SCUOLA DI DOTTORATO

UNIVERSITÀ DEGLI STUDI DI MILANO-BICOCCA

Department of Earth and Environmental Sciences

PhD program in Chemical, Geological, and Environmental Sciences Cycle XXXV

Curriculum in Geological Sciences

Unravelling coupled surface-deep Earth processes in the Southern and Patagonian Andes through numerical modelling constrained by integrated datasets

PAIVA MULLER, Veleda Astarte

Registration number 854379

Tutor: Prof. Paolo Frattini

Supervisor: Prof. Pietro Sternai

Co-supervisor: Prof. Christian Sue

Coordinator: Prof. Marco Giovanni Malusa'

ACADEMIC YEAR 2022

À perte de vue un domaine de neige et de roc s'offre à lui, dans le silence et le mystère de l'infini. Les montagnes sont un monde à part : elles sont moins une partie de la planète qu'un royaume indépendant, insolite et mystérieux, où les seules armes pour s'aventurer sont la volonté et l'amour.

(Gaston Rébuffat, Neige et Roc)

INDEX

Abstract

The Southern and Patagonian Andes constitute an orographic barrier to Pacific westerly winds, thus conditioning the climate and water/ice distribution in southern South America. Andean orogeny occurs since at least the Cretaceous, driven by oceanic subduction beneath the South American continent. Their high elevations in extra tropical latitudes condition the occurrence of fluvio-glacial erosion that control, at least partially, the surface uplift, the rock exhumation, and the localization of deformation and volcanism. This thesis is composed of regional and local studies of the geologic evolution of the Southern and Patagonian Andes from the orogenic onset to the present day, focusing on the links between deep-Earth and surface processes. Comparisons with other subduction orogens, such as the Cascade Range, and collisional orogens, such as the European Alps, are presented to provide a more general view of tectonic-climate interactions.

The southern Patagonian Andes (south of 46 °S) are characterised by Late Cretaceous to Miocene fold-and-thrust belts and magmatic complexes currently located above an asthenospheric window. Meta-volcano-sedimentary rocks from the Late Jurassic-Early Cretaceous Rocas Verdes Basin (RVB) outcrop in the internal orogenic zone. Metamorphic thermodynamic modelling, zircon U-Pb, and and phengite $^{40}Ar/^{39}Ar$ geochronology in RVB rocks allow us to determine the onset of the Andean orogeny between ~83 and 70 Ma through their tectonic underthrusting down to ~23 km. This phase was followed by Late Cretaceous foreland subsidence, and Miocene compression, plutonism, and ridge subduction. We also perform inverse modelling of apatite and zircon (U-Th-Sm)/He data from the rocks of the Torres del Paine (TdP, 51 °S) and the Fitz Roy (FzR, 49 °S) massifs. The newly produced data allows us to quantify the partitioning between the tectonic and climate forcing on the regional uplift and rock exhumation. An episode of fast exhumation in the FzR between 10.5 and 8.5 Ma is interpreted as forced by mantle upwelling during ridge subduction at that latitude. A shared episode of fast exhumation at ~6.5 Ma in both massifs records the onset of Patagonian glaciations, followed by a quiescence of exhumation up to 2 Ma. The last acceleration of the exhumation from 2 Ma to present-day is likely linked to a shift in the glacial-interglacial cyclicity.

In the Southern Andes Volanic Zone (33-46 °S) a westward migration of the volcanic arc is observed south of 40 °S, where orographic precipitation forces eastward migration of the topographic water divide. We use thermo-mechanical numerical modelling to test the hypothesis of a windward migration of the volcanic arc front forced by enhanced orographic erosion. Results show that asymmetric erosion entails a leeward topography shift and generates an asymmetric windward-verging system of crustal structures that may serve as preferential conduit for the magma upwelling. We therefore suggest that orography drives not only an eastward migration of the topographic water divide, but also a westward migration of the magma ascent and volcanic arc front.

The region around the Southern Patagonian Icefield (SPI, 49-51 °S) shows extremely fast geodetically measured rock uplift rates (up to 40 mm/yr), which are currently ascribed to the lithospheric rebound since the post- Little Ice Age (LIA) deglaciation. We perform geodynamic thermo-mechanical modelling to quantitatively assess the role of the asthenospheric window underneath the SPI in affecting the magnitude of observed present-day rock uplift. Our modelling results suggest that mantle potential temperatures higher than the common standard by up to 150-200 °C are required to generate rates of postglacial rebound in the order of tens of mm/yr. Also, our experiments show that not only the post-LIA deglaciation, but also the post- Last Glacial Maximum (~21000 years ago) deglaciation likely contributes to the present day uplift rates.

Riassunto

Le Ande Meridionali e Patagoniche costituiscono una barriera orografica ai venti occidentali del Pacifico, condizionando così il clima e la distribuzione di acqua e ghiaccio nel Sud America meridionale. L'orogenesi andina si verifica almeno dal Cretaceo, guidata dalla subduzione di litosfera oceanica sotto il continente sudamericano. Le loro altezze elevate a latitudini extra-tropicali condizionano l'erosione fluvio-glaciali che condiziona, almeno in parte, il loro sollevamento, l'esumazione delle rocce e la localizzazione di deformazioni e vulcanismo. Questa tesi è composta da studi regionali e locali sull'evoluzione geologica delle Ande Meridionali e Patagoniche dall'inizio dell'orogenesi fino ai giorni nostri, concentrandosi sui legami tra i processi della Terra profonda e quelli di superficie. Vengono presentati confronti con altri orogeni di subduzione, come la Cascade Range, e orogeni collisionali, come le Alpi Europee, per fornire una visione più generale delle interazioni tettonica-clima.

Le Ande Patagoniche meridionali (a sud di 46°S) sono caratterizzate da cinture di pieghe e sovrascorrimenti dal tardo Cretaceo al Miocene e da complessi magmatici attualmente situati sopra una finestra astenosferica. Nella zona orogenica interna affiorano rocce metavulcaniche sedimentarie del bacino di *Rocas Verdes* (RVB) del tardo Giurassico-inizio Cretaceo. La modellizzazione termodinamica metamorfica, la geocronologia U-Pb su zircone e $^{40}Ar/^{39}Ar$ su fengiti nelle rocce del RVB ci permettono di determinare l'inizio dell'orogenesi andina tra ca. 83 e 70 Ma attraverso il loro sottoscorrimento tettonico fino a ~23 km. Questa fase è stata seguita dalla subsidenza dell'avampaese nel tardo Cretaceo e da compressione, plutonismo e subduzione della dorsale oceanica nel Miocene. La modellizzazione inversa dei dati (U-Th-Sm)/He su apatite e zircone provenienti dalle rocce dei massicci di Torres del Paine (TdP, 51 °S) e del Fitz Roy (FzR, 49 °S) permette di quantificare la suddivisione tra le forzanti tettoniche e climatiche sul sollevamento regionale e sull'esumazione delle rocce. Un episodio di esumazione rapida nel FzR tra ca. 10,5 e 8,5 Ma è interpretato come forzato dalla risalita del mantello durante la subduzione della dorsale a quella latitudine. Un episodio condiviso di esumazione rapida a ca. 6,5 Ma in entrambi i massicci registra l'inizio delle glaciazioni patagoniche, seguito da una quiescenza dell'esumazione fino a ca. 2 Ma. L'ultima accelerazione dell'esumazione da ca. 2 Ma a oggi è probabilmente legata alla ciclicità glaciale-interglaciale.

Nella Ande Meridionali (33-46 °S) si osserva una migrazione verso ovest dell'arco vulcanico a sud di 40 °S, dove le precipitazioni orografiche causano la migrazione verso est dello spartiacque topografico. Utilizziamo la modellizzazione numerica termo-meccanica per verificare l'ipotesi di una migrazione verso ovest del fronte dell'arco vulcanico, forzata da una maggiore erosione orografica. I risultati mostrano che l'erosione asimmetrica comporta uno spostamento della topografia verso est e genera un sistema asimmetrico di strutture crostali che possono fungere da condotto preferenziale per la rissalita del magma. Suggeriamo quindi che l'orografia non solo guida una migrazione verso est dello spartiacque topografico, ma anche una migrazione verso ovest del fronte di risalita del magma e dell'arco vulcanico.

La regione intorno al ghiacciaio della Patagonia Meridionale (SPI, 49-51 °S) mostra tassi di sollevamento della roccia misurati geodeticamente estremamente rapidi (fino a 40 mm/anno), attualmente attribuiti al sollevamento litosferico dalla deglaciazione successiva alla Piccola Era Glaciale (LIA). Eseguiamo una modellizzazione geodinamica termomeccanica per valutare quantitativamente il ruolo della finestra astenosferica sotto lo SPI nell'influenzare l'entità del sollevamento osservato oggi. I risultati della modellizzazione suggeriscono che sono necessarie temperature potenziali del mantello più alte dello standard comune, fino a 150-200 °C, per generare tassi di sollevamento postglaciale dell'ordine di decine di mm/anno. Inoltre, i nostri esperimenti mostrano che non solo la deglaciazione post-LIA, ma anche quella successiva all'Ultimo Massimo Glaciale (~21000 anni fa) contribuisce probabilmente ai tassi di sollevamento attuali.

Chapter 1. Introduction

1. Interactions between deep and surface Earth processes

The size, geometry, and morphology of an orogen evolve as a function of tectonic and mantle processes that drive the motion of rock masses in the deep Earth, and climate-controlled erosional processes that redistribute rock masses at the surface (Koons, 1990; Willett et al., 1993; Willett, 1999; Bonnet et al., 2008; Berger et al., 2008; Whipple, 2009; Muller et al., 2022; Val and Willenbring, 2022). To a first order, orogenic systems in convergent tectonic settings behave like accretionary wedges that grow horizontally and vertically by the incoming rock mass flux (Fig. 1a; Davis et al., 1983; Koons, 1990; Willett et al., 1993; Dahlen, 1990). Internal thrusts and folds accommodate the growth of an accretionary wedge, until the wedge attains a critical surface slope and slipping along its basal thrust (i.e., "*decollement*") occurs (Fig. 1b, see Dahlen, 1990 for theory and equations). The topographic wedge can be divided into a pro-wedge, the half wedge facing the accretionary flux direction, and a retro-wedge in the back half, with a topographic divide separating them (Fig. 1a, Koons, 1990; Willett, 1999). Surface erosion removes material from the topographic wedge, changing its critical state, size and shape, and localising the strain in the regions of erosional unload (Koons, 1990; Willett, 1999; Whipple and Tucker, 1999; Beaumont et al., 2001; Bonnet et al., 2008; Berger et al., 2008; Whipple, 2009, Wolf et al., 2021). Unloading generated by erosion results in rock uplift that restores the critical state of the accretionary wedge. The wedge size decreases if the accretionary flux is slower than erosion (Fig. 1a; Dahlen, 1990; Willett, 1999; Whipple, 2009; Wolf et al., 2021). If the accretionary flux is similar to the erosion rate, the mechanical and topographic equilibrium is maintained in the wedge and deeper parts of the lithosphere are continuously driven towards the surface. This mechanism allows metamorphic and plutonic complexes, and eventually parts of the mantle, to be exhumed at the surface (Fig. 1b; Koons, 1990; Willet, 1999; Whipple and Tucker, 1999; Beaumont et al., 2001, 2004; Koons et al., 2002; Whipple, 2009). The architecture of orogens is thus controlled by a combination between tectonic accretion and surface erosion.

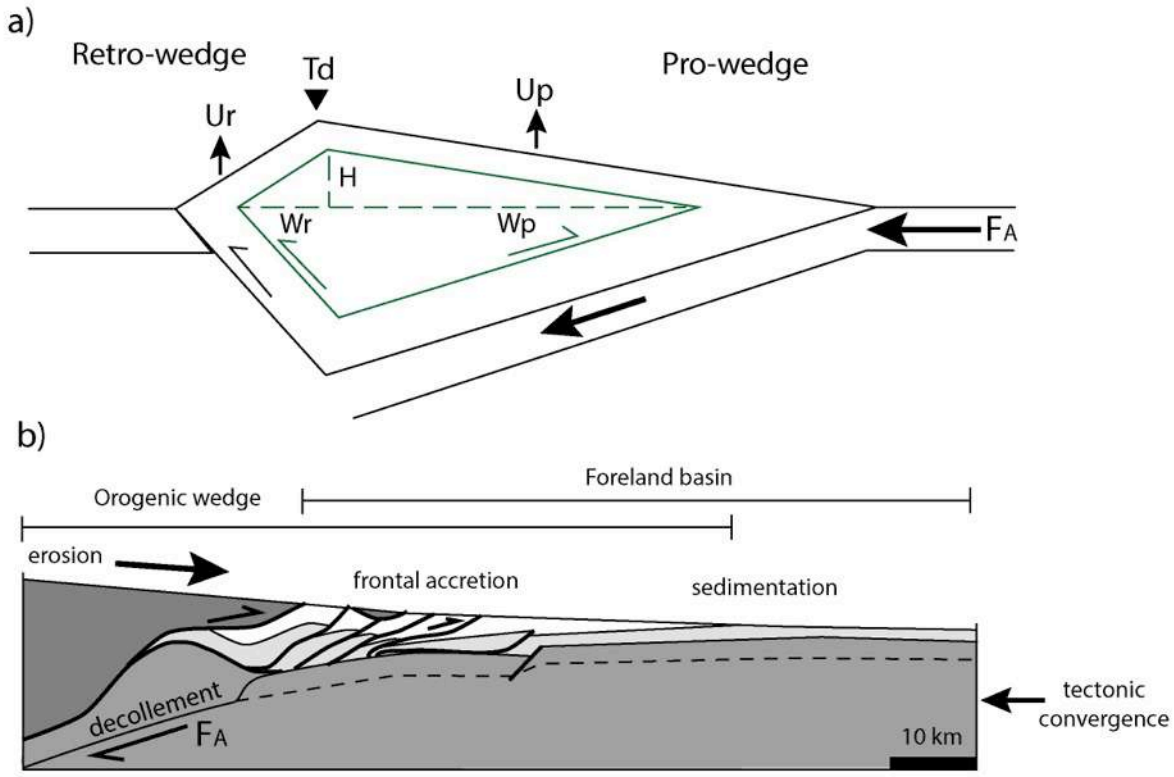

Fig. 1. a) Schematic accretionary wedge (adapted from Whipple, 2009) showing that for a constant accretionary flux (F_A) at the base of the wedge, high erosion rates lead to wedge size reduction (green wedge) and increase the uplift rates, Ur and Up, and decrease the width, Wr and Wp, at the retro-wedge and the pro-wedge, respectively. The downward black triangle indicates the position of the Topographic divide, and H is the height of the topographic divide with respect to an horizontal datum at the bottom of the topography (dashed green line). **b) Schematic accretionary wedge in a foreland system (adapted from Bonnet et al., 2008).** Horizontal tectonic compression generates an accretionary flux (F_A) with crustal shortening and thickening accommodated by thrusts within the wedge, and a *decollement* at the base of the wedge. Frontal accretion involves the basement (dark grey strata) and the foreland units (light grey and white strata). At the surface, erosion occurs in the topographically uplifted region, resulting in sedimentation in the foreland basin.

Erosion by running water is a function of the drainage area and the surface slope (i.e., stream power law, Whipple and Tucker, 1999). A particularly relevant aspect in the frame of this thesis is that, once orogens form a topographic barrier to atmospheric circulation, erosion is often enhanced on the windward side of the topographic wedge where precipitation rates are higher (Fig. 2a). On the leeward side of the wedge, instead, a rain shadow tends to be developed due to the low precipitation rates and consequently lower exhumation rates (Whipple, 2009). Geodynamic models show that enhanced erosion concentrated in the pro-wedge generates a topographic asymmetry by decreasing the elevation and translating the topographic divide towards the leeside (Fig. 2b; Willett, 1999). In the opposite case, when erosion is higher in the retro-wedge, this asymmetry occurs but is less pronounced because of the accretionary flux in the opposite direction (Willett, 1999; Val and Willenbring, 2022).

Crustal-scale shear zones and exhumation are localised on the more eroded side of the accretionary wedge (Fig. 2c). Much of past research on the surface-deep Earth processes coupling aims at disentangling the relative contributions of surface erosion, including orographic effects, and the accretionary flux direction and magnitude exert on the geometry, size and shape of the accretionary wedges (Koons, 1990; Willett et al., 1993; Willett, 1999; Beaumont et al., 2001; Whipple, 2009), but the matter is still elusive (Wolf et al., 2021; Val and Willenbring, 2022).

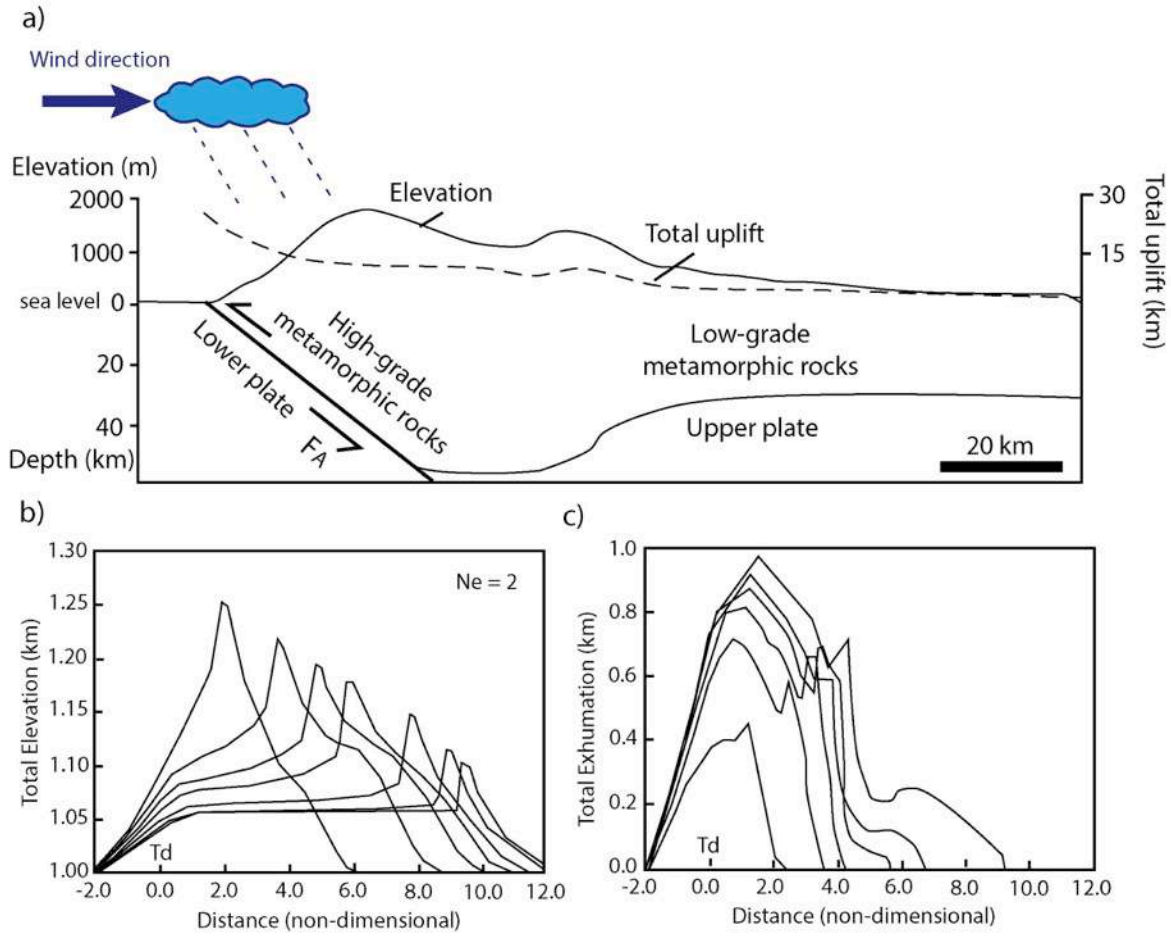

Fig. 2. a) Schematic representation of the effect of orography in an orogenic wedge (adapted from Koons, 1990). The wind brings moisture from one main direction, and precipitation and erosion are concentrated in the windward side of the topography due to the orographic effect. The accretionary flux (F_A) has the same direction than the wind, and the strain is concentrated windward. A main windward thrust accommodates the exhumation of high-grade metamorphic rocks formed at more than 40 km depth. The total uplift and the elevation increase towards the windward side of the orogen. **b) Elevation and c) exhumation vs. distance** (non-dimensional), calculated for asymmetric erosion (higher leftward by a factor of 2, given by the erosion number, Ne, = 2) acting in an initially symmetric topographic wedge (adapted from Willett, 1999).

Erosion also depends on the predominant process at play, and the partitioning between fluvial and glacial erosion impacts greatly on the shape of topography and on the overall

magnitude and spatial distribution of uplift and erosion rates (Fig. 3; Braun et al., 1999; Bockelhurst and Whipple, 2006; Berger and Spotila, 2008; Berger et al., 2008; Herman et al., 2011, 2018; Sternai et al., 2011, 2012, 2016; Valla et al., 2011; Champagnac et al., 2014). In case of protracted tectonic uplift, the orogen's maximum elevation is controlled by crustal strength (Beaumont et al., 2004) and, according to some authors, glacial erosion (e.g., Egholm et al., 2009). The theory of the glacial buzzsaw postulates that efficient glacial erosion, generally generated by warm-based glaciers that easily trigger ice and land sliding (Paterson, 1994), rapidly erodes excess of topography above the glacier's equilibrium line altitude (ELA, Fig. 3), the altitude at which ice mass balance is equal to zero (Brozovic et al., 1997; Montgomery et al., 2001; Mitchell and Montgomery, 2006; Foster et al., 2008; Egholm et al., 2009). In the Late Cenozoic, the global lowering of the glacier's ELA seems to have increased average erosion rates in orogenic belts (Molnar, 2004; Shuster et al., 2005; Berger and Spotila, 2008; Valla et al., 2011; Herman et al., 2013, 2018; Herman and Champagnac, 2016). Regional climate control on the glacier's ELA and the temperature of glaciers, however, is highly dependent on latitude (Egholm et al., 2009, Herman et al., 2013; Herman and Brandon, 2015), and cold-based glaciers at high latitudes can act as a shield to erosion (Thomson et al., 2010), allowing tectonics to uplift the orogeny undisturbed.

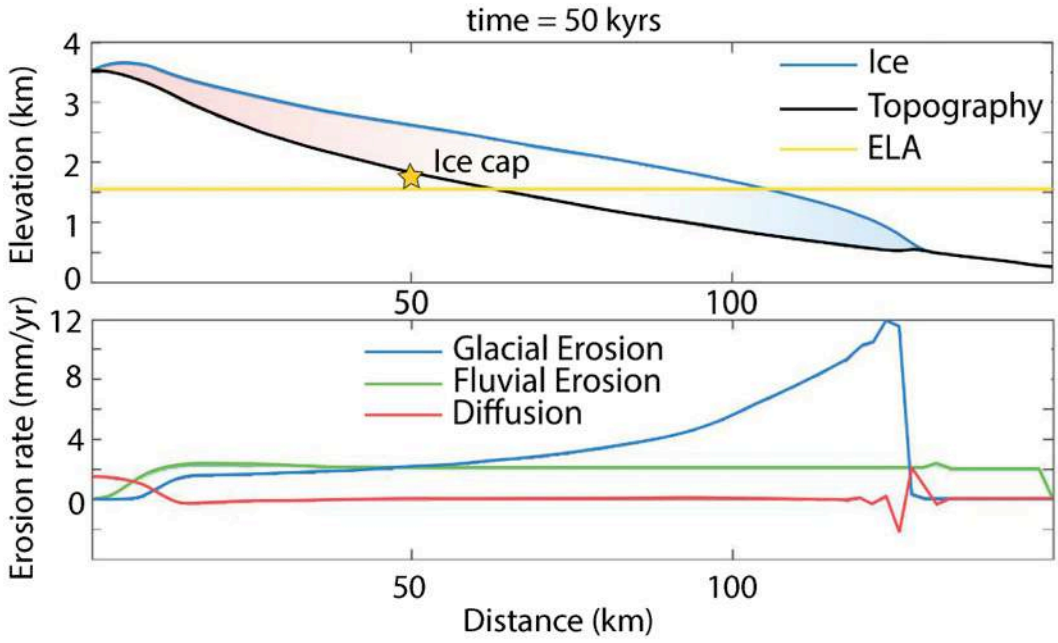

Fig. 3. Numerical model for the temporal evolution of a glacial cycle over an inclined topography, after 50 kyrs (Sternai et al., 2016), the red area in the glacier means the accumulation zone, and the blue area is the ablation zone, below the glacier's equilibrium line altitude (ELA). The yellow star is the reference point at which the surface load variations through time and mean glacial erosion are computed. Glacial erosion rates are 6 times higher than the fluvial erosion rates at the measured point.

Amongst the most prominent effects of glaciation on surface elevations is the isostatic subsidence and uplift of the lithosphere due to the building and melting of continental ice sheets (England and Molnar, 1990; Watts, 2001; Turcotte and Schubert, 2002; Stüwe, 2002). Much of the observed vertical displacements around glaciated regions as observed today via, for instance, vertical GPS measurements and remote sensing (e.g., Interferometry Satellite Images), is in fact postglacial lithospheric isostatic rebound. In addition to glacial melting and erosion unloading the lithosphere and enhancing uplift rates (England and Molnar, 1990; Watts, 2001; Sternai et al., 2016), a growing number of studies point to increased magmatic/volcanic activity and degassing during deglaciation, with specific case studies from, for example, Kamchatka, Iceland, Alaska, and the Southern Andes (Gudmundsson, 1986; Jellinek et al., 2004; Geier and Bindeman, 2011; Sigvaldason et al., 1992; Crowley et al., 2015; Mora and Tassara, 2019). Models suggest that the decompression generated by lithospheric unloading due to deglaciation and erosion can modulates rock and mantle melting at depth (Jull and McKenzie, 1996; Geier and Bindeman, 2011; Sternai et al., 2016, 2020; Mora and Tassara, 2019). Additionally, faulting and fracturing, gravitational failure, and magmatic gas exsolution can further affect the lithospheric transfer and eruption of magma during deglaciation (Fig. 4, Geier and Bindeman, 2011). While the link between glacial unloading and magmatism has attracted considerable attention, the effect of other surface processes (e.g., orographic erosion, sea level changes) on the magma productivity is still elusive.

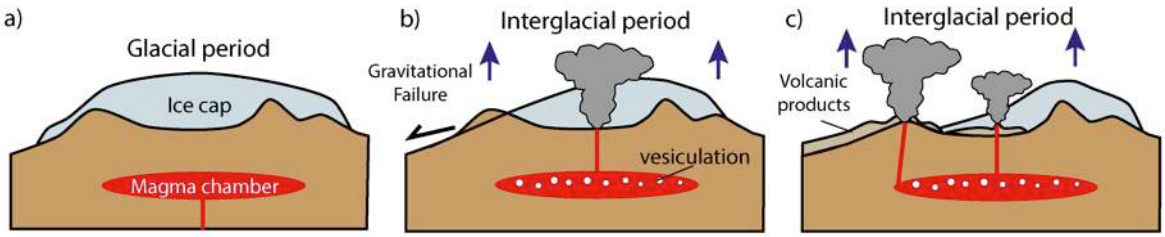

Fig. 4: Schematic relationships between glacial periods and volcanic activity (adapted from Geier and Bindeman, 2011). a) Glacial period over a crustal magma chamber. b) Onset of an interglacial period with ice retreat, lithospheric isostatic uplift (blue arrows), enhanced magma vesiculation, gravitational failure, and caldera collapse. c) Active volcanism during ice retreat, lithospheric isostatic uplift (blue arrows), and volcanic products fill topographic depressions.

2. Natural case study

Identifying and quantifying topographic changes in time and relating them to the underlying climate and tectonic forcings are challenging (e.g., Egholm et al., 2009; Thomson,

2010; Herman et al., 2013, 2018; Champagnac et al., 2014; Fox et al., 2015, 2016). To this aim, available techniques are, for example, landscape evolution numerical and geodynamic modelling (van der Beek and Braun, 1998; Herman and Braun, 2008; Tucker and Hancock, 2010; Braun et al., 2012; Croissant and Braun, 2014) constrained by integrated field stratigraphic, structural, and geomorphological observations, low-temperature thermochronology, and geophysical data (Sternai et al., 2012; Fosdick et al., 2013; Fox et al., 2015, 2016; Ehlers, 2005; McQuarrie and Ehlers, 2017). In the frame of this thesis, these techniques are applied to the Southern (33 – 46 °S) and Patagonian (46 – 56 °S) Andes which, as described in more detail hereafter, show evidence of prominent north-south variations in the tectonic and magmatic histories and cross through a pronounced latitudinal climate gradient. Therefore, these ranges are the ideal setting to investigate how deep and surface Earth processes interact to form orogenic belts.

The Andes Cordillera is an example of subduction-type orogeny, in which oceanic plates enter in subduction beneath a continental plate, generating accretionary wedges, seismicity, magmatism, and foreland subsidence across the western South America (Ramos, 1999). The Andes are currently generated by the subduction of the Nazca and Antarctic oceanic plates, and can be subdivided in four large sectors: the Northern, Central, Southern and Austral (or Patagonian) Andes (Fig. 5; Barazangi and Isacks, 1976; Mpodozis and Ramos, 1990; Ramos, 1999; Folguera and Ramos, 2011). Fold-and-thrust belts, volcanic arcs (if present) and lithospheric thickness across these sectors show different architectures as a result of long-lived subduction (at least 150 Ma) and ancient inherited tectonic histories (Ramos, 1999, 2010; Mpodozis and Ramos, 1990, 2008; Hervé et al., 2007). The stratigraphic record and structures allow paleo-reconstructions of the deformational and volcanic arc front positions, mainly associated with shifts in the subduction velocity and slab dip angle (Ramos, 1999, Folguera and Ramos, 2011). The Andes have an average altitude of 4000 m above sea level, 200 to 700 km of wideness and 8900 km of extension, distributed by 50 ° of latitude in the Earth's southern hemisphere. The impressive size of this mountain belt exert an important control on Earth's atmospheric dynamics and climate, conditioning in great part the distribution of moisture in South America and the southern Hemisphere (Garreaud et al., 2009).

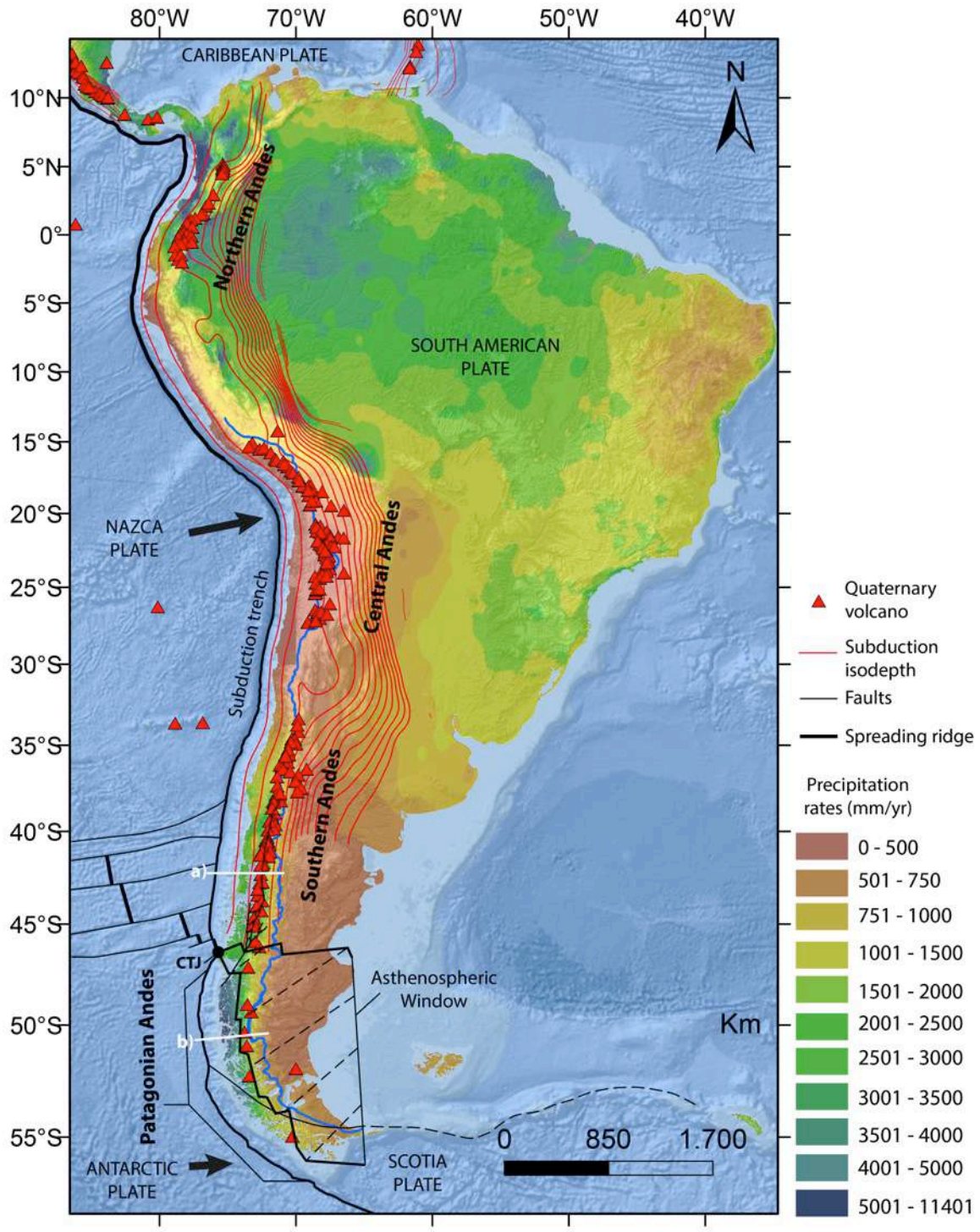

Fig. 5. Present-day tectonic and climate overview of the Andes, with the annual precipitation rates (mm/yr, Hijmans et al., 2005), the slab isodepths (Hayes et al., 2018), the Quaternary volcanoes (Global Volcanoes Program, 2022); the position of the topographic water divide (blue line), the subduction trench (black bold line) the spreading ridge and transform faults separating the Nazca and the Antarctic plates, the Chile Triple Junction (CTJ), the asthenospheric window (Breitsprecher and Thorkelson, 2009), the subduction vectors (DeMets, 2010), and the location of the cross-sections (a) and (b) of Fig. 6.

The Southern Andes, also subdivided in southern Central Andes (~33 – 40 °S) and northern Patagonian Andes (~ 40 – 46 °S) (Folguera and Ramos, 2011), are located over a

segment of subduction of the Nazca Plate with slab dip angle of ~25-30 ° (Barazangi and Isacks, 1976; Tassara and Echaurren, 2012; Hayes et al., 2018) and ~ 7 cm/yr of convergence velocity (DeMets et al., 2010). They show high seismicity and active arc volcanism along the Southern Andes Volcanic Zone (Ramos, 1999, Cembrano and Lara, 2009). The general structure of the Southern Andes is composed of Late Cretaceous to Holocene sedimentary and volcanic rocks imbricated with Paleozoic metamorphic basement by trench-verging thrusts in the fore-arc, and continent-vergent thrusts in the retro-arc (Mpodozis and Ramos, 2008; Giambiagi et al., 2012; Riesner et al., 2018; Horton, 2021; Echaurren et al., 2016, 2022). In the transition from the northern to the southern part (~ at 40 °S) the predominant compressive regime changes to strike-slip along the Liquiñe-Ofqui Fault Zone (LOFZ, Figs. 5 and 6a), coincident with the location of arc volcanoes at this sector of the belt (Cembrano et al., 2000, 2002; Cembrano and Lara, 2009; Orts et al., 2012; Echaurren et al., 2016, 2022). The southern boundary of the Southern Andes and the LOFZ is the Chile Triple Junction (CTJ), which marks the separation between the Nazca and the Antarctic plates by the oceanic Chile spreading ridge, entering in subduction beneath the South American Plate (Fig. 5) (Cande and Leslie, 1986, Breitsprecher and Thorkelson, 2009).

The Patagonian Andes south of the CTJ (~ 46 – 56 °S) are partially above an asthenospheric window generated by spreading ridge subduction and asthenospheric upwelling. This window started to open at ~54 °S and ~16 Ma, and has widened and migrated towards its current position through several episodes of ridge and transform fault subduction (Cande and Leslie, 1986; Ramos and Kay, 1992; Breitspreceher and Thorkelson, 2009, Stevens Goddard and Fosdick, 2019). Its opening and migration is driven by the different rates of subduction between the Nazca-Farallon and the Antarctic Plate, of ~7 and ~2 cm/yr, respectively, which result in a shorter Antarctic slab with respect to the Nazca-Farallon slab, opening a window with no slab where the asthenosphere upwells. Over the present-day asthenospheric window there is no arc volcanism, and from 49 °S to 56 °S there are few Quaternary volcanoes composing the Austral Andes Volcanic Zone (Ramos and Kay, 1992; Stern and Kilian, 1996; Stern et al., 2007; Ramos, 2005).

The Geologic history of the southern Patagonian Andes is marked by the closure of the Late Jurassic – Early Cretaceous ocean-floored Rocas Verdes Basin (Dalziel, 1974; Mpodozis and Ramos, 1990; Klepeis et al., 2010; Calderón et al., 2012, Muller et al., 2021). Its closure in the Late Cretaceous caused the accretion of the South American Continent and the continental block bearing the Jurassic – Cretaceous Southern Patagonian Batholith (Hervé et al., 2007). Deformed units of the Rocas Verdes Basin compose the internal part of the

Patagonian-Magallanes Fold-and-Thrust Belt, imbricated with Late Cretaceous units of the Magallanes foreland basin by continent-vergent thrusts (Fig. 6b) (Fosdick et al., 2011; Betka et al., 2015). The closure of the Rocas Verdes Basin played an important role in the bending of the southern tip of South America and separation from the Antarctic Peninsula (Poblete et al., 2016; Muller et al., 2021).

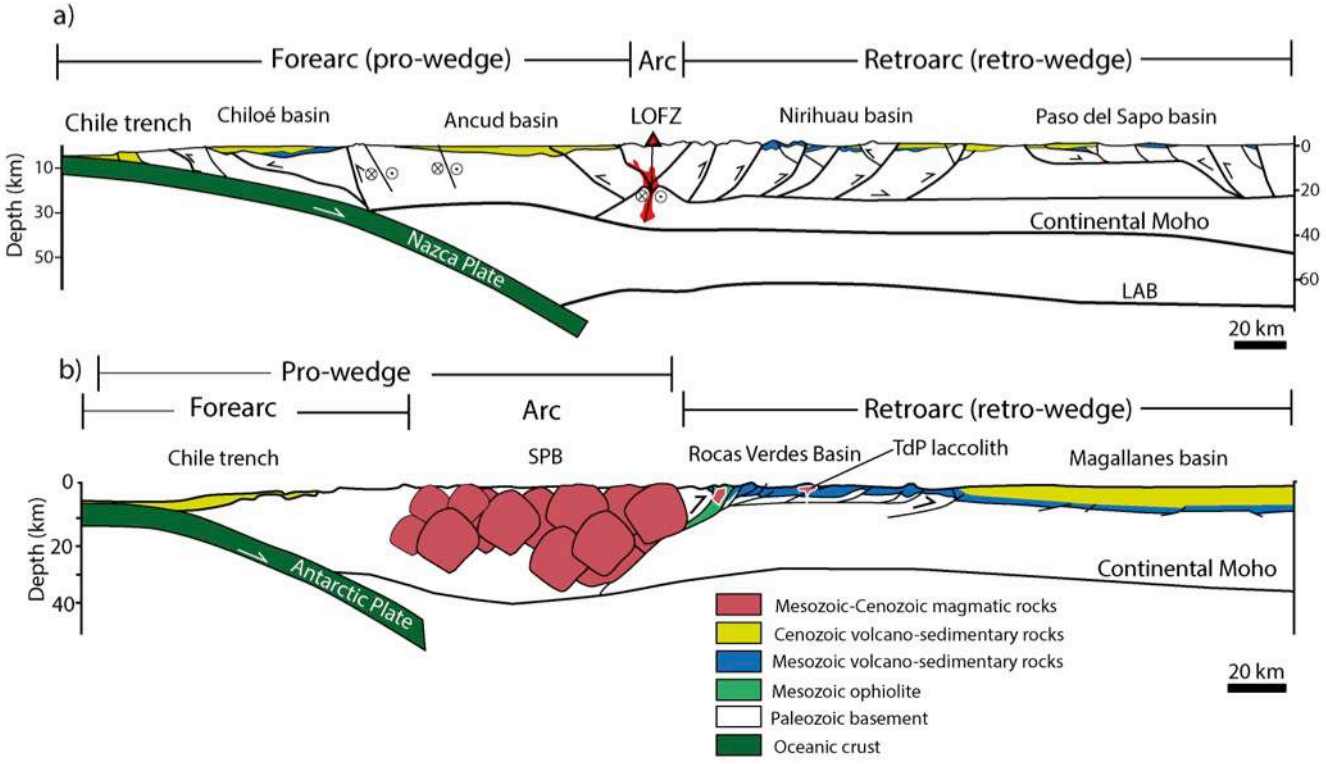

Fig. 6. Schematic cross-sections of the Southern (a) and the Patagonian Andes (b). a) The Southern Andes at ~42.5 °S (adapted from Echaurren et al., 2022) showing the trench-vergent pro-wedge and the continent-vergent retro-wedge, separated by the strike-slip Liquiñe-Ofqui Fault Zone (LOFZ) and active volcanism in the Southern Andes Volcanic Zone. **b) The southern Patagonian Andes at ~51 °S (adapted from Fosdick et al., 2011)** with the fore-arc region and the Southern Patagonian Batholith (SPB) forming the pro-wedge, and the Inverted Rocas Verdes Basin, and the Magallanes basin imbricated in the Patagonian fold-and-thrust belt and forming the retro-wedge. The Late Miocene Torres del Paine (TdP) laccolith intrudes the Mesozoic rocks of the fold-and-thrust belt. LAB: Lithospheric-Asthenospheric Boundary.

In the Southern Andes the climate shifts from desertic and semi-arid in the northern sector, to temperate in the southern sector, where precipitation rates are as high as 4 mm/yr in the western side of the orogenic wedge (Garreaud et al., 2009). The mountain elevations also decrease from north to south, from an average of ~4000 to 1500 m. This climate gradient is associated with the shift in the main wind's direction, from roughly orogen's parallel in the northern sector, to orogen's perpendicular in the southern sector (Garreaud et al., 2009, 2013). In the southern Patagonian Andes, the present-day precipitation rates are the highest along the strike of the belt, reaching 6000 mm/yr, and continental ice sheets are over the

central orogen. The high precipitation rates, however, are concentrated on the western side of the orogen, and the eastern side forms a rain shadow due to the orographic effect of the mountain belt (Blisniuk et al., 2006; Garreaud et al., 2013; Fosdick et al., 2013). This orographic gradient must occur since at least the middle Miocene (Thomson et al., 2001; Blisniuk et al., 2005, 2006), but possibly since the Late Cretaceous (Fosdick et al., 2013), due to the onset of tectonic compression with lithospheric shortening and tectonic uplift of the Southern and Patagonian Andes (Strecker et al., 2007; Fosdick et al., 2011). The onset of Patagonian Glaciations at ~ 7 Ma as a consequence of Late Cenozoic global cooling (Raymo and Ruddiman, 1992; Ruddiman and Raymo, 1997; Zachos et al., 2001) is recorded by the appearance of glacio-fluvial and glacial sedimentary deposits, glacial landforms, and acceleration of the exhumation rates (Mercer and Sutter, 1982; Rabassa et al., 2005, Rabassa, 2008; Kaplan et al., 2009; Lagabrielle et al., 2010; Fosdick et al., 2013; Georgieva et al., 2016, 2019; Willett et al., 2020). In central Patagonia (~ 46 °S), major geomorphological modifications occur at ~ 3 Ma, uplifting and disconnecting the eastern foreland catchments from the central Cordillera (Fig. 7, Lagabrielle et al., 2010, Scalabrino et al., 2010). This shift is associated with an acceleration of tectonic uplift due to the Chile ridge collision with the subduction trench at the CTJ (Lagabrielle et al., 2010; Scalabrino et al., 2010; Georgieva et al., 2019), and increase in the glacial-interglacial cyclicity (Willett et al., 2020). From ~ 2 Ma to present-day, the location of the maximum precipitation has migrated southward, from ~ 44 to ~ 50 °S, suggested a result of global cooling (Herman and Brandon, 2015).

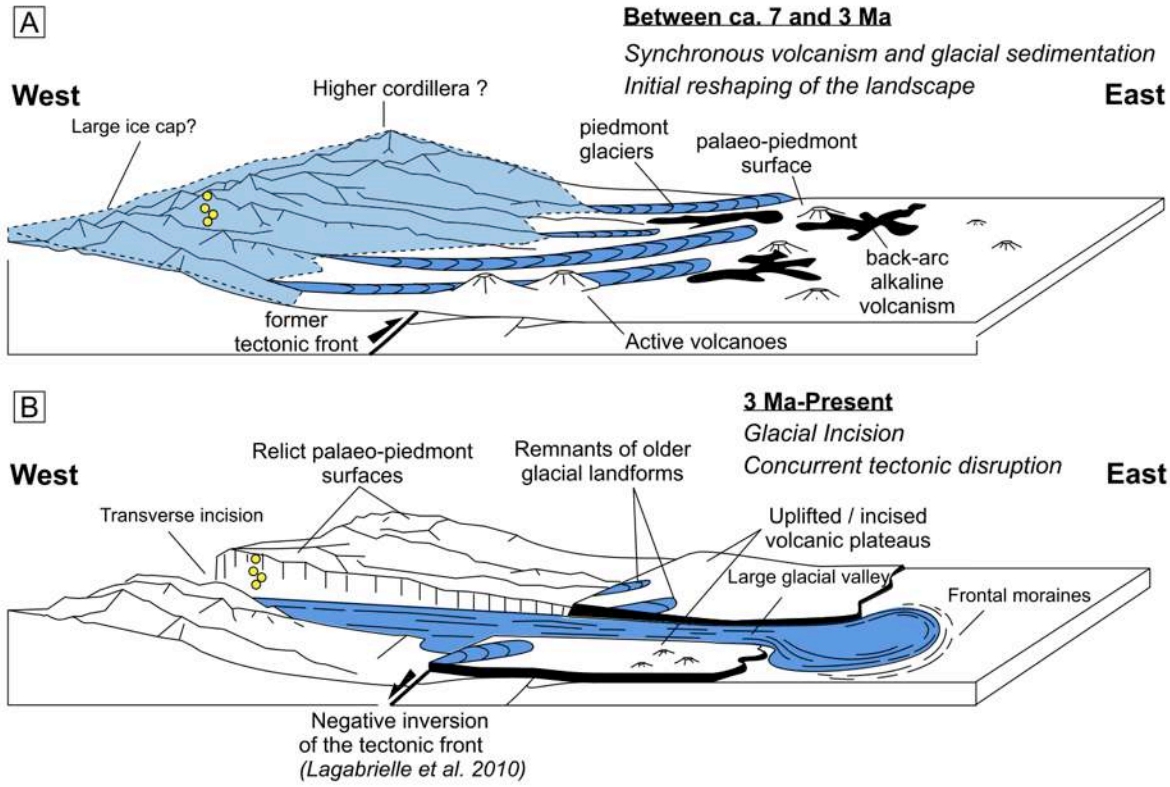

Fig. 7. Schematic landscape evolution of the Patagonian Andes at ~ 46 °S (Lagabrielle et al., 2010; Georgieva et al., 2019). A) The onset of Patagonian Glaciations at 7 Ma has covered the mountain belt with a thick ice sheet, reshaping the landscape and carving glacial valleys towards the foreland. B) The thicker ice sheet has vanished and glaciers were constrained to deep and long valleys in the foreland causing transverse incision. This episode is coincident with tectonic subsidence of the central Andean domain and uplift of the foreland domain, associated with the Chile ridge collision with the subduction trench.

3. Thesis specific targets and structure

Using the Southern and Patagonian Andes as natural case study, this thesis addresses some of the interactions between surface and deep Earth processes described above. In particular, the relationships between crustal strain and rock burial/exhumation during convergence are addressed by the study presented in Chapter 2 (Muller et al., 2021). The relationships between Late Cenozoic fluvio-glacial erosion, rock exhumation, and mantle upwelling are addressed in Chapter 3 (Muller et al., in prep. a). The relationships between orographic erosion, crustal strain, and migration of the supra-subduction magmatic arc are addressed in Chapter 4 (Muller et al., 2022). Finally, the relationships between present-day vertical displacement rates and the ongoing deglaciation, with particular focus on the role of the asthenospheric window underneath the Patagonian Andes, are addressed in Chapter 5 (Muller et al., in prep. b). Altogether, Chapters 2-5 include several breakthroughs in the field of the surface-deep Earth processes coupling; for instance, the characterization of the depths

and timing of formation and exhumation of metamorphic complexes of the Patagonian fold-and-thrust belt; the quantification of the contributions by asthenospheric upwelling and glaciation to rock exhumation in the southern Patagonian Andes; the first recognition and quantification of an orographic control on the location of the Southern Andes Volcanic Zone (and continental volcanic arcs in general); and the quantification of the mantle potential temperature required to explain present-day rates of postglacial rebound in the Patagonian Andes.

These major breakthroughs allow us to propose new applications of geo-thermo-chronological methods to quantify the partitioning between deep-Earth and surface processes during mountain building, and ways to the use geodynamic numerical models to understand poorly constrained links between lithospheric, mantle, and surface processes, as outlined in detail in Chapter 6. Two additional papers that I contributed to are included in Appendix A and B. These general contributions highlight additional ways of coupling between the surface and deep Earth, further supporting the relevance of research on the topic and, therefore, of this PhD thesis.

References - Chapter 1

Barazangi, M., & Isacks, B. L. (1976). Spatial distribution of earthquakes and subduction of the Nazca plate beneath South America. *Geology*, *4*(11), 686-692.

Beaumont, C., Jamieson, R. A., Nguyen, M. H., & Lee, B. (2001). Himalayan tectonics explained by extrusion of a low-viscosity crustal channel coupled to focused surface denudation. *Nature*, *414*(6865), 738-742.

Beaumont, C., Jamieson, R. A., Nguyen, M. H., & Medvedev, S. (2004). Crustal channel flows: 1. Numerical models with applications to the tectonics of the Himalayan‐Tibetan orogen. *Journal of Geophysical Research: Solid Earth*, *109*(B6).

Berger, A. L., & Spotila, J. A. (2008). Denudation and deformation in a glaciated orogenic wedge: The St. Elias orogen, Alaska. *Geology*, *36*(7), 523-526.

Berger, A. L., Gulick, S. P., Spotila, J. A., Upton, P., Jaeger, J. M., Chapman, J. B., Worthington, L.A., Pavlis, T.L., Ridgway, K.D., Willems, B.A., & McAleer, R. J. (2008). Quaternary tectonic response to intensified glacial erosion in an orogenic wedge. *Nature Geoscience*, *1*(11), 793-799.

Betka, P., Klepeis, K., & Mosher, S. (2015). Along-strike variation in crustal shortening and kinematic evolution of the base of a retroarc fold-and-thrust belt: Magallanes, Chile 53° S–54° S. *Bulletin*, *127*(7-8), 1108-1134.

Blisniuk, P. M., Stern, L. A., Chamberlain, C. P., Idleman, B., & Zeitler, P. K. (2005). Climatic and ecologic changes during Miocene surface uplift in the Southern Patagonian Andes. *Earth and Planetary Science Letters*, *230*(1-2), 125-142.

Blisniuk, P. M., Stern, L. A., Chamberlain, C. P., Zeitler, P. K., Ramos, V. A., Sobel, E. R., Haschke, M., Strecker, M.R., & Warkus, F. (2006). Links between mountain uplift, climate, and surface processes in the southern Patagonian Andes. In *The Andes* (pp. 429-440). Springer, Berlin, Heidelberg.

Bonnet, C., Malavieille, J., & Mosar, J. (2008). Surface processes versus kinematics of thrust belts: impact on rates of erosion, sedimentation, and exhumation–Insights from analogue models. *Bulletin de la Société géologique de France*, *179*(3), 297-314.

Braun, J., Van Der Beek, P., Valla, P., Robert, X., Herman, F., Glotzbach, C., Pedersen, V., Perry, C., Simon-Labric, T., & Prigent, C. (2012). Quantifying rates of landscape evolution and tectonic processes by thermochronology and numerical modelling of crustal heat transport using PECUBE. *Tectonophysics*, *524*, 1-28.

Braun, J., Zwartz, D., & Tomkin, J. H. (1999). A new surface-processes model combining glacial and fluvial erosion. *Annals of Glaciology*, *28*, 282-290.

Breitsprecher, K., & Thorkelson, D. J. (2009). Neogene kinematic history of Nazca–Antarctic–Phoenix slab windows beneath Patagonia and the Antarctic Peninsula. *Tectonophysics*, *464*(1-4), 10-20.

Brocklehurst, S. H., & Whipple, K. X. (2006). Assessing the relative efficiency of fluvial and glacial erosion through simulation of fluvial landscapes. *Geomorphology*, *75*(3-4), 283-299.

Brozovic, N., Burbank, D. W., & Meigs, A. J. (1997). Climatic limits on landscape development in the northwestern Himalaya. *Science*, *276*(5312), 571-574.

Calderón, M., Fosdick, J. C., Warren, C., Massonne, H. J., Fanning, C. M., Cury, L. F., Schwanethal, J., Fonseca, P.E., Galaz, G., & Herve, F. (2012). The low-grade Canal de las Montañas Shear Zone and its role in the tectonic emplacement of the Sarmiento Ophiolitic Complex and Late Cretaceous Patagonian Andes orogeny, Chile. *Tectonophysics*, *524*, 165-185.

Cande, S. C., & Leslie, R. B. (1986). Late Cenozoic tectonics of the southern Chile trench. *Journal of Geophysical Research: Solid Earth*, *91*(B1), 471-496.

Cembrano, J., & Lara, L. (2009). The link between volcanism and tectonics in the southern volcanic zone of the Chilean Andes: a review. *Tectonophysics*, *471*(1-2), 96-113.

Cembrano, J., Lavenu, A., Reynolds, P., Arancibia, G., López, G., & Sanhueza, A. (2002). Late Cenozoic transpressional ductile deformation north of the Nazca–South America–Antarctica triple junction. *Tectonophysics*, *354*(3-4), 289-314.

Cembrano, J., Schermer, E., Lavenu, A., & Sanhueza, A. (2000). Contrasting nature of deformation along an intra-arc shear zone, the Liquiñe–Ofqui fault zone, southern Chilean Andes. *Tectonophysics*, *319*(2), 129-149.

Champagnac, J. D., Valla, P. G., & Herman, F. (2014). Late-Cenozoic relief evolution under evolving climate: A review. *Tectonophysics*, *614*, 44-65.

Croissant, T., & Braun, J. (2014). Constraining the stream power law: a novel approach combining a landscape evolution model and an inversion method. *Earth surface dynamics*, *2*(1), 155-166.

Crowley, J. W., Katz, R. F., Huybers, P., Langmuir, C. H., & Park, S. H. (2015). Glacial cycles drive variations in the production of oceanic crust. *Science*, *347*(6227), 1237-1240.

Dahlen, F. A. (1990). Critical taper model of fold-and-thrust belts and accretionary wedges. *Annual Review of Earth and Planetary Sciences*, *18*, 55.

Dalziel, I. W., de Wit, M. J., & Palmer, K. F. (1974). Fossil marginal basin in the southern Andes. *Nature*, *250*(5464), 291-294.

Davis, D., Suppe, J., & Dahlen, F. A. (1983). Mechanics of fold-and-thrust belts and accretionary wedges. *Journal of Geophysical Research: Solid Earth*, *88*(B2), 1153-1172.

DeMets, C., Gordon, R. G., & Argus, D. F. (2010). Geologically current plate motions. *Geophysical journal international*, *181*(1), 1-80.

Echaurren, A., Encinas, A., Sagripanti, L., Gianni, G., Zambrano, P., Duhart, P., & Folguera, A. (2022). Fore-to-retroarc crustal structure of the north Patagonian margin: How is shortening distributed in Andean-type orogens?. *Global and Planetary Change*, *209*, 103734.

Echaurren, A., Folguera, A., Gianni, G., Orts, D., Tassara, A., Encinas, A., Giménez, M, & Valencia, V. (2016). Tectonic evolution of the North Patagonian Andes (41–44 S) through recognition of syntectonic strata. *Tectonophysics*, *677*, 99-114.

Egholm, D. L., Nielsen, S. B., Pedersen, V. K., & Lesemann, J. E. (2009). Glacial effects limiting mountain height. *Nature*, *460*(7257), 884-887.

Ehlers, T. A. (2005). Crustal thermal processes and the interpretation of thermochronometer data. *Reviews in Mineralogy and Geochemistry*, *58*(1), 315-350.

England, P., & Molnar, P. (1990). Surface uplift, uplift of rocks, and exhumation of rocks. *Geology*, *18*(12), 1173-1177.

Folguera, A., & Ramos, V. A. (2011). Repeated eastward shifts of arc magmatism in the Southern Andes: a revision to the long-term pattern of Andean uplift and magmatism. *Journal of South American Earth Sciences*, *32*(4), 531-546.

Fosdick, J. C., Grove, M., Hourigan, J. K., & Calderon, M. (2013). Retroarc deformation and exhumation near the end of the Andes, southern Patagonia. *Earth and Planetary Science Letters*, *361*, 504-517.

Fosdick, J. C., Romans, B. W., Fildani, A., Bernhardt, A., Calderón, M., & Graham, S. A. (2011). Kinematic evolution of the Patagonian retroarc fold-and-thrust belt and Magallanes foreland basin, Chile and Argentina, 51 30′ S. *Bulletin*, *123*(9-10), 1679-1698.

Foster, D., Brocklehurst, S. H., & Gawthorpe, R. L. (2008). Small valley glaciers and the effectiveness of the glacial buzzsaw in the northern Basin and Range, USA. *Geomorphology*, *102*(3-4), 624-639.

Fox, M., Herman, F., Kissling, E., & Willett, S. D. (2015). Rapid exhumation in the Western Alps driven by slab detachment and glacial erosion. *Geology*, *43*(5), 379-382.

Fox, M., Herman, F., Willett, S. D., & Schmid, S. M. (2016). The exhumation history of the European Alps inferred from linear inversion of thermochronometric data. *American Journal of Science*, *316*(6), 505-541.

Garreaud, R. D. (2009). The Andes climate and weather. *Advances in Geosciences*, *22*, 3-11.

Garreaud, R., Lopez, P., Minvielle, M., & Rojas, M. (2013). Large-scale control on the Patagonian climate. *Journal of Climate*, *26*(1), 215-230.

Georgieva, V., Gallagher, K., Sobczyk, A., Sobel, E. R., Schildgen, T. F., Ehlers, T. A., & Strecker, M. R. (2019). Effects of slab-window, alkaline volcanism, and glaciation on thermochronometer cooling histories, Patagonian Andes. *Earth and Planetary Science Letters*, *511*, 164-176.

Georgieva, V., Melnick, D., Schildgen, T. F., Ehlers, T. A., Lagabrielle, Y., Enkelmann, E., & Strecker, M. R. (2016). Tectonic control on rock uplift, exhumation, and topography above an oceanic ridge collision: Southern Patagonian Andes (47 S), Chile. *Tectonics*, *35*(6), 1317-1341.

Geyer, A., & Bindeman, I. (2011). Glacial influence on caldera-forming eruptions. *Journal of Volcanology and Geothermal Research*, *202*(1-2), 127-142.

Giambiagi, L., Mescua, J., Bechis, F., Tassara, A., & Hoke, G. (2012). Thrust belts of the southern Central Andes: Along-strike variations in shortening, topography, crustal geometry, and denudation. *Bulletin*, *124*(7-8), 1339-1351.

Global Volcanism Program, 2023. [Database] Volcanoes of the World (v. 5.0.2; 23 Jan 2023). Distributed by Smithsonian Institution, compiled by Venzke, E. https://doi.org/10.5479/si.GVP.VOTW5-2022.5.0

Gudmundsson, A. (1986). Mechanical aspects of postglacial volcanism and tectonics of the Reykjanes Peninsula, southwest Iceland. *Journal of Geophysical Research: Solid Earth*, *91*(B12), 12711-12721.

Hayes, G. P., Moore, G. L., Portner, D. E., Hearne, M., Flamme, H., Furtney, M., & Smoczyk, G. M. (2018). Slab2, a comprehensive subduction zone geometry model. *Science*, *362*(6410), 58-61.

Herman, F., & Brandon, M. (2015). Mid-latitude glacial erosion hotspot related to equatorial shifts in southern Westerlies. *Geology*, *43*(11), 987-990.

Herman, F., & Braun, J. (2008). Evolution of the glacial landscape of the Southern Alps of New Zealand: Insights from a glacial erosion model. *Journal of Geophysical Research: Earth Surface*, *113*(F2).

Herman, F., & Champagnac, J. D. (2016). Plio-Pleistocene increase of erosion rates in mountain belts in response to climate change. *Terra Nova*, *28*(1), 2-10.

Herman, F., Beaud, F., Champagnac, J. D., Lemieux, J. M., & Sternai, P. (2011). Glacial hydrology and erosion patterns: a mechanism for carving glacial valleys. *Earth and Planetary Science Letters*, *310*(3-4), 498-508.

Herman, F., Braun, J., Deal, E., & Prasicek, G. (2018). The response time of glacial erosion. *Journal of Geophysical Research: Earth Surface*, *123*(4), 801-817.

Herman, F., Seward, D., Valla, P. G., Carter, A., Kohn, B., Willett, S. D., & Ehlers, T. A. (2013). Worldwide acceleration of mountain erosion under a cooling climate. *Nature*, *504*(7480), 423-426.

Herve, F., Pankhurst, R. J., Fanning, C. M., Calderón, M., & Yaxley, G. M. (2007). The South Patagonian batholith: 150 my of granite magmatism on a plate margin. *Lithos*, *97*(3-4), 373-394.

Hijmans, R. J., Cameron, S. E., Parra, J. L., Jones, P. G. & Jarvis, A. (2005). Very high resolution interpolated climate surfaces for global land areas. *Int. J. Climatol.* **25**, 1965–1978.

Horton, B. K., Capaldi, T. N., & Perez, N. D. (2022). The role of flat slab subduction, ridge subduction, and tectonic inheritance in Andean deformation. *Geology*.

Jellinek, A. M., Manga, M., & Saar, M. O. (2004). Did melting glaciers cause volcanic eruptions in eastern California? Probing the mechanics of dike formation. *Journal of Geophysical Research: Solid Earth*, *109*(B9).

Jull, M., & McKenzie, D. (1996). The effect of deglaciation on mantle melting beneath Iceland. *Journal of Geophysical Research: Solid Earth*, *101*(B10), 21815-21828.

Kaplan, M. R., Strelin, J. A., Schaefer, J. M., Denton, G. H., Finkel, R. C., Schwartz, R., Putnam, A.E., Vandergoes, M.J., Goehring, B.M., & Travis, S. G. (2011). In-situ cosmogenic 10Be production rate at Lago Argentino, Patagonia: implications for late-glacial climate chronology. *Earth and Planetary Science Letters*, *309*(1-2), 21-32.

Klepeis, K., Betka, P., Clarke, G., Fanning, M., Hervé, F., Rojas, L., Mpodozis, C, & Thomson, S. (2010). Continental underthrusting and obduction during the Cretaceous closure of the Rocas Verdes rift basin, Cordillera Darwin, Patagonian Andes. *Tectonics*, *29*(3).

Koons, P. O. (1990). Two-sided orogen: Collision and erosion from the sandbox to the Southern Alps, New Zealand. *Geology*, *18*(8), 679-682.

Koons, P. O., Zeitler, P. K., Chamberlain, C. P., Craw, D., & Meltzer, A. S. (2002). Mechanical links between erosion and metamorphism in Nanga Parbat, Pakistan Himalaya. *American Journal of Science*, *302*(9), 749-773.

Lagabrielle, Y., Scalabrino, B., Suarez, M., & Ritz, J. F. (2010). Mio-Pliocene glaciations of Central Patagonia: New evidence and tectonic implications. *Andean Geology*, *37*(2), 276-299.

McQuarrie, N., & Ehlers, T. A. (2017). Techniques for understanding fold-and-thrust belt kinematics and thermal evolution. *Linkages and feedbacks in orogenic systems*, *213*, 25-54.

Mercer, J. H., & Sutter, J. F. (1982). Late Miocene—earliest Pliocene glaciation in southern Argentina: implications for global ice-sheet history. *Palaeogeography, Palaeoclimatology, Palaeoecology*, *38*(3-4), 185-206.

Mitchell, S. G., & Montgomery, D. R. (2006). Influence of a glacial buzzsaw on the height and morphology of the Cascade Range in central Washington State, USA. *Quaternary Research*, *65*(1), 96-107.

Molnar, P. (2004). Late Cenozoic increase in accumulation rates of terrestrial sediment: How might climate change have affected erosion rates?. *Annu. Rev. Earth Planet. Sci.*, *32*, 67-89.

Montgomery, D. R., Balco, G., & Willett, S. D. (2001). Climate, tectonics, and the morphology of the Andes. *Geology*, *29*(7), 579-582.

Mora, D., & Tassara, A. (2019). Upper crustal decompression due to deglaciation-induced flexural unbending and its role on post-glacial volcanism at the Southern Andes. *Geophysical Journal International*, *216*(3), 1549-1559.

Mpodozis, C., & Ramos, V. (1990). The andes of Chile and Argentina.

Mpodozis, C., & Ramos, V. A. (2008). Jurassic tectonics in Argentina and Chile: Extension, oblique subduction, rifting, drift and collisions?. *Revista de la Asociación Geologica Argentina*, *63*(4), 481-497.

Muller, V. A., Calderón, M., Fosdick, J. C., Ghiglione, M. C., Cury, L. F., Massonne, H. J., ... & Sternai, P. (2021). The closure of the Rocas Verdes Basin and early tectono-metamorphic evolution of the Magallanes Fold-and-Thrust Belt, southern Patagonian Andes (52–54° S). *Tectonophysics*, *798*, 228686.

Muller, V. A., Sternai, P., Sue, C., Simon-Labric, T., & Valla, P. G. (2022). Climatic control on the location of continental volcanic arcs. *Scientific Reports*, *12*(1), 1-13.

Muller V.A.P., Sue C. Valla P., Sternai P., Simon-Labric T., Martinod J., Ghiglione M., Baumgartner L., Herman F., Reiners P., Gautheron C., Grujic D., Shuster D., Braun J. (in prep. a) Exhumation response to climate, tectonic and mantle forcing in the southern Patagonian Andes (Torres del Paine and Fitz Roy plutonic complexes).

Muller V.A.P., Sternai P., Sue C. (in prep. b) The role of the asthenospheric window and deglaciation on the present-day uplift of the southern Patagonian Andes.

Orts, D. L., Folguera, A., Encinas, A., Ramos, M., Tobal, J., & Ramos, V. A. (2012). Tectonic development of the North Patagonian Andes and their related Miocene foreland basin (41 30′-43 S). *Tectonics*, *31*(3).

Paterson, W. S. B. (1994). *Physics of glaciers*. Butterworth-Heinemann.

Poblete, F., Roperch, P., Arriagada, C., Ruffet, G., de Arellano, C. R., Hervé, F., & Poujol, M. (2016). Late Cretaceous–early Eocene counterclockwise rotation of the Fueguian Andes and evolution of the Patagonia–Antarctic Peninsula system. *Tectonophysics*, *668*, 15-34.

Rabassa, J. (2008). Late cenozoic glaciations in Patagonia and Tierra del Fuego. *Developments in quaternary sciences*, *11*, 151-204.

Rabassa, J., Coronato, A. M., & Salemme, M. (2005). Chronology of the Late Cenozoic Patagonian glaciations and their correlation with biostratigraphic units of the Pampean region (Argentina). *Journal of South American Earth Sciences*, *20*(1-2), 81-103.

Ramos, V. A. (1999). Plate tectonic setting of the Andean Cordillera. *Episodes Journal of International Geoscience*, *22*(3), 183-190.

Ramos, V. A. (2005). Seismic ridge subduction and topography: Foreland deformation in the Patagonian Andes. *Tectonophysics*, *399*(1-4), 73-86.

Ramos, V. A. (2010). The tectonic regime along the Andes: Present-day and Mesozoic regimes. *Geological Journal*, *45*(1), 2-25.

Ramos, V. A., & Kay, S. M. (1992). Southern Patagonian plateau basalts and deformation: backarc testimony of ridge collisions. *Tectonophysics*, *205*(1-3), 261-282.

Ramos, V. A., Niemeyer, H., Skarmeta, J., & Mun, J. (1982). Magmatic evolution of the austral Patagonian Andes. *Earth-Science Reviews*, *18*(3-4), 411-443.

Raymo, M. E., & Ruddiman, W. F. (1992). Tectonic forcing of late Cenozoic climate. *Nature*, *359*(6391), 117-122.

Riesner, M., Lacassin, R., Simoes, M., Carrizo, D., & Armijo, R. (2018). Revisiting the crustal structure and kinematics of the Central Andes at 33.5 S: Implications for the mechanics of Andean mountain building. *Tectonics*, *37*(5), 1347-1375.

Ruddiman, W. F., Raymo, M. E., Prell, W. L., & Kutzbach, J. E. (1997). The uplift-climate connection: a synthesis. In *Tectonic uplift and climate change* (pp. 471-515). Springer, Boston, MA.

Scalabrino, B., Lagabrielle, Y., Malavieille, J., Dominguez, S., Melnick, D., Espinoza, F., Suarez, M, & Rossello, E. (2010). A morphotectonic analysis of central Patagonian Cordillera: Negative inversion of the Andean belt over a buried spreading center?. *Tectonics*, *29*(2).

Shuster, D. L., Ehlers, T. A., Rusmoren, M. E., & Farley, K. A. (2005). Rapid glacial erosion at 1.8 Ma revealed by 4He/3He thermochronometry. *Science*, *310*(5754), 1668-1670.

Sigvaldason, G. E., Annertz, K., & Nilsson, M. (1992). Effect of glacier loading/deloading on volcanism: postglacial volcanic production rate of the Dyngjufjöll area, central Iceland. *Bulletin of Volcanology*, *54*(5), 385-392.

Stern, C. R., & Kilian, R. (1996). Role of the subducted slab, mantle wedge and continental crust in the generation of adakites from the Andean Austral Volcanic Zone. *Contributions to mineralogy and petrology*, *123*(3), 263-281.

Stern, C. R., Moreno, H., López-Escobar, L., Clavero, J. E., Lara, L. E., Naranjo, J. A., ... & Skewes, M. A. (2007). Chilean volcanoes.

Sternai, P., Caricchi, L., Castelltort, S., & Champagnac, J. D. (2016). Deglaciation and glacial erosion: A joint control on magma productivity by continental unloading. *Geophysical Research Letters*, *43*(4), 1632-1641.

Sternai, P., Caricchi, L., Pasquero, C., Garzanti, E., van Hinsbergen, D. J., & Castelltort, S. (2020). Magmatic forcing of Cenozoic climate?. *Journal of Geophysical Research: Solid Earth*, *125*(1), e2018JB016460.

Sternai, P., Herman, F., Champagnac, J. D., Fox, M., Salcher, B., & Willett, S. D. (2012). Pre-glacial topography of the European Alps. *Geology*, *40*(12), 1067-1070.

Sternai, P., Herman, F., Fox, M. R., & Castelltort, S. (2011). Hypsometric analysis to identify spatially variable glacial erosion. *Journal of Geophysical Research: Earth Surface*, *116*(F3).

Stevens Goddard, A. L., & Fosdick, J. C. (2019). Multichronometer thermochronologic modelling of migrating spreading ridge subduction in southern Patagonia. *Geology*, *47*(6), 555-558.

Strecker, M. R., Alonso, R. N., Bookhagen, B., Carrapa, B., Hilley, G. E., Sobel, E. R., & Trauth, M. H. (2007). Tectonics and climate of the southern central Andes. *Annual Review of Earth and Planetary Sciences*, *35*(1), 747-787.

Stüwe, K. (2002). *Geodynamics of the Lithosphere* (p. 449). Berlin: Springer.

Tassara, A., & Echaurren, A. (2012). Anatomy of the Andean subduction zone: three-dimensional density model upgraded and compared against global-scale models. *Geophysical Journal International*, *189*(1), 161-168.

Thomson, S. N., Brandon, M. T., Tomkin, J. H., Reiners, P. W., Vásquez, C., & Wilson, N. J. (2010). Glaciation as a destructive and constructive control on mountain building. *Nature*, *467*(7313), 313-317.

Thomson, S. N., Hervé, F., & Stöckhert, B. (2001). Mesozoic-Cenozoic denudation history of the Patagonian Andes (southern Chile) and its correlation to different subduction processes. *Tectonics*, *20*(5), 693-711.

Tucker, G. E., & Hancock, G. R. (2010). Modelling landscape evolution. *Earth Surface Processes and Landforms*, *35*(1), 28-50.

Turcotte, D. L., & Schubert, G. (2002). *Geodynamics*. Cambridge university press.

Val, P., & Willenbring, J. K. (2022). Across-strike asymmetry of the Andes orogen linked to the age and geometry of the Nazca plate. *Geology*, *50*(12), 1341-1345.

Valla, P. G., Shuster, D. L., & Van Der Beek, P. A. (2011). Significant increase in relief of the European Alps during mid-Pleistocene glaciations. *Nature geoscience*, *4*(10), 688-692.

Van Der Beek, P., & Braun, J. (1998). Numerical modelling of landscape evolution on geological time-scales: a parameter analysis and comparison with the south-eastern highlands of Australia. *Basin Research*, *10*(1), 49-68.

Watts, A. B. (2001). *Isostasy and Flexure of the Lithosphere*. Cambridge University Press.

Whipple, K. X. (2009). The influence of climate on the tectonic evolution of mountain belts. *Nature geoscience*, *2*(2), 97-104.

Whipple, K. X., & Tucker, G. E. (1999). Dynamics of the stream-power river incision model: Implications for height limits of mountain ranges, landscape response timescales, and research needs. *Journal of Geophysical Research: Solid Earth*, *104*(B8), 17661-17674.

Willett, C. D., Ma, K. F., Brandon, M. T., Hourigan, J. K., Christeleit, E. C., & Shuster, D. L. (2020). Transient glacial incision in the Patagonian Andes from~ 6 Ma to present. *Science advances*, *6*(7), eaay1641.

Willett, S. D. (1999). Orogeny and orography: The effects of erosion on the structure of mountain belts. *Journal of Geophysical Research: Solid Earth*, *104*(B12), 28957-28981.

Willett, S., Beaumont, C., & Fullsack, P. (1993). Mechanical model for the tectonics of doubly vergent compressional orogens. *Geology*, *21*(4), 371-374.

Wolf, S. G., Huismans, R. S., Muñoz, J. A., Curry, M. E., & van der Beek, P. (2021). Growth of collisional orogens from small and cold to large and hot—Inferences from geodynamic models. *Journal of Geophysical Research: Solid Earth*, *126*(2), e2020JB021168.

Zachos, J., Pagani, M., Sloan, L., Thomas, E., & Billups, K. (2001). Trends, rhythms, and aberrations in global climate 65 Ma to present. *science*, *292*(5517), 686-693.

Chapter 2. Article 1

The closure of the Rocas Verdes Basin and early tectono-metamorphic evolution of the Magallanes Fold-and-Thrust Belt, southern Patagonian Andes (52-54°S)

Muller, Veleda A.P.[a,b] *, Calderón, Mauricio[c], Fosdick, Julie C.[d], Ghiglione, Matias C.[e], Cury, Leonardo F.[a], Massonne, Hans-Joachim [f,g], Fanning, C. Mark.[h], Warren, Clare J.[i], Ramírez de Arellano, Cristobal[c], Sternai, Pietro[b]

[a] Lamir Institute, Earth Science Sector - Geology Department, Universidade Federal do Paraná, Av. Cel. Francisco H. dos Santos 210, Curitiba, Brazil.

[b] Dipartimento di Scienze dell'Ambiente e della Terra, Università degli Studi di Milano-Bicocca, Piazza della Scienza 4, Milan, Italy.

[c] Carrera de Geología, Facultad de Ingeniería, Universidad Andres Bello, Sazié 2119, Santiago, Chile.

[d] Department of Geosciences, University of Connecticut, 354 Mansfield Road, U-1045, Storrs, Connecticut 06269, USA.

[e] Instituto de Estudios Andinos "Don Pablo Groeber", Universidad de Buenos Aires, CONICET, Buenos Aires, Argentina.

[f] School of Earth Sciences, China University of Geosciences, Lumo Road 388, 430074 Wuhan, China

[g] Fakultät Chemie, Universität Stuttgart, Pfaffenwaldring 55, D-70174 Stuttgart, Germany.

[h] Research School of Earth Sciences, Australian National University, Canberra, Australia.

[i] School of Environment, Earth & Ecosystem Sciences, The Open University, Milton Keynes MK7 6AA, United Kingdom

*Corresponding author

E-mail addresses: v.paivamuller@campus.unimib.it; mauricio.calderon@unab.cl; julie.fosdick@uconn.edu; matias@gl.fcen.uba.ar; cury@ufpr.br; h-j.massonne@mineralogie.uni-stuttgart.de; mark.fanning@anu.edu.au; clare.warren@open.ac.uk; cristobal.ramirez@unab.cl; pietro.sternai@unimib.it

Abstract:

The *Western Domain* of the Magallanes Fold-and-Thrust Belt (MFTB) between 52°-54°S is part of a poorly studied hinterland region of the southernmost Andean Cordillera. This domain consists of NNW-SSE trending tectonic slices of pre-Jurassic basement units and Late Jurassic-Early Cretaceous ophiolitic complexes and volcano-sedimentary successions of the Rocas Verdes Basin (RVB). New detrital zircon U-Pb ages of metatuffs and metapsammopelites constrain episodes of Late Jurassic rift-related volcanism (ca. 160 Ma) followed by Early Cretaceous sedimentation (ca. 125 Ma) during the opening of the RVB. Shear bands developed in the RVB units further record the initial phases of the Andean Orogeny. The 30-km wide thrust stack located on top of the *Eastern Tobífera Thrust* consists of mylonitic metatuffs, metapelites and metabasalts with a NE-verging brittle-ductile S_1* foliation. Phengite-bearing metatuffs commonly record pressure-temperature (P-T) conditions between ~3-6 kbar and ~210-460 °C, consistent with underthrusting of the RVB beneath the parautochthonous magmatic arc in the west. Peak metamorphic conditions of ~6 kbar and 460 °C are derived from a metapsammopelitic schist with textures of contact metamorphism overprinting early mylonitic structures (at least S_1*). A back-arc quartz-diorite, intruded at ca. 83 Na, is in contact with the metapsammopelites and constrain the minimum age of deformation at deep crustal depths. Campanian-Maastrichtian (ca. 70-73 Ma) $^{40}Ar/^{39}Ar$ phengite dates from a mylonitic metapelite indicate the timing of thrusting and backthrusting during the initial uplift of the underthrusted crustal stack. These findings reveal a ~400 km along-strike connection of mylonite belts in a continent-verging thrust structure that became active at the onset of the Andean orogeny during the closure of the Rocas Verdes back-arc marginal basin.

KEYWORDS: Rocas Verdes Basin; Patagonian Andes; fold-and-thrust belt; shear zones.

1. Introduction

The Andes constitute the archetype of a subduction-related orogen, where compressional stresses due to ocean-continent subduction control mountain building throughout shortening and thickening of the upper continental lithosphere (Dewey and Bird, 1970; Dalziel, 1986; Ramos, 1999; Schellart, 2008; Horton et al., 2018). However, extensional stresses were dominant during Gondwana tectonic dispersal in the early Mesozoic (Cox, 1992, Pankhurst et al., 1998; Dalziel et al., 2013; Braz et al., 2018). At this time, Pacific marginal and back-arc basins opened, leading to seafloor spreading at the northern and southern tips of South America (Dalziel et al, 1974; Stern and De Wit, 2003; Braz et al., 2018) and development of tectonic environments similar to those in present-day East Asia (Schellart and Lister, 2005). Tectonic inversion and closure of a proto-oceanic basin in southernmost South America occurred in the Late Cretaceous, possibly due to accelerated spreading rates in the opening of the South Atlantic (Dalziel, 1981). This shift resulted in ophiolite-bearing thrust sheets emplaced on the South American continent (Dalziel et al., 1974, Klepeis et al., 2010; Calderón et al., 2012). These deformed remnants of back-arc basin lithosphere preserve the stratigraphy, structures, and metamorphism of the extensional and compressional phases in western South America (Dalziel et al., 1974; Stern and De Wit, 2003; Kraemer, 2003; Calderón et al., 2007; Poblete et al., 2016).

The Andean fold-and-thrust belts are generally segmented along-strike, with thrust sheets involving just the sedimentary cover, versus those that include crystalline basement, known as thin- or thick-skinned sectors, respectively (Coward, 1983; Pfiffner, 2006; Lacombe and Bellahsen, 2016). The typical Andean configuration includes deeper (i.e., thick-skinned) structures to the west-hinterland, which became progressively shallow (i.e., thin-skinned) cratonward to the east. Commonly, initially thin-skinned sectors have been affected by re-activation of deep-seated structures and initiation of thick-skinned deformation (Lacombe and Bellahsen, 2016). Therefore, pre-Cenozoic inherited structures appear to have exerted a major control on the style of deformation during Andean crustal shortening (Winslow, 1982; Allmendinger et al., 1983; Kley et al., 1999; Ramos et al., 2004; Fosdick et al., 2011; Likerman et al., 2013). In this context, shear zones that developed at different crustal depths played an important role in accommodating contractional deformation during Andean orogenesis, and may have transferred shortening between different fold-and-thrust belt domains in a time-progressive construction (Price and McClay, 1981; Davis et al., 1983; Platt, 1986; Selzer et al., 2007). Estimates of pressure-temperature (P-T) conditions coupled

to the study of the structures are crucial to resolving the polarity and depth of tectonic burial and exhumation of the fold-and-thrust belts (Ernst, 1972; Miyashiro, 1973; Platt, 1986; Jamieson et al., 1998; Ernst, 2005; Agard et al., 2009; Massonne and Willner, 2008; Jolivet et al., 2010).

This study focuses on the early history of the Andean Orogeny in southernmost Patagonia, where the changes in stress conditions from an extensional to compressive regime, thereby closing the proto-oceanic Late Jurassic-Early Cretaceous Rocas Verdes Basin (RVB, Dalziel et al., 1974). Remnants of this back-arc basin are currently exposed in the hinterland domain of the Magallanes Fold-and-Thrust Belt (MFTB), located to the east of the Patagonian Batholith (Fig. 1). Several paleogeographic models have been proposed to explain the closure and inversion of the RVB (Dalziel, 1981; Cunningham et al., 1991; Kraemer, 2003; Fildani and Hessler, 2005; Calderón et al., 2007; Rapalini et al., 2008, 2015; Klepeis, 2010; Calderón et al., 2012; Fosdick et al., 2011; Poblete et al., 2016; Eagles, 2016). This tectonic event resulted in the ~ 90° counter-clockwise rotation of the southern tip of South America, where the orogenic belts change in orientation from north-south to west-east, a feature known as the Patagonian Orocline (Cunningham et al., 1991; Kraemer, 2003; Rapalini et al., 2008; Poblete et al., 2016; Eagles et al., 2016). The onset of thrust loading of RVB units during its tectonic inversion promoted topographic loading of the foreland lithosphere and development of the Magallanes-Austral Basin to the east (Wilson, 1991; Fildani and Hessler, 2005; Romans et al., 2011; Fosdick et al., 2014). Generally, models agree that the RVB was closed by mid-Cretaceous time due to the relative motion of a microplate against the South American Plate (cf. Eagles, 2016). However, many fundamental aspects of this tectonic transition remain poorly known, including the plate kinematics, the consumption (or not) of the oceanic floor by a west-directed subduction, the mechanisms of basin shortening, and the overall timing of events. The segment under investigation connects the N-S oriented Patagonian Andes and the E-W oriented Fuegian Andes (52°-54°S, 1A), encompassing the Seno Skyring and Seno Otway (Fig. 2). This segment is less studied compared to the northern and southern parts of the deformed RVB.

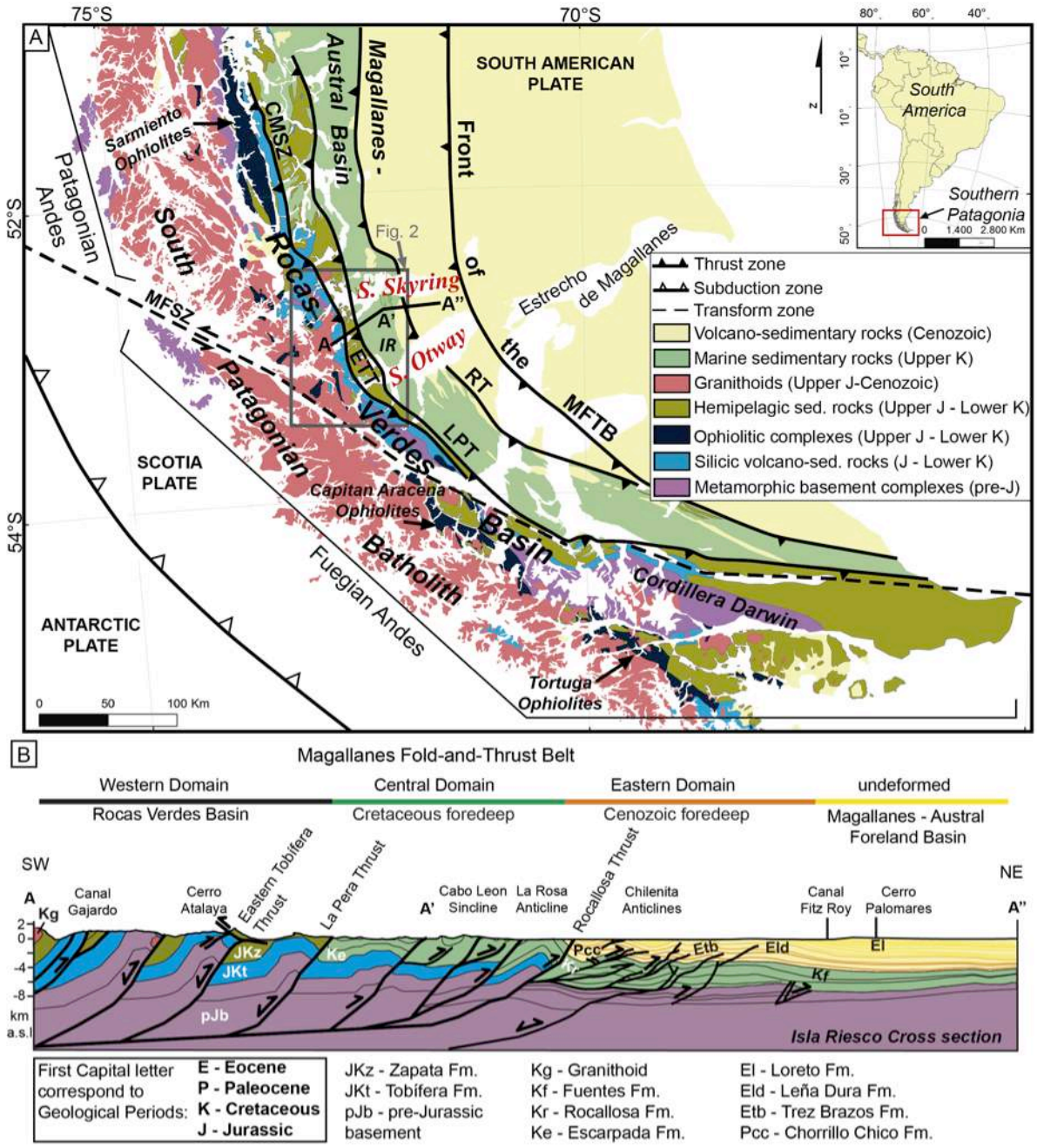

Figure 1: A) Simplified geological map of the southern Patagonian and Fuegian Andes, modified after SERNAGEOMIN (2003). Gray box indicates the study area (detail in Fig. 2) in the region of Seno Skyring and Seno Otway, and the location of cross section A-A'-A'' of Isla Riesco: B) geological cross section interpreted from 2-D seismic lines by ENAP. Abbreviations: IR - Isla Riesco; CMSZ - *Canal de las Montañas Shear Zone* (Calderón et al., 2012); ETT - *Eastern Tobífera Thrust*; LPT - *La Pera Thrust*; RT - *Rocallosa Thrust*; MFSZ - *Magallanes-Fagnano Shear Zone*; the front of the MFTB (Magallanes Fold-and-Thrust Belt) is defined in Fosdick et al. (2011).

We bring new regional and local structural observations, geochronology, and thermobarometry datasets to reconstruct the early history of the study region. The regional structure of the thick- and thin-skinned domains of the MFTB at this latitude is constructed from seismic-reflection data and surface exposure field data (Fig. 1 B). Stratigraphic and

structural field observations allow construction of local cross sections at Canal Gajardo (Fig. 3 A) and Estero Wickham (Fig. 3 B), where initial east-vergent thin-skinned deformation is superimposed by thick-skinned deformation. New Sensitive High Resolution Ion Micro Probe (SHRIMP) U-Pb analyses in detrital zircons provide constraints on the timing of deposition of the volcanic and sedimentary units of the RVB. SHRIMP U-Pb zircon crystallization ages of dioritic plutons that cross-cut mylonitic rocks of the MFTB provide a bracket for the timing of deep ductile deformation, which correlates with the timing of tectonic emplacement of the *Sarmiento Ophiolitic Complex*. The P-T constraints obtained from silicic mylonites and metapsammopelitic schists allow us to estimate the tectonic burial depth reached during the underthrusting of the RVB successions. Finally, $^{40}Ar/^{39}Ar$ in-situ dating of phengitic white mica from a mylonitic metapelite constrains the age of out-of-sequence thrusting and backthrusting in the hinterland *Western Domain* of the MFTB, which was responsible for the Late Cretaceous uplift of the orogenic belt. Based on these new data, we propose and discuss a geodynamic reconstruction of the along-strike exhumation history of the RVB units between the southern Patagonian and the Fuegian Andes.

2. Geological setting

2.1. Stratigraphy of the Magallanes-Fold-and-Thrust Belt

The early phase of Jurassic tectonic dispersal of Gondwanan landmasses was accompanied by the development of a wide volcanic rift zone in southwestern South America (Dalziel et al., 1974; Bruhn et al., 1978; Pankhurst et al., 1998, 2000). In this context, the inception of the RVB occurred in the Middle Jurassic by rifting of the pre-Jurassic basement complexes, which were overlain by Jurassic pyroclastic, volcaniclastic and sedimentary successions (Bruhn et al., 1978; Forsythe and Allen, 1980; Dalziel, 1981; Stern and De Wit, 2003, Calderón et al., 2007; Hervé et al., 2008, 2010a).

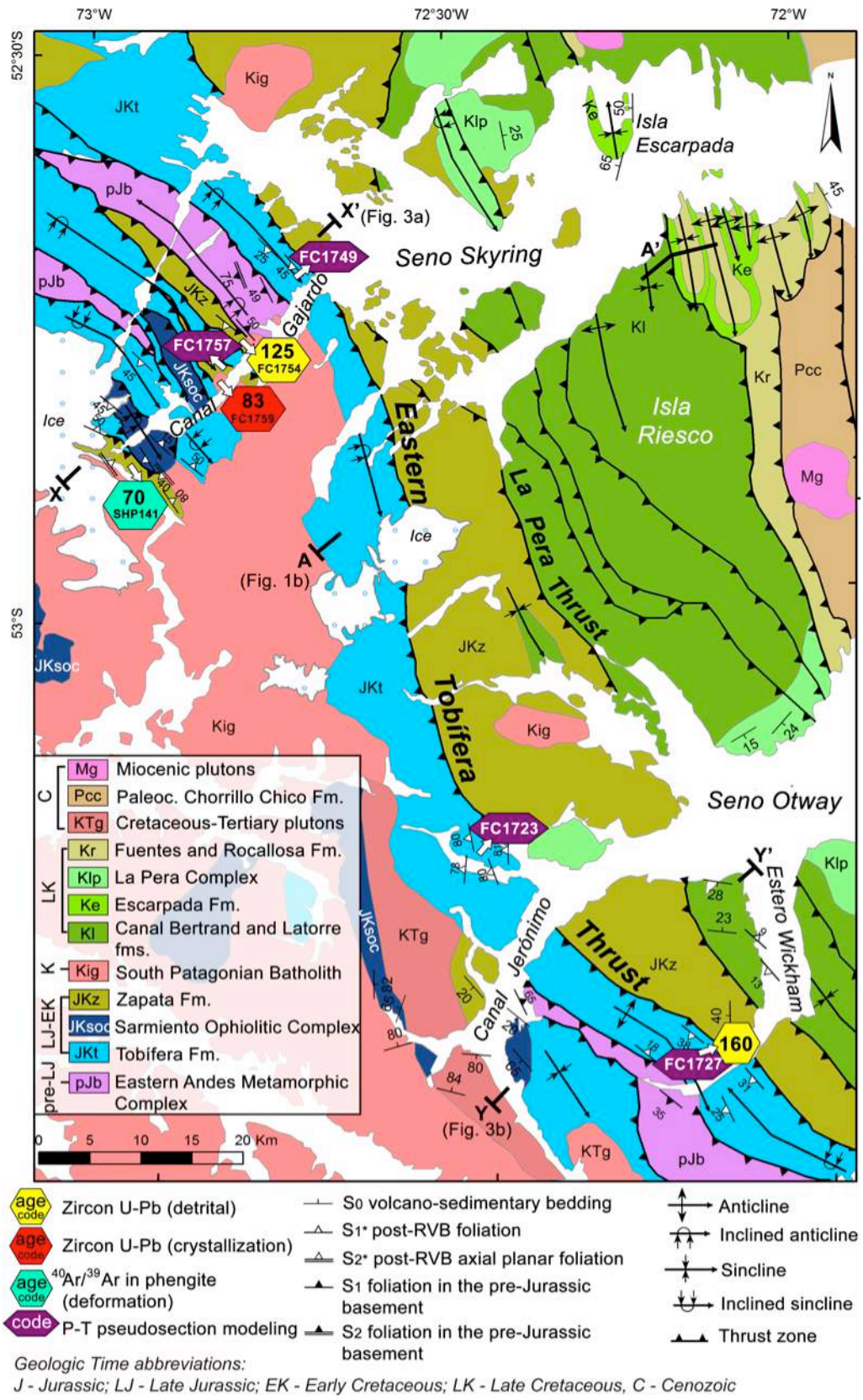

Figure 2: Geological map of the study area modified after SERNAGEOMIN (2003) and Betka (2013). Sample locations for rock samples collected for P-T pseudosection modelling are shown in purple hexagons with their respective field code. The sample locations of new geochronologic analyses with SHRIMP zircon U-Pb and $^{40}Ar/^{39}Ar$ in white mica are shown in the hexagons containing the respective mean ages in millions of years ago (Ma) and the field code is below. Cross sections of the Isla Riesco A-A'-A'', Canal Gajardo X-X', and Estero Wickham Y-Y' are shown in Fig. 1b, 3a and 3b, respectively.

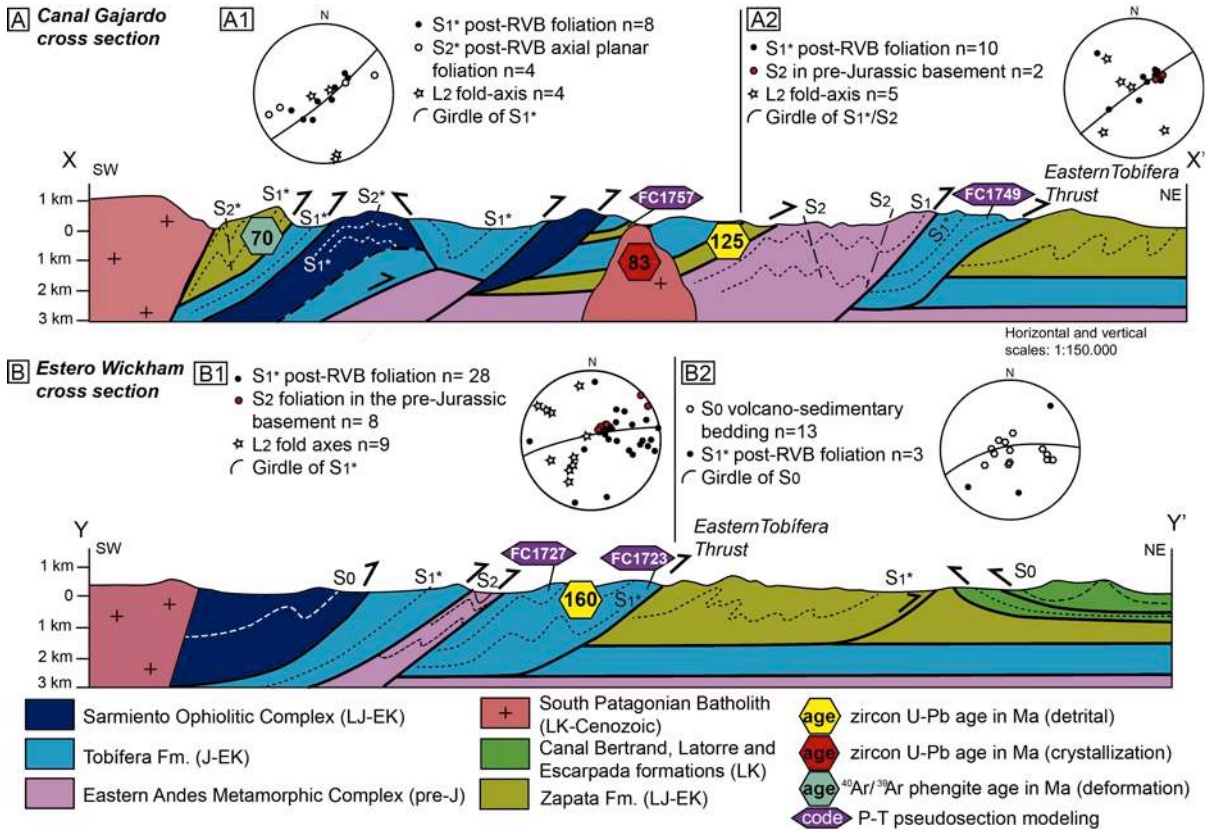

Figure 3: **Simplified geologic cross sections and structural data from the Patagonian Andes** (refer to Fig. 2 for locations): A) Canal Gajardo (X-X') and B) Estero Wickham (Y-Y') modified after Harambour (2002) and Betka et al. (2015). Structural data from volcano-sedimentary bedding, metamorphic foliations, fold axes and axial planes are portrayed in stereographic projections above the respective sectors: A1) western and central areas of Canal Gajardo; A2) eastern area of Canal Gajardo; B1) western area of Canal Jerónimo and Estero Wickham; B2) northern area of Estero Wickham. The analyzed rock samples for P-T pseudosection modelling are shown in purple hexagons with their respective field code. The schematic location of new geochronologic analyses with SHRIMP zircon U-Pb and $^{40}Ar/^{39}Ar$ in white mica are shown in the hexagons containing the respective mean ages in millions of years ago (Ma).

The continental basement in Patagonia comprises Paleozoic to early Mesozoic accretionary complexes of the proto-Pacific subduction zone (Nelson et al., 1980; Kohn et al., 1993; Hervé et al., 2003, 2008, 2010a; Hervé and Fanning, 2003; Willner et al., 2004; Hyppolito et al., 2016, Angiboust et al., 2017, 2018; Suárez et al., 2019). The Paleozoic-Early Triassic *Eastern Andes Metamorphic Complex* extends from the Ultima Esperanza region (~51°S) to the Estrecho de Magallanes (Fig. 1A), and consists of low-grade metapsammopelitic schists with minor intercalations of marbles and metabasic bodies (Forsythe and Allen, 1980; Allen, 1982; Hervé et al., 2003, Hervé et al., 2008; Betka et al., 2015). To the east, the basement of the Magallanes-Austral Basin consists of the high-grade *Tierra del Fuego Igneous and Metamorphic Complex* overlain by Jurassic rift-related silicic volcanic rocks (Hervé et al., 2010a). To the south of Estrecho de Magallanes, the Paleozoic-Mesozoic *Cordillera Darwin Metamorphic Complex* comprises medium to high-grade

metapelitic schists, metabasalts, and Jurassic metarhyolites metamorphosed in the Late Cretaceous (Nelson et al., 1980; Kohn et al., 1993, 1995; Hervé et al., 2008; Hervé et al., 2010b; Klepeis et al., 2010, Maloney et al., 2011).During the early rift-stage of the RVB the depocenters were filled with silicic lava flows, volcaniclastic successions (mostly tuffs and ignimbrites), and sedimentary fluxes of coarse- and fine-grained siliciclastic detritus belonging to the Tobífera Fm. (Fig. 2; Dalziel et al., 1974; Bruhn et al., 1978; Forsythe and Allen, 1980; Dalziel, 1981; Allen, 1982; Wilson, 1991; Pankhurst et al., 1998, 2000; Calderón et al., 2007). Rift volcanism and sedimentation lasted from ca. 170 to 140 Ma (Pankhurst et al., 2000; Calderón et al., 2007; Hervé et al., 2007a; Malkowski et al., 2015a) and fossiliferous siltstones (with ammonites, belemnites, and inoceramids) indicate a predominant submarine deposition during the Early Cretaceous (Allen, 1982; Fuenzalida and Covacevich, 1988; Wilson, 1991). Volcanism was partially coeval with the first phase of plutonism of the *South Patagonian Batholith*, represented by granites and gabbros of 157 to 144 Ma (Hervé et al., 2007a), which bounds the RVB to the west (Figs. 1 and 2).

Progressive lithospheric stretching within the back-arc region resulted in oceanic-type lithosphere formation along mid-ocean-ridge spreading centers, located between the South America cratonic margin and a microplate bearing the southwestern magmatic arc, represented by the Early Cretaceous components of the South Patagonian and Fuegian batholiths (Katz, 1964; Dalziel et al., 1974; Stern, 1979; Dalziel, 1981; Hervé et al., 1984; Stern and De Wit, 2003; Hervé et al., 2007a). In the southern Patagonian Andes, mafic and bimodal igneous suites were emplaced along-strike within the *Sarmiento Ophiolitic Complex* (Calderón et al., 2007; Fig. 1 A). The oceanic remnants consist of pillow and massive basalts with intercalations of cherts and siltstones, underlain by sheeted dyke complexes, minor gabbros and rare plagiogranites (Dalziel et al., 1974; Dalziel, 1981; Allen, 1982; Stern and De Wit, 2003; Calderón et al., 2007). In the Fuegian Andes, the northwestern edge of the Scotia Plate, these remnants are referred as the Tortuga and Capitan Aracena ophiolitic complexes (Fig. 1 A; Calderón et al., 2013).

The following regional sag phase of basin evolution constituted a Late Jurassic to Early Cretaceous marine transgression recorded by deposition of hemipelagic successions of the Zapata (Patagonian Andes), Erezcano (Isla Riesco) and Yaghan/Beauvoir (Fuegian Andes) formations, covering the ophiolitic and the silicic volcaniclastic rocks (Dalziel, 1981; Allen, 1982; Fuenzalida and Covacevich, 1988; Wilson, 1991; Calderón et al., 2007; McAtamney et al., 2011). These units are are dominated by shale-rich successions over ~1000 m in thickness in the Patagonian Andes, and nearly ~3000 m in thickness in the

Fuegian Andes (Cortés, 1964; Suárez and Pettigrew, 1976; Allen, 1982; Wilson, 1991; Fildani and Hessler, 2005). The upper stratigraphic section bears intercalations of sandy turbidites that progressively increase in thickness towards the overlapping Canal Bertrand (Fig. 2; Mpodozis et al., 2007; McAtamney et al., 2011). The facies transition to turbidites is interpreted to reflect an increase in sediment supply and higher depositional energy linked to the beginning of Andean deformation, resulting in cratonward thrusting of the MFTB and subsidence in the east-foreland (Wilson, 1991; Harambour, 1998; Fildani et al., 2003, 2008; Fildani and Hessler, 2005; McAtamney et al., 2011; Malkowski et al., 2015b). These diachronous Aptian-Albian to Turonian maximum sedimentation ages delimitate the end of deposition in the RVB and onset of the foreland stage in the Magallanes-Austral Basin, from north to south (Fildani et al., 2003; Barbeau Jr. et al., 2009; Fosdick et al., 2011; Ghiglione et al., 2015; Malkowski et al., 2015b).

The Upper Cretaceous sedimentary successions of the Magallanes-Austral Basin vary stratigraphically along-strike due to changes in the geometry of the depocenters, controlled by the geometry of inherited extensional faults and the structural evolution of the fold-and-thrust belt (Winslow, 1982; Kraemer, 1998; Fildani and Hessler, 2005; Ghiglione et al., 2009; Bernhardt et al., 2011; Fosdick et al., 2011, McAtamney et al., 2011; Romans et al., 2011; Malkowski et al., 2015b). In the study area, the interface between the RVB and Magallanes-Austral Basin is generally dominated by sand-rich turbidites of the Canal Bertrand Fm. (Wilson, 1991; Fildani and Hessler, 2005; McAtamney et al., 2011), interbedded with mafic volcanic and volcaniclastic rocks of La Pera Complex (Stern et al., 1991; Prades, 2008; Anguita, 2010). These units are capped by deep marine shale-rich successions of the Latorre Fm. (Fig. 2; Mpodozis et al., 2007; McAtamney et al., 2011). The turbidites within the upper section of the Latorre Fm. represent the transition from hemipelagic sedimentation to deep-marine turbiditic clast-supported conglomerates of the Escarpada Fm., deposited at ca. 80 Ma (McAtamney et al., 2011). The overlying Maastrichtian Fuentes and Rocallosa formations, which consist of intercalated mudstones, sandstones, and limestones, record the transition from a shelf to deltaic environment (Charrier and Lahsen, 1969; Castelli et al., 1992; Mpodozis et al., 2007), reflecting the regional shallowing of the Magallanes-Austral Basin during the Late Cretaceous.

2.2. Structural segmentation of the Magallanes Fold-and-Thrust Belt

The MFTB can be divided into three main structural domains (Figs. 1 B and 3; after Alvarez-Marrón et al., 1993): (1) The *Western Domain*, which is the focus of this study, comprises Jurassic-Lower Cretaceous RVB units and pre-Jurassic basement complexes deformed by thick-skinned tectonics; (2) the *Central Domain,* which exposes Upper Cretaceous foredeep units of the Magallanes-Austral Basin within a thick-skinned system dominated by basement-involved inversion structures; and (3) the *Eastern Domain*, defined by outcropping Paleogene foredeep units of the Magallanes-Austral Basin, dominated by thin-skinned deformation.

The *Western Domain* transferred shortening towards the external domains by linking upper crustal thrust faults to deep detachment faults within the pre-Jurassic basement and near the top of the Tobífera Fm. (Alvarez-Marrón, 1993; Harambour, 2002; Kraemer, 2003; Klepeis et al., 2010; Fosdick et al., 2011; Betka et al., 2015). East-vergent detachment faults formed in the earliest Late Cretaceous due to inversion of the RVB, accommodated 30-40 km of shortening of the MFTB in the Patagonia sector (Fosdick et al., 2011; Betka et al., 2015) and 50-100 km of shortening in the Fuegian sector (Kohn et al., 1995; Klepeis et al., 2010; Rojas and Mpodozis, 2006). This phase may have included partial consumption of the proto-oceanic lithosphere by west-directed subduction (Kraemer, 2003). Out-of-sequence thrusting and backthrusting within the RVB succession may have initiated in the Late Cretaceous and continued throughout the Paleogene, leading to deformation of the Upper Cretaceous foreland units of the Magallanes-Austral Basin (Kohn et al., 1995; Harambour, 2002; Kraemer, 2003; Rapalini et al., 2008; Klepeis et al., 2010; Fosdick et al., 2011; Betka et al., 2015). Inversion of inherited-basement faults from the rift phase is taken as an important uplift mechanism during this phase (Winslow, 1982; Alvarez-Marron, 1993; Harambour, 2002; Kraemer, 2003; Rapalini et al., 2008; Fosdick et al., 2011; Likerman et al., 2013; Betka et al., 2015). From the Late Oligocene to Middle Miocene, the deformation progressed eastward into the foreland region but led to overall less shortening and lower foreland propagation rates (Fosdick et al., 2011). Along the margins of the thrust domains, shallow thrusts rooted in the pre-Jurassic - Tobífera Fm. interface (Fig. 1 B) exhibit a forward-breaking sequence (Alvarez-Marrón et al., 1993), and contributed to exhumation of the MFTB (Fosdick et al., 2011, 2013).

2.2.1. Western Domain of the MFTB

The Upper Jurassic Rocas Verdes ophiolites show mutual cross-cutting relationships with the intrusive bodies of the *South Patagonian Batholith* in the westernmost part of the MFTB (Dalziel, 1981; Stern and De Wit, 2003; Hervé et al., 2007a; Calderón et al., 2007). North of the study zone in the Cordillera Sarmiento (~51-52°S; Fig. 1 A), the *Canal de las Montañas Shear Zone* places the ophiolites in thrust contact with the Zapata and Tobífera formations, resulting in a regional cratonward tectonic vergence (Calderón et al., 2012). This km-wide shear zone is defined by mylonitic metatuffs, metapelites and metabasalts derived from the RVB volcano-sedimentary successions. The P-T metamorphic constraints recorded in felsic mylonites of ~250-400 °C and ~5-7 kbar are addressed to a phase of underthrusting of the oceanic and thinned continental lithosphere of the RVB before ca. 85 Ma (Calderón et al., 2012). In the Fuegian Andes (~54-56°S) the Tortuga and Capitan Aracena ophiolitic complexes are thrusted over the basement and volcano-sedimentary units of the RVB, and intruded by several back-arc plutons at ca. 90-80 Ma (Fig. 1 A; Nelson et al., 1980; Hervé et al., 1984; Cunningham, 1995; Klepeis et al., 2010; Calderón et al., 2013).

The mylonitic belts within the RVB successions are cross-cut by out-of-sequence cratonward thrusts and trenchward backthrusts, dated between ca. 70 and 40 Ma (Kohn et al., 1995; Harambour, 2002; Kraemer, 2003; Rapalini et al., 2008; Klepeis et al., 2010; Fosdick et al., 2011; Maloney et al., 2011; Betka et al., 2015). The trench-parallel imbricated arrangement of the *Western Domain* of the MFTB is constituted by structural duplexes of the Tobífera and Zapata formations, tectonically intercalated with the pre-Jurassic basement complexes (Allen, 1982; Fosdick et al., 2011; Calderón et al., 2012). The apatite and zircon fission tracks and (U-Th)/He cooling ages show a protracted history of deep exhumation of the *Western Domain* of the MFTB until the Miocene (Thomson et al., 2001; Fosdick et al., 2013).

In the Fuegian Andes, the *Cordillera Darwin Metamorphic Complex* comprises high-grade kyanite- and garnet-bearing schists, Jurassic orthogneisses and metamorphosed volcano-sedimentary rocks of the RVB (Hervé et al., 2010b; Klepeis et al., 2010). Metamorphic petrology and geochronological studies indicate that the metamorphic complexes were buried to ~35 km depths, during collision of the parautochthonous magmatic arc against the South American continental margin, before ca. 73 Ma (Dalziel, 1986; Kohn et al., 1993, 1995; Cunningham, 1995; Klepeis et al., 2010; Maloney et al., 2011). The

exhumation is interpreted to have resulted from a late deep-seated thrusting phase in the Paleogene (Nelson, 1982; Kohn et al., 1995; Klepeis et al., 2010; Maloney et al., 2011).

2.2.2. Central Domain of the MFTB

The *La Pera Thrust* fault places the Zapata Fm. onto the Upper Cretaceous volcano-sedimentary rocks of the Canal Bertrand, Latorre, and Escarpada formations (Fig. 1 A and B; Mpodozis et al., 2007; McAtamney et al., 2011). The Upper Cretaceous units record east-verging thrusts and open-to-closed folds of regional scale, gradually decreasing in amplitude from west to east.

Seismic surveys across the *Central Domain* show the west-to-east structural transition from inverse steep, east-verging faults to high-angle west-and-east dipping normal faults rooted in the pre-Jurassic basement, which seemingly represent deep-seated inherited horst-graben structures (Winslow, 1982; Wilson, 1991; Harambour, 1998; Fosdick et al., 2011; Likerman et al., 2013; Betka et al., 2015).

2.2.3. Eastern Domain of the MFTB

The *Rocallosa Thrust* bounds the Central and Eastern domains, defining the transition between thick-skinned to predominantly thin-skinned deformation (Fig. 1 B). The *Eastern Domain* comprises the Upper Cretaceous Fuentes and Rocallosa formations, both of which are affected by shallow thrust faults, and the weakly folded Cenozoic Chorrillo Chico, Tres Brazos, Leña Dura and Loreto formations (Kley et al., 1999; McAtamney et al., 2011; Betka et al., 2015).

3. Methods

3.1. Structural and petrographic analysis

Field descriptions were collected from 36 outcrops to the west of Seno Otway and Seno Skyring (Fig. 2). Analysis of 70 thin sections yielded the determination of the mineral assemblages, textures, and microstructures in different samples belonging to the West and Central domains of the MFTB; 9 of these thin section samples were oriented to determine microscopic kinematic shear sense indicators (Table 1).

The structural data of foliations, lineations, and volcano-sedimentary bedding were plotted in stereographic diagrams, at equal-angle projections (Fig. 3), and in the geological map of Fig. 2 complemented with previously published geological and structural data (SERNAGEOMIN, 2003; Betka, 2013).

The structural cross section of the MFTB of Fig. 1 B is based on field data and 2-D seismic surveys done by ENAP (cf. Harambour, 1998). The structural cross section at Canal Gajardo (Fig. 3 A) and Estero Wickham (Fig. 3 B) are proposed on the basis of new field and geochronological data and data from previous works (Harambour, 2002; Betka et al., 2015).

3.2. SHRIMP zircon U-Pb geochronology

In an attempt to constrain the maximum depositional age of the different tectonic slices of the *Western Domain* of the MFTB, zircon grains have been separated from a silicic metatuff of the Tobífera Fm. (FC1727) at Estero Wickham, and a metapsammopelitic rock of the Zapata Fm. (FC1754) at Canal Gajardo. To constrain a relative age of deformation in RVB units, zircon grains were separated from a quartz-diorite pluton (FC1759) intruding the Tobífera and Zapata thrust sheets in Canal Gajardo (Figs. 2 and 3 A). The U-Pb analyses were carried out using SHRIMP II (FC1727 and FC1759; six scan data) and SHRIMP RG (FC1754; four scan data) at the Research School of Earth Sciences, Australian National University, in Canberra. Analytical techniques essentially follow those given in Williams (1998), the U/Pb ratios calibrated using analyses of the Temora reference zircon (Black et al, 2003). The data have been processed using the SQUID Excel Macro of Ludwig (2000) with corrections for common Pb made using the measured $^{238}U/^{206}Pb$ and $^{207}Pb/^{206}Pb$ ratios following Tera and Wasserburg (1972) as outlined in Williams (1998); see Table 2 A-C. Uncertainties in weighted mean age calculations are reported at the one σ level. The geological time-scale used follows the Chronostratigraphic Chart 2018 by IUGS-ICS (www.stratigraphy.org).

3.3. $^{40}Ar/^{39}Ar$ geochronology

To constrain the age of deformation in the *Western Domain* of the MFTB, up to 500 µm-long and 100 µm-wide phengite mats (mix of crystals) from a mylonitic metapelite of the Zapata Fm. (SHP141) in Canal Gajardo (Fig. 2) were analyzed by *in situ* $^{40}Ar/^{39}Ar$ analysis. The in-situ dating provides textural control, and the range of yielded ages provide insights

into the metamorphic and structural evolution of the sample. The analysis was performed in the Open University $^{40}Ar/^{39}Ar$ Laboratory. Polished thick sections of this sample were broken into 5x5 mm^2 squares, washed in acetone and distilled water before packing into foil packets, and air dried at ambient temperature. Mica mats were analyzed by spot-dating using an SPI SP25C 1090 nm laser focused through a Leica microscope, coupled to an automated extraction system and a Nu Noblesse mass spectrometer; laserprobe diameter is 50 μm. Neutron fluency was monitored using the GA1550 biotite standard with an age of 98.79 ± 0.54 Ma (Renne et al., 1998). J values were calculated by linear interpolation between two bracketing standards (and given in Table 3); a standard was included between every 8 and 10 samples in the irradiation tube. Results were corrected for blanks, ^{37}Ar decay and neutron-induced interference reactions. Typical blank measurements are included for each sample and sample run in Table 3; tabled data are blank corrected. Background measurements bracket every 1–2 spots. The correction factors used were: $(^{39}Ar/^{37}Ar)Ca=0.00065$, $(^{36}Ar/^{37}Ar)Ca=0.000265$, $(^{40}Ar/^{39}Ar)K=0.0085$ based on analyses of Ca and K salts. Analyses were also corrected for mass spectrometer discrimination. The branching ratio of Renne et al. (2011) was used. The major-element composition of white mica crystals was measured with the electron probe micro analyzer, described below.

3.4. Bulk-rock X-ray fluorescence spectrometry

Three silicic metatuffs of the Tobífera Fm. (FC1723, FC1727, and FC1749) and one metapsammopelite of the Zapata Fm. (FC1757) were selected to constrain the P-T conditions of metamorphism at different structural levels within the MFTB (Fig. 2) through the construction of phase diagrams (cf. Massonne and Willner, 2008). The whole rock major-element composition was determined with a PHILIPS PW 2400 X-ray fluorescence (XRF) spectrometer at Universität Stuttgart, using glass discs prepared from rock powder and Spectromelt®. The results are presented in Table 4. The procedures of thermodynamic modelling are described below (section 3.6). All samples show dynamic recrystallization and syntectonic growth of very fine-grained white mica and chlorite defining the main foliation. A brief petrographic description of mineral assemblages and textures is provided in section 4.2.

3.5. Mineral analyses with the electron probe micro analyzer (EPMA)

We analyzed the major-element compositions of phengite, chlorite, epidote, feldspar, and biotite present in four selected samples. The white mica composition on sample SHP141 was also analyzed to discuss the meaning of $^{40}Ar/^{39}Ar$ *in situ* dating. The mineral chemical composition was determined using the EPMA CAMECA SX100 at Universität Stuttgart, with 5 wavelength-dispersive spectrometers and an energy-dispersive system. Operating conditions were an acceleration voltage of 15 kV, a beam current of 15 nA, a beam size of 1–3 μm or a focused beam (for very small crystals), and 20 seconds counting time on the Kα peak (Ba: Lα) and on the background for each element. The standards used were natural wollastonite (Si, Ca), natural orthoclase (K), natural albite (Na), natural rhodonite (Mn), synthetic Cr_2O_3 (Cr), synthetic TiO_2 (Ti), natural hematite (Fe), natural baryte (Ba), synthetic MgO (Mg), synthetic Al_2O_3 (Al) and synthetic NiO (Ni). The PaP correction procedure provided by CAMECA was applied. Analytical errors of this method are given by Massonne (2012). Representative mineral compositions are given in Table 5.

3.6. Thermodynamic modelling

P-T isochemical phase diagrams (i.e., pseudosections) contoured by isopleths regarding the chemical composition and modal contents of syntectonic minerals (e.g. white mica, chlorite, epidote) were calculated using the software package PERPLE_X 6.8.0 (cf. Connolly, 1990) to constrain P-T conditions of regional metamorphism in the four selected samples. We used the thermodynamic input parameters provided by Holland and Powell (1998, updated 2002) for minerals and aqueous fluids. The solid-solution models, selected from those included in PERPLE_X 6.8.0, were by (1) Holland et al. (1998): Chl(HP) for chlorite; (2) Holland and Powell (1998): Ctd(HP) for chloritoid, Ep(HP) for epidote, Gt(HP) for garnet, Omph(HP) for Na-bearing clinopyroxene, Pheng(HP) for potassic white micas, TiBio(HP) for biotite; (3) Massonne and Willner (2008) and Massonne (2010): Act (M) for actinolite, Mica(M) for paragonite, Stlp(M) for stilpnomelane, Carp(M) for carpholite, Pu(M) for pumpellyite; (4) Fuhrman and Lindsley (1988): feldspar for plagioclase and alkali feldspar; and (5) Andersen and Lindsley (1988): MtUl(A) for ulvospinel and magnetite. The model IlGkPy for ilmenite-geikielite-pyrophanite is based on ideal mixing of the three end members. The calculated mineral assemblages for the analyzed samples are shown in Table 6 with the respective modal compositions.

4. Results

In the study region, the NNW-SSE-trending thrust sheets of volcano-sedimentary rocks of the Tobífera and Zapata formations are imbricated to the northeast in a cratonward thrust wedge, with variably shallow to steep dip angles. The tectonic repetition of the Tobífera Fm. over the older Zapata Fm. is characteristic of duplex structures in the *Western Domain* of the MFTB. The hanging wall of the easternmost duplex of the *Western Domain*, the *Eastern Tobífera Thrust* (Figs. 2 and 3) is characterized by moderately strained phengite-bearing mylonites suitable for P-T metamorphic constraints. To the east, the Zapata Fm. is thrust over the Upper Cretaceous successions of Canal Bertrand, Latorre and Escarpada formations along the *La Pera Thrust*.

The ophiolitic complexes consist of tectonic slices of pillow basalts and foliated metabasalts intercalated within the Tobífera thrust sheets at Canal Gajardo. The pre-Jurassic basement rocks are thrust onto Tobífera thrust sheets. Plutonic rocks of the *South Patagonian Batholith* are located to the west of the MFTB, and satellite plutons cross-cut the MFTB (Figs. 2 and 3).

Metamorphic/mylonitic foliations S_1* and S_2* in the Tobífera and Zapata formations and *Sarmiento Ophiolitic Complex* are distinguished by an asterisk (*) to separate them from S_1 and S_2 foliations of the pre-Jurassic basement rocks because they may have different tectonic origin. However, S_1* in RVB units and S_2 in the pre-Jurassic basement are related to the same tectonic event, as discussed below.

4.1. Mesoscale Structures

In the westernmost area of Canal Gajardo, a thrust sheet containing the Zapata Fm. consists of metapsammopelitic rocks with a S_1* foliation crenulated by mm-to-cm closed folds. An axial planar S_2* foliation is NW-SE-striking and dips ~70° to the northeast. These rocks are thrust over crenulated silicic metatuffs and metapsammitic rocks of the Tobífera Fm. and show a NW-SE-trending S_1* foliation dipping between 40° and 80° to the west and to the east (Figs. 2 and 3 A1). The doubly dipping structure of S_1* is due to open folds with tens of meters wavelength.

The greenish foliated metabasalts of the *Sarmiento Ophiolitic Complex* in the western area of Canal Gajardo show a NW-SE-striking S_1* schistosity, variably dipping ~15-20° either to the southwest and northeast (Figs. 2 and 3 A1). To the east, a thrust sheet containing

silicic metatuffs of the Tobífera Fm. is backthrust over the ophiolites by NW-SE-striking fault zones that dip 45° to the northeast. Further east the S_1* foliation in metatuffs dips to the southwest. These rocks are thrust over a second tectonic slice of mafic rocks of the *Sarmiento Ophiolitic Complex* (Figs. 2 and 3 A1), constituted of metabasalts with locally preserved pillow structures of up to 30 cm diameter, interleaved within metatuffs of the Tobífera Fm. (Figs. 2 and 3 A1).

To the east of the ophiolitic slices in the central area of Canal Gajardo, metarhyolites, silicic metatuffs, and shales of the Tobífera Fm. are thrust onto mylonitic metapsammopelitic rocks of the Zapata Fm. (Figs. 2 and 3 A1), resembling the geometry of an imbricated duplex. The metapsammopelitic rocks show a crenulated NW-SE-striking S_1* foliation that dips ~25° to the southwest (e.g. FC1754). Near satellite quartz-diorite plutons (e.g. FC1759; Figs. 2 and 3 A1) the S_1* foliation in metasedimentary rocks is overprinted by a hornfels texture possibly generated by contact metamorphism (e.g. FC1757).

At the central area of Canal Gajardo the western Zapata and Tobífera duplex is thrust over a tectonic slice of the pre-Jurassic basement complexes (Figs. 2 and 3 A2). The pre-Jurassic basement rocks consist of metapsammopelitic schists (e.g. FC1753) with an early S_1 foliation tightly folded by an up to 5 cm wavelength asymmetric crenulation cleavage S_2 that may present a S-C geometry. The S_2 foliation strikes NNW-SSE and dips ~25-50° to the southwest (Figs. 2 and 3 A2), being subparallel to the metamorphic/mylonitic S_1* schistosity in the juxtaposed Tobífera and Zapata thrust sheets. The fold hinges trend NW-SE and plunge from 30° to 70° to the northwest, asymmetry of fold limbs suggest a tectonic transport to the north.

At the eastern area of Canal Gajardo, mylonitic silicic metatuffs with metric intercalations of dark metapelitic rocks of the Tobífera Fm. (e.g. FC1749) constitute the hanging wall of the NW-SE-striking *Eastern Tobífera Thrust* (Figs. 2 and 3 A2). The S_1* foliation is subparallel to the sedimentary bedding and dips ~20-40° to the southwest. NE-trending stretching lineations with asymmetric sigma-shaped porphyroclasts contained in the volcano-sedimentary interface indicate a shear sense to the northeast (Table 1).

At Isla Escarpada in Seno Skyring (Fig. 2) the N-S trending eastern flank of the Escarpada Syncline exposes a thick succession of clast-supported conglomerates and conglomeratic sandstones of the Escarpada Fm. Where studied, the strata dip between 50° and 65° to the west.

Within the western reaches of Canal Jerónimo, mafic lapilli-tuffs, basalts, and andesites with metric intercalations of shales and greywackes are mapped as part of the

Sarmiento Ophiolitic Complex (Figs. 2 and 3 B1). The mafic volcaniclastic rocks are variably folded showing steep stratification.

At the central area of Canal Jerónimo the pre-Jurassic metamorphic basement rocks crop-out in the hanging wall between two thrust sheets of the Tobífera Fm. (Figs. 2 and 3 B1). The NW-SE-striking S_1 schistosity in metapelitic schists is tightly folded (of ~30 cm wavelength) with subvertical axial planes defining the S_2 crenulation cleavage. This cleavage strikes NW-SE and dips from 20 to 65° generally to the southwest, but with some limbs dipping to the northeast, parallel to the thrust zone juxtaposing it onto the Tobífera Fm. (Fig. 3 B1).

At the northern area of Canal Jerónimo (Isla Santa María) silicic metatuffs of the Tobífera Fm. (e.g. FC1723) preserve the volcaniclastic bedding subparallel to the S_1* mylonitic cleavage, striking NNW-SSE and dipping ~80° to the west (Figs. 2 and 3 B1). A group of NNE-SSW-striking 1-10 cm thick quartz veins and tension gashes cut obliquely the mylonitic planes (S_1*), present echelon geometries and monoclinal cm-sized folds with sinistral east-vergence. Brittle normal faults, which have resulted in ~1-3 cm displacements of quartz veins and the S_1* cleavage, strike to the NNW-SSE and dip ~85° to the east.

At the southern area of Estero Wickham folded successions of silicic metatuffs with intercalations of shale-rich siliciclastic rocks of the Tobífera Fm. (e.g. FC1727 and FC1728) are internally folded and imbricated (Fig. 4). A ~20 m wavelength anticline of these successions is in the hanging wall of a NW-SE-striking thrust zone dipping ~40° to the west (Fig. 4 A). The NNW-SSE-striking axial plane is nearly subvertical. A brittle-ductile NW-SE-striking mylonitic S-C-type cleavage (S_1*) dips 30-60° to the southwest, and is oblique to the volcano-sedimentary bedding (Figs. 3 B1 and 4). In the footwall, the shale-rich beds bear 15 cm- thick layers of sandstones, which are boudinaged and dip ~30° to the southwest (Fig. 4 D). The S_1* mylonitic cleavage is oblique to the sedimentary bedding, strikes NW-SE and dips ~ 40° to the southwest. Further east, the Tobífera Fm. is thrust upon the Zapata Fm. through the *Eastern Tobífera Thrust* and dips ~35° to the southwest (Figs. 2 and 3 B1).

At the northern area of Estero Wickham the hundred-meter thick successions of siltstones belonging to the Canal Bertrand Fm. (Figs. 2 and 3 B2) are backthrusted onto the Zapata Fm. The sedimentary bedding (S_0) in Canal Bertrand Fm. strikes WNW-ESE and dips ~20-30° to the north and to the south. Siltstones show a NW-SE-trending cleavage, dipping ~10° to the southwest and northeast, in which few granitic lithic grains up to 0.7 cm in size are rotated and show shear sense indicators to the northeast (Table 1). Variations in the dip direction of S_0 and the cleavage reveal open folds of tens of meters wavelength.

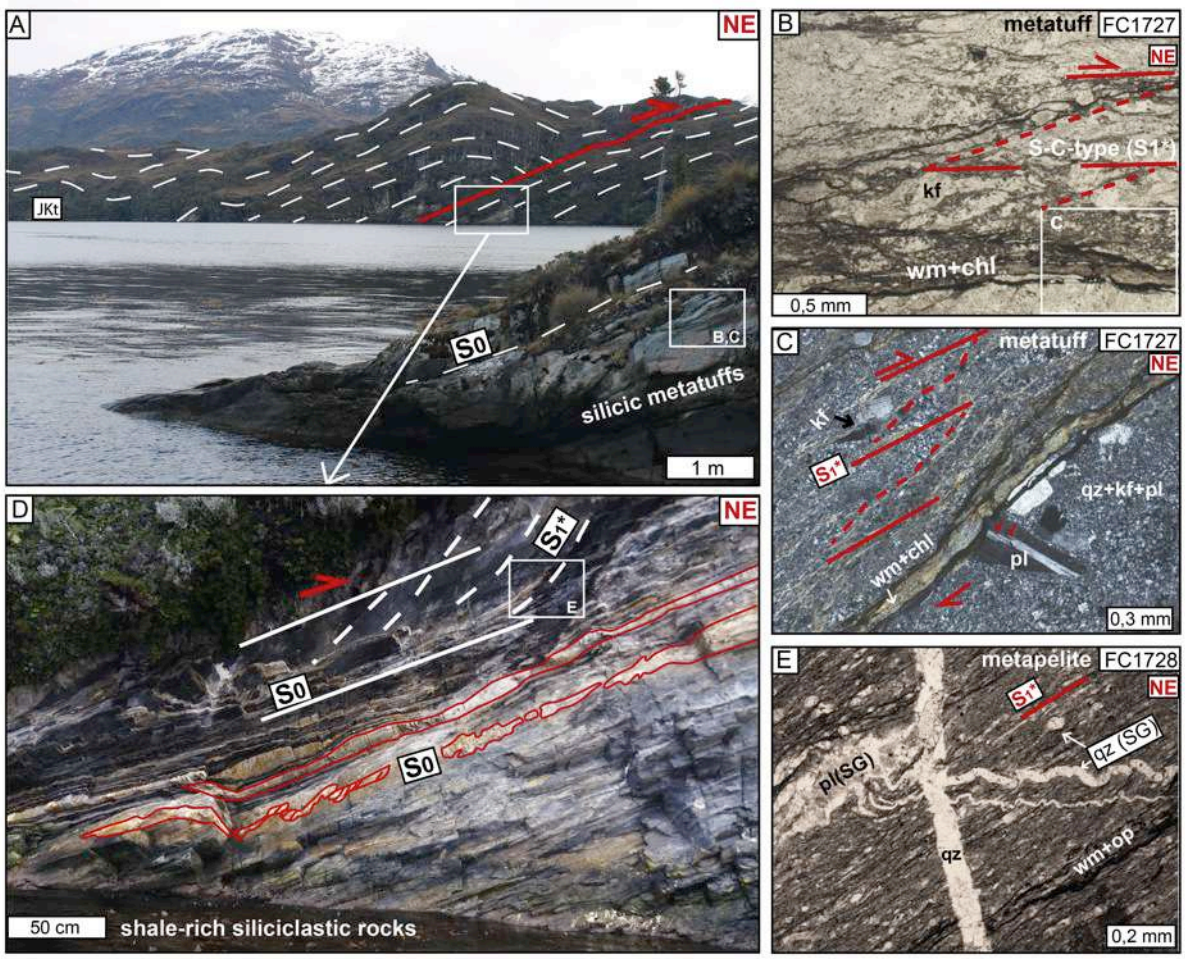

Figure 4: Field photographs and photomicrographs of the mylonitic rocks of Tobífera Fm. in the hanging wall of the *Eastern Tobífera Thrust* at Estero Wickham: A) internal thrust contact within the folded Tobífera Fm.; B) photomicrograph of oriented thin section of silicic metatuff (FC1727, plane polarized light) showing the mylonitic S-C-type foliation (S_1*) in micaceous domains, and quartz and feldspar porphyroclasts with sigma-shaped strain shadows; C) photomicrograph of detail at sample FC1727 (crossed polarized light) showing ruptured plagioclase and sigma-shaped alkali feldspar, truncated by mica-rich cleavage domains of S_1*. D) Shale-rich intercalations within Tobífera Fm. in the foot wall of the thrust fault showed in A, cm-thick sandy layers are boudinaged and folded, an internal S_1* mylonitic foliation is oblique to the bedding S_0; E) photomicrograph of mylonitic metapelite (FC1728, plane polarized light) showing the S_1* mylonitic foliation, plagioclase and quartz porphyroclasts have sigma shapes and can be recrystallized to subgrains (SG).

4.2. Microstructures

4.2.1. Pre-Jurassic basement rocks

In metapsammopelitic schists at Canal Gajardo the S_1 foliation is defined by discontinuous up to 1 cm thick, discontinuous microlithons, mainly composed of up to 100 µm-sized polycrystalline quartz, and discontinuous mm-thick cleavage domains of up to 100 µm wide crystals of white mica with minor proportions of chlorite and opaques. The S_1 foliation is crenulated into up to 1 cm asymmetric tight folds with a 1 mm- spaced axial planar S_2 crenulation cleavage, defined by irregular planes of opaques. S_2 planes cross-cut

perpendicularly the S_1 foliation causing reverse displacements of S_1 fold limbs to the north, interpreted as shear-sense indicators accordingly to meso-scale structures. The S_2 foliation is oblique and subparallel to the S_1* foliation observed in metatuffs and metasedimentary rocks of RVB, suggesting a common deformational event in the pre-Jurassic basement and the RVB units.

Metapelitic schists at Estero Wickham are composed of up to 100 μm-sized quartz, white mica, chlorite, opaque minerals and accessory apatite. Anastomosed cleavage domains constituted mainly of white mica present two oblique preferential planes, suggesting a S-C-type mylonitic foliation with shear sense to the northeast (Fig. 5 A, Table 1). Sigmoidal microlithons of polygonal quartz show undulose extinction and subgrains with core-mantle texture, which are indicators of dynamic recrystallization.

4.2.2. Sarmiento Ophiolitic Complex

Remnants of ophiolitic rocks at the central area of Canal Gajardo correspond to greenish pillow basalts composed of up to 100 μm-sized tremolite-actinolite, plagioclase, chlorite, epidote, white mica, and titanite; carbonate is restricted to inter-pillow domains. Foliated metabasalts in the westernmost ophiolitic slice at Canal Gajardo contain up to 2 mm-sized porphyroblasts of actinolite and matrix consisting of up to 500 μm-sized plagioclase, chlorite, actinolite, titanite, epidote, quartz, carbonate, and traces of opaques. Cleavage domains (~100-300 μm thick) composed of preferentially orientated mats of chlorite and actinolite define the S_1* foliation; these domains are discontinuous with sigmoidal geometry, suggesting a shear sense to the northeast (Fig. 5 B). Asymmetrically deformed porphyroblasts of actinolite indicate a shear sense to the north (Table 1). The S_1* foliation is crenulated into disharmonic open mm-folds with an incipient axial planar S_2* foliation, and cross-cut by up to 1 mm thick veins of carbonate.

4.2.3. Tobífera Fm.

Mylonitic silicic metatuffs at Canal Gajardo (e.g. FC1749) bear up to 1 mm-sized porphyroclasts (15-20%) of quartz and minor plagioclase; sigma-shaped quartz porphyroclasts show asymmetric strain shadows of quartz, white mica, and opaques (Fig. 5 C); plagioclase is commonly fractured and exhibits trails of fluid inclusions truncated by cleavage domains of white mica and chlorite. Cleavage domains are anastomosed and define

the mylonitic S_1* foliation with shear sense indicators to the northeast (Fig. 5 C; Table 1). The matrix is composed of up to 100 µm-sized quartz, feldspars, white mica, chlorite, and opaques. The dark metapelitic rocks intercalated within metatuffs bear up to 700 µm-sized porphyroclasts of microcrystalline quartz and subhedral opaques surrounded by asymmetric strain fringes of quartz, and fragmented by domino-type structures suggesting shear sense to the northeast (Fig. 5 D). The matrix is composed of preferred-oriented platy quartz, clay minerals and opaque crystals smaller than 100 µm defining the S_1* mylonitic cleavage.

Mylonitic silicic metatuffs at Canal Jerónimo (e.g. FC1723) bear mm-to-cm-sized porphyroclasts (<5%) of quartz, feldspar, and rhyolitic lithics lacking intracrystalline deformation, surrounded by asymmetric strain shadows of quartz with flakes of white mica. The recrystallized matrix is composed of up to 100 µm-sized quartz, white mica, chlorite, plagioclase, and non-oriented radial zoisite. Preferred orientation of mica in two oblique planes suggests an S-C-type mylonitic cleavage (S_1*) with shear sense to the northeast (Table 1). Late brittle structures such as quartz tension-gashes, show dextral and sinistral shear-sense indicators. At Canal Jerónimo a sedimentary breccia belonging to the Tobífera Fm. is constituted of mm-to-cm-sized rectangular clasts of polydeformed schist in a quartzose recrystallized matrix.

Mylonitic silicic metatuffs at Estero Wickham (e.g. FC1727) consist of up to 1 mm-sized and sigma-shaped porphyroclasts (5%) of quartz, alkali feldspar and plagioclase, which are internally fractured; their rims are truncated by cleavage domains of preferred-oriented micaceous and opaque minerals, formed through pressure-solution processes. Two oblique preferential planes define a S-C-type mylonitic cleavage (S_1*) with shear-sense indicators to the northeast (Fig. 4 B-C; Table 1). The matrix is dynamically recrystallized and composed of aggregates of up to 100 µm-sized quartz and feldspar, and preferred-oriented flakes of white mica and chlorite, opaques, and traces of titanite. The intercalated shale-rich metapelitic rocks bear sigma-shaped micron-sized grains of quartz, surrounded by anastomosed domains of preferred-oriented white mica, plagioclase, and accessory epidote, chlorite and opaques, defining a S_1* mylonitic cleavage (Fig. 4 E). Early quartz veins are crenulated and disrupted by cleavage domains of S_1*. Late quartz veins are undeformed and crosscut S_1*.

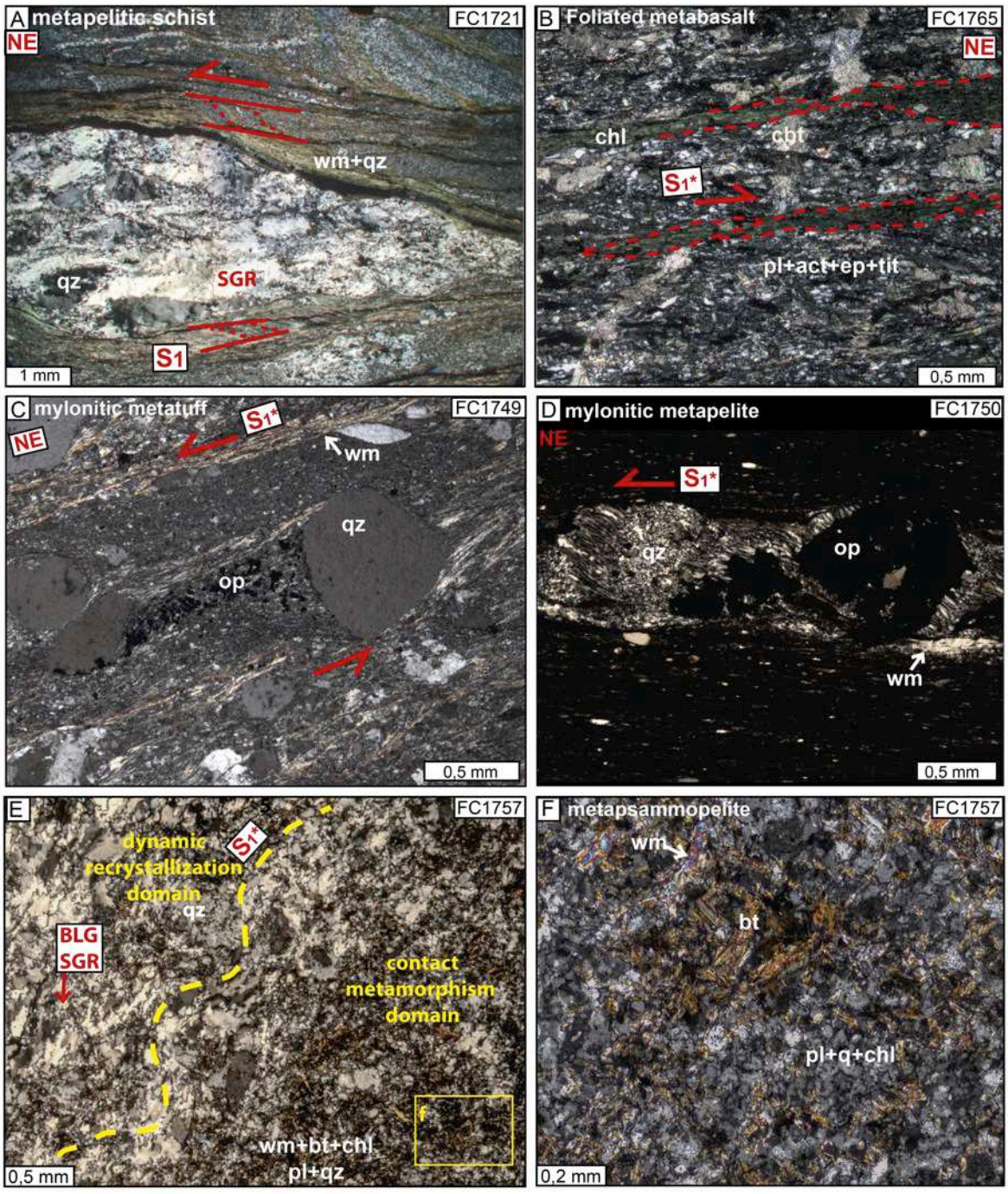

Figure 5: Photomicrographs of representative lithologies of the *Western Domain* of the MFTB: A) metapelitic schist of the pre-Jurassic basement (FC1721, crossed polarized light) with two oblique preferential planes suggesting a S-C-type mylonitic foliation with shear sense to the northeast; sigmoidal microlithons of quartz show undulose extinction and subgrains with core-mantle texture; B) foliated metabasalt of the *Sarmiento Ophiolitic Complex* (FC1765, crossed polarized light) with the S_1* schistosity defined by cleavage domains of chlorite with sigmoidal geometries that suggest shear sense to the northeast; C) mylonitic silicic metatuff of the Tobífera Fm. (FC1749, crossed polarized light) with cleavage domains of white mica defining the S_1* schistosity, quartz porphyroclasts are ruptured and displaced with strain shadows of quartz and opaques suggesting shear sense to the northeast; D) mylonitic metapelite of the Tobífera Fm. (FC1750, crossed polarized light) with porphyroclasts of quartz and opaques with asymmetric strain fringes of quartz, and fragmented by domino-type structures suggesting shear sense to the northeast; E) metapsammopelite of the Zapata Fm. (FC1757, crossed polarized light) showing the folded relict foliation (S_1*) defined by quartz with bulging and subgrain rotation, it is overprinted by contact metamorphism that is characterized by non-oriented white mica, biotite, chlorite, and plagioclase; F) zoom in the decussed biotite and white mica of sample FC1757.

4.2.4. Zapata Fm.

Mylonitic metapsammopelites at Canal Gajardo (e.g. FC1754) are composed of 1-2 mm-thick microlithons of up to 500 μm-sized microcrystalline quartz with polygonal contacts, and anastomosed 0.5-1 mm-thick cleavage domains of up to 100 μm-sized crystals of white mica, chlorite, epidote, and opaques defining the S_1* foliation. This is crenulated into 1-to-10 mm wavelength open folds, with an axial planar S_2* crenulation cleavage defined by opaque-rich discontinuous layers. The rocks affected by contact metamorphism (e.g. FC1757) show up to 100 μm-sized crystals of biotite with decussate texture, white mica, plagioclase, quartz, epidote, and chlorite with no preferential orientation overprinting a relict fabric of S_1* (Fig. 5 E-F). The domains with relict S_1* foliation are 0.5 mm-wide bands with up to 300 μm-sized preferred oriented quartz with bulging and subgrain rotation, indicating dynamic recrystallization, with disharmonic folds of 1 mm wavelength (Fig. 5 E).

Metapsammopelitic rocks at the westernmost thrust sheet of Canal Gajardo are composed of up to 100 μm-sized quartz, white mica, opaques, and traces of chlorite and epidote. The preferred orientation of micas define the S_1* foliation that is crenulated; opaque-rich cleavage domains define an axial planar foliation S_2*. Mylonitic metapelites (e.g. SHP141) show a foliation defined by cleavage domains composed of up to 500 μm-long and 100 μm-wide aggregates of white mica, and chlorite smaller than 100 μm; and up to 100 μm-thick microlithons of quartz, albite, and traces of epidote and actinolite smaller than 100 μm.

4.2.5. Satellite plutons of the South Patagonian Batholith

The *Western Domain* of the MFTB is intruded by different igneous bodies (plutons and dykes) of quartz-diorite (e.g. FC1759), composed of up to 1 cm-sized crystals of subhedral plagioclase, uralitized clinopyroxene and variably chloritized hornblende, and up to 500 μm-sized interstitial quartz, and traces of subhedral magmatic titanite and opaques. Sample FC1759 was collected from an undeformed part of the pluton there the unit does not exhibit recrystallization textures.

4.2.6. Upper Cretaceous Units of the Magallanes-Austral Basin

The fine-grained siltstones of Canal Bertrand Fm. are composed of mm-sized detrital plagioclase and quartz in a matrix of up to 100 μm-sized clay minerals, white mica, chlorite, and opaques, cemented by carbonate. A cleavage defined by preferred orientation of

chlorite, white mica, and opaque minerals is oblique to the sedimentary bedding. Rotated mm-to-cm-sized granite clasts in coarse-grained rocks show asymmetric strain shadows of micaceous and opaque minerals, indicating a sense of shear to the northeast (Table 1).

Clast-supported conglomerates of the Escarpada Fm. show imbricated well-rounded up to 10 cm-sized clasts of low sphericity. The main lithotypes of the clasts are shales, foliated rhyolites, aphanitic and porphyritic igneous rocks, and metasedimentary rocks. The matrix is composed of crystals of white mica, clay minerals and carbonates smaller than 10 μm. The compositional diversity of clasts is akin to those lithologies observed in the *Western Domain* of the MFTB, and thus considered here as a potential sediment source to submarine conglomerates deposited during the Late Cretaceous phase of sedimentation in the Magallanes-Austral Basin (cf. McAtamney et al., 2011). Further provenance analysis and stratigraphic study of these units is necessary to confirm this correlation.

4.3. Geochronology

4.3.1. Zircon U-Pb Geochronology

The zircon grains from the mylonitic silicic metatuff of the *Eastern Tobífera Thrust* (FC1727) predominantly show oscillatory zoning, indicating igneous crystallization, although many grains also have darker cathodoluminescent (CL) cores (higher U; Fig. 6 A). As the aim of this study was to determine the zircon crystallization age, 22 analyses were made on the brighter CL outer areas and whole grains, with only 4 darker CL cores analyzed (Table 2 A; Fig. 6 A). The dominant age grouping is at ca. 160 Ma with a subordinate tail at ca. 168 Ma and two other scattered Lower Jurassic and Upper Triassic analyses (Table 2 A; Fig. 6 A). Importantly, the calculated radiogenic $^{206}Pb/^{238}U$ ages do not vary significantly between rim and core in few analyzed grains. Analysis of one diffuse core records the presence of an older Triassic age (Table 2 A; Fig. 6 A). In terms of the dominant age grouping for analyses of the oscillatory zoned zircon, a weighted mean $^{206}Pb/^{238}U$ age for 21 analyses gives 159.9 ± 1.1 Ma (MSWD=1.4).

For the mylonitic metapsammopelite of the Zapata Fm. (FC1754), a random sampling of the total zircon fraction was poured onto double sided tape and prepared for detrital zircon analyses. The zircons range from euhedral prisms with bipyramidal terminations to sub-rounded/rounded grains; the CL images show a high proportion of zoned igneous internal

features (Fig. 6 B). Analysis of 70 grains records a wide range in detrital ages with significant Early Cretaceous, Permian, and Ordovician groupings (Fig. 6 B). The predominant Early Cretaceous grouping, comprising 28 analyses, can be arbitrarily unmixed in three groups (Fig. 6 C): there is a more prominent subgroup at ca. 130 Ma (n=14); a lesser sub-grouping around 125 Ma (n=12) and a minor cluster near 135 Ma (n=2). Minor components of Devonian, early Cambrian, Neoproterozoic, Mesoproterozoic and Archean ages are recorded in 12 analyzed grains (Table 2 B, Fig. 6 B). The scattered dates of 15 grains, ranging between 250 Ma and 290 Ma, suggest the presence of a Permian cluster near ca. 280 Ma. There are minor scattered clusters at ca. 410 Ma (n=4), ca. 470 Ma (n=8), and ca. 540 Ma (n=3).

Only five zircon grains were recovered from the heavy mineral concentrate for the hornblende quartz-diorite at Canal Gajardo (FC1759). All 5 grains show zoned igneous CL internal structures and record upper Cretaceous $^{206}Pb/^{238}U$ ages around 84-80 Ma (Fig. 6 D). Excluding a high U analysis with the youngest $^{206}Pb/^{238}U$ age, the weighted mean is 83.2 ± 1.0 Ma (MSWD = 0.45; Table 2 C, Fig. 6 D).

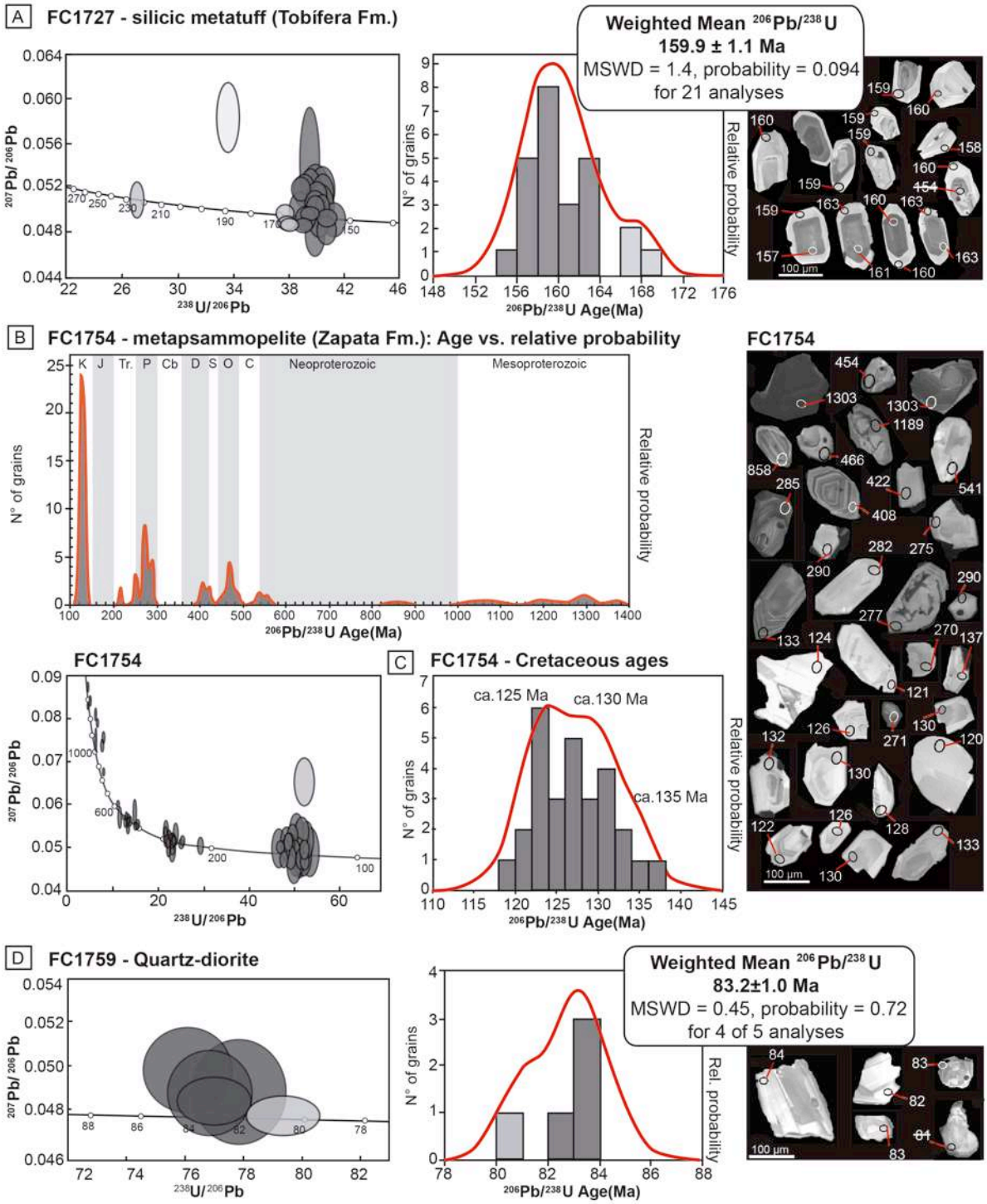

Figure 6: SHRIMP zircon U-Pb results: A) Tera-Wasserburg concordia plot, age versus relative probability diagram, weighted mean age, and demonstrative analyzed zircon grains from mylonitic silicic metatuff of the Tobífera Fm. (FC1727); B) Age versus relative probability diagram, Tera-Wasserburg concordia plot, and representative analyzed zircon grains from the metapsammopelite of Zapata Fm. (FC1754), and C) age versus relative probability diagram for the Cretaceous ages; D) Tera-Wasserburg concordia plot, age versus relative probability diagram with weighted mean age, and analyzed zircon grains from quartz-diorite (FC1759) intruding thrust sheets of Canal Gajardo.

4.3.2. $^{40}Ar/^{39}Ar$ geochronology

Mats of white mica from the mylonitic metapelite of the Zapata Fm. (SHP141) from the western Canal Gajardo (Fig. 7 A) were dated *in situ* using an IR laserprobe for $^{40}Ar/^{39}Ar$ analyses. Representative major-element compositions of the analyzed white mica crystals (see Table 5) indicate their phengite composition with Si a.p.f.u. (atoms per formula unit) > 3.3, as shown in the classification diagram of Fig. 8 A, and Mg# = $Mg^{+2}/(Mg^{+2}+Fe^{+2})$ between 0.7 and 0.85. In chlorite Mg# is ~0.6.

Ten of eleven analysis spots (Table 3) on mats of ~100 μm-sized phengite yielded a weighted mean of 71.1 ± 1 Ma (MSWD = 5.9). The asymmetric distribution of data and MSWD higher than 1 (Fig 7 B) suggest more than one population within the dataset. The five youngest dates form a consistent group with a mean age of 70.2 ± 0.4 Ma; six dates can be grouped in an interval between 71 and 73 Ma, and one significantly older 75.5 ± 1.6 Ma date was excluded from the analysis due to its high error.

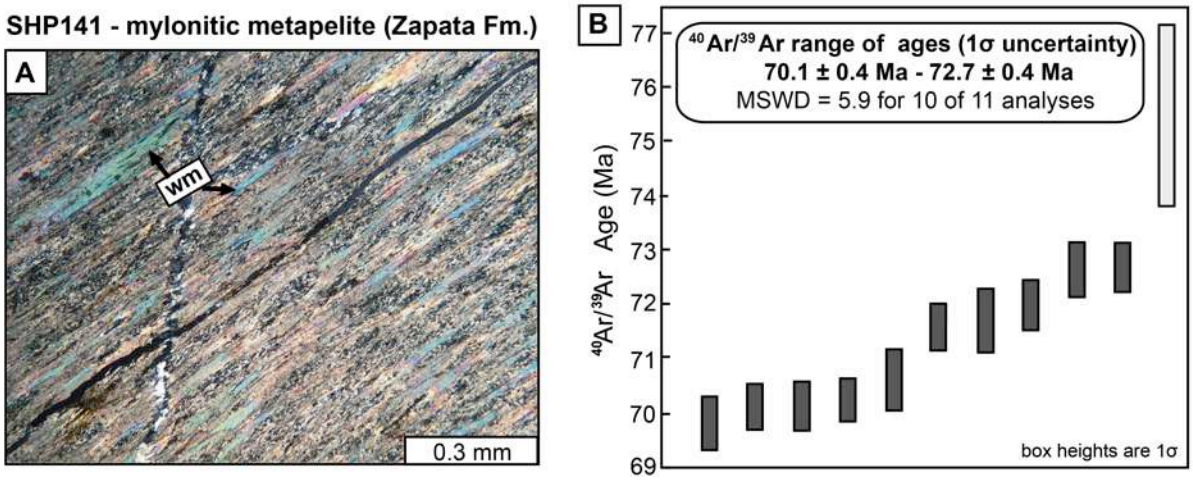

Figure 7: **A) Photomicrograph of mylonitic metapelite of Zapata Fm. (SHP141) with mats of phengite (crossed polarized light), and B) diagram of *in-situ* $^{40}Ar/^{39}Ar$ dates with errors reported at the 1 σ level**, the light gray bar (spot 7, Table 3) is considered an outlier.

4.4. P-T Constraints

The P-T pseudosection modelling of four samples was used to constrain the depth of tectonic burial and temperature during the development of mylonitic bands in the hanging wall of the *Eastern Tobífera Thrust* and in the westernmost part of the MFTB. The metatuff samples were chosen because they present a well-preserved mylonitic foliation defined by metamorphic minerals that allow to constrain the P-T conditions of dynamic recrystallization.

The metapsammopelite sample was chosen because it exhibits a hornfels texture defined by biotite, white mica, chlorite, and plagioclase, caused by contact metamorphism overprinting the S_1* foliation with dynamic recrystallization microstructures in quartz. This sample is located near the quartz-diorite pluton that was dated, allowing thus the relative dating of the different tectonic events in the *Western Domain* of the MFTB. To construct the P-T pseudosections we used the bulk-rock major-element composition (Table 4) and the mineral chemistry (Table 5) of these samples.

4.4.1. Petrography and mineral composition

Representative chemical compositions of white mica, chlorite, feldspar, biotite, and epidote of the analyzed samples are presented in Table 5. Classification diagrams for white mica (Ernst, 1963), chlorite (Foster, 1962) and feldspar (Deer et al., 1963) are shown in Figure 8 A-C, respectively. To characterize feldspar, we used the molar fraction $X_{Na} = Na^{+}/(Na^{+}+Ca^{+2}+K^{+})$. Epidote is characterized by the $Fe^{+3}/(Al+Fe^{+3})$ ratio = XFe^{3+}. Approximated modal compositions of analyzed samples are listed in Table 6 with the calculated compositions obtained from the P-T pseudosection modelling.

The silicic metatuff of the Tobífera Fm. at Canal Gajardo (FC1749) consists of quartz (~55%; including 15% of porphyroclasts), plagioclase (~25%; including 5% of porphyroclasts), white mica (15%), chlorite (5%) and traces of opaques. The Si and Al contents of phengitic white mica vary between 3.20 and 3.60 a.p.f.u. and 2.05 and 2.30 a.p.f.u., respectively (Fig. 8 A). The 5 μm-sized laths of chlorite (mostly absent in the mineral assemblage) have Si content of 3.13 a.p.f.u. and X_{Mg} of 0.8, and can be classified as diabanite (Fig. 8 B). Plagioclase porphyroclasts and interstitial grains of fine-grained dynamically recrystallized matrix are albite in composition (X_{Na} of 0.95- 0.99; Fig. 8 C).

The mylonitic metapsammopelite of the Zapata Fm. at Canal Gajardo (FC1757) is composed by quartz (55%), plagioclase (25%), white mica (10%), biotite (5%), chlorite (4%), epidote (1%) and traces of opaques. Biotite is characterized by Mg# varying between 0.41 and 0.44. White mica shows Si and Al contents ranging between 3.12 and 3.30 a.p.f.u. and 2.15 and 2.60 a.p.f.u., respectively (Fig. 8 A). Chlorite is classified as ripidiolite with X_{Mg} of ~0.50 and Si contents around 2.78 a.p.f.u. (Fig. 8 B). Plagioclase is oligoclase with X_{Na} varying between 0.69 and 0.73 (Fig. 8 C).

The mylonitic silicic metatuff at Canal Jerónimo (FC1723) is composed of quartz (~55%; including 5% of porphyroclasts), white mica (30%), chlorite (10%), plagioclase

(4%), epidote (1%) and traces of opaques. The phengitic composition of white mica is characterized by Si and Al contents varying between 3.10 and 3.30 a.p.f.u. and 2.35 and 2.60 a.p.f.u., respectively (Fig. 8 A). Two main groups of chlorite compositions were identified and correspond to clinochlore (Si = ~2.9 a.p.f.u.; X_{Mg} = ~0.8) and ripidiolite (Si = ~2.6 a.p.f.u.; X_{Mg} = ~ 0.4) (Fig. 8 B). Few grains show high X_{Mg} (~0.8) and higher Si content (>3.1 a.p.f.u.) (Fig. 8 B). Albite composition (X_{Na} of 0.95- 0.99; Fig. 8 C) was determined in porphyroclasts and within the quartz-rich recrystallized matrix. Epidote is classified as clinozoisite (*sensu* Seki, 1959), with XFe^{3+} = 0.10-0.12.

The mylonitic silicic metatuff at Estero Wickham (FC1727) consists of quartz (~50%; including 5% of porphyroclasts), plagioclase (25%), K-feldspar (5%), white mica (15%), chlorite (5%) and traces of opaques. The white mica is phengite, with Si and Al contents varying between 3.30 and 3.45 a.p.f.u. and 1.9 and 2.1 a.p.f.u., respectively (Fig. 8 A). Chlorite is classified as ripidolite with X_{Mg} between 0.40-0.44 and low Si contents (~2.8 a.p.f.u.; Fig. 8 B). Plagioclase is albite in composition (Fig. 8 C).

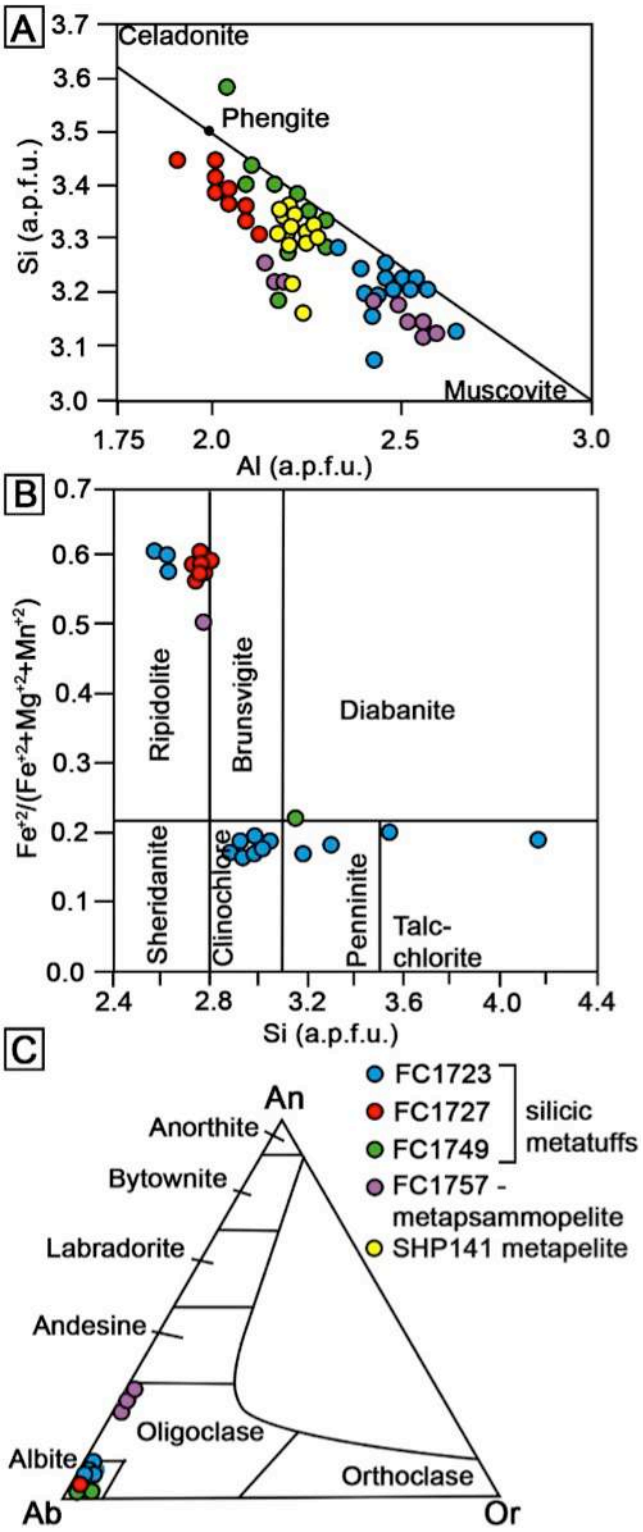

Figure 8: Diagrams of mineral chemical classification based on major element composition of white mica, chlorite, and feldspar, measured with the EPMA in samples FC1723. FC1727. FC1749 and SHP141: A) White mica solid solutions celadonite-phengite-muscovite based on Si (a.p.f.u.) versus Al (a.p.f.u.) (Ernst. 1963); B) chlorite compositions based on the ratio X_{Fe} versus Si (a.p.f.u.) (Foster. 1962); C) feldspar triangular diagram based on the alkali ratio X_{Na} with Anorthite – Albite – Orthoclase end members (Deer et al., 1963).

4.4.2. P-T Pseudosection Modelling

In the four selected samples the thermodynamic modelling was achieved in the TiMNCKMFASHO (TiO_2–MnO–Na_2O–CaO–K_2O–FeO–MgO–Al_2O_3–SiO_2–H_2O–O_2) system, within the range of pressures between 2 and 7 kbar and temperatures between 150

and 550°C. Bulk-rock compositions are presented in Tables 4 A (raw data) and 4 B (with corrections and normalization). The O_2 content is related to 10% of the iron to be trivalent suggested by the presence of magnetite in the rock. CaO was corrected due to presence of apatite. The percentage of oxides was normalized to 100% (Table 4 B). The H_2O content of each sample was based on the loss on ignition from the XRF analysis, with a maximum 4 wt% to guarantee a free hydrous fluid phase in the P-T pseudosection.

For the mylonitic silicic metatuff at Canal Gajardo (FC1749) the isopleths for Si = 3.36 a.p.f.u. in white mica (average value) and #Mg = 0.75 in chlorite (average value) intersect at ~3-4 kbar and ~210-250°C (Fig. 9 A). This is consistent with $X_{Na} > 0.95$ in plagioclase, predicted to be stable at temperature above 190ºC. At 3.5 kbar and 230°C the calculated volume percent of the mineral assemblage is quartz (46%), plagioclase (27%), white mica (16%), chlorite (3%), stilpnomelane (1%), clinopyroxene (0.2%), titanite (0.1%), plus water (6.7%). No rutile was detected under the microscope, but a good correspondence exists for major phases. Stilpnomelane and clinopyroxene were also not identified under the microscope; these minerals may have been decomposed by weathering, but other reasons for the presence of these phases in the calculation result such as imperfect solid-solution models are possible as well.

In the P-T pseudosection for the metapsammopelite with textures of contact metamorphism belonging to the Zapata Fm. at Canal Gajardo (FC1757) the intersection of the isopleths for Si = 3.18 a.p.f.u. in phengitic white mica (average value), the X_{Na} of 0.70 in plagioclase (average value), and Mg# of 0.44 in biotite (average = 0.42) match at ~5-6 kbar and 430-460°C (Fig. 9 B). At 5.5 kbar and 440°C the calculated volume percent of the mineral assemblage is quartz (55%), feldspar (19.5%), white mica (7%), biotite (2%), chlorite (3%), epidote (5%), and titanite (0.5%) plus water (8%). The isopleths of Mg# in chlorite (average = 0.48) do not intersect this field, probably because chlorite is not in equilibrium with biotite, phengite and plagioclase. According to the diagram, chlorite with of Mg# = 0.48 occur between temperatures of 230-250°C and may be result of retrograde metamorphism. Magnetite may be present as opaque mineral.

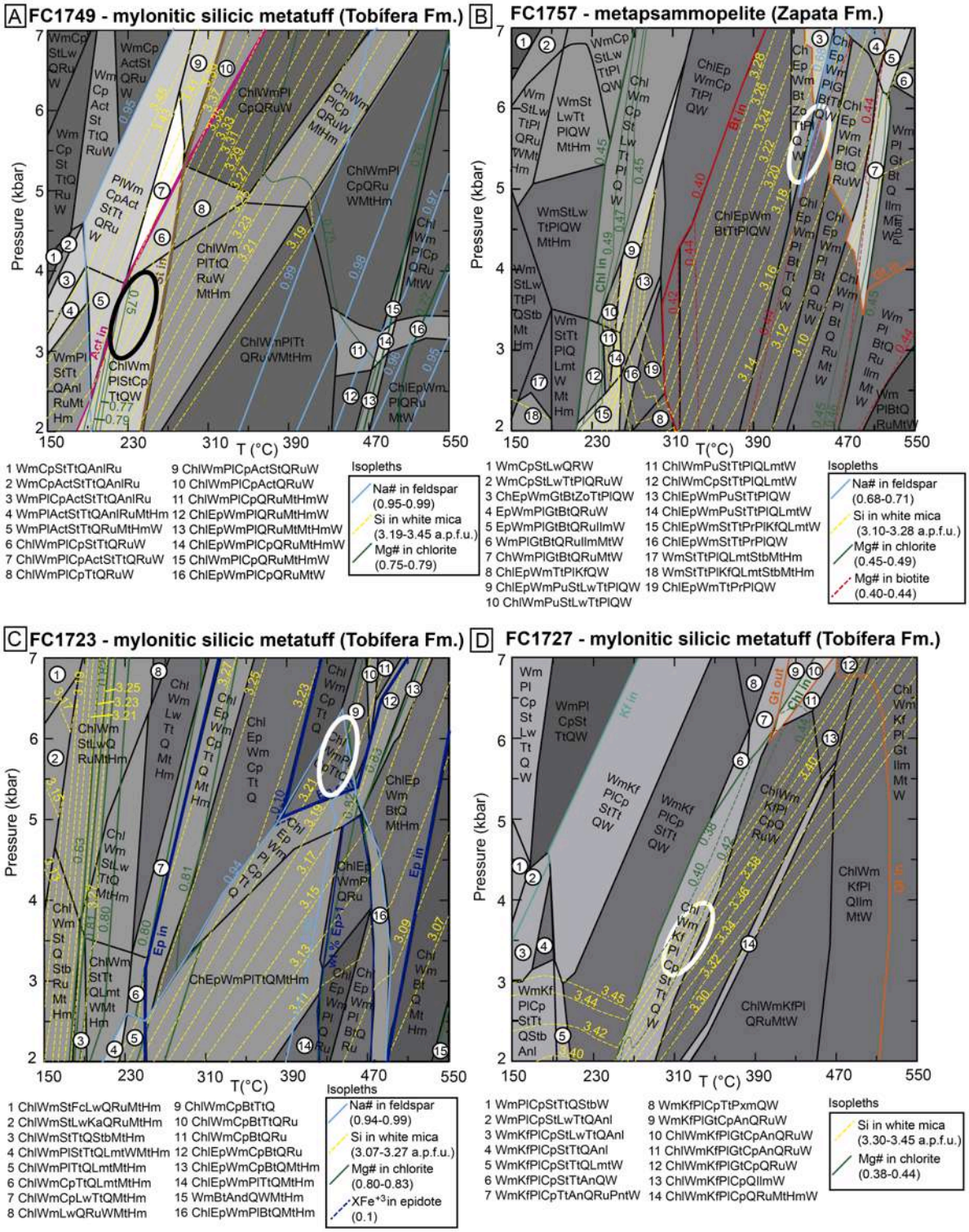

1 WmCpStTtQAnlRu
2 WmCpActStTtQAnlRu
3 WmPlCpActStTtQAnlRu
4 WmPlActStTtQAnlRuMtHm
5 WmPlActStTtQRuMtHmW
6 ChlWmPlCpStTtQRuW
7 ChlWmPlCpActStTtQRuW
8 ChlWmPlCpTtQRuW
9 ChlWmPlCpActStQRuW
10 ChlWmPlCpActQRuW
11 ChlWmPlCpQRuMtHmW
12 ChlEpWmPlQRuMtHmW
13 ChlEpWmPlQRuMtMtHmW
14 ChlEpWmPlCpQRuMtHmW
15 ChlWmPlCpQRuMtHmW
16 ChlEpWmPlCpQRuMtW

1 WmCpStLwQRW
2 WmCpStLwTtPlQRuW
3 ChEpWmGtBtZoTtPlQW
4 EpWmPlGtBtQRuW
5 EpWmPlGtBtQRuIlmW
6 WmPlGtBtQRuIlmMtW
7 ChWmPlGtBtQRuMtW
8 ChlEpWmTtPlKfQW
9 ChlEpWmPuStLwTtPlQW
10 ChlWmPuStLwTtPlQW
11 ChlWmPuStTtPlQLmtW
12 ChlWmCpStTtPlQLmtW
13 ChlEpWmPuStTtPlQW
14 ChlEpWmPuStTtPlQLmtW
15 ChlEpWmStTtPrPlKfQLmtW
16 ChlEpWmStTtPrPlQW
17 WmStTtPlQLmtStbMtHm
18 WmStTtPlKfQLmtStbMtHm
19 ChlEpWmTtPrPlQW

1 ChlWmStFcLwQRuMtHm
2 ChlWmStLwKaQRuMtHm
3 ChlWmStTtQStbMtHm
4 ChlWmPlStTtQLmtWMtHm
5 ChlWmPlTtQLmtMtHm
6 ChlWmCpTtQLmtMtHm
7 ChlWmCpLwTtQMtHm
8 ChlWmLwQRuWMtHm
9 ChlWmCpBtTtQ
10 ChlWmCpBtTtQRu
11 ChlWmCpBtQRu
12 ChlEpWmCpBtQRu
13 ChlEpWmCpBtQMtHm
14 ChlEpWmPlTtQMtHm
15 WmBtAndQWMtHm
16 ChlEpWmPlBtQMtHm

1 WmPlCpStTtQStbW
2 WmPlCpStLwTtQAnl
3 WmKfPlCpStLwTtQAnl
4 WmKfPlCpStTtQAnl
5 WmKfPlCpStTtQLmtW
6 WmKfPlCpStTtAnQW
7 WmKfPlCpTtAnQRuPntW
8 WmKfPlCpTtPxmQW
9 WmKfPlGtCpAnQRuW
10 ChlWmKfPlGtCpAnQRuW
11 ChlWmKfPlGtCpAnQRuW
12 ChlWmKfPlGtCpQRuW
13 ChlWmKfPlCpQIlmW
14 ChlWmKfPlCpQRuMtHmW

Figure 9: Calculated P-T pseudosections and selected isopleths for the analyzed samples with ellipses indicating the estimated P-T field of regional metamorphism: A) mylonitic silicic metatuff (FC1749,Tobífera Fm.) - P-T at ~3-4 kbar and ~210-250 °C; B) metapsammopelite (FC1757, Zapata Fm.) - P-T at ~5-6 kbar and ~430-460 °C, the maximum T may be related with contact metamorphism; .C) mylonitic silicic metatuff (FC1723, Tobífera Fm.) - P-T at ~5.3-6.3 kbar and ~420-460 °C; D) mylonitic silicic metatuff (FC1727, Tobífera Fm.) - P-T at ~3-4 kbar and ~300-340 °C. Mineral abbreviations: Wm - white mica; Chl - chlorite; Kf - alkali feldspar; Pl - plagioclase; Cp - clinopyroxene; Ep - epidote; St - stilpnomelane; Bt - biotite; Tt - titanite; Gt - garnet; Q - quartz; Act - actinolite; Lw - lawsonite; Stb - stilbite; Anl - analcite; Ilm - ilmenite; Fc - carpholite; Mt - magnetite; Hm - hematite; Lmt - laumontite; Zo - zoisite; Ru - rutile; And - andalusite; An - annite; Ka - kaolinite; Pu - pumpellyite; Pr - prehnite; Pnt - pyrophanite; Pxm - pyroxmangite; W - water.

In the P-T pseudosection for mylonitic silicic metatuff at Canal Jerónimo (FC1723) the intersection of the isopleths for Si = 3.21 a.p.f.u. in phengite (average value), X_{Na} = 0.99 in plagioclase (average value), Mg# = 0.82 in chlorite (clinochlore, average value) match at ~5.3-6.3 kbar and 420-460°C (Fig. 9 C). At 6 kbar and 450°C the calculated mineral assemblage is: quartz (55%), white mica (31%), chlorite (10%), plagioclase (0.5%), clinopyroxene (0.5%), plus water (3%). The disappearance of trace amounts of predicted clinopyroxene could be related to thermal increase accompanied by rising albite and epidote modal contents. However, an imperfect thermodynamic solid-solution model for Na-bearing clinopyroxene or other factors (e.g., selected O_2 content) could also account for the appearance of low amounts of clinopyroxene in the calculation results.

In the P-T pseudosection calculated for mylonitic silicic metatuff FC1727 the intersections of the isopleths for Si = 3.36-3.45 a.p.f.u. in phengite (average = 3.38), and Mg# between 0.40 and 0.42 in chlorite (average = 0.40) occur in the range 3-4 kbar at 300-340°C (Fig. 9 D). In consideration of plagioclase being almost pure albite, these conditions probably refer to the metamorphic peak. The calculated mineral assemblage at 3.8 kbar and 330°C is quartz (42%), plagioclase (30%), alkali feldspar (7%), white mica (13%), chlorite (2%), clinopyroxene (0.4%), titanite (0.2%), plus water (5.4%). Clinopyroxene and titanite were not identified in the petrographic thin section, maybe due to weathering. A good correspondence exists for major phases.

5. Discussion

5.1. Episodic magmatism and paleogeography of the Rocas Verdes Basin

The timing of magmatism during the Late Jurassic evolution of the RVB sheds important light on along-strike development of the extensional marginal basin during its ca. 40-50 myr history in southern South America. Our new ca. 160 Ma U-Pb zircon age from the silicic metatuff at Estero Wickham (FC1727 of the Tobífera Fm., Fig. 2 and 6 A) constrains the maximum depositional age of precursor silicic tuffs of the Tobífera Fm. It brings the age of Tobífera explosive silicic volcanism to the early Late Jurassic (Oxfordian) at this latitude of the orogenic system (~53°30'S). At this time, the Patagonian continental block (linked to South America) must have had continental connection with the Kalahari Craton to the northeast and the East Antarctic Craton to the southwest (Fig. 10 A, Dalziel et al., 2013).

Three older zircons of ca. 168 Ma and one of ca. 185 Ma (Fig. 6 A) likely reflect xenocrystic inheritance or reworking of zircons from different Jurassic volcano-sedimentary sources. The Upper Triassic date in the diffuse core of one zircon was either incorporated into the original rhyolitic magma by upper crustal assimilation processes, or included into the pyroclastic and/or volcanoclastic deposits, during erosion of pre-Jurassic basement complexes.

Near Canal Jerónimo (~53°S) the ca. 157 Ma crystallization age of gabbros belonging to the *South Patagonian Batholith* (Hervé et al., 2007a) – at that time representing the parautochthonous magmatic arc to the west of the RVB (Fig. 10 A) – suggest coeval bimodal magmatism between 160-155 Ma. Clearly younger silicic magmatism is reported in northern areas (~49°-52°S), with Tithonian-Berriasian U-Pb zircon ages from metatuffs and hypabyssal rhyolitic rocks of the Tobífera Fm. ranging between ca. 154 and 140 Ma (Pankhurst et al., 2000; Calderón et al., 2007; Malkowski et al., 2015a; Zerfass et al., 2017), and ca. 150 Ma bimodal igneous suites of the *Sarmiento Ophiolitic Complex* (~51°30'S; Calderón et al., 2007). In extra-Andean Patagonia, silicic volcanic and volcaniclastic rocks buried beneath the sedimentary in-fill of the Magallanes-Austral basin (~53°S) have been dated at ca. 176 Ma (Pankhurst et al., 2000). Farther south, coeval and slightly older metatuffs at Cordillera Darwin (~55°S, Fuegian Andes) range in age between ca. 168 and ca. 162 Ma (Hervé et al., 2010b; Klepeis et al., 2010).

In this context, our ca. 160 Ma age reveals older rift-related volcanic events to the south of the RVB, and an episodic character of silicic volcanism during continental rifting. This finding may indicate that silicic magmatism and basin accommodation for deposition of volcanic rocks was controlled by the pre-Jurassic lithosphere-scale structures within the continental basement. Furthermore, our chronological data agree with northward younging ages that support the south to north unzipping mode of the opening of the RVB (cf. Stern and De Wit, 2003; Malkowski et al., 2015a), at least for the Patagonian sector of the southernmost Andes. However, ages of mafic magmatism in the southernmost ophiolitic complexes located in Larsen Harbor (South Georgia Island), constrained by U-Pb zircon in plagiogranites, yielded crystallization ages of ca. 150 Ma (Mukasa and Dalziel, 1996), similar to the northern Sarmiento Ophiolitic Complex (Calderón et al., 2007). The progressive widening of the RVB and development of mid-ocean-ridge type spreading centers was established in Tierra de Fuego even later, with the emplacement of the Tortuga Ophiolitic Complex between 130-120 Ma (Calderón et al., 2013). Therefore, the silicic magmatism within the RVB seems to have been episodic during the rift-related opening of the RVB controlled by inherited basement structures, and subsequent seafloor spreading in mid-ocean-

ridge type centers to the south-west (Fig. 10 A). The opening of the RVB is partially coeval with the opening of the Weddell Sea and the massive extension between South America and Africa that starts at ca. 130 Ma (Dalziel et al., 2013, Poblete et al., 2016).

The youngest cluster of detrital zircon dates of the metapsammopelite at Canal Gajardo (FC1754; Zapata Fm.) indicates a maximum depositional age of ca. 125 Ma at these latitudes (~52°30'-53°S). This age is coherent with the Barremian-Albian (ca. 130-100 Ma) age interval of the sandy upper sections of the Zapata/Erezcano and Beauvoir/Yaghan formations (Fildani et al., 2003; Calderón et al., 2007; Fosdick et al., 2011; Barbeau Jr. et al., 2009; Klepeis et al., 2010; Hervé et al., 2010b; Malkowski et al., 2015b), in southern Patagonia and Tierra del Fuego, respectively. The dominant detrital zircon age clusters (ca. 130 ± 1 Ma and 124 ± 1 Ma) suggest their derivation from volcanic and plutonic rocks from the westernmost magmatic arc now exposed in the *South Patagonian Batholith* (Hervé et al., 2007a). The secondary Paleozoic and subordinate older zircon populations indicate recycling of the pre-Jurassic basement complexes, with similar pre-Jurassic detrital zircon age distribution to those of metamorphic complexes in southern Patagonia (Hervé et al., 2003, 2008). This correlation accounts for incipient exhumation of the basement complexes during continental lithospheric stretching (Fig. 10 A), which may have shed sediments to the depocenters of the RVB (Fildani et al., 2003; Calderón et al., 2007).

5.2. Mylonites from the *Western Domain* of the MFTB and the *Eastern Tobífera Thrust*: underthrusting of the RVB and craton-ward transfer of shortening

Retro-arc deformation across the MFTB is linked to closure and inversion of the RVB that transferred shortening from southwest to northeast, leading to orogenic widening and consolidation. However, few through-going tectonic structures associated with RVB closure have been correlated along this orogenic belt. The mylonitic rocks from the Tobífera and Zapata formations located in the hanging wall of the *Eastern Tobífera Thrust* (~52°-54°S; Figs. 2, and 3 A2 and B2) and from the *Canal de las Montañas Shear Zone* (~51°-52°S; Calderón et al., 2012, Fig. 1) share craton-ward sense of shearing, low-grade metamorphic conditions, and a Late Cretaceous age. Taken together, we thus interpret these shear zones as a single continuous structure that extends from 51°S to 54°S within Tobífera and Zapata lithotypes, formed during the tectonic burial of the RVB successions. The *Canal de las Montañas Shear Zone* represents the sole thrust of the tectonic emplacement of the *Sarmiento Ophiolitic Complex* over the continental margin (Calderón et al., 2012). Here, we suggest that

the mylonitic zones on top of the *Eastern Tobífera Thrust* also have a relevant role in the progressive underthrusting of oceanic and continental crust of the RVB (Fig. 10 B).

A partitioned deformation is observed in the mylonites of the *Western Domain*, where more competent quartz-feldspathic metatuffs experienced brittle-ductile deformation whereas less competent mica-rich metapelites and metapsammopelites exhibit dominant ductile features (*sensu* Hirth and Tullis, 1994). The coexistence of brittle and ductile structures suggest deformation at intermediate depths (~10 – 20 km depth, according to Stipp et al., 2002; Fossen and Cavalcante, 2017). The pervasive S_1* foliation in these lithotypes is seemingly related to northeast-vergent simple shearing dominated by pressure-solution processes.

The westward increase in the magnitude of ductile deformation across the strike of the *Western Domain* of the MFTB is interpreted from mesoscopic and microscopic observations at Canal Gajardo, regardless of the lithology. At the innermost part of the *Western Domain* tight folding of the S_1* foliation occurred, and transposition zones developed through the axial planar S_2* foliation. The S_1* and S_2* foliations are sub-parallel to thrusts that mark the contacts between thrust sheets of Zapata and Tobífera formations, mafic ophiolitic bodies, and the pre-Jurassic basement complexes (Figs. 2 and 3 A1). Enhanced ductile deformation can be due to a release of fluids from dehydrated protoliths (metasedimentary and metavolcanic rocks) through deep shear zones, which may form an underthrusting interface (Tullis et al., 1982, 1996; van Staal et al., 2001; Massonne and Willner, 2008; Roche et al., 2018). In addition, magmatic hydrothermal fluids and increasing temperature may be due to the emplacement of satellite plutons of the *South Patagonian Batholith*. Thus, the development of S_1* and S_2* must have occurred in deep shear zones with hot fluid circulation within the RVB succession being underthrusted westwards beneath the parautochthonous magmatic arc (Fig. 10 B).

A critical wedge geometry is proposed from mechanical models of fold-and-thrust belts (Davis et al., 1983; Dahlen, 1990) and previous hypotheses regarding the RVB closure (Nelson et al., 1980; Gealey et al., 1980; Kohn et al., 1995; Harambour, 2002; Hervé et al., 2007b; Calderón et al., 2009, 2012; Klepeis et al., 2010). In pre-Jurassic metasedimentary rocks the S_2 foliation is subparallel to the RVB S_1* foliation. The time of formation of the S_2 foliation in the pre-Jurassic basement is not clear, but the correlation with the ductile structures of the RVB suggest a common Andean deformational event, in which the pre-Jurassic basement was underthrusted together with the RVB successions.

The *Eastern Tobífera Thrust* delimitates the mylonitic zones of the *Western Domain* of the MFTB in the east, emplacing brittle-ductile sheared rocks from the RVB over the Zapata rocks that show no ductile deformation nor metamorphism (Figs. 2 and 3). The uplift of deep ductile structures of the MFTB is ascribed to out-of-sequence craton-vergent thrusting and trench-vergent backthrusting from the end of Late Cretaceous to the early Oligocene (Nelson et al., 1980; Kohn et al., 1995; Harambour, 2002; Kraemer, 2003; Hervé et al., 2007b; Calderón et al., 2009, 2012; Klepeis et al., 2010; Maloney et al., 2011; Fosdick et al., 2011; Betka et al., 2015). The origin of the *Eastern Tobífera Thrust* may be associated with this protracted deformational event of uplift of the MFTB, and represents an important surface of juxtaposition of the deeply deformed successions with shallowly deformed successions (Fig. 10 C). Cross-cutting structures between the first-generation structures, resulting from the phase of deep underthrusting of the RVB, and the second-generation structures, resulting from the uplift of the MFTB are locally found (Betka et al., 2015). Inherited structures from the rift phase in the basement are reactivated during thrusting and backthrusting (Fig. 10 C), allowing the transfer of deformation to the east onto the Upper Cretaceous foreland basin (Nelson et al., 1980; Harambour, 2002; Rapalini et al., 2008; Fosdick et al., 2011; Betka et al., 2015). The reactivation of inherited faults in the basement and imbrication of the basement slices in the *Western Domain* of the MFTB resulted in a thick-skinned deformation superimposed to an early thin-skinned deformation (*sensu* Lacombe and Bellasen, 2016).

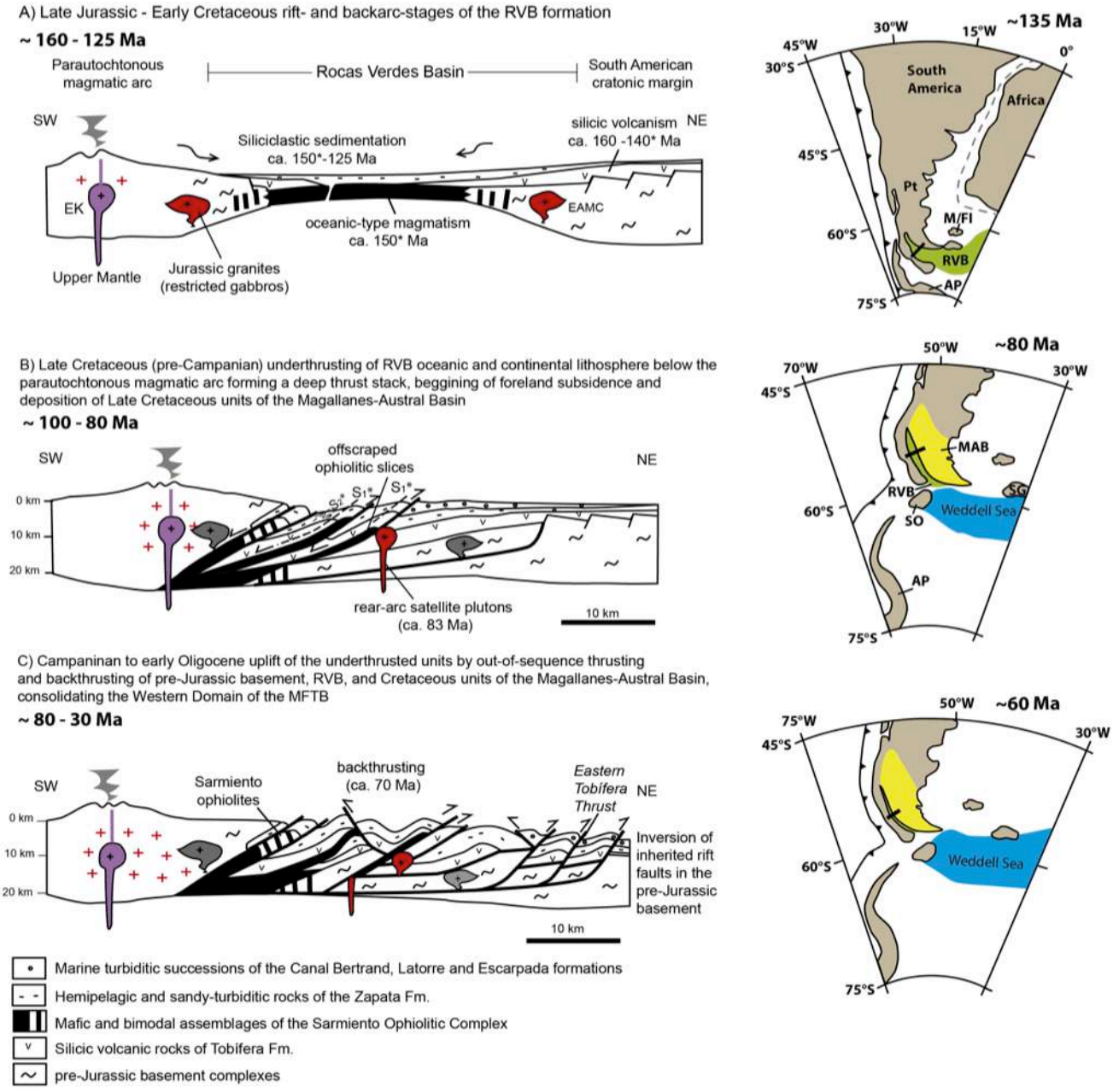

Figure 10: Schematic SW-NE geologic cross sections summarizing the proposed tectonic evolution of the RVB and the Patagonian orogenic belt between the latitudes 52 to 54°S. Respective paleogeographic reconstructions adapted from Dalziel et al. (2013) and Poblete et al. (2016) are shown on the right hand side with the approximated location of cross-sections indicated by a black bold line. Abbreviations: AP – Antarctic Peninsula, MAB – Magallanes-Austral Basin, M/FI – Malvinas/Falkland Islands, SG: South Georgia Island, SO: South Orkney Island, Pt – Patagonia, RVB – Rocas Verdes Basin. A) Late Jurassic to Early Cretaceous phases of opening of RVB due to rifting and coeval silicic volcanism of the Tobífera Fm.; seafloor spreading of the Rocas Verdes oceanic lithosphere; and the hemipelagic and siliciclastic sedimentation of the Zapata Fm. from sources including the incipient *South Patagonian Batholith*, pre-Jurassic basement horsts, and Tobífera topographic highs. The dashed line in the paleogeographic reconstruction is the approximated continental boundary between South America and Africa before the opening of the Atlantic Ocean, which starts at ca. 130 as well as the Weddel Sea opening. B) Late Cretaceous pre-Campanian underthrusting of the oceanic and continental lithosphere of the RVB beneath the parautochthonous magmatic arc. During this time, a northeast verging underthrusted crustal stack developed, reaching ~23 km depth (as recorded by samples that underwent greenschist-facies metamorphism). Offscraping of ophiolitic slices occurred along shear zones with fluids from dehydrated buried rocks. The development of S_1* foliation formed due to shearing in ductile shear zones and its crenulation within inner zones of the belt generated transposition by the S_2* foliation. In the paleogeographic reconstruction the yellow area represents the sediments of the Magallanes-Austral Basin, the Weddell Sea is in a

relatively quiet period, and the Antarctic Peninsula and the South Georgia Island are separated from the South American continent. C) Campanian to early Oligocene phase of uplift and exhumation of the underthrusted crustal stack by of out-of-sequence thrusting and backthrusting within the RVB successions, the location of the Eastern Tobífera Thrust is approximated. Inversion of inherited normal faults account for imbrications with the pre-Jurassic basement and resulted in a thick-skinned arrangement of the Western Domain of the MFTB, which transferred deformation to the Upper Cretaceous units of the Magallanes-Austral Basin.

5.3. Timing and thermobarometric conditions during the closure of the Rocas Verdes Basin

The development of brittle-ductile and ductile mylonitic fabrics in tectonically buried supracrustal rocks is controlled by the local geothermal gradient, plate boundary conditions, and the lithology of buried rocks (Ernst, 1971, 1972; Miyashiro, 1973; Tullis et al., 1982; Maruyama et al., 1996; Hirth and Tullis, 1994; Stipp et al., 2002; Wakabayashi and Dilek, 2003; Massonne and Willner, 2008; Fossen and Cavalcante, 2017). The mylonitic metatuffs of the *Western Domain* present a phengite+chlorite+quartz+albite metamorphic assemblage forming the S_1* foliation, typical of low-temperature metamorphic belts (McNamara, 1965; Vidal and Parra, 2000; Massonne and Willner, 2008; Bucher and Grapes, 2011). Pseudosection modelling shows that the metatuff at Canal Gajardo (FC1749) experienced prehnite-pumpellyite-facies metamorphism (~3-4 kbar and 210-250ºC), whereas the metatuff at Estero Wickham (FC1727) was metamorphosed at greenschist-facies conditions (~3-4 kbar and 300-340°C). Higher P-T conditions of greenschist-facies metamorphism (~ 5.3-6.3 kbar and 420-460°C) compared with the other analyzed metatuffs were estimated for the metatuff at Canal Jeronimo (FC1723). These P-T conditions are similar to those derived for the metapsammopelite at Canal Gajardo (FC1757, ~5-6 kbar and 430-460°C) based on the compositions of non-oriented biotite, muscovite, and plagioclase that overprinted oriented and folded bands of dynamically recrystallized quartz. From this textural feature, we interpret the estimated P-T conditions as recording local contact metamorphism in the metapsammopelite. The similarity between the P-T conditions estimated for samples FC1723 and FC1757 could mean that the metatuff of Canal Jeronimo was slightly affected by contact metamorphism as well, explaining the occurrence of randomly oriented epidote in the metatuff. Although contact metamorphism may have affected these rocks locally, systematic pressure increases with temperature suggest a geotherm of regional metamorphism through about 3.5 kbar and 280°C, and 5.5 kbar and 430°C.

P-T constraints broadly agree with those derived for rocks in the *Canal de las Montañas Shear Zone* (~ 250-400°C, 6-7 kbar; Hervé et al., 2007b; Calderón et al., 2012). Thus we associate these and the studied rocks with a ~ 400 km long mylonitic and

metamorphic belt of the Patagonian sector of the MFTB. Assuming intermediate geothermal gradients (~20°C/km; Miyashiro, 1973; Maruyama et al., 1996; Zheng et al., 2016) these rocks reached crustal depths between 10-23 km (Fig. 10 B). The dehydration of volcanic and sedimentary successions at depths of ~20 km would have released fluids that circulated along major thrusts, thereby favoring the offscraping and imbrication of ophiolitic tectonic slices in the underthrusted crustal stack (Massonne and Willner, 2008). These units crop out at Canal Gajardo (Figs. 1 and 2 A).

The metapsammopelite belonging to the Zapata Fm. at Canal Gajardo is located near the ca. 83 Ma quartz diorite pluton (FC1754), which is hypothesized here as the source of local thermal perturbation. With this interpretation on the timing of the thermal perturbation, combined with the fact that both the dated quartz diorite and the metamorphic minerals in the metapsammopelite are undeformed, we use this age constraint as the minimum age of dynamic recrystallization of the foliated bands (at least S1*) at Canal Gajardo. Similarly, Santonian-Campanian crystallization ages of satellite plutons emplaced in the *Western Domain* of the MFTB to the north of the study area (ca. 85-80 Ma between 51-52°S) and in the Fuegian Andes (ca. 86 Ma between 54-55°S), were interpreted as the minimum age of RVB underthrusting (Klepeis et al., 2010; Calderón et al. 2012). However, some of the Late Cretaceous satellite plutons near the study region show anisotropic fabrics near pluton margins, indicating that crustal deformation proceeded during the magmatic arc construction (Hervé et al., 2007a; Klepeis et al., 2010; Fosdick et al., 2011; Betka et al., 2015). Deep shear zones may control the ascent of the back-arc plutons especially during the extensional phases after orogenic thickening (Laurent et al., 2015). In this context, the analyzed quartz-diorite was likely emplaced after (or possible during the later stages of) the phase of underthrusting of the RVB units (that generated the S_1* foliation). The absence of deformational fabrics observed within the quartz diorite sample suggests that deformation migrated to shallower crustal levels some time before 83 Ma, and/or that the deformed parts of the intrusion and imbricated units of RVB were eroded or obscured by cover. Finally, we note that the ca. 83 Ma age is coeval with a pronounced zircon U-Pb age peak (ca. 80-66) present in detrital zircon age spectra from the Cenozoic Magallanes-Austral Basin successions (Fosdick et al., 2020), thereby providing additional indirect evidence for this phase of Late Cretaceous arc magmatism.

The syntectonic phengite of a mylonitic metapelite from the western part of Canal Gajardo yields a cluster of $^{40}Ar/^{39}Ar$ dates at ca. 70 Ma, with an older single-grain ages as old as ca. 73 Ma. We note that the grain size of phengite (up to 100 μm) is too small for any

chemical zoning of micas relating to different episodes of crystallization to be recognized. Additionally, this age variability also may have been caused by a combination of analytical uncertainty, deformation, grain boundary effects and geological variability in the micas. The mineral assemblage in the sample is phengite+chlorite+zoisite+albite, which is consistent with greenschist-facies conditions of regional metamorphism, in accordance with P-T constraints from mylonitic rocks of the *Western Domain* (of ~3-6 kbar and ~210-460 °C). Under the assumption that Ar mobility is mainly linked to thermally controlled volume diffusion, the retention of radiogenic Ar depends on the crystal size and temperature of metamorphism (Warren et al., 2012). In 100 μm grains, the retention of radiogenic Ar at temperatures < 350°C (the average estimated regional temperature) over 2 mya is between 90-95%. However, at ~460 °C (the maximum regional temperature), Ar retention would decrease to ~35% over the same time interval (Warren et al., 2012). A possible reheating event may therefore have caused partial resetting of the deformational age. However, the recorded age is considerably younger than the nearby intrusion (ca. 83 Ma), what also reinforces the fact that the analysed quartz-diorite sample is from the inner undeformed part of the pluton and that its external parts could be deformed.

Our preferred interpretation is that the 70 Ma phengite age records the timing of syntectonic mineral growth during deformation. This interpretation is consistent with Coniacian-Maastrichtian $^{40}Ar/^{39}Ar$ dates in metamorphic minerals and U-Pb dates in monazite recorded in the *Cordillera Darwin Metamorphic Complex*, which have been interpreted as recording the timing of deformation (Kohn et al., 1995; Maloney et al., 2011). Ductile thrusting in this complex operated at deep structural levels (~35 km) between 90-70 Ma, while backthrusting was concentrated in the shallow structural levels during the same interval (Kohn et al., 1995; Klepeis et al., 2010; Maloney et al., 2011). We thus interpret the ca. 73-70 Ma $^{40}Ar/^{39}Ar$ dates as recording the timing of deformation during the protracted exhumation history of mylonite belts in both the southern Patagonian and Fuegian Andes, but without further data the meaning of the dates older than 71 Ma cannot be tested. Campanian-Maastrichtian dynamic recrystallization in shallow crustal depths is consistent with the phase of out-of-sequence thrusting and backthrusting occurring until the early Oligocene (Kohn et al., 1995; Kraemer, 2003; Klepeis et al., 2010; Maloney et al., 2011; Fosdick et al., 2011; Betka et al., 2015), associated with the formation of the *Eastern Tobífera Thrust*. This episode is related to the uplift and extrusion of the underthrusted crustal stack in the *Western Domain* of the MFTB (Fig. 10 C). In the paleogeographic context, the Weddell Sea was in a relatively quiet tectonic period until 60 Ma, the Antarctic Peninsula was separated from South

America and the ophiolite-bearing South Georgia Island was displaced to the east of the Fuegian Andes (Fig. 10 B-C; Gee and Kent, 2007; Dalziel et al., 2013; Poblete et al., 2016).

Finally, the phases of deformation and metamorphism that occurred between the Santonian and Maastrichtian reflects different magnitudes of hinterland exhumation between the southern Patagonian and Fuegian Andes. Along-strike of the southern Patagonian Andes (51°-54°S), linking our study region with the *Canal de las Montañas Shear Zone*, the exhumation of low-grade metamorphic rocks, dynamically recrystallized at crustal depths ranging between ~10 and 23 km, begins between ca. 83-70 Ma. Contrastingly, in the Fuegian Andes (54°-56° S) the metasedimentary rocks of the *Cordillera Darwin Metamorphic Complex* – a unique culmination of Paleozoic to Lower Cretaceous sedimentary successions metamorphosed at upper amphibolite facies during the Cretaceous – indicate exhumation of deeply buried rocks formed at ~35 km depth before ca. 73 Ma (Kohn et al., 1993, 1995; Klepeis et al., 2010; Maloney et al., 2011). Thus, the thermobarometric constraints show that the tectonic underthrusting of the RVB successions before the Campanian due to arc-continent collision involved deep shear zones, which were uplifted during the Late Cretaceous and Paleogene with a higher magnitude in the Fuegian Andes.

6. Conclusions

New field data, microstructural analysis, thermobarometry, U-Pb and $^{40}Ar/^{39}Ar$ geochronology from the southern Patagonian Andes provide kinematic, P-T, and time constraints on the opening and closure of the RVB. Zircon U-Pb ages constrain the maximum depositional ages of episodic silicic volcanism at ca. 160 Ma, and the hemipelagic sedimentation to ca. 125 Ma. The geographical distribution of silicic volcanic rocks in sub-basins, controlled by the geometry of pre-Jurassic rifting structures within the continental basement, was followed by mafic magmatism in mid-ocean ridge-type spreading centers located to the west and southwest of the paleo-continental margin. New microstructural data and P-T metamorphic constraints of 3-6 kbar and ca. 210-460°C in mylonitic silicic volcanic and metapsammopelitic rocks of RVB are compatible with tectonic underthrusting of the RVB's oceanic and continental crust in a deep crustal stack. West- and southwest-ward shear zones recorded in at least one brittle-ductile foliation (S_1*) in the *Western Domain* of the MFTB suggests tectonic accretion during the RVB closure, indicating tectonic burial to 10-23 km depths beneath the edge of the parautochthonous magmatic arc. The mylonitic and metamorphic belt extending from the *Canal de las Montañas Shear Zone* to the study area

(~50-54ºS) constitute a ~400 km long lithospheric-scale structure that accommodated east- and northeast-verging shearing beneath the underthrusted crustal stack. Deformation migrated from this structure to shallow crustal levels prior to ca. 83 Ma, when Campanian satellite intrusions of quartz diorite caused contact metamorphism in the foliated metavolcano-sedimentary rocks. Finally, the ca. 70-73 Ma $^{40}Ar/^{39}Ar$ syntectonic phengite ages suggest a phase of Campaninan-Maastrichtian out-of-sequence thrusting and backthrusting, culminating with uplift and exhumation of the *Western Domain* of the MFTB.

7. Acknowledgements

This work was funded by the Fondecyt Project Nº 1161818 in Chile and by LAMIR/UFPR/PETROBRAS Research Project Nº 2016/00141-1 in Brazil. Special thanks to Alison Halton (The Open University) by the ^{40}Ar-^{39}Ar data processing, Andrea Stevens Goddard (Indiana University), Fernanda Torres (Andrés Bello University) and Diego Rojo (Arturo Prat University) for their support during field work, and the crew of the Marypaz II that made possible the navigation through the Patagonian fjords. We also thank all LAMIR (Federal University of Paraná) team for their technical and intellectual support during this research. Salvador Harambour kindly provided field data and the sample SHP141. This study is also part of the project MIUR – Dipartimenti di Eccellenza 2018–2022, Department of Earth and Environmental Sciences, University of Milano-Bicocca. PS was supported by the Italian MIUR (Rita Levi Montalcini grant, DM 694-26/2017). We acknowledge outstanding revisions and suggestions by Valentin Laurent, an anonymous reviewer, and the editor Philippe Agard.

TABLES:

Table 1: List of *in situ* oriented samples showing the attitude of foliation corresponding to S_1* in RVB units, the thin section orientation, and the respective shear sense interpreted from asymmetric microtectonic and/or mesoscale structures. The attitudes are dip direction/dip angle.

Locality	Coordinates	Unit	Lithology	Sample	S_0	S_1*	Thin section	Plane	Shear sense
Canal Jerónimo	S53° 22.038' W72° 25.660'	pre-Jurassic basement	Metapelitic schist	FC1721		235 32	199 55	xz	NE
Isla Santa Cruz (Canal Jerónimo)	S53° 12.592' W72° 28.992'	Tobífera Fm.	Mylonitic metatuff	FC1723		265 85	309 31	yz	NE-sinistral
Estero Wickham	S53° 25.090' W72° 09.259'	Tobífera Fm.	Mylonitic metatuff	FC1727		230 25	89 90	xz	NE
Estero Wickham	S53° 23.663' W72° 07.333'	Tobífera Fm.	Metapsammite	FC1729		175 28	119 60	xz	NE
Estero Wickham	S53° 18.979' W72° 06.379'	Latorre Fm.	Slate	FC1731	170 9	10 22	189 75	xz	NE
Canal Gajardo	S52° 43.218' W72° 43.841'	Tobífera Fm.	Mylonitic metatuff	FC1749		230 25	296 80	xz	NE
Canal Gajardo	S52° 45.421' W72° 46.252'	pre-Jurassic basement	Metapsammopelitic schist	FC1753		230 49	158 90	xz	N
Canal Gajardo	S52° 51.004' W72° 58.737'	Sarmiento Ophiolite	Foliated metabasalt	FC1763		225 20	349 85	yz	N
Canal Gajardo	S52° 51.004' W72° 58.737'	Sarmiento Ophiolite	Foliated metabasalt	FC1765		25 45	159 80	yz	NE

Table 2 A: SHRIMP U-Pb results for zircon crystals within the silicic metatuff of the Tobífera Fm. (FC1727) at Estero Wickham.

							Total			Radiogenic			Age (Ma)	
Grain.	**U**	**Th**	**Th/U**	**^{206}Pb***	**^{204}Pb/**	**f206**	**^{238}U/**		**^{207}Pb/**		**^{206}Pb/**		**^{206}Pb/**	
spot	**(ppm)**	**(ppm)**		**(ppm)**	**^{206}Pb**	**%**	**^{206}Pb**	**±**	**^{206}Pb**	**±**	**^{238}U**	**±**	**^{238}U**	**±**
1.1	411	249	0.61	8.9	0.000336	0.14	39.80	0.48	0.0504	0.0011	0.0251	0.0003	159.8	1.9
2.1	299	133	0.45	6.5	-	0.35	39.55	0.49	0.0520	0.0012	0.0252	0.0003	160.4	2.0
2.2	3035	1556	0.51	66.1	0.000090	0.68	39.47	0.44	0.0547	0.0030	0.0252	0.0003	160.2	1.9
3.1	154	66	0.43	3.3	0.000270	<0.01	39.87	0.56	0.0489	0.0019	0.0251	0.0004	159.8	2.3
3.2	476	264	0.55	9.9	0.000107	0.01	41.28	0.50	0.0492	0.0009	0.0242	0.0003	154.3	1.9
4.1	426	239	0.56	9.4	-	0.31	39.06	0.46	0.0517	0.0010	0.0255	0.0003	162.5	1.9
4.2	1776	922	0.52	38.6	0.000027	0.07	39.49	0.41	0.0498	0.0004	0.0253	0.0003	161.1	1.7
5.1	2689	1582	0.59	60.8	0.000012	<0.01	37.97	0.39	0.0490	0.0004	0.0263	0.0003	167.7	1.7
6.1	3119	1607	0.52	70.3	0.000043	<0.01	38.11	0.39	0.0489	0.0003	0.0263	0.0003	167.1	1.7
7.1	571	388	0.68	12.3	0.000022	0.11	39.82	0.46	0.0502	0.0008	0.0251	0.0003	159.7	1.8
8.1	262	151	0.58	5.6	0.000478	0.34	40.48	0.51	0.0519	0.0013	0.0246	0.0003	156.8	2.0
8.2	1563	602	0.39	33.0	0.000072	0.03	40.64	0.43	0.0494	0.0005	0.0246	0.0003	156.7	1.7
9.1	332	212	0.64	7.1	-	<0.01	40.16	0.49	0.0492	0.0011	0.0249	0.0003	158.5	1.9
10.1	831	491	0.59	18.4	0.000155	0.34	38.89	0.42	0.0520	0.0007	0.0256	0.0003	163.1	1.8
10.2	2490	1368	0.55	54.8	0.000024	<0.01	39.02	0.41	0.0487	0.0004	0.0256	0.0003	163.3	1.7
11.1	237	133	0.56	5.1	0.000256	0.26	40.22	0.53	0.0513	0.0013	0.0248	0.0003	157.9	2.1
12.1	385	203	0.53	8.5	0.000129	0.12	38.79	0.46	0.0503	0.0010	0.0258	0.0003	163.9	1.9
13.1	420	215	0.51	9.0	0.000180	0.15	40.03	0.50	0.0504	0.0010	0.0249	0.0003	158.8	2.0
14.1	457	250	0.55	9.8	0.000134	0.25	39.94	0.46	0.0513	0.0009	0.0250	0.0003	159.0	1.8
15.1	151	70	0.46	3.8	0.002035	1.08	33.64	0.52	0.0584	0.0020	0.0294	0.0005	186.8	2.9
16.1	190	83	0.44	4.1	0.000334	0.34	39.95	0.54	0.0520	0.0015	0.0249	0.0003	158.8	2.2

17.1	615	387	0.63	13.5	0.000130	<0.01	39.20	0.44	0.0493	0.0008	0.0255	0.0003	162.4	1.8
18.1	609	373	0.61	12.9	0.000156	<0.01	40.62	0.47	0.0482	0.0008	0.0246	0.0003	157.0	1.8
19.1	264	91	0.35	8.4	-	0.01	27.03	0.33	0.0510	0.0010	0.0370	0.0005	234.1	2.8
20.1	1250	1063	0.85	28.5	0.000022	0.03	37.70	0.40	0.0497	0.0005	0.0265	0.0003	168.7	1.8
21.1	628	463	0.74	13.6	0.000281	0.17	39.75	0.50	0.0506	0.0008	0.0251	0.0003	159.9	2.0
22.1	297	144	0.48	6.3	0.000257	0.17	40.40	0.51	0.0505	0.0012	0.0247	0.0003	157.4	2.0

Notes:

1. Uncertainties given at the 1σ level.

2. Error in Temora reference zircon calibration was 0.31% for the analytical session (not included in above errors but required when comparing data from different mounts).

3. f_{206} % denotes the percentage of ^{206}Pb that is common Pb.

4. Correction for common Pb for the U/Pb data has been made using the measured $^{238}U/^{206}Pb$ and $^{207}Pb/^{206}Pb$ ratios following Tera and Wasserburg (1972) as outlined in Williams (1998).

Table 2 B: SHRIMP U-Pb results for zircon crystals within a metapsammopelite of the Zapata Fm. (FC1754) at Canal Gajardo.

							Total Ratios					Radiogenic Ratios				Age (Ma)				
Grain.	**U**	**Th**	**Th/U**	**^{206}Pb***	**^{204}Pb/**	**f206**	**^{238}U/**		**^{207}Pb/**		**^{206}Pb/**		**^{207}Pb/**		**^{207}Pb/**		**^{206}Pb/**		**^{207}Pb/**		**%**
spot	**(ppm)**	**(ppm)**		**(ppm)**	**^{206}Pb**	**%**	**^{206}Pb**	**±**	**^{206}Pb**	**±**	**^{238}U**	**±**	**^{235}U**	**±**	**^{206}Pb**	**±**	**r**	**^{238}U**	**±**	**^{206}Pb**	**±**	**Disc**
1.1	568	76	0.13	79	0.000041	0.07	6.186	0.068	0.0755	0.0016	0.1615	0.0018	1.669	0.040	0.0749	0.0016	0.460	965	10	1066	43	9
2.1	773	596	0.77	14	0.000138	0.23	46.956	0.558	0.0506	0.0009	0.0212	0.0003						136	2			
3.1	257	75	0.29	28	-	<0.01	7.902	0.096	0.0757	0.0008	0.1266	0.0015	1.321	0.022	0.0757	0.0008	0.740	768	9	1087	22	29
4.1	357	387	1.08	6	0.000457	0.36	48.655	0.676	0.0515	0.0014	0.0205	0.0003						131	2			
5.1	111	72	0.65	2	-	0.12	48.813	0.975	0.0496	0.0025	0.0205	0.0004						131	3			
6.1	207	75	0.36	15	-	0.01	11.495	0.146	0.0583	0.0009	0.0870	0.0011						538	7			
7.1	319	36	0.11	21	-	<0.01	13.196	0.161	0.0548	0.0008	0.0759	0.0009						472	6			
8.1	251	79	0.31	17	0.000042	<0.01	12.658	0.160	0.0564	0.0009	0.0791	0.0010						490	6			
9.1	348	120	0.34	14	0.000139	<0.01	21.841	0.271	0.0520	0.0009	0.0458	0.0006						289	4			
10.1	480	59	0.12	31	-	0.04	13.199	0.151	0.0568	0.0007	0.0757	0.0009						471	5			
11.1	300	326	1.08	130	0.000015	0.02	1.989	0.023	0.1861	0.0007	0.5027	0.0057	12.886	0.154	0.1859	0.0007	0.952	2625	25	2706	6	3
12.1	57	40	0.70	1	0.002984	2.15	51.867	1.424	0.0656	0.0036	0.0189	0.0005						120	3			
13.1	272	241	0.89	8	0.000415	0.04	29.215	0.394	0.0508	0.0012	0.0342	0.0005						217	3			
14.1	139	79	0.57	2	0.001976	0.23	48.675	0.865	0.0505	0.0021	0.0205	0.0004						131	2			
15.1	95	43	0.45	2	0.000831	0.69	50.506	1.051	0.0540	0.0028	0.0197	0.0004						126	3			
16.1	281	88	0.31	49	-	<0.01	4.928	0.058	0.0838	0.0007	0.2030	0.0024	2.354	0.033	0.0841	0.0007	0.828	1191	13	1295	16	8
17.1	409	257	0.63	15	-	<0.01	22.987	0.279	0.0501	0.0009	0.0436	0.0005						275	3			
18.1	138	96	0.69	2	0.000783	<0.01	49.936	0.933	0.0453	0.0021	0.0201	0.0004						128	2			
19.1	114	57	0.50	2	-	0.33	48.319	0.947	0.0513	0.0025	0.0206	0.0004						132	3			
20.1	273	111	0.40	18	0.000107	0.07	13.335	0.166	0.0569	0.0009	0.0749	0.0010						466	6			

21.1	560	216	0.39	22	0.000030	0.24	21.577	0.251	0.0540	0.0008	0.0462	0.0005					291	3		
22.1	292	102	0.35	11	0.000172	0.02	22.738	0.293	0.0520	0.0011	0.0440	0.0006					277	4		
23.1	418	113	0.27	26	0.000043	0.06	13.708	0.159	0.0565	0.0007	0.0729	0.0009					454	5		
24.1	462	81	0.17	52	0.000011	0.02	7.625	0.087	0.0678	0.0006	0.1311	0.0015	1.223	0.018	0.0677	0.0006	0.769	794	8	858	20	7
25.1	429	94	0.22	24	-	0.10	15.304	0.179	0.0557	0.0007	0.0653	0.0008						408	5			
26.1	125	56	0.45	2	0.000568	0.16	49.166	0.918	0.0499	0.0023	0.0203	0.0004						130	2			
27.1	78	75	0.96	3	0.000313	<0.01	22.393	0.414	0.0514	0.0020	0.0447	0.0008						282	5			
28.1	67	36	0.53	3	0.000423	<0.01	23.000	0.444	0.0504	0.0022	0.0436	0.0009						275	5			
29.1	52	22	0.42	1	0.001169	0.30	51.146	1.381	0.0509	0.0039	0.0195	0.0005						124	3			
30.1	269	100	0.37	5	0.000921	0.15	47.963	0.709	0.0499	0.0015	0.0208	0.0003						133	2			
31.1	570	313	0.55	101	-	<0.01	4.850	0.053	0.0844	0.0006	0.2062	0.0022	2.402	0.031	0.0845	0.0006	0.856	1209	12	1303	13	7
32.1	55	29	0.53	1	-	0.13	53.278	1.428	0.0494	0.0037	0.0187	0.0005						120	3			
33.1	108	38	0.35	6	0.000390	0.40	14.735	0.223	0.0585	0.0018	0.0676	0.0010						422	6			
34.1	172	122	0.71	6	-	<0.01	23.342	0.338	0.0516	0.0014	0.0428	0.0006						270	4			
35.1	47	25	0.54	1	0.002269	10.69	46.656	1.295	0.1334	0.0069	0.0191	0.0006						122	4			
36.1	746	309	0.41	29	0.000041	<0.01	22.141	0.248	0.0515	0.0006	0.0452	0.0005						285	3			
37.1	90	39	0.43	1	0.000431	0.45	52.517	1.136	0.0520	0.0028	0.0190	0.0004						121	3			
38.1	122	52	0.43	2	0.000452	<0.01	50.652	0.972	0.0480	0.0023	0.0198	0.0004						126	2			
39.1	391	245	0.63	51	-	<0.01	6.596	0.074	0.0792	0.0006	0.1517	0.0017	1.667	0.024	0.0797	0.0007	0.797	911	10	1189	17	23
40.1	72	37	0.52	1	0.000004	0.19	46.566	1.056	0.0503	0.0030	0.0214	0.0005						137	3			
44.2	1692	29	0.02	95	0.000034	0.04	15.360	0.160	0.0552	0.0004	0.0651	0.0007						406	4			
41.1	929	778	0.84	34	0.000037	0.03	23.328	0.257	0.0519	0.0006	0.0429	0.0005						271	3			
42.1	77	48	0.62	3	0.000644	0.18	21.716	0.400	0.0535	0.0020	0.0460	0.0009						290	5			
43.1	81	30	0.37	6	-	<0.01	11.429	0.185	0.0577	0.0015	0.0876	0.0014						541	9			
44.1	193	42	0.22	22	-	<0.01	7.471	0.094	0.0739	0.0009	0.1338	0.0017	1.364	0.024	0.0739	0.0009	0.714	810	10	1038	25	22

45.1	749	356	0.47	28	0.000040	0.04	23.156	0.259	0.0520	0.0007	0.0432	0.0005							272	3	
46.1	128	62	0.48	2	0.000286	0.07	50.985	0.945	0.0491	0.0023	0.0196	0.0004							125	2	
47.1	169	109	0.64	3	0.000247	0.48	49.656	0.885	0.0524	0.0022	0.0200	0.0004							128	2	
48.1	137	53	0.39	5	0.000156	0.25	23.736	0.374	0.0536	0.0016	0.0420	0.0007							265	4	
49.1	672	38	0.06	44	0.000017	0.04	13.238	0.145	0.0568	0.0005	0.0755	0.0008							469	5	
50.1	782	58	0.07	61	-	0.20	11.051	0.119	0.0604	0.0005	0.0903	0.0010							557	6	
51.1	695	159	0.23	45	-	<0.01	13.276	0.147	0.0559	0.0006	0.0754	0.0008							468	5	
52.1	242	160	0.66	4	0.000314	<0.01	51.601	0.793	0.0479	0.0017	0.0194	0.0003							124	2	
53.1	64	32	0.50	1	0.000710	0.05	51.977	1.306	0.0488	0.0033	0.0192	0.0005							123	3	
54.1	439	264	0.60	8	0.000364	<0.01	47.684	0.628	0.0478	0.0012	0.0210	0.0003							134	2	
55.1	609	501	0.82	21	-	0.09	25.214	0.290	0.0519	0.0008	0.0396	0.0005							251	3	
56.1	99	53	0.54	2	0.000184	0.60	51.418	1.043	0.0533	0.0027	0.0193	0.0004							123	3	
57.1	56	25	0.46	1	0.001789	0.09	49.985	1.326	0.0493	0.0035	0.0200	0.0005							128	3	
58.1	374	222	0.59	6	-	<0.01	52.133	0.718	0.0473	0.0013	0.0192	0.0003							123	2	
59.1	215	107	0.50	38	0.000084	0.14	4.805	0.059	0.0844	0.0008	0.2078	0.0025	2.384	0.039	0.0832	0.0009	0.737	1217	14	1274	22 4
60.1	226	86	0.38	43	0.000004	0.01	4.488	0.054	0.0874	0.0007	0.2228	0.0027	2.683	0.039	0.0874	0.0007	0.827	1297	14	1368	16 5
61.1	157	80	0.51	22	0.000040	0.07	6.082	0.078	0.0812	0.0009	0.1643	0.0021	1.827	0.033	0.0806	0.0010	0.710	981	12	1213	25 19
62.1	440	89	0.20	82	-	<0.01	4.588	0.051	0.0833	0.0006	0.2180	0.0024	2.510	0.033	0.0835	0.0006	0.849	1271	13	1281	13 1
63.1	463	224	0.48	31	-	0.10	12.878	0.147	0.0575	0.0007	0.0776	0.0009							482	5	
64.1	591	369	0.62	20	0.000070	<0.01	24.969	0.292	0.0513	0.0008	0.0401	0.0005							253	3	
65.1	132	64	0.49	2	0.000356	<0.01	50.719	0.929	0.0470	0.0022	0.0198	0.0004							126	2	
66.1	301	198	0.66	5	0.000355	0.16	52.215	0.757	0.0497	0.0015	0.0191	0.0003							122	2	
67.1	144	69	0.48	2	0.000513	0.04	50.052	0.906	0.0489	0.0022	0.0200	0.0004							127	2	
68.1	250	234	0.93	4	-	<0.01	49.160	0.740	0.0479	0.0016	0.0204	0.0003							130	2	
69.1	621	502	0.81	23	0.000158	<0.01	23.175	0.267	0.0513	0.0007	0.0432	0.0005							272	3	

70.1	970	459	0.47	56	0.000010	0.02	14.872	0.160	0.0553	0.0005	0.0672	0.0007	419	4

Notes:

1. Uncertainties given at the 1σ level.

2. Error in Temora reference zircon calibration was 0.31% for the analytical session (not included in above errors but required when comparing data from different mounts).

3. f_{206} % denotes the percentage of ^{206}Pb that is common Pb.

4. For areas older than ca. 800 Ma correction for common Pb made using the measured $^{204}Pb/^{206}Pb$ ratio.

5. For areas younger than ca. 800 Ma correction for common Pb made using the measured $^{238}U/^{206}Pb$ and $^{207}Pb/^{206}Pb$ ratios following Tera and Wasserburg (1972) as outlined in Williams (1998).

6. For % Disc. 0% denotes a concordant analysis.

Table 2 C: SHRIMP U-Pb results for zircon crystals separated from a quartz-diorite satellite pluton of the *South Patagonian Batholith* (FC1759) intruding the RVB units at Canal Gajardo.

							Total			Radiogenic			Age (Ma)	
Grain.	**U**	**Th**	**Th/U**	**^{206}Pb***	**^{204}Pb/**	**f206**	**^{238}U/**		**^{207}Pb/**		**^{206}Pb/**		**^{206}Pb/**	
spot	**(ppm)**	**(ppm)**		**(ppm)**	**^{206}Pb**	**%**	**^{206}Pb**	**±**	**^{206}Pb**	**±**	**^{238}U**	**±**	**^{238}U**	**±**
1.1	452	353	0.78	5.1	0.000023	0.27	76.06	0.99	0.0498	0.0013	0.0131	0.0002	84.0	1.1
2.1	1459	1346	0.92	16.3	-	0.09	76.92	0.84	0.0484	0.0007	0.0130	0.0001	83.2	0.9
3.1	454	277	0.61	5.1	-	0.14	76.81	0.96	0.0488	0.0013	0.0130	0.0002	83.3	1.0
4.1	1840	1077	0.59	19.9	0.000113	0.02	79.33	0.85	0.0478	0.0006	0.0126	0.0001	80.7	0.9
5.1	293	177	0.60	3.2	-	0.15	77.85	1.07	0.0489	0.0016	0.0128	0.0002	82.2	1.1

Notes:

1. Uncertainties given at the 1σ level.
2. Error in Temora reference zircon calibration was 0.31% for the analytical session (not included in above errors but required when comparing data from different mounts).
3. f_{206} % denotes the percentage of ^{206}Pb that is common Pb.
4. Correction for common Pb for the U/Pb data has been made using the measured ^{238}U/^{206}Pb and ^{207}Pb/^{206}Pb ratios following Tera and Wasserburg (1972) as outlined in Williams (1998).

Table 3: $^{40}Ar/^{39}Ar$ data of the mylonitic metapelite of Zapata Fm. (SHP141) at Canal Gajardo.

Comment	^{40}Ar	+/-	^{39}Ar	+/-	^{38}Ar	+/-	37Ar	+/-	^{36}Ar	+/-	$^{40}Ar^*/^{39}Ar$	+/-	Age	+/-	+/- (no J error)	39/40	+/-	36/40	+/-	37/39	+/-	38/39	+/-
spot 1	285971.96	777.91	75407.84	140.34	2.74	2.27	5990.66	135.88	76.35	1.72	3.49	0.01	**72.0**	**0.4**	0.28	0.26	0	0	0	0.08	0	3.6E-05	3.01E-05
spot 2	285233.26	768.11	77111.30	130.32	1.09	1.90	5497.19	135.93	58.83	1.53	3.47	0.01	**71.6**	**0.4**	0.26	0.27	0	0.	0	0.07	0	1.4E-05	2.47E-05
spot 3	365927.21	1810.14	100863.27	290.69	7.75	2.19	13219.52	135.98	69.45	1.81	3.42	0.02	**70.6**	**0.5**	0.42	0.28	0	0	0	0.13	0	7.7E-05	2.18E-05
spot 4	331500.75	1212.63	92878.29	210.51	5.66	1.97	5673.16	136.03	58.14	1.44	3.38	0.02	**69.8**	**0.5**	0.32	0.28	0	0	0	0.06	0	6.1E-05	2.12E-05
spot 5	227792.46	573.68	59978.87	110.28	3.88	1.83	2937.69	136.12	54.68	1.44	3.53	0.01	**72.7**	**0.4**	0.27	0.26	0	0	0	0.05	0	6.5E-05	3.06E-05
spot 6	367902.47	2209.53	101346.00	210.51	6.66	1.60	9301.34	136.16	51.96	1.44	3.48	0.02	**71.7**	**0.6**	0.47	0.28	0	0	0	0.09	0	6.6E-05	1.58E-05
*spot 7	51762.21	288.73	7702.62	33.13	2.27	1.46	2603.01	136.21	78.86	1.81	3.66	0.08	**75.5**	**1.7**	1.62	0.15	0	0	0	0.34	0.02	2.9E-04	1.90E-04
spot 8	243961.90	886.03	63503.03	150.37	1.46	2.12	5401.96	136.25	67.81	1.72	3.52	0.02	**72.6**	**0.5**	0.36	0.26	0	0	0	0.09	0	2.3E-05	3.33E-05
spot 9	895338.53	1631.85	256476.77	290.77	8.77	4.38	10441.22	304.03	74.02	1.61	3.40	0.01	**70.2**	**0.4**	0.15	0.29	0	0	0	0.04	0	3.4E-05	1.71E-05
spot 10	210864.66	377.74	57991.27	93.28	5.29	4.12	6743.26	304.16	46.21	1.34	3.40	0.01	**70.1**	**0.4**	0.22	0.28	0	0	0	0.12	0.01	9.1E-05	7.10E-05
spot 11	162905.01	346.13	43676.13	78.25	4.02	4.09	3142.52	304.25	48.46	1.43	3.40	0.01	**70.1**	**0.4**	0.28	0.27	0	0	0	0.07	0.01	9.2E-05	9.35E-05

Corrections:
1. Atmospheric 40/36 correction: 298.56 (Lee et al., 2006)
2. 40/36 discimination value: 295
3. J value: 0.011546801 +/- 0.5% calculated using standard GA1550, with an age of 99.738 +/- 0.104Ma, Renne et al. (2011)
4. Potassium correction applied: 0.0085 +/-4.25E-05
5. Calcium ^{36}Ar correction applied: 0.000265 +/-1.325E-06
6. Calcium ^{39}Ar correction applied: 0.00065 +/-3.25E-06 blank corrected using average of days blanks
7. Decay constant of Renne et al. (2011)
8. ^{37}Ar and ^{39}Ar corrected for decay between irradiation and analysis irradiation: 100MWH
9. Analysis: Nu Instruments Noblesse

*Spot 7 is an outlier and was not used to calculate the mean age

Table 4: Major-element compositions of the mylonitic silicic metatuffs of Tobífera Fm. (FC1723, FC1727, FC1749) and the metapsammopelite of Zapata Fm. (FC1757): A) Original XRF data; B) Corrected and normalized to 100% data.

A	**FC1723**	**FC1727**	**FC1749**	**FC1757**	**B**	**FC1723**	**FC1727**	**FC1749**	**FC1757**
SiO_2	72.25	77.48	77.67	79.00	SiO_2	73.11	77.20	76.68	78.35
TiO_2	0.09	0.12	0.07	0.25	TiO_2	0.09	0.12	0.06	0.25
Al_2O_3	13.33	11.41	11.69	9.58	Al_2O_3	13.48	11.36	11.64	9.50
Fe_2O_3	1.68	1.52	1.05	2.06	FeO	1.53	1.36	0.93	1.84
MnO	0.01	0.03	0.03	0.03	O_2	0.01	0.01	0.01	0.01
MgO	3.69	0.61	1.54	0.75	MnO	0.01	0.03	0.03	0.03
CaO	0.26	0.08	0.06	1.90	MgO	3.73	0.61	1.52	0.75
Na_2O	0.65	3.68	3.63	2.42	CaO	0.26	0.08	0.06	1.80
K_2O	3.04	2.59	1.65	1.11	Na_2O	0.66	3.67	3.58	2.40
P_2O_5	0.00	0.00	0.00	0.07	K_2O	3.08	2.58	1.63	1.10
Sum	95.00	97.51	97.39	97.17	H_2O	4.05	2.99	3.95	3.97
					Sum	100	100	100	100

Corrections:
1. O_2 = FeO*0.05*0.1113 (relative to 10% of trivalent iron)
2. CaO=CaO-(280.4/212.92)*P2O5
3. H_2O based on loss on ignition of each sample
4. Normalized to 100%

Table 5: Representative electron microprobe analyses (in wt%) of phengitic white mica (pheng), chlorite (chl), biotite (bt), epidote (ep), and feldspar (fs) in metatuffs of Tobífera Fm. (FC1723, FC1727, FC1749), metapsammopelite (FC1727), and metapelite (SHP141) of Zapata Fm.

Sample	**FC 1723**	**FC 1727**	**FC 1749**	**FC 1757**	**SHP 141**		**FC 1723**	**FC 1723**	**FC 1727**	**FC 1749**	**FC 1757**		**FC 1757**		**FC 1723**		**FC 1723**	**FC 1727**	**FC 1749**	**FC 1757**
Mineral	pheng	pheng	pheng	pheng	pheng		chl	chl	chl	chl	chl		bt		ep		fs	fs	fs	fs
SiO_2	49.63	49.76	51.97	49.01	48.61	SiO_2	35.61	23.68	25.24	33.73	26.41	SiO_2	35.58	SiO_2	38.19	SiO_2	67.79	69.41	68.06	62.28
TiO_2	0.01	0.15	0.05	0.25	0.08	TiO_2	0	0.02	0.02	0.02	0.01	TiO_2	2.87	TiO_2	0.02	TiO_2	0	0	0	0.01
Al_2O_3	32.8	25.73	29.64	28.29	27.61	$Al2O_3$	26.7	20.94	18.4	23.13	19.83	Al_2O_3	17.44	Al_2O_3	29.73	Al_2O_3	19.78	19.42	19.5	24.57
FeO	0.89	3.8	0.81	0.18	1.14	FeO	7.53	31.3	30.91	11.33	26.96	FeO	21.35	Cr_2O_3	0	Cr_2O_3	0	0	0	0
Fe_2O_3	0	1.29	0	4.89	1.83	MnO	0.04	0.36	0.77	0.36	0.58	Fe_2O_3	0	Fe_2O_3	5.68	Fe_2O_3	0.13	0	0.12	0.24
MnO	0	0.05	0	0.05	0.07	MgO	21.35	11.33	12.06	21.65	14.55	MnO	0.27	Mn_2O_3	0	Mn_2O_3	0	0	0	0
MgO	2.21	3.18	3.59	3.83	3.78	H_2O	13.41	10.95	10.93	12.89	11.36	MgO	8.69	MgO	0.05	MgO	0	0	0.01	0
CaO	0.05	0.01	0.02	0.03	0.02	Total	104.64	98.58	98.34	103.12	99.71	CaO	0.02	CaO	24.25	CaO	0.28	0.12	0.11	5.74
Na_2O	0.28	0.08	0.09	0.1	0.04							Na_2O	0.01	Na_2O	0	Na_2O	11.99	11.78	12.03	8.63
K_2O	10.65	10.66	10.81	11.61	10.73	Si	6.37	5.19	5.54	6.28	5.58	K_2O	9.95	H_2O	1.94	K_2O	0.04	0.06	0.05	0.13
BaO	0.29	0.14	0.16	0.16	0	Al iv	1.63	2.81	2.46	1.72	2.42	BaO	0.21	Total	99.86	BaO	0.02	0.02	0	0.01
H_2O	4.61	4.42	4.64	4.57	4.42	sum4	8	8	8	8	8	H_2O	3.92			Total	100.03	100.82	99.89	101.6
Total	101.42	99.27	101.76	102.97	98.33	Al vi	3.99	2.6	2.3	3.35	2.51	Total	100.3	Si	2.96					
						Ti	0	0	0	0	0			Ti	0	Si	2.97	3.01	2.98	2.72
Si	6.46	6.76	6.72	6.44	6.59	Fe2+	1.13	5.74	5.68	1.76	4.76	Si	2.72	Al	2.71	Al	1.02	0.99	1.01	1.27
Al iv	1.54	1.24	1.28	1.56	1.41	Mn	0.01	0.07	0.14	0.06	0.1	Al iv	1.28	Cr	0	Fe3	0	0	0	0.01
sum4	8	8	8	8	8	Mg	5.69	3.7	3.95	6.01	4.58	Ti	0.16	Fe3	0.33	Ti	0	0	0	0
Al vi	3.49	2.87	3.23	2.82	3	sum6	10.82	12.11	12.07	11.18	11.96	Al vi	0.29	Mg	0.01	su1	3.99	4	3.99	4
Ti	0	0.02	0	0.02	0.01	H	16	16	16	16	16	Fe2	1.37	sum6	3.05	Ba	0	0	0	0
Fe2+	0.1	0.43	0.09	0.02	0.13	Compo-sitions						Fe3	0	Ca	2.01	Ca	0.01	0.01	0.01	0.27
Fe3+	0	0.13	0	0.48	0.19	xSi	1.18	0.59	0.77	1.14	0.79	Mn	0.02	Na	0	Na	1.02	0.99	1.02	0.73
Mn	0	0.01	0	0.01	0.01	Mg#	0.83	0.39	0.41	0.77	0.49	Mg	0.99	sum8	2.01	K	0	0	0	0.01
Mg	0.43	0.64	0.69	0.75	0.76	Fe#	0.17	0.61	0.59	0.23	0.51	sum6	2.83	H	1	su2	1.03	1	1.03	1.01

sum6	4.02	4.1	4.02	4.1	4.1	Ca	0	Compo-sitions		Compo-nents				
Ca	0.01	0	0	0	0	Na	0	Ps [Fe/(Al+Fe)]	0.11	Anorthite	0.01	0.01	0.01	0.27
Ba	0.01	0.01	0.01	0.01	0	K	0.97			High Albite	0.99	0.99	0.99	0.73
Na	0.07	0.02	0.02	0.03	0.01	Ba	0.01			K Feldspar	0	0	0	0.01
K	1.77	1.85	1.78	1.95	1.86	sum8	0.98							
sum8	1.86	1.88	1.82	1.98	1.87	H	2							
H	4	4	4	4	4	Compo-sitions								
Compo-nents						xAl	0.15							
Ms	0.7	0.51	0.61	0.57	0.6	Mg#	0.42							
Wm_Phl	0.01	0.05	0.01	0.05	0.05									
Al_Cel	0.2	0.23	0.32	0.22	0.25									
Fe_Al_Cel	0.04	0.15	0.04	0.01	0.04									
Pg	0.04	0.01	0.01	0.01	0.01									
Ti_Mn_Ca_Wm	0.01	0.05	0.01	0.14	0.05									
xOH	1	1	1	1	1									

Abbreviations: Ms - muscovite; Wm - white mica; Phl - phlogopite; Cel - celadonite; Pg - paragonite; Ps - pistacite; Structural formulae and various parameters (mainly molar fractions X of end member components) were calculated using the CALCMIN software (Brandelik, 2009) as follows: biotite O= 11, all Fe is divalent; white mica valences = 42, cations without interlayer cations ≤12.1; chlorite O= 28, all Fe is divalent; feldspar O=8; ilmenite O= 3, cations = 2.

Table 6: Modal (mod) and calculated (calc) composition of the samples analyzed for P-T pseudosection modelling showing interpreted P and T calculations. Abbreviations: Q – quartz; Pl – plagioclase; Kfs – alkaline feldspar; Wm – white mica; Bt – biotite; Ep – epidote; Tt – titanite; Op – opaques; Stlp – stilpnomelane; Cpx – clinopyroxene.

	FC1749		**FC1757**		**FC1723**		**FC1727**	
Mineral	Mod	Calc	Mod	Calc	Mod	Calc	Mod	Calc
Q	55	46	55	55	55	55	50	42
Pl	25	27	25	19.5	4	0.5	25	30
Kfs							5	7
Wm	15	16	10	7	30	31	15	13
Chl	5	3	4	3	10	10	5	2
Bt			5	2				
Ep			1	5	1			
Tt		0.1		0.5				0.2
Op	tr.		tr.		tr.		tr.	
Stlp		1						
Cpx		0.2				0.5		0.4
water		6.7		8		3		5.4
P (kbar)		3.5		5.5		6		3.8
T (C)		230		440		450		330

References – Chapter 2

Agard, P., Yamato, P., Jolivet, L., Burov, E. 2009. Exhumation of oceanic blueschists and eclogites in subduction zones: timing and mechanisms. Earth-Science Reviews, 92(1-2), 53-79. doi.org/10.1016/j.earscirev.2008.11.002

Allen, R.B. 1982. Geología de la Cordillera Sarmiento, Andes Patagónicos, entre los 51º00' y 52º15' Lat. S, Magallanes, Chile. Servicio Nacional de Geología y Minería, Boletín 38, 1-46.

Allmendinger, R.W., Ramos, V.A., Jordan, T.E., Palma, M., Isacks, B.L. 1983. Paleogeography and Andean structural geometry, northwest Argentina. Tectonics, 2(1), 1-16. doi.org/10.1029/TC002i001p00001

Alvarez-Marrón, J., McClay, K.R., Harambour, S., Rojas, L., Skarmeta, J. 1993. Geometry and evolution of the frontal part of the Magallanes foreland thrust and fold belt (Vicuna-Area), Tierra del Fuego, Southern Chile. American Association of Petroleum Geologist Bulletin, 77, 1904–1921. doi.org/10.1306/BDFF8F74-1718-11D7-8645000102C1865D

Andersen, D.J., Lindsley, D.H. 1988. Internally consistent solution models for Fe-Mg-Mn-Ti oxides; Fe-Ti oxides. American Mineralogist, 73(7-8), 714-726.

Angiboust, S., Cambeses, A., Hyppolito, T., Glodny, J., Monié, P., Calderón, M., Juliani, C. 2018. A 100-my-long window onto mass-flow processes in the Patagonian Mesozoic subduction zone (Diego de Almagro Island, Chile). Geological Society of America Bulletin, 130(9-10), 1439-1456. doi.org/10.1130/B31891.1

Angiboust, S., Hyppolito, T., Glodny, J., Cambeses, A., Garcia-Casco, A., Calderón, M., Juliani, C. 2017. Hot subduction in the middle Jurassic and partial melting of oceanic crust in Chilean Patagonia. Gondwana Research, 42, 104-125. Doi.org/10.1016/j.gr.2016.10.007

Anguita, N.G. 2010. Petrogénesis de diques lamprofídicos postectónicos y su relación con el magmatismo shoshonítico Cretácico de la Formación Barros Arana y el Complejo La Pera, Magallanes, XII Región, Chile. Undergraduate Thesis, Universidad de Chile, Santiago, 237 p. (unpublished)

Barbeau Jr., D.L., Olivero, E,B., Swanson-Hysell, N.L., Zahid, K.M., Murray, K.E., Gehrels, G.E. 2009. Detrital-zircon geochronology of the eastern Magallanes foreland basin: Implications for Eocene kinematics of the northern Scotia Arc and Drake Passage. Earth and Planetary Science Letters, 284(3-4), 489-503. doi.org/10.1016/j.epsl.2009.05.014

Bernhardt, A., Jobe, Z.R., Lowe, D.R. 2011. Stratigraphic evolution of a submarine channel-lobe complex system in a narrow fairway within the Magallanes foreland basin, Cerro Toro Formation, southern Chile. Marine and Petroleum Geology, 28(3), 785-806. doi.org/10.1016/j.marpetgeo.2010.05.013

Betka, P., Klepeis, K., Mosher, S. 2015. Along-strike variation in crustal shortening and kinematic evolution of the base of a retroarc fold-and-thrust belt: Magallanes, Chile 53°S–54°S. Geological Society of America Bulletin, 127 (7–8), 1108-1134. doi.org/10.1130/B31130.1

Betka, P.M. 2013. Structure of the Patagonian fold-thrust belt in the Magallanes region of Chile, 53°-55° S Lat. PhD Thesis, The University of Texas at Austin, 224 p. https://repositories.lib.utexas.edu/handle/2152/23239

Black, L.P., Kamo, S.L., Allen, C.M., Aleinikoff, J.N., Davis, D.W., Korsch, R.J., Foudoulis, C. 2003. TEMORA 1: a new zircon standard for Phanerozoic U–Pb geochronology. Chemical Geology, 200, 155-170. doi.org/10.1016/S0009-2541(03)00165-7

Brandelik, A., 2009. CALCMIN–an EXCELTM Visual Basic application for calculating mineral structural formulae from electron microprobe analyses. Computers & Geosciences 35 (7), 1540–1555

Braz, C., Seton, M., Flament, N., Müller, R.D. 2018. Geodynamic reconstruction of an accreted Cretaceous back-arc basin in the Northern Andes. Journal of Geodynamics, 121, 115-132.

Bruhn, R.L., Stern, C.R., de Wit, M.J. 1978. Field and geochemical data bearing on the development of a Mesozoic volcano-tectonic rift zone and back-arc basin in southernmost South America. Earth and Planetary Science Letters, 41(1), 32-46. doi.org/10.1016/0012-821X(78)90039-0

Bucher, K., Grapes, R. 2011. Petrogenesis of metamorphic rocks. Springer Science & Business Media.

Calderón, M., Fildani, A., Hervé, F., Fanning, C.M. 2007. Late Jurassic bimodal magmatism in the northern sea-floor remnant of the Rocas Verdes Basin, southern Patagonian Andes. Journal of the Geological Society of London, 164, 1011-1022. doi.org/10.1144/0016-76492006-102

Calderón, M., Fosdick, J., Alvarez, J., Sanchez, A., Galaz, G. 2009. Doubly-vergent structures in metamorphic rocks that enclose the Sarmiento Ophiolite Complex at Senos Lolos and Encuentros, Southern Patagonian Andes (51-52°S). XII Congreso Geológico Chileno, Santiago.

Calderón, M., Fosdick, J.C., Warren, C., Massonne, H.-J., Fanning, C.M., Cury, L.F., Schwanethal, J., Fonseca, P.E., Galaz, G., Gaytán, D., Hervé, F. 2012. The low-grade Canal de las Montañas Shear Zone and its role in the tectonic emplacement of the Sarmiento Ophiolitic Complex and Late Cretaceous Patagonian Andes orogeny, Chile. Tectonophysics, 524, 165-185. doi.org/10.1016/j.tecto.2011.12.034

Calderón, M., Prades, C. F., Hervé, F., Avendaño, V., Fanning, C. M., Massonne, H.-J., Theye, T., Simonetti, A. 2013. Petrological vestiges of the Late Jurassic-Early Cretaceous transition from rift to back-arc basin in southernmost Chile: New age and geochemical data from the Capitán Aracena, Carlos III, and Tortuga ophiolitic complexes. Geochemical Journal, 47(2), 201-217. doi.org/10.2343/geochemj.2.0235

Castelli, J.C., Robertson, R., Harambour, A. 1992. Evaluación Geológica y Petrolera, bloques Ultima Esperanza Sur e Isla Riesco. Informe Archivo Técnico ENAP, Santiago, 59 p. (unpublished).

Charrier, R., Lahsen, A. 1969. Stratigraphy of Late Cretaceous-Early Eocene, Seno Skyring--Strait of Magellan Area, Magallanes Province, Chile. AAPG Bulletin, 53(3), 568-590. doi.org/10.1306/5D25C69D-16C1-11D7-8645000102C1865D

Connolly, J.A.D. 1990. Multivariable phase diagrams; an algorithm based on generalized thermodynamics. American Journal of Science, 290(6), 666-718. doi.org/10.2475/ajs.290.6.666

Cortés, R. 1964. Estratigrafía y un estudio de paleocorrientes del flysch Cretáceo del Depto. de Ultima Esperanza: Santiago, Chile. Undergraduate Thesis, Universidad Técnica de Estado, 117 p. (unpublished)

Coward, M.P. 1983. Thrust tectonics, thin skinned or thick skinned, and the continuation of thrusts to deep in the crust. Journal of Structural Geology, 5(2), 113-123. doi.org/10.1016/0191-8141(83)90037-8

Cox, K.G. 1992. Karoo igneous activity, and the early stages of breakup of Gondwanaland. In Magmatism and the causes of continental breakup (Storey, B.C.; Alabaster, T.; Pankhurst, R.J.; editors). Geological Society, Special Publications 68: 137-148.

Cunningham, W.D. 1995. Orogenesis at the southern tip of the Americas: the structural evolution of the Cordillera Darwin metamorphic complex, southernmost Chile. Tectonophysics, 244, 197-229. doi.org/10.1016/0040-1951(94)00248-8

Cunningham, W.D., Klepeis, K.A., Gose, W.A., Dalziel, I.W. 1991. The Patagonian Orocline: New paleomagnetic data from the Andean magmatic arc in Tierra del Fuego, Chile. Journal of Geophysical Research: Solid Earth, 96(B10), 16061-16067.

Dahlen, F. A. 1990. Critical taper model of fold-and-thrust belts and accretionary wedges. Annual Review of Earth and Planetary Sciences, 18(1), 55-99.

Dalziel, I.W., De Wit, M.J., Palmer, K.F. 1974. Fossil marginal basin in the southern Andes. Nature, 250, 291-294.

Dalziel, I.W., Lawver, L.A., Norton, I.O., Gahagan, L.M. 2013. The Scotia Arc: genesis, evolution, global significance. Annual Review of Earth and Planetary Sciences, 41.

Dalziel, I.W.D. 1981. Back-arc extension in the southern Andes: A review and critical reappraisal. Royal Society of London Philosophical Transactions A, 300, 319-335. doi.org/10.1098/rsta.1981.0067

Dalziel, I.W.D. 1986. Collision and Cordilleran orogenesis: an Andean perspective. In: Coward, M.P., Ries, A.C. (Eds.), Collision Tectonics. Geological Society of London Special publications, 19, 389-404. doi.org/10.1144/GSL.SP.1986.019.01.22

Davis, D., Suppe, J., Dahlen, F.A. 1983. Mechanics of fold-and-thrust belts and accretionary wedges. Journal of Geophysical Research: Solid Earth, 88(B2), 1153-1172. doi.org/10.1029/JB088iB02p01153

Deer, W.A., Rowie, R.A., Zussman, J. 1963. Rock Forming Minerals. 1st ed., vol. 4, London, Longman.

Dewey, J.F., Bird, J.M. 1970. Mountain belts and the new global tectonics. Journal of Geophysical Research, 75(14), 2625-2647. doi.org/10.1029/JB075i014p0262

Eagles, G. 2016. Plate kinematics of the Rocas Verdes Basin and Patagonian orocline. Gondwana Research, 37, 98-109.

Ernst, W.G. 1963. Significance of phengitic micas from low-grade schists. American Mineralogist: Journal of Earth and Planetary Materials, 48(11-12), 1357-1373.

Ernst, W.G. 1971. Metamorphic zonations on presumably subducted lithospheric plates from Japan, California and the Alps. Contributions to Mineralogy and Petrology, 34(1), 43-59.

Ernst, W.G. 1972. Occurrence and mineralogic evolution of blueschist belts with time. American Journal of Science, 272(7), 657-668. doi.org/10.2475/ajs.272.7.657

Ernst, W.G. 2005. Alpine and Pacific styles of Phanerozoic mountain building: subduction-zone petrogenesis of continental crust. Terra Nova, 17(2), 165-188. doi.org/10.1111/j.1365-3121.2005.00604.x

Fildani, A., Cope, T.D., Graham, S.A., Wooden, J.L. 2003. Initiation of the Magallanes foreland basin: Timing of the southernmost Patagonian Andes orogeny revised by detrital zircon provenance analysis. Geology, 31, 1081-1084. doi.org/10.1130/G20016.1

Fildani, A., Hessler, A.M. 2005. Stratigraphic record across a retroarc basin inversion: Rocas Verdes-Magallanes Basin, Patagonian Andes, Chile. Geological Society of America Bulletin, 117, 1596-1614. doi.org/10.1130/B25708.1

Fildani, A., Romans, B., Fosdick, J.C., Crane, W.D., Hubbard, S.M., 2008. Orogenesis of the Patagonian Andes as reflected by basin evolution in southernmost South America. Arizona Geological Society Digest 22, 259–268.

Forsythe, R., Allen, R.B. 1980. The basement rocks of Península Staines, Región XII, Province of Última Esperanza, Chile. Revista Geológica de Chile, 10, 3-15. doi.org/10.5027/andgeoV7n2-a01

Fosdick, J.C., Graham, S.A., Hilley, G.E. 2014. Influence of attenuated lithosphere and sediment loading on flexure of the deep-water Magallanes retroarc foreland basin, Southern Andes: Tectonics, 33, 12, 2505–2525. Doi:10.1002/2014TC003684.

Fosdick, J.C., Grove, M., Hourigan, J.K., Calderon, M. 2013. Retroarc deformation and exhumation near the end of the Andes, southern Patagonia. Earth and Planetary Science Letters, 361, 504-517. doi.org/10.1016/j.epsl.2012.12.007

Fosdick, J.C., Romans, B.W., Fildani, A., Bernhardt, A., Calderón, M., Graham, S.A. 2011. Kinematic evolution of the Patagonian retroarc fold-and-thrust belt and Magallanes foreland basin, Chile and Argentina, 51°30's. Geological Society of America Bulletin 123, 1679-1698. doi.org/10.1130/B30242.1

Fosdick, J.C., VanderLeest, R.V., Bostelmann, J.E., Leonard, J.S., Ugalde, R., Oyarzún, J.L., and Griffin, M. 2020. Revised timing of Cenozoic Atlantic incursions and changing hinterland sediment sources during southern Patagonian orogenesis, Lithosphere. doi.org/10.2113/2020/8883099.

Fossen, H., Cavalcante, G. C. G. 2017. Shear zones–A review. Earth-Science Reviews, 171, 434-455.

Foster, M.D. 1962. Interpretation and a classification of the chlorite. US Geological Survey Professional Paper, 414, 1-33.

Fuenzalida, R., Covacevich, V. 1988. Volcanismo y bioestratigrafía del Jurásico y Cretácico Inferior en la Cordillera Patagónica, Región de Magallanes, Chile. In: V Congreso Geológico Chileno 3, H159-H183.

Fuhrman, M.L., Lindsley, D.H. 1988. Ternary-feldspar modelling and thermometry. American Mineralogist, 73(3-4), 201-215.

Gealey, W.K. 1980. Ophiolite obduction mechanism. In: Panayiotou, A. (Ed.), Ophiolites. Proceedings International Ophiolite Symposium, Cyprus. Cyprus Geological Survey, Nicosia, 228-243.

Gee, J.S., Kent, D.V. 2007. Source of oceanic magnetic anomalies and the geomagnetic polarity time scale. doi.org/10.7916/D8DV1V8P

Ghiglione, M.C., Naipauer, M., Sue, C., Barberón, V., Valencia, V., Aguirre-Urreta, B., Ramos, V.A. 2015. U-Pb zircon ages from the northern Austral basin and their correlation with the Early Cretaceous exhumation and volcanism of Patagonia. Cretaceous Research, 55, 116-128. doi.org/10.1016/j.cretres.2015.02.006

Ghiglione, M.C., Suarez, F., Ambrosio, A., Da Poian, G., Cristallini, E.O., Pizzio, M.F., Reinoso, R.M. 2009. Structure and evolution of the Austral Basin fold-thrust belt, southern Patagonian Andes. Revista de la Asociación Geológica Argentina, 65(1), 215-226.

Harambour, S. 1998. Structural evolution of the Magallanes Block, Magallanes (Austral) Basin, offshore Argentina, South Atlantic. MSc thesis, Royal Holloway, University of London, Royal Holloway New College, 136 p. (unpublished)

Harambour, S. 2002. Deep seated thrusts in the frontal part of the Magallanes fold and thrust belt, Ultima Esperanza, Chile. XV Congreso Geológico Argentino, 3. El Calafate, Argentina, p. 230. CD ROM.

Hervé, F., Calderón, M., Fanning, C.M., Kraus, S., and Pankhurst, R.J. 2010a. SHRIMP chronology of the Magallanes Basin basement, Tierra del Fuego: Cambrian plutonism and Permian high-grade metamorphism. Andean Geology, 37(2), 253-275. ISSN: 0718-7092

Hervé, F., Calderón, M., Faúndez, V. 2008. The metamorphic complexes of the Patagonian and Fuegian Andes. Geological Acta, 6, 43-53. ISSN: 1695-6133

Hervé, F., Fanning, C.M. 2003. Early Cretaceous subduction of continental crust at the Diego de Almagro archipelago, southern Chile. Episodes, 26, 285-289.

Hervé, F., Fanning, C.M., Pankhurst, R.J. 2003. Detrital zircon age patterns and provenance of the metamorphic complexes of southern Chile. Journal of South America Earth Sciences, 16, 107-123. doi.org/10.1016/S0895-9811(03)00022-1

Hervé, F., Fanning, C.M., Pankhurst, R.J., Mpodozis, C., Klepeis, K., Calderón, M., Thomson, S.N. 2010b. Detrital zircon SHRIMP U–Pb age study of the Cordillera Darwin Metamorphic Complex of Tierra del Fuego: sedimentary sources and implications for the evolution of the Pacific margin of Gondwana. Journal of the Geological Society, 167(3), 555-568. doi.org/10.1144/0016-76492009-124

Hervé, F., Massonne, H.-J., Calderón, M., Theye, T. 2007b. Metamorphic P-T conditions of Late Jurassic rhyolites in the Magallanes fold and thrust belt, Patagonian Andes, Chile. Journal of Iberian Geology 33, 5-16. ISSN: 1886-7995.

Hervé, F., Pankhurst, R.J., Fanning, C.M., Calderón, M., Yaxley, G.M. 2007a. The South Patagonian batholith: 150 my of granite magmatism on a plate margin. Lithos 97, 373-394. doi.org/10.1016/j.lithos.2007.01.007

Hervé, M., Suárez, M., Puig, A. 1984. The Patagonian Batholith S of Tierra del Fuego, Chile: timing and tectonic implications. Journal of the Geological Society, 141(5), 909-917. doi.org/10.1144/gsjgs.141.5.0909

Hirth, G., Tullis, J. 1994. The brittle-plastic transition in experimentally deformed quartz aggregates. Journal of Geophysical Research: Solid Earth, 99(B6), 11731-11747. doi.org/10.1029/93JB02873

Holland, T., Baker, J., Powell, R. 1998. Mixing properties and activity-composition relationships of chlorites in the system MgO-FeO-Al_2O_3-SiO_2-H_2O. European Journal of Mineralogy, 395-406. doi.org/10.1127/ejm/10/3/0395

Holland, T.J.B., Powell, R. 1998. An internally consistent thermodynamic data set for phases of petrological interest. Journal of Metamorphic Geology 16, 309-343. doi.org/10.1111/j.1525-1314.1998.00140.x

Horton, B.K. 2018. Tectonic regimes of the central and southern Andes: Responses to variations in plate coupling during subduction. Tectonics, 37(2), 402-429. doi.org/10.1002/2017TC004624

Hyppolito, T., Angiboust, S., Juliani, C., Glodny, J., Garcia-Casco, A., Calderon, M., Chopin, C. 2016. Eclogite-, amphibolite- and blueschist-facies rocks from Diego de Almagro Island (Patagonia): Episodic accretion and thermal evolution of the Chilean subduction interface during the Cretaceous. Lithos, 264, 422-440. doi.org/10.1016/j.lithos.2016.09.001

Jamieson, R.A., Beaumont, C., Fullsack, P., Lee, B. 1998. Barrovian regional metamorphism: Where's the heat?. Geological Society, London, Special Publications, 138(1), 23-51. doi.org/10.1144/GSL.SP.1996.138.01.03

Jolivet, L., Trotet, F., Monié, P., Vidal, O., Goffé, B., Labrousse, L., Agard, P. 2010. Along-strike variations of P–T conditions in accretionary wedges and syn-orogenic extension, the HP–LT Phyllite–Quartzite Nappe in Crete and the Peloponnese. Tectonophysics, 480(1-4), 133-148. doi.org/10.1016/j.tecto.2009.10.002

Katz, H.R. 1964. Some new concepts on geosynclinal development and mountain building at the southern end of South America. 22nd International Geological Congress, India, Proceedings, New Delhi 4, 242-255.

Klepeis, K., Betka, P., Clarke, G., Fanning, M., Hervé, F., Rojas, L., Mpodozis, C., Thomson, S.N. 2010. Continental underthrusting and obduction during the Cretaceous closure of the Rocas Verdes rift basin, Cordillera Darwin, Patagonian Andes. Tectonics, 29(3), TC3014. doi:10.1029/2009TC002610.

Kley, J., Monaldi, C.R., Salfity, J.A. 1999. Along-strike segmentation of the Andean foreland: causes and consequences. Tectonophysics, 301(1-2), 75-94. doi.org/10.1016/S0040-1951(98)90223-2

Kohn, M.J., Spear, F.S., Dalziel, I.D. 1993. Metamorphic P-T paths from Cordillera Darwin, a core complex in Tierra del Fuego, Chile: Journal of Petrology, 34, 519-542. doi.org/10.1093/petrology /34 .3 .519.

Kohn, M.J., Spear, F.S., Harrison, T.M., Dalziel, I.W.D. 1995. 40Ar/39Ar geochronology and P-T-t paths from the Cordillera Darwin metamorphic complex, Tierra del Fuego, Chile. Journal of Metamorphic Geology, 13(2), 251-270. doi.org/10.1111/j.1525-1314.1995.tb00217.x

Kraemer, P.E. 1998. Structure of the Patagonian Andes: Regional balanced cross section at 50 S, Argentina. International Geology Review, 40(10), 896-915. doi.org/10.1080/00206819809465244

Kraemer, P.E. 2003. Orogenic shortening and the origin of the Patagonian orocline (56 S. Lat). Journal of South American Earth Sciences, 15(7), 731-748.

Lacombe, O., Bellahsen, N. 2016. Thick-skinned tectonics and basement-involved fold–thrust belts: insights from selected Cenozoic orogens. Geological Magazine, 153(5-6), 763-810. doi.org/10.1017/S0016756816000078

Laurent, V., Beaudoin, A., Jolivet, L., Arbaret, L., Augier, R., Rabillard, A., Menant, A. 2015. Interrelations between extensional shear zones and synkinematic intrusions: The example of Ikaria Island (NE Cyclades, Greece), Tectonophysics, 651, 152-171. ISSN: 0040-1951

Lee, J.Y., Marti, K., Severinghaus, J.P., Kawamura, K., Yoo, H.S., Lee, J.B., Kim, J.S. 2006. A redetermination of the isotopic abundances of atmospheric Ar. Geochimica et Cosmochimica Acta, 70(17), 4507-4512.

Likerman, J., Burlando, J.F., Cristallini, E.O., Ghiglione, M.C. 2013. Along-strike structural variations in the Southern Patagonian Andes: insights from physical modelling. Tectonophysics, 590, 106-120. doi.org/10.1016/j.tecto.2013.01.018

Ludwig, K.R. 2000. SQUID 1.00, A User's Manual. Berkeley Geochronology Center Special Publication, 2, 2455.

Malkowski, M.A., Grove, M., Graham, S.A. 2015a. Unzipping the Patagonian Andes—Long-lived influence of rifting history on foreland basin evolution. Lithosphere, 8(1), 23-28. doi.org/10.1130/L489.1

Malkowski, M.A., Sharman, G.R., Graham, S.A., Fildani, A. 2015b. Characterization and diachronous initiation of coarse clastic deposition in the Magallanes–Austral retroarc foreland basin, Patagonian Andes. Basin Research, 29, 298-326. doi.org/10.1111/bre.12150

Maloney, K.T., Clarke, G.L., Klepeis, K.A., Fanning, C.M., and Wang, W. 2011. Crustal growth during back-arc closure: Cretaceous exhumation history of Cordillera Darwin, southern Patagonia. Journal of Metamorphic Geology, 29(6), 649-672. doi: 10 .1111 /j.1525-1314 .2011 .00934 .x

Maruyama, S., Liou, J.G., Terabayashi, M. 1996. Blueschists and eclogites of the world and their exhumation. International Geology Review, 38(6), 485-594. doi.org/10.1080/00206819709465347

Massonne, H.-J. 2010. Phase relations and dehydration behaviour of calcareous sediments at very-low to low grade metamorphic conditions. Periodico di Mineralogia, 79(2), 21-43.

Massonne, H.-J. 2012. Formation of amphibole and clinozoisite-epidote in eclogite owing to fluid infiltration during exhumation in a subduction channel. Journal of Petrology, 53, 1969-1998. doi.org/10.1093/petrology/egs040

Massonne, H.-J., Willner, A. 2008. Phase relations and dehydration behaviour of psammopelites and mid-ocean ridge basalt at very-low to low grade metamorphic conditions. European Journal of Mineralogy 20, 867-879. doi.org/10.1127/0935-1221/2008/0020-1871

McAtamney, J., Klepeis, K., Mehrtens, C., Thomson, S., Betka, P., Rojas, L., Snyder, S. 2011. Along-strike variability of back-arc basin collapse and the initiation of sedimentation in the Magallanes foreland basin, southernmost Andes (53–54.5°S). Tectonics, 30 (5), TC5001. doi.org/10.1029/2010TC002826

McNamara, M. 1965. The lower greenschist facies in the Scottish Highlands. Geologiska Föreningen i Stockholm Förhandlingar, 87(3), 347-389.

Miyashiro, A. 1973. Paired and unpaired metamorphic belts. Tectonophysics, 17(3), 241-254. doi.org/10.1016/0040-1951(73)90005-X

Mpodozis, C., Alvarez, P., Elgueta, S., Mella, P., Hervé, F., Fanning, M. 2007. Revised Cretaceous stratigraphy of the Magallanes foreland basin at Seno Skyring: Regional implications of new SHRIMP age data on detrital zircon populations. In GEOSUR 2007 International Congress on the Geology and Geophysics of the Southern Hemisphere: Santiago, Chile, Pontificia Universidad Católica de Chile, abstract, p. 106.

Mukasa, S.B., Dalziel, I.W. 1996. Southernmost Andes and South Georgia Island, North Scotia Ridge: zircon U-Pb and muscovite 40Ar39Ar age constraints on tectonic evolution of Southwestern Gondwanaland. Journal of South American Earth Sciences, 9(5-6), 349-365.

Nelson, E.P. 1982. Post-tectonic uplift of the Cordillera Darwin orogenic core complex: Evidence from fission track geochronology and closing temperaturetime relationship. Journal of the Geolological Society, 139, 755-761. Doi.org/10.1144/gsjgs.139.6.0755

Nelson, E.P., Dalziel, I.W.D., Milnes, A.G. 1980. Structural geology of the Cordillera Darwin; collisional style orogenesis in the southernmost Chilean Andes. Eclogae Geologie Helvetica, 73(3), 727-751.

Pankhurst, R.J., Leat, P.T., Sruoga, P., Rapela, C.W., Márquez, M., Storey, B.C., Riley, T R. 1998. The Chon Aike province of Patagonia and related rocks in West Antarctica: a silicic large igneous province. Journal of Volcanology and Geothermal Research, 81(1-2), 113-136. doi.org/10.1016/S0377-0273(97)00070-X

Pankhurst, R.J., Riley, T.R., Fanning, C.M., Kelley, S.P. 2000. Episodic silicic volcanism in Patagonia and the Antarctic Peninsula: Chronology of magmatism associated with the break-up of Gondwana. Journal of Petrology, 41, 605-625. doi.org/10.1093/petrology/41.5.605

Pfiffner, O.A. 2006. Thick-skinned and thin-skinned styles of continental contraction. Special papers-Geological Society of America, 414, 153.

Platt, J.P. 1986. Dynamics of orogenic wedges and the uplift of high-pressure metamorphic rocks. Geological Society of America Bulletin, 97(9), 1037-1053. doi.org/10.1130/0016-7606(1986)97<1037:DOOWAT>2.0.CO;2

Poblete, F., Roperch, P., Arriagada, C., Ruffet, G., Ramírez de Arellano, C., Hervé, F., Poujol, M. 2016. Late Cretaceous–early Eocene counterclockwise rotation of the Fueguian Andes and evolution of the Patagonia–Antarctic Peninsula system. Tectonophysics, 668, 15-34.

Prades, C.F.K. 2008. Petrología y metamorfismo de las rocas basálticas en Isla Capitán Aracena, Isla Carlos III y Estero La Pera, Región de Magallanes, Chile. Undergraduate Thesis, Departamento de Geología, Universidad de Chile, 136 p. (unpublished) http://repositorio.uchile.cl/handle/2250/104950

Price, N.J., McClay, K.R. (Eds.). 1981. Thrust and nappe tectonics. Geological Society of London.

Ramos, V. 1999. Plate tectonic setting of the Andean Cordillera. Episodes, 22, 183-190. doi.org/10.18814/epiiugs/1999/v22i3/005

Ramos, V.A., Zapata, T., Cristallini, E., Introcaso, A. 2004. The Andean thrust system: latitudinal variations in structural styles and orogenic shortening. In: McClay, K. (ed.), Thrust Tectonics and Hydrocarbon Systems, American Association of Petroleum Geologists: Memoir, AAPG, Tulsa, 82, 30–50.

Rapalini, A.E., Calderón, M., Singer, S., Hervé, F., Cordani, U. 2008. Tectonic implications of a paleomagnetic study of the Sarmiento Ophiolitic Complex, southern Chile. Tectonophysics 452, 29-41. doi.org/10.1016/j.tecto.2008.01.005

Rapalini, A., Peroni, J., Luppo, T., Tassone, A., Cerredo, M.E., Esteban, F., Lippai, H., Franciscovilas, J., 2015. Palaeomagnetism of Mesozoic magmatic bodies of the Fuegian Cordillera: implications for the formation of the Patagonian Orocline. Geological Society 425 (1), 65–80. https://doi.org/10.1144/SP425.3.

Renne, P.R., Balco, G., Ludwig, K.R., Mundil, R., Min, K. 2011. Response to the comment by WH Schwarz et al. on "Joint determination of 40K decay constants and 40Ar∗/40K for the Fish Canyon sanidine standard, and improved accuracy for 40Ar/39Ar geochronology" by PR Renne et al.(2010). Geochimica et Cosmochimica Acta, 75(17), 5097-5100.

Renne, P.R., Swisher, C.C., Deino, A.L., Kramer, D.B., Owens, T.L., DePaolo, D.J. 1998. Intercalibration of standards, absolute ages and uncertainities in 40Ar/39Ar dating. Chemical Geology ,145, 117-152. doi.org/10.1016/S0009-2541(97)00159-9

Roche, V., Sternai, P., Guillou-Frottier, L., Menant, A., Jolivet, L., Bouchot, V., Gerya, T. 2018. Emplacement of metamorphic core complexes and associated geothermal systems controlled by slab dynamics. Earth and Planetary Science Letters, 498, 322-333. doi.org/10.1016/j.epsl.2018.06.043

Rojas, L., Mpodozis, C. 2006. Geología estructural de la Faja Plegada y Corrida del sector chileno de Tierra del Fuego, Andes patagónicos australes. In Congreso Geológico Chileno, No. 11: Actas (Vol. 1).

Romans, B.W., Fildani, A., Hubbard, S.M., Covault, J.A., Fosdick, J.C., Graham, S.A. 2011. Evolution of deep-water stratigraphic architecture, Magallanes Basin, Chile. Marine and Petroleum Geology, 28, 612-628. doi.org/10.1016/j.marpetgeo.2010.05.002

Schellart, W.P. 2008. Overriding plate shortening and extension above subduction zones: a parametric study to explain formation of the Andes Mountains. Geological Society of America Bulletin, 120, 1441-1454. doi.org/10.1130/B26360.1

Schellart, W.P., Lister, G.S. 2005. The role of the East Asian active margin in widespread extensional and strike-slip deformation in East Asia. Journal of the Geological Society, 162(6), 959-972.

Seki, Y. 1959. Relation between chemical composition and lattice constants of epidote. American Mineralogist: Journal of Earth and Planetary Materials, 44(7-8), 720-730.

Selzer, C., Buiter, S.J., Pfiffner, O.A. 2007. Sensitivity of shear zones in orogenic wedges to surface processes and strain softening. Tectonophysics, 437(1-4), 51-70. doi.org/10.1016/j.tecto.2007.02.020

SERNAGEOMIN, 2003. Mapa Geológico de Chile: digital version. Geological Base scale 1:1.000.000. Chile Government, Servicio Nacional de Geología y Minería.

Stern, C.R. 1979. Open and closed system igneous fractionation within two Chilean ophiolites and the tectonic implications. Contribution to Mineralogy and Petrology 68, 243-258.

Stern, C.R., De Wit, M.J. 2003. Rocas Verdes ophiolites, southernmost South America: remnants of progressive stages of development of oceanic-type crust in a continental margin back-arc basin. Geological Society of London, Special Publications, 218, 665-683. doi.org/10.1144/GSL.SP.2003.218.01.32

Stern, C.R., Mohseni, P.P., Fuenzalida, P.R. 1991. Petrochemistry and tectonic significance of Lower Cretaceous Barros Arana Formation basalts, southernmost Chilean Andes. Journal of South American Earth Sciences, 4(4), 331-342. doi.org/10.1016/0895-9811(91)90005-6

Stipp, M., Stünitz, H., Heilbron, M., Schmid, D.W. 2002. The eastern Tonale fault zone: a natural laboratory for crystal plastic deformation of quartz over a temperature range from 250 to 700 °C. Journal of Structural Geology, 24, 1861-1884. doi.org/10.1016/S0191-8141(02)00035-4

Suárez, M., Pettigrew, T.H. 1976. An upper Mesozoic island-arc–back-arc system in the southern Andes and South Georgia. Geological Magazine, 113(4), 305-328. doi.org/10.1017/S0016756800047592

Suárez, R., González, P.D., Ghiglione, M.C. 2019. A review on the tectonic evolution of the Paleozoic-Triassic basins from Patagonia: Record of protracted westward migration of the pre-Jurassic subduction zone. Journal of South American Earth Sciences, 102256. doi.org/10.1016/j.jsames.2019.102256

Tera, F., Wasserburg, G. 1972. U-Th-Pb systematics in three Apollo 14 basalts and the problem of initial Pb in lunar rocks. Earth and Planetary Science Letters 14, 281-304. doi.org/10.1016/0012-821X(72)90128-8

Thomson, S.N., Hervé, F., Stöckhert, B. 2001. Mesozoic-Cenozoic denudation history of the Patagonian Andes (southern Chile) and its correlation to different subduction processes. Tectonics, 20(5), 693-711. doi.org/10.1029/2001TC900013

Tullis, J., Snoke, A.W., Todd, V.R. 1982. Significance and petrogenesis of mylonitic rocks. Geology, 10, 227-230. doi.org/10.1130/0091-7613(1982)10<227:SAPOMR>2.0.CO;2

Tullis, J., Yund, R., Farver, J. 1996. Deformation-enhanced fluid distribution in feldspar aggregates and implications for ductile shear zones. Geology, 24(1), 63-66. doi.org/10.1130/0091-7613(1996)024<0063:DEFDIF>2.3.CO;2

van Staal, C.R., Rogers, N., Taylor, B.E. 2001. Formation of low-temperature mylonites and phyllonites by alkali-metasomatic weakening of felsic volcanic rocks during progressive, subduction-related deformation. Journal of Structural Geology, 23(6-7), 903-921. doi.org/10.1016/S0191-8141(00)00163-2

Vidal, O., Parra, T. 2000. Exhumation paths of high-pressure metapelites obtained from local equilibria for chlorite–phengite assemblages. Geological Journal, 35(3-4), 139-161. doi.org/10.1002/gj.856

Wakabayashi, J., Dilek, Y. 2003. What constitutes 'emplacement' of an ophiolite?: Mechanism and relationship to subduction initiation and formation of metamorphic soles. In: Dilek, Y., Robinson, P.T. (Eds.), Ophiolites in Earth History: Geological Society, London, Special Publications, 218, 427-447. doi.org/10.1144/GSL.SP.2003.218.01.22

Warren, C.J., Hanke, F., Kelley, S.P. 2012. When can muscovite 40Ar/39Ar dating constrain the timing of metamorphic exhumation?. Chemical Geology, 291, 79-86. doi.org/10.1016/j.chemgeo.2011.09.017

Williams, I.S. 1998. U-Th-Pb geochronology by ion microprobe. In: McKibben, M.A., Shanks III, W.C., Ridley, W.I. (Eds.), Applications of Microanalytical Techniques to Understanding Mineralizing Processes: Reviews in Economic Geology, 107, 1-35.

Willner, A.P., Hervé, F., Thomson, S.N., Massonne, H.-J. 2004. Converging PT-paths of Mesozoic HP-LT metamorphic units (Diego de Almagro Island, Southern Chile, 51°30pS): Evidence for juxtaposition during late shortening of an active continental margin. Mineralogy and Petrology, 81, 43-84.

Wilson, T.J. 1991. Transition from back-arc to foreland basin development in southernmost Andes: Stratigraphic record from the Ultima Esperanza District, Chile. Geological Society of America Bulletin, 103, 98-111. doi.org/10.1130/0016-7606(1991)103<0098:TFBATF>2.3.CO;2

Winslow, M.A. 1982. The structural evolution of the Magallanes Basin and neotectonics in the southernmost Andes. Antarctic Geoscience, 143-154.

Zerfass, H., Ramos, V.A., Ghiglione, M.C., Naipauer, M., Belotti, H.J., Carmo, I.O. 2017. Folding, thrusting and development of push-up structures during the Miocene tectonic inversion of the Austral Basin, Southern Patagonian Andes (50°S). Tectonophysics. 699, 102-120. doi.org/10.1016/j.tecto.2017.01.010

Zheng, Y., Chen, R., Xu, Z., Zhang, S. 2016. The transport of water in subduction zones. Science China Earth Sciences, 59(4), 651-682.

Chapter 3. Article 2

Quantification of the mantle and climate forcing to the exhumation of the southern Patagonian Andes (Torres del Paine 51 °S and Fitz Roy 49 °S massifs)

Veleda P. Muller[1], Christian Sue[2,3], Pierre G. Valla[2], Pietro Sternai[1], Thibaud Simon-Labric[4], Cécile Gautheron[2,5], Kurt Coffey[6], Matthias Bernet[2], Djordie Grujic[7], Lukas Baumgartner[8], Frédéric Herman[8], Matias Ghiglione[9], Peter Reiners[9], David Shuster[6], Chelsea Willett[6], Joseph Martinod[2], Jean Braun[2,11]

[1] Dipartimento di Scienze dell'Ambiente e della Terra (DISAT), Università degli Studi di Milano-Bicocca, Piazza della Scienza 4, Milan, Italy.
[2] Institute des Sciences de la Terre (ISTerre), Université Grenoble Alpes, Université Savoie Mont Blanc, CNRS, IRD, IFSTTAR, Université Gustave Eiffel, Grenoble – Chambèry, France.
[3] Université de Franche-Comté, 25000 Besançon, France
[4] Centre de Géologie Oisans Alpes, Musée des Minéraux, 38520 Bourg-d'Oisans, France
[5] Geosciences Paris Saclay, Université Paris Saclay, CNRS, Orsay, France.
[6] Department of Geography, Department of Earth and Planetary Science, University of California – Berkeley, USA
[7] Department of Earth and Environmental Sciences, Dalhousie University, Halifax, Canada.
[8] Institut des Sciences de la Terre (ISTE), Université de Lausanne, CH-1015 Lausanne, Switzerland
[9] Instituto de Estudios Andinos "Don Pablo Groeber", Universidad de Buenos Aires, CONICET, Buenos Aires, Argentina
[9] Department of Geosciences, University of Arizona, Tucson, USA
[11] Helmholtz-Zentrum Potsdam, University of Potsdam, Potsdam, Germany

E-mail adresses: v.paivamuller@campus.unimib.it; christian.sue@univ-grenoble-alpes.fr; pierre.valla@univ-grenoble-alpes.fr; pietro.sternai@unimib.it; thibaud.simon-labric@asso-cgo.fr; cecile.gautheron@univ-grenoble-alpes.fr; kcuffey@berkeley.edu; Joseph.Martinod@univ-smb.fr; matias@gl.fcen.uba.ar; Lukas.Baumgartner@unil.ch; Frederic.Herman@unil.ch; reiners@email.arizona.edu; Djordje.Grujic@Dal.Ca; dshuster@berkeley.edu; jean.braun@gfz-potsdam.de; matthias.bernet@univ-grenoble-alpes.fr

Abstract

The modern topography of the southern Patagonian Andes shows conspicuous landscapes with deep incised glacial valleys surrounded by mountain peaks protruding ~1-2 km above the current glacier's equilibrium line altitude. The respective contributions and spatio-temporal variability of tectonic convergence, mantle upwelling, and climate-controlled erosion to rock exhumation and relief evolution are still poorly constrained. Late Cretaceous – Miocene lithospheric shortening in the retroarc of the belt generated fold-and-thrust belts, later intruded by Late Miocene plutonic complexes. Two of these plutonic complexes form the core of the Fitz Roy (49 °S) and Torres del Paine (51 °S) massifs and part of the highest topography of the southern Patagonian Andes. These massifs are currently located above an asthenospheric window formed by northward migrating subduction of oceanic ridge segments, a process initiated at ~54 °S and ~16 Ma. Late Miocene onset of major glaciations generated drastic geomorphological changes via erosional processes. Here, we present inverse thermal modelling outputs based on a new low-temperature thermochronology dataset with zircon and apatite (U-Th-Sm)/He ages within the two massifs, complemented by new apatite $^{4}He/^{3}He$ data in Torres del Paine. Our results show a short period of rapid rock exhumation recorded in the Fitz Roy massif between ~10.5 and 8.5 Ma, synchronous with ridge subduction at ~49 °S. Such signal is not observable in Torres del Paine, given that ridge subduction occurred earlier than pluton emplacement at this location. We thus associate this early rock exhumation episode to mantle upwelling and crustal shortening as consequence of ridge subduction at 49 °S. Both massifs record a pulse of rapid rock exhumation between ~6.5 and 5.5 Ma, interpreted as the onset of the Patagonian glaciations at around 50°S, resulting in spatially variable erosion and relief evolution (~1-3 km of erosion). After a period of erosional quiescence at the Miocene/Pliocene transition, increase in rock exhumation from ~2-3 Ma to present day is interpreted as the result of alpine valley carving through efficient glacial erosion, which has been promoted by reinforced glacial-interglacial cyclicity. We thus highlight the importance of along-strike large-scale thermochronological studies to better assess spatio-temporal variations in tectonic, mantle, and surface processes forcing on mountain building.

1. Introduction

Along subduction and continental collision zones, orogens grow and evolve according to a long-term balance between incoming masses by tectonic accretion and outgoing masses by climate-driven erosion (Dahlen, 1990; Ruddiman et al., 1997; Willett et al., 1999; Egholm et al., 2009; Koppes and Montgomery, 2009). Compression is primarily accommodated by thrusts and transpressive faults that lead to lithospheric shortening, thickening, and uplift (Dahlen, 1990; Willett, 1999). At depths, lithospheric slab subduction and upper mantle dynamics modulate the stress and thermal state of the crust, thereby affecting the surface uplift (Molnar et al., 1993; Heuret and Lallemand, 2005; Conrad and Husson, 2009; Guillaume et al., 2010; Faccena et al., 2013; Sternai et al., 2019). At the surface, erosion shapes the relief of orogens, exhuming rocks in topographic highs and generating sedimentation in topographic depressions (England and Molnar, 1990; Whipple and Tucker, 1999; Willett, 1999; Brocklehurst, 2010; Whipple, 2009; Champagnac et al., 2014). Since climate-controlled erosion and deep-seated processes are intrinsically linked and operate at various spatial and temporal scales, quantifying their relative contributions to rock exhumation and landscape evolution in orogenic settings is a primary but still elusive goal.

The erosional mass outflux largely depends on the partitioning between glacial processes that widen and deepen valleys (Brocklehurst and Whipple, 2006; Herman et al., 2011, 2018; Sternai et al., 2011; Shuster et al., 2005, 2011; Sternai et al., 2013), and fluvial erosion that forms valleys with relief that depend on the local slope and water discharge (Willett, 1999; Whipple and Tucker, 1999; Braun and Willett, 2013). Changes in global climate, such as the increase in global cooling during the late Cenozoic and associated onset of glaciations, generate cyclic shifts in the fluvial/glacial erosion and associated transience in the landscape and uplift (Egholm et al., 2009; Koppes and Montgomery, 2009; Valla et al., 2011; Herman et al., 2013, 2018; Fox et al., 2015). At orogenic scale, the glacier's Equilibrium Line Altitude (ELA) may limit the elevation of glaciated mountain ranges, independent of the tectonic uplift rate (Egholm et al., 2009). Other studies, however, suggested that the tectonic uplift modulates both the fluvial and glacial erosion rates in orogens (Koppes and Montgomery, 2009). The control of glacial erosion on the elevation and topographic relief of mountain ranges is complex and depends on factors such as the bedrock physical properties, previous mountain slope, basal thermal gradient of ice sheets, etc. (Sternai et al., 2013; Pedersen and Egholm, 2013). The basal temperature of ice sheets, in particular, modulates glacial erosion rates such that wet and warm-based glaciers are more

prone to generate glacier sliding and thus higher erosion rates (Pedersen and Egholm, 2013), whereas dry and cold-based glaciers shield the underneath bedrock from erosion, allowing topographic growth due to tectonic uplift (Thomson et al., 2010).

The typical steep and high topographic relief of glaciated mountain belts with deeply incised valleys exposes lithospheric rocks that were once deeply buried (e.g., Champagnac et al., 2014). Generally, crystalline rocks that formed at depth (i.e., magmatic and metamorphic rocks) offer a higher resistance to erosion compared to soft rocks formed near the surface (i.e., volcano-sedimentary rocks), and tend to form prominent peaks in Alpine valleys (Egholm et al., 2009; Shuster et al., 2011; Herman et al., 2013; Champagnac et al., 2014). Low-temperature thermochronometric bedrock ages vary systematically with elevation, low elevation rocks being more recently exhumed, and age-elevation relationships allow estimating regional exhumation rates (Braun, 2002; Reiners and Brandon, 2006). Dating crystalline rocks in elevation transects using low-temperature thermochronology provide robust information to unravel the exhumation history of orogenic regions, potentially recording the effects of glacial erosion and tectonic uplift on the topographic relief evolution.

In the southern Patagonian Andes glacial landscapes and related sedimentary deposits were proposed to have evolved since the onset of Patagonian glaciations in the Late Miocene (~7 Ma; Mercer and Sutter, 1982; Zachos et al., 2001; Thomson et al., 2001; Rabassa, 2008; Lagabrielle et al., 2010; Georgieva et al., 2016, 2019; Willett et al., 2020). Currently, the Northern Patagonian (NPI, 46 – 47 °S), the Southern Patagonian (SPI, 48 – 52 °S) and the Cordillera Darwin (CDI, 54 °S) icefields are located above the central orogenic zone. This study focuses on the rocks in the eastern proximity of the SPI, where mountain peaks rise above the current glaciers' ELA, which has been oscillating between ~0.5 and 2 km above sea level during glacial/interglacial periods, at least since the Last Glacial Maximum (~21000 years ago) (Broecker and Denton, 1990; Davies, 2020). Miocene plutonic complexes intruding deformed Mesozoic sedimentary rocks constitute most of these high peaks, and the geomorphology is of steep valleys close to the ice fields, and gentle valleys towards the eastern continental foreland (Fosdick et al., 2013). The entire region is lying above an asthenospheric window (Fig. 1) currently originating at the Chile Triple Junction at ~46 °S (Cande and Leslie, 1986; Breitsprecher and Thorkelson, 2009). The asthenospheric window opened through events of spreading ridge and transform fault subduction. Ridge collision with the trench generated compressive deformation events in the orogen, which episodically migrated northward, from 54 °S at ~16 Ma, 49 °S at ~12 Ma, and 47 °S at ~3 Ma (Fig. 1)

(Cande and Leslie, 1986; Thomson et al., 2001; Ramos, 2005; Lagabrielle et al., 2010; Breitsprecher and Thorkelson, 2009; Guillaume et al., 2009; Scalabrino et al., 2010; Fosdick et al., 2013; Stevens Goddard and Fosdick, 2019, Georgieva et al., 2016, 2019). Mantle upwelling during ridge subduction is expected to have generated long-wavelength surface uplift of the continent, following the northward motion of the Chile Triple Junction (Guillaume et al., 2009, 2013).

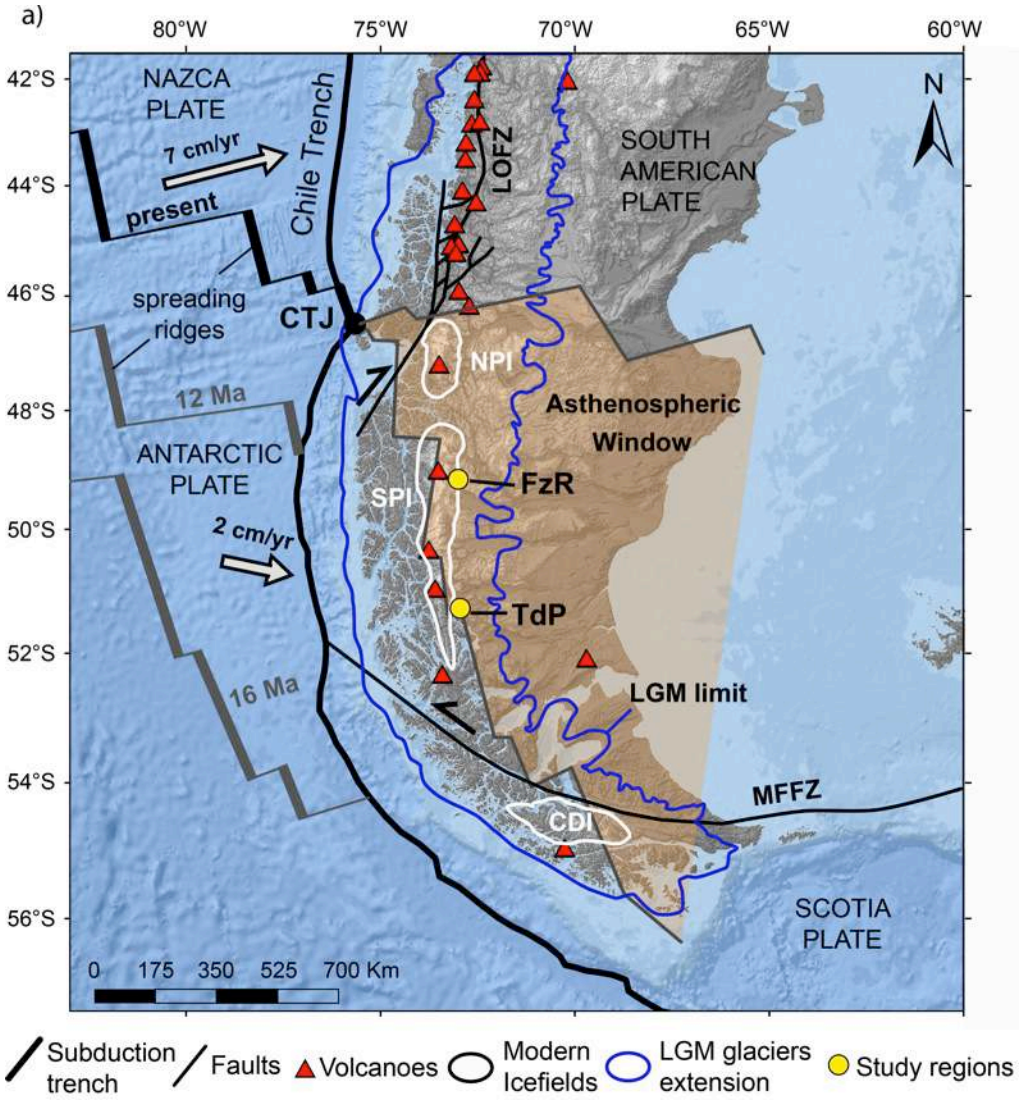

Fig. 1. Geodynamic context of the southern Patagonian Andes. The orange region is the current asthenospheric window, and the Chile Triple Junction (CTJ) is where the Chile Ridge is currently subducting. The black and grey lines between the Nazca and the Antarctic plates are the present day, and the older positions (at 16 and 12 Ma), respectively, of the spreading ridges and transform faults separating the plates (Breitsprecher and Thorkelson, 2009). The grey arrows show the velocity and approximate direction of subduction of the Nazca and Antarctic plates (DeMets et al., 2010). Red triangles are Quaternary volcanoes (Global Volcanism Program, 2023). Low-temperature thermochronometric data presented in this study are from the Torres del Paine (TdP) and Fitz Roy (FzR) massifs (yellow circles), located in the eastern border of the Southern Patagonian Icefield (SPI, white line). The region delimited by the blue line was covered by glaciers during the Last Glacial Maximum (LGM) at ~21000 years (adapted from Thorndycraft et al., 2019). Other abbreviations: NPI: Northern Patagonian Icefield, CDI: Cordillera Darwin Icefield, MFFZ: Magallanes-Fagnano Fault Zone, LOFZ: Liquiñe-Ofqui Fault Zone.

In this study, we present a new low-temperature thermochronometric dataset from two of the most emblematic massifs of the Southern Patagonia Andes, the Fitz Roy (FzR) and the Torres del Paine (TdP) (Figs. 1-3). These two regions are located south of the northward migrating CTJ, and thus may have recorded the effects of ridge subduction and asthenospheric window opening besides those of the local onset of Late Cenozoic glaciations (Ramos, 2005; Guillaume et al., 2009, 2013; Fosdick et al., 2013; Stevens Goddard and Fosdick, 2019). They are also located far from the damage zones of the transpressive Liquiñe-Ofqui and the Magallanes-Fagnano fault zones, allowing us to dismiss a potential influence on regional exhumation and/or reheating associated to these major structures (Thomson et al., 2001; Lagabrielle et al., 2010; Guillaume et al., 2013). Because these two massifs are located ~200 km apart in the N-S direction the comparative study of their exhumation records allow us to interpret local and/or regional transient processes, shedding new light on the main drivers of mountain building and respective partitioning.

2. Geologic context

2.1. Geodynamic setting

The FzR and the TdP massifs are located in the retroarc of the southern Patagonian Andes, to the east of the main N-S oriented drainage divide and the Southern Patagonian Batholith (SPB). The SPB is made of subduction-related plutons crystallized from the Late Jurassic to the Neogene intruding Paleozoic metamorphic complexes (Hervé et al., 2007). The amalgamation of the continental block bearing the SPB with the South American continent occurred in the Late Cretaceous through the closure of the ocean-floored backarc Rocas Verdes Basin (Calderón et al., 2012; Maloney et al., 2013; Muller et al., 2021). Crustal shortening and thickening in the retroarc led to foreland subsidence towards the east, and deposition of marine siliciclastic deposits of the Late Cretaceous Magallanes-Austral foreland basin (Fildani et al., 2003; Fosdick et al., 2011; Malkowski et al., 2017). After the break-up of the Farallon Plate into the Nazca Pate at ~25 Ma, the increase in convergence velocity generated eastward thrust propagation into the foreland basin, finally composing the N-S oriented Patagonian-Magallanes fold-and-thrust belt (Figs. 2 and 3) (Suárez et al., 2000; Kraemer, 2003; Ghiglione et al., 2009; Fosdick et al., 2011, 2013; Betka et al., 2015). Late Miocene small and undeformed plutonic complexes intrude the Patagonian fold-and-thrust belt distributed for ~800 km along the strike of the mountain belt (Ramírez de Arellano et al.,

2012). In the Fitz Roy massif, the Chaltén Plutonic Complex is located at ~49 °S and is composed of granitic to gabbroic rocks crystallized between ca. 16.90 and 16.37 Ma (Ramírez de Arellano et al., 2012). Hornblende-thermobarometry from this plutonic complex indicates an early magmatic emplacement at around 8-10 km depth and rapid exhumation up to ~6-4 km depth during the syn-magmatic phase (Ramírez de Arellano, 2011). Currently, these plutonic complexes are exposed, for example, in the Mount Fitz Roy (3405 m.a.s.l.) and Cerro Torre (3128 m.a.s.l.) (Fig. 2). The Torres del Paine Plutonic Complex, located at ~51 °S, is a laccolith with feeder dikes of granitic to gabbroic composition, emplaced at ~2-4 km depth, as constrained from contact-metamorphic assemblages such as prehnite-anorthite (Putlitz et al., 2001), and crystallized between ca. 12.4 Ma and 12.6 Ma (Leuthold et al., 2012). The culminant points of the TdP massif are the Cerro Paine Grande (2884 m.a.s.l), composed of Late Cretaceous metasedimentary siliciclastic rocks, and the Torre Central (2460 m.a.s.l.), composed of granitic rocks from the Torres del Paine Plutonic Complex (Fig. 3).

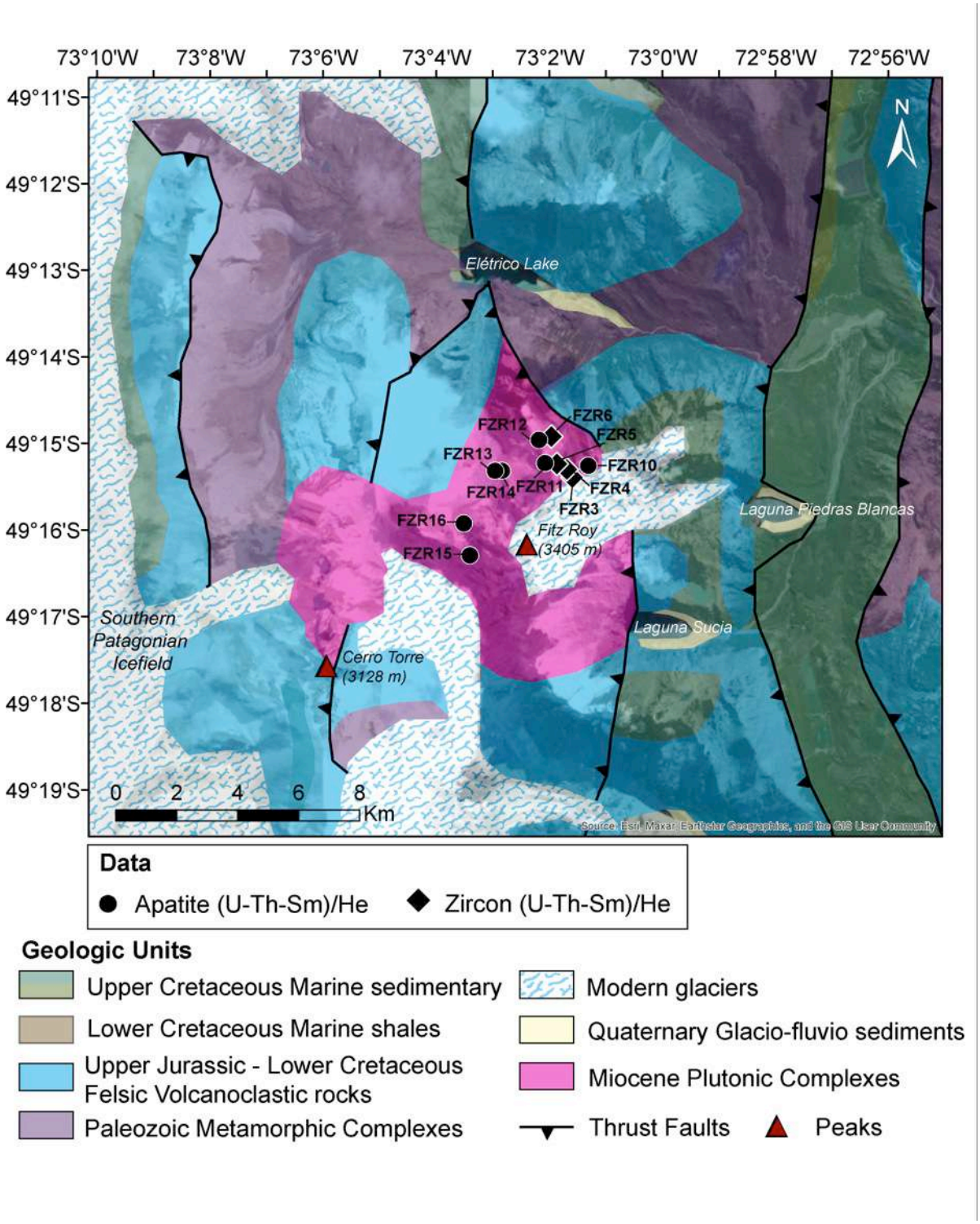

Fig. 2. Geological map of the Fitz Roy Massif (FzR, Argentina) with sample locations (modified from SEGEMAR, 2011, background satellite photo is from Google Earth). Major topographic peaks are indicated by red triangles. See Fig. 1 for location within the Southern Patagonian Andes.

The faster Nazca Plate subduction with respect to the Antarctic Plate generated a much longer Nazca slab than the Antarctic slab (DeMets et al., 2010; Hayes et al., 2018), with space for mantle upwelling in an asthenospheric window beneath the South American

Continent (Fig. 1; Cande and Leslie, 1986; Ramos and Kay, 1992; Lagabrielle et al., 2004, 2007; Ramos, 2005; Breitsprecher and Thorkelson, 2009). Asthenospheric upwelling and tectonic compression due to ridge and transform faults collision with the subduction trench contributed to an increase in rock uplift rates around the CTJ (~ 46 °S) over the last ca. 3 Ma (Thomson et al., 2001; Lagabrielle et al., 2004, 2007, 2010; Guillaume et al., 2009; Georgieva et al., 2016, 2019). Between ~12 and 6 Ma the slab window broadened between latitudes ~ 51 – 48 °S, and the dynamic uplift related to the asthenospheric flow was estimated of up to ~800 m (Guillaume et al., 2009). The Chaltén Plutonic Complex (FzR massif) was emplaced before this time window whereas the TdP laccolith was emplaced at around 12 Ma (Ramírez de Arellano et al., 2012). Whether these plutonic complexes record the progressive northward propagation of asthenospheric upwelling and tectonic compression due to ridge collision is still a matter of investigation (Fosdick et al., 2013; Stevens Goddard and Fosdick, 2019). One of the effects of the absence of a subducting slab in the asthenospheric window is the cancelation of arc volcanism (Ramos, 2005), but basaltic extensional volcanism occur in the eastern foreland recording the migrating episodes of ridge subduction (Ramos and Kay, 1992; Breitsprecher and Thorkelson, 2009). Amongst the six Quaternary volcanoes of the Austral Andes Volcanic Zone (Stern et al., 1984; Global Volcanism Program, 2023), the Lautaro (~ 49 °S) and the Reclus (~ 51 °S) volcanoes are located more than 20 km distant from the study regions (Fig. 1), and we assume no thermal influence from recent volcanism on the analyzed samples.

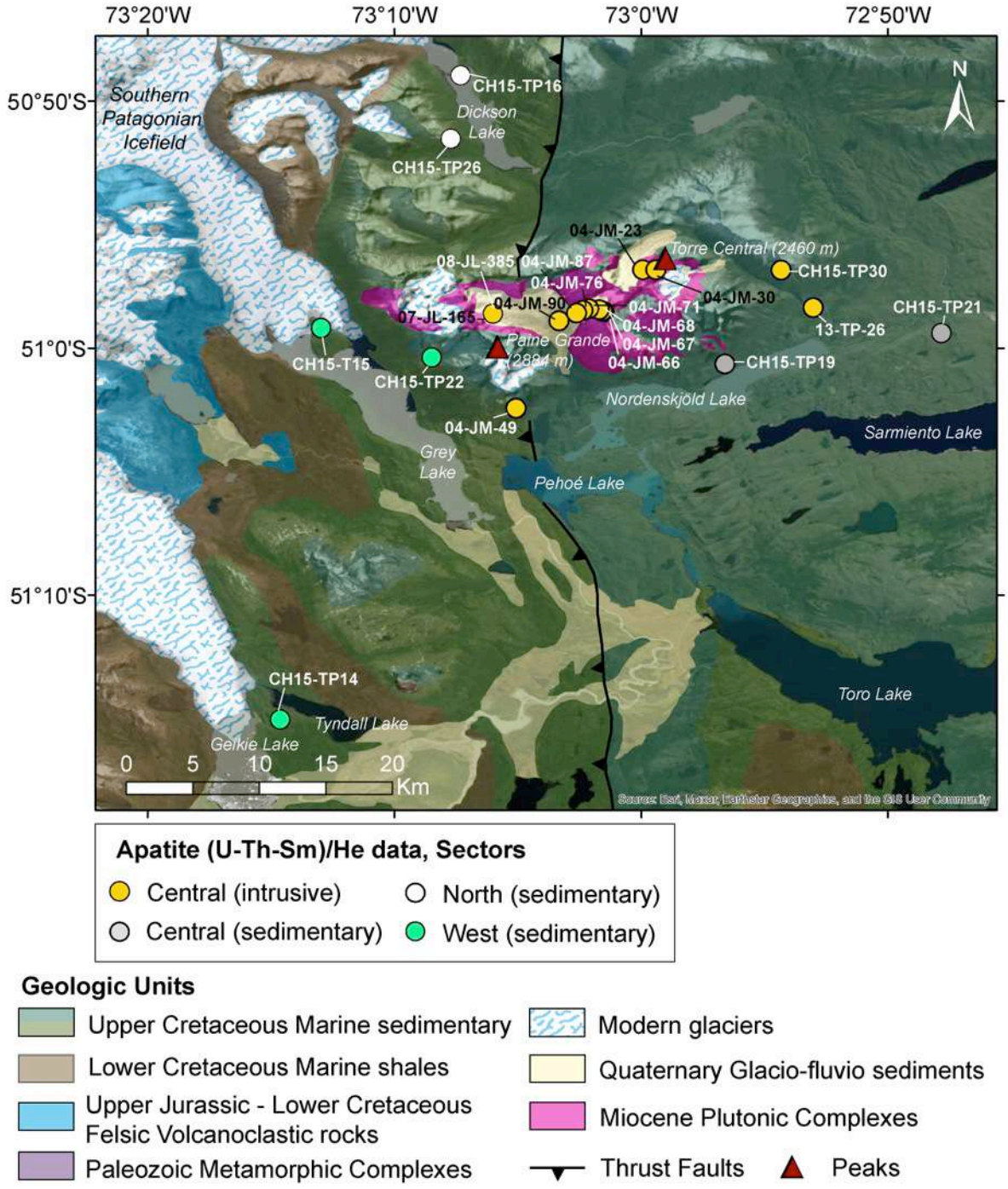

Fig. 3. Geological map of the Torres del Paine massif (TdP, Chile) with sample locations (modified from Fosdick et al., 2013, background satellite photo from Google Earth). Major topographic peaks are indicated by red triangles. See Fig. 1 for location within the Southern Patagonian Andes.

2.2. Paleoclimatic setting and thermochronologic record

The southern Patagonian Andes are approximately perpendicular to the main winds dominated by the westerlies, thus acting as an orographic barrier since at least the early Miocene (Blisniuk et al., 2006; Fosdick et el., 2013). As a result, the precipitation rates are higher than 4000 mm/yr on the windward side of the orogen, where the SPB is located, whereas the region located to the east of the topographic divide, including the FzR and the TdP massifs, is in a rain shadow (Blisniuk et al., 2006; Fosdick et al., 2013; Herman and Brandon, 2015). Low-temperature thermochronologic ages from the SPB range from ~60 to 10 Ma, being generally younger eastward and suggesting an eastward migration of the topographic divide and exhumation front (Thomson et al., 2001, 2010). In the Patagonian fold-and-thrust belt, including the Torres del Paine region, the exhumation ages range between ca. 22 – 10 Ma ascribed to thrust-driven exhumation, and ca. 7 – 3 Ma associated with glacio-fluvial erosion (Thomson et al., 2010; Fosdick et al., 2013; Herman and Brandon, 2015).

The onset of Patagonian Glaciations around 7 Ma is supported by stratigraphic and geomorphologic evidence, including glacial troughs, striations and moraine deposits up to 100 km eastward distant from the sediment sources (Mercer and Sutter, 1982; Zachos et al., 2001; Singer et al., 2004; Rabassa et al., 2005, 2011; Lagabrielle et al., 2010). At the region around the CTJ, cooling ages between ca. 4 – 3 Ma were associated with both changing glacial cyclicity, and active faulting due to spreading ridge and transform faults interaction with the orogen (Thomson et al., 2001; Lagabrielle et al., 2010; Scalabrino et al., 2010; Georgieva et al., 2016, 2019; Willett et al., 2020). The maximum extent of the Cordilleran ice sheet (the Great Patagonian Glaciation) has been dated at ~1.1 Myr, and was subsequently followed by glacial episodes that reveal a gradual shrinking of the ice extent (Kaplan et al., 2004; Singer et al., 2004; Hein et al., 2011). During the Last Glacial Maximum (LGM at ~21000 years), the region between ~38 – 56 °S formed the Patagonian Ice Sheet represented in Fig. 1 (Kaplan et al., 2004; Glasser et al., 2008; Davies and Glasser, 2012; Thorndycratf et al., 2018; Davies, 2020). An orogen-scale southward increase in exhumation ages below 49 °S was interpreted as a decrease in the erosional efficiency due to bedrock shielding by cold-based glaciers at high latitudes (Thomson et al., 2010; Herman and Brandon, 2015). However, the effects of cold-based glacier on long-term bedrock exhumation, and whether topographic relief in the Southern Patagonian Andes may surpass the glacier's ELA due to bedrock protection, are still open discussions.

3. Materials and Methods

3.1. Sample locations and processing

In the present study, we collected two new datasets of bedrock low-temperature thermochronology data from the FzR and TdP massifs. Sampled bedrock outcrops are spatially distributed within the massifs, with a sampling strategy along elevation profiles when possible (Figs. 2 and 3). The FzR profile covers around 660-m elevation (Figs. 2 and 4a) and 3-4 km of horizontal distance, with 7 samples collected for apatite (U-Th-Sm)/He data (AHe) and 4 samples for zircon (U-Th-Sm)/He data (ZHe), from magmatic rocks of the Chaltén Plutonic Complex (Tables 1-2). In the TdP massifs, investigated samples are distributed in three main sectors (Central, North and West, Fig. 3) and have been collected for AHe data, with two samples from the Central sector having also apatite $^{4}He/^{3}He$ data (Figs. 3 and 4 b, Table 3 a-c and Table S1). The Central sector covers around 1600-m elevation over around 15-km of horizontal distance, with 15 magmatic samples from the TdP plutonic complex and 2 metasedimentary samples from the Patagonian fold-and-thrust belt located near the Lago Nordenskjöld (Fig. 3). The West and North sectors have few samples, and extend over around 630-m and 550-m elevation respectively (Fig. 3). The West sector is comprised of 3 samples from the metasedimentary rocks to the west of the TdP plutonic complex, while the North sector has only 2 samples from the metasedimentary rocks near the Lago Dickson (Fig. 3). Apatite and zircon crystals were extracted from bedrock samples using crushing followed by standard magnetic and heavy-liquid separation techniques. Preparation included selection of grains for euhedral shape, uniform size and absence of inclusion.

3.2. AHe and ZHe thermochronology data

In the present study, we used both the ZHe and AHe systems which are based on the radioactive decay of the parent nuclides ^{238}U, ^{235}U, ^{232}Th, and ^{147}Sm, to the daughter nuclide ^{4}He in a single apatite or zircon crystal (Farley, 2002; Reiners and Brandon, 2006). According to equations given in Dodson (1973, 1979) the ratio between the parents and the daughter nuclides provides the crystal age in its so-called "effective closure temperature", Tc. Inside the given Tc ranges, however, ^{4}He can be partially lost from the zircon or apatite crystal and He ages of several individual grains can vary depending on each grain's chemical composition and the time that a given sample has experienced in this "partial retention zone"

(Reiners et al., 2005). This zone can be estimated between around 180 and 70 °C, and 80 and 30 °C for the ZHe and AHe systems, respectively (Farley, 2002; Ehlers and Farley, 2003; Reiners et al., 2004, 2005; Gautheron et al., 2009; 2020). The He retentivity and associated closure temperature of AHe and ZHe systems also vary according to the composition and the thermal history that causes radiation damage in the analysed crystal (Dodson, 1973; Farley, 2002; Reiners and Brandon, 2006; Gautheron et al., 2009, 2020). The ZHe system is highly sensitive to radiation damage, and ^{4}He diffusivity can strongly increase with low radiation damage, decreasing the closure temperature (Gautheron et al., 2009; 2020). In general, zircon with young crystallisation ages will present low radiation damage, with increased diffusivity of ^{4}He, and thus low resulting ZHe closure temperature, which can be relatively similar to the lower-temperature systems such as AHe (Reiners et al., 2005; Gautheron et al., 2009, 2020; Gérard et al., 2022). The FzR plutonic complex is relatively young (ca. 12.5 Ma; Ramírez de Arellano et al., 2012), and we used the Activation Energy (E_a) and the initial Diffusion coefficient (D_0) calculated by Gautheron et al. (2020), to estimate the closure temperature of the ZHe system between 87 and 108 °C for the FzR samples (Table S2).

AHe thermochronometry was performed following standard procedures (House et al., 2000) at the ARHDL of University of Arizona (USA) for magmatic samples of TdP, and at the Berkeley Geochronology Center (USA) for metasedimentary samples of TdP and ^{4}He/^{3}He data. AHe thermochronometry of FzR magmatic samples was performed in the GEOPS Laboratory in the Paris-Saclay University (Paris, France), and ZHe thermochronometry was performed in the UTHHE Laboratory of University of Dalhouise (Halifax, Canada) following the methods of Reiners et al. (2004, 2005) and Landry et al. (2016). Full analytical details for ZHe, AHe and ^{4}He/^{3}He data production are given in the Supplementary Information.

3.3. Inverse thermal modelling

In this study, we used inverse thermal modelling to interpret new AHe and ZHe data in terms of rock cooling histories, and eventually to discuss the timing and spatial differences in exhumation histories between the TdP and FzR massifs. To this aim, we used the QTQt model (Gallagher, 2012), which is based on a Bayesian Markov-Chain Monte-Carlo approach to statistically explore different temperature-time (T-t) paths for multiple samples distributed along an elevation profile. For predicting ^{4}He diffusion in a crystal, the software uses the raw contents of ^{238}U, ^{232}Th and ^{147}Sm, and the spherical grain radius estimated from grain measurements in the laboratory. For AHe data, we used the ^{4}He diffusion kinetic parameters

from the radiation damage and annealing model of Flowers et al. (2009). For the ZHe data, we estimated and input E_a and D_0 parameters for each individual zircon grain to further investigate He diffusion in zircon (see Supplementary Information and Table S2 for details; Gérard et al., 2022). Then, we conducted several thermal inversions for FzR massif and TdP sectors (Central, West and North, Fig. 3) with shared input parameters in QTQt. First, we prescribed a geothermal gradient of 35±10 °C/km, according to the ~70-90 mW/m^2 thermal flow of the region predicted by Ávila and Dávila (2018). The geothermal gradient is allowed to vary with time within the 35±10 °C/km range, and no reheating was allowed due to the lack of evidence of reheating events in the studied FzR and TdP regions during the late Miocene to Plio-Quaternary periods (Ramírez de Arellano et al., 2012). We considered an atmospheric lapse rate of 6±2 °C/km, and a present-day temperature of 1±1 °C to ensure model simulations reaching surface temperature for modern conditions. We also constrained the initial thermal constraints using 275±25 °C and 16 ±1 Ma and 12±1 Ma, for the FzR and TdP massifs, respectively. For the metasedimentary samples (West and North sectors of TdP massif), we do not impose any initial thermal constraint, and re-heating is not allowed given the lack of evidence of thermal events after Early Cenozoic low-grade metamorphism during basin thrusting (Klepeis et al., 2010; Fosdick et al., 2011). For thermal inversion, QTQt's approach is based on a linear interpolation between the highest and the lowest elevation samples to randomly predict thermal paths and shared geothermal gradients of all samples in an elevation profile (Figs. 5 and 6, S1-4) that best predicts observed thermochronological data in a consistent manner (Gallagher, 2012). QTQt inverse simulations were done for high numbers of iterations (in the 10,000 – 35,0000 range of individual models) to ensure the reliability of the model predictions.

Finally, we used thermal inversion modelling (Schildgen et al., 2010) to interpret ^{4}He/^{3}He thermochronometry data in two TdP samples (Fig. 3). To explore possible changes in ^{4}He diffusivity through time, all cooling paths (~20-30 10^3 iterations for each sample) began at 150 °C, well above the accumulation of radiation damage effects (Flowers et al., 2009) and ended after 10 Myr at the modern surface temperature (arbitrary prescribed at ~1 °C). Following each specified cooling path, the model first calculated an AHe age that was compared to the measured age. If the predicted age was within 1 standard deviation (SD) of the mean measured age (Table 3), a model ^{4}He/^{3}He ratio evolution was calculated using the same analytical heating schedule as the sample and compared to observed ratios. This approach allows a random-search scheme to identify cooling histories that are compatible

with the observations based on the computation of misfit statistics (M; mean of squared residuals weighted by the individual uncertainties in the ratio measurements; Schildgen et al., 2010); we set a misfit limit M~2, which corresponds to the 99% confidence level. Thermal histories yielding M>4 are excluded by the data, 2<M<4 are marginally acceptable, and M<2 are good fits to the data.

4. Results

4.1. AHe and ZHe thermochronology data

We present all analytical details and AHe and ZHe data in Tables 1-3. For illustration, we report in Figure 4 both single-grain and average AHe and ZHe corrected ages in age-elevation diagrams.

The FzR dataset (Fig. 4a) reveals single-grain ZHe ages ranging from 6 to 13 Ma, with single-grain dispersion increasing for low-elevation samples. Mean ZHe ages are relatively similar around 8-10 Ma along the elevation profile, potentially indicating fast rock cooling/exhumation during that period. FzR single-grain AHe ages range between 3 and 9 Ma and mean AHe ages cluster around 6-8 Ma, with no clear age-elevation relationship.

For the TdP massif, new AHe data from the Central sector (Fig. 4 b) show similar ages for metasedimentary and magmatic samples, with mean AHe ages ranging between around 4 and 11 Ma which all reflect cooling and exhumation posterior to the plutonic intrusion phase. In addition, we can observed a break-in slope in the age-elevation relationship around 7-8 Ma and ~1400-m elevation, potentially indicating an increase in rock cooling/exhumation at this time, and the exhumation of a paleo- partial retention zone above (note the apparent higher dispersion in single-grain AHe ages for samples above 1400 m). Samples from the North and West sectors have been collected at lower elevations (i.e. below 1000-m elevation, Fig. 4 b) and mean AHe ages range between 6 and 10 Ma, reflecting slower/older rock cooling/exhumation than for the Central sector.

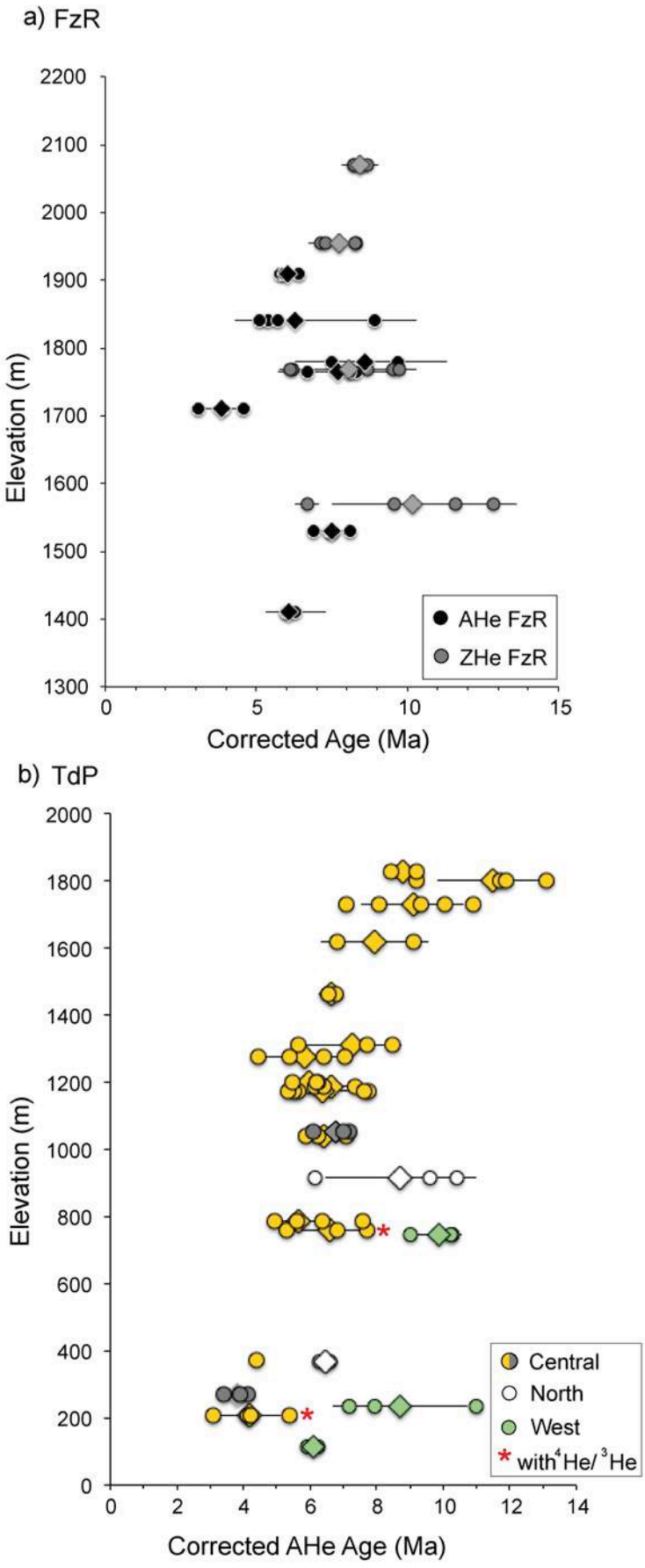

Fig. 4. Age-elevation relationships for FzR and TdP massifs. a) ZHe and AHe data for the FzR massif: single grain apatite and zircon (U-Th-Sm)/He ages are indicated by circles, and mean ages with 1σ errors (standard deviation of the single-grain ages) by diamonds. b) AHe data for the TdP massif: single-grain apatite and zircon (U-Th-Sm)/He ages are indicated by circles, and mean ages with 1σ errors (standard deviation of the single-grain ages) by diamonds. Two samples with $^4He/^3He$ data are marked by a red asterisk. Colors correspond to different zones of the TdP massif (Central, West and North), grey samples are sedimentary and yellow are magmatic from the Central transect, according to the legend in Fig. 3, and as explained in the text. Full analytical details for AHe and ZHe data are given in Tables 1-3.

4.2. QTQt thermal inversion results

We present the results of QTQt thermal inversion modelling with the relative probabilities of expected T-t paths for the highest and lowest elevation samples of each elevation transect in Figs. 5 and 6. The expected models for all the samples of each transect, interpolated from the highest and the lowest elevation ones, are shown in the Supplementary Figs. S1-4, together with the observed vs. predicted ages diagrams, and the thermal gradient predicted for the inversion within the imposed range of 35 ± 10 °C geothermal gradient, that gradually shifts to the atmospheric (lapse rate) gradient of 6 ± 1 °C during rock exhumation towards the surface. Using the T-t paths and the output geothermal gradients, we can estimate exhumation rates for the different periods of time, chosen based on major observed changes in output T-t paths.

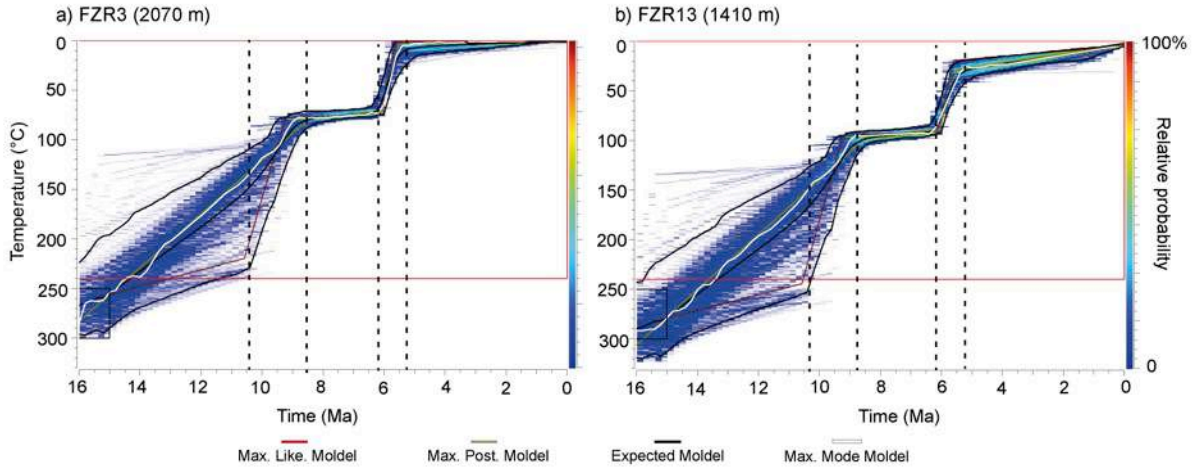

Fig. 5. QTQt thermal modelling outputs for the FzR massif. Inverse thermal modelling is based on AHe and ZHe data presented in Fig. 4 a. Selected output results for (a) the highest sample FZR3 (2070 m) and (b) the lowest sample FZR13 (1410 m). Note that output thermal histories for other FzR samples are linearly interpolated between these two end members (Fig. S1 a). Both panels show the relative probability for the thermal history, as well as the expected model (weighted mean model) and its 95% confidence intervals (black solid lines) and the maximum-likelihood model (best-fitting model, red line), the maximum posterior model (green line), and the maximum mode model (white line). Black dashed lines highlight key time periods with major changes in cooling rates. The black box indicates the initial thermal constraints and the redbox is representing general T-t priors.

QTQt inversion results for the FzR massif suggest a multi-stage cooling history (Figs. 5 and S1). Using both ZHe and AHe data, the expected (weighted mean) thermal histories show an unconstrained cooling from the imposed initial magmatic temperature (above 275 °C) and age (around 16 Ma) constraints, to a temperature range between 230 and 110 °C at ca. 10.5 Ma. At this time, predicted T-t paths become steeper and better constrained up to

~8.5 Ma, revealing an increase in cooling rate of 20-70 °C/Ma (Fig. 5). Between ~8.5 and ~6.5-6 Ma, the output thermal history reveal a quiescent phase with slow cooling at around 4-5 °C/Ma. At ~ 6.5-6 Ma, both high- and low-elevation samples were rapidly cooled at around 70 °C/Ma during a short period of maximum 1.5 Ma. The highest sample (FZR3, Fig. 5a) reached surface temperatures at this early Pliocene time, while the lowest elevation sample (FZR13, Fig. 5b) still experienced gradual cooling at ~5 °C/Ma with a slight increase up to ~20 °C/Ma at ~1 Ma.

For the TdP massif, thermal inverse modelling using QTQt provided variable information on the regional exhumation history from the different sectors. For the Central sector (Figs. 6 a,b and S2) the expected T-t paths from the dense AHe dataset (Fig. 4 b) first show rapid cooling from the imposed magmatic temperature/age constraints to a temperature range of 70-130 °C at ~11.5 Ma. This cooling signal has no real geological meaning since it reflects the thermal adjustment to the shallow intrusion depth of the TdP Plutonic Complex (note that the Central sector includes also two metasedimentary samples, which we assume were re-heated by the intrusion of the TdP plutonic complex). TdP samples of the Central sector then cooled very slowly up to ~6.5 Ma, when they experienced an increase in cooling rate from <1 °C/Ma up to ~90-120 °C/Ma. This fast exhumation phase was relatively short (~0.5 Ma), ending at around 6 Ma, when the highest elevation sample (04-JM-66, Fig. 6 a) reached surface temperatures. The lowest elevation sample (13-TP-26, Fig. 6 b) shows a quiescent period until around 2 Ma (slow cooling <1 °C/Ma) when it experienced an increase in cooling rate up to 30 °C/Ma. It is worth noting that the output thermal history is relatively well constrained over the Late Miocene to Plio-Quaternary period because of the dense AHe dataset and well prescribed AHe age-elevation relationship (Fig. 4 b)

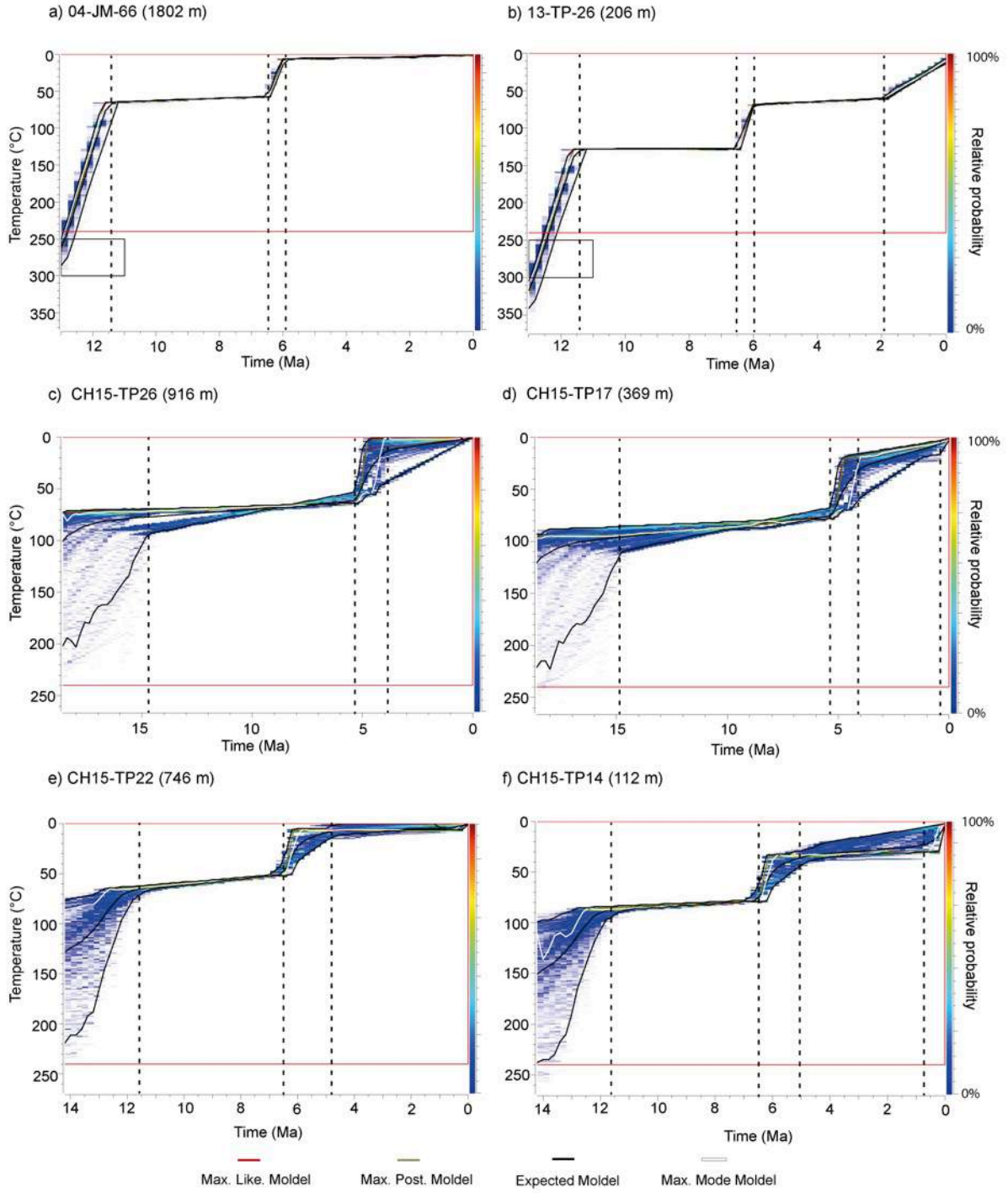

Fig. 6. QTQt thermal modelling outputs for the TdP massif. Inverse thermal modelling is based on AHe data presented in Fig. 4 b. Selected output results for (a-b) the Central sector, with the highest 04-JM-66 (a, 1802 m) and lowest 13-TP-26 (b, 206 m) elevation samples; (c-d) the North sector, with the highest CH15-26 (c, 916 m) and lowest CH15-TP17 (d, 369 m) elevation samples; and (e-f) the West sector, with the highest CH15-TP22 (e, 746 m) and lowest CH15-TP14 (f, 112 m) elevation samples. Note that output thermal histories for other TdP samples are linearly interpolated between the two end members for each sector (Figs. S2, S3 and S4). All panels show the relative probability for the thermal history, as well as the expected model (weighted mean model) and its 95% confidence intervals (black solid lines) and the maximum-likelihood model (best-fitting model, red line), the maximum posterior model (green line), and the maximum mode model (white line). Key time periods with major changes in cooling rates are by black dashed lines. The black box indicates the initial thermal constraints, and the redbox is representing general T-t priors.

For the North and West sectors of the TdP Massif (metasedimentary samples, Fig. 4 b), the AHe dataset is less dense and output model predictions are less constrained. For the North sector, there is no output constraint on the thermal histories until around 15 Ma (Fig. 6 c,d). The output thermal history reveals slow cooling between ~15 and ~5.25 Ma, with an estimated cooling rate < 2 °C/Ma, followed by a short cooling episode (between ~5.25 and 4 Ma) of ~40-60 °C/Ma. The low-elevation sample (Fig. 6 d) also recorded subsequent cooling after 4 Ma, but this phase is relatively unconstrained although a potential acceleration in cooling rate may occur at ~0.5 Ma (from ~20 up to 40 °C/Ma, Fig. 6 d). For the West sector, the expected T-t paths (Fig. 6 e,f) are not well constrained until ~12 Ma, when the relative probability for the cooling histories becomes well constrained and defines a slow cooling trend at around 4 °C/Ma. At ~6.5 Ma, the sample cooling was accelerated to ~25-30 °C/Ma for a short period of ~1.5 Ma, bringing the high-elevation sample (Fig. 6 e) to surface temperatures. After this time-interval, the low-elevation sample was cooled slowly to the surface (~2 °C/Ma), with a possible late-stage exhumation increase at ~0.5 Ma (up to 80 °C/Ma).

In TdP metasedimentary samples (West and North sectors), we have only limited constraints on the regional exhumation for the North sector since ca. 15 Ma (Fig. 6 c,d) and no information from the West sector before the emplacement age of the TdP Plutonic Complex at ~12 Ma (Fig. 6 e,f). Potential cooling/exhumation events before 15 Ma would have therefore not been recorded by the AHe dataset in the TdP massif. All TdP sectors show a short episode of fast cooling between around 6.5 and 4 Ma, which is common between the magmatic and the metasedimentary samples, and a potential delay (or lower resolution in timing) for this event north of the TdP laccolith. Finally, a late-stage cooling episode is revealed for all low-elevation samples (Fig. 6 b,d,f), but the timing of onset for this episode appears spatially variable, being earlier (~2 Ma) for the Central sector compared to the West and North sectors (~0.5 Ma).

4.3. $^{4}He/^{3}He$ thermal histories

Inverse thermal modelling of $^{4}He/^{3}He$ data shows variable resolution for the two TdP samples (Central sector, Fig. 7). $^{4}He/^{3}He$ data resolution is relatively low for sample 13-TP-26 (Fig. 7 c-d), resulting in unconstrained output cooling histories over the last 10 Ma, although significant cooling (> 40-50 °C) had still occurred for this sample since ca. 5-6 Ma.

^{4}He/^{3}He data resolution is much higher for sample 04-JM-90 (Fig. 7 a) and associated output cooling histories (Fig. 7 b) suggest fast cooling until around 6 Ma before a quiescent period with low cooling rates. This thermal history is relatively similar to QTQt outcomes for the Central sector (Fig. 6 a,b). Finally, a late-stage cooling episode is recorded since ~2 Ma, coherent with QTQt thermal predictions for the low-elevation sample (Fig. 6 b).

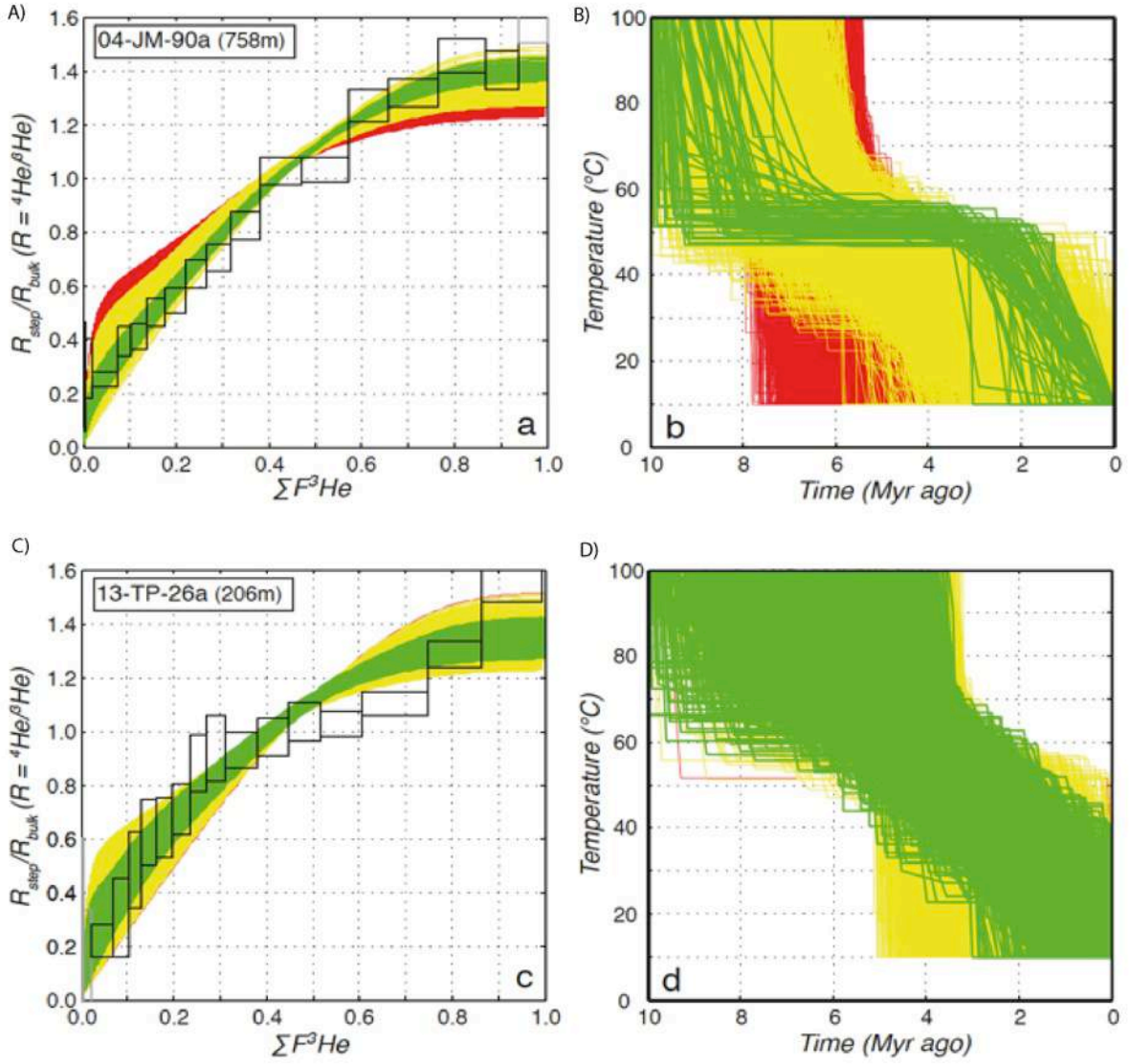

Fig. 7. ^{4}He/^{3}He thermochronometry of TdP massif (see Figs. 3-4 for locations and details). Observed ^{4}He/^{3}He ratio evolution diagrams, and model cooling paths for 04-JM-90a (a-b), and 13-TP-26a (c-d). The measured ^{4}He/^{3}He ratios of each degassing step (R_{step}) are normalised to the bulk ratio (R_{bulk}) and plotted versus the cumulative ^{3}He release fraction ($\sum F^3He$). Boxes indicate ±1σ (vertical) and integration steps (horizontal). Coloured lines show the predicted ^{4}He/^{3}He ratio evolution diagrams (a, c) for arbitrary cooling paths between 150 and 10 °C (b, d). Each coloured path predicts the observed AHe age of the sample to within ±1σ (cooling paths failing to predict the AHe age are not shown); red and yellow cooling paths are excluded by the ^{4}He/^{3}He data, whereas green cooling paths are permitted (see text for details, and Supplementary Table S1 for analytical details).

5. Discussion

5.1. Ridge subduction and asthenospheric upwelling forcing

An episode of increase in rock exhumation rates from ~0.7 km/Ma to 1-1.4 km/Ma (resulting from the cooling rate divided by the predicted geothermal gradient, Fig. S1) is recorded between ca. 10.5 and 8.5 Ma only in the FzR massif. This event predates by some million years the onset of Late Cenozoic Glaciations in Patagonia at ca. 7 Ma (Mercer and Sutter, 1982), and roughly coincides with spreading ridge subduction beneath the FzR between ca. 12-8 Ma (Cande and Leslie, 1986; Ramos, 2005; Lagabrielle et al., 2010; Guillaume et al., 2009b, 2013; Breitsprecher and Thorkelson, 2009). Our estimated rock exhumation rate of ~1 km/Ma from ZHe and AHe thermochronometry is well explained by Late Miocene continental compression and eastward fold-and-thrust belt propagation in response to the spreading-ridge subduction (Thomson, 2001; Ramos, 2005; Scalabrino et al., 2010; Guenthner et al., 2010; Lagabrielle et al., 2004, 2010; Georgieva et al., 2016, 2019; Stevens Goddard and Fosdick, 2019). Furthermore, a dynamic uplift forced by the asthenospheric flow implies that the effects of erosion on rock exhumation are amplified over the incipient asthenospheric window opening at depth at ~ 49 °S (Fig. 8 a) (Conrad and Husson, 2005; Guillaume et al., 2010; Faccenna et a., 2013; Sternai et al., 2016).

In the TdP Massif no episode of fast cooling before the Miocene/Pliocene transition appears in our T-t models, but AHe ages around 12 Ma are found in high altitude samples (Fig. 4 b). These older cooling ages suggest that the analysed samples were in the partial retention zone of the AHe system from 12 to 9 Ma. Exhumation ages between 12 and 10 Ma previously obtained in the TdP massif were associated to thermal resetting during pluton emplacement (Fosdick et al., 2013). Surface dynamic uplift due to mantle upwelling in the region of TdP is not well constrained, and less plausible than in the FzR Massif because the TdP is located to the south of the region where the spreading ridge has been subducting since ~12 Ma (Fig. 8 a).

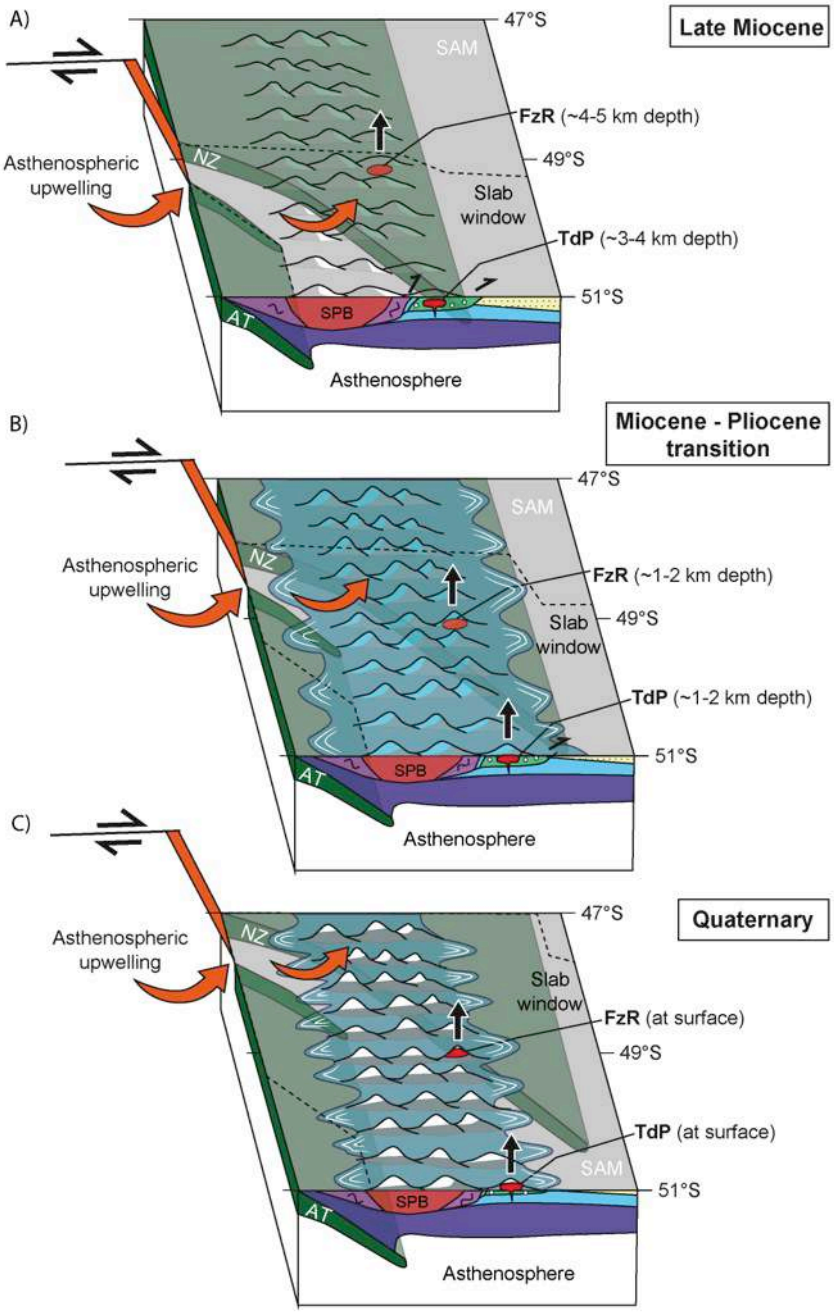

Fig. 8. Block-diagram with the interpretation of the geodynamic and landscape evolution of the southern Patagonian Andes from the Late Miocene to the Quaternary. A) At the Late Miocene (~12 Ma), the spreading ridge between the Nazca Plate (NZ) and the Antarctic Plate (AT) was subducting beneath the South American Plate (SAM) at ~49 °S, asthenospheric upwelling caused dynamic uplift and part of the rock exhumation in the FzR massif. Deformation in the fold-and-thrust belts was active, generating crustal thickening and additional topography. The Chaltén Plutonic Complex was already emplaced at ~4-5 km depth in the Fitz Roy region whereas the Torres del Paine Laccolith was being emplaced at 2-3 km depth. The Southern Patagonian Batholith (SPB) was already emplaced in the core of the orogen. Topography was growing by a combination of thrust tectonics, dynamic uplift, and erosion. B) At the Miocene – Pliocene transition the spreading ridge was subducting at ~48 °S, the dynamic uplift was thus occurring in the north of the studied regions. The fold-and-thrust belt and the intrusions were being exhumed mainly due to the onset of Patagonian Glaciations. C) In the Quaternary the subducting spreading ridge was at ~ 47 °S. The mountain belt was being exhumed mainly due to glacio-fluvial erosion, with carving of deep valleys and exposing the mountain peaks. The plutonic complexes must be near the surface. Black arrows highlight the uplifting regions, orange arrows highlight the region of asthenospheric upwelling.

5.2. Late-Miocene to Plio-Quaternary glacial-fluvial erosion forcing

Both the FzR and the TdP massifs share an episode of abrupt acceleration in rock exhumation between ca. 6.5 Ma and 6-4.5 Ma. The onset of increased exhumation rate is synchronous with the reported stratigraphic, geomorphologic (Mercer and Sutter, 1982; Lagabrielle et al., 2004, 2007, 2009, 2010; Rabassa et al., 2005, 2011; Rabassa, 2008), and thermochronologic (Thomson et al., 2001; Glodny et al., 2008; Thomson et al., 2010; Fosdick et al., 2013; Georgieva et al., 2016, 2019; Willett et al., 2020) evidence of the onset of Patagonian glaciations between ca. 7 and 6 Ma in the Southern Patagonian Andes. The Andean topography, therefore, quickly responded to the transition from fluvial-dominated to glacial-dominated erosion (Fig. 8 b), as proposed for other alpine environments (Egholm et al., 2009; Shuster et al., 2005; 2011; Valla et al., 2011; Herman et al., 2013; Champagnac et al., 2014). Modeled exhumation rates for this time interval are estimated between ~0.6 and 3 km/Ma, but both the magnitude and duration of this event depend on the analysed sector of the TdP and FzR massifs. The limited exhumation in the North and West sectors of the TdP massif compared to that of the Central sector, can be possibly explained by selective glacial erosion with potential glacial bedrock shielding in the West/North sectors, which are closer to the present-day/past icefield (Rabassa, 2008, Lagabrielle et al., 2010). A similar explanation can be proposed for the Plio-Quaternary exhumation, where delayed onset of increased exhumation rate in the North/West sectors compared to the Central sector of TdP and the FzR massif (located in a more external position) is observed. Efficient erosion of high-elevation topography from glacial and periglacial processes during the late Miocene would have resulted in a net decrease of ice accumulation area and hence in ice extent, ice flux, and consequently in glacial erosion (Pedersen and Egholm 2013; Sternai et al., 2013). Such a negative feedback has also been proposed to explain the Late Pleistocene gradual shrinking of the Southern Patagonian Icefield (Fig. 8 c; Kaplan et al., 2009), and likely explains the short-lived erosion pulse we identified at southern Patagonia at the late-Miocene/Pliocene transition (Christeleit et al., 2017; Willet et al., 2020).

Pliocene low exhumation rates (~0.025 – 0.035 km/Ma) recorded in the FzR and TdP massifs indicate erosional quiescence following high but transient glacial erosion in the Southern Patagonian Andes (Christeleit et al., 2017; Willet et al., 2020). The late-stage Quaternary exhumation is mainly recorded in low-elevation samples and in $^{4}He/^{3}He$ thermochronometric data, but its onset between ca. 2 and 0.5 Ma depends on the study region

(Figs. 5-6, and S1-4) and thermochronometric system (Fig. 7). North of the studied regions (~ 46 – 47 °S), stratigraphic records from glacial moraines indicate a shift of the drainage network after ~3 Ma, resulting in a major landscape change from smooth piedmont surface with extensive icefields in the foreland, to long west-east oriented and channelized glacial lobes (Lagabrielle et al., 2010). Tectonic uplift of the eastern foreland of Patagonia could have conditioned or at least favoured such geomorphological shift and induced west-east incision of deep glacial valleys (Lagabrielle et al., 2010; Georgieva et al., 2019). The recent acceleration in exhumation in the Southern Patagonia Andes can thus be associated with the Plio-Quaternary increase in glacial-interglacial cyclicity, enhanced glacial erosional processes, and icefield drainage reorganization in Patagonia possibly linked to tectonic activity (Fig. 8c).

Previous studies suggested a potential increase in mountain erosion as early as ~3 Ma, in response to climate-driven glacial processes (Shuster et al., 2005; 2011; Herman et al., 2013; Fox et al., 2015). An increase in the duration of glacial-interglacial cyclicity occurred at ~1.2 Ma according to deep-sea water $\delta^{18}O$ data (Lisiecki and Raymo, 2007; Lisiecki, 2010). By periodically switching between glacial and fluvial conditions, and by changing associated vegetation and soil cover, geomorphic processes would remain transient (Molnar, 2004; Herman and Champagnac, 2013), maintaining landscape disequilibrium and in turn enhancing erosion rates (Egholm et al., 2009; Champagnac et al., 2014). An increase in exhumation rates in several mountainous regions worldwide after ~2 Ma (Herman et al., 2013) is associated with the onset of or enhanced glaciations at mid latitudes, including the New-Zealand Alps (Shuster et al., 2011), Alaska and British Columbia (Shuster et al., 2005; Berger et al., 2008) or the European Alps (Haeuselmann et al., 2007; Valla et al., 2011; Glotzbach et al., 2011; Fox et al., 2015, 2016). The onset of glaciation in southern Patagonia between ca. 7 and 6 Ma (Mercer and Sutter, 1982; Rabassa, 2008; Lagabrielle et al., 2010), much earlier than at mid-latitudes, indicates a progressive latitudinal migration of the maximum glacial extent and thus points to a gradual increase in global cooling from the latest Miocene to the Quaternary.

6. Conclusions

The Southern Patagonian Andes recorded a long history of interactions between tectonics and climate processes. The North-South orientation of the Andean belt allows us to investigate spatial and temporal variations of these interactions. We found

thermochronometric evidence for the ridge subduction and opening of an asthenospheric window to force rock exhumation of the Fitz Roy massif in the Andean cordillera. This event accounts for ~1 km of rock exhumation over the late Miocene due to spreading ridge subduction, continental compression, uplift and increased erosion at ~49 °S. In the Torres del Paine massif, this event is not clearly recorded by low-temperature thermochronometric data, possibly due to the already attenuated surface response to ridge collision and mantle upwelling when the pluton emplaced at 51 °S.

The onset of glaciations generates a regional signal of rapid rock exhumation in southern Patagonia between ca. 6.5 and 4.5 Ma at ~49-51 °S in the eastern cordillera. A period of slow rock exhumation until the Quaternary suggests erosional quiescence, possibly reflecting bedrock shielding by extensive icefields covering the Southern Patagonian Andes. A last Quaternary episode of accelerated rock exhumation is recorded in our thermochronometric dataset, and coincides with worldwide increase in mountain erosion rates ascribed to glacial-interglacial cycles (e.g., Herman et al., 2013). This climatic transition generated a geomorphological shift from smooth landforms to deep incised glacial valleys, exposing the Torres del Paine and the Fitz Roy plutonic complexes at high elevations.

Table 1. Zircon (U-Th-Sm)/He (ZHe) data for Fitz Roy (FzR) samples.

Sample N°	Latitude/ Longitude (°S/°W)	Elevation (m)	U (ppm)	Th (ppm)	Sm (ppm)	^{4}He (nmol/g)	F_T	Corrected Age (Ma)	1σ error (Ma)
FZR3-1			205.76	91.50	5.99	7.9	0.78	8.24	0.5
FZR3-2			284.29	100.81	2.45	11.1	0.79	8.47	0.5
FZR3-3			506.73	156.89	3.37	18.8	0.78	8.24	0.5
FZR3-4			516.96	138.72	2.51	19.7	0.78	8.50	0.5
FZR3-5			513.12	198.42	2.59	21	0.77	8.69	0.5
FZR3	**49.2566/ 49.2566/**	**2070**						**8.4 ± 0.2**	
FZR4-1			371.29	140.86	3.46	13.6742	0.76	8.30	0.5
FZR4-3			309.55	109.25	2.52	11.6129	0.78	8.26	0.5
FZR4-4			1128.8	326.58	3.95	34.5965	0.75	7.14	0.4
FZR4-5			715.56	234.09	2.93	23.664	0.78	7.31	0.4
FZR4	**49.2550/ 73.0281**	**1955**						**7.7 ± 0.6**	
FZR5-1			904.21	321.40	7.38	35.659	0.78	8.66	0.5
FZR5-2			271.41	96.76	3.14	11.343	0.75	9.54	0.6
FZR5-3			412.40	310.97	5.73	12.060	0.74	6.22	0.4
FZR5-4			527.95	246.47	6.48	22.495	0.73	9.72	0.6
FZR5-5			529.41	268.56	5.24	14.285	0.73	6.11	0.4
FZR5	**49.2540/ 73.0311**	**1758**						**8.0 ± 1.8**	
FZR6-1			1157.2	380.03	8.43	66.359	0.77	12.87	0.7
FZR6-2			1221.7	476.31	9.30	62.1423	0.75	11.59	0.7
FZR6-3			1021.0	290.08	4.19	41.4346	0.74	9.58	0.6
FZR6-4			403.02	141.72	2.78	11.6276	0.74	6.68	0.4
FZR6	**49.2487/ 73.0327**	**1569**						**10.2 ± 2.7**	

Notes. Ft = age correction factor (Farley et al., 1996). Bold numbers are mean ages calculated from the single-grain replicates; 1σ error for mean ages is standard deviation of replicate ages. Analytical uncertainties are around 6% of the corrected age.

Table 2. Apatite (U-Th-Sm)/He (AHe) data for Fitz Roy (FzR) samples.

Sample N°	Latitude/ Longitude (°S/°W)	Elevation (m)	U (ppm)	Th (ppm)	Sm (ppm)	^{4}He (nmol/g)	F_T	Corrected Age (Ma)	1σ error (Ma)
FZR10-M			13.3	38.20	277.30	0.7164	0.73	7.50	0.4
FZR10-N			53.3	168.00	436.10	3.6462	0.73	9.70	0.6
FZR10	**49.2543/ 73.0319**	**1780**						**8.6 ± 1.6**	
FZR11-A			3.5	12.00	103.00	0.1645	0.80	5.40	0.3
FZR11-D			8.00	19.90	170.50	0.5211	0.77	8.90	0.5
FZR11-E			23.5	38.6	122.40	0.8126	0.80	5.70	0.3
FZR11-L			14.4	46.4	344.1	0.5685	0.73	5.10	0.3
FZR11	**49.2538/ 73.0346**	**1840**						**6.2 ± 1.4**	
FZR12-E			7.3	20.6	136.3	0.3699	0.78	6.70	0.4
FZR12-M			23.60	68.00	381.9	1.3324	0.71	8.30	0.5
FZR12-N			15.30	45.80	250.0	0.9303	0.76	8.10	0.5
FZR12	**49.2493/ 73.0364**	**1765**						**7.7 ± 0.9**	
FZR13-B			26.9	46.2	140.1	0.9689	0.77	6.00	0.4
FZR13-F			7.9	22.8	83.5	0.3726	0.84	6.00	0.4
FZR13-L			71.3	135.8	461.4	2.4651	0.69	6.30	0.4
FZR13	**49.2553/ 73.0473**	**1410**						**6.1 ± 0.2**	
FZR14-A			10.0	17.40	105.90	0.4436	0.81	6.90	0.4
FZR14-D			11.10	30.50	186.50	0.6317	0.74	8.10	0.5
FZR14-E			10.50	29.40	183.30	0.5682	0.75	7.50	0.5
FZR14-F			6.70	19.50	76.10	0.3979	0.85	7.40	0.4
FZR14-G			9.80	24.90	100.20	0.5531	0.84	7.50	0.5
FZR14	**49.2586/ 73.0493**	**1530**						**7.5 ± 0.4**	
FZR15-A			28.30	72.10	150.80	1.1287	0.78	5.80	0.3
FZR15-D			27.30	78.10	130.80	1.1801	0.80	5.90	0.4
FZR15-F			36.30	106.90	214.30	1.6033	0.75	6.40	0.4
FZR15	**49.2715/ 73.0568**	**1910**						**6.03 ± 0.3**	
FZR16-A			13.70	40.90	131.70	0.3928	0.78	3.90	0.2
FZR16-C			14.20	40.20	109.10	0.3345	0.82	3.10	0.1
FZR16-E			12.20	38.50	68.90	0.4431	0.83	4.60	0.3
FZR16	**49.2654/ 73.0586**	**1710**						**3.9 ± 0.7**	

Notes. Ft = age correction factor (Farley et al., 1996). Bold numbers are mean ages calculated from the single-grain replicates; 1σ error for mean ages is standard deviation of replicate ages. Analytical uncertainties are <1, ~3 and ~2% for respectively U, Th and Sm measurements; and <1% for ^{4}He measurements.

Table 3 a. Apatite (U-Th-Sm)/He (AHe) data for Torres del Paine (TdP) samples, Central transect

Sample N°	Latitude/ Longitude (°S/°W)	Elevation (m)	U (ppm)	Th (ppm)	Sm (ppm)	^{4}He (nmol/g)	F_T	Corrected Age (Ma)	1σ error (Ma)
04-JM-66ap1			8.24	10.14	442.43	0.5064	0.73	11.73	0.37
04-JM-66ap2			5.08	11.16	291.29	0.2884	0.73	9.18	0.23
04-JM-66ap3			8.80	13.26	397.58	0.5035	0.64	11.89	0.39
04-JM-66ap4			32.38	40.96	575.75	2.1827	0.74	13.09	0.30
04-JM-66	**50.97541/ 73.02521**	**1802**						**11.5 ±1.6**	
04-JM-67ap1			7.48	16.91	290.23	0.3888	0.76	8.06	0.13
04-JM-67ap2			54.20	75.26	1128.1	3.3644	0.75	10.91	0.15
04-JM-67ap3			8.95	21.13	442.59	0.5862	0.81	9.32	0.14
04-JM-67ap4			53.89	67.27	996.05	2.0018	074	7.09	0.11
04-JM-67ap5			14.32	30.91	647.52	0.7859	0.65	10.04	0.36
04-JM-67	**50.97492/ 73.02651**	**1731**						**9.1 ± 1.5**	
04-JM-68ap1			4.21	11.59	161.99	0.2777	0.80	9.10	0.26
04-JM-68ap2			8.36	15.41	309.23	0.3266	0.73	6.82	0.27
04_JM-68	**50.97405/ 73.02843**	**1619**						**8.0 ±1.6**	
04-JM-71ap1			36.14	89.26	701.25	1.4274	0.81	5.66	0.07
04-JM-71ap2			15.06	25.06	508.50	0.7787	0.79	8.49	0.11
04-JM-71ap4			19.80	26.18	579.96	0.8193	0.75	7.71	0.20
04-JM-71	**50.97342/ 73.03557**	**1310**						**7.3 ±1.5**	
04-JM-76ap1			15.16	21.64	466.10	0.5671	0.69	7.35	0.41
04-JM-76ap2			21.13	41.25	503.38	0.6776	0.65	6.15	0.37
04-JM-76ap3			41.16	42.22	539.89	1.2375	0.69	6.41	0.15
04-JM-76	**50.97449/ 73.03936**	**1189**						**6.6 ±0.6**	
04-JM-87ap1			11.13	31.79	448.11	0.4242	0.66	6.25	0.44
04-JM-87ap2			21.89	50.81	291.15	1.1062	0.84	7.11	0.08
04-JM-87ap3			17.95	25.52	588.59	0.5842	0.75	5.88	0.11
04-JM-87	**50.97638/ 73.04372**	**1042**						**6.4 ±0.6**	
04-JM-90ap1			28.04	22.82	254.31	0.6745	0.71	5.30	0.21
04-JM-90ap2			12.72	28.50	352.84	0.6312	0.77	7.71	0.24
04-JM-90ap3			22.29	29.92	312.20	0.8225	0.77	6.80	0.22
04-JM-90	**50.98166/ 73.05553**	**758**						**6.6 ±1.2**	
08-JL-385ap1			18.63	64.77	185.97	0.7070	0.68	5.66	0.09
08-JL-385ap2			2.26	0.98	0.26	0.0516	0.70	5.54	0.48
08-JL-385ap3			11.19	33.64	270.29	0.5420	0.67	7.74	0.21
08-JL-385ap4			26.70	60.46	397.62	0.7461	0.62	5.35	0.21
08-JL-385ap5			44.77	128.8	299.38	2.1480	0.69	7.61	0.09
08-JL-385	**50.97669/ 73.10013**	**1175**						**6.4 ±1.2**	
07-JL-160ap2			5.15	23.37	208.06	0.2691	0.73	6.23	0.14
07-JL-160ap3			5.31	21.81	145.68	0.2308	0.74	5.46	0.13
07-JL-160ap4			9.10	30.81	181.90	0.3915	0.71	6.19	0.08
07-JL-160	**50.97677/ 73.10036**	**1200**						**6.0 ±0.4**	

07-JL-165ap4			20.82	40.34	222.66	0.7432	0.70	6.44	0.08
07-JL-165ap4			16.74	54.39	250.27	0.4926	0.69	4.44	0.11
07-JL-165ap4			42.74	93.24	317.60	1.7486	0.71	7.05	0.09
07-JL-165ap4			21.33	43.42	285.72	0.6064	0.65	5.39	0.18
07-JL-165	**50.97718/ 73.10087**	**1275**						**5.8 ±1.2**	
04-JM-49ap1			10.49	42.26	416.58	0.5313	0.74	6.39	0.10
04-JM-49ap2			9.48	26.59	348.45	0.3671	0.75	5.61	0.10
04-JM-49ap3			8.18	24.67	330.62	0.2606	0.68	4.93	0.13
04-JM-49ap4			8.39	24.17	285.54	0.4567	0.77	7.60	0.09
04-JM-49	**51.04051/ 73.08473**	**785**						**6.1 ±1.2**	
04-JM-30ap1			9.11	12.77	501.27	0.4878	0.79	9.18	0.43
04-JM-30ap2			15.84	38.02	671.08	0.8212	0.71	8.46	0.22
04-JM-30	**50.94709/ 72.99015**	**1830**						**8.8 ±0.5**	
04-JM-23ap1			6.20	14.94	317.04	0.2792	0.77	6.77	0.26
04-JM-23ap2			6.71	12.86	352.67	0.2289	0.65	6.53	0.77
04-JM-23	**50.94713/ 72.99902**	**1461**						**6.7 ±0.2**	
13-TP-26-a			16.83	90.36	60.46	0.4760	0.74	3.08	0.04
13-TP-26-z-BR			10.58	40.02	53.35	0.4560	0.77	5.37	0.06
13-TP-26-y-BR			9.84	34.29	46.39	0.3130	0.77	4.11	0.05
13-TP-26-x			11.34	45.61	51.81	0.3860	0.75	4.22	0.04
13-TP-26	**50.9728/ 72.8839**	**206**						**4.2 ±0.9**	
CH15-19	**51.01057/ 72.94342**	**372**	0.242	3.323	23.645	0.024	0.82	**4.4±0.5**	
CH15-TP21_x			4.888	30.028	51.404	0.179	0.78	3.42	0.06
CH15-TP21_y			11.27	13.099	34.121	0.24	0.73	4.14	0.08
CH15-TP21_z			3.741	16.706	13.093	0.126	0.78	3.91	0.08
CH15-TP21	**50.98973/ 72.79723**	**268**						**3.8±0.4**	
CH15_TP30_x			1.727	11.361	16.025	0.142	0.81	7.19	0.11
CH15_TP30_y			1.48	11.285	19.511	0.125	0.77	7.01	0.15
CH15_TP30_z			1.081	11.826	12.423	0.097	0.75	6.1	0.36
CH15_TP30	**50.94726/ 72.90560**	**1053**						**6.8±0.6**	

Notes. Ft = age correction factor (Farley et al., 1996). Bold numbers are mean ages calculated from the single-grain replicates; 1σ error for mean ages is standard deviation of replicate ages. Analytical uncertainties are <1, ~3 and ~2% for respectively U, Th and Sm measurements; and <1% for ^{4}He measurements.

Table 3 b. Apatite (U-Th-Sm)/He (AHe) data for Torres del Paine (TdP) samples, West transect

Sample N°	Latitude/ Longitude (°S/°W)	Elevation (m)	U (ppm)	Th (ppm)	Sm (ppm)	^{4}He (nmol/g)	F_T	Corrected Age (Ma)	1σ error (Ma)
CH15-TP14_x			11.82	86.65	46.439	0.877	0.81	6.25	0.07
CH15-TP14_z			1.66	15.596	23.078	0.13	0.75	5.91	0.12
CH15-TP14	**51.25035/ 73.24379**	**112**						**6.1±0.2**	
CH15-TP15_x			5.023	6.437	21.903	0.219	0.76	7.93	0.15
CH15-TP15_y			3.03	20.962	20.081	0.235	0.76	7.17	0.18
CH15-TP15_z			2.684	18.609	34.048	0.299	0.70	10.99	0.2
CH15-TP15	**50.98633/ 73.21632**	**235**						**8.7±2**	
CH15_TP22_x			9.93	7.017	18.153	0.493	0.75	10.28	0.15
CH15_TP22_y			2.909	16.841	14.915	0.23	0.69	9.04	0.36
CH15_TP22_z			0.857	23.269	12.324	0.253	0.73	10.24	0.84
CH15_TP22	**51.00625/ 73.14149**	**746**						**9.8±0.7**	

Notes. Ft = age correction factor (Farley et al., 1996). Bold numbers are mean ages calculated from the single-grain replicates; 1σ error for mean ages is standard deviation of replicate ages. Analytical uncertainties are <1, ~3 and ~2% for respectively U, Th and Sm measurements; and <1% for ^{4}He measurements.

Table 3 c. Apatite (U-Th-Sm)/He (AHe) data for Torres del Paine (TdP) samples, North transect

Sample N°	Latitude/ Longitude (°S/°W)	Elevation (m)	U (ppm)	Th (ppm)	Sm (ppm)	^{4}He (nmol/g)	F_T	Corrected Age (Myr)	1σ error (Ma)
CH15-TP17_y			2.355	15.135	25.211	0.164	0.79	6.3	0.18
CH15_TP17_z			1.852	15.597	36.746	0.151	0.73	6.61	0.17
CH15_TP17	**50.81598/ 73.12218**	**369**						**6.46±0.2**	
CH15_TP26_x			31.341	49.473	53.996	1.849	0.82	9.6	0.1
CH15_TP26_y			34.892	41.442	41.455	1.131	0.76	6.13	0.08
CH15_TP26_z			13.306	23.852	38.619	0.848	0.78	10.41	0.12
CH15_TP26	**50.85859/ 73.12883**	**916**						**8.71±2.27**	

Notes. Ft = age correction factor (Farley et al., 1996). Bold numbers are mean ages calculated from the single-grain replicates; 1σ error for mean ages is standard deviation of replicate ages. Analytical uncertainties are <1, ~3 and ~2% for respectively U, Th and Sm measurements; and <1% for ^{4}He measurements.

Supplementary Material

Zircon (U-Th-Sm)/He (ZHe) thermochronometry

Zircon single-grains were processed at the Dalhousie Noble Gas Extraction Laboratory (Halifax, Canada) for (U-Th-Sm)/He dating. They were analyzed following the methods described following the methods of Reiners et al. (2004, 2005) and Landry et al. (2016), in parallel with Fish Canyon Tuff standards. Zircon grains were measured and observed under binoculars to avoid any inclusion and/or fracture, before being packed into a Nb foil envelope. ^{4}He was then extracted from each aliquot in an in-house built He extraction line with successive 15-min-heatings under a focused beam of a 45 W diode laser (1250 °C), until ^{4}He yields were under 1% of total. After adding a known amount of purified ^{3}He spike, ^{3}He/^{4}He ratios were measured with a Pfiffer Vaccuum Prisma quadrupole mass spectrometer. Typical 1σ errors are in range of 1.5–2%. Fish Canyon Tuff (FTC) zircon standards were included to ensure accuracy, reproducibility, and reliability of the data. After He extraction, zircons were dissolved in high-pressure dissolution vessels with concentrated HF and HNO_3 at 200 °C for 96 h. Prior to dissolution, samples were spiked with mixed ^{235}U, ^{230}Th, and ^{149}Sm spikes. Isotopic ratios were measured with iCAP Q inductively coupled plasma mass spectrometry (ICP-MS). Additional blank analyses controlled the analytical accuracy. The raw data were reduced using a Helios software package.

ZHe ages for the Chaltén Plutonic Complex (Fitz Roy massif) are relatively similar to AHe ages presented in this study (Tables 1-2, Fig. 4 a). Following the recent studies of Gérard et al. (2022) and Gautheron et al. (2020, 2022), we propose that such age similarity between the ZHe and the AHe systems result from the low ∝-dose in the zircon crystals, calculated between 6 x 10^{15} and 5.3 x 10^{16} (∝/g) (Table S2), and linked with a low ^{4}He retention. The ∝-dose is the total radiation damage accumulated in the crystal lattice, and depends on the age-effective uranium concentration, eU (Table S2), and the time since the crystal began to accumulate damage. The low radiation damage and associated low ^{4}He retention in the zircon crystals of the FzR is most probably explained by the young emplacement age of the Chaltén Plutonic Complex (ca. 12.5 Ma, Ramírez de Arellano et al., 2012). In the following, we estimate the changes in He retention for zircon crystals by calculating the impact of low ∝-dose on He diffusivity in zircon, that we subsequently relate to the effective closure temperature, Tc, of the ZHe system (Dodson, 1979; Gautheron et al., 2020, 2022; Gérard et al., 2022) (Table S2). We calculate the initial diffusion coefficient D_0

as a function of the damage fraction (f), estimated in terms of ∝-dose normalized to the total number of atoms in 1g of zircon (Nasdala et al., 2001) and the diffusion coefficient for a zero-damage crystal (1.6 x 10^{-7} m^2/s, Table 4 in Gautheron et al., 2020). Typical damage fraction for low-damaged zircon will be in the 0.01 to 1 % zone. With time, damage content in zircon will increase and the damage fraction will be higher (Gautheron et al., 2020). The activation Energy, Ea, was estimated in base to the ∝-dose as well with a similar value of 133 kJ/mol for all zircon crystals, as an intermediate value (Fig. 8 of Gautheron et al., 2020) for young zircons with ∝-dose in the order of 10^{15} and 10^{16}. In the inverse QTQt thermal modelling, instead of inputting a thermal model for the He diffusion, we input the activation energy, Ea, and the calculate diffusion coefficient D_0 as shown in Table S2. The resulting Tc between 87 and 108 °C, and the ∝-Dose between 6 x 10^{15} and 5.3 x 10^{16} (∝/g) of the zircon crystals of the Chaltén Plutonic Complex can help to fill current gaps in our knowledge about low ∝-dose zircon behaviour, since few studies recognized natural examples with this kinetic behaviour (Gérard et al, 2022).

Apatite (U-Th-Sm)/He (AHe) and ^{4}He/^{3}He thermochronometry

For TdP AHe data, single-crystal aliquots of apatite were wrapped in Pt or Nb foils and degassed by laser heating. At the University of Arizona and the Berkeley Geochronology Center, ^{4}He abundances were measured using ^{3}He isotope dilution and quadrupole mass spectrometry (House et al., 2000). Net signal intensities were interpolated to the inlet time of the gas into the mass spectrometer, and then compared to the corresponding mean signal from reference gas aliquots of known absolute amounts analyzed by the same procedure. Degassed aliquots were then dissolved and U, Th and Sm concentrations were measured by isotope dilution using ICP-MS.

For FzR AHe data, individual apatite grains were encapsulated in Pt tubes before heating under high vacuum conditions at high temperature (1,050°C ±50°C using an infrared diode laser) twice for 5 min at GEOPS laboratory (Université Paris-Saclay, France). The released ^{4}He gas was mixed with a known amount of ^{3}He, purified, and the gas was analyzed using a Prisma Quadrupole. The ^{4}He content was determined by isotope dilution method. Subsequently, apatite crystals were dissolved in 100 µL of HNO_3 5 N solution containing known amount of ^{235}U, ^{230}Th, ^{149}Sm, and ^{42}Ca. The solution was heated at 70°C during 3 h and after a cooling time, 900 µL of distilled water was added. The final solution was analyzed using an ELEMENT XR ICP-MS and the ^{238}U, ^{230}Th, and ^{147}Sm concentrations and apatite

weight (using the Ca content) were determined following the methodology proposed by Evans et al. (2005). More details about the analytical procedure can be found in Recanati et al. (2017).

Durango apatite crystals were also analyzed during the same period to ensure the data quality. Replicate analyses of Durango apatite yielded a <5% reproducibility compared to the reference age. An α-ejection correction was applied to calculate the (U-Th-Sm)/He (AHe) age (Farley et al., 1996). The one-sigma error on each AHe age amounts to around 8%, reflecting the analytical error and the uncertainty on the FT ejection factor correction. Sample locations and details, as well as all individual AHe ages, crystal characteristics and mean ages appear in Tables 2 and 3.

In $^{4}He/^{3}He$ thermochronometry (Shuster and Farley, 2004), the natural spatial distribution of radiogenic ^{4}He is constrained by stepwise degassing and $^{4}He/^{3}He$ analysis of a sample containing synthetic, homogeneously distributed, proton-induced ^{3}He. Approximately 50 mg of apatite grains were packaged into Sn foil and exposed to ~$5x10^{15}$ protons cm^{-2} with incident energy of ~220 MeV over a continuous ~5-hour period at the Francis H. Burr Proton Therapy Center (Boston, USA). Euhedral crystals free of visible mineral inclusions were selected using the above criteria; crystal dimensions were measured using a calibrated binocular microscope. Individual crystals were then sequentially heated in multiple steps under ultra-high vacuum using a feedback-controlled 70-W diode laser, with temperature measured with a coaxially aligned optical pyrometer at the Noble Gas Thermochronometry Laboratory (Berkeley Geochronology Center, USA). The molar ^{3}He abundance and the $^{4}He/^{3}He$ ratio were measured for each heating step using calibrated pulse-counting sector-field mass spectrometry and corrected for blank contributions to ^{3}He and ^{4}He (uncertainties in blank corrections are propagated into ratio uncertainties). All stepwise $^{4}He/^{3}He$ degassing data are given in Tables S2 a, b. A few heating steps yielded $^{4}He/^{3}He$ ratios that plot well outside analytical uncertainty relative to contiguous heating steps and therefore result in evolving ratios that do not monotonically increase over the course of certain stepped heating analyses. Potential explanations for these anomalous ratios include: (i) inaccuracy in the ^{4}He blank correction for a particular heating step, or (ii) small cracks within the crystal that were not visible via optical microscopy. To minimize the influence of anomalous $^{4}He/^{3}He$ ratios and simultaneously place some constraint on the most likely cooling scenarios, these data (open grey boxes in Fig. 7 a, c) were excluded from the calculation of misfit statistics.

Somehow, inclusion of these data would result in lower levels of confidence in the excluded cooling paths, with most of the constraint therefore derived from the AHe age alone.

Supplementary Figures

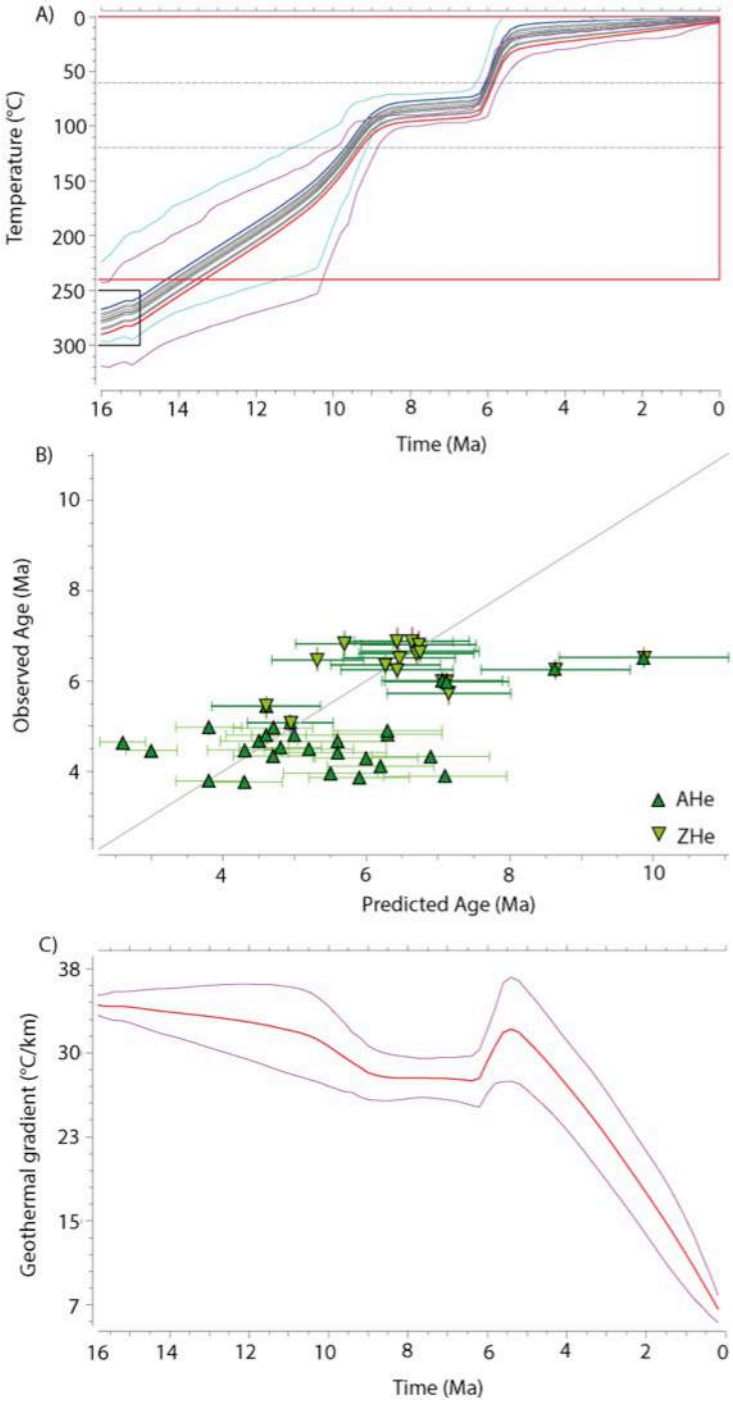

Fig. S1 - QTQt thermal modelling outputs for the FzR massif. A) Expected (weighted mean) T-t model based on AHe and ZHe data presented in Fig. 4 a, the red line correspond to the output thermal history for the highest elevation sample, and the blue line to the output thermal history for the lowest elevation sample, the grey lines are output thermal histories of the intermediate samples. The cyan and magenta lines bound the 95% confidence interval of the expected model for the lowest and the highest elevation samples, respectively. The black box indicates the initial thermal constraints, and the redbox is representing general T-t priors. B) Observed vs. the predicted age diagram with the single-grain AHe (green triangles) and ZHe (downward green triangles) corrected ages plotted to show the statistical fit of the model. C) The geothermal gradient (red line) and 95% of confidence interval (magenta lines) predicted for the inversion thermal modelling. Note that the late-stage evolution is reflecting the gradual transition form geothermal (35 $\pm$ 10 °C/km) to atmospheric (lapse rate, 6 $\pm$ 2 °C/km) gradient during rock exhumation towards the surface.

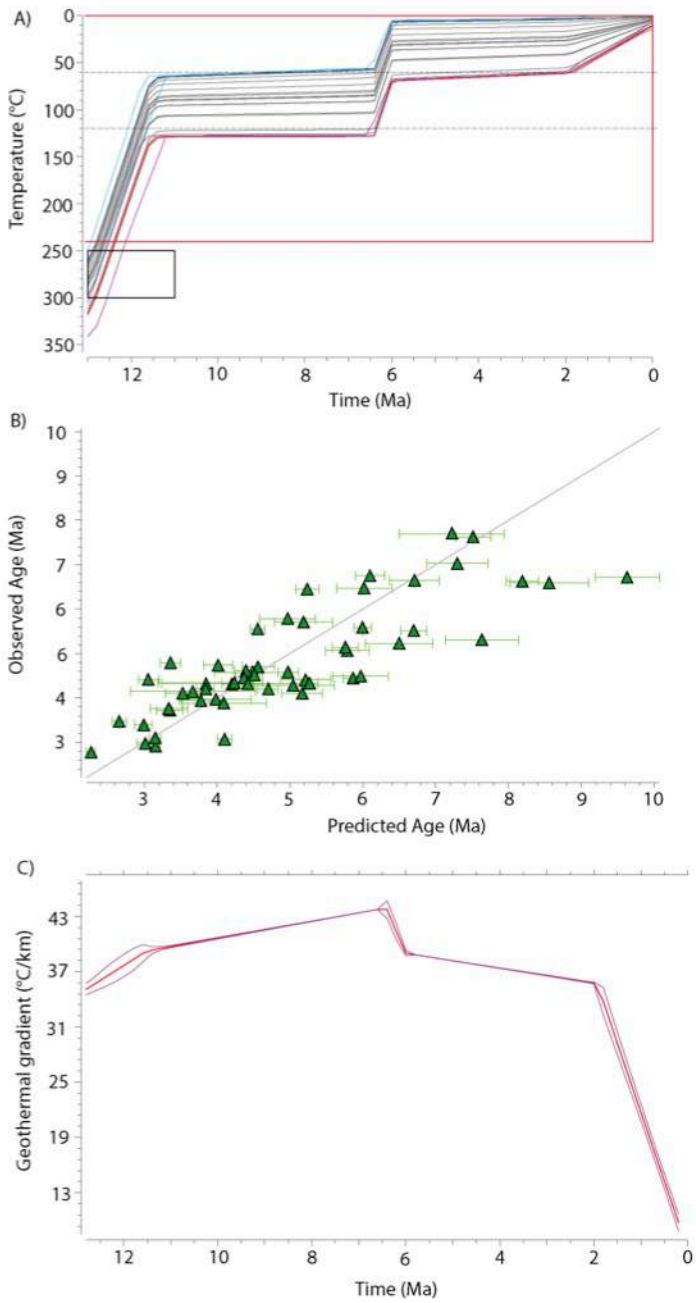

Fig. S2 - QTQt thermal modelling outputs for the TdP massif, Central transect. A) Expected (weighted mean) T-t model based on AHe data presented in Fig. 4 b, the red line correspond to the output thermal history for the highest elevation sample, and the blue line to the output thermal history for the lowest elevation sample, the grey lines are output thermal histories of the intermediate samples. The cyan and magenta lines bound the 95% confidence interval of the expected model for the lowest and the highest elevation samples, respectively. The black box indicates the initial thermal constraints, and the redbox is representing general T-t priors. B) Observed vs. the predicted age diagram with the single-grain AHe corrected ages (green triangles) plotted to show the statistical fit of the model. C) The geothermal gradient (red line) and 95% of confidence interval (magenta lines) predicted for the inversion thermal modelling. Note that the late-stage evolution is reflecting the gradual transition form geothermal (35 $\pm$ 10 °C/km) to atmospheric (lapse rate, 6 $\pm$ 2 °C/km) gradient during rock exhumation towards the surface.

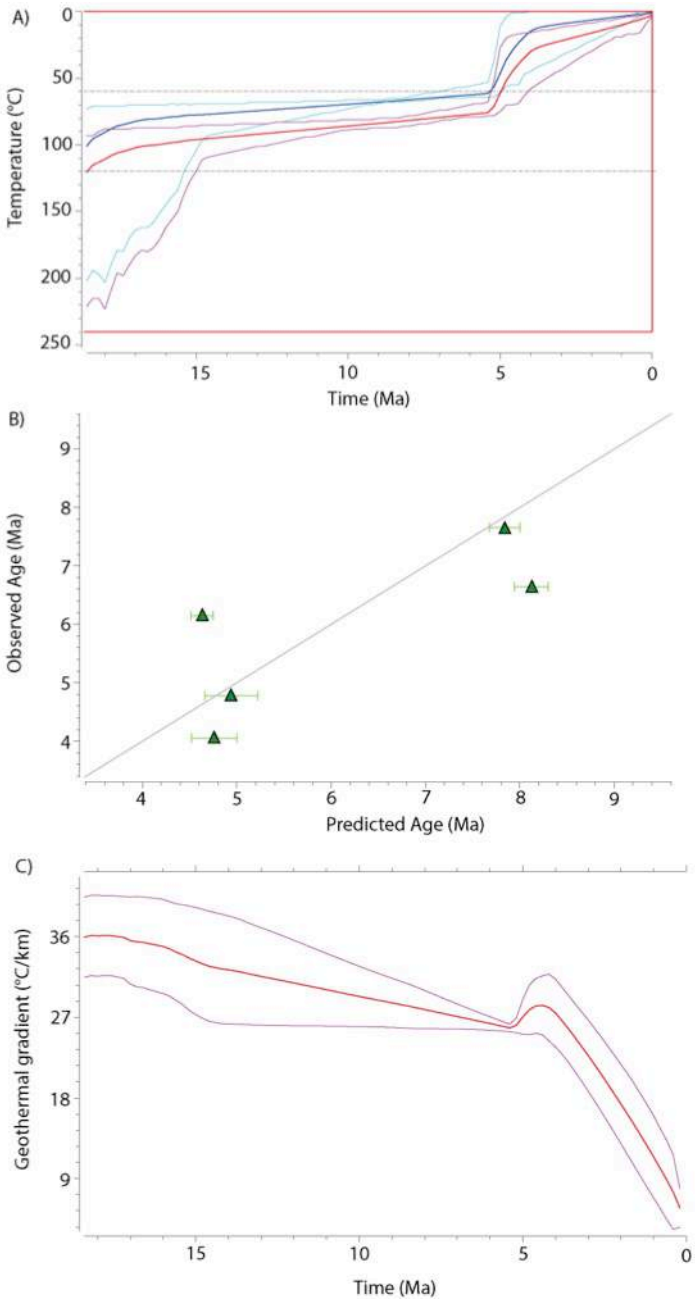

Fig. S3 - QTQt thermal modelling outputs for the TdP massif, North transect. A) Expected (weighted mean) T-t model based on AHe data presented in Fig. 4 b, the red line correspond to the output thermal history for the highest elevation sample, and the blue line to the output thermal history for the lowest elevation sample. The cyan and magenta lines bound the 95% confidence interval of the expected model for the lowest and the highest elevation samples, respectively. The redbox is representing general T-t priors. B) Observed vs. the predicted age diagram with the single-grain AHe corrected ages (green triangles) plotted to show the statistical fit of the model. C) The geothermal gradient (red line) and 95% of confidence interval (magenta lines) predicted for the inversion thermal modelling. Note that the late-stage evolution is reflecting the gradual transition form geothermal (35 $\pm$ 10 °C/km) to atmospheric (lapse rate, 6 $\pm$ 2 °C/km) gradient during rock exhumation towards the surface.

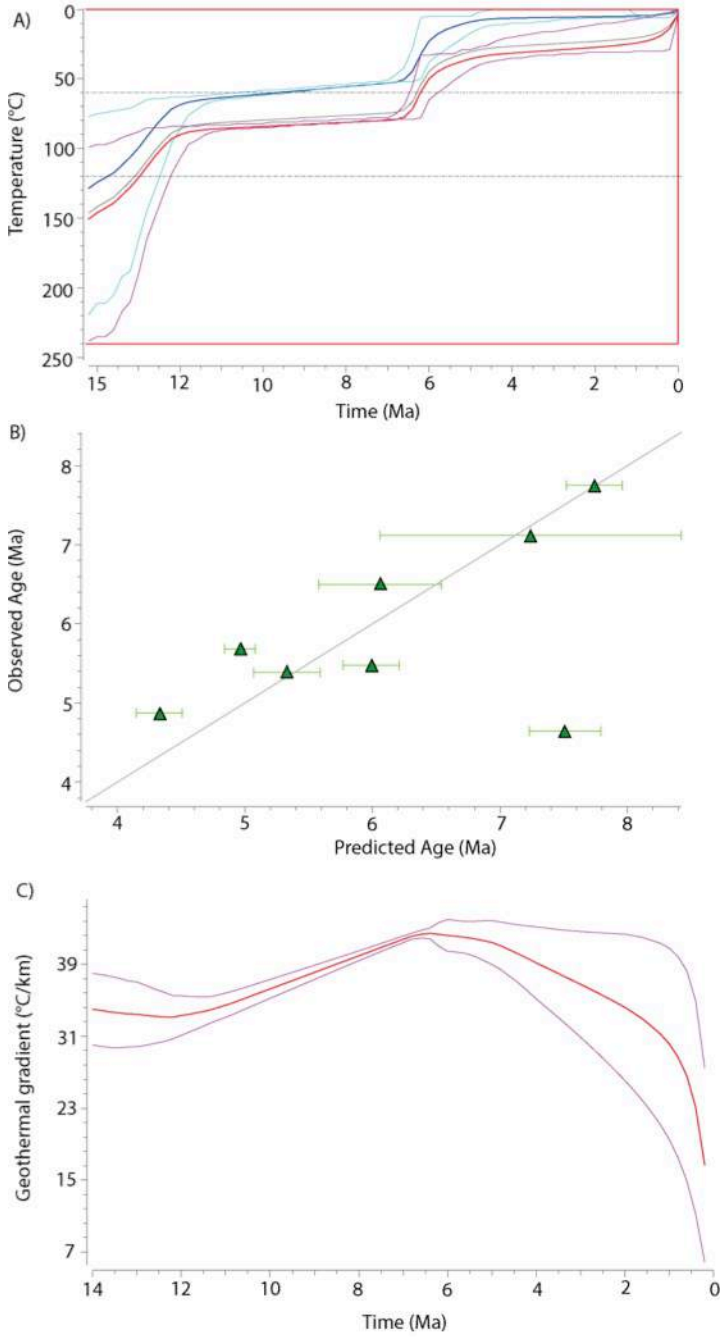

Fig. S4 - QTQt thermal modelling outputs for the TdP massif, West transect. A) Expected (weighted mean) T-t model based on AHe data presented in Fig. 4 b, the red line correspond to the output thermal history for the highest elevation sample, and the blue line to the output thermal history for the lowest elevation sample. The cyan and magenta lines bound the 95% confidence interval of the expected model for the lowest and the highest elevation samples, respectively. The redbox is representing general T-t priors. B) Observed vs. the predicted age diagram with the single-grain AHe corrected ages (green triangles) plotted to show the statistical fit of the model. C) The geothermal gradient (red line) and 95% of confidence interval (magenta lines) predicted for the inversion thermal modelling. Note that the late-stage evolution is reflecting the gradual transition form geothermal (35 $\pm$ 10 °C/km) to atmospheric (lapse rate, 6 $\pm$ 2 °C/km) gradient during rock exhumation towards the surface.

Supplementary Tables

Table S1 a. Stepwise $^{4}He/^{3}He$ degassing data for Torres del Paine sample 04-JM-90a.

04-JM-90a (758 m)						
Step	Temperature* (°C)	Duration (hours)	^{3}He ($x10^{6}$ atoms)	(±) ($x10^{6}$ atoms)	$^{4}He/^{3}He$	(±)
1	210	0.2	0.006	0.001	2058.40	6513.08
2	225	0.5	0.049	0.004	391.81	303.77
3	260	0.38	0.096	0.007	437.33	163.28
4	300	0.51	0.444	0.022	376.70	39.49
5	300	0.66	0.233	0.014	589.97	82.25
6	310	0.66	0.287	0.017	612.92	70.86
7	330	0.46	0.297	0.017	746.94	78.31
8	340	0.45	0.349	0.019	815.25	72.20
9	350	0.48	0.377	0.020	965.31	77.20
10	350	0.66	0.421	0.021	1054.30	75.91
11	370	0.53	0.503	0.024	1233.72	76.86
12	400	0.48	0.723	0.029	1537.27	72.97
13	410	0.5	0.799	0.031	1542.67	69.22
14	420	0.56	0.700	0.029	1902.99	89.92
15	440	0.63	0.864	0.032	1971.67	80.89
16	475	0.5	0.803	0.031	2183.20	94.58
17	500	0.5	0.590	0.026	2101.45	110.96
18	600	0.5	0.489	0.023	2391.61	141.96
19	700	0.5	0.006	0.001	9494.85	26907.71
20	900	0.5	0.010	0.001	659.04	1768.82

Notes. *Temperatures of these analyses are approximate, and controlled to ±50 °C.
BDL: Below Detection Limit.
Effective model: a = 59.9 µm; U = 21.0 ppm; Th = 27.1 ppm.
Single-grain replicates: (U-Th-Sm)/He age = 6.60 ±1.22 Ma; mean replicates a = 60.3 µm.

Table S1 b. Stepwise $^{4}He/^{3}He$ degassing data for Torres del Paine sample 13-TP-26a.

13-TP-26a (206 m)						
Step	Temperature* (°C)	Duration (hours)	^{3}He ($x10^{6}$ atoms)	(±) ($x10^{6}$ atoms)	$^{4}He/^{3}He$	(±)
1	210	0.2	0.010	0.001	BDL	BDL
2	225	0.5	0.137	0.010	9.68	38.31
3	260	0.38	0.299	0.018	6.56	19.96
4	300	0.51	0.947	0.035	17.33	4.95
5	300	0.66	0.657	0.029	24.36	11.64
6	310	0.66	0.570	0.026	38.46	11.12
7	330	0.46	0.617	0.028	49.51	9.70
8	340	0.45	0.674	0.029	50.97	8.84
9	350	0.48	0.766	0.031	56.26	7.51
10	350	0.66	0.708	0.030	69.94	8.53
11	370	0.53	0.813	0.032	74.44	9.58
12	400	0.48	1.373	0.043	74.09	5.37
13	410	0.5	1.318	0.042	77.77	5.66
14	420	0.56	1.380	0.043	82.26	5.62
15	440	0.63	1.850	0.051	81.79	3.72
16	475	0.5	2.793	0.063	87.70	3.39
17	500	0.5	2.323	0.057	102.05	3.94
18	600	0.5	2.594	0.061	122.40	4.74
19	700	0.5	0.135	0.010	307.72	63.39
20	900	0.5	0.053	0.005	670.05	254.61

Notes. *Temperatures of these analyses are approximate, and controlled to ±50 °C.
BDL: Below Detection Limit.
Effective model: a = 61.0 μm; U = 12.2 ppm; Th = 52.6 ppm.
Single-grain replicates: (U-Th-Sm)/He age = 4.20 ±0.94 Ma; mean replicates a = 60.8 μm.

Table S2. Estimates of the radiation damage, kinetic He diffusion parameters and closure temperature of the ZHe system in the Fitz Roy massif samples in a scenario in which the low ∝-dose is linked to the relatively young age of the pluton of ca. 12.5 Ma (Ramírez de Arellano, 2012). The ∝-dose, f and D_0 estimates were calculated based in Geutheron et al. (2020), using a common E_a value of 133 kJ/mol (see text for details), and the Tc estimate were based in Dodson (1979).

Zircon (U-Th-Sm)/He data	Corrected Age ± 1σ (Ma)	eU (ppm)	∝-dose	Ea (J/mol)	f (%)	D_0 (m^2/s)	Tc (°C)
zFZR3-1	8,24	226,86	6,11797E+15	133000	0,2	0,00008	90,6
zFZR3-2	8,47	307,51	8,51577E+15	133000	0,2	0,00008	91,16
zFZR3-3	8,24	542,86	1,4624E+16	133000	0,6	2,66667E-05	99,15
zFZR3-4	8,50	548,91	1,52487E+16	133000	0,6	2,66667E-05	99,15
zFZR3-5	8,69	577,81	1,64245E+16	133000	0,6	2,66667E-05	98,83
FZR3	8,43 ± 0,19						
zFZR4-1	8,30	403,74	1,09639E+16	133000	0,5	0,000032	95,7
zFZR4-3	8,26	334,71	9,03723E+15	133000	0,2	0,00008	90,3
zFZR4-4	7,14	1204,03	2,81155E+16	133000	1	0,000016	100,69
zFZR4-5	7,31	769,46	1,83981E+16	133000	0,8	0,00002	101,56
FZR4 AV	7,75 ± 0,61						
zFZR5-1	8,66	978,23	2,77215E+16	133000	1	0,000016	103,44
zFZR5-2	9,54	293,70	9,1662E+15	133000	0,3	5,33333E-05	91,26
zFZR5-3	6,22	484,01	9,85664E+15	133000	0,2	0,00008	87,73
zFZR5-4	9,72	584,72	1,8603E+16	133000	0,8	0,00002	98,09
zFZR5-5	6,11	591,26	1,18174E+16	133000	0,5	0,000032	94,26
FZR5 AV	8,05 ± 1,77						
zFZR6-1	12,87	1244,72	5,23982E+16	133000	2	0,000008	108,37
zFZR6-2	11,59	1331,37	5,05061E+16	133000	2	0,000008	106,56
zFZR6-3	9,58	1087,78	3,40949E+16	133000	1,5	1,06667E-05	103,3
zFZR6-4	6,68	435,66	9,51279E+15	133000	0,2	0,00008	87,38
FZR6 AV	10,18 ± 2,70						

Eu is the age-effective uranium concentration, **Ea** is the activation energy, **f** is the damage fraction, **D_0** is the initial diffusion coefficient, and **Tc** is the effective closure temperature of the ZHe system.

References - Chapter 3

Ávila, P., & Dávila, F. M. (2018). Heat flow and lithospheric thickness analysis in the Patagonian asthenospheric windows, southern South America. *Tectonophysics*, *747*, 99-107.

Berger, A. L., Gulick, S. P., Spotila, J. A., Upton, P., Jaeger, J. M., Chapman, J. B., ... & McAleer, R. J. (2008). Quaternary tectonic response to intensified glacial erosion in an orogenic wedge. *Nature Geoscience*, *1*(11), 793-799.

Betka, P., Klepeis, K., & Mosher, S. (2015). Along-strike variation in crustal shortening and kinematic evolution of the base of a retroarc fold-and-thrust belt: Magallanes, Chile 53° S–54° S. *Bulletin*, *127*(7-8), 1108-1134.

Blisniuk, P. M., Stern, L. A., Chamberlain, C. P., Zeitler, P. K., Ramos, V. A., Sobel, E. R., Haschke, M., Strecker, M.R., & Warkus, F. (2006). Links between mountain uplift, climate, and surface processes in the southern Patagonian Andes. In *The Andes* (pp. 429-440). Springer, Berlin, Heidelberg.

Braun, J. (2002). Quantifying the effect of recent relief changes on age–elevation relationships. *Earth and Planetary Science Letters*, *200*(3-4), 331-343.

Braun, J., & Willett, S. D. (2013). A very efficient O (n), implicit and parallel method to solve the stream power equation governing fluvial incision and landscape evolution. *Geomorphology*, *180*, 170-179.

Breitsprecher, K., & Thorkelson, D. J. (2009). Neogene kinematic history of Nazca–Antarctic–Phoenix slab windows beneath Patagonia and the Antarctic Peninsula. *Tectonophysics*, *464*(1-4), 10-20.

Brocklehurst, S. H. (2010). Tectonics and geomorphology. *Progress in Physical Geography*, *34*(3), 357-383.

Brocklehurst, S. H., & Whipple, K. X. (2006). Assessing the relative efficiency of fluvial and glacial erosion through simulation of fluvial landscapes. *Geomorphology*, *75*(3-4), 283-299.

Broecker, W. S., & Denton, G. H. (1990). The role of ocean-atmosphere reorganizations in glacial cycles. *Quaternary science reviews*, *9*(4), 305-341.

Calderón, M., Fosdick, J. C., Warren, C., Massonne, H. J., Fanning, C. M., Cury, L. F., Schwanethal, J., Fonseca, P.E., Galaz, G., & Herve, F. (2012). The low-grade Canal de las Montañas Shear Zone and its role in the tectonic emplacement of the Sarmiento Ophiolitic Complex and Late Cretaceous Patagonian Andes orogeny, Chile. *Tectonophysics*, *524*, 165-185.

Cande, S. C., & Leslie, R. B. (1986). Late Cenozoic tectonics of the southern Chile trench. *Journal of Geophysical Research: Solid Earth*, *91*(B1), 471-496.

Champagnac, J. D., Valla, P. G., & Herman, F. (2014). Late-Cenozoic relief evolution under evolving climate: A review. *Tectonophysics*, *614*, 44-65.

Christeleit, E. C., Brandon, M. T., & Shuster, D. L. (2017). Miocene development of alpine glacial relief in the Patagonian Andes, as revealed by low-temperature thermochronometry. *Earth and Planetary Science Letters*, *460*, 152-163.

Conrad, C. P., & Husson, L. (2009). Influence of dynamic topography on sea level and its rate of change. *Lithosphere*, *1*(2), 110-120.

Dahlen, F. A. (1990). Critical taper model of fold-and-thrust belts and accretionary wedges. *Annual Review of Earth and Planetary Sciences*, *18*, 55.

Davies, B. J., & Glasser, N. F. (2012). Accelerating shrinkage of Patagonian glaciers from the Little Ice Age (~ AD 1870) to 2011. *Journal of Glaciology*, *58*(212), 1063-1084.

Davies, B. J., Darvill, C. M., Lovell, H., Bendle, J. M., Dowdeswell, J. A., Fabel, D., García, J.-L., Geiger, A., Glasser, N.F., Gheorghiu, D.M., Harrison, S., Hein, A. S., Kaplan, M. R., Martin, J.R.V., Mendelova, M., Palmer, A., Pelto, M., Rodés, A., Sagredo, E.A., Smedley, R.K., & Thorndycraft, V. R. (2020). The evolution of the Patagonian Ice Sheet from 35 ka to the present day (PATICE). *Earth-Science Reviews*, *204*, 103152.

DeMets, C., Gordon, R. G., & Argus, D. F. (2010). Geologically current plate motions. *Geophysical journal international*, *181*(1), 1-80.

Dodson, M. H. (1973). Closure temperature in cooling geochronological and petrological systems. *Contributions to Mineralogy and Petrology*, *40*(3), 259-274.

Dodson, M. H. (1979). Theory of cooling ages. In *Lectures in isotope geology* (pp. 194-202). Springer, Berlin, Heidelberg.

Egholm, D. L., Nielsen, S. B., Pedersen, V. K., & Lesemann, J. E. (2009). Glacial effects limiting mountain height. *Nature*, *460*(7257), 884-887.

Ehlers, T. A., & Farley, K. A. (2003). Apatite (U–Th)/He thermochronometry: methods and applications to problems in tectonic and surface processes. *Earth and Planetary Science Letters*, *206*(1-2), 1-14.

England, P., & Molnar, P. (1990). Surface uplift, uplift of rocks, and exhumation of rocks. *Geology*, *18*(12), 1173-1177.

Evans, N. J., Byrne, J. P., Keegan, J. T., & Dotter, L. E. (2005). Determination of uranium and thorium in zircon, apatite, and fluorite: Application to laser (U-Th)/He thermochronology. *Journal of Analytical Chemistry*, *60*(12), 1159-1165.

Faccenna, C., Becker, T. W., Conrad, C. P., & Husson, L. (2013). Mountain building and mantle dynamics. *Tectonics*, *32*(1), 80-93.

Farley, K. A. (2002). (U-Th)/He dating: Techniques, calibrations, and applications. *Reviews in mineralogy and geochemistry*, *47*(1), 819-844.

Farley, K. A., Wolf, R. A., & Silver, L. T. (1996). The effects of long alpha-stopping distances on (U-Th)/He ages. *Geochimica et cosmochimica acta*, *60*(21), 4223-4229.

Fildani, A., Cope, T. D., Graham, S. A., & Wooden, J. L. (2003). Initiation of the Magallanes foreland basin: Timing of the southernmost Patagonian Andes orogeny revised by detrital zircon provenance analysis. *Geology*, *31*(12), 1081-1084.

Fosdick, J. C., Grove, M., Hourigan, J. K., & Calderon, M. (2013). Retroarc deformation and exhumation near the end of the Andes, southern Patagonia. *Earth and Planetary Science Letters*, *361*, 504-517.

Fosdick, J. C., Romans, B. W., Fildani, A., Bernhardt, A., Calderón, M., & Graham, S. A. (2011). Kinematic evolution of the Patagonian retroarc fold-and-thrust belt and Magallanes foreland basin, Chile and Argentina, 51 30′ S. *Bulletin*, *123*(9-10), 1679-1698.

Fox, M., Herman, F., Kissling, E., & Willett, S. D. (2015). Rapid exhumation in the Western Alps driven by slab detachment and glacial erosion. *Geology*, *43*(5), 379-382.

Fox, M., Herman, F., Willett, S. D., & Schmid, S. M. (2016). The exhumation history of the European Alps inferred from linear inversion of thermochronometric data. *American Journal of Science*, *316*(6), 505-541.

Garreaud, R., Lopez, P., Minvielle, M., & Rojas, M. (2013). Large-scale control on the Patagonian climate. *Journal of Climate*, *26*(1), 215-230.

Gautheron, C., Djimbi, D. M., Roques, J., Balout, H., Ketcham, R. A., Simoni, E., Pik, R., Seydoux-Guillaume, A.-M., & Tassan-Got, L. (2020). A multi-method, multi-scale theoretical study of He and Ne diffusion in zircon. *Geochimica et Cosmochimica Acta*, *268*, 348-367.

Gautheron, C., Tassan-Got, L., Barbarand, J., & Pagel, M. (2009). Effect of alpha-damage annealing on apatite (U–Th)/He thermochronology. *Chemical Geology*, *266*(3-4), 157-170.

Gautheron, C., Hueck, M., Ternois, S., Heller, B., Schwartz, S., Sarda, P., & Tassan-Got, L. (2022). Investigating the Shallow to Mid-Depth (> 100–300° C) Continental Crust Evolution with (U-Th)/He Thermochronology: A Review. *Minerals*, *12*(5), 563.

Georgieva, V., Gallagher, K., Sobczyk, A., Sobel, E. R., Schildgen, T. F., Ehlers, T. A., & Strecker, M. R. (2019). Effects of slab-window, alkaline volcanism, and glaciation on thermochronometer cooling histories, Patagonian Andes. *Earth and Planetary Science Letters*, *511*, 164-176.

Georgieva, V., Melnick, D., Schildgen, T. F., Ehlers, T. A., Lagabrielle, Y., Enkelmann, E., & Strecker, M. R. (2016). Tectonic control on rock uplift, exhumation, and topography above an oceanic ridge collision: Southern Patagonian Andes (47 S), Chile. *Tectonics*, *35*(6), 1317-1341.

Gérard, B., Robert, X., Grujic, D., Gautheron, C., Audin, L., Bernet, M., & Balvay, M. (2022). Zircon (U-Th)/He closure temperature lower than apatite thermochronometric systems: reconciliation of a paradox. *Minerals*, *12*(2), 145.

Ghiglione, M. C., Suarez, F., Ambrosio, A., Da Poian, G., Cristallini, E. O., Pizzio, M. F., & Reinoso, R. M. (2009). Structure and evolution of the Austral Basin fold-thrust belt, southern Patagonian Andes. *Revista de la Asociación Geológica Argentina*, *65*(1), 215-226.

Glasser, N., & Jansson, K. (2008). The glacial map of southern South America. *Journal of Maps*, *4*(1), 175-196.

Global Volcanism Program, 2023. [Database] Volcanoes of the World (v. 5.0.1; 19 Dec 2022). Distributed by Smithsonian Institution, compiled by Venzke, E. https://doi.org/10.5479/si.GVP.VOTW5-2022.5.0

Glodny, J., Gräfe, K., Echtler, H., & Rosenau, M. (2008). Mesozoic to Quaternary continental margin dynamics in South-Central Chile (36–42 S): the apatite and zircon fission track perspective. *International Journal of Earth Sciences*, *97*(6), 1271-1291.

Glotzbach, C., van der Beek, P. A., & Spiegel, C. (2011). Episodic exhumation and relief growth in the Mont Blanc massif, Western Alps from numerical modelling of thermochronology data. *Earth and Planetary Science Letters*, *304*(3-4), 417-430.

Guenthner, W. R., Barbeau Jr, D. L., Reiners, P. W., & Thomson, S. N. (2010). Slab window migration and terrane accretion preserved by low-temperature thermochronology of a magmatic arc, northern Antarctic Peninsula. Geochemistry, Geophysics, Geosystems, 11(3).

Guillaume, B., Gautheron, C., Simon-Labric, T., Martinod, J., Roddaz, M., & Douville, E. (2013). Dynamic topography control on Patagonian relief evolution as inferred from low temperature thermochronology. *Earth and Planetary Science Letters*, *364*, 157-167.

Guillaume, B., Martinod, J., Husson, L., Roddaz, M., & Riquelme, R. (2009b). Neogene uplift of central eastern Patagonia: dynamic response to active spreading ridge subduction?. *Tectonics*, *28*(2).

Guillaume, B., Moroni, M., Funiciello, F., Martinod, J., & Faccenna, C. (2010). Mantle flow and dynamic topography associated with slab window opening: Insights from laboratory models. *Tectonophysics*, *496*(1-4), 83-98.

Haeuselmann, P., Granger, D. E., Jeannin, P. Y., & Lauritzen, S. E. (2007). Abrupt glacial valley incision at 0.8 Ma dated from cave deposits in Switzerland. Geology, 35(2), 143-146.

Hayes, G. P., Moore, G. L., Portner, D. E., Hearne, M., Flamme, H., Furtney, M., & Smoczyk, G. M. (2018). Slab2, a comprehensive subduction zone geometry model. *Science*, *362*(6410), 58-61.

Hein, A. S., Dunai, T. J., Hulton, N. R., & Xu, S. (2011). Exposure dating outwash gravels to determine the age of the greatest Patagonian glaciations. *Geology*, *39*(2), 103-106.

Herman, F., & Brandon, M. (2015). Mid-latitude glacial erosion hotspot related to equatorial shifts in southern Westerlies. *Geology*, *43*(11), 987-990.

Herman, F., & Brandon, M. (2015). Mid-latitude glacial erosion hotspot related to equatorial shifts in southern Westerlies. *Geology*, *43*(11), 987-990.

Herman, F., Beaud, F., Champagnac, J. D., Lemieux, J. M., & Sternai, P. (2011). Glacial hydrology and erosion patterns: a mechanism for carving glacial valleys. *Earth and Planetary Science Letters*, *310*(3-4), 498-508.

Herman, F., Braun, J., Deal, E., & Prasicek, G. (2018). The response time of glacial erosion. *Journal of Geophysical Research: Earth Surface*, *123*(4), 801-817.

Herman, F., Braun, J., Deal, E., & Prasicek, G. (2018). The response time of glacial erosion. *Journal of Geophysical Research: Earth Surface*, *123*(4), 801-817.

Herman, F., Seward, D., Valla, P. G., Carter, A., Kohn, B., Willett, S. D., & Ehlers, T. A. (2013). Worldwide acceleration of mountain erosion under a cooling climate. *Nature*, *504*(7480), 423-426.

Herve, F., Pankhurst, R. J., Fanning, C. M., Calderón, M., & Yaxley, G. M. (2007). The South Patagonian batholith: 150 my of granite magmatism on a plate margin. *Lithos*, *97*(3-4), 373-394.

Heuret, A., & Lallemand, S. (2005). Plate motions, slab dynamics and back-arc deformation. *Physics of the Earth and Planetary Interiors*, *149*(1-2), 31-51.

House, M. A., Kohn, B. P., Farley, K. A., & Raza, A. (2002). Evaluating thermal history models for the Otway Basin, southeastern Australia, using (U-Th)/He and fission-track data from borehole apatites. *Tectonophysics*, *349*(1-4), 277-295.

Kaplan, M. R., Ackert Jr, R. P., Singer, B. S., Douglass, D. C., & Kurz, M. D. (2004). Cosmogenic nuclide chronology of millennial-scale glacial advances during O-isotope stage 2 in Patagonia. *Geological Society of America Bulletin*, *116*(3-4), 308-321.

Klepeis, K., Betka, P., Clarke, G., Fanning, M., Hervé, F., Rojas, L., Mpodozis, C, & Thomson, S. (2010). Continental underthrusting and obduction during the Cretaceous closure of the Rocas Verdes rift basin, Cordillera Darwin, Patagonian Andes. *Tectonics*, *29*(3).

Koppes, M. N., & Montgomery, D. R. (2009). The relative efficacy of fluvial and glacial erosion over modern to orogenic timescales. *Nature Geoscience*, *2*(9), 644-647.

Kraemer, P. E. (2003). Orogenic shortening and the origin of the Patagonian orocline (56 S. Lat). *Journal of South American Earth Sciences*, *15*(7), 731-748.

Lagabrielle, Y., Scalabrino, B., Suarez, M., & Ritz, J. F. (2010). Mio-Pliocene glaciations of Central Patagonia: New evidence and tectonic implications. *Andean Geology*, *37*(2), 276-299.

Lagabrielle, Y., Goddéris, Y., Donnadieu, Y., Malavieille, J., & Suarez, M. (2009). The tectonic history of Drake Passage and its possible impacts on global climate. *Earth and Planetary Science Letters*, *279*(3-4), 197-211.

Lagabrielle, Y., Suárez, M., Malavieille, J., Morata, D., Espinoza, F., Maury, R. C., Scalabrino, B., Barbero, L., Cruz, R., Rossello, E., & Bellon, H. (2007). Pliocene extensional tectonics in the Eastern Central Patagonian Cordillera: geochronological constraints and new field evidence. *Terra Nova*, *19*(6), 413-424.

Lagabrielle, Y., Suárez, M., Rossello, E. A., Hérail, G., Martinod, J., Régnier, M., & de la Cruz, R. (2004). Neogene to Quaternary tectonic evolution of the Patagonian Andes at the latitude of the Chile Triple Junction. *Tectonophysics*, *385*(1-4), 211-241.

Landry, K. R., Coutand, I., Whipp Jr, D. M., Grujic, D., & Hourigan, J. K. (2016). Late Neogene tectonically driven crustal exhumation of the Sikkim Himalaya: Insights from inversion of multithermochronologic data. *Tectonics*, *35*(3), 833-859.

Leuthold, J., Müntener, O., Baumgartner, L. P., Putlitz, B., Ovtcharova, M., & Schaltegger, U. (2012). Time resolved construction of a bimodal laccolith (Torres del Paine, Patagonia). *Earth and Planetary Science Letters*, *325*, 85-92.

Lisiecki, L. E., & Raymo, M. E. (2007). Plio–Pleistocene climate evolution: trends and transitions in glacial cycle dynamics. *Quaternary Science Reviews*, *26*(1-2), 56-69.

Lisiecki, L. E. (2010). A benthic δ13C-based proxy for atmospheric pCO2 over the last 1.5 Myr. *Geophysical Research Letters*, *37*(21).

Malkowski, M. A., Sharman, G. R., Graham, S. A., & Fildani, A. (2017). Characterisation and diachronous initiation of coarse clastic deposition in the Magallanes–Austral foreland basin, Patagonian Andes. *Basin Research*, *29*, 298-326.

Maloney, K. T., Clarke, G. L., Klepeis, K. A., & Quevedo, L. (2013). The Late Jurassic to present evolution of the Andean margin: Drivers and the geological record. *Tectonics*, *32*(5), 1049-1065.

Mercer, J. H., & Sutter, J. F. (1982). Late Miocene—earliest Pliocene glaciation in southern Argentina: implications for global ice-sheet history. *Palaeogeography, Palaeoclimatology, Palaeoecology*, *38*(3-4), 185-206.

Molnar, P., England, P., & Martinod, J. (1993). Mantle dynamics, uplift of the Tibetan Plateau, and the Indian monsoon. *Reviews of Geophysics*, *31*(4), 357-396.

Muller, V. A., Calderón, M., Fosdick, J. C., Ghiglione, M. C., Cury, L. F., Massonne, H. J., Fannin, C. M., Warren, C., Ramírez de Arellano, C. & Sternai, P. (2021). The closure of the Rocas Verdes Basin and early tectono-metamorphic evolution of the Magallanes Fold-and-Thrust Belt, southern Patagonian Andes (52–54° S). *Tectonophysics*, *798*, 228686.

Nasdala, L., Wenzel, M., Vavra, G., Irmer, G. and Kober, B. (2001) Metamictisation of natural zircon: accumulation versus thermal annealing of radioactivity-induced damage. *Contrib. Min. Petrol*. 141, 125-144.

Pedersen, V. K., & Egholm, D. L. (2013). Glaciations in response to climate variations preconditioned by evolving topography. *Nature*, *493*(7431), 206-210.

Putlitz, B., Baumgartner, L.P., Oberhaensli, R., Diamond, L., Altenberger, U. (2001). The Torres del Paine Laccolith (Chile); intrusion and metamorphism. XI Goldschmidt Conference, Abstract No. 3534. Hot Springs, United States.

Rabassa, J. (2008). Late cenozoic glaciations in Patagonia and Tierra del Fuego. *Developments in quaternary sciences*, *11*, 151-204.

Rabassa, J., Coronato, A. M., & Salemme, M. (2005). Chronology of the Late Cenozoic Patagonian glaciations and their correlation with biostratigraphic units of the Pampean region (Argentina). *Journal of South American Earth Sciences*, *20*(1-2), 81-103.

Rabassa, J., Coronato, A., & Martinez, O. (2011). Late Cenozoic glaciations in Patagonia and Tierra del Fuego: an updated review. *Biological Journal of the Linnean Society*, *103*(2), 316-335.

Ramírez de Arellano, C. (2011). *Petrology and chemistry of the Chaltén Plutonic Complex and implications on the magmatic and tectonic evolution of the Southernmost Andes (Patagonia) during the Miocene* (Doctoral dissertation, Université de Lausanne, Faculté des géosciences et de l'environnement).

Ramírez de Arellano, C., Putlitz, B., Müntener, O., & Ovtcharova, M. (2012). High precision U/Pb zircon dating of the Chaltén Plutonic Complex (Cerro Fitz Roy, Patagonia) and its relationship to arc migration in the southernmost Andes. *Tectonics*, *31*(4).

Ramos, V. A. (2005). Seismic ridge subduction and topography: Foreland deformation in the Patagonian Andes. *Tectonophysics*, *399*(1-4), 73-86.

Ramos, V. A., & Kay, S. M. (1992). Southern Patagonian plateau basalts and deformation: backarc testimony of ridge collisions. *Tectonophysics*, *205*(1-3), 261-282.

Recanati, A., Gautheron, C., Barbarand, J., Missenard, Y., Pinna-Jamme, R., Tassan-Got, L., ... & Gallagher, K. (2017). Helium trapping in apatite damage: Insights from (U-Th-Sm)/He dating of different granitoid lithologies. *Chemical Geology*, *470*, 116-131.

Reiners, P. W. (2005). Zircon (U-Th)/He thermochronometry. *Reviews in Mineralogy and Geochemistry*, *58*(1), 151-179.

Reiners, P. W., & Brandon, M. T. (2006). Using thermochronology to understand orogenic erosion. *Annual Review of Earth and Planetary Sciences*, *34*(1), 419-466.

Reiners, P. W., Spell, T. L., Nicolescu, S., & Zanetti, K. A. (2004). Zircon (U-Th)/He thermochronometry: He diffusion and comparisons with 40Ar/39Ar dating. *Geochimica et cosmochimica acta*, *68*(8), 1857-1887.

Ruddiman, W. F., Raymo, M. E., Prell, W. L., & Kutzbach, J. E. (1997). The uplift-climate connection: a synthesis. In *Tectonic uplift and climate change* (pp. 471-515). Springer, Boston, MA.

Scalabrino, B., Lagabrielle, Y., Malavieille, J., Dominguez, S., Melnick, D., Espinoza, F., Suarez, M, & Rossello, E. (2010). A morphotectonic analysis of central Patagonian Cordillera: Negative inversion of the Andean belt over a buried spreading center?. *Tectonics*, *29*(2).

Shuster, D. L., Cuffey, K. M., Sanders, J. W., & Balco, G. (2011). Thermochronometry reveals headward propagation of erosion in an alpine landscape. *Science*, *332*(6025), 84-88.

Shuster, D. L., Ehlers, T. A., Rusmoren, M. E., & Farley, K. A. (2005). Rapid glacial erosion at 1.8 Ma revealed by 4He/3He thermochronometry. *Science*, *310*(5754), 1668-1670.

Shuster, D. L., Farley, K. A., Sisterson, J. M., & Burnett, D. S. (2004). Quantifying the diffusion kinetics and spatial distributions of radiogenic 4He in minerals containing proton-induced 3He. *Earth and Planetary Science Letters*, *217*(1-2), 19-32.

Singer, B. S., Ackert Jr, R. P., & Guillou, H. (2004). 40Ar/39Ar and K-Ar chronology of Pleistocene glaciations in Patagonia. *Geological Society of America Bulletin*, *116*(3-4), 434-450.

Stern, C. R., Futa, K., & Muehlenbachs, K. A. R. L. I. S. (1984). Isotope and trace element data for orogenic andesites from the Austral Andes. In *Andean magmatism* (pp. 31-46). Birkhäuser Boston.

Sternai, P., Avouac, J. P., Jolivet, L., Faccenna, C., Gerya, T., Becker, T. W., & Menant, A. (2016). On the influence of the asthenospheric flow on the tectonics and topography at a collision-subduction transition zones: Comparison with the eastern Tibetan margin. *Journal of Geodynamics*, *100*, 184-197.

Sternai, P., Herman, F., Fox, M. R., & Castelltort, S. (2011). Hypsometric analysis to identify spatially variable glacial erosion. *Journal of Geophysical Research: Earth Surface*, *116*(F3).

Sternai, P., Herman, F., Valla, P. G., & Champagnac, J. D. (2013). Spatial and temporal variations of glacial erosion in the Rhône valley (Swiss Alps): Insights from numerical modelling. *Earth and Planetary Science Letters*, *368*, 119-131.

Sternai, P., Sue, C., Husson, L., Serpelloni, E., Becker, T. W., Willett, S. D., Faccenna, C., Di Giulio, A., Spada, G., Jolivet, L., Valla, P., Petit, C. Nocquet, J.-M, Walpersdorf, A., & Castelltort, S. (2019). Present-day uplift of the European Alps: Evaluating mechanisms and models of their relative contributions. *Earth-Science Reviews*, *190*, 589-604.

Stevens Goddard, A. L., & Fosdick, J. C. (2019). Multichronometer thermochronologic modelling of migrating spreading ridge subduction in southern Patagonia. *Geology*, *47*(6), 555-558.

Suárez, M., De La Cruz, R., & Bell, C. M. (2000). Timing and origin of deformation along the Patagonian fold and thrust belt. *Geological Magazine*, *137*(4), 345-353.

Thomson, S. N., Brandon, M. T., Tomkin, J. H., Reiners, P. W., Vásquez, C., & Wilson, N. J. (2010). Glaciation as a destructive and constructive control on mountain building. *Nature*, *467*(7313), 313-317.

Thomson, S. N., Hervé, F., & Stöckhert, B. (2001). Mesozoic‐Cenozoic denudation history of the Patagonian Andes (southern Chile) and its correlation to different subduction processes. *Tectonics*, *20*(5), 693-711.

Thorndycraft, V. R., Bendle, J. M., Benito, G., Davies, B. J., Sancho, C., Palmer, A. P., .Fabel, D., Medialdea, A., & Martin, J. R. (2019). Glacial lake evolution and Atlantic-Pacific drainage reversals during deglaciation of the Patagonian Ice Sheet. *Quaternary Science Reviews*, *203*, 102-127.

Valla, P. G., Shuster, D. L., & Van Der Beek, P. A. (2011). Significant increase in relief of the European Alps during mid-Pleistocene glaciations. *Nature geoscience*, *4*(10), 688-692.

Wenzens, G. (2006). Terminal moraines, outwash plains, and lake terraces in the vicinity of Lago Cardiel (49 S; Patagonia, Argentina)—evidence for Miocene Andean foreland glaciations. *Arctic, Antarctic, and Alpine Research*, *38*(2), 276-291.

Whipple, K. X. (2009). The influence of climate on the tectonic evolution of mountain belts. *Nature geoscience*, *2*(2), 97-104.

Whipple, K. X., & Tucker, G. E. (1999). Dynamics of the stream‐power river incision model: Implications for height limits of mountain ranges, landscape response timescales, and research needs. *Journal of Geophysical Research: Solid Earth*, *104*(B8), 17661-17674.

Willett, C. D., Ma, K. F., Brandon, M. T., Hourigan, J. K., Christeleit, E. C., & Shuster, D. L. (2020). Transient glacial incision in the Patagonian Andes from~ 6 Ma to present. *Science advances*, *6*(7), eaay1641.

Willett, S. D. (1999). Orogeny and orography: The effects of erosion on the structure of mountain belts. *Journal of Geophysical Research: Solid Earth*, *104*(B12), 28957-28981.

Zachos, J., Pagani, M., Sloan, L., Thomas, E., & Billups, K. (2001). Trends, rhythms, and aberrations in global climate 65 Ma to present. *science*, *292*(5517), 686-693.

Chapter 4. Article 3

Climatic control on the location of continental volcanic arcs

Veleda A. P. Muller*[1], Pietro Sternai[1], Christian Sue[2,3], Thibaud Simon-Labric[4], Pierre G. Valla[2]

*Corresponding Author

[1]Dipartimento di Scienze dell'Ambiente e della Terra (DISAT), Università degli Studi di Milano-Bicocca, Piazza della Scienza, 4, Milan, Italy. v.paivamuller@campus.unimib.it; pietro.sternai@unimib.it

[2]Institute des Sciences de la Terre (ISTerre), Université Grenoble Alpes, Université Savoie Mont Blanc, CNRS, IRD, IFSTAR, Université Gustave Eiffel, 38000 Grenoble, France. christian.sue@univ-grenoble-alpes.fr; pierre.valla@univ-grenoble-alpes.fr

[3]University of Franche-Comté, 25000 Besançon, France.

[4]Centre de Géologie Oisans Alpes, Musée des Minéraux, 38520 Bourg-d'Oisans, France. thibaud.simon-labric@asso-cgo.fr

Abstract

Orogens and volcanic arcs at continental plate margins are primary surface expressions of convergent plate tectonics. Although it is established that climate affects the shape, size, and architecture of orogens via orographic erosion gradients, the ascent of magma through the crust and location of volcanoes along magmatic arcs have been considered insensitive to erosion. However, available data reveal westward migration of late-Cenozoic volcanic activity in the Southern Andes and Cascade Range where orography drives an eastward migration of the topographic water divide by increased precipitation and erosion along west-facing slopes. Thermomechanical numerical modelling shows that orographic erosion and the associated leeward topographic migration may entail asymmetric crustal structures that drive the magma ascent toward the region of enhanced erosion. Despite the different tectonic histories of the Southern Andes and the Cascade Range, orographic erosion is a shared causal mechanism that can explain the late-Cenozoic westward migration of the volcanic front along both magmatic arcs.

Introduction

Volcanic arcs at convergent plate margins are located above the zone of dehydration of a subducting oceanic plate, leading to partial melting of mantle rocks at depths around ~100 km, depending on the mean slab dip angle, convergence velocity and thermal structure of the slab and mantle wedge[1–4]. Assuming a vertical magma transfer from the mantle melting zone to the upper crust in subduction settings[4], slab rollback and trench retreat lead to arc migration towards the subducting plate, whereas slab flattening and trench advancement force the migration of the arc front towards the continent[3,5,6]. In addition to processes that change the depth and position of the mantle melting zone, lithospheric brittle-ductile shear zones serve as fundamental conduits to drive the magma ascent to the surface, thereby affecting the location of the volcanic arc front with respect to the magma source in the mantle and crust[7–10]. The evolution of lithospheric brittle-ductile structures, in turn, depend on the erosion patterns, besides several other factors such as inherited structures, lithology, and convergence rate[11–13]. As a general rule, under the same tectonic conditions, low erosion rates allow forming high and wide orogenic plateaus, whereas high erosion rates imply the formation of smaller orogenic wedges. The climate-tectonics feedbacks also involve orography such that, if the orogen acts as a barrier to atmospheric circulation, enhanced precipitation and erosion on upwind slopes force a leeward migration of the topography[11,13,14]. Although the climatic control on the overall orogenic architecture via surface processes has been largely investigated, its control on rock melting and magma transfer, recognized in extensional settings[15–18], has been essentially overlooked in convergent continental margins. Here, we propose that an orographic leeward migration of the topographic load may entail the upwind migration of the volcanic arc front due to formation of asymmetric crustal shear zones that allow for magma ascent through the crust, a mechanism that explains observations along the northern and southern American Cordillera.

The Cascade Range and Southern Andes case studies

The Cascade Range and Volcanic Arc (CVA) are generated by the subduction of the oceanic Juan de Fuca Plate (JDF), a remnant of the larger and long-lived Farallon Plate, beneath the western margin of the North American continent between latitudes 40–50 °N (Ref. [19,20]). Current subduction occurs at an average rate of ~4 cm/yr, increasing from ~3 to ~4.5 cm/yr from south to north[21]. The subducting plate is ~10 Ma old in its central part at ~45

°N and rejuvenates toward its northern and southern edges (Fig. 1a) providing an example of young, hot and buoyant subducting slab[19–25]. Resistance to subduction and break-up of the JDF Plate into the Explorer and the Gorda microplates is therefore increased since the last ~6 Ma in the north and south respectively[21,26,27]. Asthenospheric upwelling is proposed where break-up between the JDF and the Explorer plates occurs accommodated by the transform Nootka Fault entering into subduction[21,27], and along the southern edge of the JDF plate, nearby the Mendocino Triple Junction[19,21]. Emplacement of volcanic and plutonic rocks in the North Cascades (48-50 °N) occurs through compressive and transcurrent shear zones, such as the Straight Creek and Ross Lake fault, that accommodate the accretion of allochthonous terranes since the Mesozoic[28–30]. These shear zones were suggested as preferential conduits for the emplacement of the Chilliwack Batholith, which crystallized from ~35 to ~4 Ma and is considered of the same magmatic origin as the Quaternary Mt. Baker volcano[23,31–34] (transect Fig. 1 a,b). The volcanic arc in the North Cascades migrates from the northeast towards the southwest since at least ~4 Ma. If one considers the intrusive rocks of the Chilliwack Batholith the onset of such trend can be dated back to ~12 Ma (Ref. [23,31–33]). Conversely, in the High Cascades (40-48°N) volcanic rocks erupted since the late Miocene are preserved, providing the record of an eastward migration of the arc front[23,31–34] in a predominantly transtensional tectonic regime that extends into the Basin and Range sector[19,20,34,35].

The North Cascades interact with westerly Pacific winds, which generate ten times higher precipitation rates on western slopes with respect to the eastern side of the orogen at latitudes where the westerlies are perpendicular to the orogenic belt[36] (north of ~46° N, Fig 1a). This precipitation pattern is consistent with focused rock exhumation in the western flank of the North Cascades since ~10 Ma (Fig. 1b), suggesting that orographic effects are long term features in western North America[11,14,37–40]. While Mesozoic to Tertiary plutonic rocks and metamorphic basement are exhumed in the North Cascades due to orographic erosion, Tertiary to Quaternary volcanics are still preserved in the High Cascades[23,30,31,33,37]. Accordingly, the topographic water divide north of ~46 °N is 40-70 km more to the east and the average elevation is lower by about 500-1000 m than in the southern sector (Fig. 1a,b). The water divide migration is supposed to have occurred during the Plio-Quaternary[14]. Quaternary volcanoes north of ~46 °N commonly overlie slab isodepths <100 km and are systematically located west of the topographic water divide (Fig. 1a). Quaternary volcanoes

south of ~46 °N, instead, overlie slab isodepths ≥100 km and are found along the topographic water divide.

The Southern Andes Volcanic Zone (SVZ) is generated by the subduction of the Nazca oceanic plate below the western margin of the South American continent between latitudes 33–46 °S (Fig. 1c). Subduction occurs at an average rate of ~7 cm/yr (Ref. [41]) with an average slab dip angle of ~25 ° (Refs. [42,43]) since the late Miocene[44]. The age of the subducting oceanic plate decreases southward from ~40 Ma to present-day where the Chile Ridge is currently entering into subduction at the Chile Triple Junction (CTJ, Ref. [45]). In the southern Central Andes (33–38 °S) several fold-and-thrust belts accommodate deformation and volcanic emplacement since at least the Miocene[44,46,47]. In the northern Patagonian Andes (38–46 °S) the general compressive tectonic regime changes to transpressive accommodated by the major strike-slip Liquiñe-Ofqui Fault Zone (LOFZ) active since at least ~5 Ma, with denudation ages between ~16-10 Ma suggesting an earlier activation[48–51]. In this sector, the Patagonian Batholith is exposed, which allows for reconstructions of the magmatic arc migration since the Cretaceous[52]. Conversely, batholiths are not exposed in the Central Andes where deformed volcanic and sedimentary rocks are preserved at the surface[44,46]. Eruption and emplacement ages of volcanic and intrusive rocks south of 40 °S suggest a westward migration and narrowing of the southern volcanic front by around 50 km into the region of the LOFZ since at least the Pleistocene[47,53–55] (e.g., Tronador-Osorno transect, Fig. 1c,d).

Similarly to the Cascade Range, south of 40 °S the SVZ interacts with westerly Pacific winds perpendicular to the orogenic belt associated with significantly increased precipitation on the western slopes of the Southern Andes[36] (Fig. 1c). Exhumation ages younger than ~10 Ma are recorded in the western part of the orogen, whereas systematically older exhumation ages are recorded on the drier eastern peaks of the orogen[49,50,56] (Fig. 1d). An abrupt increase in exhumation rates since ~7 Ma is recorded in the Patagonian Andes, pinpointing the onset of Andean glaciations[40,49,56–58]. An erosion hotspot at 42-46 °S is observed in thermochronologic data 2±2 Ma (Fig. 1c, Ref. [58]). In addition, an overall decrease in mean elevation from about 3 km to 1 km and an ~70 km eastward migration of the topographic water divide further testify the long-term regional orographic effects on the Andean topography[56,59]. Quaternary stratovolcanoes overlie slab isodepths ≤100 km south of 40 °S and are systematically west of the topographic water divide (Fig. 1c) whereas, north of 40 °S, they overlie slab isodepths >100 km and are found along the main topographic divide.

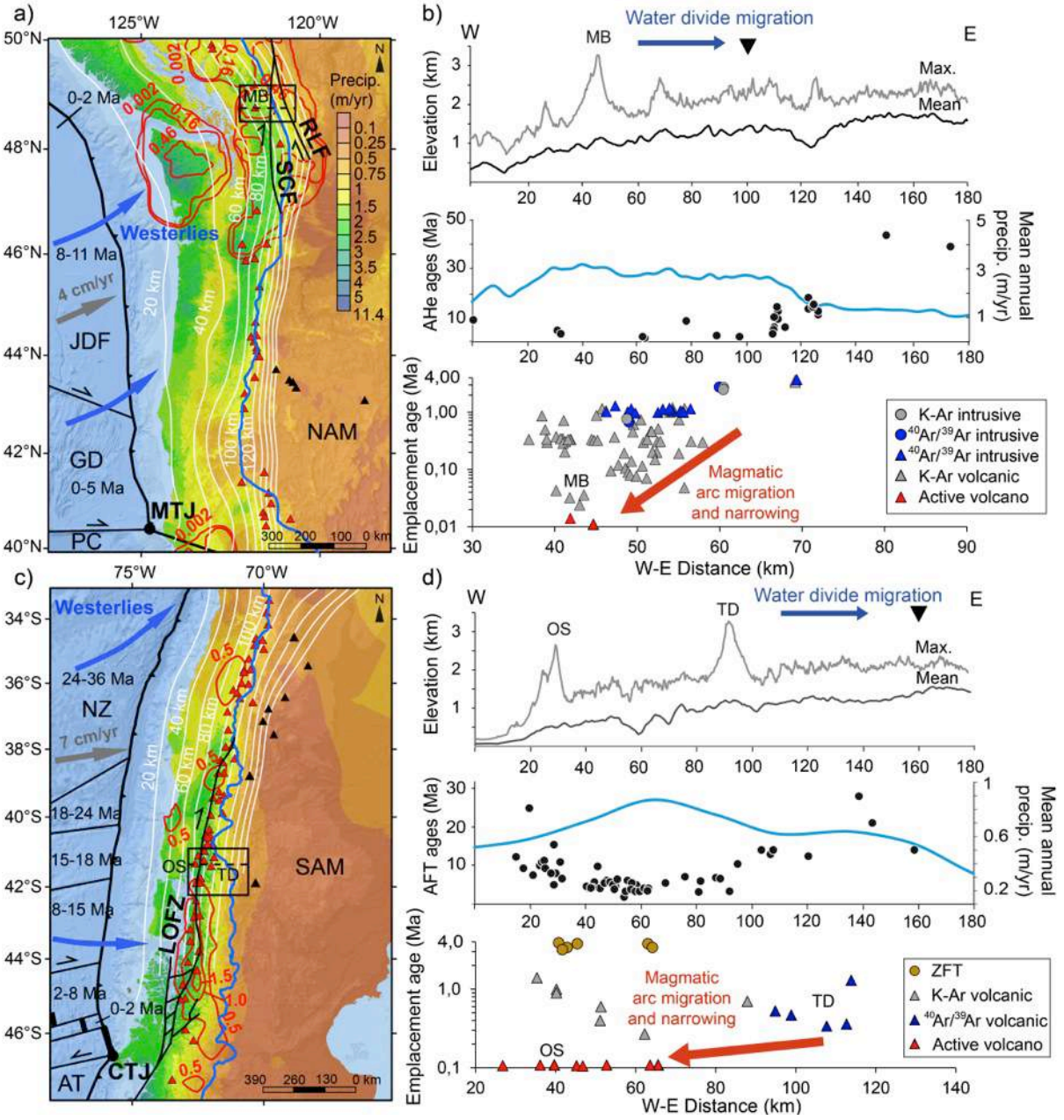

Fig. 1. Data compilation from the Cascade Range and the Southern Andes. (a, c) Maps of the Cascade Range and Southern Andes with mean annual precipitation[36] and approximated direction of westerlies winds (blue arrows), Quaternary volcanoes[60] (red triangles: arc volcanoes; black triangles: within-plate volcanoes[21,47]), convergence velocity (gray arrows)[21,41], isodepths of the top of the slab[43] (white lines), Quaternary exhumation rates[40,58] (red lines), topographic water divide (blue line), subduction trench (black line) and the age range of oceanic plates[25,45]. The insets show where the thermochronological data plotted in (b, d) were compiled (Supplementary Table 1a-d) and the dashed lines show the location of the east-west profiles through the Mt. Baker (MB) in CVA, and Osorno (OS) and Tronador (TD) volcanoes in SVZ. Abbreviations: AT: Antarctic Plate; NZ: Nazca Plate; SAM: South American Plate; NAM: North American Plate; JDF: Juan de Fuca Plate; GD: Gorda Plate; PC: Pacific Plate; CTJ: Chile Triple Junction; MTJ: Mendocino Triple Junction; LOFZ: Liquiñe-Ofqui Fault Zone; SCF: Straight Creek Fault, RLF: Ross Lake Fault. **(b, d)**. Top panels show the mean and maximum elevations (water divide location shown by the black downward triangle, blue arrows show the direction of migration of the topographic water divide). Central panels show the mean annual precipitation rates and apatite (U-Th)/He (AHe) and fission tracks (AFT) ages (Supplementary Table 1a,c and references therein). Bottom panels show emplacement ages of intrusive and volcanic rocks based on K-Ar and $^{40}Ar/^{39}Ar$ in volcanic and intrusive rocks, and zircon fission tracks (ZFT) in intrusive rocks (Supplementary Table 1b,d and references therein), red arrows represent the main sense of volcanic arc migration/narrowing.

The observed topographic leeward and volcanic arc front windward migrations, shared by both the CVA and SVZ despite the different tectonic history, suggest a potential climatic control via erosion on the long-term evolution and location of these continental volcanic arcs. Hereafter, we assess the plausibility of a coupling between crustal magma transfer and climate-controlled erosion.

Coupled geodynamic and erosion numerical modelling

We use a thermo-mechanical (visco-elasto-plastic) geodynamic numerical model coupled to the stream power erosion model (see Methods) to test the hypothesis of an upwind (i.e., westward) migration of the magma ascent and volcanic arc front forced by orography-driven topographic change. The model accounts for the continental crust, upper mantle, asthenosphere (rheological properties are shown in Supplementary Table 2) and a wedge-shaped topography up to 2.5 km high. In a first set of numerical experiments, we impose the initial topography directly above or shifted to the right with respect to a central mantle melting zone (MMZ), analogue to the region where partial melting is generated at ~100 km depth feeding crustal magma reservoirs and surface volcanoes[1–4] (Fig. 2 and Supplementary Figs. 1-4), and no erosion is imposed. This first set of numerical experiments allows us to assess changes in the magma ascent prior to and after the topographic landscape has adjusted to an orographic erosional gradient. In a second set of simulations we impose asymmetric surface erosion, with stream power erosion rates being one order of magnitude higher on left-facing slopes than on right-facing slopes. In these experiments, we consider an initial topography directly above the MMZ (Fig. 3 and Supplementary Figs. 5-8), consistently with observed exhumation rate patterns from the CVA[14,37–40] and SVZ[40,49,56–58]. The local drainage areas and topographic slopes, continuously adjusting to the progressive crustal deformation due to the emplacement of magma, modulate the erosion rates[11,61] (see eq. 13 in Methods), allowing us to address the transient evolution of magma ascent as the topography adjusts to orographic erosion. In order to isolate the effects of climate-driven orography over the crustal trajectories of magma emplacement and ascent towards the surface, we did not impose any tectonic convergence, subduction of oceanic plate, crustal accretion nor sedimentation in these experiments, which simply evolve by upwelling of buoyant magma into the crust until depletion of the MMZ over about 0.3 Ma. This is obviously an oversimplification, but it reduces the degree of complexity of the model and removes any effect from poorly constrained parameters (e.g. spatial-temporal changes in convergence rate or

thermal/mechanical/rheological properties). Although this approach does not allow to reproduce the geologic history of the CVA and SVZ in our simulations, it enables us to explore plausible orographic effects on the joint evolution of the topographic landscapes, crustal structures and magma ascent observed in these settings, that is our ultimate goal. We obviously bear this limitation in mind when framing our results in the contexts of the CVA and SVZ.

The model domain extends over 200 × 120 km (horizontal, x, and vertical, y, dimensions), resolved by 201 × 61 grid points respectively, and is distributed on an irregular Eulerian grid that accounts for a maximum resolution of 1 km along the x and y directions in the upper-central part of the model domain. 400 × 400 Lagrangian markers are randomly distributed along the x and y dimensions and used for advecting the material properties[16,62,63] (Supplementary Table 2). The material properties carried by Lagrangian markers are then interpolated onto the Eulerian grid via a 4th order Runge-Kutta interpolation scheme[62,63]. An internal free surface is simulated through a 10 -km thick layer of sticky air[62]. The velocity boundary conditions are free slip at all boundaries (x = 0 and x = 200 km; y = 0 and y = 120 km). The initial temperature gradient is piece-wise linear resulting from an adiabatic temperature gradient of 0.5 °C/km in the asthenosphere[64] and thermal boundary conditions fixed at 0 °C at the surface and 1327 °C at the lower boundary, with nil horizontal heat flux across the vertical boundaries[63]. Temperature is set to 1327 °C in the MMZ, that is initially circular with 20 km diameter and imposed in the center of the model domain at 100 km depth, consistent with estimates from the CVA[21,65] and SZV[1,66,67]. The upward transfer and emplacement of magma into the crust occurs by buoyancy through a 3 -km wide magmatic channel, which allows for a simplified representation of magmatic percolation by hydrofractures, diffusion, porous flow, and reactive flow through the rheologically stronger mantle lithosphere[63]. The bulk composition of the MMZ is ultramafic, but enrichment by 25% mafic melt is prescribed in the magmatic channel[63]. The viscosity, $\eta_{ductile}$ (Eq. 3 in Methods), of partially molten rocks (with $\xi > 0.1$, Eq. 10 in Methods) is assigned a low constant value of 10^{16} Pa s, and the $\eta_{ductile}$ upper limit is set to 10^{25} Pa s (Refs. [16,63,64]). The topographic wedge measures 2.5 km in simulations with central topography, and 1.5 km in simulations with lateral topography, consistent with the observed orography-related change in mean altitude in the CVA and SVZ (Refs. [38,39,56,59]).

The parametric study focuses on three main parameters. First, the crustal thickness (Ch) varies between 45 and 35 km, consistently with literature values[42,65]. Second, the initial

depth of the magmatic channel upper tip (Dmc), which assumes values of 15, 20, and 25 km to account for efficient/inefficient magma transfer through the crust. Values are based on estimates of the depth of the regional brittle-ductile transition (~20 km, Refs. [42,51,65]), assuming that the rheology of the upper plate crust exerts a primary control on the efficiency of magma transfer. Third, the thickness of the thermal lithosphere (Lh) varies between 90 and 100 km allowing us to account for variations of the elastic lithosphere between ~55 and ~65 km, as estimated from the regional geophysical data[42,65].

Results

Results from the first set of numerical experiments show that the emplacement of magma into the crust is accommodated by structures that affect both the brittle upper crust and the ductile lower crust. Simulations that account for an initial central topography allow the formation of symmetric crustal magma reservoirs and structures with respect to the MMZ, feeding volcanoes on both sides of the topographic wedge (Fig. 2a,b and Supplementary Figs. 1-4). Simulations that account for an initial lateral topography develop highly asymmetric crustal magma reservoirs and structures, feeding volcanoes on the opposite side of the initial topographic wedge (Fig. 2c,d and Supplementary Figs. 1-4). We define the degree of asymmetry of the resultant structures (shown by the cumulative bulk strain in Figs. 2b,d and 3) as $\delta d = dr - dl$, where dr and dl are the maximum horizontal distance between the center of the model domain and the surface fault tips to the right and left, respectively. Increasing positive and negative δd values indicate increasing asymmetry toward the right and left of the system, respectively (results in Table 1 and Fig. 4). For all tested configurations, a thin crust (Ch = 35 km) and a cold lithosphere (Lh = 100 km) facilitate the brittle strain (Fig. 2 and Supplementary Figs. 1,2). When the initial topography is lateral, the leftward asymmetry of the strain and magma ascent is enhanced (Figs. 2c-d, 3, and Supplementary Figs. 1,2). When the initial depth of the magmatic channel upper tip is deep (Dmc = 25 km), the viscous strain in the lower crust accommodates the emplacement of magma, inhibiting the formation of brittle upper crustal structures and the rise of magma to the near surface (Supplementary Figs. 1-4). When Dmc is shallow (15 km), the magma rises easily to the surface through brittle structures near the center of the model, resulting in relatively small values of δd (Fig. 4 and Supplementary Figs. 1-4). When Dmc is intermediate (20 km), brittle-ductile structures cross through the crust reaching the surface at further distance from the center of the model (Figs. 2-3, and Supplementary Figs. 1,3,4). In

the reference model (i.e., Ch = 35 km, Lh = 100 km, and Dmc = 20 km, Fig. 2), an initial lateral topography leads to $\delta d \approx -45$ km (i.e., leftward asymmetry), comparable to the observed westward migration of the magmatic arcs in the natural case studies (Fig. 1). We further remark that, in simulations with initial central topography, a symmetric set of thrusts rooted in the region of magma emplacement form a pop-up structure similar to those observed in the northern sector of the SVZ [46,47]. In the simulations with initial lateral topography, the asymmetric thrust verging towards the west is similar to the "Western Patagonian Thrust" proposed by Ref. [51].

Results from the second set of simulations show that the progressive rightward migration of the topographic divide leads to negative δd values when Ch = 35 km (Figs. 3, 4, and Supplementary Figs. 5,6). The topography migrates toward the right ~20 km in ~0.3 Ma (Fig. 3c and Supplementary Figs. 5,6), roughly consistent with the eastward migration of the water divide by ~50-70 km observed in the study regions during the Plio-Quaternary. Uplift of additional topographic peaks on the left side of the model domain occurs due to left-verging thrusts accommodating the magma ascent. We associate this topography to that of volcanic edifices west of the main topographic divide (Fig. 1). When the crust is thick (Ch = 45 km) the viscous strain accommodates almost entirely the magma emplacement and limited bulk strain accumulates along shallow brittle faults that tend to be symmetric (Fig. 3 and Supplementary Figs. 7,8). Accordingly, no topographic relief is generated on the left side of the model domain and the topography migrates to the right by ~10 km in ~0.3 Ma (Supplementary Figs. 7,8).

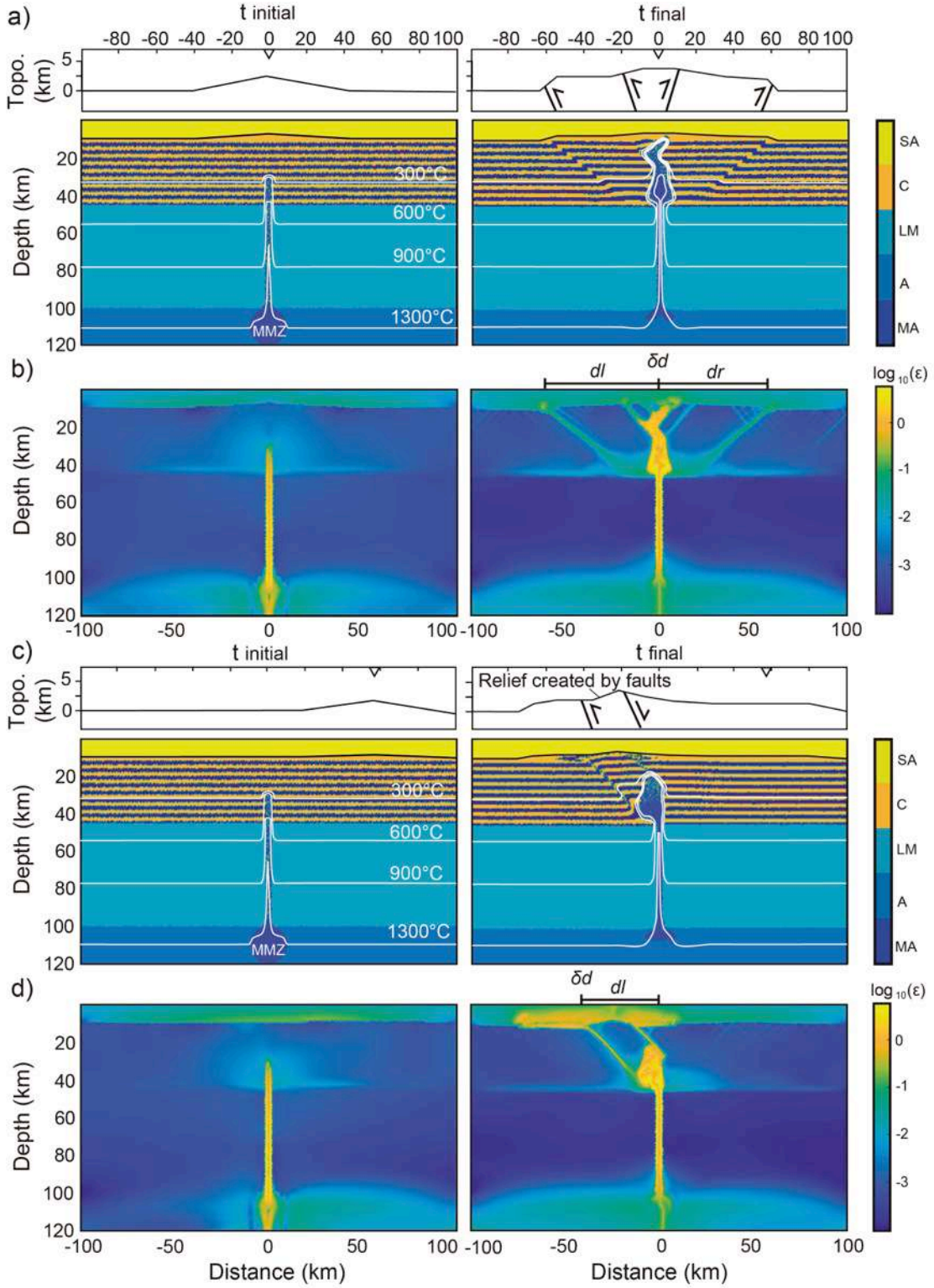

Fig. 2. Numerical outcomes of the first set of simulations (Ch = 35 km, Lh = 100 km, Dmc = 20 km). (a,c) Initial and final lithologic and thermal distribution of the reference simulations with initial central and lateral topography. The color layering in the crust shows the deformation and the vertical exaggeration of the topographic profiles is 3x. **(b,d)** Initial and final cumulative bulk strain of the same numerical simulations shown in **(a,c)**. Note the final symmetric system of brittle-ductile structures accommodating the rise of magma to near the surface with initial central topography **(a,b)**. Note the final asymmetric system of brittle-ductile structures, leading to left-verging magma ascent with initial lateral (shifted rightward) topography **(c,d)**. $\delta d = dr - dl$, where dr and dl are defined in the text. SA – sticky air; C – crust; LM – lithospheric mantle; A – asthenosphere; MA – molten asthenosphere; MMZ: mantle melting zone.

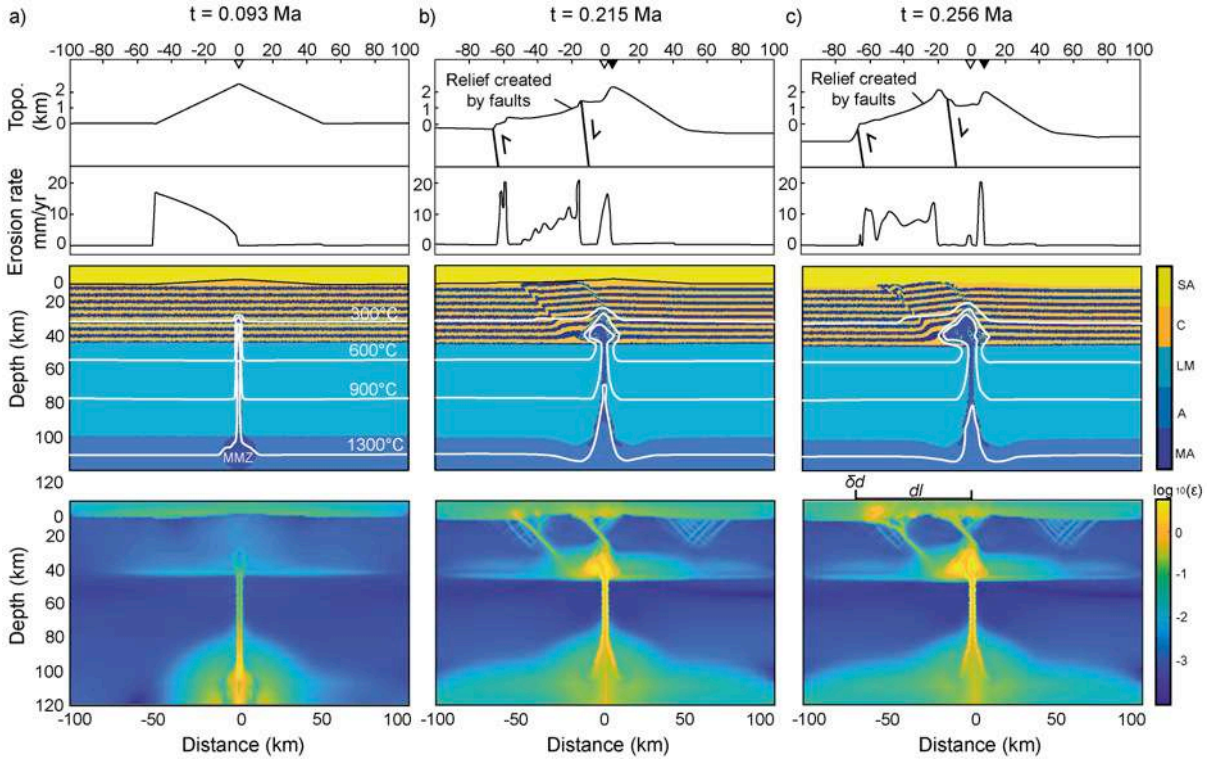

Fig. 3. Initial, intermediate and final steps of selected numerical simulation with asymmetric erosion from the second set of simulations (Ch = 35 km, Lh = 100 km, Dmc = 20 km). Topographic profile (8x vertical exaggeration) and erosion rates (top panels), lithologic and thermal distribution (middle panels), and cumulative bulk strain (lower panels) of the initial state with central topography **(a)**, early transient state **(b)**, and advanced transient state **(c)**. Note the initial water divide (white downward triangle) migrating to the right throughout the simulation (black downward triangle) due to asymmetric erosion and the final asymmetric system of brittle-ductile structures, leading to lateral magma ascent toward the opposite side of the initial topography. Abbreviations are the same as in Fig. 2.

Table 1 – Results of the parametric study. Ch: crustal thickness, **Lh**: lithospheric thickness; **Dmc**: initial depth of the magmatic channel upper tip; ***dl*** and ***dr***: maximum horizontal distances between the center of the model domain and the surface fault tips in surface to the left and to the right, respectively; $\delta d = dr - dl$ is the degree of the asymmetry of the accumulated bulk strain (negative values show asymmetry to the left).

Ch (km)	**Lh (km)**	**Dmc (km)**	**Initial**	***Orographic***	***dl* (km)**	***dr* (km)**	***δd=dr-dl***
35	90	15	Central	No	65	60	-5
35	90	20	Central	No	70	65	-5
35	90	25	Central	No	10	10	0
35	90	15	Lateral	No	50	10	-40
35	90	20	Lateral	No	50	5	-45
35	90	25	Cateral	No	64	64	0
35	100	15	Central	No	15	15	0
35	100	20	Central	No	65	65	0
35	100	25	Central	No	65	65	0
35	100	15	Lateral	No	15	5	-10
35	100	20	Lateral	No	45	0	-45
35	100	25	Lateral	No	50	10	-40
45	90	15	Central	No	90	100	10
45	90	20	Central	No	3	13	10
45	90	25	Central	No	0	0	0
45	90	15	Lateral	No	90	25	-65
45	90	20	Lateral	No	25	5	-20
45	90	25	Lateral	No	25	5	-20
45	100	15	Central	No	90	100	10
45	100	20	Central	No	90	100	10
45	100	25	Central	No	0	0	0
45	100	15	Lateral	No	90	10	-80
45	100	20	Lateral	No	90	0	-90
45	100	25	Lateral	No	30	5	-25
35	90	15	Central	Yes	93	3	-90
35	90	20	Central	Yes	95	10	-85
35	90	25	Central	Yes	25	0	-25
35	100	15	Central	Yes	70	10	-60
35	100	20	Central	Yes	70	0	-70
35	100	25	Central	Yes	70	10	-60
45	90	15	Central	Yes	10	10	0
45	90	20	Central	Yes	8	5	-3
45	90	25	Central	Yes	0	0	0
45	100	15	Central	Yes	13	5	-8
45	100	20	Central	Yes	5	5	0
45	100	25	Central	Yes	0	0	0

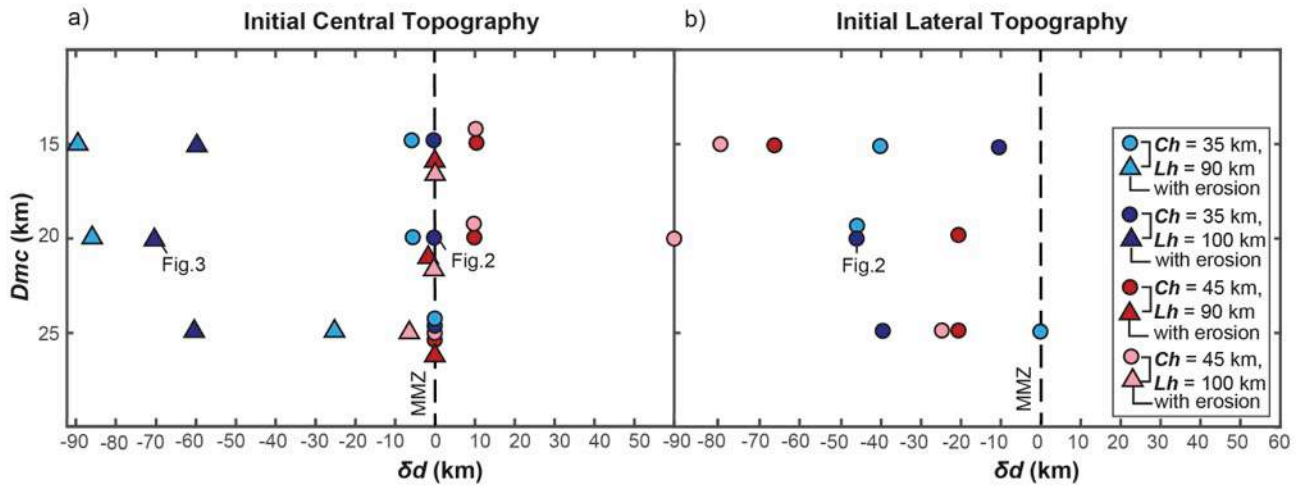

Fig. 4. Results of the parametric study. Initial depth of the magmatic channel upper tip (Dmc) vs. δd (see text), with initial central **(a)** and lateral **(b)** topography. Triangles in panel **(a)** are the results of simulations with asymmetric erosion (i.e., second set of simulations, see text). Negative values show asymmetry to the left of the mantle melting zone (MMZ) (i.e., central vertical axis of the model domain). Values of Ch and Lh are shown in the legend, cold and hot colors show simulations with thin and thick crust, respectively. See results of simulations in Figs. 2, 3, Supplementary Figs. 1-8, and Table 1.

Discussion

The break-up of the Farallon plate into the Juan de Fuca and Nazca plates in the early Miocene established a kinematic configuration similar to the present day in terms of slab partitioning and convergence rates along the American Cordillera[20,44]. Although the onset of the eastward migration of the topographic water divide in the CVA and the SVZ is uncertain, systematically younger exhumation ages on the western slopes of both the North Cascades and northern Patagonian Andes (Fig. 1) suggests that orographic effects were already established in the latest Miocene[37–39,56,57], leading to the formation of the current landform throughout the Pleistocene[14,39,58,59]. Although low-temperature thermochronometric ages constrain the onset of enhanced erosion between ~10 and ~6 Ma in the North Cascades and the Southern Andes, respectively[37,38,56], large uncertainties exist about the paleo position of topographic water divide and paleo-elevations in general. A similar issue pertains to the onset of arc front migration, which can be only roughly constrained from batholith ages[31,52], but precise information about the exact position of the paleo volcanic arc front is lacking. Our modelling results show a fast response of the crustal strain and magmatic plumbing system to orographic erosion, which adjust to topographic changes in just a few hundreds of thousands of years (Figs. 2 and 3).

In the CVA, the present-day clockwise rotation of the Oregon and Washington blocks and the counterclockwise displacement of the volcanic front since the Miocene have been

ascribed to differential along strike rollback of the Juan de Fuca slab[20,31,34,35]. However, since the magmatic source follows the rollbacking slab[1,4–6], this model requires some unjustified degree of decoupling between rollback and arc front migration[34]. In the North Cascades, the increase in the rate of arc front migration towards the southwest since ~4 Ma (Refs. [31–33]) requires faster slab rollback rates than during the late Miocene, difficult to reconcile with the transpressive regime and present northeastward displacements of the Washington block[31,34]. The presence of slab-derived magmas (i.e., adakites[68]) in southernmost and northernmost volcanoes of the CVZ may suggest shallower (i.e., closer to the trench) magma production near the breakup of the Juan de Fuca Plate into the Gorda and Explorer plates[22,24,68]. However, if the thermal gradient along the strike of the subduction system set alone the surface location of the volcanic arc, trench-ward migration of the volcanic front would be observed both in the northern and southern sectors of the CVA. Thus, the opposite sense of arc front migration in the North Cascades and in the High Cascades[34] can hardly be explained by along-strike slab age and/or thermal changes alone. Since Quaternary volcanoes are emplaced over fault systems, orographic interactions with westerly Pacific winds (Fig. 1a,b) and the mechanistic link between asymmetric erosion and crustal structures accommodating the magma ascent (Figs. 2-5) appear as a suitable along-strike differential forcing to drive the observed latitudinal arc migration front trend reversal. Magnetotelluric data (Fig. 5) show westward dipping magmatic plumbing systems in the North Cascades[69], consistent with our modelling results (Figs. 2c,d and 3) and an orographic control on the location of volcanic arc front.

In the Southern Andes, a Plio-Quaternary magmatic arc narrowing toward the west has been related to the steepening of a formerly shallow slab[55] or a decrease in convergence velocity[54]. South of ~40 °S, Plio-Pleistocene strain localization along the transpressive system of the LOFZ has been ascribed to oblique convergence of the Nazca Plate and the CTJ approaching its current position[48–50], driving the ascent of magmas and setting the observed trench-ward deflection of the SVZ[8,48,49,54] (Fig. 1c). Geophysical imaging of the deep crust and mantle show that the crustal magma reservoirs of the Osorno volcano are located up to 10 km east of the volcanic edifice[70], consistent with our modelling results and hypothesis of focused orographic erosion facilitating the strain and magma ascent across the windward side of orogens[11–13] (Fig. 5). Field evidence regarding the presence of the west vergent "Western Patagonian Thrust"[51] reinforces our proposal of asymmetric faults assisting magma ascent towards the west. Also in agreement with previous studies[8], our models

indicate that orographic erosion of a thin crust facilitates the formation of major structures, suggesting that orographic erosion may have contributed to the activation, or re-activation, of the LOFZ. Heat advection from the younger slab and the CTJ in the south can likely enhance this effect. The Nazca Plate is younger toward its southern edge (CTJ) and thus the thermal regime of the subduction is likely higher in the northern Patagonian Andes[53,67]. However, no slab-derived magmas are found in the whole SVZ[8,52,66,71] and the depth of the source of partial melting is unlikely to change significantly along the strike of the belt[1,52,67]. Differences in magma composition along the strike of the SVZ show a tendency toward more mafic magmas in the south. This trend can be simply explained by a reduced crust-magma interaction due to the thinner crust in this sector[8,66,71], which also promotes the orographic forcing on the magma ascent proposed here (Fig. 4).

We propose a common explanation to the westward migration of the volcanic arc fronts in the North Cascades and the northern Patagonian Andes, located several thousands of kilometers apart and in different tectonic/structural settings, by the shared orographic interactions between topography and westerly Pacific winds (Fig. 5). The climatic control on magmatism would occur not only through a forcing from ice building-melting and erosion on the magma production[15,72], but also through orography and topographic change facilitating crustal strain and magma transfer verging toward the region of enhanced precipitation and erosion. Because volcanic arcs provide a substantial contribution to the evolution of climate across timescales, this recognition provides additional evidence of the tight coupling between climate, surface processes, magmatism, and plate tectonics[73,74].

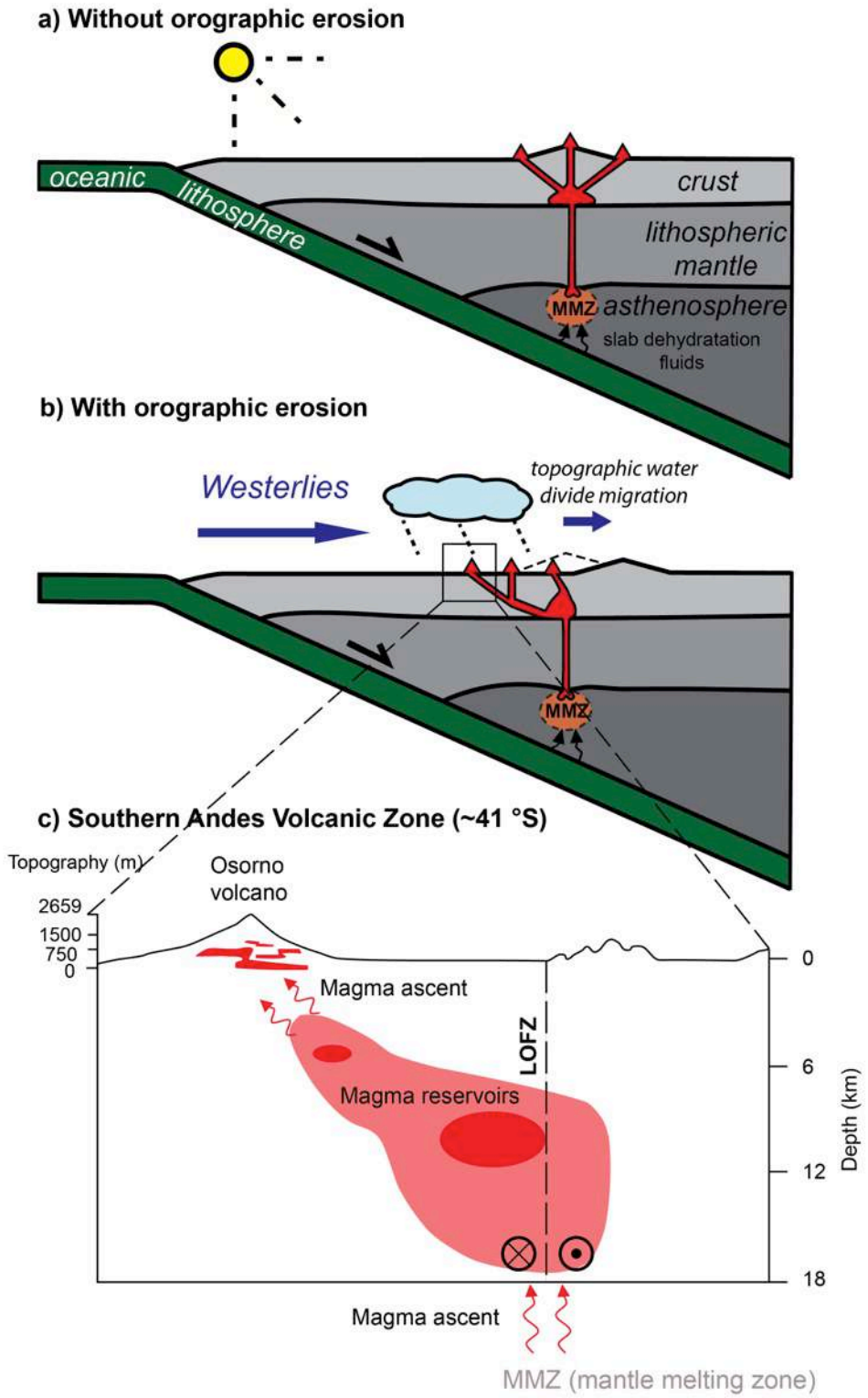

Fig. 5 - Schematic representation of the orographic forcing on the location of continental volcanic arcs. Cross-sections illustrate the magma ascent from a sub-lithospheric mantle melting zone (MMZ) to surface volcanoes (red triangles) trough newly-formed or reactivated structures. A) Analogy for orogens and volcanic arcs without orographic erosion, and **B)** with orographic erosion gradient. In the latter case, the deformation is enhanced on the windward side and so is the magma ascent through the brittle-ductile structures. C) Schematic representation of the crustal magma reservoirs interpreted from magnetotelluric data underneath the Osorno volcano showing the marked westward magma ascent in agreement with our modelling results and the proposed orographic effect on the location of the volcanic arc front (modified after Ref. [70]).

Methods

Thermomechanical model

The numerical model is based on the finite differences with marker-in-cell technique and incorporates temperature-dependent rheologies for solid and partially-molten rocks[63]. The model accounts for (1) mechanical, (2) visco-elasto-plastic rheological, (3) thermal, and (4) partial rock melting components. A short description of the model components is provided hereafter. Additional details and full description of the numerical techniques are provided elsewhere[16,62,63].

Mechanical component

The continuity equation,

$$(1)\ \frac{\partial \rho}{\partial t} + \nabla(\rho \vec{v}) = 0,$$

where ρ is the local density, $t\ is\ time, \vec{v}$ is the velocity vector, and ∇ is the divergence operator, allows for the conservation of mass during the displacement of a geological continuum.

The momentum equation,

$$(2)\ \frac{\partial \sigma_{ij}}{\partial x_i} + \rho g_i = \rho \left(\frac{\partial v_i}{\partial t} + v_j \frac{\partial v_i}{\partial x_j}\right),$$

where σ_{ij} is the stress tensor, x_i and x_j are spatial coordinates, and g_i is the *i*-th component of the gravity vector, describes the changes in velocity of an object in the gravity field due to internal and external forces.

Rheological component

Ductile deformation is thermally activated and occurs by viscous flow. Diffusion and dislocation creep are computed based on material shear viscosity[62,63], $\eta_{ductile}$, defined as:

$$(3)\ \frac{1}{\eta_{ductile}} = \frac{1}{\eta_{diff}} + \frac{1}{\eta_{disl}},$$

with

$$\eta_{diff} = \frac{\eta_0}{2\sigma_{cr}^{n-1}} exp\left(\frac{E_a + PV_a}{RT}\right), \text{ and}$$

$$\eta_{disl} = \frac{\eta_0^{\frac{1}{n}}}{2} exp\left(\frac{E_a + PV_a}{nRT}\right) \dot{\varepsilon}_{II}^{\frac{1}{n}-1},$$

where η_{diff} and η_{disl} are the shear viscosity for diffusion and dislocation creep, respectively, η_0 is the material static viscosity, σ_{cr} is the diffusion-dislocation transition critical stress, n is the stress exponent, E_a is the activation energy, V_a is the activation volume, P is pressure, R is the gas constant, T is temperature, and $\dot{\varepsilon_{II}}$ is the second invariant of the strain rate tensor. Then, the viscous deviatoric strain rate tensor, $\dot{\varepsilon}'_{ij\,(viscous)}$, is computed as:

$$(4)\ \dot{\varepsilon}'_{ij\,(viscous)} = \frac{1}{2\eta_{ductile}}\sigma'_{ij} + \delta_{ij}\eta_{bulk}\dot{\varepsilon}_{kk} = \frac{1}{2\eta_{diff}}\sigma'_{ij} + \frac{1}{2\eta_{disl}}\sigma'_{ij} + \delta_{ij}\eta_{bulk}\dot{\varepsilon}_{kk},$$

where σ'_{ij} is the deviatoric stress tensor, δ_{ij} is the Kronecker delta, $\dot{\varepsilon}_{kk}$ is the volumetric strain rate (e.g., related to phase transformations), η_{bulk} is the bulk viscosity.

Elastic deformation is reversible and assumes proportionality of stress and strain. The elastic deviatoric strain rate tensor, $\dot{\varepsilon}'_{ij\,(elastic)}$, is computed as:

$$(5)\ \dot{\varepsilon}'_{ij\,(elastic)} = \frac{1}{2\mu}\frac{D\sigma'_{ij}}{Dt},$$

where μ is the shear modulus and $\frac{D\sigma'_{ij}}{Dt}$ is the objective co-rotational time derivative of the deviatoric stress tensor.

Plastic (or brittle) localised deformation occurs at low temperature in the upper part of the lithosphere, after reaching the absolute shear stress limit, σ_{yield}, is defined as:

$$(6)\ \sigma_{yield} = C + sin\,sin\,(\varphi)P,$$

where C is cohesion and φ is the effective internal friction angle. The plastic strain rate tensor, $\dot{\varepsilon}'_{ij\,(plastic)}$, is then computed as:

$$(7)\ \dot{\varepsilon}'_{ij\,(plastic)} = 0\ for\ \sigma_{II} < \sigma_{yield},\ \dot{\varepsilon}'_{ij\,(plastic)} = X\frac{\partial\sigma'_{ij}}{2\sigma_{II}}\ for\ \sigma_{II} \geq \sigma_{yield},$$

where X is the plastic multiplier which satisfies the plastic yielding condition $\sigma_{II} = \sigma_{yield}$.

At the lithospheric scale, all deformation mechanisms occur jointly and the overall visco-elasto-plastic rock strain rate tensor, $\dot{\varepsilon}'_{ij(bulk)}$, is defined as:

$$(8)\ \dot{\varepsilon}'_{ij(bulk)} = \dot{\varepsilon}'_{ij(viscous)} + \dot{\varepsilon}'_{ij(elastic)} + \dot{\varepsilon}'_{ij(plastic)}$$

Thermal Component

Heat conservation during advective and conductive heat transfer in the continuum is computed by the energy equation:

$$(9)\ \rho C_P \frac{DT}{Dt} - div(c\nabla T) + v\nabla T = H_r + H_s + H_a + H_l,$$

where C_P is specific heat capacity at a constant P, c is the thermal conductivity, $H_r + H_s + H_a + H_l$ are the volumetric heat productions by radiogenic, shear, adiabatic and latent heat, respectively. $H_a \propto \frac{DP}{Dt}$, $H_s = \sigma'_{ij}\dot{\varepsilon}'_{ij(viscous)}$, and H_r and H_l are the radiogenic and latent heat productions (defined in Supplementary Table 2).

Partial melting component

Partial melting occurs between the wet solidus, T_s, and dry liquidus, T_l, of the considered lithologies[75–77] (Supplementary Table 2). ξ is the volumetric fraction of melt that increases linearly with T at a constant P (Ref. [64]), so that,

$$(10)\{\ \xi = 0\ at\ T \le T_s\ \xi = \frac{(T - T_s)}{(T_l - T_s)}\ at\ T_s < T < T_l\ \xi = 1\ at\ T \ge T_l$$

The effective density, ρ_{eff}, of partially molten rocks is then computed by[16,63]:

$$(11)\ \rho_{eff} = \rho_s\ (1 - \xi + \xi \frac{\rho_l^0}{\rho_s^0}),$$

where ρ_l^0 and ρ_s^0 are the standard densities of solid and molten rocks, respectively. The solid rock density, ρ_s, is calculated as[63]:

$$(12)\ \rho_s = \rho_o\ [1 + \beta(P - P_0)] \times [1 - \alpha(T - T_0)],$$

where β is compressibility, α is thermal expansion and ρ_o, P_0, and T_0 are density, pressure and temperature of rocks at surface conditions.

Erosion model

During the fluvial incision of an uplifting topography the erosion rate, $\dot{e}$, depends primarily on channel slope, river discharge and rock type[61]. An empirical relationship was derived[11,61], such that:

$$(13)\ \dot{e} = \frac{dz}{dt} = kA^m \left|\frac{dz}{dx}\right|^n$$

where z is the elevation, A is the basin drainage area taken as a proxy for river discharge, $\left|\frac{dz}{dx}\right|$ is the magnitude of the local topographic slope, and k, m, and n are empirical parameters, usually determined by fitting models to river longitudinal profiles. While k is used as a scaling constant, different values of m and n lead to differences in the shape of river profiles, but commonly used values (e.g., $0.3< m<0.5$ and $n\approx1$) predict realistic concave-up profiles such as those observed along bedrock rivers incising uplifting topographies[11,61,78]. Although simplistic, Eq. 13 captures the main physical processes and parameter dependencies and, most important for this study, it provides the feedback mechanisms between tectonic uplift and erosion. Tectonic uplift increases slope, and the rise of topography increases drainage area, both leading to an increase in erosion rates.

Integration on a discrete topography of the top of the lithosphere allows for Eq. 13 to be solved numerically, thereby assessing surface elevation changes in response to the tectonic strain and fluvial incision[11,16]. At each time step, the surface load changes associated with modifications of the modelled landscape are computed. The orographic enhancement of precipitation, and hence fluvial erosion, is included in the surface processes model by assigning different k values (Eq. 13) on negatively (left-facing) and positively (right-facing) sloping topography.

Acknowledgements

This work is part of the project Dipartimenti di Eccellenza 2018–2022, of the Department of Earth and Environmental Sciences at the University of Milano-Bicocca, funded by the Italian Ministry of Education, MIUR. V.A.P.M. acknowledge the Erasmus Program for the period in the Institute des Sciences de la Terre, at the Université Grenoble Alpes, and the "Tectonics, Reliefs & Basins team" support in this last institution. P.S. was supported by the Italian (Rita Levi Montalcini grant, DM 694–26/2017) funded by MIUR. P.G.V. acknowledges funding from the French ANR-PIA program (ANR-18- MPGA-0006).

Andrés Echaurren and four anonymous reviewers provided useful comments that helped us improving the manuscript.

Authors Contributions

V.A.P.M. contributed to the development of the initial scientific question, performed the study and wrote the manuscript. P.S. conceived the initial scientific question, helped with the data interpretation and numerical investigation, and wrote the manuscript. C.S. contributed to the development of the initial scientific questions, helped with the interpretation of the geological data and numerical models, and contributed to manuscript writing. T.S.-L. helped with the compilation and interpretation of the geological data, and contributed to manuscript writing. P.G.V. helped with interpretation of the geological data and manuscript writing.

Data availability statement

Supplementary Tables and Figures are available for this paper.

Competing interest declaration

The authors declare no competing interests.

Corresponding Author line

Correspondence and request for materials should be addressed to V.A.P.M.

Supplementary Data

Supplementary Table 1a – Summary of apatite (U-Th)/He ages (AHe) around the Mont Baker, Cascade Range (data inside the inset of Fig. 1a, plotted in the central panel of Fig. 1b). W-E distance corresponds to the horizontal distance between each sample and the western boundary of the inset in Fig. 1a. In the field "Type", I = intrusive, V = volcanic, M = metamorphic. Geographic Coordinate System WGS 1984.

Method	Name	Longitude	Latitude	Elevation	W-E distance (km)	Age (Ma)	Error (Ma)	Type	Place of sampling	Reference
AHe	01-1	-121.1975	48.7287	1953	112	12.4	2.7	I	Skagit Gorge Profile	Simon-Labric et al., 2014
AHe	01-2	-121.1981	48.7234	1758	112	14.5	2.1	I	Skagit Gorge Profile	Simon-Labric et al., 2014
AHe	01-4	-121.2005	48.7123	1347	111	9.1	1.3	I	Skagit Gorge Profile	Simon-Labric et al., 2014
AHe	01-5	-121.2041	48.7112	1155	111	10.1	1.4	I	Skagit Gorge Profile	Simon-Labric et al., 2014
AHe	01-6	-121.2072	48.7076	904	111	6.4	0.6	I	Skagit Gorge Profile	Simon-Labric et al., 2014
AHe	01-7	-121.2083	48.70667	680	111	5.9	0.6	I	Skagit Gorge Profile	Simon-Labric et al., 2014
AHe	02-1	-121.2092	48.6999	345	110	4.3	1.0	I	Skagit Gorge Profile	Simon-Labric et al., 2014
AHe	02-2	-121.2116	48.6973	241	110	3.5	0.8	I	Skagit Gorge Profile	Simon-Labric et al., 2014
AHe	03-1	-121.0988	48.8223	1967	123	18.1	1.8	I	Ross Lake Profile	Simon-Labric et al., 2014
AHe	03-2	-121.0914	48.8182	1778	124	14.3	1.4	I	Ross Lake Profile	Simon-Labric et al., 2014
AHe	03-3	-121.0828	48.8095	1617	124	15.1	1.5	I	Ross Lake Profile	Simon-Labric et al., 2014
AHe	03-5	-121.0703	48.7943	1181	126	15.3	4.7	I	Ross Lake Profile	Simon-Labric et al., 2014
AHe	04-1	-121.0595	48.7793	692	127	11.0	2.2	I	Ross Lake Profile	Simon-Labric et al., 2014
AHe	04-2	-121.0612	48.7818	916	127	11.3	2.0	I	Ross Lake Profile	Simon-Labric et al., 2014
AHe	013D25	-120.6298	48.5743	1173	175	38.8	7.8	I	North Washington Cascades	Simon-Labric et al., 2014
AHe	013D27	-120.8371	48.6243	1033	152	43.7	6.9	I	North Washington Cascades	Simon-Labric et al., 2014
AHe	013D28	-121.0771	48.7167	628	125	15.6	3.3	I	North Washington Cascades	Simon-Labric et al., 2014
AHe	09CAS16	-121.9142	48.8797	350	32	3.4	0.7	I	North Washington Cascades	Simon-Labric et al., 2014
AHe	09CAS18	-121.9264	48.8639	854	31	4.8	1.8	I	North Washington Cascades	Simon-Labric et al., 2014
AHe	12Cas14	-121.32201	48.63378	142	98	2.4	0.6	I	North Washington Cascades	Simon-Labric et al., 2014

AHe	12Cas25	-121.39841	48.58596	116	89	2.7	0.2	I	North Washington Cascades	Simon-Labric et al., 2014
AHe	12Cas26	-122.20283	48.81322	73	0	8.7	2.7	I	North Washington Cascades	Simon-Labric et al., 2014
AHe	12Cas10	-121.17249	48.70697	280	115	5.9	0.8	I	North Washington Cascades	Simon-Labric et al., 2014
AHe	WC95-32	-121.5	48.67	300	78	8.6	0.5	I	Yellow Aster	Reiners et al., 2002
AHe	LA01A	-121.641	48.835	1651	62	1.4	0.1	I	Lake Ann pluton	Reiners et al., 2002
AHe	LA01B	-121.641	48.835	1651	62	1.4	0.1	I	Lake Ann pluton	Reiners et al., 2002
AHe	LA01C	-121.641	48.835	1651	62	1.2	0.1	I	Lake Ann pluton	Reiners et al., 2002
AHe	LA02A	-121.645	48.831	1471	62	2.2	0.1	I	Lake Ann pluton	Reiners et al., 2002
AHe	LA02B	-121.645	48.831	1471	62	2.0	0.1	I	Lake Ann pluton	Reiners et al., 2002

Supplementary Table 1b – Summary of isotopic ages <4 Ma of rocks around the Mount Baker, Cascade Range (data inside the inset of Fig. 1a, plotted in the bottom panel of Fig. 1b). In the field "Method", Wr K-Ar: $^{40}K/^{40}Ar$ in whole rock, Pl Ar-Ar: $^{40}Ar/^{39}Ar$ in plagioclase, Bt K-Ar: $^{40}K/^{40}Ar$ in biotite, Hb K-Ar: $^{40}K/^{40}Ar$ in hornblende; Active volcano: 0.01 Ma is an arbitrary recent age and the position is according to Venzke (2013). Other columns like in Table 1a.

Method	Name	Longitude	Latitude	W-E distance (km)	Age (Ma)	Error (Ma)	Rock	Type	Place of sampling	Reference
Wr K-Ar	MB-493	-121.736092	48.85944238	51.89168666	1.191	0.094	Dacite	V	Kulshan caldera suite	Hildreth et al., 2003
Wr K-Ar	MB-500	-121.840496	48.82545378	40.28829116	1.156	0.130	Andesite	V	Kulshan caldera suite	Hildreth et al., 2003
Wr K-Ar	MB-316	-121.694892	48.81849939	56.47058367	1.155	0.038	Rhyodacite	V	Kulshan caldera suite	Hildreth et al., 2003
Wr K-Ar	MB-145	-121.83771	48.82812465	40.59801732	1.060	0.010	Rhyodacite	V	Kulshan caldera suite	Hildreth et al., 2003
Wr K-Ar	MB-212	-121.70544	48.83211299	55.29837474	1.032	0.011	Rhyodacite	V	Kulshan caldera suite	Hildreth et al., 2003
Wr K-Ar	MB-276B	-121.710335	48.8006803	54.7542751	1.005	0.017	Andesite	V	Kulshan caldera suite	Hildreth et al., 2003
Wr K-Ar	MB-93	-121.871016	48.86174231	36.89636533	0.878	0.018	Andesite	V	Early extracaldera lava flows from Mt Baker	Hildreth et al., 2003
Wr K-Ar	MB-91	-121.944213	48.81745383	28.76138252	0.859	0.014	Andesite	V	Early extracaldera lava flows from Mt Baker	Hildreth et al., 2003
Wr K-Ar	MB-81	-121.722576	48.8547952	53.39378926	0.743	0.034	Andesite	V	Early extracaldera lava flows from Mt Baker	Hildreth et al., 2003
Wr K-Ar	MB-640	-121.751692	48.7804437	50.15788814	0.743	0.072	Andesite	V	Early extracaldera lava flows from Mt Baker	Hildreth et al., 2003
Wr K-Ar	MB-52	-121.851179	48.71580346	39.10098866	0.716	0.045	Basalt	V	Early extracaldera lava flows from Mt Baker	Hildreth et al., 2003
Wr K-Ar	MB-225	-121.810782	48.87193235	43.59068974	0.613	0.008	Dacite	V	Early extracaldera lava flows from Mt Baker	Hildreth et al., 2003
Wr K-Ar	MB-99	-121.748943	48.83619194	50.46346304	0.515	0.008	Andesite	V	Oldest intracaldera andesitic lava flow	Hildreth et al., 2003

Wr	K-Ar	MB-135	-121.756022	48.82547284	49.67663871	0.457	0.040	Andesite	V	Oldest intracaldera andesitic lava flow	Hildreth et al., 2003
Wr	K-Ar	MB-67	-121.895581	48.73692941	34.16627492	0.495	0.018	Andesite	V	Black Buttes stratovolcano	Hildreth et al., 2003
Wr	K-Ar	MB-63	-121.892822	48.73870224	34.47292075	0.296	0.020	Andesite	V	Black Buttes stratovolcano	Hildreth et al., 2003
Wr	K-Ar	MB-116	-121.884404	48.75031652	35.40848586	0.374	0.010	Andesite	V	Black Buttes stratovolcano	Hildreth et al., 2003
Wr	K-Ar	MB-246	-121.882644	48.76829254	35.60408894	0.346	0.009	Andesite	V	Black Buttes stratovolcano	Hildreth et al., 2003
Wr	K-Ar	MB-603	-121.881443	48.76108368	35.73750709	0.343	0.005	Andesite	V	Black Buttes stratovolcano	Hildreth et al., 2003
Wr	K-Ar	MB-249	-121.908457	48.77033914	32.73523793	0.339	0.011	Andesite	V	Black Buttes stratovolcano	Hildreth et al., 2003
Wr	K-Ar	MB-49	-121.807494	48.72345666	43.95615923	0.336	0.015	Andesite	V	Black Buttes stratovolcano	Hildreth et al., 2003
Wr	K-Ar	MB-119	-121.92406	48.74079732	31.00112922	0.334	0.015	Andesite	V	Black Buttes stratovolcano	Hildreth et al., 2003
Wr	K-Ar	MB-238	-121.872897	48.77809383	36.68729064	0.334	0.011	Andesite	V	Black Buttes stratovolcano	Hildreth et al., 2003
Wr	K-Ar	MB-16	-121.882363	48.78088494	35.63522097	0.306	0.013	Andesite	V	Black Buttes stratovolcano	Hildreth et al., 2003
Wr	K-Ar	MB-110	-121.874701	48.75831911	36.48678255	0.288	0.015	Andesite	V	Black Buttes stratovolcano	Hildreth et al., 2003
Wr	K-Ar	MB-615	-121.733933	48.78294894	52.13166032	0.460	0.013	Andesite	V	Satellite centers contemporaneous with Black Buttes	Hildreth et al., 2003
Wr	K-Ar	MB-61	-121.744933	48.77857099	50.90913676	0.296	0.015	Andesite	V	Satellite centers contemporaneous with Black Buttes	Hildreth et al., 2003
Wr	K-	MB-22	-121.722492	48.69735533	53.40315038	0.455	0.009	Andesite	V	Satellite centers	Hildreth et al., 2003

Ar										contemporaneous with Black Buttes	
Wr Ar	K-Ar	MB-222	-121.773225	48.73479255	47.76478584	0.366	0.010	Andesite	V	Satellite centers contemporaneous with Black Buttes	Hildreth et al., 2003
Wr Ar	K-Ar	MB-151	-121.847679	48.8093322	39.49001295	0.322	0.012	Andesite	V	Satellite centers contemporaneous with Black Buttes	Hildreth et al., 2003
Wr Ar	K-Ar	MB-589	-121.839592	48.8056525	40.38881016	0.322	0.009	Andesite	V	Satellite centers contemporaneous with Black Buttes	Hildreth et al., 2003
Wr Ar	K-Ar	MB-223	-121.786263	48.87077718	46.31572544	0.334	0.009	Andesite	V	Satellite centers contemporaneous with Black Buttes	Hildreth et al., 2003
Wr Ar	K-Ar	MB-59	-121.846814	48.72835501	39.58617675	0.333	0.012	Andesite	V	Satellite centers contemporaneous with Black Buttes	Hildreth et al., 2003
Wr Ar	K-Ar	MB-50	-121.846958	48.72205888	39.57017129	0.331	0.018	Basalt	V	Satellite centers contemporaneous with Black Buttes	Hildreth et al., 2003
Wr Ar	K-Ar	MB-89	-121.741175	48.81991379	51.32680857	0.305	0.006	Andesite	V	Ptarmigan Ridge and Table Mountain lavas	Hildreth et al., 2003
Wr Ar	K-Ar	MB-89	-121.738428	48.8207834	51.63205273	0.306	0.013	Andesite	V	Ptarmigan Ridge and Table Mountain lavas	Hildreth et al., 2003
Wr Ar	K-Ar	MB-391	-121.682982	48.85704853	57.79423382	0.301	0.005	Andesite	V	Ptarmigan Ridge and Table Mountain lavas	Hildreth et al., 2003
Wr Ar	K-Ar	MB-10	-121.698185	48.84912447	56.10465285	0.309	0.013	Andesite	V	Ptarmigan Ridge and Table Mountain lavas	Hildreth et al., 2003
Wr Ar	K-Ar	MB-488	-121.717401	48.84394205	53.96898404	0.189	0.011	Andesite	V	Ptarmigan Ridge and Table Mountain lavas	Hildreth et al., 2003
Wr Ar	K-Ar	MB-262	-121.816703	48.85220125	42.93263205	0.192	0.008	Andesite	V	Younger lavas inset along Cougar Divide	Hildreth et al., 2003
Wr	K-	MB-260	-121.818448	48.83602562	42.73874985	0.119	0.023	Andesite	V	Younger lavas inset	Hildreth et al., 2003

Ar									along Cougar Divide	
Wr	K-Ar	MB-335	-121.810038	48.84583517	43.67335604	0.105	0.008	Andesite	V	Younger lavas inset along Cougar Divide	Hildreth et al., 2003
Wr	K-Ar	MB-53	-121.848482	48.71487688	39.40082802	0.203	0.025	Andesite	V	Younger mafic outliers	Hildreth et al., 2003
Wr	K-Ar	MB-175B	-121.729466	48.63625504	52.62810201	0.094	0.021	Basalt	V	Younger mafic outliers	Hildreth et al., 2003
Wr	K-Ar	MB-193	-121.695911	48.72674642	56.35735248	0.199	0.005	Rhyodacite	V	Boulder Ridge lavas	Hildreth et al., 2003
Wr	K-Ar	MB-645	-121.762823	48.77066753	48.92082738	0.140	0.055	Andesite	V	Boulder Ridge lavas	Hildreth et al., 2003
Wr	K-Ar	MB-39	-121.764405	48.76168797	48.74504171	0.090	0.052	Andesite	V	Boulder Ridge lavas	Hildreth et al., 2003
Wr	K-Ar	MB-402	-121.761529	48.76795468	49.0646607	0.080	0.014	Andesite	V	Boulder Ridge lavas	Hildreth et al., 2003
Wr	K-Ar	MB-12	-121.793685	48.90234227	45.49086856	0.202	0.009	Andesite	V	Intracanyon lava flows	Hildreth et al., 2003
Wr	K-Ar	MB-332A	-121.792169	48.90862381	45.65937696	0.149	0.005	Dacite	V	Intracanyon lava flows	Hildreth et al., 2003
Wr	K-Ar	MB-92	-121.810141	48.89891476	43.66194695	0.114	0.009	Andesite	V	Intracanyon lava flows	Hildreth et al., 2003
Wr	K-Ar	MB-168	-121.784605	48.82667737	46.49996979	0.076	0.007	Andesite	V	Intracanyon lava flows	Hildreth et al., 2003
Wr	K-Ar	MB-232	-121.755107	48.80747006	49.77843325	0.070	0.007	Andesite	V	Intracanyon lava flows	Hildreth et al., 2003
Wr	K-Ar	MB-572	-121.677945	48.78951755	58.35403441	0.048	0.018	Andesite	V	Intracanyon lava flows	Hildreth et al., 2003
Wr	K-Ar	MB-507	-121.86605	48.71954932	37.44830161	0.043	0.005	Andesite	V	Mount Baker Stratovolcano	Hildreth et al., 2003
Wr	K-Ar	MB-520	-121.815861	48.71454637	43.02619053	0.036	0.014	Andesite	V	Mount Baker Stratovolcano	Hildreth et al., 2003

Wr K-Ar	MB-524	-121.841644	48.71660768	40.16070948	0.032	0.014	Andesite	V	Mount Baker Stratovolcano	Hildreth et al., 2003
Wr K-Ar	MB-458	-121.869629	48.80235234	37.05053313	0.024	0.016	Andesite	V	Mount Baker Stratovolcano	Hildreth et al., 2003
Wr K-Ar	MB-632	-121.888571	48.80793439	34.94531285	0.014	0.009	Andesite	V	Mount Baker Stratovolcano	Hildreth et al., 2003
Wr K-Ar	MB-46	-121.815227	48.74152949	43.09665621	0.011	0.009	Andesite	V	Mount Baker Stratovolcano	Hildreth et al., 2003
Wr K-Ar	MB-43	-121.849204	48.74277333	39.3204983	0.009	0.011	Andesite	V	Mount Baker Stratovolcano	Hildreth et al., 2003
Wr K-Ar	MB-294	-121.853373	48.79859321	38.85724294	0.009	0.007	Andesite of Roosevelt Glacier	V	Mount Baker Stratovolcano	Hildreth et al., 2003
Hb K-Ar	RWT 469A-67	-121.524993	48.86413266	75.35299663	3.6	1.0	Andesite	V	Hannegan Pass	Engels et al., 1976
Hb K-Ar	RWT 469B-67	-121.524964	48.86512286	75.35623356	3.3	1.0	Andesite	V	Hannegan Pass	Engels et al., 1976
Pl Ar-Ar	MB-618	-121.742559	48.81902926	51.1729383	0.992	0.014	Rhyodacite	V	Mount Baker Volcanic Field	Hildreth et al., 2003
Pl Ar-Ar	MB-628	-121.813914	48.8548715	43.24266407	1.015	0.018	Rhyodacite	V	Mount Baker Volcanic Field	Hildreth et al., 2003
Pl Ar-Ar	MB-212	-121.705416	48.83301237	55.30095361	1.012	0.008	Rhyodacite	V	Mount Baker Volcanic Field	Hildreth et al., 2003
Pl Ar-Ar	MB-212	-121.705416	48.83301237	55.30095361	0.994	0.015	Rhyodacite	V	Mount Baker Volcanic Field	Hildreth et al., 2003
Pl Ar-Ar	MB-212 mean	-121.705416	48.83301237	55.30095361	1.008	0.007	Rhyodacite	V	Mount Baker Volcanic Field	Hildreth et al., 2003
Pl Ar-Ar	MB-145	-121.836368	48.82721147	40.74709451	1.018	0.008	Rhyodacite	V	Mount Baker Volcanic Field	Hildreth et al., 2003
Pl Ar-Ar	MB-82-2	-121.71858	48.85115228	53.83797894	1.063	0.012	Rhyodacite	V	Mount Baker Volcanic Field	Hildreth et al., 2003

Pl Ar-Ar	MB-630	-121.727076	48.83865146	52.8937021	1.041	0.011	Rhyodacite	V	Mount Baker Volcanic Field	Hildreth et al., 2003
Pl Ar-Ar	MB-630	-121.727076	48.83865146	52.8937021	1.073	0.016	Rhyodacite	V	Mount Baker Volcanic Field	Hildreth et al., 2003
Pl Ar-Ar	MB-630 mean	-121.705416	48.83301237	55.30095361	1.008	0.007	Rhyodacite	V	Mount Baker Volcanic Field	Hildreth et al., 2003
Pl Ar-Ar	MB-287	-121.723401	48.82241724	53.30218327	1.109	0.019	Rhyodacite	V	Mount Baker Volcanic Field	Hildreth et al., 2003
Pl Ar-Ar	MB-287	-121.723401	48.82241724	53.30218327	1.111	0.015	Rhyodacite	V	Mount Baker Volcanic Field	Hildreth et al., 2003
Pl Ar-Ar	MB-287 mean	-121.727076	48.83865146	52.8937021	1.052	0.016	Rhyodacite	V	Mount Baker Volcanic Field	Hildreth et al., 2003
Pl Ar-Ar	MB-227	-121.730484	48.81169973	52.51498173	1.114	0.011	Rhyodacite	V	Mount Baker Volcanic Field	Hildreth et al., 2003
Pl Ar-Ar	MB-227	-121.730484	48.81169973	52.51498173	1.138	0.010	Rhyodacite	V	Mount Baker Volcanic Field	Hildreth et al., 2003
Pl Ar-Ar	MB-227 mean	-121.723401	48.82241724	53.30218327	1.110	0.012	Rhyodacite	V	Mount Baker Volcanic Field	Hildreth et al., 2003
Pl Ar-Ar	MB-188	-121.696986	48.84281344	56.23792518	1.149	0.010	Rhyodacite	V	Mount Baker Volcanic Field	Hildreth et al., 2003
Pl Ar-Ar	MB-583	-121.813637	48.86656395	43.27343013	1.151	0.016	Rhyodacite	V	Mount Baker Volcanic Field	Hildreth et al., 2003
Pl Ar-Ar	MB-275C	-121.71435	48.80342409	54.30803001	1.180	0.017	Rhyodacite	V	Mount Baker Volcanic Field	Hildreth et al., 2003
Pl Ar-Ar	MB-626	-121.827901	48.83972068	41.68815988	1.293	0.016	Rhyodacite	V	Mount Baker Volcanic Field	Hildreth et al., 2003
Pl Ar-Ar	MB-380	-121.536133	48.89036302	74.11497719	3.722	0.020	Ignimbrite	V	Mount Baker Volcanic Field	Hildreth et al., 2003
Pl Ar-Ar	MB-201	-121.789859	48.83482942	45.91611361	0.969	0.029	Felsite breccia	V	Mount Baker Volcanic Field	Hildreth et al., 2003
Active	-	-121.81	48.77	43.677627	0.010	-	-	-	Mount Baker Volcano	-

volcano									
Pl Ar-Ar	MB-636A	-121.79293	48.82046733	45.57479774	0.674	0.023	Granodiorite	I	Mount Baker Volcanic Field	Hildreth et al., 2003
Bt Ar-Ar	MB-333	-121.642704	48.83409025	62.27077326	2.750	0.130	Lake Ann stock	I	Mount Baker Volcanic Field	Hildreth et al., 2003
Bt K-Ar	RWT 480-67	-121.631287	48.82913807	63.53957821	2.7	0.3	Lake Ann stock	I	Chilliwack Composite Batholith	Engels et al., 1976
Bt K-Ar	DFC 1-69	-121.633725	48.83610637	63.26863455	2.5	0.1	Hornfels	I	Chilliwack Composite Batholith	Engels et al., 1976
Wr K-Ar	MB-356	-121.794313	48.81958217	45.42102482	0.764	0.163	Granodiorite	I	Kulshan caldera suite	Hildreth et al., 2003

Supplementary Table 1c – Summary of apatite fission tracks (AFT) ages around the Osorno and Tronador volcanoes, Southern Andes (data inside the inset of Fig. 1c, plotted in the central panel of Fig. 1d). W-E distance corresponds to the horizontal distance between each sample and the western boundary of the inset in Fig. 1c. Other columns like in Table 1a.

Method	Name	Longitude	Latitude	Elevation	W-E distance (km)	Age (Ma)	Error (Ma)	Rock	Type	Place of sampling	Reference
AFT	AA1	-72.6812	-41.2194	80	19.5	24.9	4.7	Granodiorite	I	Lago Llanquihue	Adriasola et al., 2006
AFT	AA102	-72.4267	-41.154	50	47.8	6.3	2.2	Tonalite	I	Petrohué	Adriasola et al., 2006
AFT	AA106	-72.4710	-42.039	5	42.9	4.3	1.5	Tonalite	I	Isla Pelada	Adriasola et al., 2006
AFT	AA11	-72.3328	-41.461	150	58.3	3.3	1.2	Granodiorite	I	Estancia Reloncaví	Adriasola et al., 2006
AFT	AA111	-72.4903	-42.022	5	40.8	4.4	1.2	Aplite	I	Isla Pelada	Adriasola et al., 2006
AFT	AA112	-72.0054	-41.0885	850	94.6	10.6	1.3	Tonalite	I	Volcan Casablanca	Adriasola et al., 2006
AFT	AA119	-72.4939	-42.1683	5	40.4	4.9	1.7	Mica-schist	M	Isla Llancahué	Adriasola et al., 2006
AFT	AA12	-72.3493	-41.488	180	56.4	4	1.3	Tonalite	I	Canutillar	Adriasola et al., 2006
AFT	AA125	-72.3946	-41.9462	100	51.4	6.5	1.2	Granite	I	Rio Blanco	Adriasola et al., 2006
AFT	AA129	-72.2897	-41.11	5	63.0	4.4	0.6	Granite	I	Lago Todos Los Santos	Adriasola et al., 2006
AFT	AA13	-72.4092	-41.501	300	49.8	4.8	0.8	Tonalite	I	Lago Chapo	Adriasola et al., 2006
AFT	AA130	-72.1242	-41.0738	5	81.4	6.1	0.8	Granite	I	Lago Todos Los Santos	Adriasola et al., 2006
AFT	AA131	-72.0718	-41.148	20	87.3	6.9	1.3	Tonalite	I	Lago Todos Los Santos	Adriasola et al., 2006
AFT	AA132	-72.1755	-41.0975	10	75.7	7.2	1.8	Tonalite	I	Lago Todos Los Santos	Adriasola et al., 2006
AFT	AA2	-72.3042	-41.3782	30	61.4	4.4	0.5	Tonalite	I	Ralún	Adriasola et al., 2006
AFT	AA20	-72.6417	-41.4456	200	23.9	11.1	1.8	Granodiorite	I	Correntoso	Adriasola et al., 2006
AFT	AA21	-72.6331	-41.4102	250	24.9	11.4	1.5	Granodiorite	I	Lago Chapo	Adriasola et al., 2006
AFT	AA22	-72.5813	-41.4383	300	30.6	10.9	1.1	Granodiorite	I	Lago Chapo	Adriasola et al., 2006
AFT	AA23	-72.6090	-41.514	450	27.6	8	1	Gneiss	M	Lago Chaiquenes	Adriasola et al., 2006
AFT	AA24	-72.6998	-41.5955	10	17.5	9.4	2	Granodiorite	I	Punta Metri	Adriasola et al., 2006
AFT	AA25	-72.7230	-41.566	20	14.9	12.5	1.6	Tonalite	I	Punta Metri	Adriasola et al., 2006
AFT	AA26	-72.668	-41.637	10	21.0	7.8	0.9	Tonalite	I	Caleta Larenas	Adriasola et al., 2006

AFT	AA27	-72.626	-41.692	200	25.7	9.3	0.8	Tonalite	I	Caleta Larenas	Adriasola et al., 2006
AFT	AA29	-72.2369	-41.4594	150	68.9	5.5	0.9	Granite	I	Rio Cochamo	Adriasola et al., 2006
AFT	AA3	-72.349	-41.5049	60	56.5	5.6	2	Tonalite	I	Estancia Reloncaví	Adriasola et al., 2006
AFT	AA30	-72.311	-41.6492	100	60.7	4	0.9	Tonalite	I	Balseo	Adriasola et al., 2006
AFT	AA31	-72.3008	-41.6667	250	61.8	4	0.9	Granite	I	Puelo Chico	Adriasola et al., 2006
AFT	AA33	-72.4672	-41.728	20	43.3	5.8	0.5	Granodiorite	I	Volcán Yates	Adriasola et al., 2006
AFT	AA34	-72.4010	-41.705	30	50.7	4.2	0.5	Tonalite	I	Volcán Yates	Adriasola et al., 2006
AFT	AA35	-72.363	-41.354	150	54.9	6.2	0.8	Tonalite	I	Termas de Ralún	Adriasola et al., 2006
AFT	AA36	-72.5890	-41.589	200	2.8	8.2	1.3	Gneiss	M	Parque Alerce Andino	Adriasola et al., 2006
AFT	AA37	-72.5726	-41.747	30	31.6	6.8	1	Tonalite	I	Chaparrano	Adriasola et al., 2006
AFT	AA39	-72.4346	-42.02	150	46.9	5.7	1.9	Tonalite	I	Rio Mariquita	Adriasola et al., 2006
AFT	AA4	-72.4022	-41.647	20	50.6	3.8	0.9	Tonalite	I	Estancia Reloncaví	Adriasola et al., 2006
AFT	AA40	-72.4484	-42.076	40	45.4	4.3	0.7	Granodiorite	I	Pichanco	Adriasola et al., 2006
AFT	AA42	-72.4027	-41.907	200	50.5	4.2	2.7	Tonalite	I	Rio Negro	Adriasola et al., 2006
AFT	AA43	-72.601	-41.9908	100	28.5	15.5	2.7	Dacite	I	Pichicolo	Adriasola et al., 2006
AFT	AA44	-72.3689	-42.18	10	54.2	3.3	0.5	Tonalite	I	F. Quintupeu	Adriasola et al., 2006
AFT	AA45	-72.4821	-42.091	5	41.7	4.3	1.2	Mica-schist	M	Isla Llancahué	Adriasola et al., 2006
AFT	AA6	-72.3424	-41.5378	20	57.2	3.8	0.9	Tonalite	I	Estancia Reloncaví	Adriasola et al., 2006
AFT	AA8	-72.3201	-41.6024	80	59.7	3.3	0.6	Granodiorite	I	Estancia Reloncaví	Adriasola et al., 2006
AFT	AA9	-72.3003	-41.5672	110	61.9	3.5	0.7	Granite	I	Estancia Reloncaví	Adriasola et al., 2006
AFT	AL122	-72.0588	-41.3606	1600	88.7	6.7	1.6	Tonalite	I	Rio Cochamo	Adriasola et al., 2006
AFT	AL137	-72.46	-41.5885	1200	44.1	9.8	1.9	Granodiorite	I	Puelo	Adriasola et al., 2006
AFT	AL152	-72.0588	-41.3606	1550	88.7	6.7	1.7	Tonalite	I	Llanada Grande	Adriasola et al., 2006
AFT	SP06b	-72.415	-41.4933	400	49.1	5.9	0.6	-	-	-	Thomson et al., 2010
AFT	SP11	-72.6	-41.73	25	28.6	5.1	1	-	-	-	Thomson et al., 2010

AFT	SP040	-71.898	-41.8	1675	106.5	13	2.2	-	-	-	Thomson et al., 2010
AFT	SP041	-71.888	-41.862	1525	107.7	14.2	3.3	-	-	-	Thomson et al., 2010
AFT	SP046	-72.13	-42.062	1450	80.8	3.4	0.5	-	-	-	Thomson et al., 2010
AFT	SP048	-71.928	-41.903	275	103.2	14.1	2.7	-	-	-	Thomson et al., 2010
AFT	SP057	-72.03	-41.395	1325	91.9	3.5	1.1	-	-	-	Thomson et al., 2010
AFT	SP061	-72.337	-41.995	1650	57.8	3.9	0.7	-	-	-	Thomson et al., 2010
AFT	SP062	-72.33	-42.072	1325	58.6	5.1	0.6	-	-	-	Thomson et al., 2010
AFT	SP066	-72.373	-41.947	125	53.8	2	0.8	-	-	-	Thomson et al., 2010
AFT	SP067	-72.647	-41.408	250	23.4	10.2	1.5	-	-	-	Thomson et al., 2010
AFT	SP128	-71.568	-42.03	300	143.2	21	2	-	-	-	Thomson et al., 2010
AFT	SP133	-71.43	-41.098	250	158.6	14	1.7	-	-	-	Thomson et al., 2010
AFT	SP137	-71.777	-41.578	450	120.1	12.5	3.9	-	-	-	Thomson et al., 2010
AFT	SP139	-71.612	-41.593	300	138.4	28.1	5.2	-	-	-	Thomson et al., 2010

Supplementary Table 1d – Summary of isotopic ages < 4 Ma of rocks around the Osorno and Tronador volcanoes, Southern Andes (data inside the inset of Fig. 1c, plotted in the bottom panel of Fig. 1d). In the field "Method", ZFT: zircon fission tracks, Wr K-Ar: $^{40}K/^{40}Ar$ in whole rock, Wr Ar-Ar: $^{40}Ar/^{39}Ar$ in whole rock, Active volcano: 0.1 Ma is an arbitrary recent age and the position is according to Venzke (2013). Other columns like in Table 1a.

Method	Name	Longitude	Latitude	Elevation	W-E Horizontal distance (km)	Age (Ma)	Error (Ma)	Rock	Type	Place of sampling	Reference
ZFT	AA106	-72.4710	-42.0391	5	42.895	3.4	0.3	Tonalite	I	Isla Pelada	Adriasola et al., 2006
ZFT	AA111	-72.4903	-42.02187	5	40.754	3.9	0.3	Aplite	I	Isla Pelada	Adriasola et al., 2006
ZFT	AA129	-72.2897	-41.11029	5	63.049	3.8	0.2	Granite	I	Lago Todos los Santos	Adriasola et al., 2006
ZFT	AA40	-72.4484	-42.07639	40	45.412	3.8	0.3	Granodiorite	I	Pichanco	Adriasola et al., 2006
ZFT	AA45	-72.4821	-42.09051	5	41.670	3.2	0.5	Mica-schist	M	Isla Llancahué	Adriasola et al., 2006
ZFT	BR409	-72.2795	-41.41409	200	64.183	3.4	0.8	Granite	I	Puente Las Trancas, Ralún	Adriasola et al., 2006
Wr K-Ar	XC-288	-72.3970	-40.91695		51.122	0.4	0.1	Basalt	V	Estratos de Chapuco	Lara et al., 2001
Wr K-Ar	XC-289	-72.3954	-40.95834		51.302	0.6	0.5	Basalt	V	Estratos de Chapuco	Lara et al., 2001
Wr K-Ar	HO-46	-72.4952	-40.95695		40.205	1	0.3	Basalt	V	Estratos de Chapuco	SNGM-BRGM,1995
Wr K-Ar	HO-46	-72.4952	-40.95695		40.205	0.9	0.3	Basalt	V	Estratos de Chapuco	Lara et al., 2001
Wr K-Ar	60385	-72.5391	-41.30917		35.326	1.4	0.2	Basalt	V	Estratos de Hueñu Hueñu	Moreno et al.,1985
Wr K-Ar	090185-3	-72.2970	-41.44603		62.241	0.27	0.14	Basalt	V	Estratos de Reloncavi	Moreno et al., 1985
Wr K-Ar	P273b	-72.0661	-41.3359		87.897	0.7	0.4	basalt	V	Volcán Cuernos del Diablo	SNGM-BRGM, 1995
Wr Ar-Ar	XB-29	-72.0033	-41.22027		94.880	0.53	0.127	basalt	V	Tronador Volcanic Group	Mella et al., 2005
Wr Ar-Ar	XB-32	-71.9675	-41.18701		98.860	0.47	0.036	basalt	V	Tronador Volcanic Group	Mella et al., 2005

Wr Ar-Ar	XM-7	-71.8432	-41.14895		112.674	0.36	0.05	basalt	V	Tronador Volcanic Group	Mella et al., 2005
Wr Ar-Ar	XM-22	-71.8877	-41.20374		107.730	0.34	0.041	basalt	V	Tronador Volcanic Group	Mella et al., 2005
Wr K-Ar	XM-23	-71.8327	-41.18705		113.838	1.3	0.3	dacite	V	Tronador Volcanic Group	Mella et al., 2005
Active volcano	-	-72,2667	-40.98333	2493	65.609	0.1	-	-	-	Puntiagudo Cordon Cenizos	-
Active volcano	-	-72,4333	-41.05	1715	47.086	0.1	-	-	-	Osorno	-
Active volcano	-	-72,5	-41.1	2652	39.677	0.1	-	-	-	Osorno	-
Active volcano	-	-72,5333	-41.13333	1082	35.972	0.1	-	-	-	Osorno	-
Active volcano	-	-72,2667	-41.18333	260	65.609	0.1	-	-	-	Cayutue La Vigueria	-
Active volcano	-	-72,2833	-41.28333	500	63.757	0.1	-	-	-	Cayutue La Vigueria	-
Active volcano	-	-72,6167	-41.33333	2015	26.710	0.1	-	-	-	Cabulco	-
Active volcano	-	-72,3833	-41.78333	2111	52.643	0.1	-	-	-	Yate	-
Active volcano	-	-72,45	-41.86667	1572	45.234	0.1	-	-	-	Hornopirén	-
Active volcano	-	-72,6167	-41.88333	1670	26.710	0.1	-	-	-	Apagado	-

Supplementary Table 2 – Material properties used in the numerical experiments.

	P_0^s, ρ_0^l (km/m^3)	E_a (kJ/mol)	V_a (m^3/mol)	n	C (Mpa)	Visc. flow law	Sin (ϕ_{eff})	c (W/m/K)	μ (Gpa)	C_p (J/kg/K)	Hr (μW/m^3)	H_l (kJ/kg)	α (1/k)	β (1/Pa)	$T_{solidus}$ (K)	$T_{liquidus}$ (K)
Crust	2800 (solidus) 2400 (liquidus)	154	0	2.3	10	Wet Qz.	0.2	0.64+807/(T+77)	10	1000	1	300	3x10^{-5}	1x10^{-11}	889 + 17900 /(P+54)+ 20200/(P+54)^2 at P <1200 Mpa; 831 + 0.06 P at P > 1200 Mpa	1262 + 0.09 P
Lithospheric mantle	3250 (solidus) 2200 (liquidus)	532	10	3.5	10	Dry Ol.	0.6	0.73+1293/(T+77)	67	1000	0.022	400	3x10^{-5}	1x10^{-11}	1394 + 0.132899 P-0.000005104P^2 at P < 1000 Mpa, 2212 + 0.030819 (P-10000) at P >1000 Mpa	2073 + 0.114 P
Asthenospheric mantle	3250 (solidus) 2200 (liquidus)	532	10	3.5	10	Dry Ol.	0.6	0.73+1293/(T+77)	67	1000	0.022	400	3x10^{-5}	1x10^{-11}	1394 + 0.132899 P-0.000005104 P^2 at P < 1000 Mpa, 2212 + 0.030819 (P-1000) at P>10000 Mpa	2073 + 0.114 P
MMZ and 75% of the magma channel	3250 (solidus) 1800 (liquidus)	471	0	4.0	10	Wet Ol.	0	0.73+1293/(T+77)	67	1000	0.022	400	3x10^{-5}	1x10^{-11}	1240 + 49800/(P+323) at P<2400 Mpa, 1266 + 0.114 P + 0.000005 P^2 at P>2400 Mpa	2073 + 0.114 P
Basalt 25% of the magma channel	3100 (solidus), 1800 (liquidus)	154	0	2.3	10	Wet Qz.	0	1.18+474/(T+77)	25	1000	0.25	380	3x10^{-5}	1x10^{-11}	973-70400/(P+354)+77800000 at P<1600 935+0.0035 P + 0.0000062 P^2 at P>1600	1423 + 0.105 P

ρ_l^0 and ρ_s^0 are the standard densities of solid and molten rocks, respectively; E_a is the activation energy; V_a is the activation volume; $\boldsymbol{n}$ is the stress exponent; $\boldsymbol{C}$ is cohesion; φ is the effective internal friction angle; $\boldsymbol{C_p}$ is the specific heat capacity; $\boldsymbol{c}$ is thermal conductivity; μ is the shear modulus; $\boldsymbol{H_r}$ and $\boldsymbol{H_l}$ are the radiogenic and latent heat productions, respectively; α is thermal expansion; β is compressibility; T_s and T_l are the solidus and liquidus temperatures, respectively. Qz and Ol are quartzite and olivine, respectively. All rheological and partial melting laws/parameters are based on experimental rock mechanics and petrology (Ranalli, 1995; Hirschmann, 2000; Johannes, 1985; Turcotte, 2002).

Supplementary Figures

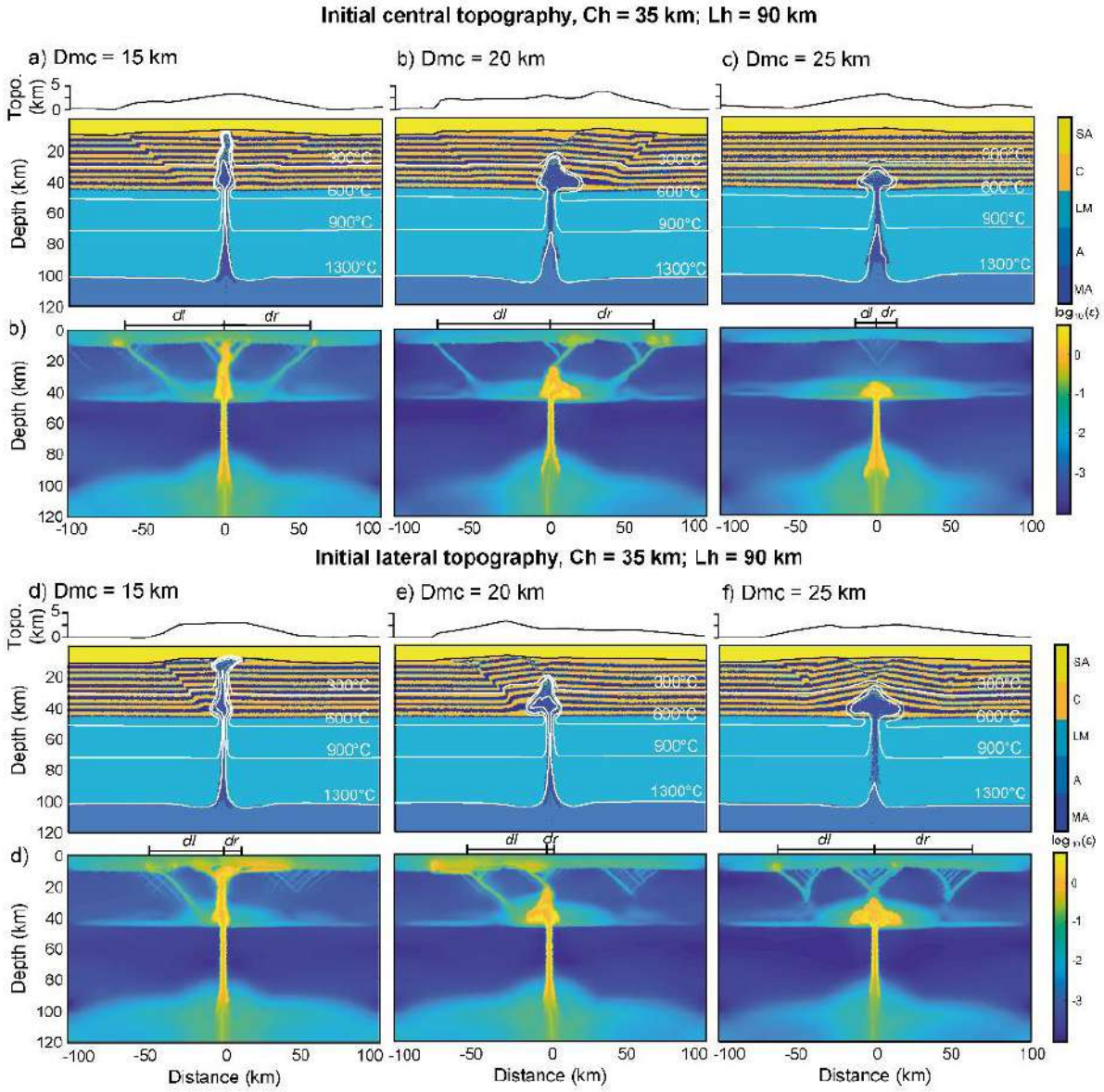

Supplementary Fig. 1. Final steps of simulations accounting for Ch = 35 km and Lh = 90 km. Symbols and definitions are the same of Fig. 2. **a-c)** The initial central topography is centered above the MMZ. **d-f)** The initial topography is laterally shifted (rightward) respect to the MMZ.

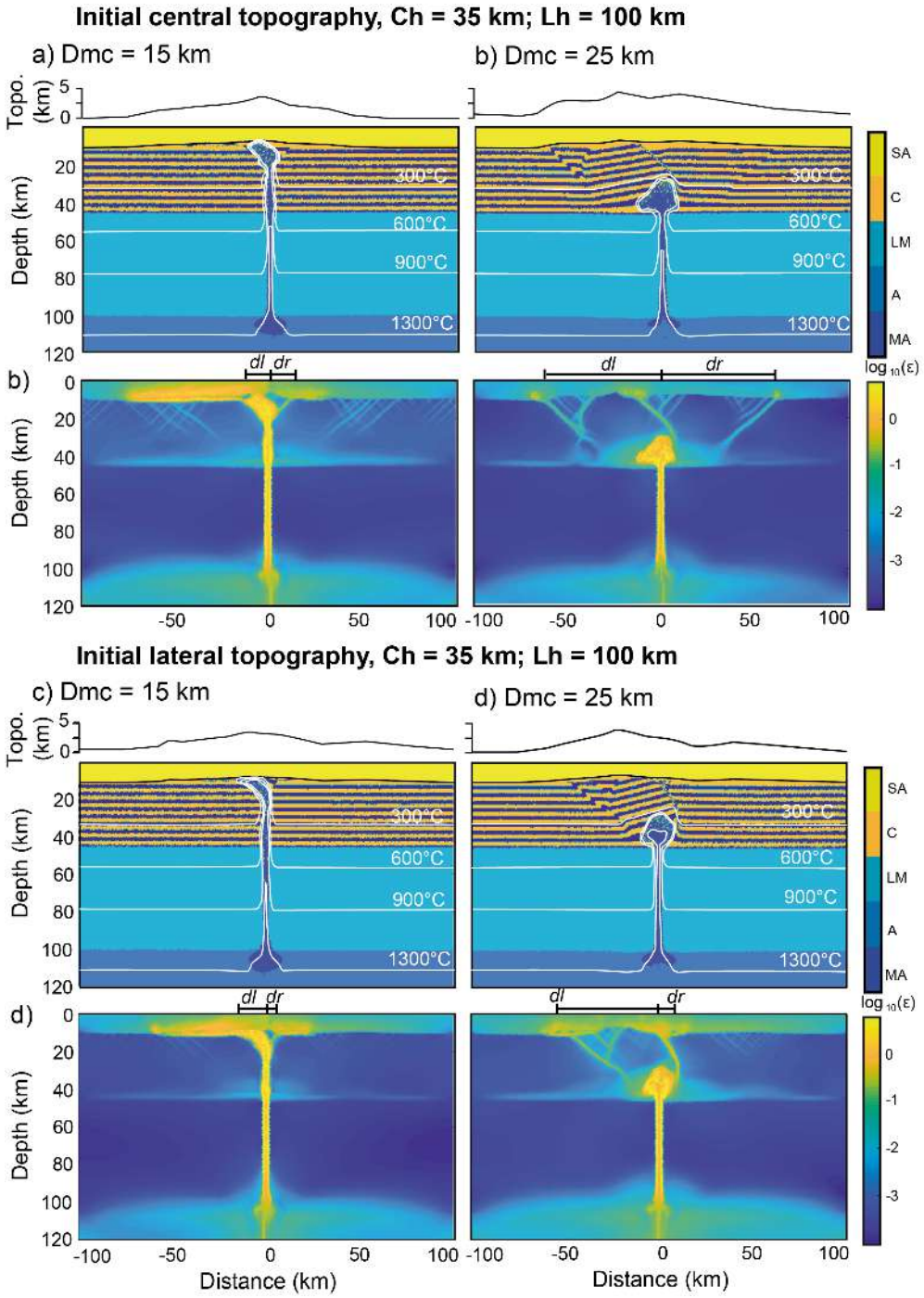

Supplementary Fig. 2. Final steps of simulations accounting for Ch = 35 km and Lh = 100 km. Symbols and definitions are the same of Fig. 2. **a, b)** The initial topography is centered above the MMZ. **c, d)** The initial topography is laterally shifted (rightward) respect to the MMZ.

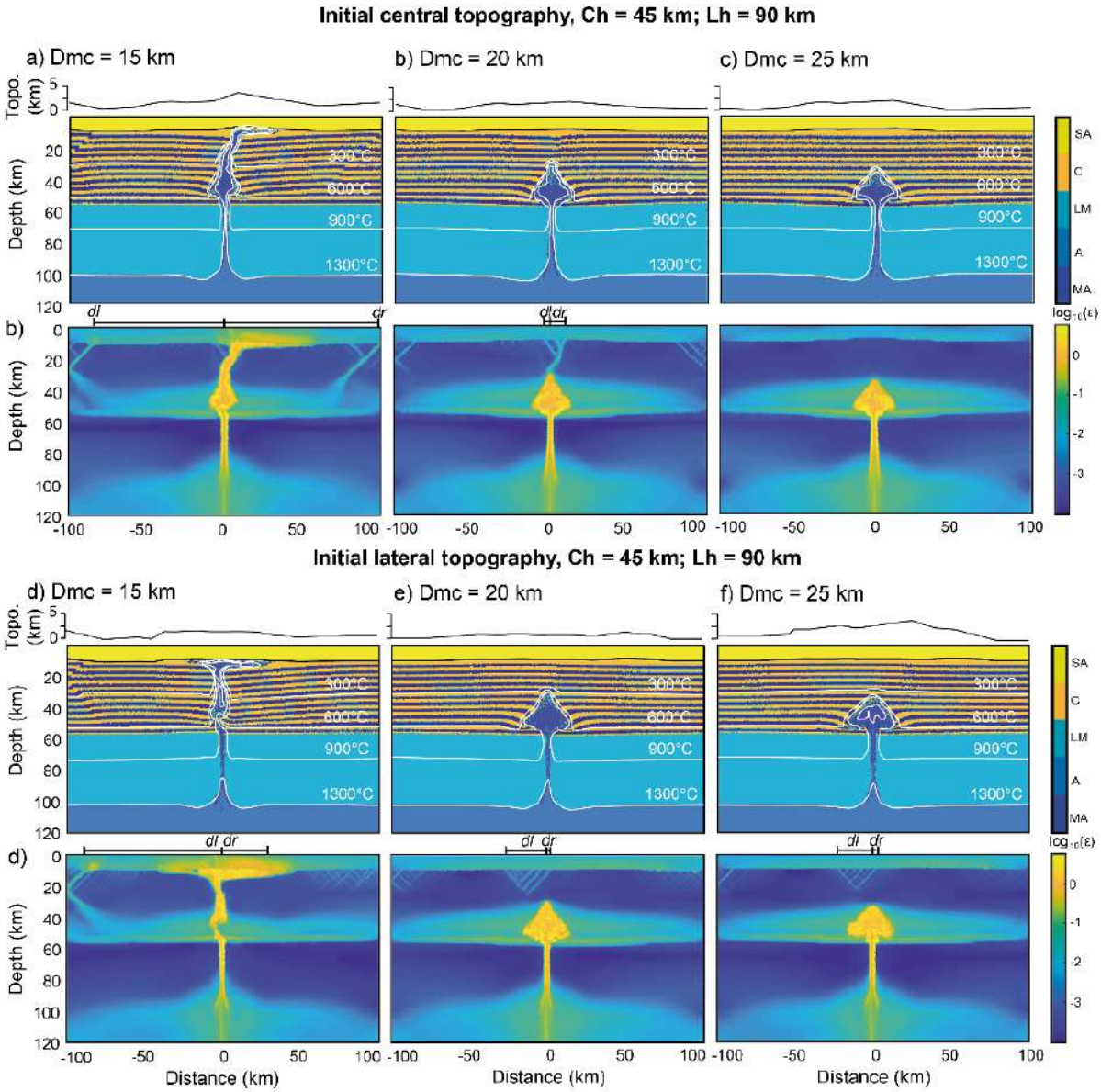

Supplementary Fig. 3. Final steps of simulations accounting for Ch = 45 km and Lh = 90 km. Symbols and definitions are the same of Fig. 2. **a-c)** The initial topography is centered above the MMZ. **d-f)** The initial topography is laterally shifted (rightward) respect to the MMZ.

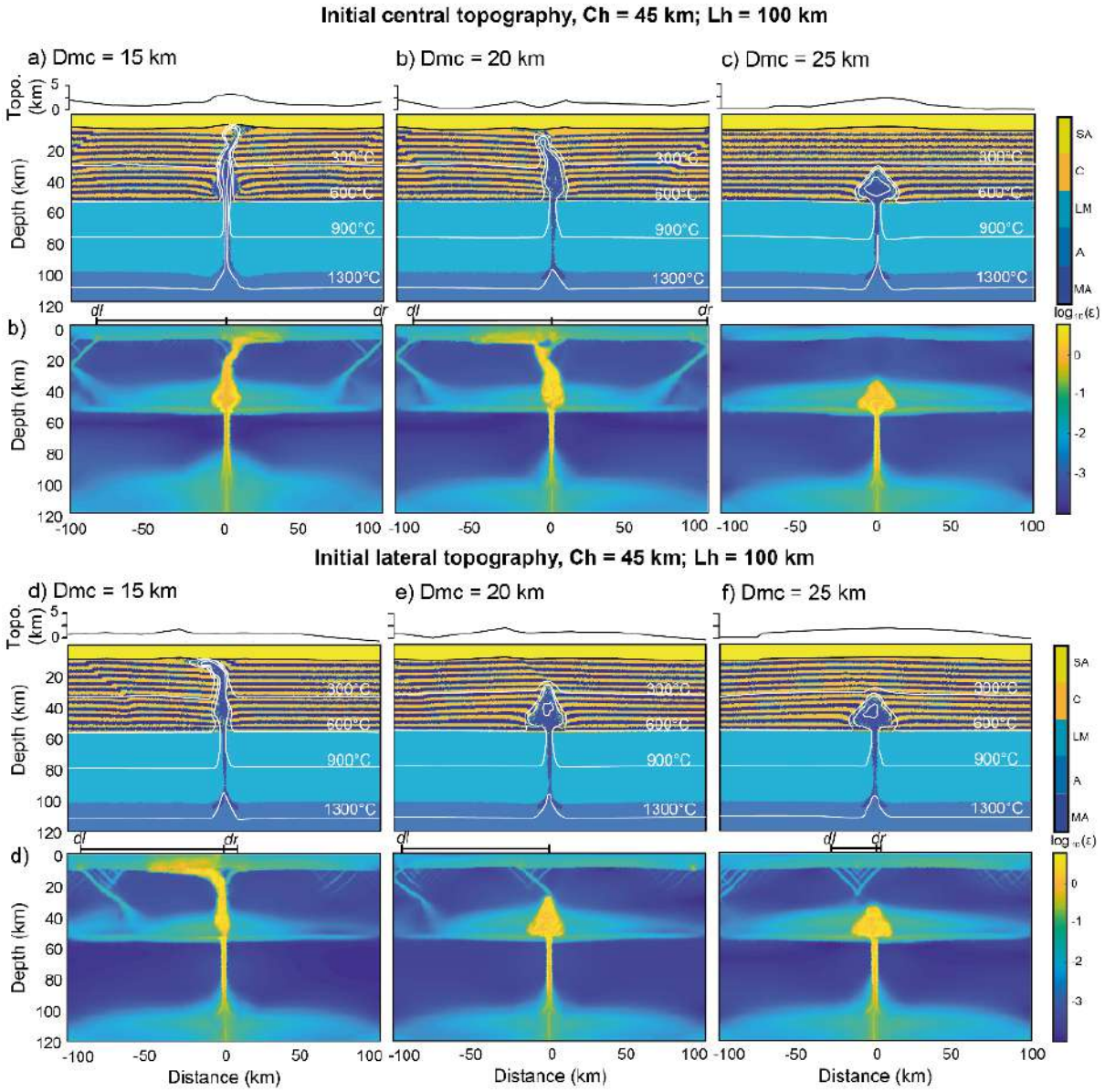

Supplementary Fig. 4. Final steps of simulations accounting for Ch = 45 km and Lh = 100 km. Symbols and definitions are the same of Fig. 2. **a-c)** The initial topography is centered above the MMZ. **d-f)** The initial topography is laterally shifted (rightward) respect to the MMZ.

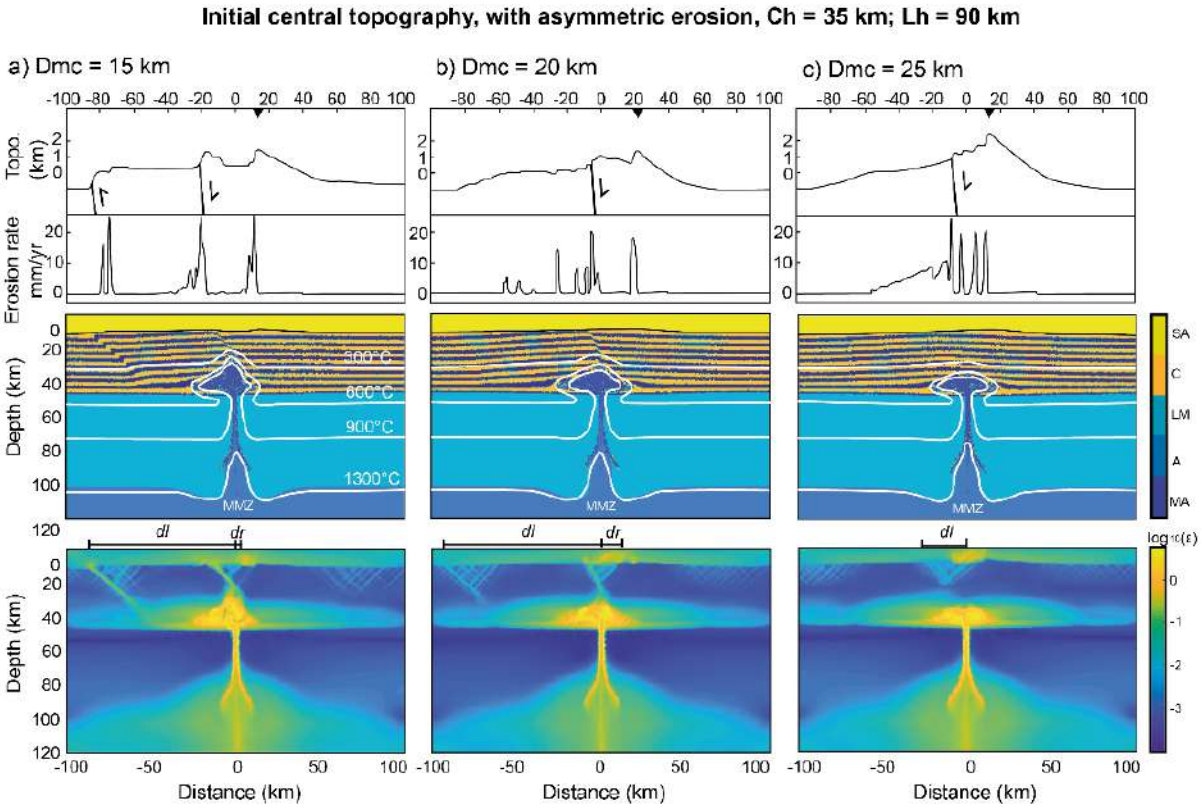

Supplementary Fig. 5. Final steps of simulations accounting for Ch = 35 km and Lh = 90 km with asymmetric erosion. Symbols and definitions are the same of Fig. 3. a-c) The initial topography is centered above the MMZ.

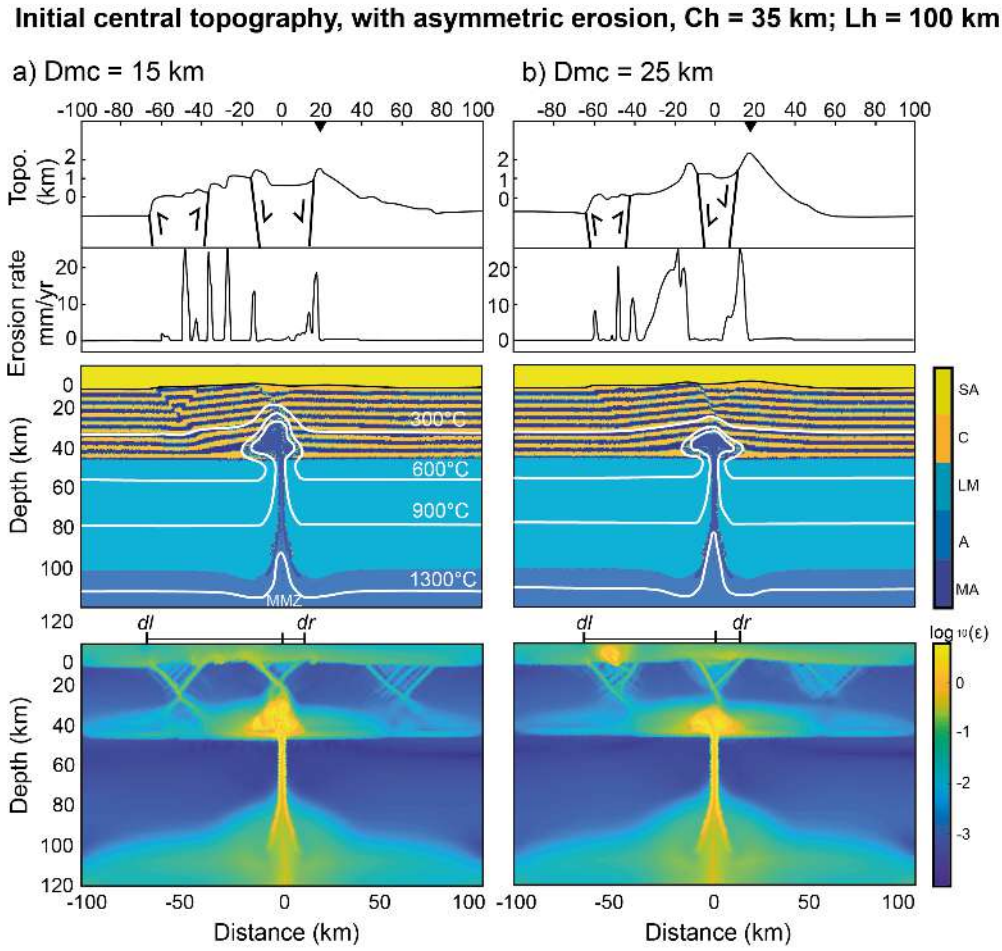

Supplementary Fig. 6. Final steps of simulations accounting for Ch = 35 km and Lh = 100 km with asymmetric erosion. Symbols and definitions are the same of Fig. 3. a-b) The initial topography is centered above the MMZ.

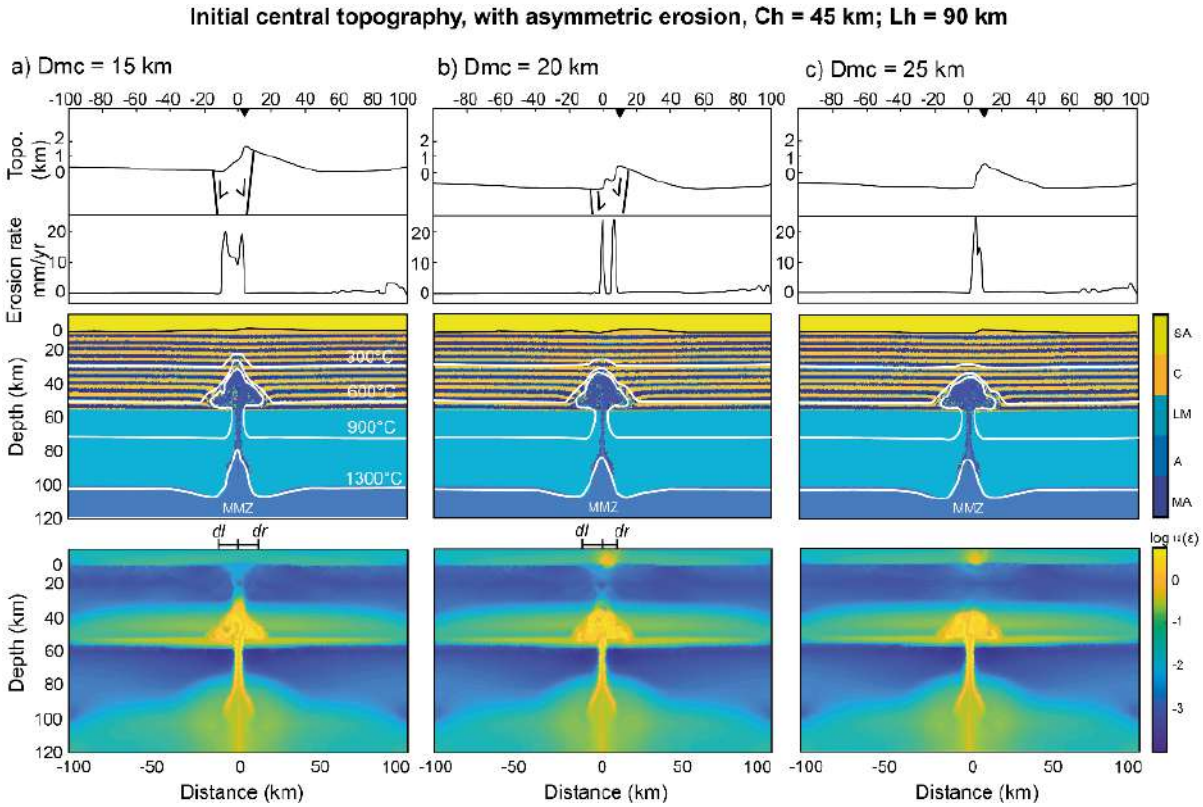

Supplementary Fig. 7. Final steps of simulations accounting for Ch = 45 km and Lh = 90 km with asymmetric erosion. Symbols and definitions are the same of Fig. 3. a-c) The initial topography is centered above the MMZ.

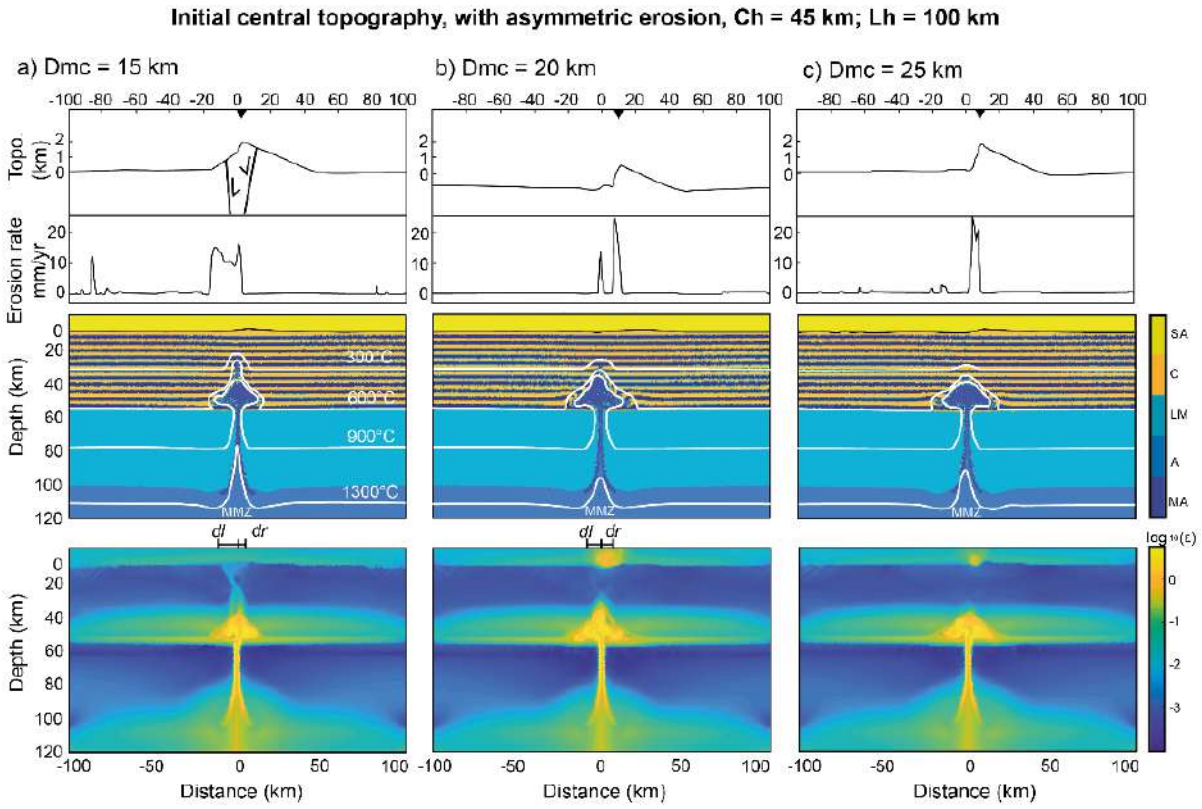

Supplementary Fig. 8. Final steps of simulations accounting for Ch = 45 km and Lh = 100 km with asymmetric erosion. Symbols and definitions are the same of Fig. 3. a-c) The initial topography is centered above the MMZ.

References – Chapter 4

1. England, P., Engdahl, R. & Thatcher, W. Systematic variation in the depths of slabs beneath arc volcanoes. *Geophys. J. Int.* **156**, 377–408 (2004).

2. England, P. & Wilkins, C. A simple analytical approximation to the temperature structure in subduction zones. *Geophys. J. Int.* **159**, 1138–1154 (2004).

3. Syracuse, E. M. & Abers, G. A. Global compilation of variations in slab depth beneath arc volcanoes and implications. *Geochemistry, Geophys. Geosystems* **7**, 1–18 (2006).

4. England, P. C. & Katz, R. F. Melting above the anhydrous solidus controls the location of volcanic arcs. *Nature* **467**, 700–703 (2010).

5. Heuret, A. & Lallemand, S. Plate motions, slab dynamics and back-arc deformation. *Phys. Earth Planet. Inter.* **149**, 31–51 (2005).

6. Gianni, G. M. & Luján, S. P. Geodynamic controls on magmatic arc migration and quiescence. *Earth-Science Rev.* **218**, (2021).

7. Petford, N., Cruden, A. R., McCaffrey, K. J. W. & Vigneresse, J. L. Granite magma formation, transport and emplacement in the Earth's crust. *Nature* **408**, 669–673 (2000).

8. Cembrano, J. & Lara, L. The link between volcanism and tectonics in the southern volcanic zone of the Chilean Andes: A review. *Tectonophysics* **471**, 96–113 (2009).

9. Reyes, E. C. *et al.* Subduction zone fluids and arc magmas conducted by lithospheric deformed regions beneath the central Andes. *Sci. Rep.* 1–12 (2021) doi:10.1038/s41598-021-02430-9.

10. Maccaferri, F., Acocella, V. & Rivalta, E. How the differential load induced by normal fault scarps controls the distribution of monogenic volcanism. *Geophys. Res. Lett.* **42**, 7507–7512 (2015).

11. Willett, S. D. Orogeny and orography: The effects of erosion on the structure of mountain belts. *J. Geophys. Res. Solid Earth* **104**, 28957–28981 (1999).

12. Horton, B. K. Erosional control on the geometry and kinematics of thrust belt development in the central Andes. *Tectonics* **18**, 1292–1304 (1999).

13. Whipple, K. X. The influence of climate on the tectonic evolution of mountain belts. *Nat. Geosci.* **2**, 97–104 (2009).

14. Simon-Labric, T. *et al.* Low-temperature thermochronologic signature of rangedivide migration and breaching in the North Cascades. *Lithosphere* **6**, 473–482 (2014).

15. Jull, M. & McKenzie, D. The effect of deglaciation on mantle melting beneath Iceland. *J. Geophys. Res.* **101**, 21815–21828 (1996).

16. Sternai, P. Surface processes forcing on extensional rock melting. *Sci. Rep.* **10**, 1–14 (2020).

17. Sternai, P. *et al.* Effects of asthenospheric flow and orographic precipitation on continental rifting. *Tectonophysics* **820**, 229120 (2021).

18. Stüwe, K., Robl, J., Turab, S. A., Sternai, P. & Stuart, F. M. Feedbacks between sea-floor spreading, trade winds and precipitation in the Southern Red Sea. *Nat. Commun.* **13**, 1–8 (2022).

19. Severinghaus, J. & Atwater, T. Cenozoic geometry and thermal state of the subducting slabs beneath western North America. *Geol. Soc. Am. Bull.* **176**, 1–22 (1990).

20. Schellart, W. P., Stegman, D. R., Farrington, R. J., Freeman, J. & Moresi, L. Cenozoic tectonics of Western North America controlled by evolving width of Farallon slab. *Science (80-.).* **329**, 316–319 (2010).

21. Long, M. D. The Cascadia Paradox: Mantle flow and slab fragmentation in the Cascadia subduction system. *J. Geodyn.* **102**, 151–170 (2016).

22. Yogodzinski, G. M. *et al.* Geochemical evidence for the melting of subducting oceanic lithosphere at plate edges. *Nature* **409**, 500–503 (2001).

23. Mullen, E. K., Weis, D., Marsh, N. B. & Martindale, M. Primitive arc magma diversity: New geochemical insights in the Cascade Arc. *Chem. Geol.* **448**, 43–70 (2017).

24. Defant, M. J. & Drummond, M. S. Mount St. Helens: potential example of the partial melting of the subducted lithosphere in a volcanic arc. *Geology* **21**, 547–550 (1993).

25. Wilson, D. S. Confidence intervals for motion and deformation of the Juan de Fuca Plate. *J. Geophys. Res.* **98**, (1993).

26. Rohr, K. M. M. & Tryon, A. J. Pacific-North America plate boundary reorganization in response to a change in relative plate motion: Offshore Canada. *Geochemistry, Geophys. Geosystems* **11**, 1–26 (2010).

27. Mullen, E. K. & Weis, D. Evidence for trench-parallel mantle flow in the northern Cascade Arc from basalt geochemistry. *Earth Planet. Sci. Lett.* **414**, 100–107 (2015).

28. Brown, E. H. Structural geology and accretionary history of the Northwest Cascades system, Washington and British Columbia (USA, Canada). *Geol. Soc. Am. Bull.* **99**, 201–214 (1987).

29. Dickinson, W. R. Evolution of the North American Cordillera. *Annu. Rev. Earth Planet. Sci.* **32**, 13–45 (2004).

30. Haugerud, R. *et al.* Geologic Map of the North Cascade Range , Washington. *Bull. Geol. Soc. Am.* **120**, 2940 (2009).

31. Mullen, E. K., Paquette, J. L., Tepper, J. H. & McCallum, I. S. Temporal and spatial evolution of Northern Cascade Arc magmatism revealed by LA–ICP–MS U–Pb zircon dating. *Can. J. Earth Sci.* **55**, 443–462 (2018).

32. Hildreth, W., Fierstein, J. & Lanphere, M. Eruptive history and geochronology of the Mount Baker volcanic field, Washington. *Bull. Geol. Soc. Am.* **115**, 729–764 (2003).

33. du Bray, E. A. & John, D. A. Petrologic, tectonic, and metallogenic evolution of the Ancestral Cascades magmatic arc, Washington, Oregon, and northern California. *Geosphere* **7**, 1102–1133 (2011).

34. Wells, R. E. & McCaffrey, R. Steady rotation of the Cascade arc. *Geology* **41**, 1027–1030 (2013).

35. Priest, G. R. Volcanic and tectonic evolution of the Cascade Volcanic Arc, central Oregon. *J. Geophys. Res.* **95**, (1990).

36. Hijmans, R. J., Cameron, S. E., Parra, J. L., Jones, P. G. & Jarvis, A. Very high resolution interpolated climate surfaces for global land areas. *Int. J. Climatol.* **25**, 1965–1978 (2005).

37. Reiners, P. W. *et al.* Late Miocene exhumation and uplift of the Washington Cascade Range. *Geology* **30**, 767–770 (2002).

38. Reiners, P. W., Ehlers, T. A., Mitchell, S. G. & Montgomery, D. R. Coupled spatial variations in precipitation and long-term erosion rates across the Washington Cascades. *Nature* **426**, 645–647 (2003).

39. Mitchell, S. G. & Montgomery, D. R. Polygenetic topography of the Cascade Range, Washington State,

USA. *Am. J. Sci.* **306**, 736–768 (2006).

40. Herman, F. *et al.* Worldwide acceleration of mountain erosion under a cooling climate. *Nature* **504**, 423–426 (2013).

41. DeMets, C., Gordon, R. G. & Argus, D. F. Geologically current plate motions. *Geophys. J. Int.* **181**, 1–80 (2010).

42. Tassara, A. & Echaurren, A. Anatomy of the Andean subduction zone: Three-dimensional density model upgraded and compared against global-scale models. *Geophys. J. Int.* **189**, 161–168 (2012).

43. Hayes, G. P. *et al.* Slab2, a comprehensive subduction zone geometry model. *Science (80-.).* **362**, 58–61 (2018).

44. Maloney, K. T., Clarke, G. L., Klepeis, K. A. & Quevedo, L. The Late Jurassic to present evolution of the Andean margin: Drivers and the geological record. *Tectonics* **32**, 1049–1065 (2013).

45. Tebbens, S. F. *et al.* The Chile ridge: A tectonic framework. *J. Geophys.* **102**, 12035–12059 (1997).

46. Giambiagi, L., Mescua, J., Bechis, F., Tassara, A. & Hoke, G. Thrust belts of the southern Central Andes: Along-strike variations in shortening, topography, crustal geometry, and denudation. *Bull. Geol. Soc. Am.* **124**, 1339–1351 (2012).

47. Folguera, A. & Ramos, V. A. Repeated eastward shifts of arc magmatism in the Southern Andes: A revision to the long-term pattern of Andean uplift and magmatism. *J. South Am. Earth Sci.* **32**, 531–546 (2011).

48. Cembrano, J. *et al.* Late Cenozoic transpressional ductile deformation north of the Nazca-South America-Antarctica triple junction. *Tectonophysics* **354**, 289–314 (2002).

49. Thomson, S. N. Late Cenozoic geomorphic and tectonic evolution of the Patagonian Andes between latitudes 42°S and 46°S: An appraisal based on fission-track results from the transpressional intra-arc Liquiñe-Ofqui fault zone. *Bull. Geol. Soc. Am.* **114**, 1159–1173 (2002).

50. Adriasola, A. C., Thomson, S. N., Brix, M. R., Hervé, F. & Stöckhert, B. Postmagmatic cooling and late Cenozoic denudation of the North Patagonian Batholith in the Los Lagos region of Chile, 41°-42°15′S. *Int. J. Earth Sci.* **95**, 504–528 (2006).

51. Echaurren, A. *et al.* Fore-to-retroarc crustal structure of the north Patagonian margin: How is shortening distributed in Andean-type orogens? *Glob. Planet. Change* **209**, (2022).

52. Castro, A. *et al.* Secular variations of magma source compositions in the North Patagonian batholith from the Jurassic to Tertiary: Was mélange melting involved? *Geosphere* **17**, 766–785 (2021).

53. Mella, M. *et al.* Petrogenesis of the Pleistocene Tronador Volcanic Group, Andean Southern Volcanic Zone. *Rev. Geol. Chile* **32**, 131–154 (2005).

54. Lara, L. E. & Folguera, A. The Pliocene to Quaternary narrowing of the Southern Andean volcanic arc between 37° and 41°s latitude. *Spec. Pap. Geol. Soc. Am.* **407**, 299–315 (2006).

55. Haschke, M. *et al.* Central and Southern Andean Tectonic Evolution Inferred from Arc Magmatism. *The Andes* 337–353 (2006) doi:10.1007/978-3-540-48684-8_16.

56. Thomson, S. N. *et al.* Glaciation as a destructive and constructive control on mountain building. *Nature* **467**, 313–317 (2010).

57. Glodny, J., Gräfe, K., Echtler, H. & Rosenau, M. Mesozoic to Quaternary continental margin dynamics in South-Central Chile (36-42°S): The apatite and zircon fission track perspective. *Int. J. Earth Sci.* **97**, 1271–1291 (2008).

58. Herman, F. & Brandon, M. Mid-latitude glacial erosion hotspot related to equatorial shifts in southern Westerlies. *Geology* **43**, 987–990 (2015).

59. Montgomery, D. R., Balco, G. & Willett, S. D. Climate, tectonics, and the morphology of the Andes. *Geology* **29**, 579–582 (2001).

60. Venzke, E. Global Volcanism Program. *Volcanoes of the World* (2013) doi:https://doi.org/10.5479/si.GVP.VOTW4-2013.

61. Whipple, K. X. & Tucker, G. E. Dynamics of the stream-power river incision model: Implications for the height limits of mountain ranges, landscape response timescales, and research need. *J. Geophys. Res.* **104**, 661–674 (1999).

62. Gerya, T. V. & Yuen, D. A. Robust characteristics method for modelling multiphase visco-elasto-plastic thermo-mechanical problems. *Phys. Earth Planet. Inter.* **163**, 83–105 (2007).

63. Gerya, T. V. *Introduction to Geodynamic Numerical Modelling*. (Cambridge University Press, 2019).

64. Turcotte, D. L. & Schubert, G. *Geodynamics*. (Cambridge University Press, 2002).

65. Zhao, D. & Hua, Y. Anisotropic tomography of the Cascadia subduction zone. *Phys. Earth Planet. Inter.* **318**, 106767 (2021).

66. Hildreth, W. & Moorbath, S. Crustal contributions to arc magmatism in the Andes of Central Chile. *Contrib. to Mineral. Petrol.* **98**, 455–489 (1988).

67. Völker, D., Kutterolf, S. & Wehrmann, H. Comparative mass balance of volcanic edifices at the southern volcanic zone of the Andes between 33°S and 46°S. *J. Volcanol. Geotherm. Res.* **205**, 114–129 (2011).

68. Defant, M. J.; Drummont, M. S. Derivation of some modern arc magmas by melting of young subducted lithosphere. *Nature* **347**, 662–665 (1990).

69. Wannamaker, Philip E.; Evans, Rob L.; Bedrosian, Paul A.; Unsworth, Martyn J.; Maris, Virginie; McGary, S. Segmentation of plate coupling, fate of subduction fluids, and modes of arc magmatism in Cascadia, inferred from magnetotelluric resistivity. *Geochemistry, Geophys. Geosystems* 4230–4253 (2014) doi:10.1002/2014GC005509.Received.

70. Díaz, D., Zúñiga, F. & Castruccio, A. The interaction between active crustal faults and volcanism: A case study of the Liquiñe-Ofqui Fault Zone and Osorno volcano, Southern Andes, using magnetotellurics. *J. Volcanol. Geotherm. Res.* **393**, 106806 (2020).

71. López Escobar, Á., Cembrano, J. & Moreno, H. Geochemistry and tectonics of the Chilean Southern Andes basaltic Quaternary volcanism (37-46°S). *Andean Geol.* **22**, 219–234 (1995).

72. Sternai, P., Caricchi, L., Castelltort, S. & Champagnac, J. D. Deglaciation and glacial erosion: A joint control on magma productivity by continental unloading. *Geophys. Res. Lett.* **43**, 1632–1641 (2016).

73. Sternai, P. Feedbacks between internal and external Earth dynamics. in *Dynamics of Plate Tectonics and Mantle Convection* (ed. Joao Duarte) (2022).

74. Sternai, P. *et al.* Magmatic Forcing of Cenozoic Climate? *J. Geophys. Res. Solid Earth* **125**, 1–22 (2020).

75. Ranalli, G. *Rheology of Earth*. (Springer Sciences and Business Media, 1995).

76. Hirschmann, M. M. Mantle solidus: Experimental constraints and the effects of peridotite composition. *Geochemistry, Geophys. Geosystems* **1**, (2000).

77. Johannes, W. The significance of experimental studies for the formation of migmatites. in *Migmatites* (ed. Ashworth, J. R.) (Blackie & Son Ltd, USA Chapman & Hall, 1985).

78. Sternai, P. *et al.* Pre-glacial topography of the European Alps. *Geology* **40**, 1067–1070 (2012).

References Supplementary Data

Adriasola, A. C., Thomson, S. N., Brix, M. R., Hervé, F. & Stöckhert, B. Postmagmatic cooling and late Cenozoic denudation of the North Patagonian Batholith in the Los Lagos region of Chile, 41°-42°15′S. *Int. J. Earth Sci.* 95, 504–528 (2006).

Engels, J.C., Tabor, R. W., Miller, F.K., Obradovich, J. D. Summary of K-Ar, Rb-Sr, U-Pb, Pba, and fission-track ages of rocks from Washington State prior to 1975 (exclusive of Columbia Plateau basalts). *Miscellaneous Field Studies Map 710* (1976).

Hildreth, W., Fierstein, J. & Lanphere, M. Eruptive history and geochronology of the Mount Baker volcanic field, Washington. *Bull. Geol. Soc. Am.* 115, 729–764 (2003).

Hirschmann, M. M. Mantle solidus: Experimental constraints and the effects of peridotite composition. *Geochemistry, Geophys. Geosystems* 1, (2000).

Johannes, W. *The significance of experimental studies for the formation of migmatites. in Migmatites* (ed. Ashworth, J. R.) (Blackie & Son Ltd, USA Chapman & Hall, 1985).

Lara, L. ., Rodríguez, C. ., Moreno, H. . & Pérez de Arce, C. Geocronología K-Ar y geoquímica del volcanismo plioceno superior-pleistoceno de los Andes del sur (39-42°S). *Rev. Geol. Chile* 28, (2001).

Mella, M. et al. Petrogenesis of the Pleistocene Tronador Volcanic Group, Andean Southern Volcanic Zone. *Rev. Geol. Chile* 32, 131–154 (2005).

Moreno, H., Varela, J., López, L., Munizaga, F., and Lahsen, A. *Geología y riesgo volcánico del volcán Osorno y centros eruptivos menores: Unpublished report No. OICB-06C to ENDESA-CORFO*, 212 p. (1985).

Ranalli, G. *Rheology of Earth.* (Springer Sciences and Business Media, 1995).

Reiners, P. W. et al. Late Miocene exhumation and uplift of the Washington Cascade Range. *Geology* 30, 767–770 (2002).

SERNAGEOMIN-BGRM. *Carta metalogénica X región sur: Servicio Nacional de Geología y Minería.* (1995).

Simon-Labric, T. et al. Low-temperature thermochronologic signature of rangedivide migration and breaching in the North Cascades. *Lithosphere* 6, 473–482 (2014).

Thomson, S. N. et al. Glaciation as a destructive and constructive control on mountain building. *Nature* 467, 313–317 (2010).

Turcotte, D. L. & Schubert, G. *Geodynamics.* (Cambridge University Press, 2002).

Venzke, E. *Global Volcanism Program.* Volcanoes of the World (2013). doi:https://doi.org/10.5479/si.GVP.VOTW4-2013.

Chapter 5. Article 4

Fast postglacial uplift in the Southern Patagonian Andes due to the asthenospheric window underneath

Veleda A. P. Muller[1], Pietro Sternai[1], Christian Sue[2,3]

[1] Dipartimento di Scienze dell'Ambiente e della Terra (DISAT), Università degli Studi di Milano-Bicocca, Piazza della Scienza 4, Milan, Italy.

[2] Institute des Sciences de la Terre (ISTerre), Université Grenoble Alpes, Université Savoie Mont Blanc, CNRS, IRD, IFSTTAR, Université Gustave Eiffel, Grenoble, France.

[3] Université de Franche Comté, Besançon, France.

Abstract

The Patagonian Icefields are remnants of glaciers building and melting in the southern Patagonian Andes since the latest Miocene. Their Last Glacial Maximum was reached ~21 kyrs ago, and there are records of an acceleration of deglaciation rates since the Little Ice Age (LIA) ~400 yrs ago. The southern Patagonian Andes overlie an asthenospheric window where mantle upwelling increases the heat flow across much of the South American lithosphere. GPS measured vertical uplift rates between 10-40 mm/yr are currently ascribed to post-LIA glacial rebound. However, these vertical uplift rates are one order of magnitude higher than the measured uplift rates due to deglaciation in collisional orogens (e.g., the European Alps), which rises questions about the role of the asthenospheric window in driving the surface displacements. Here, we perform geodynamic thermo-mechanical numerical modelling to estimate the surface uplift rates induced by post-LIA and post-LGM deglaciation of an ice sheet accounting for temperature dependent rheologies and different thermal regimes in the asthenosphere. For plausible lithosphere and mantle rheologies, the maximum uplift rate is <2 mm/yr if the mantle potential temperature is bellow 1265 °C. Modeled uplift rates approach observed values when the mantle potential temperature is increased by 150-200 °C. We conclude that the asthenospheric window plays a key role in controlling the magnitude of regional present-day uplift rates. Furthermore, higher mantle potential temperatures implies mantle viscosities between 10^{16}-10^{18} Pa s which, in turn, imply that post-LGM deglaciation contributes by approximately 20% to the observed fast uplift rates in the southern Patagonian Andes, the rest pertaining to post-LIA rebound.

1. Introduction

Vertical displacements of the Earth's surface with respect to the geoid occur in response to the motion of crustal and mantle rock masses driven by plate tectonics and the redistribution of the surface rock, water and ice masses by surface processes (e.g., Watts, 2001; Turcotte and Schubert, 2002). For instance, excess of topography in orogenic regions due to convergence deflects the lithosphere downward, whereas unloading by erosion and ice melting causes upward deflection of the lithosphere, known as 'isostatic' adjustment. The magnitude of surface uplift rates is set primarily by the lithosphere and asthenosphere viscosities, which depend, amongst other factors, on the thermal field at depth (Ranalli, 1997; Kauffman et al., 1997; England and Molnar, 1990; Watts, 2001; Turcotte and Schubert, 2002; Klemann et al., 2007). Although the theory that relates surface load changes and isostatic adjustments is well developed, recognizing and quantifying expressions of such dynamics in natural settings is difficult. Here, we use thermo-mechanical numerical modelling to quantitatively characterize the isostatic adjustment of the southern Patagonian Andes due to the deglaciation with particular focus on the relative role of the viscosity structure at depth.

The southern Patagonian Andes in the South American Continent are located above a transition zone between the subducting Antarctic Plate and a wide asthenospheric window opening between the Antarctic and Nazca oceanic plates at depth (Fig. 1a; Cande and Leslie, 1986). The Chile Triple Junction (CTJ) at ~46 °S delimits the surface tip of the asthenospheric window, which opened during the last ~16 Ma from south to north. First order effects of the asthenospheric flow on the surface continental geology are the inhibition of arc volcanism in favour of retroarc magmatism, forward propagation of the fold-and-thrust belt, and rock uplift (Ramos and Kay, 1992; Ramos, 2005; Breitsprecher and Thorkelson, 2009; Guillaume et al., 2009; Lagabrielle et al., 2010; Georgieva et al., 2016). Rock uplift due to asthenospheric upwelling, in particular, was estimated as < 0.15 mm/yr in the last 3 Ma over an area of about 100000 km^2 around the CTJ latitude (Guillaume et al., 2009). The heat flow was calculated as >100 mW/m^2 near the CTJ, ~70-90 mW/m^2 in the center of the asthenospheric window (~50 °S), and 50-60 mW/m^2 near its northern boundary (~46 °S) (Ávila and Dávila, 2018).

The southern Patagonian Andes were covered by the Patagonian Ice Sheet in the Last Glacial Maximum (LGM) ~21-14 kyrs ago, which covered an estimated area of 400000 km^2 and volume of 525000 km^3 (Fig. 1 a; McCulloch, 2000; Hulton et al., 2002; Rabassa, 2008; Glasser and Jansson, 2008; Glasser et al., 2005; Hein et al., 2010; Boex et al, 2013; Moreno et

al., 2015; Bendle et al., 2017; Thorndycraft et al., 2019). Ice thickness in the LGM varied by sector, being thicker (i.e., ~1500-2500 m) in mountainous regions between 44 and 52 °S, and thinner (i.e., ~500 m) towards the periphery of the ice sheet (Hulton et al., 2002). The Patagonian Ice Sheet experienced cycles of glacial advance and retreat to form the present day Northern Patagonian Icefield that covers an area of ~3976 km^2, and the Southern Patagonian Icefield (SPI) that covers an area of ~13219 km^2 (Millan et al., 2019). The present-day ice thickness varies between 100 and 1800 m depending on the analysed sector, with a mode of 250 m in the SPI (Millan et al., 2019).

GPS and remote sensing data allow us to measure the ongoing rock vertical uplift rates, which are extremely high (~40 mm/yr) in the vicinity of the SPI (Fig. 1b), and gradually decrease toward its peripheral parts (Ivins and James, 2004; Dietrich et al., 2010; Lange et al., 2014). These uplift rates are currently ascribed to lithospheric viscoelastic isostatic adjustment to the deglaciation following the Little Ice Age (LIA, with apex around 1630 AD), responsible for ~503 km^3 of iceloss (Ivins and James, 1999; Rignot et al., 2003; Klemann et al., 2007; Dietrich et al., 2010; Glasser et al., 2011; Davies and Glasser, 2012; Lange et al., 2014). The ice loss since the LGM is estimated as about 500000 km^3 (McCulloch et al., 2000; Hulton et al., 2002; Bendle et al., 2017; Thorndycraft et al., 2019) but, due to its long timespan, its effects on the present-day uplift were considered negligible compared to those related to post-LIA deglaciation (Aniya, 1997; Ivins and James, 1999). The estimates of ice volume and ice loss throughout the last glacial and interglacial, however, are only crudely estimated based on the preserved glacial morphologies, geochronological data, and remote sensing (Mercer and Sutter, 1982; Aniya, et al., 1996, 1997; Ivins and James, 1999, McCulloth, 2000; Hulton, 2002; Rabassa, 2008; Davies and Glasser, 2012; Torndycraft et al., 2019)

Previous investigations of the regional viscoelastic glacial isostatic adjustment infer a very low viscosity asthenosphere (~ 1.6 x 10^{18} Pa s) and a thin elastic lithosphere (~36.5±5.3 km) to reproduce the uplift rates of ~40 mm/yr forced by ~400 yrs of post-LIA unloading (Ivins and James, 1999, 2004; Klemann et al., 2007; Langue et al., 2014). The presence of low viscosities at depth is consistent with abnormally high temperatures due to the asthenospheric window underneath the SPI, but temperature and viscosity were treated independently in previous investigations (Ivins and James, 1999, 2004; Klemann et al., 2007; Lange et al, 2013). Besides, the mantle viscoelastic relaxation time to surface unloading varies between 10^2 to 10^5 yrs depending on the asthenosphere viscosity (Ranalli, 1997; Turcotte and Schubert,

2002), implying that a contribution from post-LGM deglaciation to the present-day uplift rate cannot be ruled out.

Here, we perform fully coupled thermo-mechanical numerical geodynamic experiments forced by surface unloading equivalent to post-LIA and post-LGM ice melting. Numerical experiments account for positive thermal anomalies in the asthenosphere to asses the role of the asthenospheric window in setting the mantle viscosity and associated postglacial rebound. We focus on magnitude, rather than the pattern, of the inferred surface uplift rates, which we compare to that of the GPS-measured rock uplift rates to constrain plausible thermal and viscosity structures at depth as well as the timing of rebound.

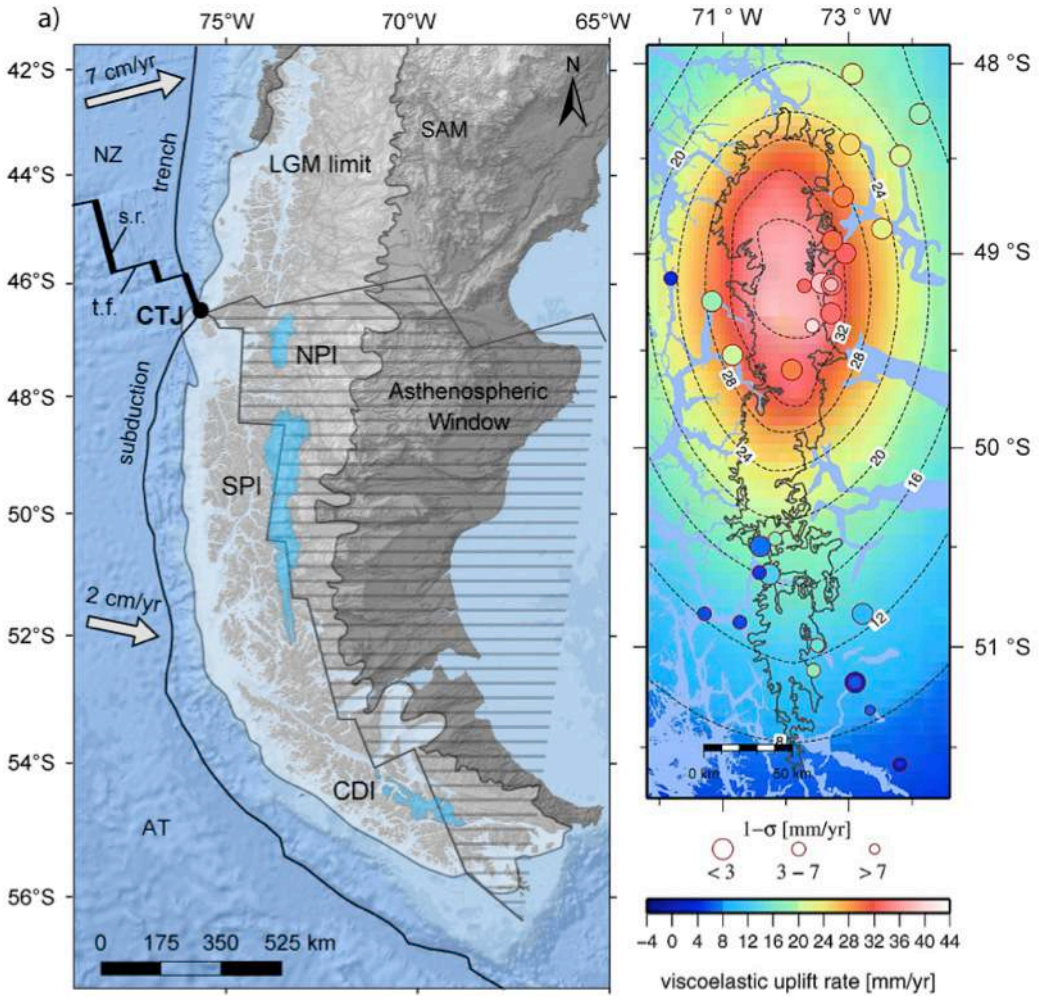

Fig. 1: A) Map of southern Patagonia with the Southern Patagonian Icefield (SPI), Northern Patagonian Icefield (NPI), and the Cordillera Darwin Icefield (CDI) highlighted in light blue, the approximated extension of the icefields in the Last Glacial Maximum ~21 kyrs ago (LGM limit), and the approximated extension of the present-day asthenospheric window (dashed region) beneath the South American Continent (SAM). In the Pacific Ocean there are the spreading ridges (s.r., thick black lines) and the transform faults (t.f., thin black lines) that separate the Nazca (NZ) and the Antarctic (AT) plates, the subduction trench is highlighted by the black line around the continent. The arrows show the approximated direction of the subduction of the oceanic plates with the velocity marked above. B) The region of the SPI and the location of the GPS stations (circles) used to calculate the viscoelastic uplift rates in Lange et al. (2014), the size of the circles represents the range of uplift values obtained from each individual GPS station.

2. Methodology

2.1. Reference model setup

The model domain, scaled on the study region, is 700 km wide and 120 km thick (see Supplementary Table 1 for layer's rheological properties). From top to bottom, the model accounts for 10 km of 'sticky' air, 30 km of continental crust (with rheology of quartzite, Ranalli, 1995), 30 km of lithospheric mantle, and 50 km of asthenospheric mantle (with rheology of dry olivine, Ranalli, 1995), in agreement with literature data (e.g., Klemann et al., 2007). On the top of the crust and in the middle of the model domain we impose a 2 km thick and 70 km wide ice layer (Fig. 2 a). The ice load distribution does not change throughout the simulations, but we simulate post-LIA and post-LGM deglaciation by reducing the ice density through time (see also section 2.3).

The initial geotherm is piece-wise linear resulting from an adiabatic temperature gradient of 0.5 °C/km in the asthenosphere (Turcotte and Schubert, 2002) and thermal boundary conditions fixed at 0 °C at the surface, 1300 °C at the bottom of the lithosphere, and 1325 °C at the bottom of the model, with nil horizontal heat flux across the vertical boundaries. In the reference setup, the lithosphere-asthenosphere boundary is imposed at 70 km depth. The rheologic and thermal structures of the reference model give a lithospheric elastic thickness, *Te* (*sensu* Burov and Diament, 1995), of ~30 km, a value comparable to previous estimates underneath the SPI based on visco-elastic modelling from GPS data (36.5 $\pm$ 5.3 km, Dietrich et al., 2010; Lange et al., 2014), and based on heat flow data (between 25 and 40 km, Ávila and Dávila, 2018).

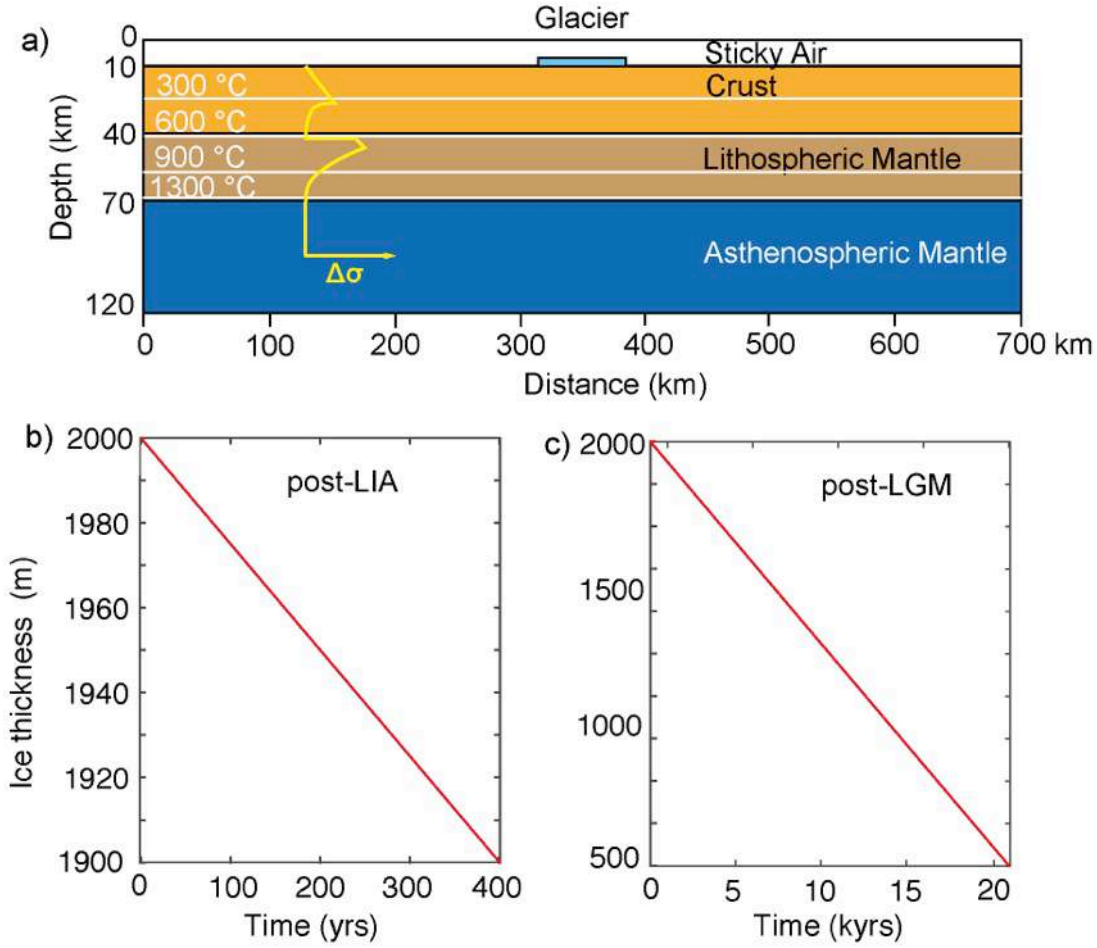

Fig. 2. Reference numerical model setup. A) Thermo-mechanical numerical model domain with rheological layers (Supplementary Table 1), isotherms (white lines), and yield strength ($\Delta\sigma$) profile (yellow line). Diagrams for the function of ice thickness vs. time used in the numerical experiments to simulate post-LIA (b) and post-LGM (c) deglaciation.

2.2. Numerical model

We use a fully coupled thermo-mechanical, visco-elasto-plastic, numerical geodynamic model to quantify the effect of thermal anomalies in the mantle on the magnitude of surface uplift rates due to deglaciation. The numerical model uses the finite differences with marker-in-cell technique, resolved by 51 × 61 nodes in x and y directions, respectively, distributed on a Eulerian grid that accounts for a maximum resolution of 1 km along the y direction in the upper part of the model domain, and ~13 km in the x direction. 400 × 400 Lagrangian markers are randomly distributed along the x and y dimensions and used for advecting the material properties (Gerya and Yuen, 2007; Gerya et al., 2019). The material properties carried by Lagrangian markers are then interpolated onto the Eulerian grid via a 4th order Runge-Kutta interpolation scheme. An internal free surface is simulated through the 10

-km thick layer of sticky air. The velocity boundary conditions are free slip at all boundaries (x = 0 and x = 700 km; y = 0 and y = 120 km).

We provide a short overview of the governing equations hereafter, while a detailed description of numerical technique can be found, for instance, in Gerya and Yuen (2007), Gerya et al. (2019), Sternai et al. (2020), and Muller et al. (2022). The continuity equation allows for the conservation of mass during the displacement of a geological continuum:

(1) $\frac{\partial \rho}{\partial t} + \nabla(\rho v) = 0$

where ρ is the local density, t is time, v is the velocity vector, and ∇ is the divergence operator. The momentum equation describes the changes in velocity of an object in the gravity field due to internal and external forces:

(2) $\frac{\partial \sigma_{ij}}{\partial x_i} + \rho g_i = \rho \left(\frac{\partial v_i}{\partial t} + v_j \frac{\partial v_i}{\partial x_j} \right)$

where σ_{ij} is the stress tensor, x_i and x_j are spatial coordinates, and g_i is the *i*-th component of the gravity vector. The energy equation allows for the conservation of energy during advective and conductive heat transfer in the continuum:

(3) $\rho C_P \frac{DT}{Dt} - div(c\nabla T) + v\nabla T = H_r + H_s + H_a + H_l$

where *P* is pressure, T is temperature, C_P is specific heat capacity at a constant *P*, c is the thermal conductivity, $H_r + H_s + H_a + H_l$ are the volumetric heat productions by radiogenic, shear, adiabatic and latent heat, respectively. $H_a \propto \frac{DP}{Dt}$, $H_s = \sigma'_{ij}\dot{\varepsilon}'_{ij(viscous)}$, and H_r and H_l are the radiogenic and latent heat productions. Ductile deformation is thermally activated generating viscous flow, which involves diffusion and dislocation creep, calculated according to the material shear viscosity:

(4) $\frac{1}{\eta_{ductile}} = \frac{1}{\eta_{diff}} + \frac{1}{\eta_{disl}}$

with

$\eta_{diff} = \frac{\eta_0}{2\sigma_{cr}^{n-1}} exp\left(\frac{E_a + PV_a}{RT}\right)$, and

$\eta_{disl} = \frac{\eta_0^{\frac{1}{n}}}{2} exp\left(\frac{E_a + PV_a}{nRT}\right) \dot{\varepsilon}_{II}^{\frac{1}{n}-1}$

where η_{diff} and η_{disl} are the shear viscosity for diffusion and dislocation creep, respectively, η_0 is the material static viscosity, σ_{cr} is the diffusion-dislocation transition critical stress, *n* is the stress exponent, E_a is the activation energy, V_a is the activation volume, *P* is pressure, *R* is the gas constant, *T* is temperature, and $\dot{\varepsilon}_{II}$ is the second invariant of the strain rate tensor. The viscous deviatoric strain rate tensor, $\dot{\varepsilon}'_{ij\ (viscous)}$, is defined by:

(5) $\dot{\varepsilon}'_{ij\,(viscous)} = \frac{1}{2\eta_{ductile}}\sigma'_{ij} + \delta_{ij}\eta_{bulk}\dot{\varepsilon}_{kk} = \frac{1}{2\eta_{diff}}\sigma'_{ij} + \frac{1}{2\eta_{disl}}\sigma'_{ij} + \delta_{ij}\eta_{bulk}\dot{\varepsilon}_{kk}$

where σ'_{ij} is the deviatoric stress tensor, δ_{ij} is the Kronecker delta, $\dot{\varepsilon}_{kk}$ is the volumetric strain rate (e.g., related to phase transformations), and η_{bulk} is the bulk viscosity. The reversible elastic deformation is defined by the elastic deviatoric strain rate tensor, $\dot{\varepsilon}'_{ij\,(elastic)}$, as:

(6) $\dot{\varepsilon}'_{ij\,(elastic)} = \frac{1}{2\mu}\frac{\check{D}\sigma'_{ij}}{Dt}$

where μ is the shear modulus and $\frac{\check{D}\sigma'_{ij}}{Dt}$ is the objective co-rotational time derivative of the deviatoric stress tensor. The plastic deformation, brittle and localised, occurs at low temperature at the upper part of the lithosphere after that the absolute shear stress limit, σ_{yield}, is reached:

(7) $\sigma_{yield} = C + \sin(\varphi)P.$

where C is cohesion and φ is the effective internal friction angle. The plastic strain rate tensor, $\dot{\varepsilon}'_{ij\,(plastic)}$, is defined by:

(8) $\dot{\varepsilon}'_{ij\,(plastic)} = 0\ for\ \sigma_{II} < \sigma_{yield}, \dot{\varepsilon}'_{ij\,(plastic)} = \mathcal{X}\frac{\partial\sigma'_{ij}}{2\sigma_{II}}\ for\ \sigma_{II} \geq \sigma_{yield}$

where $\mathcal{X}$ is the plastic multiplier which satisfies the plastic yielding condition $\sigma_{II} = \sigma_{yield}$. The bulk strain rate tensor, $\dot{\varepsilon}'_{ij(bulk)}$, integrates the viscous, elastic and plastic deformation:

(9) $\dot{\varepsilon}'_{ij(bulk)} = \dot{\varepsilon}'_{ij(viscous)} + \dot{\varepsilon}'_{ij(elastic)} + \dot{\varepsilon}'_{ij(plastic)}$

2.3. Modelling approach

Computing the surface load, *L*, as

(10) $L = \rho_{ice} g h_{ice},$

where ρ_{ice} is the density of the ice, *g* is the gravity acceleration, and h_{ice} is the ice thickness, the model is forced by the progressive unloading due to linear melting of the synthetic ice cap (Fig. 2). We run two sets of experiments based on the estimated volume of ice loss since the LGM (~75% in ~21 kyrs) and the LIA (~5% in ~400 yrs) (McCulloth et al., 2000; Hulton et al., 2002; Glasser et al., 2011; Boex et al., 2013; Bendle et al., 2017; Millan et al., 2019). Assuming a 70 km wide ice cap (i.e., 1/10 of the model width, approximately equivalent to the average width of the SPI today), the percentages above result in the melting of 100 m and 1500 m of ice in 400 yrs and in 21 kyrs, respectively (Fig. 2 b,c). We stress that,

since we focus on the magnitude and not the pattern of postglacial rebound, results are largely independent of the assumed width of the ice cap. The surface uplift rate is calculated through time as the surface elevation change resulting from the modelled strain field divided by the viscoelastic timestep. The parametric study focuses on the mantle potential temperature (*sensu* McKenzie and Bickle, 1988) which accounts for positive thermal anomalies, TA, of up to 200 °C in steps of 50 ° C (added to the reference mantle potential temperature of 1265 °C), to mimic the presence of a slab window at depth.

3. Results

Results are shown in Table 1 and Figs. 3-5. Overall, increasing the asthenospheric temperature decreases the viscosity of the asthenosphere, with significant effects on the magnitude and pattern of the velocity field. The asthenosphere viscosity ranges between 10^{22} and 10^{19} Pa s in simulations with TA equal to 0, 50 and 100 °C, whereas it ranges between 10^{18} and 10^{16} Pa s in simulations with TA equal to 150 and 200 °C (Fig. 3 a-d). Lithospheric warming due to increasing TA also leads to a moderate reduction of the overall lithospheric viscosity, thereby decreasing the integrated lithospheric strength (*Te*).

In agreement with the theory of lithosphere flexure (e.g., Turcotte and Schubert, 2002), the post-LIA deglaciation triggers uplift in the region covered by the shrinking ice cap and subsidence in the neighbouring regions (Figs. 3-5). For TA equal to 0, 50, and 100 °C the initial maximum uplift rates are less than 2 mm/yr in the center of the model. For TA of 150 and 200 °C, the initial maximum uplift rates reach up to ~14 and 26 mm/yr, respectively, in the center of the model (Fig. 4 b). During the 400 years of deglaciation, the maximum uplift rate increases in the center of the model, reaching up to ~20 and 28 mm/yr with a TA equal to 150 and 200 °C, respectively, and up to ~2 mm/yr with a TA equal to 0, 50 and 100 °C (Figs. 4 c, d). Observing the maximum uplift rates versus time for the post-LIA deglaciation (Fig. 6 a), one can recognize that TA equal to 0, 50 and 100 °C generates a slower increase of the maximum uplift rate compared to that of simulations where TA equal to 150 and 200 °C. When deglaciation ends the maximum uplift rate drops to ~0 mm/yr in ~ 100 years if TA equals to 0, 50 and 100 °C, whereas it takes >1000 years is TA equals to 150 °C or 200 °C (Fig. 6 a).

Table 1 – Maximum uplift rates derived from the numerical simulations for the parametric study that considers: a thermal anomaly (TA) of 0, 50, 100, 150 and 200 °C, during 500 years and 25000 years to simulate the post-LIA and the post-LGM deglaciation, respectively. In the simulations the post-LIA deglaciation stops at 400 years, and the post-LGM deglaciation stops at 21000 years, the last timestep shown in the table for both experiments are thus after the cessation of deglaciation. Fig. 6 is a plot of the calculated maximum uplift rates vs. time for each tested TA, for both experiments.

Thermal Anomaly (°C)	**max. uplift rate (mm/yr)**					
0	1,487616	1,404141	1,311538	1,231416	1,212055	1,201007
50	0,764477	0,315201	1,03729	1,581134	2,027777	0,270842
100	0,486062	0,83436	1,52349	1,982825	0,409559	0,229386
150	7,719348	13,321857	17,988805	20,933763	14,962459	10,492216
200	21,171616	25,857969	27,306896	28,201894	6,813495	2,699061
Time since LIA deglaciation onset (years)	**0**	**100**	**200**	**300**	**400**	**500**
Thermal Anomaly (°C)	**max. uplift rate (mm/yr)**					
0	0,240966	0,358934	0,883904	1,365068	1,972565	1,200874
50	0,236484	0,441587	1,15048	1,993024	2,901279	1,478978
100	0,205707	0,707683	1,15048	3,714884	4,90923	2,403842
150	0,251128	5,163112	6,149255	6,743781	7,469746	1,924015
200	2,750999	5,762251	6,855096	7,271318	7,872445	1,364
Time since LGM deglaciation onset (years)	**0**	**5000**	**10000**	**15000**	**20000**	**25000**

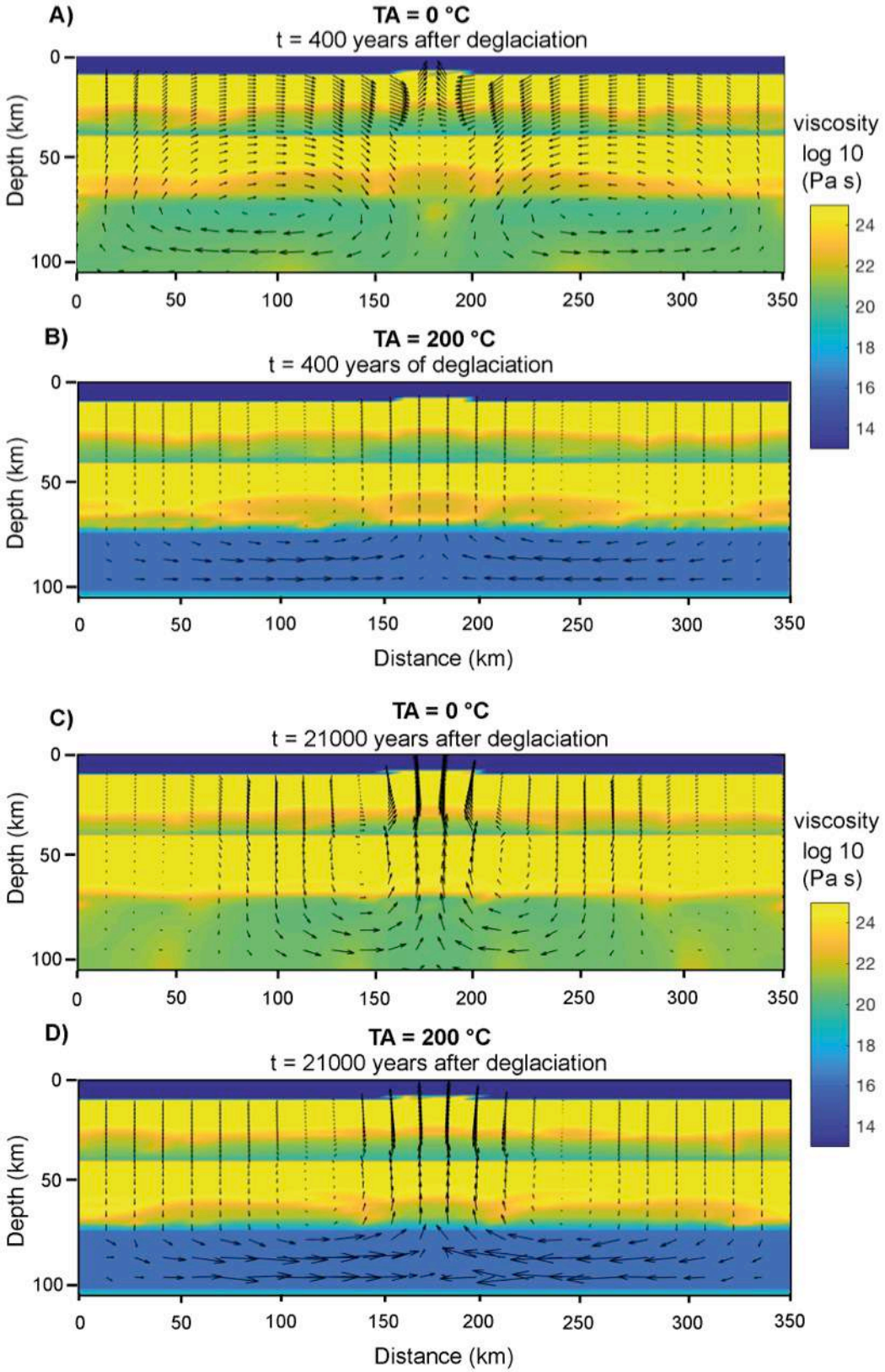

Fig. 3. Distribution of viscosity and velocity vectors in the simulations. A) With an asthenospheric thermal anomaly (TA) of 0 °C, and **B)** with a TA = 200 °C ~ 400 years after the onset of post-LIA deglaciation. **C)** With an asthenospheric thermal anomaly (TA) of 0 °C, and **D)** with a TA = 200 °C ~ 21000 years after the onset of post-LGM deglaciation.Velocity vectors have not the same scale in the two simulations and serve for visualization of the velocity flow.

In the post-LGM experiments with TA equal to 0, 50, and 150 °C, the initial maximum uplift rate is less than 0.7 mm/yr in the center of the model. When TA equals to 150 or 200 °C, the maximum uplift rate reach up to 6 mm/yr in the center of the model (Fig. 5 b). During the second half of deglaciation the maximum uplift rate increases to 5 mm/yr if TA equal to 0, 50 and 100 °C (Fig. c,d). For any tested TA, the maximum uplift rate increases with time during the deglaciation. The drop of the maximum uplift rate to ~0 mm/yr after the end of the deglaciation takes more than 10000 years to occur regardless of TA (Fig. 6 b).

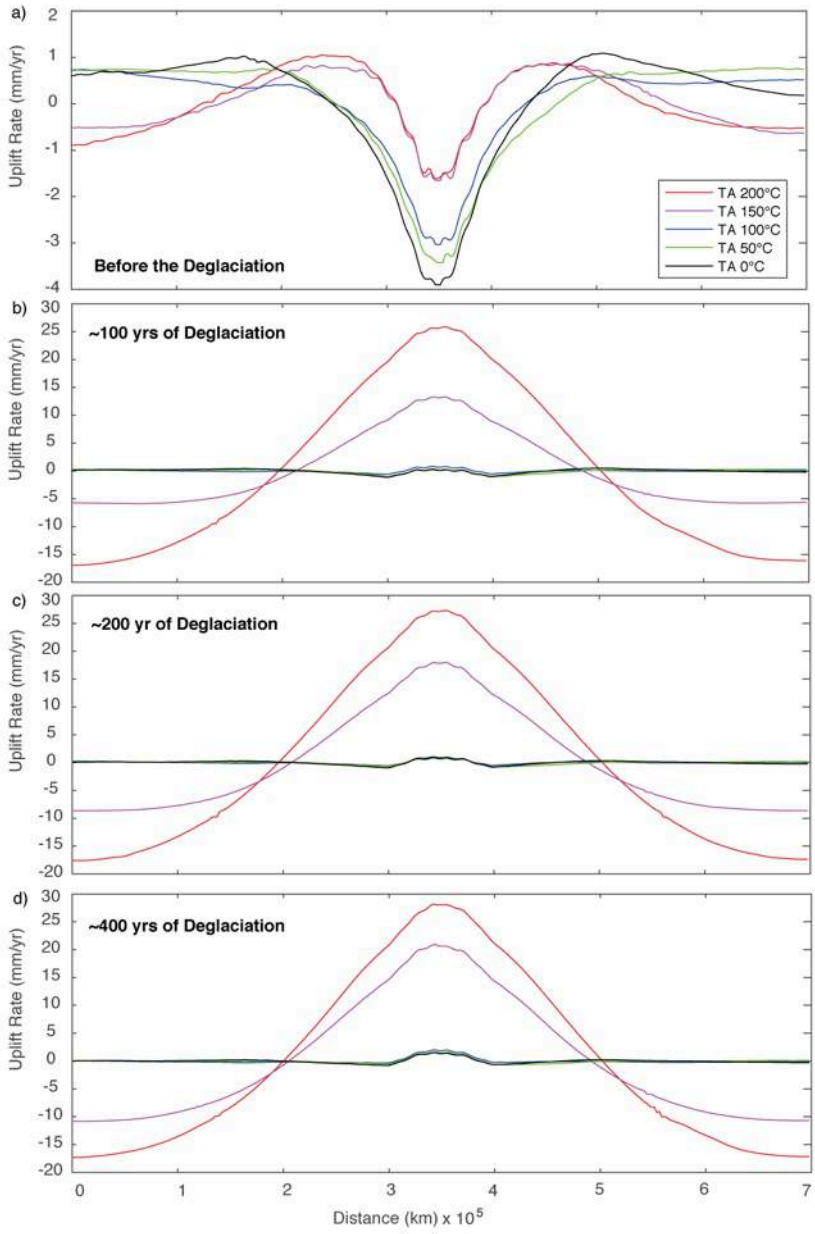

Fig. 4. Surface uplift rates vs. distance in the model domain for the post-LIA 400 years of deglaciation. A) Before the beginning of deglaciation; B) t = ~100 years of deglaciation; C) t = ~200 years of deglaciation; D) t = ~400 years of deglaciation. Different line colors correspond to the thermal anomaly (TA) imposed at the asthenosphere.

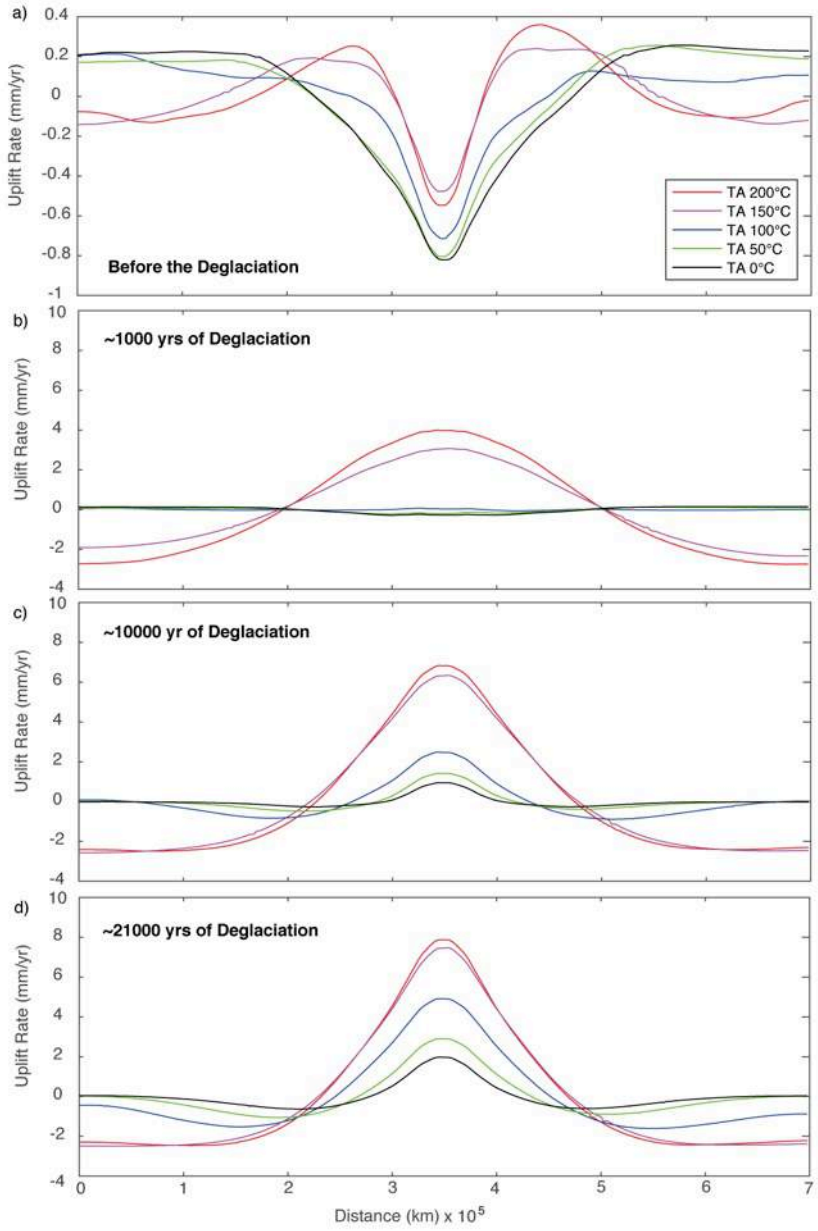

Fig. 5. Surface uplift rates vs. distance in the model domain for the post-LGM 21000 years of deglaciation. A) Before the beginning of deglaciation; B) t = ~1000 years of deglaciation; C) t = ~10000 years of deglaciation; D) t = ~210000 of deglaciation. Different line colors correspond to the imposed asthenospheric thermal anomaly (TA).

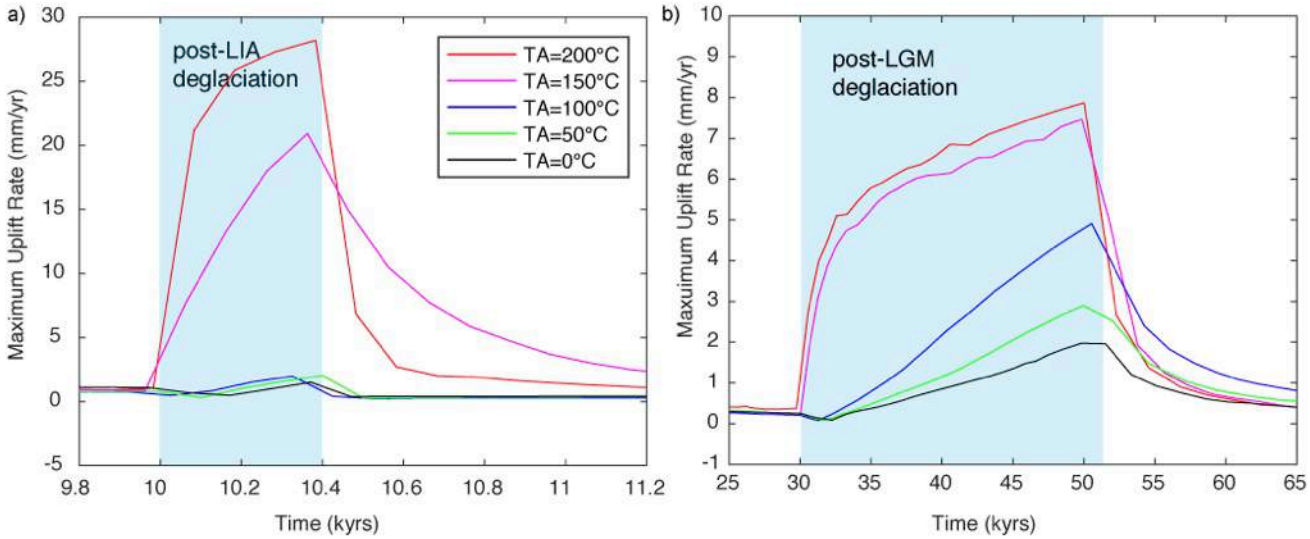

Fig. 6. Maximum uplift rates vs. time for each simulation with different asthenospheric thermal anomalies (TA). A) Simulations for the post-LIA deglaciation accounting for a drop of the glacier thickness of 100 m in 400 years, highlighted in blue; B) Simulations for the post-LGM deglaciation accounting for a drop of the glacier thickness of 1500 m in 21000 years, highlighted in blue.

4. Discussion

Our modelling is simplistic in that we impose a linear and uniform ice loss instead of a more realistic ice-sheet melting pattern in space and time. This choice is due to the fact that actual data reporting on the SPI melting velocities and associated redistribution of the surface masses cover time spans much shorter than the post-LIA and post-LGM time windows investigated here (Anyia et al., 1996, 1997; Rignot et al., 2003; Ivins and James, 2004; Willis et al., 2012). As previously highlighted (Hulton et al., 2002; Rabassa et al., 2008, 2011; Glasser et al., 2011; Davis and Glasser, 2012; Bendle et al., 2017), constraints regarding the ice-sheet mass balance and melting velocities throughout the time windows of interest are difficult to obtain from the preserved geomorphological, stratigraphic and geochronological records. We also assume a homogeneous lithosphere and neglect lateral viscosity variations in the mantle (Klemann et al., 2007), which is obviously an oversimplification given the long-term southern Andean orogenic history and present-day configuration (Cande and Leslie, 1986; Ramos, 2005). However, our fully coupled numerical thermo-mechanical geodynamic models provide realistic uplift rates that one can compare to observations bearing these limitations in mind. Following the example of previous studies (Ivins and James, 1999, 2004; Klemann et al., 2007; Dietrich et al., 2010; Lange et al., 2014), we discuss our results assuming that GPS-measured rock uplift rates are mostly related to the deglaciation history and only marginally controlled by longer term geodynamics.

It is noteworthy that surface uplift rates inferred from experiments without asthenospheric thermal anomaly are comparable to uplift rates measured in collisional orogens such as the European Alps (Sue et al., 2007; Serpelloni et al., 2013; Walpersdorf et al., 2015) and the Himalayas (Larson et al., 1999). As these collisional orogens are characterized by a thicker lithosphere (Geissler et al., 2010; Ravikumar et al., 2020), they are likely less sensitivity to mantle dynamics than the southern Patagonian Andes (Ivins and James, 1999, Klemann et al., 2007). In the European Alps post-LGM deglaciation is responsible for some 50% of the present day uplift rates (Sternai et al. 2019), but other sources of uplift exist such as slab break-off and asthenospheric upwelling (Handy et al, 2015; Fox et al., 2016; Sternai et al., 2019). High uplift rates (>25 mm/yr) inferred from our experiments with an asthenospheric thermal anomaly between 150-200 °C are comparable to uplift rates measured in non-collisional regions such as in Alaska (Larsen et al., 2005) and Greenland (Khan et al., 2007). In both these regions, high uplift rates are ascribed to post-LIA deglaciation, but a low viscosity asthenosphere (<10^{20} Pa s) is required to reach up to such values (Larsen et al., 2005). We remark, however, that assuming that high uplift rates are associated only to short lived and recent deglaciation episodes may be erroneous considering that the mantle relaxation time after load/unload episodes may reach up to 10^5 years (Turcotte and Schubert, 2002). The maximum uplift rate reached with high TA (150-200 °C) during post-LIA deglaciation is between 25 and 30 mm/yr, still lower than the maximum uplift rate measured by GPS in the SPI region (Dietrich et al., 2010, Langue et al., 2014). Under the same thermal conditions, the maximum uplift rate reached for the post-LGM deglaciation is of ~8 mm/yr. Therefore, our results suggest both long- and short-term deglaciation contribute to the present-day uplift rate, the magnitude of which is primarly controlled by the low-viscosity asthenospheric window due to high mantle potential temperatures.

Further support to this conclusion is provided by estimates of the mantle relaxation time, τ_r, as (Turcotte and Schubert, 2002):

$$(11)\,\tau_r = \frac{4\pi v}{g\lambda}$$

where v is the asthenosphere viscosity, λ is the width of the ice sheet, and g is the gravity acceleration. Substituting mantle viscosities between 10^{16} and 10^{18} Pa s and a glacier width of 70 km in Eq. 11 leads to between ~ 6000 and 600000 years of mantle relaxation time. This time range is considerably longer than the post-LIA deglaciation and includes full Pleistocene glacial-interglacial cycles (Ruddiman and Raymo, 1986). Additionally, our numerical simulations show that a short time of deglaciation such as during the 400 years of

post-LIA is not enough to stabilize the asthenospheric flow when the asthenosphere has a high viscosity (Fig. 3 a). The time for the mantle to respond to unload generated by deglaciation is of ~10000 years as shown in the post-LGM simulation for a TA = 0 °C (Fig. 3 c). This lead us to interpret a glacial rebound caused not only since the LIA but also since the LGM and possibly since longer deglaciation cycles recorded in Patagonia (e.g., Rabassa et al., 2008).

The thermal control on mantle viscosity accounts an increase of 2 to 14 times of the maximum uplift rate if comparing TA ≤100 °C with TA ≥ 150 °C. A thermal increase higher than 200 °C, however, seems unrealistic, given that it would decrease the mantle viscosities to less than 10^{16} Pa s, which is already an extreme value if we compare with standard asthenospheric viscosities (Turcotte and Schubert, 2002) and regions over an asthenospheric widow such as the southern Patagonian Andes (Ivins and James, 1999; Robertson Maurice and Wiens, 2003; Klemann et al., 2007; Lange et al., 2014; Ávila and Dávila, 2018). We thus limit our results to the thermal asthenospheric anomaly of 200 °C, and conclude that the asthenospheric window role for the fast surface uplift rates is not only that of producing 'dynamic' uplift as previously defined and estimated (Conrad and Husson, 2009; Guillaume et al., 2009), but also by decreasing mantle viscosity and generating additional heat in the lithosphere.

5. Conclusions

Thermo-mechanical numerical modelling suggests that fast postglacial rebound in the Patagonian Ice Sheets are to a large extent controlled by abnormally high sub-lithospheric temperatures by 150-200 °C due to the asthenospheric window underneath the Patagonian Andes. Such thermal anomaly decreases the asthenospheric viscosity to 10^{16}-10^{18} Pa s, allowing surface uplift rates by post-LIA isostatic rebound to reach values around 25 mm/yrs and surface uplift rates by post-LGM isostatic rebound to reach values around 25 mm/yrs, thereby filling the outstandingly high observational budget (~40 mm/yr).

Supplementary Material

Supplementary Table 1 – Material properties used in the numerical experiments.

	P_0^s (km/m^3)	E_a (kJ/mol)	V_a (m^3/mol)	n	C (Mpa)	Visc. flow law	Sin (ϕ_{eff})	c (W/m/K)	μ (Gpa)	C_p (J/kg/K)	Hr (µW/m^3)	H_l (kJ/kg)	α (1/k)	β (1/Pa)
Crust	2800	154	0	2.3	10	Wet Qz.	0.2	0.64+807/(T+77)	10	1000	1	300	3x10^{-5}	1x10^{-11}
Lithospheric mantle	3250	532	10	3.5	10	Dry Ol.	0.6	0.73+1293/(T+77)	67	1000	0.022	400	3x10^{-5}	1x10^{-11}
Asthenospheric mantle	3250	532	10	3.5	10	Dry Ol.	0.6	0.73+1293/(T+77)	67	1000	0.022	400	3x10^{-5}	1x10^{-11}
Ice	920	154	0	2.3	10		0	0.73+1293/(T+77)	67	1000	0.022	400	3x10^{-5}	1x10^{-11}

ρ_l^0 is the standard densities of solid rocks; E_a is the activation energy; V_a is the activation volume; $\boldsymbol{n}$ is the stress exponent; $\boldsymbol{C}$ is cohesion; φ is the effective internal friction angle; $\boldsymbol{C_p}$ is the specific heat capacity; $\boldsymbol{c}$ is thermal conductivity; μ is the shear modulus; $\boldsymbol{H_r}$ and $\boldsymbol{H_l}$ are the radiogenic and latent heat productions, respectively; α is thermal expansion; β is compressibility. Qz and Ol are quartzite and olivine, respectively. All rheological and partial melting laws/parameters are based on experimental rock mechanics and petrology (Ranalli, 1995; Hirschmann, 2000; Johannes, 1985; Turcotte, 2002).

References – Chapter 5

Aniya, M. (1996). Holocene variations of Ameghino glacier, southern Patagonia. *The Holocene*, *6*(2), 247-252.

Aniya, M., Sato, H., Naruse, R., Skvarca, P., & Casassa, G. (1997). Recent glacier variations in the Southern Patagonia icefield, South America. *Arctic and Alpine Research*, *29*(1), 1-12.

Ávila, P., & Dávila, F. M. (2018). Heat flow and lithospheric thickness analysis in the Patagonian asthenospheric windows, southern South America. *Tectonophysics*, *747*, 99-107.

Bendle, J. M., Palmer, A. P., Thorndycraft, V. R., & Matthews, I. P. (2017). High-resolution chronology for deglaciation of the Patagonian Ice Sheet at Lago Buenos Aires (46.5 S) revealed through varve chronology and Bayesian age modelling. *Quaternary Science Reviews*, *177*, 314-339.

Boex, J., Fogwill, C., Harrison, S., Glasser, N. F., Hein, A., Schnabel, C., & Xu, S. (2013). Rapid thinning of the late Pleistocene Patagonian Ice Sheet followed migration of the Southern Westerlies. *Scientific Reports*, *3*(1), 1-6.

Bourgois, J., Cisternas, M. E., Braucher, R., Bourlès, D., & Frutos, J. (2016). Geomorphic records along the general Carrera (Chile)–Buenos Aires (Argentina) glacial lake (46–48 S), climate inferences, and glacial rebound for the past 7–9 ka. *The Journal of Geology*, *124*(1), 27-53.

Breitsprecher, K., & Thorkelson, D. J. (2009). Neogene kinematic history of Nazca–Antarctic–Phoenix slab windows beneath Patagonia and the Antarctic Peninsula. *Tectonophysics*, *464*(1-4), 10-20.

Burov, E. B., & Diament, M. (1995). The effective elastic thickness (T e) of continental lithosphere: What does it really mean?. *Journal of Geophysical Research: Solid Earth*, *100*(B3), 3905-3927.

Cande, S. C., & Leslie, R. B. (1986). Late Cenozoic tectonics of the southern Chile trench. *Journal of Geophysical Research: Solid Earth*, *91*(B1), 471-496.

Champagnac, J. D., Molnar, P., Anderson, R. S., Sue, C., & Delacou, B. (2007). Quaternary erosion-induced isostatic rebound in the western Alps. *Geology*, *35*(3), 195-198.

Conrad, C. P., & Husson, L. (2009). Influence of dynamic topography on sea level and its rate of change. *Lithosphere*, *1*(2), 110-120.

Davies, B. J., & Glasser, N. F. (2012). Accelerating shrinkage of Patagonian glaciers from the Little Ice Age (~ AD 1870) to 2011. *Journal of Glaciology*, *58*(212), 1063-1084.

Dietrich, R., Ivins, E. R., Casassa, G., Lange, H., Wendt, J., & Fritsche, M. (2010). Rapid crustal uplift in Patagonia due to enhanced ice loss. *Earth and Planetary Science Letters*, *289*(1-2), 22-29.

England, P., & Molnar, P. (1990). Surface uplift, uplift of rocks, and exhumation of rocks. *Geology*, *18*(12), 1173-1177.

Fox, M., Herman, F., Willett, S. D., & Schmid, S. M. (2016). The exhumation history of the European Alps inferred from linear inversion of thermochronometric data. *American Journal of Science*, *316*(6), 505-541.

Georgieva, V., Melnick, D., Schildgen, T. F., Ehlers, T. A., Lagabrielle, Y., Enkelmann, E., & Strecker, M. R. (2016). Tectonic control on rock uplift, exhumation, and topography above an oceanic ridge collision: Southern Patagonian Andes (47 S), Chile. *Tectonics*, *35*(6), 1317-1341.

Gerya, T. (2019). *Introduction to numerical geodynamic modelling*. Cambridge University Press.

Gerya, T. V., & Yuen, D. A. (2007). Robust characteristics method for modelling multiphase visco-elasto-plastic thermo-mechanical problems. *Physics of the Earth and Planetary Interiors*, *163*(1-4), 83-105.

Geissler, W. H., Sodoudi, F., & Kind, R. (2010). Thickness of the central and eastern European lithosphere as seen by S receiver functions. *Geophysical Journal International*, *181*(2), 604-634.

Glasser, N. F., Harrison, S., Jansson, K. N., Anderson, K., & Cowley, A. (2011). Global sea-level contribution from the Patagonian Icefields since the Little Ice Age maximum. *Nature Geoscience*, *4*(5), 303-307.

Glasser, N. F., Jansson, K. N., Harrison, S., & Rivera, A. (2005). Geomorphological evidence for variations of the North Patagonian Icefield during the Holocene. *Geomorphology*, *71*(3-4), 263-277.

Glasser, N., & Jansson, K. (2008). The glacial map of southern South America. *Journal of Maps*, *4*(1), 175-196.

Guillaume, B., Martinod, J., Husson, L., Roddaz, M., & Riquelme, R. (2009). Neogene uplift of central eastern Patagonia: dynamic response to active spreading ridge subduction?. *Tectonics*, *28*(2).

Handy, M. R., Ustaszewski, K., & Kissling, E. (2015). Reconstructing the Alps–Carpathians–Dinarides as a key to understanding switches in subduction polarity, slab gaps and surface motion. International Journal of Earth Sciences, 104(1), 1-26.

Hein, A. S., Hulton, N. R., Dunai, T. J., Sugden, D. E., Kaplan, M. R., & Xu, S. (2010). The chronology of the Last Glacial Maximum and deglacial events in central Argentine Patagonia. *Quaternary Science Reviews*, *29*(9-10), 1212-1227.

Hirschmann, M. M. (2000). Mantle solidus: Experimental constraints and the effects of peridotite composition. *Geochemistry, Geophysics, Geosystems*, *1*(10).

Hulton, N. R., Purves, R. S., McCulloch, R. D., Sugden, D. E., & Bentley, M. J. (2002). The last glacial maximum and deglaciation in southern South America. *Quaternary Science Reviews*, *21*(1-3), 233-241.

Ivins, E. R., & James, T. S. (1999). Simple models for late Holocene and present-day Patagonian glacier fluctuations and predictions of a geodetically detectable isostatic response. *Geophysical Journal International*, *138*(3), 601-624.

Ivins, E. R., & James, T. S. (2004). Bedrock response to Llanquihue Holocene and present-day glaciation in southernmost South America. *Geophysical Research Letters*, *31*(24).

Johannes, W. (1985). The significance of experimental studies for the formation of migmatites. In: *Migmatites*, Ed. Ashworth, J. R. Blackie & Son Ltd, USA Chapman & Hall.

Kaufmann, G., Wu, P., & Wolf, D. (1997). Some effects of lateral heterogeneities in the upper mantle on postglacial land uplift close to continental margins. Geophysical Journal International, 128(1), 175-187.

Khan, S. A., Wahr, J., Stearns, L. A., Hamilton, G. S., van Dam, T., Larson, K. M., & Francis, O. (2007). Elastic uplift in southeast Greenland due to rapid ice mass loss. *Geophysical Research Letters*, *34*(21).

Klemann, V., Ivins, E. R., Martinec, Z., & Wolf, D. (2007). Models of active glacial isostasy roofing warm subduction: Case of the South Patagonian Ice Field. *Journal of Geophysical Research: Solid Earth*, *112*(B9).

Lagabrielle, Y., Scalabrino, B., Suarez, M., & Ritz, J. F. (2010). Mio-Pliocene glaciations of Central Patagonia: New evidence and tectonic implications. *Andean Geology*, *37*(2), 276-299.

Lange, H., Casassa, G., Ivins, E. R., Schröder, L., Fritsche, M., Richter, A., Groh, A., & Dietrich, R. (2014). Observed crustal uplift near the Southern Patagonian Icefield constrains improved viscoelastic Earth models. *Geophysical Research Letters*, *41*(3), 805-812.

Larsen, C. F., Motyka, R. J., Freymueller, J. T., Echelmeyer, K. A., & Ivins, E. R. (2005). Rapid viscoelastic uplift in southeast Alaska caused by post-Little Ice Age glacial retreat. *Earth and planetary Science letters*, *237*(3-4), 548-560.

Larson, K. M., Bürgmann, R., Bilham, R., & Freymueller, J. T. (1999). Kinematics of the India-Eurasia collision zone from GPS measurements. *Journal of Geophysical Research: Solid Earth*, *104*(B1), 1077-1093.

Martinod, J., Pouyaud, B., Carretier, S., Guillaume, B., & Hérail, G. (2016). Geomorphic Records along the General Carrera (Chile)–Buenos Aires (Argentina) Glacial Lake (46°–48° S), Climate Inferences, and Glacial Rebound for the Past 7–9 ka: A discussion. The Journal of Geology, 124(5), 631-635.

Mckenzie, D. A. N., & Bickle, M. J. (1988). The volume and composition of melt generated by extension of the lithosphere. *Journal of petrology*, *29*(3), 625-679.

Millan, R., Rignot, E., Rivera, A., Martineau, V., Mouginot, J., Zamora, R., Uribe, J., Lenzano, G., De Fleurian, B., Li, X., Gim, Y., & Kirchner, D. (2019). Ice thickness and bed elevation of the Northern and Southern Patagonian Icefields. *Geophysical Research Letters*, *46*(12), 6626-6635.

Mitrovica, J. X. (1996). Haskell [1935] revisited. *Journal of Geophysical Research: Solid Earth*, *101*(B1), 555-569.

Moreno, P. I., Denton, G. H., Moreno, H., Lowell, T. V., Putnam, A. E., & Kaplan, M. R. (2015). Radiocarbon chronology of the last glacial maximum and its termination in northwestern Patagonia. *Quaternary Science Reviews*, *122*, 233-249.

Muller, V. A., Sternai, P., Sue, C., Simon-Labric, T., & Valla, P. G. (2022). Climatic control on the location of continental volcanic arcs. *Scientific Reports*, *12*(1), 1-13.

Rabassa, J. (2008). Late cenozoic glaciations in Patagonia and Tierra del Fuego. *Developments in quaternary sciences*, *11*, 151-204.

Ramos, V. A. (2005). Seismic ridge subduction and topography: Foreland deformation in the Patagonian Andes. *Tectonophysics*, *399*(1-4), 73-86.

Ramos, V. A., & Kay, S. M. (1992). Southern Patagonian plateau basalts and deformation: backarc testimony of ridge collisions. *Tectonophysics*, *205*(1-3), 261-282.

Ranalli, G. (1997). Rheology of the lithosphere in space and time. *Geological Society, London, Special Publications*, *121*(1), 19-37.

Ravikumar, M., Singh, B., Pavan Kumar, V., Satyakumar, A. V., Ramesh, D. S., & Tiwari, V. M. (2020). Lithospheric density structure and effective elastic thickness beneath Himalaya and Tibetan Plateau: Inference from the integrated analysis of gravity, geoid, and topographic data incorporating seismic constraints. *Tectonics*, *39*(10), e2020TC006219.

Robertson Maurice, S. D., Wiens, D. A., Koper, K. D., & Vera, E. (2003). Crustal and upper mantle structure of southernmost South America inferred from regional waveform inversion. *Journal of Geophysical Research: Solid Earth*, *108*(B1).

Rignot, E., Rivera, A., & Casassa, G. (2003). Contribution of the Patagonia Icefields of South America to sea level rise. *Science*, *302*(5644), 434-437.

Ruddiman, W. F., Raymo, M., & McIntyre, A. (1986). Matuyama 41,000-year cycles: North Atlantic Ocean and northern hemisphere ice sheets. *Earth and Planetary Science Letters*, *80*(1-2), 117-129.

Serpelloni, E., Faccenna, C., Spada, G., Dong, D., & Williams, S. D. (2013). Vertical GPS ground motion rates in the Euro-Mediterranean region: New evidence of velocity gradients at different spatial scales along the Nubia-Eurasia plate boundary. *Journal of Geophysical Research: Solid Earth*, *118*(11), 6003-6024.

Steinberger, B., & O'Connell, R. J. (1998). Advection of plumes in mantle flow: implications for hotspot motion, mantle viscosity and plume distribution. *Geophysical Journal International*, *132*(2), 412-434.

Sternai, P. (2020). Surface processes forcing on extensional rock melting. *Scientific reports*, *10*(1), 1-13.

Sternai, P., Sue, C., Husson, L., Serpelloni, E., Becker, T. W., Willett, S. D., Faccenna, C., Di Giulio, A., Spada, G., Jolivet, L., Valla, P., Petit, C., Nocquet, J.-M., Walpersdorf, A., & Castelltort, S. (2019). Present-day uplift of the European Alps: Evaluating mechanisms and models of their relative contributions. *Earth-Science Reviews*, *190*, 589-604.

Sue, C., Delacou, B., Champagnac, J. D., Allanic, C., & Burkhard, M. (2007). Aseismic deformation in the Alps: GPS vs. seismic strain quantification. *Terra Nova*, *19*(3), 182-188.

Thorndycraft, V. R., Bendle, J. M., Benito, G., Davies, B. J., Sancho, C., Palmer, A. P., .Fabel, D., Medialdea, A., & Martin, J. R. (2019). Glacial lake evolution and Atlantic-Pacific drainage reversals during deglaciation of the Patagonian Ice Sheet. *Quaternary Science Reviews*, *203*, 102-127.

Turcotte, D. L., & Schubert, G. (2002). *Geodynamics*. Cambridge university press.

Walpersdorf, A., Sue, C., Baize, S., Cotte, N., Bascou, P., Beauval, C., Collard, P, Daniel, G., Dyer, H., Grasso, J.-R., Hautecoeur, O., Helmstetter, A., Hok, S., Langlais, M., Menard, G., Mousavi, Z., Ponton, F., Rizza, M., Rolland, L., Souami, D., & Martinod, J. (2015). Coherence between geodetic and seismic deformation in a context of slow tectonic activity (SW Alps, France). *Journal of Geodynamics*, *85*, 58-65.

Watts, A. B. (2001). *Isostasy and Flexure of the Lithosphere*. Cambridge University Press.

Willis, M. J., Melkonian, A. K., Pritchard, M. E., & Rivera, A. (2012). Ice loss from the Southern Patagonian ice field, South America, between 2000 and 2012. *Geophysical research letters*, *39*(17).

Chapter 6. Conclusions and Future Perspectives

This thesis includes several aspects of the geologic history of the Southern and the Patagonian Andes from the onset of Andean orogeny to present-day, focusing on the coupling between tectonic and climate processes. In the first two studies, I used the geo-thermochronologic methods U-Pb, $^{40}Ar/^{39}Ar$, and (U-Th-Sm)/He to constrain the time, depths, and rates of rock burial and exhumation, disentangling the tectonic/mantle from the climatic contribution to mountain building. In the last two studies, I used geodynamic numerical modelling to explore the thermo-mechanical coupling between erosion, strain, volcanism, deglaciation, mantle flow, and rock uplift. These studies were based on the Quaternary to present-day distribution of volcanoes and ice caps in the Southern and Patagonian Andes constrained by vertical GPS, seismic tomography, and low-temperature thermochronology data. Results show new mechanisms of tectonic and climate coupling, such as orography and volcanic arc location, and mantle potential temperatures and rock uplift, which can apply to other mountain and volcanic belts.

It is established that the one of main geological links between tectonics and climate is erosion which, by generating differential spatio-temporal unload at surface, exerts an important control of the distribution of lithospheric strain, uplift, and exhumation (Willet et al., 1999, Whipple and Tucker, 1999, Beaumont et al., 2001; Whipple and Meade, 2004). Through a comparative analysis of the Southern Andes and Cascade Range, we further recognize that asymmetric erosion caused by enhanced precipitation on the orographic side of mountain belts can force a windward migration not only of the strain, but also of the magma ascent, consequently localising volcanic activity on the more eroded side of the belt (Muller et al., 2022). This result is important because it shows for the first time that a climate forcing on volcanic activity occurs not only by deglaciation and sea-level changes (Jull and McKenzie, 1996; Geier and Bindeman, 2011; Sternai et al., 2016, 2020), but also due to orography (Muller et al., 2022).

The Patagonian-Magallanes fold-and-thrust belt is an example of continent-ward verging belt formed between ca. 83 to 70 Ma after a period of extension in the backarc Rocas Verdes Basin between ca. 160 and 125 Ma (Muller et al., 2021). Our geochronologic and thermodynamic modelling results show that the internal zones of the Patagonian fold-and-thrust belt were buried down to 23 km depth beneath the pre-Late Cretaceous magmatic arc, and then exhumed to about 10 km between ca. 73 – 70 Ma (Muller et al., 2021). The heritage of the Late Cretaceous compression controls the deformation style in the Andean subduction

margin, characterised by intense deformation in the retro-wedge rather than in the pro-wedge (Fig. 1 b, c; Echaurren et al., 2022). These results are difficult to reconcile with analytical and numerical models of e.g., Willett, 1999, predicting the effects of orography on the wedge deformation and exhumation patterns (see Chapter 1, Fig. 2). Since this was the initial orogenic phase of the deformation in the southern Patagonia Andes, as well as in most of the other orogenic sector of the Andes (Fig. 1 a, Horton et al., 2018), we suggest that the effects of orography were negligible at that time, and tectonics was the major control on the distribution of strain and exhumation within the orogenic wedge (Horton et al., 2018; Val and Willenbring, 2022).

We recognize a Late Cenozoic partitioning between tectonic and climatic processes in controlling the exhumation pattern based on zircon and apatite (U-Th-Sm)/He thermochronometers (Muller et al., in prep. a). For the first time, we are able to distinguish and quantify the contribution of ridge subduction and the onset of Patagonian glaciation to the exhumation of the Patagonian Andes, as ~ 1 km/Ma between 10.5 and 8.5 Ma and ~ 0.6 – 3 km/Ma between 6.5 and 4.5 Ma, respectively. We further recognize that the effects of glaciation on rock exhumation are not uniform and seem to depend on the glacier's thickness and temperature. The episode of quiescence of rock exhumation between 6-4.5 to 3-0.5 Ma (Muller et al., in prep. a; Fosdick et al., 2013; Guillaume et al., 2013; Georgieva et al., 2016, 2019; Willett, 2020) from 46 to 51 °S suggest glacier's shielding of the Patagonian Ice Sheet, in accordance with the hypothesis of glaciation as a constructive control on mountain building (Thomson et al., 2010). Increased glacial erosion in the Quaternary involved a transition from thick protective glaciers to narrow effectively erosional glacial valleys. Enhanced Quaternary rock exhumation rates in different sectors of the southern Patagonian Andes are similar to other glaciated orogens such as the European Alps and the New Zealand Alps, suggesting a global change in the glacial-interglacial cyclicity in the Quaternary (Valla et al., 2011; Shuster et al., 2011).

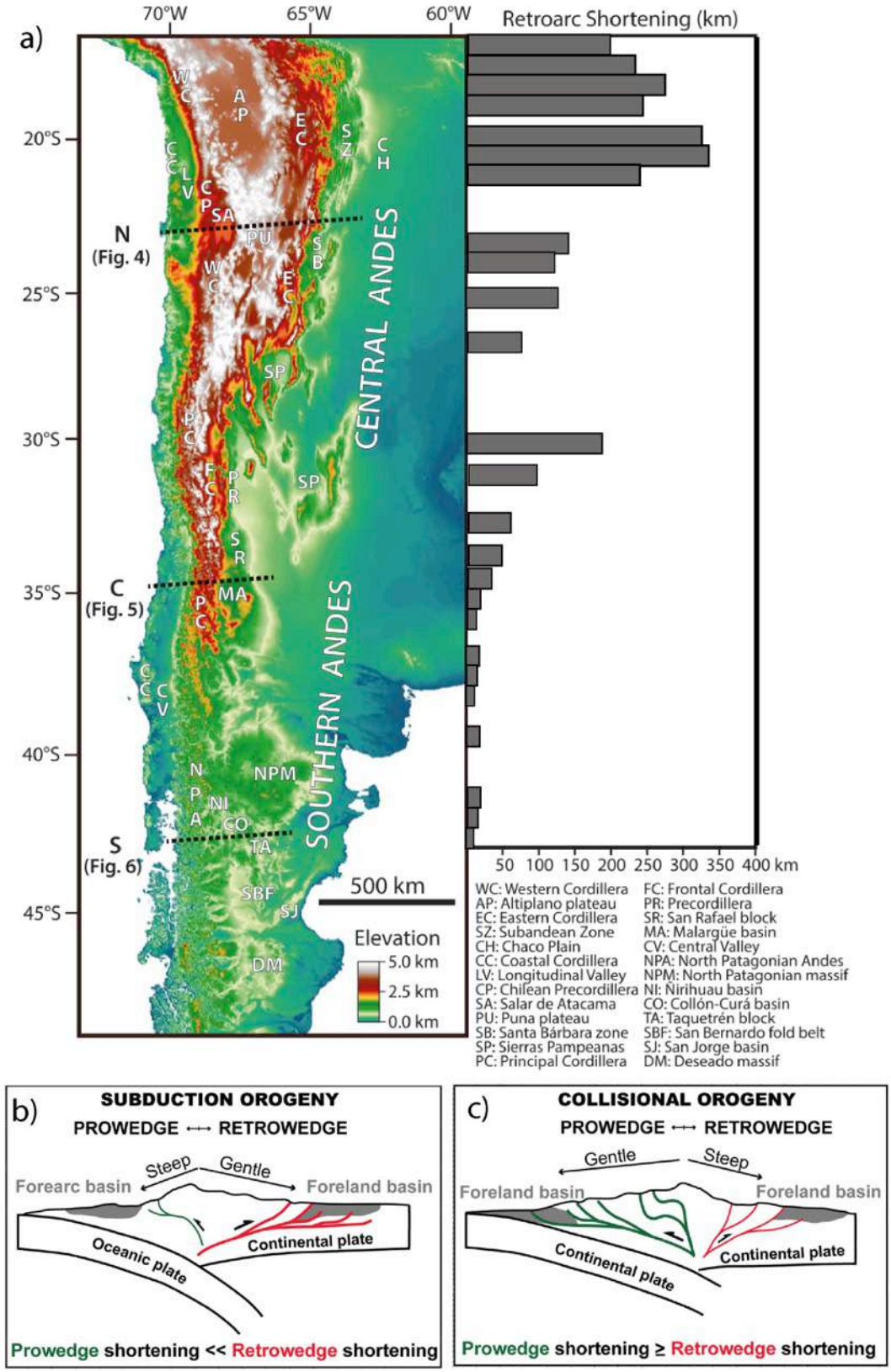

Fig. 1. a) Digital elevation map with plot of the retroarc crustal shortening along the strike of the Central and Southern Andes (Horton et al., 2018 and references therein). b) Schematic orogenic wedges in subduction (c) and collisional (b) orogens (Echaurren et al., 2022), showing the systematic difference in the localisation of deformation between the two orogenic types. The subduction orogens tend to concentrate the deformation in the retro-wedge, whereas collisional orogens tend to develop doubly-vergent orogenic wedges.

Our results from numerical geodynamic modelling show that mantle potential temperatures from the asthenospheric window control the magnitude of present-day high uplift rates due to post-glacial rebound in the southern Patagonian Andes (~ 40 mm/yr) (Muller et al., in prep. b). A minimal thermal anomaly of 150 °C of the mantle potential temperature is necessary to reduce the asthenosphere viscosity to less than 10^{18} Pa s and generate rock uplift rates of the order of tens of mm/yr, highlighting the relevance of deep-Earth conditions in setting surface displacements. Also, we test the effects of the post- Last Glacial Maximum deglaciation and conclude that long-term post-glacial rebound contributes to increase the uplift rates, and not only short-term deglaciation such as the post- Little Ice Age deglaciation. This kind of mechanism has operated also in the glacial-interglacial cycles during the Late Cenozoic thus having a role also in the long-term history of rock uplift and exhumation of the Torres del Paine and Fitz Roy massifs.

Mountain ranges like the Andes, the North American Cordillera, the Himalayas and the European Alps control global atmospheric and oceanic circulation affecting climate and ecology over millions of years (Ruddiman and Kutzbach, 1989). As shown throughout this thesis, orography, partitioning between glacial and fluvial erosion, subduction, and mantle dynamics play a role in mountain building. I focused on the long-lived tectonic and climatic history of a subdcution orogen, but the tectonic and climatic interactions addressed here take place also in collisional orogens. As in the Fitz Roy and Torres del Paine massifs of the southern Patagonian Andes, the external and the internal crystalline massifs of the Western Alps form high topographic relief in a glacial environment. They were exhumed betweeen ~35 to 20 Ma by crustal scale shortening structures due to collision between the European and the Adria plates, after oceanic subduction (Handy et al., 2010; Stüwe and Schuster, 2010; Rubatto et al., 2011; Schmid and Kissling, 2000; Lipptisch et al., 2003; Schimd et al., 2004; Rosenberg et al., 2018; Manzotti et al., 2018). The Western Alps were also subject to rapid exhumation since ~5 Ma, which is associated to glaciation, slab break-off, mantle upwelling and crustal tectonics (e.g., Delacou et al., 2004; Sue et al., 2007; Valla et al., 2011; Glotzbach et al., 2011; Fox et al., 2015, 2016; Sternai et al., 2019). However, there are several uncertainties regarding the rates and timing of deep-seated and surface processes that exhume these complexes. In my future projects, I envisage comparative analyses using available and newly produced data from subduction and collisional orogens to further elucidate the partitioning between climate-controlled erosion and lithospheric structures in exhuming crystalline complexes, and affecting the architecture of orogenic wedges.

To do this, I want to produce new geo-thermochronological data togheter with a stratigraphically controlled field work, to quantitatively constrain rates and depths of burial and exhumation periods in other orogenic settings. I then want to apply new geodynamic thermo-mechanical (e.g., Gerya, 2019; Sternai, 2020, Muller et al., 2022) and landscape evolution (e.g., Braun and Willett, 2013; Croissant and Braun, 2014) numerical models accounting for subduction and continental collision, to test how the geometry and coupling between the plates, mantle dynamics, and fluvial and glacial erosion, affect the topographic expressions of orogenic processes (Fig. 2). The objective is to isolate the effects of tectonic and surface processes, and track, for example, the pressure and temperature of specific markers during tectonic and surface processes, and the evolution of erosion-exhumation rates at surface (Fig. 2). Proposed studies are to decouple the mantle, the tectonic and the climate contributions to the exhumation of the crystalline massifs of the European Alps, Southern Patagonia, Himalaya, and Cascade Range. Like this, I want to contribute to advance the state-of-the art of geo-thermochronoligcal methods and their application to understand and the mechanisms of mountain building and basin generation, eventually linking this knowledge to new urgent research areas such as energy and water resources and natural hazards.

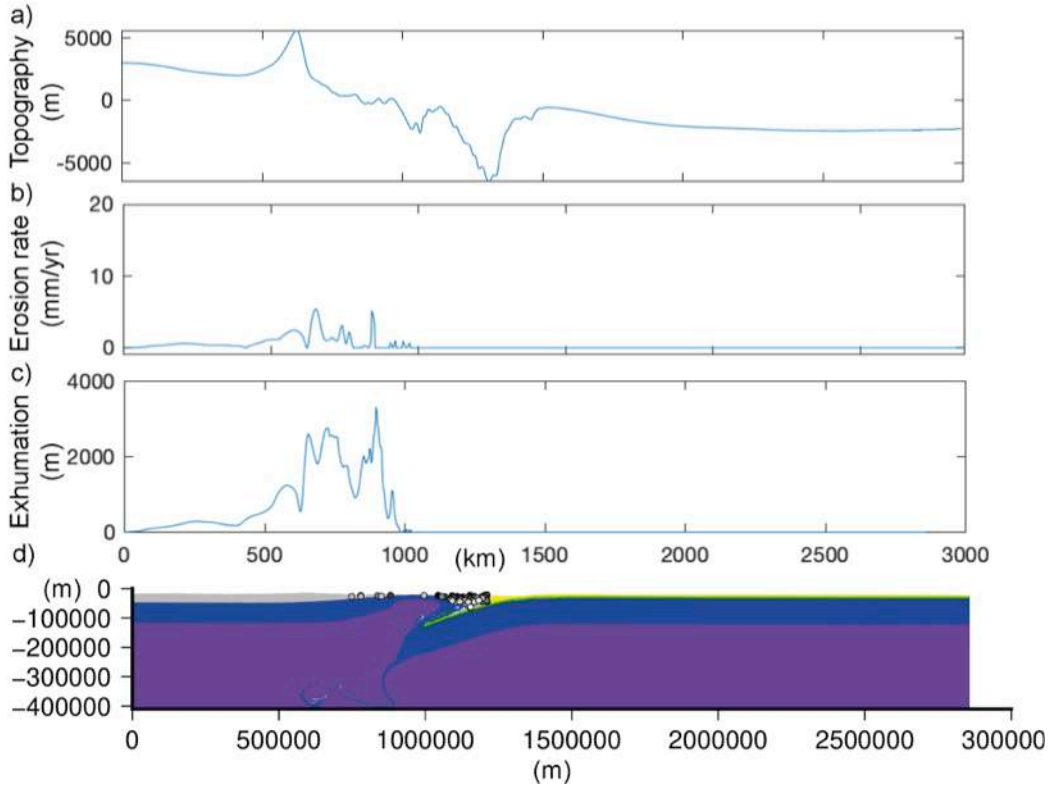

Fig. 2: Example of preliminary test of 2D coupled geodynamic and surface thermo-mechanical numerical model, where the stream-power erosion is coupled to a subduction setting, the circles in the lower panel are markers which are used to track P-T-t paths during the model evolution. The bottom panel show Earth layer's distribution and markers (a), the upper panels show the topography (b), erosion rate (c), and exhumation (d) calculated from the movement of markers.

References – Chapter 6

Braun, J., & Willett, S. D. (2013). A very efficient O (n), implicit and parallel method to solve the stream power equation governing fluvial incision and landscape evolution. *Geomorphology*, *180*, 170-179.

Croissant, T., & Braun, J. (2014). Constraining the stream power law: a novel approach combining a landscape evolution model and an inversion method. *Earth surface dynamics*, *2*(1), 155-166.

Delacou, B., Sue, C., Champagnac, J. D., & Burkhard, M. (2004). Present-day geodynamics in the bend of the western and central Alps as constrained by earthquake analysis. *Geophysical Journal International*, *158*(2), 753-774.

Echaurren, A., Encinas, A., Sagripanti, L., Gianni, G., Zambrano, P., Duhart, P., & Folguera, A. (2022). Fore-to-retroarc crustal structure of the north Patagonian margin: How is shortening distributed in Andean-type orogens?. *Global and Planetary Change*, *209*, 103734.

Fosdick, J. C., Grove, M., Hourigan, J. K., & Calderon, M. (2013). Retroarc deformation and exhumation near the end of the Andes, southern Patagonia. *Earth and Planetary Science Letters*, *361*, 504-517.

Fox, M., Herman, F., Kissling, E., & Willett, S. D. (2015). Rapid exhumation in the Western Alps driven by slab detachment and glacial erosion. *Geology*, *43*(5), 379-382.

Fox, M., Herman, F., Willett, S. D., & Schmid, S. M. (2016). The exhumation history of the European Alps inferred from linear inversion of thermochronometric data. *American Journal of Science*, *316*(6), 505-541.

Georgieva, V., Gallagher, K., Sobczyk, A., Sobel, E. R., Schildgen, T. F., Ehlers, T. A., & Strecker, M. R. (2019). Effects of slab-window, alkaline volcanism, and glaciation on thermochronometer cooling histories, Patagonian Andes. *Earth and Planetary Science Letters*, *511*, 164-176.

Georgieva, V., Melnick, D., Schildgen, T. F., Ehlers, T. A., Lagabrielle, Y., Enkelmann, E., & Strecker, M. R. (2016). Tectonic control on rock uplift, exhumation, and topography above an oceanic ridge collision: Southern Patagonian Andes (47 S), Chile. *Tectonics*, *35*(6), 1317-1341.

Gerya, T. (2019). *Introduction to numerical geodynamic modelling*. Cambridge University Press.

Geyer, A., & Bindeman, I. (2011). Glacial influence on caldera-forming eruptions. *Journal of Volcanology and Geothermal Research*, *202*(1-2), 127-142.

Glotzbach, C., van der Beek, P. A., & Spiegel, C. (2011). Episodic exhumation and relief growth in the Mont Blanc massif, Western Alps from numerical modelling of thermochronology data. *Earth and Planetary Science Letters*, *304*(3-4), 417-430.

Guillaume, B., Gautheron, C., Simon-Labric, T., Martinod, J., Roddaz, M., Douville, E. (2013). Dynamic topography control on Patagonian relief evolution as inferred from low temperature thermochronology. Earth Planet. Sci. Lett. 364, 157–167. https://doi.org/10.1016/j.epsl.2012.12.036.

Handy, M. R., Schmid, S. M., Bousquet, R., Kissling, E., & Bernoulli, D. (2010). Reconciling plate-tectonic reconstructions of Alpine Tethys with the geological–geophysical record of spreading and subduction in the Alps. *Earth-Science Reviews*, *102*(3-4), 121-158.

Horton, B. K. (2018). Tectonic regimes of the central and southern Andes: Responses to variations in plate coupling during subduction. *Tectonics*, *37*(2), 402-429.

Jull, M., & McKenzie, D. (1996). The effect of deglaciation on mantle melting beneath Iceland. *Journal of Geophysical Research: Solid Earth*, *101*(B10), 21815-21828.

Lippitsch, R., Kissling, E., and Ansorge, J. (2003). Upper mantle structure beneath the Alpine orogen from high-resolution teleseismic tomography. *Journal of Geophysical Research- Solid Earth*, v. 108, n. B8, http://dx.doi.org/10.1029/2002JB002016

Manzotti, P., Bosse, V., Pitra, P., Robyr, M., Schiavi, F., & Ballèvre, M. (2018). Exhumation rates in the Gran Paradiso Massif (Western Alps) constrained by in situ U–Th–Pb dating of accessory phases (monazite, allanite and xenotime). *Contributions to Mineralogy and Petrology*, *173*, 1-28.

Muller V.A.P., Sternai P., Sue C. (in prep. b) The role of the asthenospheric window and deglaciation on the present-day uplift of the southern Patagonian Andes.

Muller V.A.P., Sue C. Valla P., Sternai P., Simon-Labric T., Martinod J., Ghiglione M., Baumgartner L., Herman F., Reiners P., Gautheron C., Grujic D., Shuster D., Braun J. (in prep. a) Exhumation response to climate, tectonic and mantle forcing in the southern Patagonian Andes (Torres del Paine and Fitz Roy plutonic complexes).

Muller, V. A., Calderón, M., Fosdick, J. C., Ghiglione, M. C., Cury, L. F., Massonne, H. J., Fannin, C. M., Warren, C., Ramírez de Arellano, C. & Sternai, P. (2021). The closure of the Rocas Verdes Basin and early tectono-metamorphic evolution of the Magallanes Fold-and-Thrust Belt, southern Patagonian Andes (52–54° S). *Tectonophysics*, *798*, 228686.

Muller, V. A., Sternai, P., Sue, C., Simon-Labric, T., & Valla, P. G. (2022). Climatic control on the location of continental volcanic arcs. *Scientific Reports*, *12*(1), 1-13.

Rosenberg, C. L., Schneider, S., Scharf, A., Bertrand, A., Hammerschmidt, K., Rabaute, A., & Brun, J. P. (2018). Relating collisional kinematics to exhumation processes in the Eastern Alps. *Earth-Science Reviews*, *176*, 311-344.

Rubatto, D., Regis, D., Hermann, J., Boston, K., Engi, M., Beltrando, M., & McAlpine, S. R. (2011). Yo-yo subduction recorded by accessory minerals in the Italian Western Alps. *Nature Geoscience*, *4*(5), 338-342.

Ruddiman, W. F., & Kutzbach, J. E. (1989). Forcing of late Cenozoic northern hemisphere climate by plateau uplift in southern Asia and the American West. *Journal of Geophysical Research: Atmospheres*, *94*(D15), 18409-18427.

Schmid, S. M., & Kissling, E. (2000). The arc of the western Alps in the light of geophysical data on deep crustal structure. *Tectonics*, *19*(1), 62-85.

Schmid, S. M., Fügenschuh, B., Kissling, E., and Schuster, R. (2004). Tectonic map and overall architecture of the Alpine orogen. *Eclogae Geologicae Helvetiae*, v. 97, n. 1, p. 93–117, http://dx.doi.org/10.1007/ s00015-004-1113-x

Shuster, D. L., Cuffey, K. M., Sanders, J. W., & Balco, G. (2011). Thermochronometry reveals headward propagation of erosion in an alpine landscape. *Science*, *332*(6025), 84-88.

Sternai, P. (2020). Surface processes forcing on extensional rock melting. *Scientific reports*, *10*(1), 1-13.

Sternai, P., Caricchi, L., Castelltort, S., & Champagnac, J. D. (2016). Deglaciation and glacial erosion: A joint control on magma productivity by continental unloading. *Geophysical Research Letters*, *43*(4), 1632-1641.

Sternai, P., Caricchi, L., Pasquero, C., Garzanti, E., van Hinsbergen, D. J., & Castelltort, S. (2020). Magmatic forcing of Cenozoic climate?. *Journal of Geophysical Research: Solid Earth*, *125*(1), e2018JB016460.

Sternai, P., Sue, C., Husson, L., Serpelloni, E., Becker, T. W., Willett, S. D., Faccenna, C., Di Giulio, A., Spada, G., Jolivet, L., Valla, P., Petit, C. Nocquet, J.-M, Walpersdorf, A., & Castelltort, S. (2019). Present-day uplift of the European Alps: Evaluating mechanisms and models of their relative contributions. *Earth-Science Reviews*, *190*, 589-604.

Stüwe, K., & Schuster, R. (2010). Initiation of subduction in the Alps: Continent or ocean?. *Geology*, *38*(2), 175-178.

Sue, C., Delacou, B., Champagnac, J. D., Allanic, C., & Burkhard, M. (2007). Aseismic deformation in the Alps: GPS vs. seismic strain quantification. *Terra Nova*, *19*(3), 182-188.

Thomson, S. N., Brandon, M. T., Tomkin, J. H., Reiners, P. W., Vásquez, C., & Wilson, N. J. (2010). Glaciation as a destructive and constructive control on mountain building. *Nature*, *467*(7313), 313-317.

Val, P., & Willenbring, J. K. (2022). Across-strike asymmetry of the Andes orogen linked to the age and geometry of the Nazca plate. *Geology*, *50*(12), 1341-1345.

Valla, P. G., Shuster, D. L., & Van Der Beek, P. A. (2011). Significant increase in relief of the European Alps during mid-Pleistocene glaciations. *Nature geoscience*, *4*(10), 688-692.

Watts, A. B. (2001). *Isostasy and Flexure of the Lithosphere*. Cambridge University Press.

Whipple, K. X. (2009). The influence of climate on the tectonic evolution of mountain belts. *Nature geoscience*, *2*(2), 97-104.

Whipple, K. X., & Meade, B. J. (2004). Controls on the strength of coupling among climate, erosion, and deformation in two-sided, frictional orogenic wedges at steady state. *Journal of Geophysical Research: Earth Surface*, *109*(F1).

Whipple, K. X., & Tucker, G. E. (1999). Dynamics of the stream-power river incision model: Implications for height limits of mountain ranges, landscape response timescales, and research needs. *Journal of Geophysical Research: Solid Earth*, *104*(B8), 17661-17674.

Willett, C. D., Ma, K. F., Brandon, M. T., Hourigan, J. K., Christeleit, E. C., & Shuster, D. L. (2020). Transient glacial incision in the Patagonian Andes from~ 6 Ma to present. *Science advances*, *6*(7), eaay1641.

Willett, S. D. (1999). Orogeny and orography: The effects of erosion on the structure of mountain belts. *Journal of Geophysical Research: Solid Earth*, *104*(B12), 28957-28981.

Acknowledgements

I acknowledge enormously my supervisor Pietro Sternai and my co-supervisor Christian Sue who provided me scientific, infrastructure, and psychological basis to do this PhD, with several opportunities of learning new techniques and scientific concepts, and interacting with other researchers. I thank them a lot for believe in my potential and the support to bring me to Europe, in Milan and in Grenoble, places that really become my home for these three years. I acknowledge a lot Prof. Pierre Valla who provided data and helped to supervise the thermochronology section of this thesis. Many thanks to Geologist Thibaud Simon-Labric who also provided data, support, and ideas for the orography and thermochronology sections of this thesis. Many thanks also to my Master's supervisor Mauricio Calderón, who brought me to the field in Patagonia and stayed connected during my PhD, helping to supervise the section of geochronology and petrology of this work. I acknowledge also Profs. Cécile Gautheron, Matthias Bernett, Josepth Martinod, and Laurent Husson for insightful discussions and help in the modelling and methodological development of this thesis. Finally I acknowledge Profs. Leonardo Cury and Anelize Bahniuk, who although not involved in this PhD project, provided me the basis of research in the Lamir Institute in Brazil, and provided me the initial opportunity of studying and going to Patagonia. I acknowledge the DISAT in the University of Milano-Bicocca and the ISTerre in the Universtié Grenoble Alps for the infrastructure to realize this PhD. I also thank the Erasmus program for the financial support to go to the Université Grenoble Alpes.

I acknowledge a lot my family, who supported me to do this PhD abroad and made me grow in a discovering environment with curiosity and exploration. They also helped me to keep strong in the difficult moments and stimulated me to continue in the path of research that I choose. I acknowledge my friends from Brazil that are an important reason of why I am passionate for Geology, and specially the ones who still follow my progress in science and life. I thank a lot the friends I did during this PhD, specially Sofia Locchi, Chiara Crippa, Melisa Mariel, Luis Antonio Cipriano Marcos, Malcon Celorio, Leoncio Cabrera, Marion Roger, Xiong Ou, Hester Blommaert, Victoria Mowbray, Annet Baken, Gino de Gelder, Lara Maldanis, Jacopo Targa, Lucca Castrogiovanni, Silvestro Lanciaprima, and Clara Rossi, who were always with me, when crying of happiness or sadness. I hope to continue strong on my passions thanks to all of you.

Veleda Astarte Paiva Muller

APPENDIX A – Article contribution 1

Effects of asthenospheric flow and orographic precipitation on continental rifting

Pietro Sternai[1], Veleda Astarte Paiva Muller[1], Laurent Jolivet[2], Eduardo Garzanti1, Giacomo Corti[3], Claudia Pasquero[1], Andrea Sembroni[4], Claudio Faccena[5]

[1] Department of Earth and Environmental Sciences, University of Milano-Bicocca, Italy
[2] Sorbonne Université, CNRS-INSU, Institut des Sciences de la Terre Paris, ISTeP, UMR 7193, Paris, France
[3] Consiglio Nazionale delle Ricerche, Istituto di Geoscienze e Georisorse, via G. La Pira, 4, 50121, Firenze, Italy
[4] Dipartimento di Beni Culturali, Università di Bologna, Bologna, Italy
[5] Dipartimento Scienze, Università Roma Tre, Rome, Italy

Abstract

Asthenosphere-lithosphere interactions modulated by surface processes generate outstanding topographies and sedimentary basins, but the nature of these interactions and the mechanisms through which they control the evolution of extensional tectonic settings are elusive. Basal lithospheric shearing due to plume-related mantle flow leads to extensional lithospheric rupturing and associated magmatism, rock exhumation, and topographic uplift away from the plume axis by a distance inversely proportional to the lithospheric elastic thickness. When moisturized air encounters a topographic barrier, it rises, decompresses, and saturates, leading to enhanced erosion on the windward side of the uplifted terrain. Orographic precipitation and asymmetric erosional unloading facilitate strain localization and lithospheric rupturing on the wetter and more eroded side of an extensional system. This simple analytical model is validated against petro-thermo-mechanical numerical experiments where a rheologically stratified lithosphere above an asthenospheric plume is subject to fluvial erosion proportional to stream power during extension. Our modelling results are consistent with Paleogene mantle upwelling and flood basalts in Ethiopia synchronous to distal initiation of lithospheric stretching/rupturing in the Gulf of Aden, which progressively propagates into the Red Sea. The present-day asymmetric topography and extensional structures in the Main Ethiopian Rift may also be an effect of a Neogene-to-present orographic erosional gradient. Although inherently related to the lithosphere rheology, the evolution of continental rifts appears even more conditioned by the mantle and surface dynamics than previously thought.

Keywords: asthenosphere-lithosphere interactions; orography; continental rifting; East African Rift system

1. Introduction

The topography of extensional tectonic settings raised fundamental questions regarding asthenospheric upwelling (e.g., Hager, et al., 1985; Lithgow-Bertelloni & Silver, 1998; Moucha & Forte, 2011), the mechanisms of continental stretching/breakup (e.g., Fitton, 1983; Buck, 1991), the lithosphere-asthenosphere boundary (e.g., Buck, 2004; Koptev, et al., 2015) and the lithosphere rheology (e.g., Ziegler & Cloetingh, 2004; Burov, 2011). On the one hand, heterogeneous inherited lithospheric structures affect the asthenospheric flow and produce complex, asymmetric topographies across these settings (e.g., Burov & Gerya, 2014; Koptev, et al., 2016). On the other hand, primary plumes rising from the core-mantle boundary through the lower mantle spread out variably at the 670 and 410 km discontinuities (e.g., Wilson, 1963; Condie, 2001; Courtillot, et al., 2003). The dynamic traction and thermal anomaly involved by the upwelling of primary plumes can trigger upwelling of secondary asthenospheric plumes in the upper mantle (e.g., Bijwaard & Spakman, 1999; Brunet & Yuen, 2000; Nikishin, et al., 2002), which generate topographies of up to several hundreds of meters (dynamic topography), thereby providing a substantial contribution to the continental lithospheric stretching, warming, and rupturing (e.g., Houseman and England, 1986; Lithgow-Bertelloni & Silver, 1998; Kendall & Lithgow-Bertelloni, 2016). Continental rifting and associated surface evolution are thus commonly debated in terms of a dominant partitioning between asthenospheric plumes and lithospheric far-field forces (e.g., Ziegler & Cloetingh, 2004; Foulger & Hamilton, 2014).

The topography generated by extensional strain is subject to erosion and sediment deposition which, acting at similar rates to those of tectonic extension, affect the stratigraphic (e.g., Van Balen, et al., 1995), geomorphologic (e.g., Petit, et al., 2007; Sembroni & Molin, 2018), structural (e.g., Burov & Cloetingh, 1997; Burov & Poliakov, 2001), metamorphic (e.g., England & Richardson, 1977) and magmatic (e.g., Maccaferri et al., 2014; Sternai, 2020) records of continental rifts. Prominent erosion and sediment deposition above an extensional setting drive a ductile flow in the lower crust directed outward from the zone of lithospheric necking/rupturing, thereby fostering the extensional strain, mantle upwelling, rift-shoulder uplift, and tectonic exhumation of deeper rocks (e.g., Burov & Cloetingh, 1997). The pressure and thermal anomalies at depth due to surface processes modulate the mantle decompression and crustal anatectic partial melting during lithospheric extension (e.g., Jull & McKenzie, 1996; Sternai, et al., 2017; Armitage, et al., 2019; Sternai, 2020). Surface load changes above an extensional magmatic province affect the stress pattern within the elastic

upper crust, modulating the propagation of dykes, the pressure/overpressure field at depth, exsolution of gasses, and, thus, the probability of volcanic eruptions (e.g., Jellinek & De Paolo, 2003, Jellinek, et al., 2004; Hooper, et al., 2011; Maccaferri, et al., 2011). Because magmatism assists extensional lithospheric rupturing (e.g., Buck, 2004; Kendall, et al., 2005), the control of surface processes on both magmatism and the slip along extensional structures may influence the location, migration, segmentation or failure of continental rifts (e.g., Sternai, 2020).

Representations of surface processes where hillslope-controlled erosion is a function of the local slope reveal only first-order effects of surface processes on continental rifting. Bedrock fluvial incision, proportional to local slope, river discharge, precipitations, and rock type, plays a primary role in creating local relief in form of valleys in fast-evolving areas (e.g., Hovius, et al., 1997; Willett, 1999; Whipple, 2009). Hillslope processes then move materials from the valley flanks onto the valley floor, where rivers can transport it out of the system. As local relief increases, the rate of hillslope erosion accelerates, so that the rate of fluvial incision sets the downcutting rate of the entire landscape and the overall erosional flux. Orographic perturbation of the regional climate produces systems where a dominant storm track draws moisture and precipitation on the upwind side of the topographic barrier (e.g., Barry, 1981; Singh & Kumar, 1997), resulting in a strongly asymmetric fluvial erosion pattern on the two sides of the range. Although the relationships between orography and orogeny in convergent settings have been the subject of previous investigations (e.g., Willett, 1999), they are poorly known in extensional contexts.

In this paper, we investigate how asthenospheric flow and orographic precipitation influence the slip along lithospheric shear zones accommodating far-field extension, associated topographic growth, and lithospheric rupturing. A relationship between the location of lithospheric rupturing with respect to the asthenospheric plume axis and the lithosphere effective elastic thickness, T_e (Burov & Diament, 1995), is derived analytically and adapted to extensional systems subject to orographic precipitation (section 2). We then test the analytical solution against numerical models of realistic extensional visco-elasto-plastic strain of a rheologically stratified lithosphere undergoing partial rock melting and fluvial bedrock incision proportional to stream power (section 3). In doing so, we systematically document the joint effects of mantle flow and orographic precipitation on the evolution of continental rifts to a degree not attempted before (section 4). We finally discuss results in terms of the spatial pattern of lithospheric rupturing, rock exhumation, magmatic activity and topographic asymmetry in relation to the mantle flow and orography, using the

East African Rift system across the Afar triple junction from Ethiopia to Somalia as a natural example (section 5).

2. Analytical model

2.1 Rheology

Empirical constitutive relations express the yield stress of rocks as a function of strain rate, temperature, pressure and activation energy (e.g., Goetze, 1978; Ranalli & Murphy, 1987; Burov & Diament, 1995). In a generalized form, the effective strain rate, $\dot{\varepsilon}$, and stress, σ, (second invariants) are related by,

$$\dot{\varepsilon} = \Gamma\sigma^n \quad (1)$$

where the stress exponent n and the constitutive parameter Γ describe the rocks properties. Eq. (1) describes the ductile behaviour of rocks with $\Gamma = (\Gamma^*)\mathrm{e}^{(-H/RT)}$ and $2 \leq n \leq 5$, where Γ^* is a material constant that depends on the mineral grain size, H is the activation energy, R is the gas constant, and T is temperature. The following Arrhenius relationship holds for ductile creep,

$$\dot{\varepsilon} = (\Gamma^*)\mathrm{e}^{(-H/RT)}(\sigma_1 - \sigma_3)^n \quad (2)$$

where $(\sigma_1 - \sigma_3) = \sigma_d$ is the deviatoric yielding stress, defined as the difference between the maximum and minimum principal stresses, σ_1 and σ_3, respectively. The ratio of the stress to strain rate gives the effective non-Newtonian viscosity, $\mu = \sigma_d/2\dot{\varepsilon}$. For strain rates between 10^{-17}-10^{-14} s^{-1}, exceeding a critical temperature of around 250-300 °C and 600-700 °C implies ductile flow of quartz and olivine, respectively (e.g., Brace & Kohlstedt, 1980; Burov & Diament, 1995).

Following the theory reported in Burov and Diament, 1995, conditions of brittle failure in a bi-dimensional case may be approximated as,

$$\sigma_3 = \sigma_d/3.9 \text{ MPa if } \sigma_3 < 120 \text{ MPa}$$
$$\sigma_3 = \frac{\sigma_d}{2.1} - 100 \text{ MPa if } \sigma_3 \geq 120 \text{ MPa} \quad (3)$$

implying that the brittle strength of rocks is insensitive to temperature and mainly dependent on pressure via σ_d (Byerlee, 1978). Colder, upper parts of the crust and mantle deform by predominant brittle (plastic) failure, whereas warmer parts of the lithosphere deform by temperature activated creep (e.g., Mareschal & Gangi, 1977; Burov & Diament, 1995). If the yielding limit is overtaken, then rocks fail either by brittle rupturing or by

ductile creep flow. If the imposed stress is lower than the ductile or brittle strength, then no deformation occurs and the materials behave (quasi-)elastically.

Combining Eqs. (2) and (3) one can form yield-stress envelopes (Goetze & Evans, 1979), which allow us to identify resistant (elastic) zones within the lithosphere and zones of ductile or brittle failure for given strain rates and local deviatoric stress gradients. The mechanical coupling or decoupling between the crust and the underlying mantle is controlled by variations in the composition and thickness of the crust as well as by the thermal regime and the strain rate. In the case of mechanical coupling, the elastic thickness, T_e, approximately corresponds to the depth of the 700 °C isotherm, where ductile strain in the mantle becomes dominant. However, for common crustal geotherms and thicknesses, the critical ~300 °C isotherm is at mid crustal levels (e.g., Ranalli, 1995), leading to a mechanically decoupled lithosphere. Crust-mantle decoupling is accompanied by a drastic reduction of T_e, which can be estimated as (Burov & Diament, 1995)

$$T_e = \sqrt[3]{{C_e}^3 + {M_e}^3} \quad (4)$$

where C_e and M_e are the thickness of the elastic crust and mantle, respectively. Estimates of continental T_e vary widely between ~10 and 110 km, assuming globally a bimodal distribution with prominent peaks between ~25-35 km and ~65-85 km (e.g., Watts, 1992; Burov & Diament, 1995).

The kinematics of lithosphere extension may involve a range of geometries including pure shear (e.g., McKenzie, 1978), simple shear (e.g., Wernicke, 1985) and combinations of these geometries (e.g., Lister, et al., 1986; Manatschal & Bernoulli, 1999). Systems of conjugate lithospheric-scale brittle-ductile normal shear zones underlie these geometries. According to classical mechanics, a system of conjugate normal faults in the upper brittle parts of the crust and mantle forms at ~60-65° from horizontal in regions subject to extensional stress (vertical σ_1) (e.g., Anderson, 1951; Reston, 2020). As slip on high-angle faults produces topography that opposes further motion (e.g., Forsyth, 1992), the faults must rotate to lower angles to accommodate significant extension (e.g., Jackson, 1987). These faults remain active because they are sufficiently weak to allow slip at non-optimum angles and at stresses below those required to form new faults (e.g., Collettini & Sibson, 2001). Lower angle brittle-ductile failure zones transition into low-angle ductile shear zones at depth, where temperature-sensitive mechanisms such as shear heating (e.g., Fleitout & Froidevaux, 1980; Ord & Hobbs, 1989) and crystal size reduction (e.g., Rutter & Brodie,

1988) enable the lower, warmer crust and lithospheric mantle to strain following the power law relationship described by Eq. (2) (Ramsay, 1980). Field evidence, laboratory measurements and modelling studies suggest that these shear zones correspond to regions of intense permeability driving the migration of fluids (e.g., Patriat & Jolivet, 1998; Brown & Solar, 1998; Manatschal, 1999; Gottardi, et al., 2015; Roche, et al., 2018). In turn, the presence of fluids within extensional shear zones fosters the deformation and facilitates the rupturing of the continental lithosphere (e.g., Kendall, et al., 2005; Lavier & Manatschal, 2006; Gillard, et al., 2016).

2.2 Topography and surface processes

The relationships between the lithosphere rheology, T_e, and the geometry of structures accommodating the tectonic strain determine the evolution of the topography, t_{obs}. At any time, t_{obs} is the sum of isostatic and dynamic components (e.g., Watts, 2009; Faccenna, et al., 2014; Sternai, et al., 2019). The isostatic elevation of the surface topography, t_{iso}, with respect to a reference elevation, H, does not account for the flow of geological materials and depends on the density structure of the lithosphere and underlying mantle,

$$t_{iso} = \left[\frac{(\rho_a - \rho_c)}{\rho_a}\right] C + \left[\frac{(\rho_a - \rho_m)}{\rho_a}\right] M - H \quad (5)$$

where C and M are the thickness of the crust and mantle lithosphere and ρ_c, ρ_m, and ρ_a are the mean densities of the crust, mantle lithosphere and asthenosphere, respectively. The dynamic component of the topography, t_{dyn}, is related to the vertical traction and thermal anomaly that mantle convection applies at the base of the lithosphere. In case of steady convection within a homogeneous half-space subject to harmonic variations in surface temperature ($T = T_0 cos(\frac{2\pi}{\lambda} x)$, where T_0 is the ambient temperature and λ is the wavelength of the thermal perturbation), the flow due to lateral density variations results in,

$$t_{dyn} = \frac{3\epsilon T_0 \lambda}{8\pi} \cos\left(\frac{2\pi}{\lambda} x\right) \quad (6)$$

where ϵ is the coefficient of thermal expansion (Molnar, et al., 2015).

The process of fluvial incision of an uplifting topography is not well understood. However, geomorphologists have long proposed that the erosion rate, $\dot{e}$, depends primarily on channel slope, river discharge and rock type (Gilbert, 1877). An empirical relationship was derived (e.g., Howard & Kerby, 1983; Willett, 1999; Whipple & Tucker, 1999), such that

$$\dot{e} = \frac{dt_{obs}}{dt} = kA^m \left|\frac{dt_{obs}}{dx}\right|^n \quad (7)$$

where A is the basin drainage area taken as a proxy for river discharge, $\left|\frac{dt_{obs}}{dx}\right|$ is the magnitude of the local topographic slope and k, m, and n are empirical parameters, usually determined by fitting models to river longitudinal profiles. While k is used as a scaling constant, different values of m and n lead to differences in the shape of river profiles, but commonly used values (e.g., $0.3 < m < 0.5$ and $n \approx 1$) predict realistic concave-up profiles such as those observed along bedrock rivers incising uplifting topographies (e.g., Stock & Montgomery, 1999; Whipple & Tucker, 1999; Willett, 1999; Sternai, et al., 2012). Although simplistic, Eq. (7) captures the main physical processes and parameter dependencies and, most important for this study, it provides the feedback mechanisms between tectonic uplift and erosion. Tectonic uplift increases slope, and the rise of topography increases drainage area, both leading to an increase in erosion rates. It must be noted, however, that Eq. (7) does not account for sediment deposition and, thus, its use to investigate feedbacks between surface and lithospheric processes is representative of systems where the sediment routing brings the eroded material far away from the sediment source area.

2.3 Analytical model setup and mechanics

Given the theory above, consider a layered lithosphere-asthenosphere system subject to horizontal far-field extension at a rate V_{ext}, in presence of asthenospheric upwelling. We frame this system into a right-handed reference where x is parallel to V_{ext}, and y is vertical (Fig. 1). Once the asthenospheric upwelling reaches the lithosphere-asthenosphere boundary (LAB), enhanced resistance by higher viscosity mantle lithosphere forces the vertical asthenospheric flow into a flow oriented parallel to the LAB with velocity V_p. Assuming a sub-horizontal LAB, this flow assists far-field extensional forces in driving lithospheric stretching. The condition $V_p > V_{ext}$ is likely due to lower asthenosphere viscosity with respect to that of the lithosphere (e.g., Turcotte & Schubert, 2002). Opposite-sense basal lithospheric simple shearing, σ_{xy}, develops on the left- and right-hand side of the asthenospheric plume, affecting the slip along the brittle-ductile shear zones that accommodate mantle lithospheric necking and crustal stretching (Fig. 1a-d and Fig. 2a).

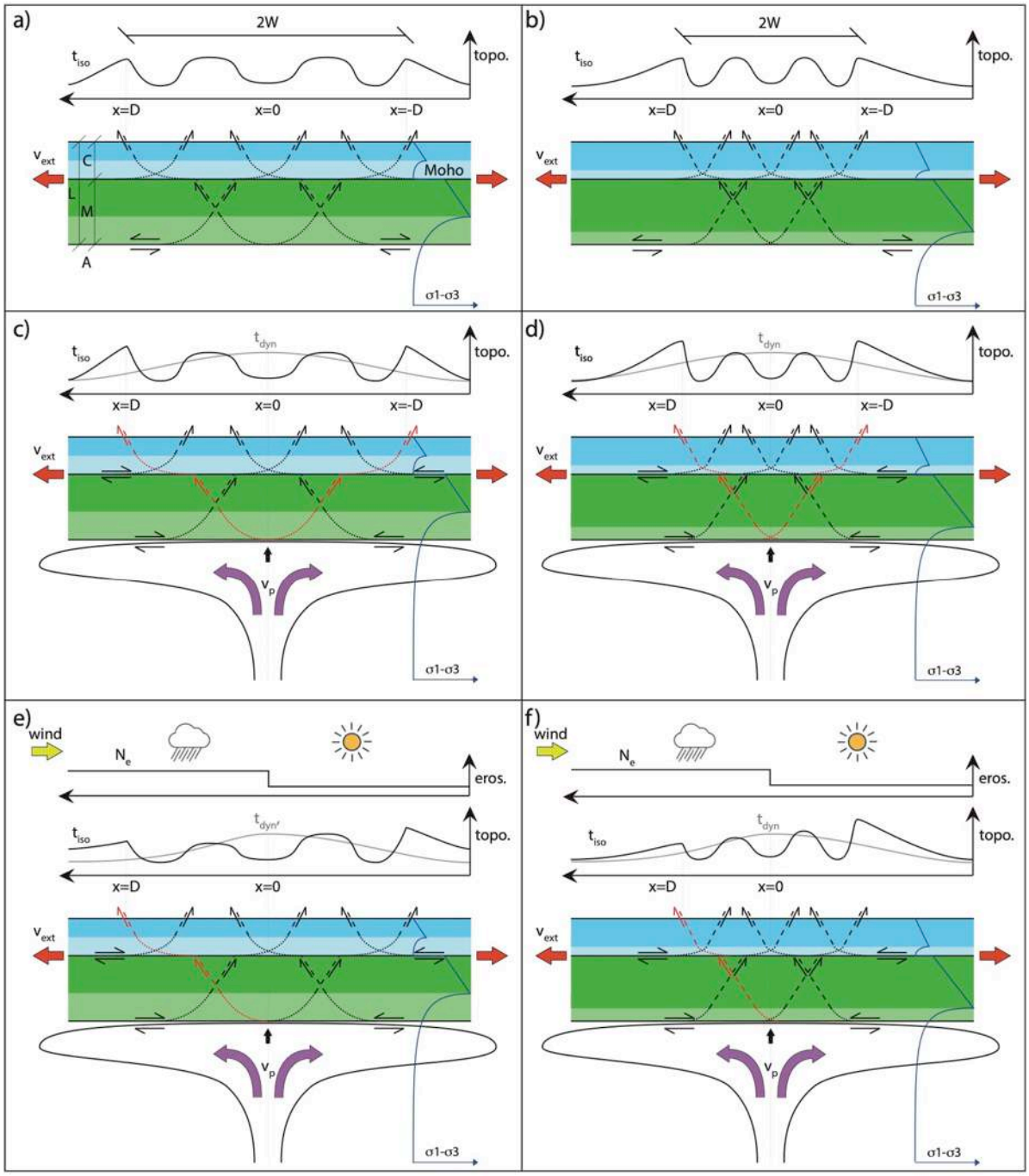

Figure 1: Sketch showing the main processes at work and the analytical model setup. Panels show the structures and topography forming during extension of a rheologically weak (a, c, e) and strong (b, d, f) lithosphere, with crust in blue and mantle lithosphere in green (dark and light tones for brittle and viscous parts, respectively). Panels (a, b) only account for the contribution of lithospheric far-field forces, panels (c-f) account for the contribution of lithospheric far-field and mantle flow-related forces and panels (e-f) further account for orographic effects. Theoretical yield stress envelops are shown in blue. Extensional shear zones represented in red accommodate most of the deformation. The crust (C), lithosphere (L), mantle lithosphere (M), asthenosphere (A) and Moho are indicated in panel (a). Dark and light blue and green colors indicate the upper and lower crust and mantle lithosphere, respectively. Other variables are defined in the text.

The role of lithospheric structures

Previous works emphasize the importance of the lithospheric thermal state and T_e in determining the mode of extension and the width of the extensional lithospheric rupturing zone (e.g., Ziegler & Cloetingh, 2004). We define $\bar{\alpha}_{(T_e)}$ as the mean angle between the orientation of the normal lithospheric shear zones and the horizontal, such that $\bar{\alpha}_{(T_e)} = \frac{1}{z}\sum_{i=1}^{z} \alpha_i$, where α_i is the i^{th} sampled values of α at depth and z is the number of sampled values of α. Because T_e evolves in time depending on the evolution of the strain, thermal state and topography during extension, a dependency between $\bar{\alpha}_{(T_e)}$ and time also exists. At any given time, however, $\bar{\alpha}_{(T_e)}$ is set by the partitioning between ductile and brittle shearing during extension, which also controls the width of the lithospheric rupturing zone in absence of an asthenospheric plume (e.g., Buck, 1991), besides pre-existing lithsopheric structures. Fossilized ductile extensional shear zones exposed in many plate margins show that α_i at depth may reach values as low as ~5-10° (e.g., Anderson, 1971; Wernicke, 1981; Jolivet, et al., 2018). However, cross-lithospheric shear zones must include a brittle part, with higher values of α_i that increase $\bar{\alpha}_{(T_e)}$. Classical rock mechanics suggests that $\alpha_{min} = \sim 20° \leq \alpha_i < \alpha_{max} = \sim 65°$ (e.g., Anderson, 1951; Reston, 2020), which we use to set the condition $\alpha_{min} = 20° \leq \bar{\alpha}_{(T_e)} \leq \alpha_{max} = 65°$ in a logistic sigmoidal function linking the cross-lithospheric $\bar{\alpha}_{(T_e)}$ to T_e, so that

$$\bar{\alpha}_{(T_e)} = \frac{a}{1 + b \cdot e^{-T_e/c}} + d \qquad (8)$$

where $a = (\alpha_{max} - \alpha_{min}) = 45°$, $d = \alpha_{min} = 20°$, b is a dimensionless scaling factor and c is a characteristic length set by the minimum thickness of the brittle lithosphere.

As described by the schematic σ_{xy} function in Fig. 2a, in presence of asthenospheric upwelling, simple shearing at the base of the lithosphere implies strain localisation and surface rupturing at a distance, $|D|$, from the plume axis, such that

$$|D| = \frac{L}{\tan(\bar{\alpha}_{(T_e)})} \qquad (9)$$

where L is the thickness of the thermal lithosphere as set by the depth of the 1300 °C isotherm (e.g., Turcotte & Schubert, 2002), although the theory can be adjusted to any other reference thickness as far as reasonable values of $\bar{\alpha}_{(T_e)}$ are used. Fig. 2 shows solutions of Eqs. (8) and (9) for the intervals $0 < T_e \leq 100$ km and $20 < L \leq 200$ km, satisfying $\lim_{T_e \to 0} \bar{\alpha}_{(T_e)} = 20°$, $\lim_{T_e \to 100} \bar{\alpha}_{(T_e)} = 65°$ and $T_e \leq L$ and with $b = 100$ and $c = 10$ km.

According to this analytical solution, if $T_e > \sim 80$ km, then $\bar{\alpha}_{(T_e)} \approx \alpha_{max}$ and $|D| \approx \frac{L}{2}$. Only rheologically coupled lithosphere (i.e., with Moho shallower than 35 km) may account for $T_e \geq 80$ km (Burov & Diament, 1995). Thus, $|D| \approx \frac{L}{2}$ represents a minimum expected value. In relatively young and hot continental lithospheres, or where the crust is thicker than 35 km, T_e is thinner than 80 km and $\bar{\alpha}_{(T_e)}$ is smaller than α_{max} leading to a higher variability of $|D|$, plausibly ranging between ~50-500 km. However, for realistic rock rheologies and common crustal thicknesses, the thicker the lithosphere the higher T_e. In the simplified case of a perfectly homogeneous and rheologically stratified lithosphere, this implies that values of $|D|$ greater than ~350-400 km are unlikely. Although estimates of $|D|$ may vary depending on the parametrization of the sigmoid function defining $\bar{\alpha}_{(T_e)}$ (i.e., parameters a, b, c, and d of Eq. 8), these general bounds appear plausible for common continental lithosphere geometries and rheologies (see also section 5).

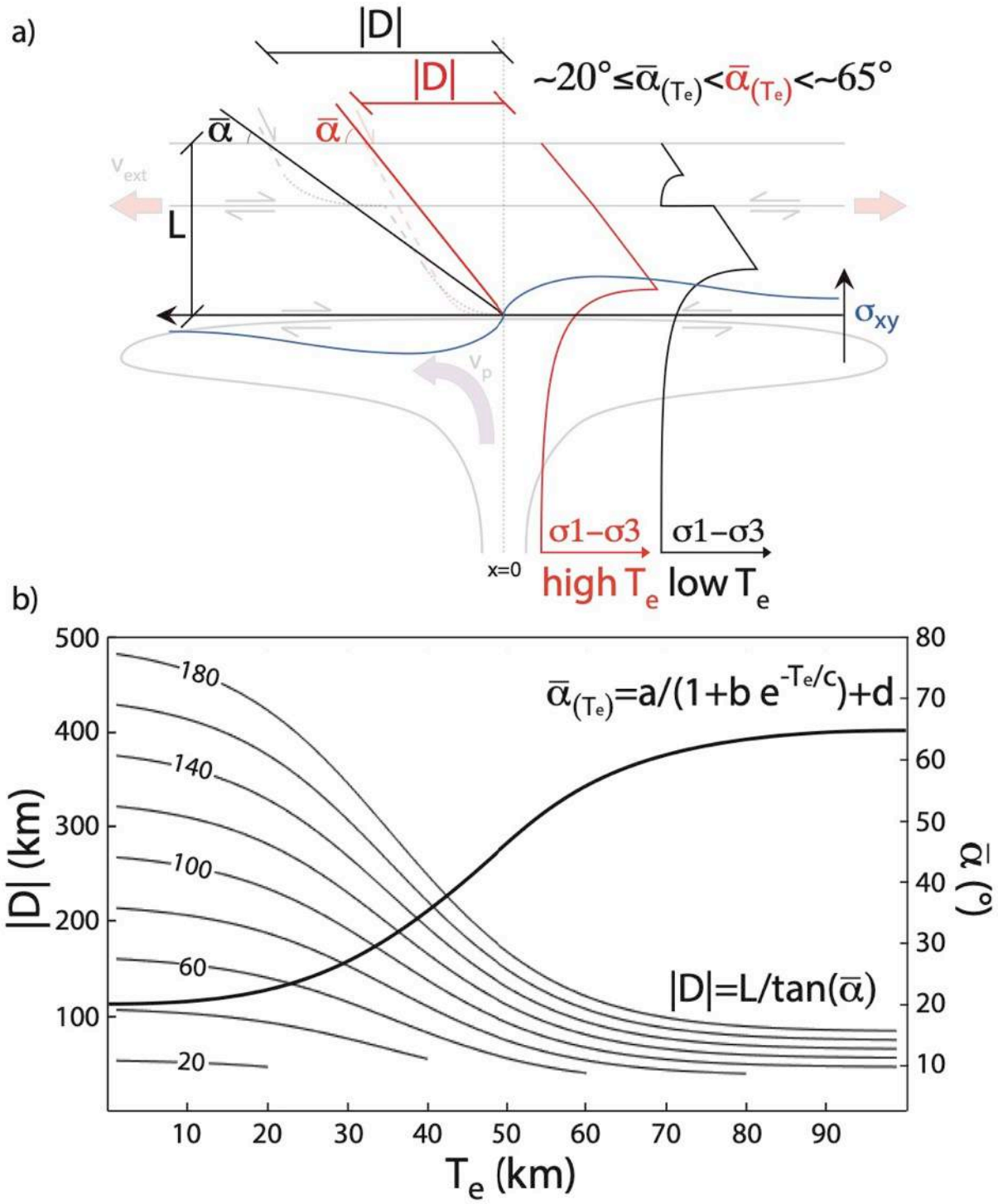

Figure 2: Boundary conditions (a) and analytical solution (b) of Eqs. 8 and 9. The light background in panel (a) is taken from Fig. 1a. The lithospheric thickness (L) gives the vertical scale. Other variables are defined in the text. In panel (b), thin lines follow the axis on the left and the thick line follows the axis on the right. Numbers along thinner lines define the lithospheric thickness (depth of the 1300 °C isotherm) in km.

The role of orographic precipitation

The isostatic elevation of the surface topography, t_{iso}, evolves in response to variations of the crust and mantle lithospheric thicknesses during extension (Eq. 5), resulting in classical horst-and-graben morphology (Fig. 1). Eq. 6 describes the initially harmonic upward deflection of the lithosphere and, thus, t_{dyn} during the rise of the mantle, which then diffuses laterally as the head of the plume spreads at the base of the lithosphere. Previous models demonstrate the effect of the erosional feedback in the sense of enhanced erosion rates where $t_{obs} = t_{iso} + t_{dyn}$ reaches high elevations, leading to enhanced deformation and exhumation in regions of high erosion rates (e.g., Burov & Cloetingh, 1997; Willett, 1999; Sternai, 2020). However, the erosional forcing is not just a function of drainage area and slope, as may be accounted for by Eq. 7. Orographic precipitation includes an asymmetric distribution resulting from the disruption of a storm track by high topography. Much of the moisture in the air mass is lost during air uplift over the mountain range, resulting in a rain shadow on the leeward side and in an enhanced erosion rate on the windward side.

General considerations regarding orographic effects in the case of a stretching lithosphere above an asthenospheric plume can be derived adapting previous analyses regarding compressive orogenic settings (Willett, 1999) to extensional settings. Assuming perfectly symmetric straining of a stretching lithosphere above an asthenospheric plume and defining the width of the overall rift topography $2W$, identical slope and drainage area characterize the basins on the two sides of the rift (Fig. 1a, b). Thus, the parameter k in Eq. 7 determines the rate of erosion on both sides of the rifting lithosphere. Using a reference depth, ψ, and length, W, to nondimensionalize the problem in the vertical and horizontal direction, respectively, two characteristic fluxes describe the system: the flux of topographic advection, $F_t \sim (V_{ext} + V_p)\psi$, due to tectonic extension, and the erosional flux out of the upper surface, $F_e \sim kW$. The erosional efficiency, N_e, is the ratio between the erosional flux out of the upper surface, F_e, and the flux of topographic advection, F_t, due to tectonic extension.

$$N_e = \frac{F_e}{F_t} \sim \frac{k2W}{(V_{ext}+V_p)\psi} \quad (10)$$

is consistent with Willett's definition of $N_e^* = \frac{4kW^2}{VC}$ (symbols adjusted to definitions provided in this manuscript; see Willett, 1999, for further detail). However, the use of a different reference depth that includes the mantle plume (i.e., $\psi = 640$ km based on the

numerical model setup described in section 3) and separating the horizontal velocity term, V, into a lithospheric extensional velocity component, V_{ext}, and a mantle plume horizontal velocity component, V_p, is more appropriate in this context. A small N_e reflects a system in which erosion rates are low either due to incision-resistant rocks or low precipitation rate. A large N_e reflects an erosional environment in which a high topography is unlikely to be produced. In the limit as $N_e \to \infty$ erosion is efficient to the point of erasing all increase in elevation and no topography exists. In the limit as $N_e \to 0$ the topography is uplifted until the mechanical limit set by rocks strength is reached. Because the rates of erosion usually vary within the same orders of magnitudes as the rates of tectonic uplift, N_e lies in a relatively small range of values representative of the local feedback between tectonics and climate.

The higher t_{obs} the higher the orographic effects on the precipitation pattern. Increased erosion rates, reflected in higher N_e on the windward side of the rifting system, reduce t_{obs}. Because the load of the topography produced during extensional deformation works against the tectonic stresses at their origins (e.g., Forsyth, 1992), the erosional removal of uplifted terrains promotes the slip along normal shear zones on the wetter and more eroded side of the topographic barrier (Fig. 1e, f). Not only a lower topography, but also enhanced exhumation and strain localisation are thus expected on the windward side of a rift topography, where eventual lithospheric rupturing at a distance $|D|$ (Eqs. 8 and 9) from the asthenospheric plume axis would occur (Figs. 1 and 2).

3. Numerical model

We test the analytical solution in Eqs. 8 and 9 and Figs. 1 and 2 by means of a coupled thermo-mechanical and surface processes numerical model. The coupled model includes three main components: (1) a rheological model, (2) a model for rock melting, and (3) an erosion model as described in more detail hereafter as well as in previous works (e.g., Gerya & Yuen, 2003; Gerya & Yuen, 2007; Gerya, 2010).

3.1 Rheological model

This model component accounts for the visco-elasto-plastic rheology of the lithosphere and asthenosphere based on rock mechanics data for a quartz-dominated crust and an olivine-dominated mantle (e.g., Ranalli, 1995; Turcotte & Schubert, 2002). In the ductile

lithosphere, the rate of strain follows a power law relationship with the stress and an exponential relationship with the temperature (Eq. 2). In the brittle (effectively plastic) lithosphere, the rocks' strength is linearly related to pressure. The elastic strain of rocks depends linearly on the stress scaled by typical Young's modulus, μ, and Poisson's ratio, ν, (Table 1).

During continental lithospheric stretching and asthenospheric plume upwelling the mass, momentum, and energy conservation equations are solved, so that

$$\begin{cases} \partial\rho_{eff}/\partial t + \nabla(\rho_{eff}\boldsymbol{v}) = 0 \\ \nabla(\boldsymbol{\sigma}) + \rho_{eff} g = 0 \\ \rho_{eff} C_p \cdot DT/Dt - \nabla(C_T \nabla T) = H_r + H_s + H_a + H_l \end{cases} \quad (11)$$

The effective density, ρ_{eff}, is the density of solid rocks at given P-T conditions. $\rho_{eff} = \rho_s\,(1 - \xi + \xi\frac{\rho_l^0}{\rho_s^0})$, with ρ_s^0 and ρ_l^0 being the standard densities of solid and molten rocks, respectively, ξ being the volumetric fraction of melt computed as described in section 3.2, and $\rho_s = \rho_0[1 + \beta(P - P_0)]\times[1 - \alpha(T - T_0)]$ where β is the compressibility, P is lithostatic pressure, and ρ_0, P_0 and T_0 are the density, pressure and temperature of rocks at surface conditions. $\boldsymbol{v}$ is the velocity vector, $\boldsymbol{\sigma}$ is the stress tensor, $\boldsymbol{g}$ is the acceleration due to gravity, C_p is the specific heat capacity, T is temperature, C_T is the thermal conductivity, and H_r, H_s, H_a, and H_l are the radiogenic, shear, adiabatic and latent heat production per unit volume, respectively (e.g., Turcotte & Schubert, 2002). The shear heat production is calculated as $H_s = \sigma'_{ij}\dot{\varepsilon}'_{ij}$, where $\boldsymbol{\sigma}'$ is the deviatoric stress tensor, $\dot{\boldsymbol{\varepsilon}}'$ is the deviatoric strain rate tensor, *i* and *j* are coordinate indices (for x and y) and repeated *ij* indices denotes summation, results from dissipation of the mechanical energy during irreversible deformation. The adiabatic heat production is computed as $H_a = T\epsilon\frac{DP}{Dt}$, where

$$Cp_{eff} = Cp + Q_l\left(\frac{\partial\xi}{\partial T}\right)_{P=const} \quad (12),$$

$$\epsilon_{eff} = \epsilon + \frac{Q_l}{T}\rho_{eff}\left(\frac{\partial\xi}{\partial P}\right)_{T=const} \quad (13),$$

where Q_l is the latent heating of the lithology of interest (Table 1).

3.2 Rock melting model

The rock-specific solidus and liquidus controls partial melting and crystallisation of magmas in the pressure-temperature domain (Table 1) (Ranalli, 1995; Turcotte & Schubert, 2002). At constant pressure, ξ is assumed to increase linearly with temperature according to the relations (e.g., Gerya, 2010; Sternai, 2020)

$$\begin{cases} \xi = 0 \quad at \quad T \leq T_s \\ \xi = \frac{(T-T_s)}{(T_l-T_s)} \quad at \quad T_s < T < T_l \\ \xi = 1 \quad at \quad T \geq T_l \end{cases} \qquad (14),$$

where T_s and T_l are the solidus and liquidus of the considered rock, respectively. The effective viscosity, η, of partially molten rocks with $\xi > 0.1$ is reduced to a constant value of 10^{16} Pa s (e.g., Burg, et al., 2009; Gerya, 2010; Sternai, 2020) simulating a viscosity drop consistent with previous estimates (e.g., Kohlstedt, 2002; Rey et al., 2009). Imposing such a high melt-content threshold for the viscosity change compensates for the lack of melt extraction processes in the numerical model and implies a very conservative assessment of the role of partial rock melting on the dynamic interactions investigated here.

3.3 Erosion model

The geometry of the top of the lithosphere as obtained from the coupled solution of Eqs. 11-14 determines the modelled t_{obs}, but separating t_{iso} and t_{dyn} requires specific settings (see Section 4). Integration on a discrete topography of the top of the lithosphere, however, allows for Eq. 7 to be solved numerically, thereby assessing surface elevation changes in response to the tectonic strain and fluvial incision (e.g., Willett, 1999; Sternai, 2020). At each time step, the surface load changes associated with modifications of the modelled landscape are computed. The orographic enhancement of precipitation, and hence fluvial erosion, is included in the surface processes model by increasing the reference $k = 3 \cdot 10^{-11}$ s^{-1} to $k = 5 \cdot 10^{-11}$ s^{-1} (Eq. 7) on positively sloping topographies. Following the approach of Willett, 1999, the resulting net erosional efficiency N_e (Eq. 10) on the two sides of the modelled orogen reflects the assumed dominant wind direction and efficiency of orographic enhancement of erosion rates, regardless of the imposed tectonic extension and lithosphere geometry.

3.4 Integrated model components, reference setup, and boundary conditions

Considering that the lithostatic pressure, P, depends on the elevation, equations 7, 11 and 14 are coupled via stress, temperature and velocity continuity conditions, adopting the finite-differences approximation scheme and a fully staggered bi-dimensional grid (e.g., Gerya & Yuen, 2003; Gerya & Yuen, 2007; Gerya, 2010). The initial domain (Fig. 3) measures 1500×650 km in the x and y dimensions, resolved by 161×61 grid points respectively. The Eulerian grid points are distributed irregularly so that the highest grid resolution of 5 km in both directions is imposed in the central-upper part of the model domain. To advect the material properties, 400×300 Lagrangian markers are distributed randomly in the model domain. A 4^{th} order Runge-Kutta interpolation scheme is used to interpolate the material properties carried by Lagrangian markers onto the Eulerian grid. The reference model assumes that both the upper and lower continental crust are 20 km thick, that is the Moho is located at 40 km depth consistently with commonly observed values (e.g., Reguzzoni, et al., 2013). The velocity boundary conditions are free slip at all boundaries (x=0 km and x=1500 km; y=0 and y=650 km). The left and right moving boundaries (x=0 km and x=1500 km) also account for x-parallel velocities equally distributed on the two boundaries, which define an extension rate of the model of 1 cm/yr. The lower moving boundary (y=650 km) also accounts for y-parallel velocity to compensate for horizontal extension and ensure mass conservation. The top surface of the lithosphere is calculated dynamically as an internal free surface through a 10 km thick layer of "sticky air" with viscosity of 10^{13} P s (e.g., Gerya, 2010; Crameri, et al., 2012). Each time step is limited by the Courant criteria (Courant, 1928). The thermal boundary conditions are 0 °C and 1600 °C for the upper and lower boundaries respectively, and nul horizontal heat flux across the vertical boundaries. The initial geothermal gradient is piece-wise linear with an adiabatic temperature gradient in the asthenosphere equal to 0.5 °C/km (e.g., Turcotte & Schubert, 2002). In the reference model, the 1300 °C isotherm at 100 km depth implies a temperature at the Moho of 530 °C. The parametric study focuses on the depth of the 1300°C isotherm as main control on the thermal lithospheric thickness and associated rheological changes. We account for younger and older continental lithospheres with the 1300 °C isotherm between 90 and 180 km depths, implying temperatures at the Moho between 580 °C and 290 °C. We initiate an asthenospheric plume by imposing a 200 km radius thermal anomaly at the base of the model domain, 200 °C warmer than the surroundings, without any imposed variation of the model's lower boundary heat flux.

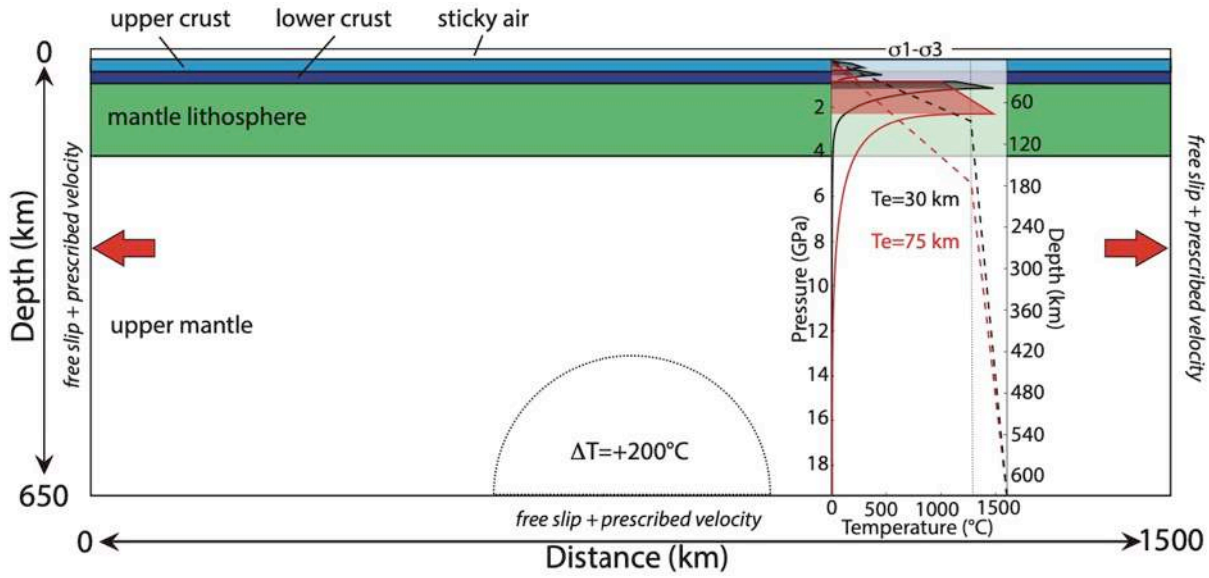

Figure 3: Numerical setup. The inset shows end-member weak (red) and strong (black) lithospheric geotherms and yield stress envelops (reference strain rate $\dot{\boldsymbol{\varepsilon}} = \mathbf{1{\times}10^{-15}}$ s^{-1}), implying $\boldsymbol{T_e}$ between 30 and 75 km. Shaded regions within the yield stress envelop highlight brittle-plastic levels.

Numerical simulations use a reference erosion number $N_e = 0.5$ (Eq. 10). When orographic enhancement of precipitation and erosion is accounted for, N_e is increased to 0.8 on upwind slopes (left-sloping topography) with respect to downwind slopes (right-sloping topography), leading to an approximate five-folds amplification of erosion rates, consistent with orographic perturbations of precipitations and erosion observed in natural settings (e.g., the Main Ethiopian Rift – e.g., Chorowicz, et al., 1998; Pik, et al., 2003; Garzanti, et al., 2006; Gani, et al., 2007; Sembroni, et al., 2016 - see also section 5.2). We remark that, provided the scaling between the parameter k and $(V_{ext} + V_p)$ in the nondimensional definition of N_e (Eq. 10), results are representative of systems subject to any tectonic extension and erosion rates.

4. Results

Evolution of lithospheric structures and topography in absence of orography

Lithospheric extension in absence of asthenospheric plume and erosion leads to distributed strain of a hot and weak lithosphere, i.e., low T_e, and localized strain along discrete structures in a cold and strong lithosphere, i.e., high T_e (Fig. 4), in agreement with previous studies (e.g., Buck, 1991; Huismans & Beaumont, 2003). The initially flat topography evolves into a horst and graben landscape, whose characteristic width and height depend on the imposed lithospheric thickness and T_e (Fig. 5). Although the time required to

break the lithosphere is inversely proportional to its strength (e.g., Huismans & Beaumont, 2011; Sternai, 2020), the location of lithospheric rupturing in the absence of plume-induced asthenospheric flow and surface processes is poorly sensitive to the imposed large variation of T_e.

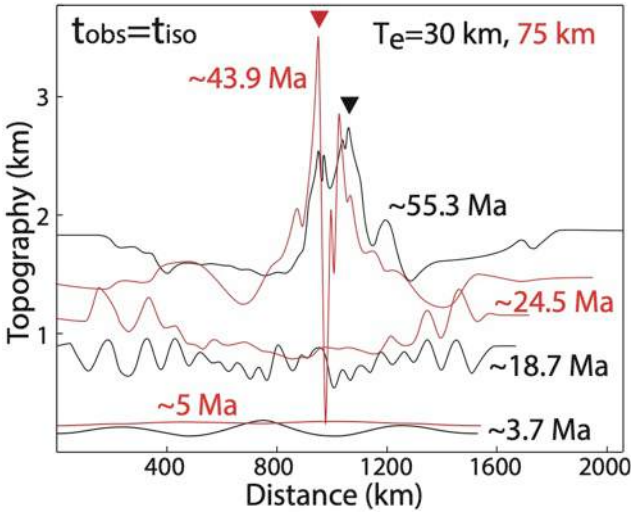

Figure 4: Evolution of the topography for the numerical experiments shown in Fig. 4a, b. Triangles pinpoint the location of lithospheric rupturing.

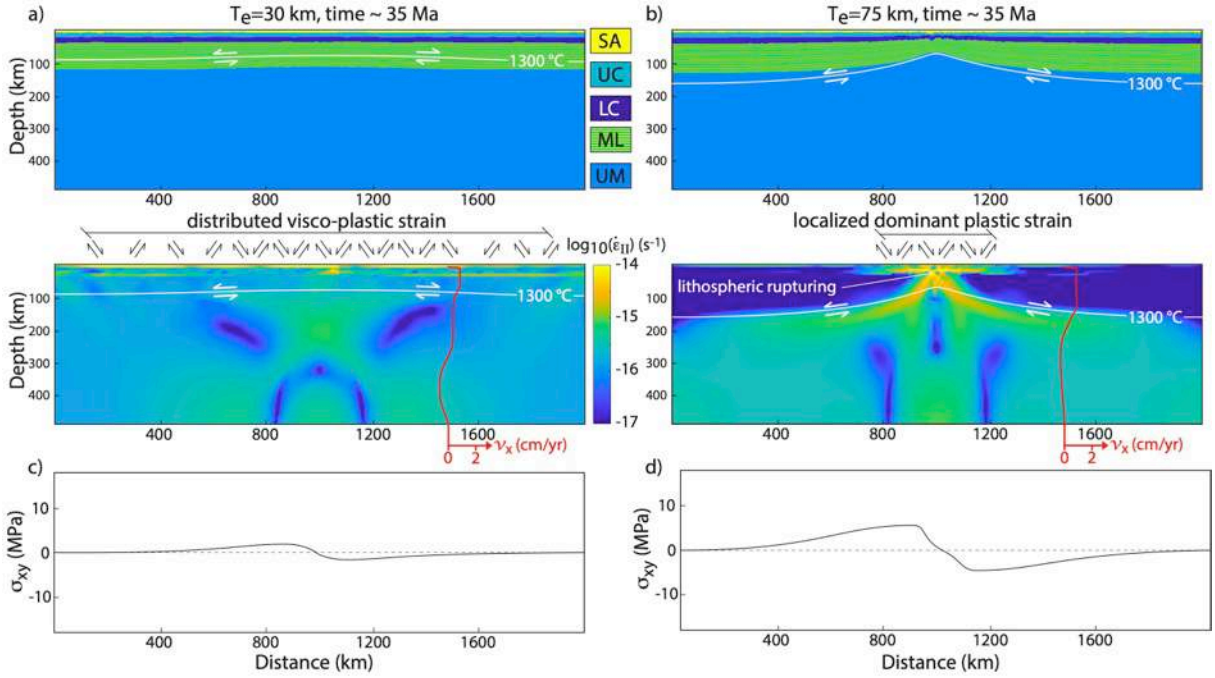

Figure 5: Numerical experiments of lithospheric extension in absence of asthenospheric plume (ΔT=0 °C) and erosion (N_e=0) for a weak (T_e=30 km, a) and strong (T_e=75 km, b) lithosphere. Upper panels show the phase distribution and lower panels show the second invariant of the strain rate tensor, $\dot{\boldsymbol{\varepsilon}}$. Depth variations of the horizontal component of the velocity vector ($\boldsymbol{v_x}$) are shown in red on the lower panels. Top-to-the-left and Top-to-the-right basal lithospheric shearing develop on the left-hand and right-hand side of the model respectively to accommodate for extension. Distributed vs. localized lithospheric strain occurs when the lithosphere is respectively weak (a) and strong (b). SA: Sticky air; UC: Upper Crust; LC: Lower Crust; ML: Mantle Lithosphere; UM: Upper Mantle. Panel (c) and (d) show the shear stress at the base of the thermal lithosphere.

Simulations that account for an asthenospheric plume in the absence of lithospheric extension and erosion (Fig. 6) allow us to assess t_{dyn} for the specific setup (Fig. 7), reaching up to ~150 m above the centre of the thermal anomaly shortly after the onset of mantle upwelling (<2 Ma). The early harmonic topographic anomaly spreads out laterally once the upwelling asthenospheric plume reaches the LAB and its flow is deviated horizontally. The upwelling and lateral spreading of the asthenospheric mantle plume at the base of the rigid lithosphere is also responsible for an upward deflection of the basal lithospheric isotherms and the delamination of the viscous part of the denser lithospheric mantle (e.g., Fig. 6a), which inhibit the decay of t_{dyn}. Subsidence by ~200 m occurs at the margins of the model domain. In agreement with previous studies (e.g., Burov & Cloetingh, 1997; Burov & Gerya, 2014), we observe that the topography at the top of a warm and thin lithosphere is more sensitive and responds more quickly to the forcing induced by the asthenospheric plume.

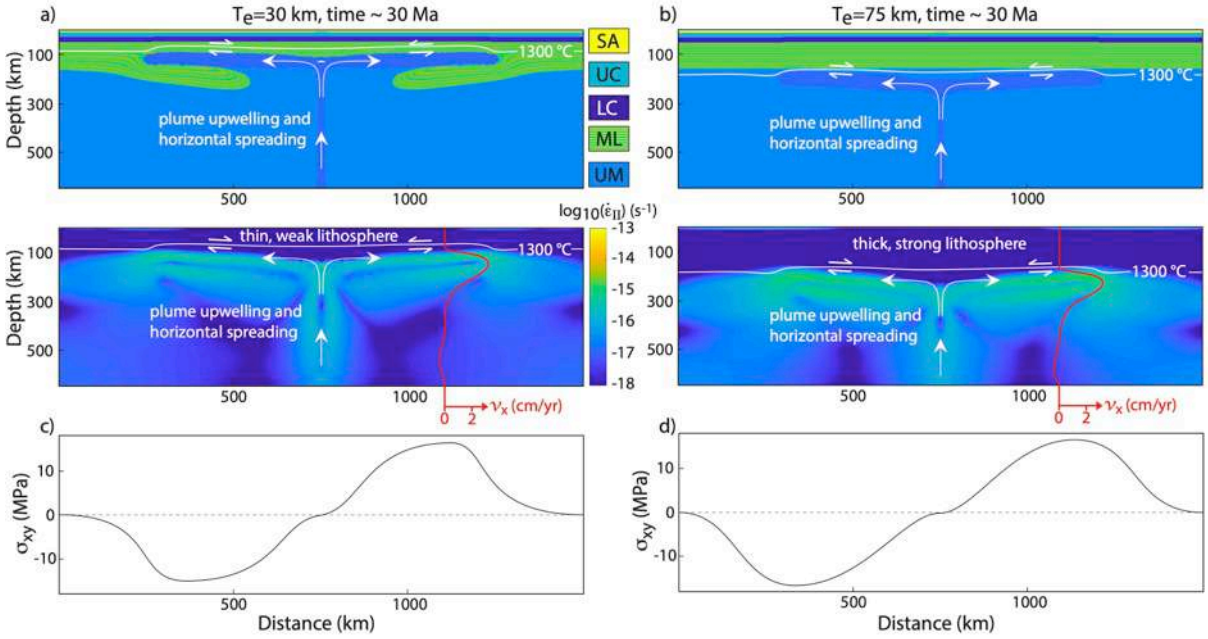

Figure 6: Numerical experiments of asthenospheric plume (ΔT=200 °C) in absence of lithospheric extension and erosion (N_e=0) for a weak (T_e=30 km, a) and strong (T_e=75 km, b) lithosphere. Upper panels show the phase distribution and lower panels show the second invariant of the strain rate tensor, $\dot{\boldsymbol{\varepsilon}}$. Depth variations of the horizontal component of the velocity vector ($\boldsymbol{v_x}$) are shown in red on the lower panels. Note the top-to-the-right and top-to-the-left basal lithospheric shearing on the left-hand and right-hand side of the model respectively (opposite to Fig. 4) due to the asthenospheric plume and associated flow. SA: Sticky air; UC: Upper Crust; LC: Lower Crust; ML: Mantle Lithosphere; UM: Upper Mantle. Panel (c) and (d) show the shear stress at the base of the thermal lithosphere.

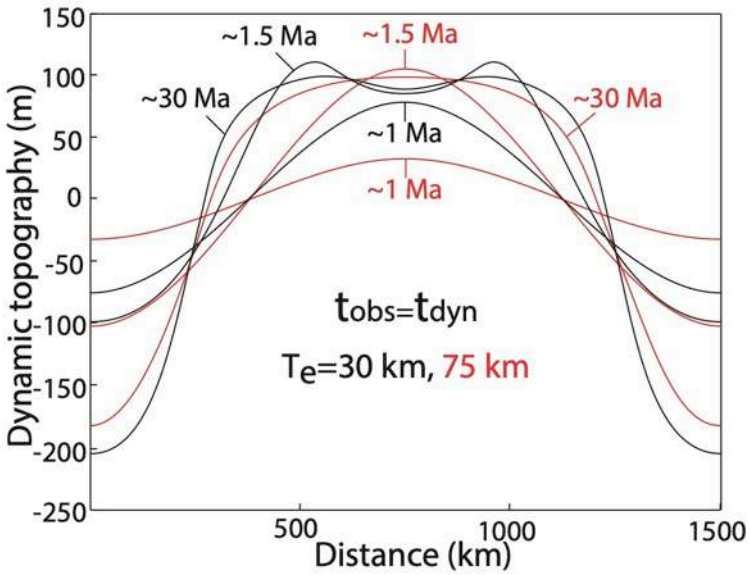

Figure 7: Evolution of the topography for the numerical experiments shown in Fig. 6a, b.

Consistently with the analytical model described in section 2 and by Figs. 1 and 2, top-to-the-right and top-to-the-left basal lithospheric shearing develop, respectively, on the left- and right-hand side of the numerical model when the lithospheric extension and asthenospheric plume act jointly (Fig. 8). Basal lithospheric shearing enhances the simple shear component of the deformation by promoting asymmetric slip along conjugate brittle-ductile shear zones accommodating lithospheric extension. The simple shearing mode of deformation is particularly effective in a hot and weak lithosphere (i.e., low T_e) subject to dominant distributed viscous strain, leading to lithospheric necking, nucleation of a partial melting zone, rock exhumation and final lithospheric rupturing at a high distance $|D|$ from the asthenospheric plume axis (Fig. 8a, b). The initial position of Lagrangian markers is determined by a pseudorandom number generator algorithm initialized by a random seed. Using the same random seed ensures the same initial pseudorandom position of Lagrangian markers for all numerical simulations presented. We remark that, although lithospheric rupturing may in principle occur on either sides of the mantle plume axis, the initial pseudorandom position of Lagrangian markers leads to rupturing on the right-hand side of the model in absence of further perturbations. $|D|$ is reduced with increasing lithospheric strength (i.e., high T_e) subject to dominant localized brittle-plastic strain in a pure shearing mode (Fig. 8c, d). Respectively wider and narrower horst and graben morphologies develop during extension above weak and strong lithospheres, reflecting distributed lithospheric necking away from the asthenospheric plume axis versus localized lithospheric rupturing nearby the asthenospheric plume axis, respectively (Fig. 9). High topography (i.e., high t_{iso} and t_{dyn})

above the zone of lithospheric rupturing is due to effective removal of high-density mantle lithospheric material replaced by hot upwelling asthenospheric material.

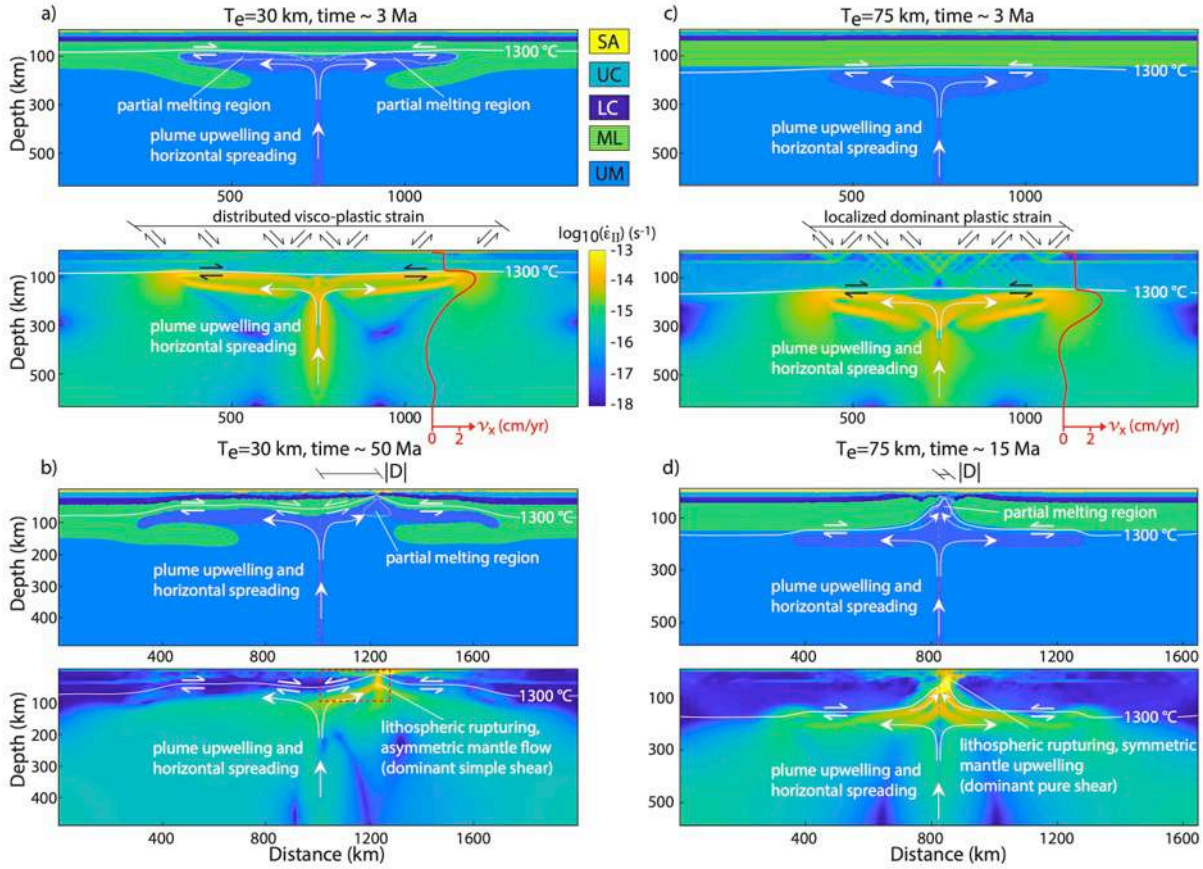

Figure 8: Numerical experiments of lithospheric extension with asthenospheric plume (ΔT=200 °C). (a, b) Case of a weak lithosphere (T_e=30 km). Partial rock melting as well as top-to-the-right and top-to-the-left basal lithospheric shearing occur on the left-hand and right-hand side of the model respectively due to the asthenospheric plume. Distributed lithospheric strain (a) and lithospheric rupturing far from the asthenospheric plume axis (b) occur. (c, d) Case of a strong lithosphere (T_e=75 km). Localized lithospheric strain (c) and lithospheric rupturing close to the asthenospheric plume axis (d) occur. Partial rock melting only occurs during later stages of the experiment (d). Depth variations of the horizontal component of the velocity vector (v_x) are shown in red on the lower panels in (a) and (c). Top-to-the-right and top-to-the-left basal lithospheric shearing occur on the left-hand and right-hand side of the model respectively due to the asthenospheric plume. The dashed, red rectangle in the lower panel of (b) shows the region expanded in Fig. 15c. SA: Sticky air; UC: Upper Crust; LC: Lower Crust; ML: Mantle Lithosphere; UM: Upper Mantle.

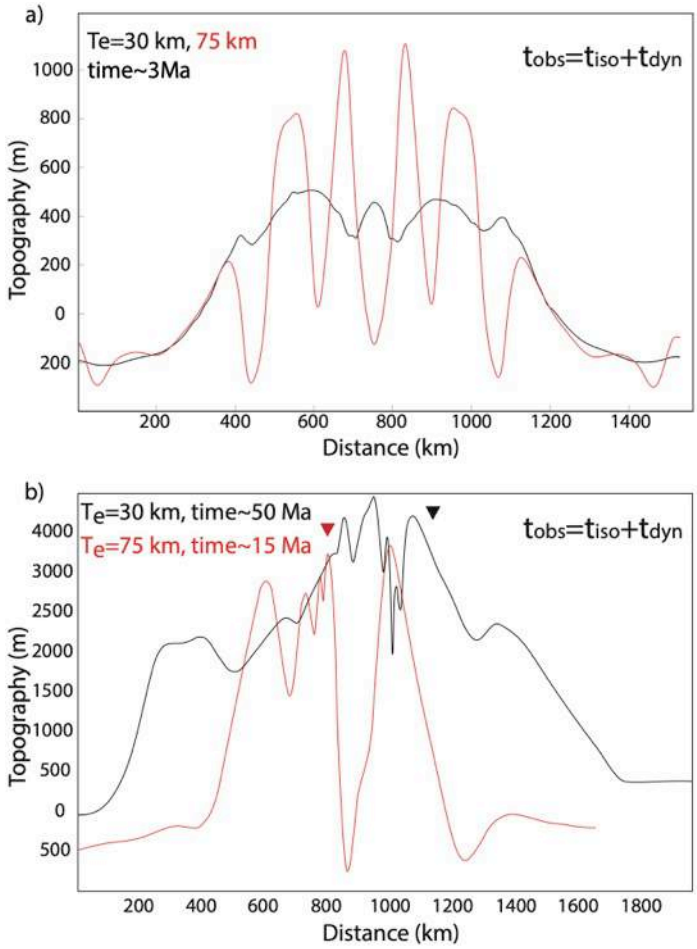

Figure 9: (a) Topography of experiments shown in Fig. 8a (black line) and Fig. 8c (red line). (b) Topography of experiments shown in Fig. 8b (black line) and Fig. 8d (red line). Triangles pinpoint the location of lithospheric rupturing.

The role of orographic precipitations

Orographically enhanced erosion rates produce asymmetric topography characterized by lower slopes and elevations on the upwind side of the range (Fig. 10-13), consistent with landscapes observed in natural settings (e.g., see section 5.2). Orographic erosion and associated asymmetric removal of the surface masses involve a modification of the strain rate by up to two orders of magnitudes on the wetter and more eroded side of the model domain. In a hot and weak lithosphere with low T_e, this effect is relevant to depths down to ~200 km, where the plume-related mantle flow is particularly fast (Fig. 10a, lower panel). In turn, the removal of the surface masses by orographic erosion facilitates partial decompression mantle melting and rock weakening (Fig. 10c, lower panel). Strain localization, associated lithospheric necking, and focused rock exhumation away from the asthenospheric plume axis thus occur on the wetter and more eroded side of the orogen (Fig. 10b, d and 11). In a strong

and cold lithosphere with high T_e, the mantle lithosphere supports the stress changes induced by orographic erosion and the effects of asymmetric surface mass removal is limited to crustal depths (Fig. 12a, lower panel, and 13). The orography-triggered feedback between erosion, strain, and rock partial melting and weakening is dampened and mantle lithospheric rupturing occurs in proximity to the asthenospheric plume axis. The asymmetric surface mass removal due to the interaction between precipitation and orography provides a preferential strain localization and exhumation path toward the wetter and more eroded side of the range for the partially molten asthenosphere upwelling within the mantle lithospheric necking zone.

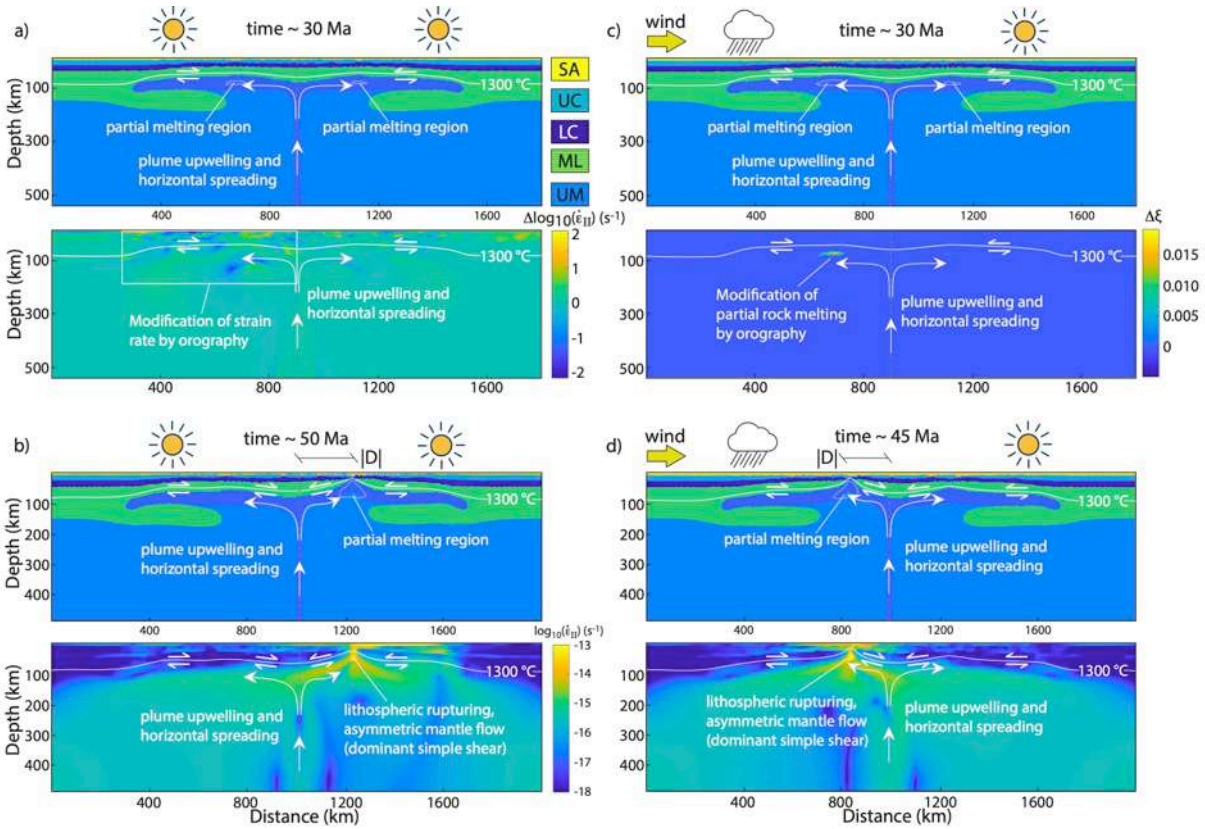

Figure 10: Numerical experiments of lithospheric extension (T_e=30 km) with asthenospheric plume (ΔT=200 °C) and erosion (N_e=0.5, 0.8). (a, b) Case without orographic precipitation (N_e=0.5 on both sides of the asthenospheric plume) at time=30 Ma and 50 Ma. (c, d) Case with orographic precipitation (N_e=0.8 left of the plume and N_e=0.5 right of the plume) at time=30 Ma and 45 Ma. The lower panel in (a) shows the difference between the second invariant of the strain rate in the simulation with and without orography (upper panels in a and c). The lower panel in (c) shows the difference between partial rock melting in the simulation with and without orography (upper panels in a and c). SA: Sticky air; UC: Upper Crust; LC: Lower Crust; ML: Mantle Lithosphere; UM: Upper Mantle.

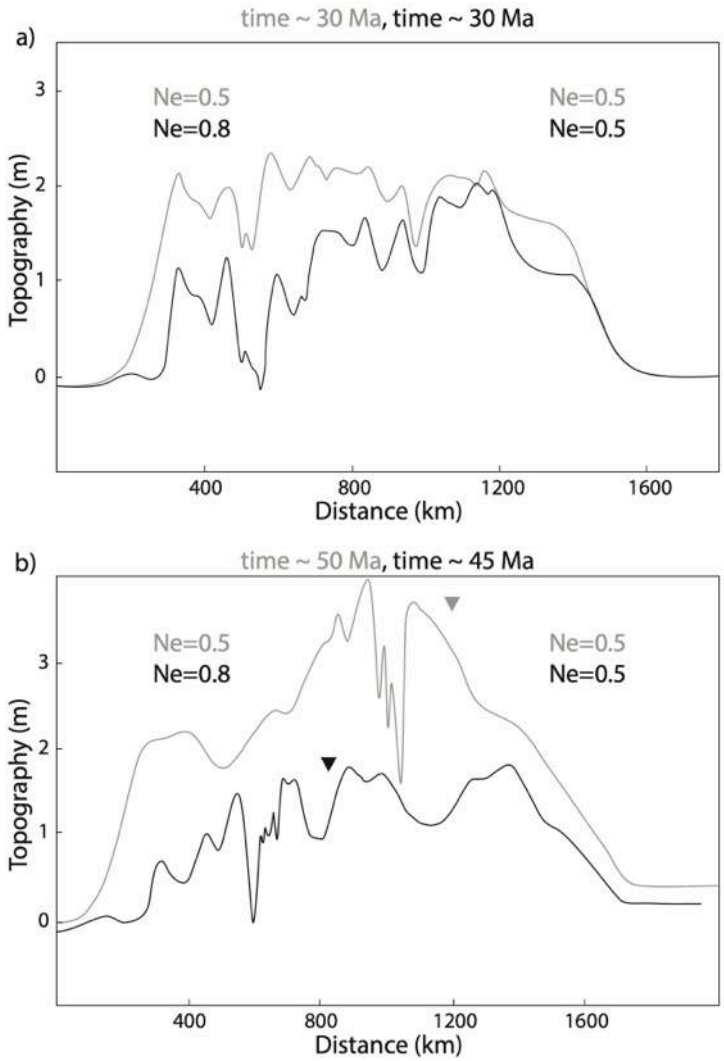

Figure 11: (a) Topography of experiments shown in Fig. 10a (gray line) and Fig. 10c (black line). (b) Topography of experiments shown in Fig. 10b (gray line) and Fig. 10d (black line). Triangles pinpoint the location of lithospheric rupturing.

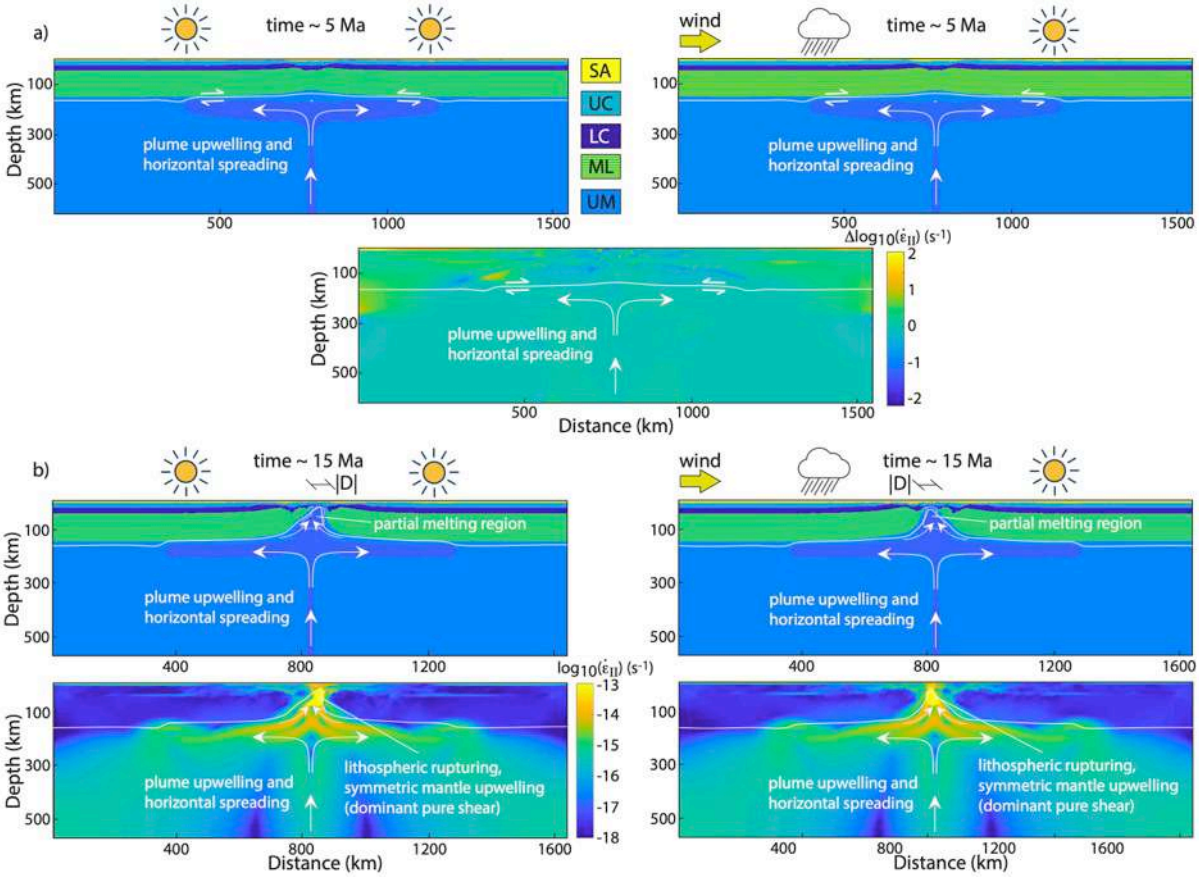

Figure 12: Numerical experiments of lithospheric extension (T_e=75 km) with asthenospheric plume (ΔT=200 °C) and erosion (N_e=0.5, 0.8). (a) Comparison between experiments without orographic precipitation (N_e=0.5 on both sides of the asthenospheric plume) and with orographic precipitation (N_e=0.8 left of the asthenospheric plume and N_e=0.5 on the right of the plume) at time=5 Ma. The lower panel shows the difference between the second invariant of the strain rate in the experiments shown in the upper panels. (b) Comparison between experiments without orography (N_e=0.5 on both sides of the asthenospheric plume) and with orography (N_e=0.8 left of the asthenospheric plume and N_e=0.5 on the right of the plume) at time=15 Ma. SA: Sticky air; UC: Upper Crust; LC: Lower Crust; ML: Mantle Lithosphere; UM: Upper Mantle.

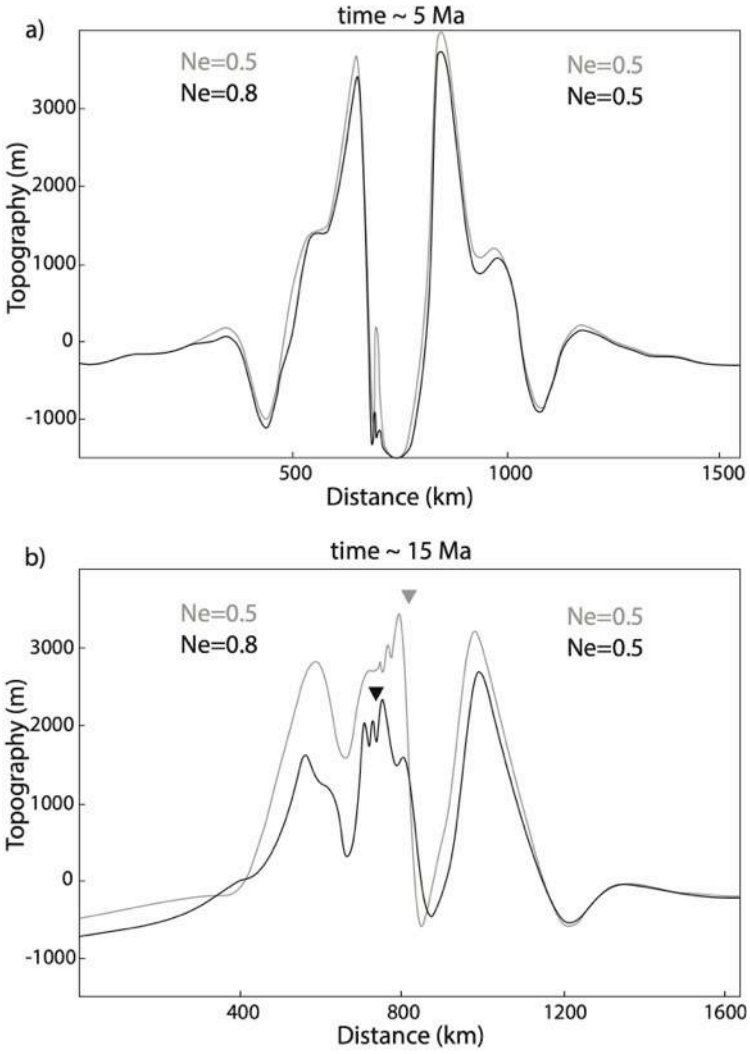

Figure 13: (a) Topography of experiments shown in Fig. 12a (upper left panel: gray line; upper right panel: black line). (b) Topography of experiments shown in Fig. 12b (left panels: gray line; right panels: black line). Triangles pinpoint the location of lithospheric rupturing.

5. Discussion

5.1 Mantle flow and orographic forcing on rifting

A chicken or egg distinction exists between "active" and "passive" rifts (e.g., Sengör & Burke, 1978; Olsen & Morgan, 2006), respectively driven by asthenospheric upwelling (e.g., Dewey & Burke, 1975; Spohn & Schubert, 1982) or far-field lithospheric extensional forces (e.g., McKenzie, 1978; McKenzie & Bickle, 1988). This distinction may hold if associated to magmatism, but it becomes questionable when associated to the driving forces of continental rifting. On the one hand, horizontal plate-boundary forces alone seem barely sufficient to produce continental lithospheric rupturing (e.g., Buck, 2004; Ziegler &

Cloetingh, 2004). On the other hand, intracontinental asthenospheric plumes are not necessarily associated with major extensional faulting (e.g., Burke & Whiteman, 1973; Le Bas, 1987; Wilson & Guiraud, 1998), suggesting that mantle flow alone cannot lead to rifting. Extension and rupturing of the continental lithosphere likely result by a combination of divergent plate-boundary forces and viscous coupling between the lithosphere and the convecting mantle (e.g., Forsyth & Uyeda, 1975; Ziegler & Cloetingh, 2004; Buiter & Torsvik, 2014; Jolivet, et al., 2018; Jolivet, et al., 2018b). It should also be noted that asthenospheric plumes may be long- or short-lived, and impingement of plumes on zones of lithospheric extension can thus affect various stages of continental rifting (e.g., Ziegler, et al., 2001; Nikishin, et al., 2002; Ziegler & Cloetingh, 2004). During these stages, mantle drag forces are strong enough to drive plate motion and the modes of continental lithospheric stretching across extensional settings (e.g., Houseman and England, 1986; White & McKenzie, 1989; Wilson & Guiraud, 1998; Doglioni, et al., 2003; Sternai, et al., 2014; Jolivet, et al., 2018; Jolivet, et al., 2018b).

Here, we document the effects of mantle drag forces on extensional shear zones (e.g., Fig. 4c,d and 6c,d), driving the location of lithospheric necking, focused partial melting, rock exhumation and final lithospheric rupturing with respect to the asthenospheric plume axis, $|D|$. We assume an initial thermal anomaly that generates mantle upwelling from 650 km to the base of the lithosphere in about 1.5 Ma, that is a characteristic mantle flow rate in the orders of the tens of cm/a (e.g., Turcotte & Schubert, 2002). The resulting sub-horizontal mantle flow at the LAB is faster than the lithospheric extension rate (e.g., see vertical velocity profiles in Fig. 6 and 8), in the order of the cm/a as commonly observed (e.g., Kreemer, et al., 2014). An increasing misfit between estimates of $|D|$ from the analytical (section 2, Eqs. 8, 9) and numerical (section 3, Eqs. 10-15) solutions is found with increasing T_e (Fig. 14). This misfit is readily explained by the fact that the analytical solution accounts for simple shearing only, whereas both pure and simple shearing are accounted for in the numerical experiments. Stretching a strong continental lithosphere characterized by high T_e leads to rifting by dominant pure shear, compromising the applicability of Eq. 9. Stretching a weak continental lithosphere with low T_e leads to rifting by dominant simple shear, which is well accounted for by both the analytical and numerical solutions. The misfit between the analytical and numerical results (Fig. 14) is thus an indicator of the partitioning between simple and pure shear during continental rifting for lithospheres characterized by different strengths (e.g., McKenzie, 1978; Wernicke, 1985; Lister, et al., 1986; Buck, 1991; Allemand

and Brune, 1991; Manatschal & Bernoulli, 1999). The inverse proportionality between T_e and $|D|$ found in both the numerical and analytical solutions indicates that a weak lithosphere is more prone to be influenced by the sub-lithospheric mantle flow and associated basal lithospheric shearing. In a perfectly homogeneous lithosphere, lithospheric necking with nucleation of a partial melting zone and focused rock exhumation leading to further strain localization and final lithospheric rupturing occur at a distance from the asthenospheric plume axis that ranges from a few tens to a few hundreds of kilometres, depending on the lithospheric strength (e.g., Figs. 8, 10, and 12).

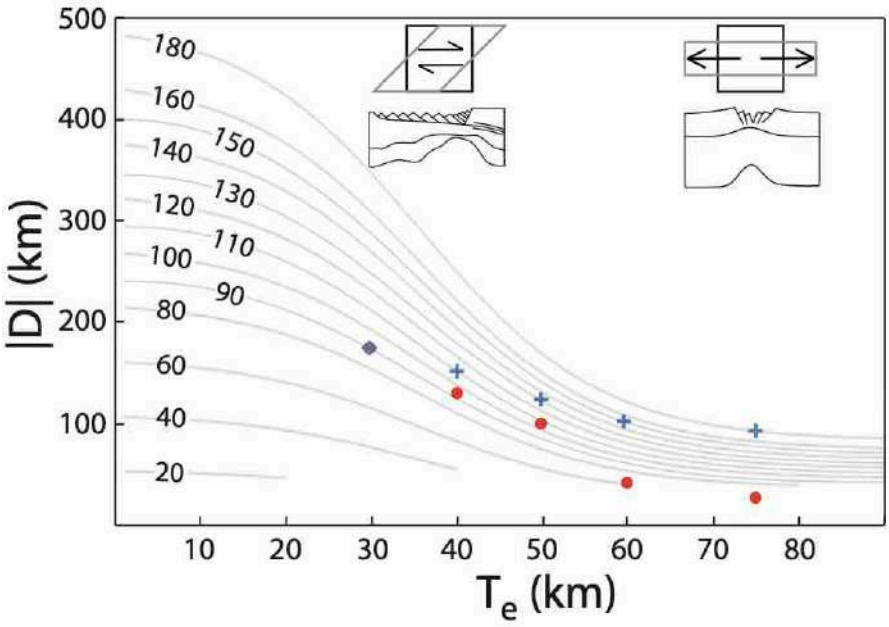

Figure 14: Comparison between analytical (blue crosses) and numerical solutions (red dots). The background plot is the same as in Fig. 2b. Note the fine match between analytical and numerical results at relatively low T_e (when dominant simple shear occurs) and increasing mismatch between analytical and numerical results at relatively high T_e (when dominant pure shear occurs). See text for further detail.

The development of prominently asymmetric extensional tectonic features is favoured by strain-dependent weakening (e.g., Zhong & Gurnis, 1996; Tackley, 1998; Huismans & Beaumont, 2003). On a local scale, deformation on faults and shear zones is inherently asymmetric. This is consistent with the inherent asymmetry of our analytical model, which only accounts for the simple shear deformation mode. In our numerical models, however, rheological weakening by partial melting only pertains to viscous strain (see section 3.2), whereas frictional-plastic strain weakening by cohesion loss or fluid pressure variations (e.g., Sibson, 1990; Buck, 1993; Huismans & Beaumont, 2003) is neglected. Yet, extensional strain localisation tens to hundreds of kilometres away from the asthenospheric plume axis does

involve an asymmetry in our numerical models. This result agrees with symmetric, asymmetric, or intermediate rift architectures arising from different combinations of pure and simple shearing (e.g., McKenzie, 1978; Wernicke, 1985; Lister, et al., 1986; Manatschal & Bernoulli, 1999), but further suggests that the mantle flow, when present, can exert a major control on the location of surface extensional strain localization, rock exhumation, and final continental lithospheric rupturing.

Strain localisation away from the asthenospheric plume axis drives asthenospheric upwelling and topographic uplift above the incipient lithospheric rupturing zone. Erosion of the uplifted topography also enhances rock exhumation, and the resulting unloading fosters partial decompression mantle melting and viscous strain (e.g., Fig. 10 and 11) (Sternai, 2020). On the one hand, the lack of a depositional term in our surface process model (i.e., Eq. 7) may lead us to overestimate the role of asymmetric erosion in setting the location of lithospheric rupturing by an extent proportional to the relevance of intramountain sediment deposition. On the other hand, the lack of strain weakening during frictional/plastic deformation in our lithospheric model, which further enhances the asymmetry of rift systems and the sensitivity of surface structures to the erosional forcing (e.g., Tackley, 1998; Huismans & Beaumont, 2003), may lead us to underestimate the role of orography and lateral erosion gradients recognized here. Overall, we consider it likely that orography and associated asymmetric removal of surface rocks promotes lithospheric rupturing on the wetter and more eroded side of a rifting continent, thereby playing a role in setting the location of lithospheric rupturing.

5.2 Comparison with the East African Rift System

Simplified models cannot capture entirely the complexity of natural systems. Yet, the outcomes of our models are consistent with several observed features in the geological record from the Afar triple junction in the East African Rift System. The most robust outcomes of our models are the spatial patterns of lithospheric rupturing, rock exhumation and magmatic activity, as well as the topographic asymmetry in relation to the asthenospheric flow and orography. It is these features and their relationships with the natural tectonics and climatic forcing that we discuss hereafter.

Mantle upwelling and distal initiation of lithospheric stretching

Asthenospheric upwelling and impinging at the base of the East African lithosphere around 45 Ma led to intense magmatism during three phases of basaltic eruptions associated with bimodal or silicic products (e.g., Rooney, 2017). The initial phase focuses on the Omo (southern Ethiopia) and Turkana Basin regions and covers a time span of about 10 Ma (~45-35 Ma). The second phase (Trap eruption) started around 31 Ma (e.g., Hofmann, et al., 1997) and is centred in NW Ethiopia and Yemen. The last phase, synchronous (~23-24 Ma) from the Red Sea margin to the Turkana Basin and partly associated with continental crust extension (e.g., Stab, et al., 2016), is less voluminous and does not result in thick basalt piles but shield volcanoes and isolated flows. About 84% of the total basalts volume is found in the Ethiopian Plateau resulting in an asymmetric distribution with respect to the Main Ethiopian Rift (MER) (Sembroni, et al., 2016). Seismic velocity modelling from wide-angle reflection/refraction profiles across the MER suggests the presence of a ~15 km thick high-velocity lower crust beneath NW Ethiopia interpreted as underplated material associated with the Trap eruption (e.g., Mackenzie, et al., 2005). As a result, the western crust of the MER is ~10 km thicker than the eastern crust. The magmatic activity pre-dates initiation of significant extension in the MER, which only began in the middle-late Miocene (e.g., Purcell, 2018; Macgregor, 2018), but is roughly synchronous to the onset of extension in the Gulf of Aden, propagating into the Red Sea since ~30-35 Ma (e.g., Wolfenden, et al., 2005; Bonini, et al., 2005; Ebinger & Sleep, 1998). Recent geophysical and field surveys across the Central Afar and Red Sea segments (e.g., Hammond, et al., 2011; Stab, et al., 2016) show that extension is distributed over a large domain with normal faults dipping mostly toward the Ethiopian side of the rift. In addition, the Yemen margin is short compared to the Afar region from the Ethiopian Plateau to the Red Sea, where a progressive thinning and a velocity gradient distributed over at least 300 km are observed (e.g., Kogan, et al., 2012). A combination of mechanical stretching and thermal weakening of the continental lithospheric mantle, similar to conditions explored in our numerical experiments, leads to a wide rift northward, in line with rare seismicity below 20 km (e.g., Yang & Chen, 2010) and early replacement of the lithospheric mantle by the channelling asthenospheric plume head underneath (e.g., Stab, et al., 2016). The asymmetry of the deformation is consistent with northward displacement of the asthenosphere relative to the lithosphere fostering the Cenozoic northward motion of Africa with respect to the Eurasian continent (e.g., Jolivet, et al., 2018; Faccenna, et al., 2013), an interpretation that is consistent with our numerical

experiments (e.g., Fig. 8a, b and Fig. 15). Eocene mantle upwelling impinging the East African lithosphere, leading to intense magmatism and onset of asymmetric extension in the Gulf of Aden propagating into the Red Sea, is also consistent with distal initiation of lithospheric stretching and magmatic activity with respect to the plume axial zone and suggests significant shear stresses at the base of and into the lithosphere. These features, also observed into our models, particularly those that assume a warm and weak lithosphere, suggest that basal simple shearing induced by the underlying asthenospheric mantle flow is a primary driver of the cross-lithospheric strain evolution of the entire East African rift system (Fig. 15). Assuming a steady mantle flux and recovering ~800 km of lithospheric stretching from the Ethiopian Plateau to the Aden-Red Sea region since the onset of extension (e.g., Stab, et al., 2016), one can estimate the horizontal distance $|D|$ between the region of initial localization of extension and the plume axial zone underneath Lake Turkana between ~200-300 km. The analytical solution in Fig. 2 thus indicates a thickness of the Oligocene African lithosphere between 80-120 km, with T_e between ~20-40 km.

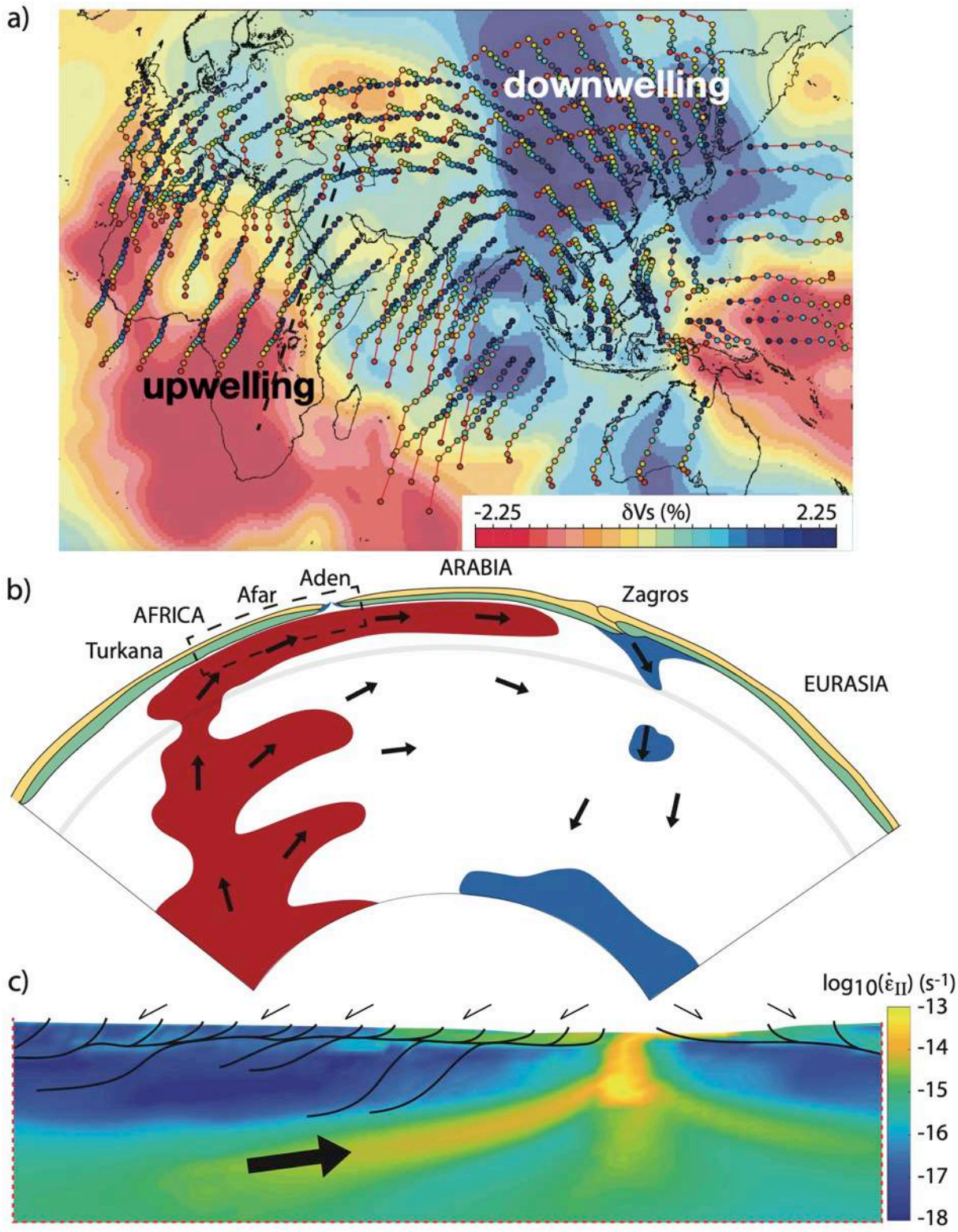

Figure 15: a) Kinematic trajectories since 50 Ma (one step every 5 Ma, from red to blue) on top of the S-wave velocity anomalies of the lower mantle (LLSVP at 2.800 km), modified after Jolivet et al., 2018 (tomography from Becker & Boschi, 2002). b) Sketch of mantle convection underneath the East African Rift, Arabia and the Zagros Range (approximate location shown by the dashed line in a) representing the low-velocity anomaly reaching further to the north in the less viscous upper mantle and the downwelling in the Tethyan subduction zone (Zagros). c) Comparison with the numerical simulation shown in Fig. 8b (zoom within the dashed, red rectangle) and the sketch of mantle convection (black dashed rectangle).

Mantle tomography models show a low velocity anomaly centred below the Afar region (e.g., Ebinger & Sleep, 1998; Lithgow-Bertelloni & Silver, 1998; Moucha & Forte, 2011; Faccenna, et al., 2013). Petrological differences between Afar and Kenyan lavas suggest that two Cenozoic plumes may have existed (e.g., George, et al., 1998; Rogers, et al., 2000), the first rising and dispersing beneath Kenya since the Eocene, and the second rising from underneath Afar, driving magmatism into the axial MER, the Afar depression and north-western Ethiopia (e.g., Bonini, et al., 1997; Kendall, et al., 2005; Ebinger, 2005; Corti, 2009; Corti, 2008). Regions of thinned lithosphere established along inherited structures channelled buoyant magmas, in turn localizing the strain, rock exhumation and lithospheric rupturing in the African-Arabian rift system (e.g., Mohr & Zanettin, 1988; Corti, 2009; Kendall, et al., 2005; Bastow, et al., 2010; Keranen, et al., 2009; Gao, et al., 2010; Obrebski, et al., 2010). Co-location of extensional strain, magmatism, and rock exhumation in our numerical experiments (e.g., Fig. 8 and 10) supports this interpretation and further suggests that basal lithospheric shearing due to the asthenospheric flow, in addition to inherited lithospheric structures (e.g., Corti, 2008; Corti, 2009; Corti, et al., 2007; Brune, et al., 2017), focuses lithospheric thinning and eventually leads to rupturing.

Evolution of topography and orographic contribution

The Ethiopian and Somalian plateaus are part of the African Superswell, a wide region of anomalously high topography (e.g., Nyblade & Robinson, 1994) that generates an east-west orographic effect involving a strong precipitation gradient across the strike of the rift. However, assessing the possible contribution of orography and lateral erosion gradients to the East African rifting dynamics is challenging because limited information regarding orographic patterns in the geological past exist and the evolution of the topography, progressively erased by erosion, is unclear. Early studies suggested uplift in Ethiopia in the late Eocene, preceding both the flood-basalt emplacement and the main rifting episodes (e.g., Dainelli, 1943; Beydoun, 1960; Mohr, 1976). Successive studies argued against major uplift before the flood-basalt event (e.g., Merla, et al., 1979; Menzies, et al., 1997), but significant erosion in Northern Ethiopia as early as 25-30 Ma ago suggests that an elevated plateau existed since at least the Oligocene (e.g., Pik, et al., 2003). A polyphase history of early Oligocene domal uplift by ~1 km followed by fast uplift of the plateau by ~2 km during the Plio-Pleistocene is plausible (e.g., Gani, et al., 2007; Baker & Mohr, 1972; Almond, 1986; Adamson & Williams, 1987; Sembroni, et al., 2016) and consistent with the thermal and

mechanical action of the recent asthenospheric plume activity at the base of the lithosphere (e.g., Pik, et al., 2003; Gani, et al., 2007; Dugda, et al., 2007; Burov & Gerya, 2014; Koptev, et al., 2016) (e.g., Fig. 7). If correct, then orographic effects and similar asymmetric erosion patterns to those observed today (Fig. 16b) may also have occurred prior to the onset of extension in the MER (e.g., Chorowicz, et al., 1998; Pik, et al., 2003; Garzanti, et al., 2006; Gani, et al., 2007; Sembroni, et al., 2016). In support to this claim, lower Miocene basaltic lava flows meandering parallel to the present rivers of the Ogaden basin (SE Ethiopia) suggest an Oligocene landscape whose configuration was similar to the present (Sembroni & Molin, 2018).

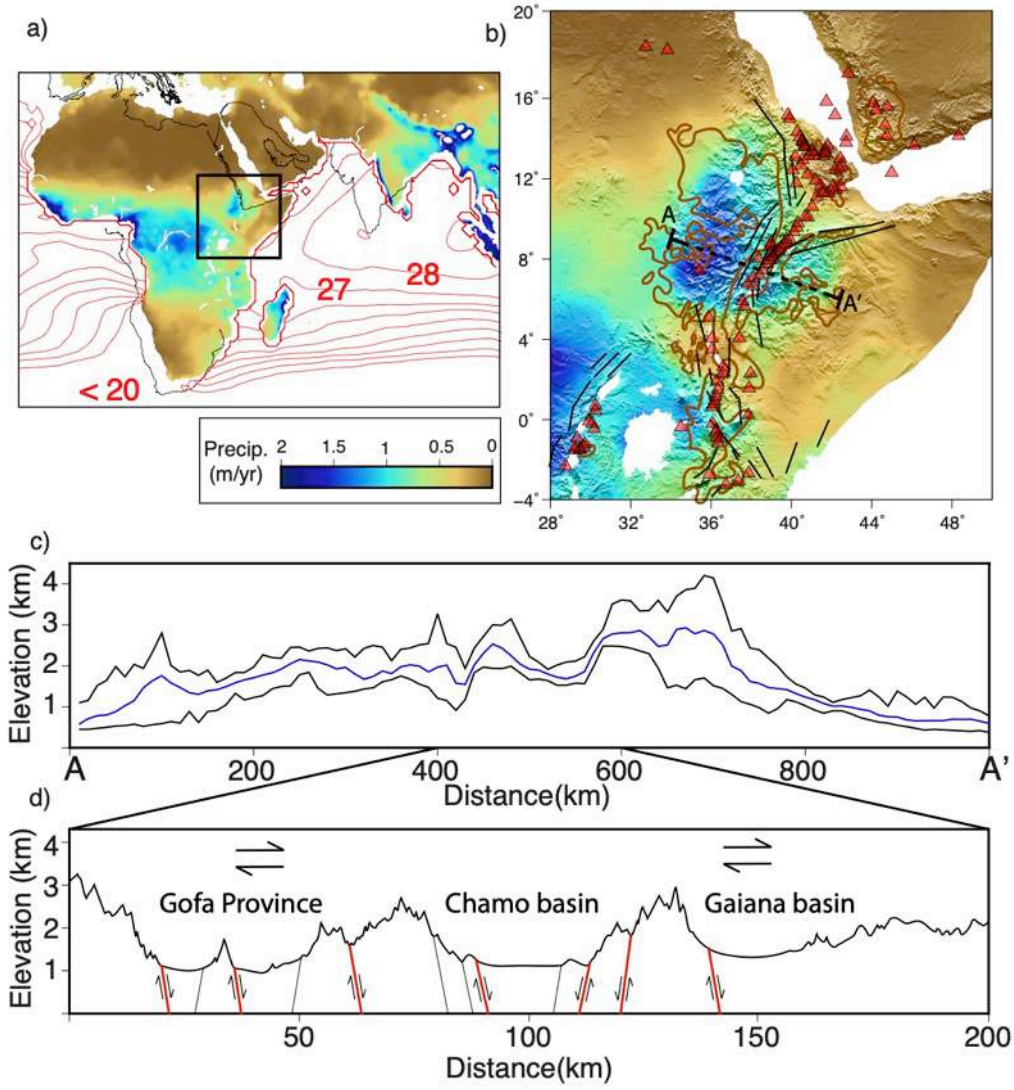

Figure 16: a) The inset shows the large-scale present-day mean annual precipitation (Willmott & Matsuura, 2001) and the sea surface temperatures (red isolines), as well as the lower Miocene paleogeography (black lines) (Seton et al., 2012). b) Mean annual precipitation, active volcanoes (Venzke, 2013), main extensional structures (black lines) and extent of Eocene flood basalts (brown line). c) 100 km wide topographic swath profile (location shown in a) and b), mean elevation in blue and min and max elevation in black). Note the overall asymmetry of the Ethiopian and Somalian plateaus due to orographic precipitation. c) Simplified profile (location shown in a-c)), modified after Corti et al., 2018 (see also references therein). Note

the tectonic asymmetry across the profile with mostly east-dipping normal boundary faults accommodating the majority of the deformation (red lines). The structural asymmetry is consistent with basal lithospheric top-to-the-east shearing. See text for more detail.

At present, the West African monsoon causes south-westerly winds to bring moist air from the equatorial Atlantic Ocean toward East Africa, where orographic air upwelling enhances rainfall on the Ethiopian side of the MER (e.g., Nicholson, 2017). Conversely, the Pacific Warm Pool and the Indonesian throughflow generate a strong east-west temperature gradient in the equatorial Indian Ocean, which leads to prevailing easterlies at low levels and westerlies aloft (i.e., air ascent and descent in the eastern and western Indian Ocean, respectively), responsible for the unusual dry conditions in easternmost equatorial Africa (e.g., Nicholson, 2017) (Fig. 16a). Because the air-sea-land thermal contrast that generates the current asymmetric precipitation in the region is related to the position of Africa with respect to the Indian and Atlantic oceans, it seems plausible that the present-day precipitation pattern was established during the early Neogene. Paleo-climate models also suggest that uplift of the Ethiopian-Somalian plateaus led the East African climate to conditions similar to present-day since at least 8 Ma (Sepulchre, et al., 2006), although such models depend on the assumed timing of topographic variations.

Exposed minimum vertical displacements of major boundary faults along the MER indicate a structural top-to-the-east asymmetry characteristic of rift sectors proximal to the marked orographic gradient (e.g., Laó-Dávila, et al., 2015; Corti, et al., 2018) (Fig. 16c, d). According to our results, the observed topographic and structural asymmetry can be explained by preferential erosion of the footwall of major east dipping extensional faults on the western side of the range (e.g., Fig. 10 and 11). The asymmetric erosion patterns and their feedback with the regional strain and exhumation may further be reflected in lithospheric-scale differences between the Ethiopian and Somalian plateaus. The lithosphere underneath the Somalian Plateau is relatively strong, homogeneous, and characterised by a thick crust. In contrast, the Ethiopian plateau stands above a more heterogeneous lithosphere, with a strong and thick crust in the northern, dryer sector (e.g., Mackenzie, et al., 2005), but a weaker and thinner crust to the south, where the modern orographic precipitation and erosion gradient is marked (e.g., Keranen & Klemperer, 2008; Keranen, et al., 2009). Our modelling results show that a higher amount of precipitation/erosion in the southwestern Ethiopian plateau may have effectively thinned the crust, possibly resulting in the marked across-MER asymmetry in bulk crustal V_p/V_s ratios, magnetotelluric data, body-wave tomography, and T_e estimates (Corti, et al., 2018, and references therein). Although not conclusive, significant off-axis

recent deformation and magmatic activity in the southwestern Ethiopian plateau along the transversal Yerer Tullu-Wellel and Goba-Bonga volcano-tectonic lineaments (e.g., Adhana, 2014; Corti, et al., 2018), in contrast to the absence of significant recent activity in the Somalian plateau, provides further support to these interpretations. The MER may thus be the first recognized example of orography-conditioned continental rift. If correct, where erosion and exhumation are unequal on the two sides of the Ethiopian-Somalian range, the exposed vertical displacement along major normal faults underestimates the structural top-to-the-east asymmetry, which reaches lithospheric scales.

6. Conclusions

We investigate the relationships between far field lithospheric extension, asthenospheric plume forces and orography in driving the mechanisms and location of extensional lithospheric strain through analytical and numerical models. Results indicate that plume-induced basal lithospheric shearing drives continental rupturing away from the asthenospheric plume axis at a horizontal distance that ranges from a few tens to several hundreds of kilometers and is inversely proportional to the lithospheric elastic thickness. Orographic precipitation and associated lateral erosion gradient drive changes in the strain rate and partial melting down to sub-lithospheric levels and promote lithospheric rupturing and/or asymmetric topography, strain and exhumation toward the wetter and more eroded side of an extensional range.

These results are consistent with the first-order geological record from the East African rift system, suggesting that the mantle flow and climate-controlled erosion gradients affected its strain, exhumation, and topographic history. Apart from the economic interest in the architecture of continental margins, the fundamental role of the mantle flow and orography in co-determining the location of continental lithospheric rupturing has far-reaching implications for our understanding of the interactions between plate tectonics and climatic changes throughout the Earth's history.

Acknowledgements

Pietro Sternai received funding for this contribution from the Italian MIUR (Rita Levi Montalcini grant, DM 694-26/2017). This work is also funded by the project MIUR –

Dipartimenti di Eccellenza 2018-2022, Department of Earth and Environmental Sciences, University of Milano-Bicocca.

Competing interests

The authors declare no conflict of interests.

Data availability

No datasets were generated during the current study, but the codes used are available from the corresponding author on request.

Table 1: Material properties used in all numerical experiments: ρ_0 (of solid and molten material) is the density, **E_a** is the activation energy, **V_a** is the activation volume, *n* is the stress exponent, **C** is the cohesion, **Qz.** and **Ol.** correspond to the abbreviations of quartzite and olivine, **φ** is the effective internal friction angle, c is the thermal conductivity, $\boldsymbol{\mu}$ is the Young's modulus, $\boldsymbol{\nu}$ is the Poisson's ratio, **C_p** is the specific heat capacity, **H_r** is the radiogenic heat production, $\boldsymbol{\alpha}$ and $\boldsymbol{\beta}$ are the thermal expansion and compressibility, respectively, $\boldsymbol{Q_l}$ is the lithology-related latent heating, and $\boldsymbol{T_s}$ and $\boldsymbol{T_l}$ are the solidus and liquidus temperature, respectively. Values are taken from Ranalli, 1995, Turcotte & Schubert, 2002, Gerya, 2010 (and references therein).

	ρ_0^s, ρ_0^l (kg/m^3)	E_a (kJ/mol)	V_a (m^3/mol)	n	C (MPa)	Viscous flow law	sin(ϕ)	C_T (W/m/K)	μ (GPa)	ν
Upper cont. crust	2800 solid 2400 molten	154	8	2.3	1	Wet Qz.	0.2	0.64+807/(T+77)	10	0.2
Lower cont. crust	3000 solid 2700 molten	238	8	3.2	1	Wet Qz.	0.2	0.64+807/(T+77)	25	0.2
Mantle	3300 solid 2700 molten	532	8	3.5	1	Dry Ol.	0.6	0.73+1293/(T+77)	67	0.2

	C_p (J/kg/K)	H_r (mW/m3)	ϵ (1/K)	β (1/Pa)	Q_l (kJ/kg)	T_s (K)	T_l (K)
Upper cont. crust	1000	1	$3x10^{-5}$	$1x10^{-11}$	300	889+17900/(P+54)+20200/(P+54)2 at P<1200 MPa, 831+0.06P at P>1200 MPa	1262+0.09P
Lower cont. crust	1000	0.5	$3x10^{-5}$	$1x10^{-11}$	380	973+70400/(P+354)+77800000/(P+354)2 at P<1600 MPa, 935+0.0035P+0.0000062P^2 at P>1600 MPa	1423+0.105P
Mantle	1000	0.02	$3x10^{-5}$	$1x10^{-11}$	400	1394+0.132899P-0.000005104P2 at P<1000 MPa, 2212+0.030819(P-10000) at P>1200 MPa	2073+0.114P

References – Appendix A

Adamson, D. & Williams, M. A., 1987. Geological setting of Pliocene rifting and deposition in the Afar Depression of Ethiopia. *Journal of Human Evolution,* Volume 16, p. 597–610.

Adhana, T. A., 2014. The occurrence of a complete continental rift type of volcanic rocks suite along the Yerer–Tullu Wellel Volcano Tectonic Lineament, Central Ethiopia. *Journal of African Earth Sciences,* Volume 99, pp. 374-385.

Allemand, P., & Brun, J. P., 1991. Width of continental rifts and rheological layering of the lithosphere. *Tectonophysics*, *188*(1-2), 63-69.

Almond, D. C., 1986. Geological evolution of the Afro-Arabian dome. *Tectonophysics,* Volume 131, p. 301–332.

Anderson, E. M., 1951. The Dynamics of Faulting. *Oliver and Boyd.*

Anderson, R. E., 1971. Thin-skin distention in the Tertiary rock of southwestern Nevada. *Geological Society of America Bulletin,* Volume 105, pp. 1019-1052.

Armitage, J., Ferguson, D. J., Petersen, K. D. & Creyts, T. T., 2019. The importance of Icelandic ice sheet growth and retreat on mantle CO2 flux. *Geophysical Research Letters,* 46(12), pp. 6451-6458.

Baker, B. H. & Mohr, P. A., 1972. Geology of the Eastern Rift System of Africa. *Geological Society of America Special Paper, Boulder Colorado.,* Volume 136, p. 67.

Barry, R. G., 1981. Mountain weather and climate. p. 313.

Bastow, I. D., Pilidou, S., Kendall, J. M. & Stuart, G. W., 2010. Melt-induced seismic anisotropy and magma assisted rifting in Ethiopia: Evidence from surface waves. *Geochemistry, Geophysics, Geosystems,* 11(6).

Becker, T. W. & Boschi, L., 2002. A comparison of tomographic and geodynamic mantle models.. *Geochemistry, Geophysics, Geosystems, ,* 3(1), p. 1003.

Beydoun, Z. R., 1960. Synopsis of the Geology of East Aden Protectorate. *XXI International Geological Congress, Copenhagen,* Volume 21, p. 131–149.

Bijwaard, H. & Spakman, W., 1999. Tomographic evidence for a narrow whole mantle plume beneath Iceland. *Earth Planet. Sci. Lett.,* Volume 166, p. 121–126.

Bonini, M. et al., 2005. Evolution of the Main Ethiopian Rift in the frame of Afar and Kenya rifts propagation. *Tectonics,* 24(1).

Bonini, M., Souriot, T., Boccaletti, M. & Brun, J. P., 1997. Successive orthogonal and oblique extension episodes in a rift zone: Laboratory experiments with application to the Ethiopian Rift. *Tectonics,* 16(2), pp. 347-362.

Brace, W. F. & Kohlstedt, D. L., 1980. Limits on lithospheric stress imposed by laboratory experiments. *Journal of Geophysical Research: Solid Earth,* 85(B11), pp. 6248-6252.

Brown, M. & Solar, G. S., 1998. Shear-zone systems and melts: feedback relations and self-organization in orogenic belts. *Journal of structural geology,* 20(2-3), pp. 211-227.

Brune, S., Corti, G. & Ranalli, G., 2017. Controls of inherited lithospheric heterogeneity on rift linkage: Numerical and analog models of interaction between the Kenyan and Ethiopian rifts across the Turkana depression. *Tectonics,* 36(9), pp. 1767-1786.

Brunet, D. & Yuen, D. A., 2000. Mantle plumes pinched in the transition zones. *Earth Planet. Sci. Lett.,* Volume 178, p. 13–27.

Buck, W. R., 1991. Modes of continental lithospheric extensions. *Journal of Geophysical Research,* 96(B12), pp. 20161-20178.

Buck, W. R., 1993. Effect of lithospheric thickness on the formation of high- and low-angle normal faults. *Geology,* Volume 21, p. 933–936.

Buck, W. R., 2004. Consequences of Asthenospheric Variability in Continental Rifting. *in Rheology and Deformation of the Lithosphere at Continental Margins (eds Karner, G. D., Taylor, B., Driscoll, N. W. & Kohlstedt, D. L.) 1–30 (Columbia Univ. Press, New York)*..

Buiter, S. & Torsvik, T. H., 2014. A review of Wilson Cycle plate margins: A role for mantle plumes in continental break-up along sutures?. *Gondwana Research,* 26(2), pp. 627-653.

Burg, J. P., Bodinier, J. L. & Gerya, T., 2009. Translithospheric mantle diapirism: geological evidence and numerical modelling of the Kondyor zoned ultramafic complex (Russian Far-East). *Journal of Petrology,* Volume 50, p. 289–321.

Burg, J. P. & Gerya, T. V., 2005. The role of viscous heating in Barrovian metamorphism of collisional orogens: thermomechanical models and application to the Lepontine Dome in the Central Alps. *Journal of Metamorphic Geology,* 23(2), pp. 75-95.

Burke, K. & Whiteman, A. J., 1973. Uplift, rifting and the break-up of Africa.. *In: Tarling, D.H., Runcorn, S.K. (Eds.), Implications of Continental Drift to the Earth Sciences. Academic Press,* p. pp. 735–755..

Burov, E., 2011. Rheology and strength of the lithosphere.. *Mar. Petrol. Geol.,* Volume 28, p. 1402–1443.

Burov, E. B. & Cloetingh, S., 1997. Erosion and rift dynamics: new thermomechanical aspects of post-rift evolution of extensional basins. *Earth and Planetary Science Letters,* Volume 150, pp. 7-26.

Burov, E. & Diament, M., 1995. The effectiveelasticthickness(Te) of continentallithosphere: What doesit really mean?. *Journal of Geophysical Research,* 100(B3), pp. 3905-3927.

Burov, E. & Gerya, T., 2014. Asymmetric three-dimensional topography over mantle plumes. *Nature,* Volume 513, pp. 85-89.

Burov, E. & Poliakov, A., 2001. Erosion and rheology controls on synrift and postrift evolution: Verifying old and new ideas using a fully coupled numerical model. *Journal of Geophysical Research: Solid Earth,* 106(B8), pp. 16461-16481.

Byerlee, J., 1978. Friction of rocks.. *In Rock friction and earthquake prediction,* pp. 615-626.

Chorowicz, J. et al., 1998. The Tana basin, Ethiopia: intra-plateau uplift, rifting and subsidence. *Tectonophysics,* 295(3-4), pp. 351-367.

Collettini, C. & Sibson, R. H., 2001. Collettini, C., Sibson, R.H., 2001. Normal faults normal friction?. *Geology,* Volume 29, p. 927–930.

Condie, K. C., 2001. Mantle plumes and their record in Earth history. *Cambridge university press..*

Corti, G., 2008. Control of rift obliquity on the evolution and segmentation of the main Ethiopian rift. *Nature Geoscience,* 1(4), pp. 258-262.

Corti, G., 2009. Continental rift evolution: from rift initiation to incipient break-up in the Main Ethiopian Rift, East Africa. *Earth-Science Reviews,* 96(1-2), pp. 1-53.

Corti, G. et al., 2018. Control of pre-rift lithospheric structure on the architecture and evolution of continental rifts: insights from the Main Ethiopian Rift, East Africa. *Tectonics,* Volume 37, pp. 477-496.

Corti, G. et al., 2018. Off-axis volcano-tectonic activity during continental rifting: Insights from the transversal Goba-Bonga lineament, Main Ethiopian Rift (East Africa). *Tectonophysics,* Volume 728-729, pp. 75-91.

Corti, G., van Wijk, J., Cloetingh, S. & Morley, C. K., 2007. Tectonic inheritance and continental rift architecture: Numerical and analogue models of the East African Rift system. *Tectonics,* 26(6).

Courant, R., 1928. On the partial difference equations of mathematical physics. *Mathematische Annalen,* Volume 100, pp. 32-74.

Courtillot, V., Davaille, A., Besse, J. & Stock, J., 2003. Three distinct types of hotspots in the Earth's mantle. *Earth and Planetary Science Letters,* 205(3-4), pp. 295-308.

Crameri, F. et al., 2012. A comparison of numerical surface topography calculations in geodynamic modelling: an evaluation of the 'sticky air'method.. *Geophysical Journal International,* 189(1), pp. 38-54.

Dainelli, G., 1943. Geologia dell'Africa Orientale. *Reale Accademia d'Italia. 3 vols..*

Dewey, J. F. & Burke, K., 1975. Hot-spots and continental break-up. *Geology,* Volume 2, p. 57–60.

Doglioni, C., Carminati, E. & Bonatti, E., 2003. Rift asymmetry and continental uplift. *Tectonics,* 22(3).

Dugda, M., Nyblade, A. A. & Julia, J., 2007. Thin lithosphere beneath the Ethiopian Plateau revealed by a joint inversion of Rayleigh Wave Group velocities and receiver functions. *Journal of Geophysical Research,* Volume 112, p. doi:10.1029/2006JB004918.

Ebinger, C., 2005. Continental break-up: the East African perspective. *Astronomy & Geophysics,* 46(2), pp. 2-16.

Ebinger, C. J. & Sleep, N. H., 1998. Cenozoic magmatism throughout east Africa resulting from impact of a single plume. *Nature,* 395(6704), pp. 788-791.

England, P. & Richardson, S. W., 1977. The influence of erosion upon the mineral facies of rocks from different metamorphic environments. *J. Geol. Sot. London,* Volume 134, pp. 201-213.

Faccenna, C. et al., 2014. Isostasy, dynamic topography, and the elevation of the Apennines of Italy. *Earth and Planetary Science Letters,* Volume 407, pp. 163-174.

Faccenna, C., Becker, T. W., Jolivet, L. & Keskin, M., 2013. Mantle convection in the Middle East: Reconciling Afar upwelling, Arabia indentation and Aegean trench rollback. *Earth and Planetary Science Letters,* Volume 375, pp. 254-269.

Fitton, G. J., 1983. Active versus passive continental rifting: Evidence from the West African rift system. *Tectonophysics,* Volume 94, p. 473–481.

Fleitout, L. & Froidevaux, C., 1980. Thermal and mechanical evolution of shear zones.. *Journal of Structural Geology,* 2(1-2), pp. 159-164.

Forsyth, D. & Uyeda, S., 1975. On the relative importance of the driving forces of plate motions. *Geophys. J. R. Astron. Soc.,* Volume 43, p. 163–200.

Forsyth, D. W., 1992. Finite extension and low-angle normal faulting. *Geology,* Volume 20, p. 27–30.

Foulger, G. R. & Hamilton, W. B., 2014. Earth science: Plume hypothesis challenged. *Nature,* 505(618).

Gani, N. D., Abdelsalam, M. G. & Gani, M. R., 2007. Blue Nile incision on the Ethiopian Plateau: pulsed plateau growth, Pliocene uplift, and hominin evolution. *GSA Today,* Volume 17, p. 4–11.

Gao, S. S., Liu, K. H. & Abdelsalam, M. G., 2010. Seismic anisotropy beneath the Afar Depression and adjacent areas: Implications for mantle flow. *Journal of Geophysical Research: Solid Earth,* 115(B12).

Garzanti, E. et al., 2006. Petrology of Nile River sands (Ethiopia and Sudan): sediment budgets and erosion patterns. *Earth and Planetary Science Letters,* 252(3-4), pp. 327-341.

George, R., Rogers, N. & Kelley, S., 1998. Earliest magmatism in Ethiopia: Evidence for two mantle plumes in one flood basalt province. *Geology,* 26(10), pp. 923-926.

Gerya, T., 2010. *Introduction to Numerical Geodynamic Modelling.* s.l.:Cambridge University Press.

Gerya, T. V. & Yuen, D. A., 2003. Characteristics-based marker-in-cell method with conservative finite-differences schemes for modelling geological flows with strongly variable transport properties. *Physics of the Earth and Planetary Interiors,* 140(4), pp. 293-318.

Gerya, T. & Yuen, D., 2007. Robust characteristics method for modelling multiphase visco-elasto-plastic thermo-mechanical problems. *Phys. Earth Planet. Inter.,* Volume 163, p. 83–105..

Gilbert, G., 1877. Geology of the Henry mountains. *Government Printing Office,* pp. 1-160.

Gillard, M., Autin, J. & Manatschal, G., 2016. Fault systems at hyper-extended rifted margins and embryonic oceanic crust: Structural style, evolution and relation to magma. *Marine and Petroleum Geology,* Volume 76, pp. 51-67.

Goetze, C., 1978. The mechanisms of creep in olivine. *Philosophical Transactions of the Royal Society of London. Series A, Mathematical and Physical Sciences,* 288(1350), pp. 99-119.

Goetze, C. & Evans, B., 1979. Stress and temperature in the bending lithosphere as constrained by experimental rock mechanics. *Geophysical Journal International,* 59(3), pp. 463-478. ISO 690.

Gottardi, R. et al., 2015. Strain and permeability gradients traced by stable isotope exchange in the Raft River detachment shear zone, Utah. *Journal of Structural Geology,* Volume 71, pp. 41-57.

Hager, B. H. et al., 1985. Lower mantle heterogeneity, dynamic topography and the geoid. *Nature,* Volume 313, p. 541–545.

Hammond, J. O. et al., 2011. The nature of the crust beneath the Afar triple junction: Evidence from receiver functions. *Geochemistry, Geophysics, Geosystems,* 12(12).

Houseman, G., & England, P., 1986. A dynamical model of lithosphere extension and sedimentary basin formation. *Journal of Geophysical Research: Solid Earth*, *91*(B1), 719-729.

Hofmann, C. et al., 1997. Timing of the Ethiopian flood basalt event and implications for plume birth and global change. *Nature,* 389(6653), pp. 838-841.

Hooper, A. et al., 2011. Increased capture of magma in the crust promoted by ice-cap retreat in Iceland. *Nature Geoscience,* Volume 4, pp. 783-786.

Hovius, N., Stark, C. P. & Allen, P. A., 1997. Sediment flux from a mountain belt derived by landslide mapping. *Geology,* 25(3), pp. 231-234.

Howard, A. D. & Kerby, G., 1983. Channel changes in badlands. *Geol. Soc. of Am. Bull.,* Volume 94, pp. 739-752.

Huismans, R. & Beaumont, C., 2011. Depth-dependent extension, two-stage breakup and cratonic underplating at rifted margins. *Nature,* Volume 473, pp. 74-79.

Huismans, R. S. & Beaumont, C., 2003. Symmetric and asymmetric lithospheric extension: Relative effects of frictional-plastic and viscous strain softening. *Journal of Geophysical Research,* 108(B10), p. 2496.

Jackson, J. A., 1987. Active normal faulting and crustal extension. *In: Coward, M.P., Dewey, J.F., Hancock, P.L. (Eds.), Continental Extensional Tectonics, Geological Society, London, Special Publication,* Volume 28, p. 3–17.

Jellinek, A. M. & De Paolo, D. J., 2003. A model for the origin of large silicic magma chambers: precursors of caldera-forming eruptions. *Bulletin of Volcanology,* 65(5), p. pp.363–381..

Jellinek, A. M., Manga, M. & Saar, M. O., 2004. Did melting glaciers cause volcanic eruptions in eastern California? Probing the mechanics of dike formation. *Journal of Geophysical Research,* Volume 109.

Jolivet, L. et al., 2018b. Mantle Flow and Deforming Continents: From India-Asia Convergence to Pacific Subduction. *Tectonics,* p. 10.1029/2018TC005036.

Jolivet, L. et al., 2018. Extensional crustal tectonics and crust-mantle coupling, a view from the geological record. *Earth-Science Reviews,* Volume 185, pp. 1187-1209.

Jull, M. & McKenzie, D., 1996. The effect of deglaciation on mantle melting beneath Iceland. *Journal of Geophysical Research,* 101(B10), pp. 21815-21828.

Kendall, J. M. & Lithgow-Bertelloni, C., 2016. Why is Africa rifting?. *Magmatic Rifting and Active Volcanism. Geological Society, London, Special Publications,* Volume 420, p. 11–30.

Kendall, J. M. et al., 2005. Magma-assisted rifting in Ethiopia. *Nature,* Volume 433, pp. 146-148.

Keranen, K. M. & Klemperer, S. L., 2008. Discontinuous and diachronous evolution of the Main Ethiopian Rift: Implications for the development of continental rifts. *Earth and Planetary Science Lettters,* Volume 265, p. doi:10.1016/j.epsl.2007.09.038..

Keranen, K. M. et al., 2009. Low lower crustal velocity across Ethiopia: Is the Main Ethiopian Rift a narrow rift in a hot craton?. *Geochemistry, Geophysics, Geosystems,* 10(5).

Kogan, L. et al., 2012. Lithospheric strength and strain localization in continental extension from observations of the East African Rift. *Journal of Geophysical Research: Solid Earth,* Volume 117(B3).

Kohlstedt, D. L. (2002). Partial melting and deformation. Reviews in mineralogy and geochemistry, 51(1), 121-135.

Koptev, A. et al., 2016. Contrasted continental rifting via plume-craton interaction: Applications to Central East African Rift. *Geoscience Frontiers,* Volume 7, pp. 221-236.

Koptev, A. et al., 2015. Dual continental rift systems generated by plume–lithosphere interaction. *Nature,* Volume 8, pp. 388-392.

Kreemer, C., Blewitt, G. & Klein, E. C., 2014. A geodetic plate motion and Global Strain Rate Model. *Geochemistry, Geophysics, Geosystems,* 15(10), pp. 3849-3889.

Laó-Dávila, D. A., Al-Salmi, H. S., Abdelsalam, M. G. & Atekwana, E. A., 2015. Hierarchical segmentation of the Malawi rift: the influence of inherited lithospheric heterogeneity and kinematics in the evolution of continental rifts. *Tectonics,* Volume 34, p. 2399–2417.

Lavier, L. & Manatschal, G., 2006. A mechanism to thin the continental lithosphere at magma-poor margins. *Nature,* 440(7082), pp. 324-328.

Le Bas, M. J., 1987. Ultra-alkaline magmatism without rifting. *Tectonophysics,* Issue 143, p. 75–84.

Lister, G. S., Etheridge, M. A. & Symonds, P. A., 1986. Detachment faulting and the evolution of passive continental margins. *Geology,* 14(3), pp. 246-250.

Lithgow-Bertelloni, C. & Silver, P. G., 1998. Dynamic topography, plate driving forces and the African superswell. *Nature,* 395(6699), p. 269.

Maccaferri, F., Rivalta, E., Keir, D., & Acocella, V., 2014. Off-rift volcanism in rift zones determined by crustal unloading. Nature Geoscience, 7(4), 297-300.

Maccaferri, F., Bonafede, M. & Rivalta, E., 2011. A quantitative study of the mechanisms governing dike propagation, dike arrest and sill formation. *Journal of Volcanology and Geothermal Research,* 208(1-2), pp. 39-50.

Macgregor, D., 2018. History of the development of Permian–Cretaceous rifts in East Africa: a series of interpreted maps through time. *Petroleum Geoscience,* 24(1), pp. 8-20.

Mackenzie, G. D., Thybo, H. & Maguire, P. K., 2005. Crustal velocity structure across the Main Ethiopian Rift: results from two-dimensional wide-angle seismic modelling. *Geophysical Journal International,* 162(3), pp. 994-1006.

Manatschal, G., 1999. Fluid-and reaction-assisted low-angle normal faulting: evidence from rift-related brittle fault rocks in the Alps (Err Nappe, eastern Switzerland). *Journal of Structural Geology,* 21(7), pp. 777-793.

Manatschal, G. & Bernoulli, D., 1999. Architecture and tectonic evolution of nonvolcanic margins: Present-day Galicia and ancient Adria. *Tectonics,* 18(6), pp. 1099-1119.

Mareschal, J. C. & Gangi, A. F., 1977. Equilibrium position of a phase boundary under horizontally varying surface loads. *Geophys J. R. Astron. Soc.,* Volume 49, pp. 757-779.

McKenzie, D., 1978. Some remarks on the development of sedimentary basins. *Barth Planet. Sci. Lett.,* Volume 40, pp. 25-32.

McKenzie, D. & Bickle, M. J., 1988. The volume and composition of melt generated by extension of the lithosphere. *Journal of petrology,* 29(3), pp. 625-679.

Menzies, M., Gallagher, K., Yelland, A. & Hurford, A. J., 1997. Volcanic and nonvolcanic rifted margins of the Red Sea and Gulf of Aden: crustal cooling and margin evolution in Yemen. *Geochimica et Cosmochimica Acta,* Volume 61, p. 2511–2527.

Merla, G. et al., 1979. Geological map of Ethiopia and Somalia and comment with a map of major landforms (scale 1:2, 000, 000).. *Consiglio Nazionale delle Ricerche, Rome,* Volume 95.

Mohr, P., 1976. The Ethiopian Rift System. *Bulletin of the Geophysical Observatory of Addis Ababa,* Volume 11.

Mohr, P. & Zanettin, B., 1988. The Ethiopian flood basalt province. *In Continental flood basalts. Springer, Dordrecht.,* pp. 63-110.

Molnar, P., England, P. C. & Jones, C. H., 2015. Mantle dynamics, isostasy, and the support of high terrain. *Journal of Geophysical Research: Solid Earth,* 120(3), pp. 1932-1957.

Moucha, R. & Forte, A. M., 2011. Changes in African topography driven by mantle convection. *Nature Geoscience,* Volume 4, p. 707–712.

Nicholson, S. E., 2017. Climate and climatic variability of rainfall over eastern Africa. *Reviews of Geophysics,* 55(3), pp. 590-635.

Nikishin, A. M. et al., 2002. Permo-Triassic intraplate magmatism and rifting in Eurasia: implications for mantle plumes and mantle dynamics. *Tectonophysics,* Volume 351, p. 3–39.

Nyblade, A. A. & Robinson, S. W., 1994. The african superswell. *Geophysical research letters,* 21(9), pp. 765-768.

Obrebski, M., Kiselev, S., Vinnik, L. & Montagner, J. P., 2010. Anisotropic stratification beneath Africa from joint inversion of SKS and P receiver functions. *Journal of Geophysical Research: Solid Earth,* 115(B9).

Olsen, K. H. & Morgan, P., 2006. Introduction: progress in understanding continental rifts. *In Developments in Geotectonics. Elsevier.,* Volume 25, pp. 3-26.

Ord, A. & Hobbs, B. E., 1989. The strength of the continental crust, detachment zones and the development of plastic instabilities.. *Tectonophysics,,* 158(1-4), pp. 269-289.

Patriat, M. & Jolivet, L., 1998. Post-orogenic extension and shallow-dipping shear zones, study of a brecciated decollement horizon in Tinos (Cyclades, Greece) Extènsion post-orogénique et zones de cisaillement. *Comptes Rendus de l'Académie des Sciences-Series IIA-Earth and Planetary Science,* 326(5), pp. 355-362.

Petit, C., Fournier, M. & Gunnell, Y., 2007. Tectonic and climatic controls on rift escarpments: Erosion and flexural rebound of the Dhofar passive margin (Gulf of Aden, Oman). *Journal of Geophysical Research: Solid Earth,* 112(B3), p. ISO 690.

Pik, R., Marty, B., Carignan, J. & Lavé, J., 2003. Stability of the Upper Nile drainage network (Ethiopia) deduced from (U–Th)/He thermochronometry: implications for uplift and erosion of the Afar plume dome. *Earth and Planetary Science Letters,,* 215(1-2), pp. 73-88.

Purcell, P. G., 2018. Re-imagining and re-imaging the development of the East African Rift. *Petroleum Geoscience,* 24(1), pp. 21-40.

Ramsay, J., 1980. Shear zone geometry: a review. *Journal of structural geology,* 2(1-2), pp. 83-99.

Ranalli, G., 1995. *Rheology of the Earth, Deformation and Flow Processes in Geophysics and Geodynamics.* s.l.:Chapman & Hall. .

Ranalli, G. & Murphy, D. C., 1987. Rheological stratification of the lithosphere. *Tectonophysics,* 132(4), pp. 281-295.

Reguzzoni, M., Sampietro, D. & Sansò, F., 2013. Global Moho from the combination of the CRUST2. 0 model and GOCE data. *Geophysical Journal International,* 195(1), pp. 222-237. ISO 690.

Reston, T., 2020. On the rotation and frictional lock-up of normal faults: Explaining the dip distribution of normal fault earthquakes and resolving the low-angle normal fault paradox. *Tectonophysics,* 720(228550).

Rey, P. F., Teyssier, C., & Whitney, D. L. (2009). The role of partial melting and extensional strain rates in the development of metamorphic core complexes. *Tectonophysics*, *477*(3-4), 135-144.

Roche, V. et al., 2018. Emplacement of metamorphic core complexes and associated geothermal systems controlled by slab rollback. *Earth and Planetary Science Letters,* Volume 498, pp. 322-333.

Rogers, N. et al., 2000. Two mantle plumes beneath the East African rift system: Sr, Nd and Pb isotope evidence from Kenya Rift basalts. *Earth and Planetary Science Letters,* 176(3-4), pp. 387-400.

Rooney, T. O., 2017. The Cenozoic magmatism of East-Africa: Part I—Flood basalts and pulsed magmatism. *Lithos,* Volume 286, pp. 264-301.

Rutter, E. H. & Brodie, K. H., 1988. The role of tectonic grain size reduction in the rheological stratification of the lithosphere. *Geologische Rundschau,* 77(1), pp. 295-307.

Sembroni, A. & Molin, P., 2018. Long-term drainage system evolution in the Wabe Shebele River basin (SE Ethiopia-SW Somalia). *Geomorphology,* Volume 320, pp. 45-63.

Sembroni, A. et al., 2016. Evolution of continental-scale drainage in response to mantle dynamics and surface processes: An example from the Ethiopian Highlands. *Geomorphology,* Volume 261, pp. 12-29.

Sengör, A. C. & Burke, K., 1978. Relative timing of rifting and volcanism on Earth and its tectonic implications. *Geophysical Research Letters,* 5(6), pp. 419-421.

Sepulchre, P. et al., 2006. Tectonic Uplift and Eastern Africa Aridification. *Science,* Volume 313, pp. 1419-1423.

Seton , M. et al., 2012. Global continental and ocean basin reconstructions since 200 Ma. *Earth-Science Reviews,* Volume 113, pp. 212-270.

Sibson, R. H., 1990. Conditions for fault-valve behaviour. *in Deformation Mechanisms, Rheology and Tectonics, edited by R. J. Knipe and E. H. Rutter, Geol. Soc. Spec. Publ.,* Volume 54, p. 15–28.

Singh, P. & Kumar, N., 1997. Effect of orography on precipitation in the western Himalayan region. *Journal of Hydrology,* 199(1-2), pp. 183-206.

Spohn, T. & Schubert, G., 1982. Convective thinning of the lithosphere: a mechanism for the initiation of continental rifting. *J. Geophys. Res.,* Volume 87, p. 4669–4681.

Stab, M. et al., 2016. Modes of rifting in magma‐rich settings: Tectono‐magmatic evolution of Central Afar. *Tectonics,* 35(1), pp. 2-38.

Sternai, P., 2020. Surface processes forcing on extensional rock melting. *Scientific Reports,* Volume doi.org/10.1038/s41598-020-63920-w.

Sternai, P. et al., 2017. Magmatic pulse driven by sea-level changes associated with the Messinian salinity crisis. *Nature Geoscience,* Volume DOI: 10.1038/NGEO3032.

Sternai, P. et al., 2012. Pre-glacial topography of the European Alps. *Geology,* 40(12), pp. 1067-1070.

Sternai, P., Jolivet, L., Menant, A. & Gerya, T., 2014. Driving the upper plate surface deformation by slab rollback and mantle flow. *Earth and Planet. Sci. Lett.,* Volume 405, pp. 110-118.

Sternai, P. et al., 2019. Present-day uplift of the European Alps: Evaluating mechanisms and models of their relative contributions. *Earth-Science Reviews,* Volume 190, pp. 589-604.

Stock, J. & Montgomery, D., 1999. Geological constraints on bedrock river incision using the stream power law. *J. Geophys.Res.,* Volume 104, pp. 4983- 4993.

Tackley, P. J., 1998. Self-consistent generation of tectonic plates in three-dimensional mantle convection. *Earth Planet. Sci. Lett.,* Volume 157, p. 9–22.

Turcotte, D. L. & Schubert, G., 2002. *Geodynamics.* Cambridge: Cambridge University Press.

Van Balen, R. T., Van der Beek, P. A. & Cloetingh, S. A., 1995. The effect of rift shoulder erosion on stratal patterns at passive margins: Implications for sequence stratigraphy. *Earth and Planetary Science Letters,* 134(3-4), pp. 527-544.

Venzke, E., 2013. Global Volcanism Program. Volcanoes of the World. Volume doi:https://doi.org/10.5479/si.GVP.VOTW4-2013.

Watts, A. B., 1992. The effective elastic thickness of the lithosphere and the evolution of foreland basins. *Basin Research,* 4(3-4), pp. 169-178. ISO 690.

Watts, A. B., 2009. *Isostasy and flexure of the lithosphere.* Cambridge: Cambridge University Press.

Wernicke, B., 1981. Low angle normal faults in the Basin and Range Province: Nappe tectonics in an extending orogene. *Nature,* Volume 291, pp. 645-648.

Wernicke, B., 1985. Uniform-sense normal simple shear of the continental lithosphere. *Canadian Journal of Earth Sciences,* 22(1), pp. 108-125.

Whipple, K. X., 2009. The influence of climate on the tectonic evolution of mountain belts. *Nature geoscience,* 2(2), p. 97.

Whipple, K. X. & Tucker, G., 1999. Dynamics of the stream-power river incision model: Impli- cations for height limits of mountain ranges, landscape response timescales, and research needs. *Journal of Geophysical Research ,* Volume 104, pp. 17661-17674.

White, R. & McKenzie, D., 1989. Magmatism at rift zones: the generation of volcanic continental margins and flood basalts. *Journal of Geophysical Research,* Volume 94, pp. 7685-7729.

Willett, S. D., 1999. Orogeny and orography: The effects of erosion on the structure of mountain belts. *Journal of Geophysical Research,* 104(b12), pp. 957-981.

Willmott, C. J. & Matsuura, K., 2001. Terrestrial air temperature and precipitation: Monthly and annual time series (1950–1999). *Center for Climatic Research, University of Delaware, Newark.,* Volume Version 1.02..

Wilson, J. T., 1963. A possible origin of the Hawaiian islands. *Canadian Journal of Physics,* Volume 41.

Wilson, M. & Guiraud, R., 1998. Late Permian to recent magmatic activity on the African – Arabian margin of Tethys. *In: McGre- gor, D.S., Moody, R.T.J., Clark-Lowes, D.D. (Eds.), Petroleum Geology of North Africa. Spec. Publ.-Geol. Soc. Lond.,* Volume 132, p. 203–225.

Wolfenden, E. et al., 2005. Evolution of a volcanic rifted margin: Southern Red Sea, Ethiopia. *Geological Society of America Bulletin,* 117(7-8), pp. 846-864.

Yang, Z. & Chen, W. P., 2010. Earthquakes along the East African Rift System: A multiscale, system-wide perspective. *Journal of Geophysical Research: Solid Earth,* Volume 115(B12).

Zhong, S. & Gurnis, M., 1996. Interaction of weak faults and non-Newtonian rheology produces plate tectonics in a 3D model of mantle flow. *Nature,* Volume 383, p. 245–247.

Ziegler, P. A. & Cloetingh, S. A., 2004. Dynamic processes controlling evolution of rifted basins. *Earth-Science Reviews,* Volume 64, pp. 1-50.

Ziegler, P. A., Cloetingh, S., Guiraud, R. & Stampfli, G. M., 2001. Peri-Tethyan platforms: constraints on dynamics of rifting and basin inversion. *In: Ziegler, P.A., Cavazza, W., Robertson, A.H.F., Crasquin-Soleau, S. (Eds.), Peri-Tethys Mem. 6: Peri- Tethyan Rift/Wrench Basins and Passive Margins. Mem. Mus. Natl. Hist. Nat., Paris,* Volume 186, p. 9–49.

APPENDIX B – Article contribution 2

Frontiers of research on coupled surface-deep Earth processes: perspectives from TOPO-EUROPE on climate and energy societal challenges

Sierd Cloetingh[1,2], Pietro Sternai[3], Eszter Békési[1], Kristóf Porkolàb[1,2], Magdala Tesauro[4,2], Alessio Lavecchia[5], Svetlana Botsyun[6], Veleda Muller[3], Alexander Koptev[6,7], François Roure[8], Todd A. Ehlers[6,9], Enrico Serpelloni[10], Liviu Matenco[2], Sébastien Castelltort[11], Taras Gerya[12], Donato Giovannelli[13,14,15,16,17], Alberto Vitale Brovarone[18,19,20], Giovanni Coletti[3], István Kovács[21], Pierre Valla[22], Jon Limberger[23,2]

1. Institute of Earth Physics and Space Science, Sopron, Hungary
2. Department of Earth Sciences, Faculty of Geosciences, Utrecht University, Utrecht, Netherlands
3. Department of Earth and Environmental Sciences, University of Milano-Bicocca, Milano, Italy
4. Dipartimento di Matematica e Geoscienze, Università di Trieste, Trieste Italy
5. Istituto Nazionale di Geofisica e Vulcanologia, Bari, Italy
6. Department of Geosciences, University of Tuebingen, Tuebingen, Germany
7. GFZ German Research Centre for Geosciences, Potsdam, Germany
8. IFP Énergies Nouvelles, Ruel Malmaison, France
9. School of Geographical and Earth Sciences, University of Glasgow, Glasgow, Scotland, UK
10. Istituto Nazionale di Geofisica e Vulcanologia, Rome, Italy
11. Department of Earth Sciences, University of Geneva, Geneva, Switzerland
12. ETH-Zurich, Institute of Geophysics, Switzerland
13. Department of Biology, University of Naples Federico II, Naples, Italy
14. National Research Council – Institute of Marine Biological Resources and Biotechnologies - CNR-IRBIM, Ancona, Italy
15. Department of Marine and Coastal Science, Rutgers University, New Brunswick, NJ, USA
16. Marine Chemistry & Geochemistry Department - Woods Hole Oceanographic Institution, MA, USA
17. Earth-Life Science Institute, Tokyo Institute of Technology, Tokyo, Japan
18. Dipartimento di Scienze Biologiche, Geologiche e Ambientali, Alma Mater Studiorum Università di Bologna, Bologna, Italy
19. Sorbonne Université, Muséum National d'Histoire Naturelle, UMR CNRS 7590, IRD, Institut de Minéralogie, de Physique des Materiaux et de Cosmochimie, IMPMC, 4 Place Jussieu, 75005, Paris, France
20. Institute of Geosciences and Earth Resources, National Research Council of Italy, Pisa, Italy
21. MTA FI Lendület Pannon LitH2Oscope Research Group, Institute of Earth Physics and Space Science, Sopron, Hungary
22. Institute of Earth Sciences (ISTerre), Université Grenoble Alpes, Université Savoie Mont Blanc, CNRS, IRD, IFSTAR, 38000, Grenoble, France
23. TNO Energy Transition, Amsterdam and Utrecht, The Netherlands

Abstract

Better understanding of the interactions between surface and deep Earth processes is fundamental for allowing the Earth Sciences to take a leading position in the dialogue with all domains of frontiers research for climate, environment, energy, geo-resources and biosphere. The International Lithosphere Program (ILP) TOPO-EUROPE initiative serves as a pan-European platform for integrated surface and deep Earth sciences, synergizing observational studies of the Earth structure and fluxes on all spatial and temporal scales with modelling of Earth processes. This review provides a survey of recent breakthroughs in quantitative understanding of coupled surface-deep Earth processes and their impact on our ability to respond to the societal challenges currently faced and secure a more sustainable ecosystem. In this context, we present key examples of domains of frontiers science with rich potential for further advances, multidisciplinary research and community building.

1. INTRODUCTION

The advent and establishment of the theory of plate tectonics in the second half the 20th century, providing an integrated explanation for the bathymetry of oceans, the relative motion of continents, the formation and evolution of orogenic belts and sedimentary basins, glaciations, greenhouse gases concentration changes over geological timescales and related evolution of oceanic and atmospheric circulation patterns embodies the last major revolution in the Earth Sciences. One of the most important recent developments of such theory and coeval improvement of mantle tomography models have been the recognition that processes occurring at the Earth surface and those taking place deep within its interiors are inherently linked. Since this recognition, the understanding of how the Earth's topography evolves has been pursued through joint investigations of the Earth's surface through sedimentology and geomorphology, and of the deep Earth through seismology and geodynamics. More and more commonly, modern geologists interpret basins' stratigraphy, volcanic and hydrothermal activity, ore formation and distribution, the morphology of landscapes, changes in sea level and surface elevation also in terms of deep geodynamic and tectonic processes. Similarly, modern geophysicists explain topographic anomalies as well as erosional and sedimentary changes via data that reports on the deeper Earth structure and dynamics. Because the surface-deep Earth processes coupling is the means for the geological cycling and storage of fundamental elements such as carbon, hydrogen, oxygen and metals, it links the evolution of life and climate to that of plate tectonics, also involving favorable aspects such as the geological conditions that allow our present-day society to function and prosper into the future. This aspect requires, amongst other, knowledge on the distribution of rock formations suitable for extraction and storage of natural compounds such as hydrocarbons, carbon dioxide, hydrogen, heat, compressed air, nuclear waste, etc. in order to develop strategies for production of energy and/or mitigation of climate and environmental changes. It further involves natural hazards related to earthquakes and the redistribution of the surface masses of rocks, water and ice. The relevance of research pertaining to the deep and surface Earth are thus enhanced through a focus on their interaction, particularly considering the threats and challenges that the current climate warming imposes on our societies.

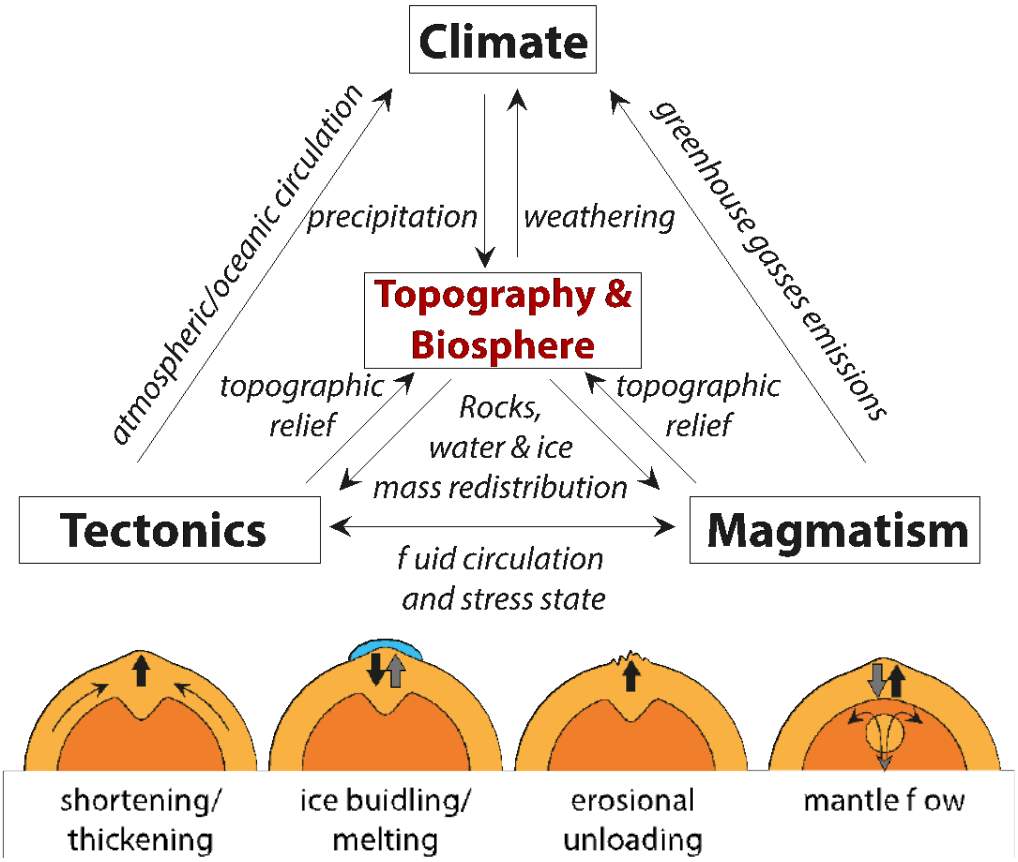

Figure 1.1: Schematic representation of the Earth System Triangle (EST), showing the main components of the Earth System and dynamic interactions. Tectonics, magmatism, and climate are intrinsically coupled with joint expressions on Earth topography. Forcings external to the EST include orbital changes as well as sun activity.

The International Lithosphere Program (ILP) launched a European multidisciplinary program in Europe under the umbrella name of TOPO-EUROPE with a workshop in 2005 and a white paper (Cloetingh et al., 2007) describing its scientific scope. The program represents a bottom-up, community effort to self-organize and cross-fertilize the disparate fields within the geological and geophysical communities. Throughout the last fifteen years the program has continued to grow. The core of the TOPO-EUROPE research activities was supported through funding of a European Collaborative Research (EUROCORES) program administered by the European Science Foundation (ESF), with 14.5 M€ allocated by 23 different member states to better understand and quantify the evolution of topography in Europe, the accompanying changes in sea level and their surface and deep Earth driving mechanisms. The ESF EUROCORES provided funding for the training of more than 60 European young researchers with widespread results published in several special volumes and papers of high-impact international journals and papers. TOPO-EUROPE has been extraordinarily successful in capacity building on a pan-European scale and inspiring large

scale collaborative research in Europe. A number of International Training Networks (ITN) funded by the European Commission for training and networking young researchers followed. The ITNs SUBITOP and TOPOMOD, for instance, have funded more than 20 young researchers together. On a national level, programs such as the TOPO-IBERIA (Garate et al., 2015) program funded by the national research council of Spain (CSIC) with an amount of 8M€ to unravel the structure and evolution of the Iberian topography, with an average elevation higher than that of Switzerland. TOPO-EUROPE also demonstrated the need for integrated European Solid Earth Scientific infrastructures and accomplished the realization of a European Plate Observatory System (EPOS) coordinated by the Italian National Institute of Geophysics and Volcanology (INGV) as part of the European Scientific Research Infrastructure (ESFRI) program. Other examples of community building in the Solid Earth science inspired by TOPO-EUROPE are the AlpArray and AdriaArray programs for deployment of dense networks of seismic stations to address first order questions about intra-crustal heterogeneities and coeval regional seismicity, orogeny and lithosphere dynamics. Overall, TOPO-EUROPE served as a trigger to bring integrative Earth Science to a position where it could more easily branch out to synergies with other disciplines such as Environmental and Climate science.

The interaction between surface and deep Earth processes is far more reaching than anticipated at the onset of the TOPO-EUROPE program and the global nature of the themes addressed by TOPO-EUROPE does not restrict its findings to Europe and its continental margins (Fig. 1.1). Despite the advances made so far, major challenges for frontier research in the domain of coupled surface-deep Earth processes have emerged, requiring to scale up present collaborative and individual research efforts as well as the integrated research approach and methodologies. In this contribution, we review several recent breakthroughs in the domain of the interaction between surface and deep Earth processes. To this aim, we follow a bottom-up sequence, starting with perspectives from the deep mantle, followed by findings from lithospheric and surface processes research. As evident from this overview, these topics cannot be treated in isolation but are intrinsically linked. Recent breakthroughs lay a solid foundation for the next TOPO-EUROPE agenda which, apart from pursuing further frontiers of research in integrated Earth Sciences, will also focus on interfacing with the biosphere, environment, and climate research.

2. EXAMPLES OF RECENT BREAKTHROUGHS IN LINKING DEEP AND SURFACE EARTH DYNAMICS

2.1 Mantle structures, dynamics and interactions with the lithosphere

Seismology has always been a fundamental source of information on the deep Earth, resulting in the widespread acceptance of an Earth structure composed of crust, mantle, and core. With further developments in seismology this first order subdivision has been refined by dividing the crust, mantle, and core into distinct layers. With the advent of plate tectonics, the concept of the lithosphere has emerged, juxtaposing the crust and the more viscous part of the upper mantle. Originally, it was assumed that heterogeneity of the Earth's structure is limited to the crust, while the mantle and core were considered as a simpler, homogeneous radial structure. This picture has dramatically changed during the past decades. In particular, advanced seismic tomography is able to detect crustl/mantle seismic velocity differences of only a few percent (Rickers et al., 2013; Plomerová et al., 2016), corresponding to temperature anomalies in the order of the tens of °C and subtle compositional changes. This allowed imaging of downgoing lithospheric slabs and uprising mantle plumes throughout the entire mantle and has provided new constraints on plate reconstructions and has also shown that there is rich diversity in the mode of subduction and mantle ascent (Arnould et al., 2020) (Fig. 2.1.1).

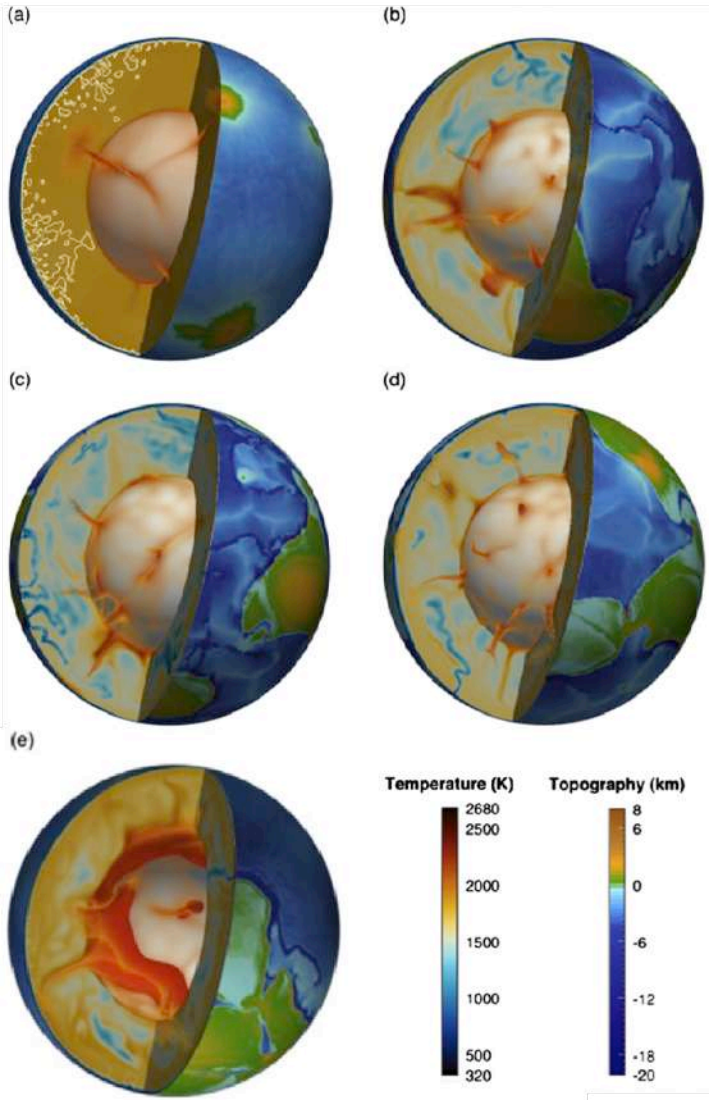

Figure 2.1.1: 3D snapshots of five different numerical simulations of global mantle convection based on different plausible parameter settings to highlight the role of plate tectonics and mantle convection in driving mantle plumes' shape and dynamics (modified after Arnould et al., 2020). Temperature is shown in the interior of the shells and topography at their surface. The white isotherm on (a) highlights small-scale convection. The red isosurface on (e) delineates basal thermochemical heterogeneities. (For interpretation of the colours in the figure(s), the reader is referred to the web version of this article.)

Importantly, the sources of vertically continuous low-velocity anomalies (Ritsema et al., 1999) interpreted as classic Morgan-type plumes originating at the base of the lower mantle (Morgan, 1971), are not randomly distributed across the core-mantle boundary but are preferentially localized within or at the boundaries of two large low shear wave velocity provinces (LLSVPs) located beneath African continent and the Pacific Ocean (French & Romanowicz, 2015). Such "primary" superplumes can also stagnate below or within the mantle transition zone (MTZ, 410-660 km) and cause numerous thermal perturbations in the upper mantle, corresponding to so-called "secondary" plumes (Courtillot et al., 2003). The MTZ might also serve as a barrier to the descent of oceanic slabs, which tend to stagnate in

its lower part (Kuritani et al., 2019) due to the jump in mantle viscosity at about 660 km depth (Forte & Mitrovica, 1996). A chemical (hydrous) component attributed to water originated from stagnant slabs (Richard & Bercovici, 2009) enhances the buoyancy of "secondary" plumes rising from the MTZ (Zhao, 2009). Despite the relatively small size of these thermo-chemical anomalies (sometimes referred to as "baby" plumes; (Koptev et al., 2021)), they have been shown to be capable of penetrating to shallow levels near the base of the crust (Cloetingh et al., 2022), forming "finger" and "mushroom"-like structures inside the overlying continental lithosphere, as detected in regional seismo-tomographic studies across the globe (Ritter et al., 2001; Lei et al., 2009).

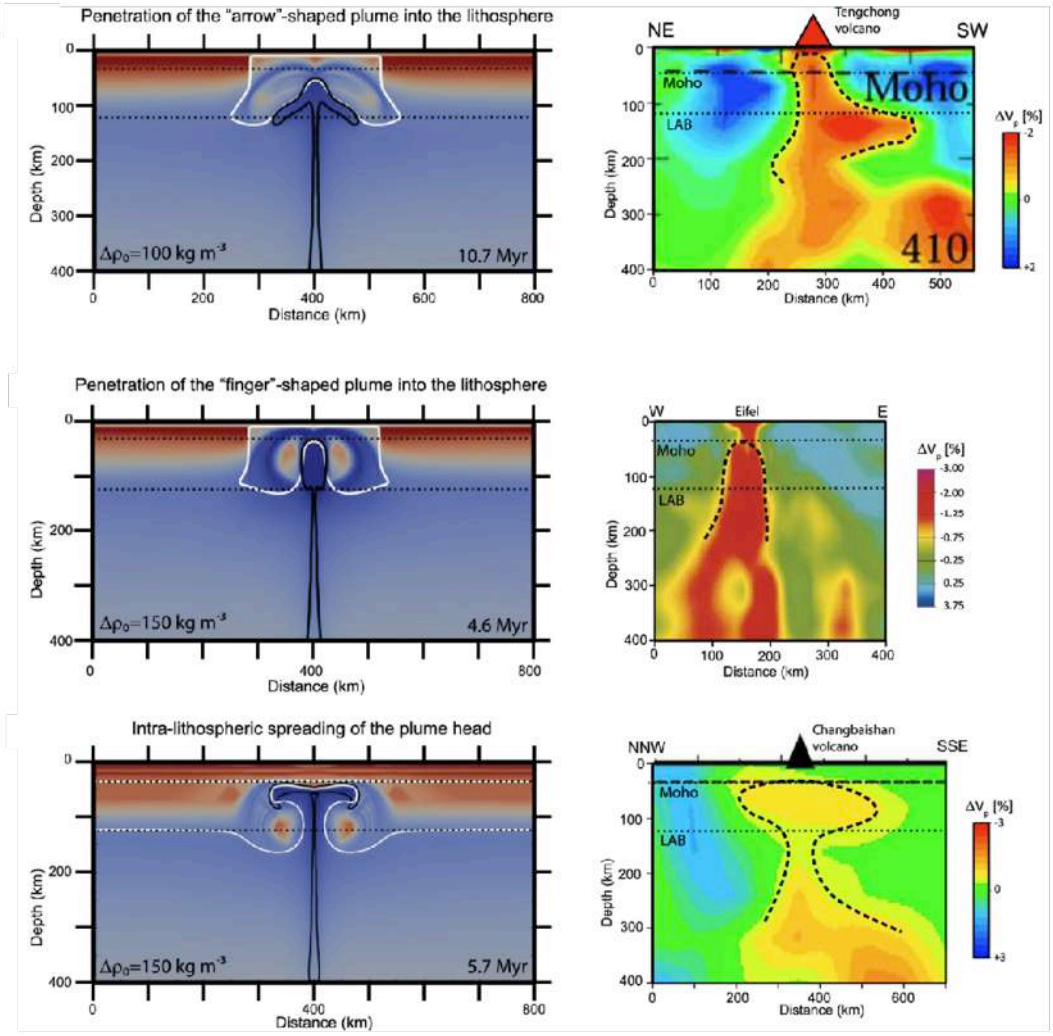

Figure 2.1.2 Comparison of modelled plume-emplacement modes (left panels) with natural examples of seismic velocity anomalies in the upper mantle (right panels). a) Modelled "arrow"-shaped plume vs. asymmetric "arrow" beneath the Tengchong volcano. b) Modelled "finger"-shaped plume vs. columnar structure in sublithospheric and lithospheric mantle below the Eifel volcanic fields. c) Advanced stage of the "finger" scenario with intra-lithospheric spreading of the plume head vs. intra-lithospheric "mushroom" underlying the Changbaishan volcanic area. Modified after Cloetingh et al., 2022.

Seismic tomography has yielded fundamentally new insights into the regional geodynamics, providing an unprecedent image in terms of resolution and coverage of the upper mantle beneath Europe and its margins, including areas such the northern Atlantic rift province (Lebedev et al., 2018; Steinberger et al., 2019), Anatolia (Medved et al., 2021; Kounoudis et al., 2020), central Europe (Zhu et al., 2012; Karousová et al., 2012). In this context, the Mediterranean area, with its rich spectrum of down going slabs and the creation of young and well-preserved back-arc systems provides an excellent natural laboratory for detailed imaging of upper mantle structures. (Rappisi et al., 2022) (Fig. 2.1.2) present the first three-dimensional (3D) anisotropic teleseismic P-wave tomography model of the upper mantle covering the entire Central Mediterranean. The tomography model is dominated by numerous fast anomalies associated with retreating, stagnant, and detached slab segments as well as relatively slower mantle structures related to slab windows and back-arc basins. P-wave seismic anisotropy in the Central Mediterranean upper mantle is strongest at 200-300 km depth and interpreted as the result of asthenospheric material flowing primarily horizontally around the rollbacking Cenozoic slabs, while sub-vertical anisotropy may reflect asthenospheric entrainment by downwelling slabs.

Recent tomography underneath the Paris Basin has documented the occurrence of a remnant of the Hercynian slab still accounting for a deep density anomaly at the base of the lithosphere, resulting in the long living subsidence observed in this intraplate sedimentary basin over the entire Mesozoic and Cenozoic (Averbuch & Piromallo, 2012). Recent tomography beneath the SE Carpathians in Romania has demonstrated the occurrence of ongoing delamination of the Moesian lithosphere, its lithospheric mantle being subducted at great depth, accounting for extremely high subsidence rates and deep focal mechanisms below the Focsani Depression, whereas its upper crustal basement and sedimentary units are progressively uplifted underneath the outer Carpathians in the Vrancea area (Bocin et al., 2013). Similar dynamics have also been proposed for the Apulian lithosphere beneath the Southern Apennines (Roure et al., 2010; Koulakov et al., 2015). In this context, the paleo-bathymetry and geodynamic evolution of the Eastern Mediterranean as a whole should be revisited, as alternative models involving the progressive delamination of the continental lithosphere of North Africa could be more realistic than the proposed and currently established oceanic nature of the Eastern Mediterranean basin.

The lithosphere-asthenosphere boundary (LAB) is a first-order structural discontinuity accommodating differential motion between tectonic plates and the underlying asthenospheric mantle (Eaton et al., 2009). A fundamental question formulated at the dawn of

plate tectonic theory has been the nature and importance of drag at the base of the lithosphere arising from mantle convective flow (Forsyth & Uyeda, 1975) versus slab pull (Conrad & Lithgow-Bertelloni, 2002) and ridge push (Artyushkov, 1973) forces. Different definitions exist on the LAB varying from a thermal definition equating it to an isotherm between ~1200-1350°C (Artemieva, 2006; Koptev & Ershov, 2011) and a seismological definition based on a decrease in seismic velocities (Rychert et al., 2005; Chen et al., 2006) and change in seismic anisotropy (Gung et al., 2003). In addition, a petrological definition has been formulated pursuing the hydrous nature of the mantle below the LAB (Kovacs et al., 2020). Previous attempts have been made to reconcile these different definitions (Artemieva, 2010). These attempts also led to the formulation of the 'pargasosphere' hypothesis (Kovács et al., 2021), where pargasitic amphibole (a hydrous double chain silicate with ~1.5 – 2 wt.%) is stable (i.e., at pressures and temperatures less than 3 GPa and 1100 °C) making the lithosphere mechanically stronger because anhydrous this hydrous mineral (along with phlogopite at higher potassium contents)s lowers the water activity by absorbing 'water' and from silicate, carbonated silicate and carbonate melts from percolating in this shallower part of the upper mantle by metasomatic reactions. This means that the lack of melts/fluids and the lower structural hydroxyl content in nominally anhydrous minerals (Girard et al., 2013; Tielke et al., 2017) both strengthens the rheology of the shallow upper mantle where hydrous minerals, pargasitic amphibole in particular, are stable. This contributes significantly to the contrast existing between the stronger and rigid outer shell: the lithosphere and the underlying mechanically weak and ductile asthenosphere.

Besides the LAB, another important horizon in older and colder plates are the mid lithospheric discontinuities (MLD) of which discovery goes back only little more than two decades (Thybo & Perchuć, 1997). The origin of MLDs is still a controversial issue as it is linked to various factors including the presence of hydrous layers ('water collector'; (Fu et al., 2022)), pargasite-rich horizons (Kovács et al., 2021)and channel flow (Yang et al., 2022). Regardless their origin, it became clear that MLDs may play a fundamental role in the initiation continental subduction (Cloetingh et al., 2021), delamination of the lower continental lithospheric mantle and removal of cratonic roots (Wang et al., 2017; Wang & Kusky, 2019; Liu et al., 2018; Wang et al., 2022). The LAB and MLD may also be genetically linked, since with the age and secular cooling of tectonic plates LAB can be transformed into MLD as 'frozen' in or 'fossil' LAB (Fischer et al., 2010; Kovács et al., 2017; Rychert et al., 2020)(Fischer et al., 2010; Kovács et al.. 2017; Rychert et al., 2020).

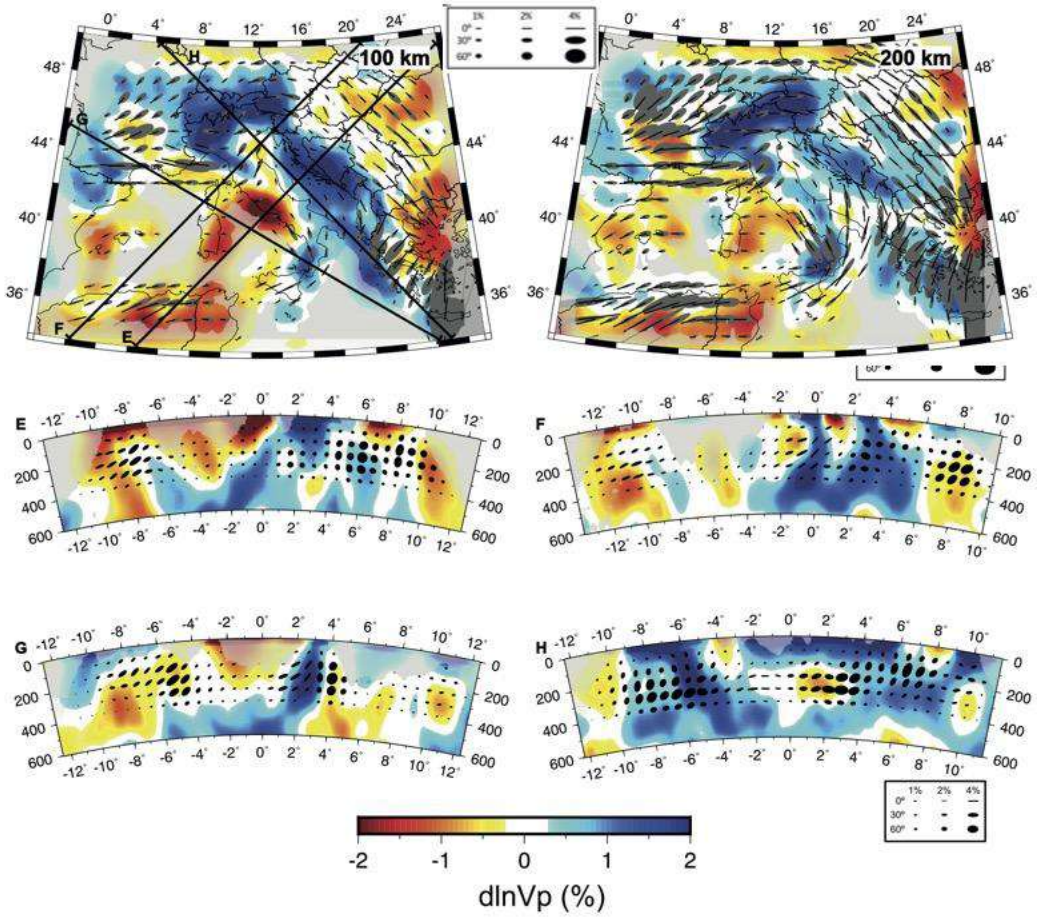

Figure 2.1.3: Horizontal and vertical cross-sections of the ani-NEWTON21 tomography model for the central Mediterranean (Rappisi e t al., 2022). Areas of poor coverage are masked in grey.

2.2 Structure of the lithosphere and rheology

A breakthrough in our understanding of the lithosphere mechanical properties was achieved by (Goetze & Evans, 1979), who first extrapolated inferences from experimental rock mechanics on olivine to geological timescales to assess the rheology of the oceanic lithosphere. Subsequent work on ocean lithospheric flexure under seamount loading and at subduction trenches validated this concept, showing that oceanic intraplate seismicity is restricted to depths shallower than the isotherm of 750°C whereas the effective elastic thickness corresponds to the depth of isotherms between 400-600 °C (Wiens & Stein, 1983; Bodine et al., 1981). The mechanically strong part of the lithosphere resides in the upper part of the lithosphere in oceanic domains. A similar approach was used to assess the rheology of the continental lithosphere. Experimental mechanic studies applied to rocks and minerals characteristic of the continental crust and upper mantle (Brace & Kohlstedt, 1980), analyses of intraplate seismicity, and quantifications of continental flexure (Cloetingh & Burov, 1996) led to a better understanding of spatial variations in the mechanical behavior of the

continental lithosphere, allowing for the definition of the effective elastic thickness (*Te*) as a proxy parameter for the rigidity and integrated strength of the lithosphere (Burov & Diament, 1995; Burov, 2011). Europe, with its wide coverage of seismological studies shedding light on the Moho and crustal as well as upper mantle structures, served as the first area to construct continental scale maps of *Te* (Tesauro et al., 2013). These maps were obtained determining temperature distribution from inversion of new seismic tomography models improved by an a-priori correction of the crustal effect (Koulakov et al., 2009). The new temperature estimates were used together with the most updated European crustal model, EuCRUST-07 (Tesauro et al., 2008) to calculate the strength distribution within the European lithosphere (Tesauro et al., 2009a). Differently from previous estimates, the new strength model adopted lateral variations of lithology and density, which were also derived from EuCRUST-07. The strength distribution was the input for the calculation of the *Te*. Both strength and *Te* models show that in western and central Europe the lithosphere is more heterogeneous and characterized by mostly mechanically decoupled crustal and mantle lithospheric layers, relatively low strength, and $Te < 30$ km (Tesauro et al., 2009a; Tesauro et al., 2009)b, whereas eastern Europe is generally more uniform, stronger, and with higher *Te* values.

These findings have led to recognition that the spatial distribution of intraplate seismicity in Europe is focused around the European Cenozoic rift system (ECRIS) and the Pannonian Carpathian system, both characterized by relatively weak lithosphere. These concepts have been subsequently expanded to other continents including North America and Australia (Tesauro et al., 2014; Tesauro et al., 2020). In North America, a high proportion of intraplate seismic events are concentrated at the edge of the cratons (Mazzotti & Stein, 2007), in areas characterized by sharp lateral variations in the lithospheric thickness (Mooney et al., 2012) and integrated strength (Tesauro et al., 2015). A correlation between seismicity and cratonic edges is also reported for the Siberian and Congo craton (Craig et al., 2011; Sloan et al., 2011). On the other hand, the intraplate earthquakes in the western part of Australia do not show a strong correlation with the edges of the cratons, but many of them occur in areas characterized by weak crust, such as the southwestern part of the Yilgarn craton. Other seismic events are located along the transition zones between the weak and strong crust, as those at the margins of the Officer basin and Musgrave Province (Tesauro et al., 2020).

The most seismically active areas around the globe are in proximity of plate boundaries, where around 90% of earthquakes occur (Sbar & Sykes, 1973). This led to the assumption of limited deformation within plates in the early formulations of the plate tectonic

theory (Isacks et al., 1968). However, a number of seismic events in intraplate regions testify stress accumulation far from plate boundaries, in areas commonly considered tectonically stable (Haldar et al., 2022). Notable regions for intraplate earthquakes include the New Madrid seismic zone (Nuttli, 1973; Page & Hough, 2014), West Malaysia (Nazaruddin & Duerrast, 2021), Costa Rica region (Tary et al., 2021), India (Haldar et al., 2022), central Brazil (Rocha et al., 2016) and Bohemia (Mittag, 2003). Typically, these regions are affected by low to moderate seismic activity, although examples of earthquakes with magnitude higher than 6 still occur. In historical times, notable examples of large earthquakes are the well-studied 1811-1812 New Madrid events in the Mississippi valley of the Central U.S., the 1988 Tennant Creek earthquakes in Australia, the 1819 and 2001 earthquakes in the Kachchh rift basin (Western India), and the 1690 Manaus and 1955 Parecis basin earthquakes in Brazil (Calais et al., 2016), and references therein). Regarding Europe, relevant examples of historic earthquakes that shook relatively stable regions are the Basel (1356), Verviers (1692), Lisbon (1755) and Nice (1887).

Intraplate earthquakes occur preferentially in areas of rifted crust, with over half of all events associated with either interior rifts or rifted continental margins, where most $M \geq 7$ earthquakes occurred (Schulte & Mooney, 2005). Several models have been suggested to provide an explanation for seismicity in stable cratonic regions. The first models suggest the presence of factors causing stress concentration, such as weakened intrusions (Campbell, 1978), intersections of faults (Talwani, 1988) and shear zones in the lower crust (Zoback, 1983). Other factors include pre-existing weak zones below the fault (Kenner & Segall, 2000), topography load change due to surface erosion (Calais et al., 2010), glacier removal (Grollimund & Zoback, 2001) and fluid flow along the fault plane (Audin et al., 2002). The important contribution of fluids at near-lithostatic pressures has also been suggested for seismic activity in southern Italy (Lavecchia et al., 2022), where recent studies highlight a strength drop and rheological switch for the Gargano promontory lower crust, causing a diffused micro-seismicity at depth greater than 20 km, in contrast to the almost totally aseismic upper basement and sedimentary cover in the region (Fig. 2.2.1). High crustal temperatures have also been suggested as a driver of seismic activity by raising the depth of the brittle ductile rock transition (Liu & Zoback, 1997). A fundamental contribution to intraplate seismicity is ascribed to far-field tectonic stresses and large-scale plate interactions, which may control the recurrence of intraplate earthquakes depending on the viscosity ratio between the two plates and the far field to local fault stress regime (So & Capitanio, 2017).

Earthquakes at crustal depth can also be triggered by mantle flow, as in the case of the 1811-1812 seismic sequences, an unprecedented sequence involving at least three M ≥ 7 main events (Hough et al., 2000). Several studies invoked the descent of the Farallon slab as the main source for high localized mantle flow below the New Madrid seismic zone (Forte et al., 2007; Becker et al., 2015), suggesting that variations in mantle flow related dynamic topography (see also section 2.3) can contribute to seismicity where convective vertical normal stress are modulated by lithospheric strength heterogeneities. It thus appears that mantle flow needs to be considered to properly quantify seismic hazard in intraplate regions.

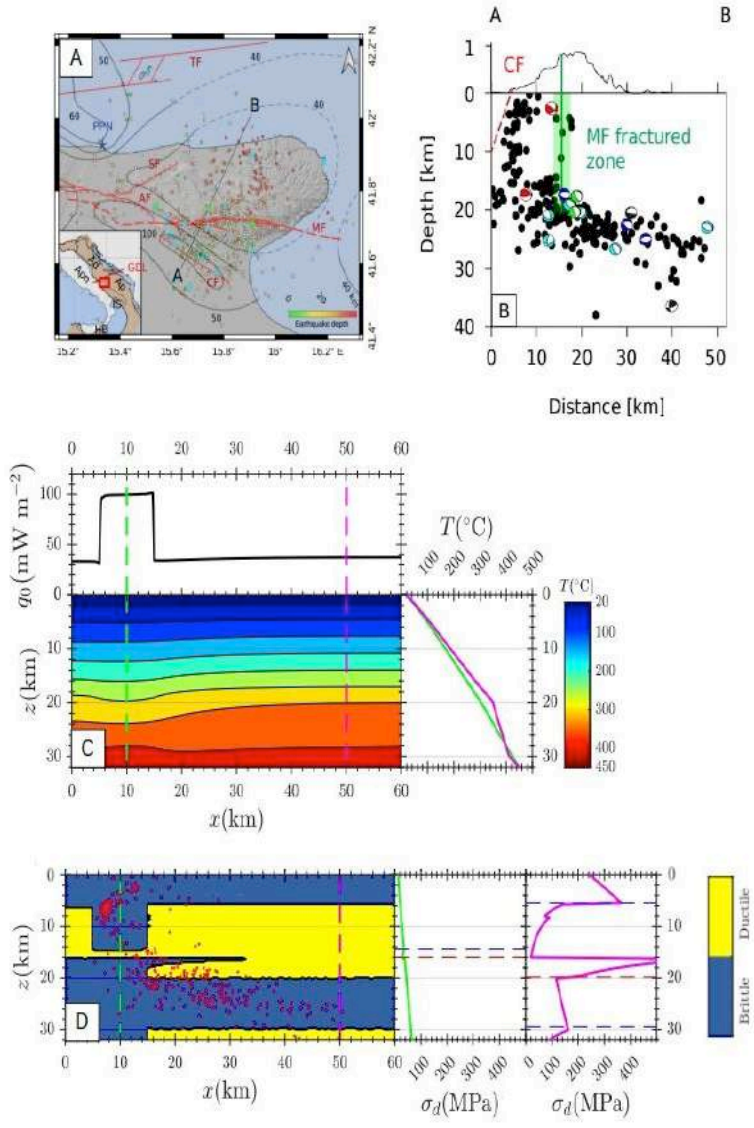

Fig. 2.2.1 – A) Map of the Gargano promontory. Inset shows its location (red square) with respect to the Adria and Apulian microplates. Colored circles indicate the depth of the earthquake hypocenters. The A-B black segment is the trace of the vertical crustal section in panel B. B) Vertical cross-section along the A-B section. Hypocenters(black circles) and focal mechanisms are projected over the vertical plane (red = normal; green = transcurrent; light blue = transpressive; dark blue = compressive; black = unknown). C) Geotherm, heat flow and rheological behavior for the Gargano promontory. Further details are given in Lavecchia et al., 2022.

Because seismic reflection profiles recorded by the petroleum industry are only rarely made available to seismologists, most seismo-tectonic maps show only the surface projection of earthquakes. Few studies using 2D or 3D seismic imagery provide accurate cross-sections where individual seismic event can be confidently plotted at depth on specific fault segments (i.e., in the Po Plain, (Turrini et al., 2014)). Intraplate deformations and diffuse seismicity in the forelands of the Alps, the Pyrenees and the Apennines imply the remobilization of fluids within the ductile lower crust; if strong coupling exists between the orogen and its foreland, far field reactivation of high angle upper to middle crustal faults at large distance from the suture may occur as long as high angle structures are still connected with the lower crust (Ziegler & Dèzes, 2006; Lavecchia et al., 2022). The construction of accurate 3D structural models at crustal scale, outlining the fault trajectories between the surface and the lower crust, still requires the acquisition of regional deep seismic reflection profiles, whereas denser seismic networks would be also required to plot individual events on the active fault segments (Roure & Howell, 2022). Ultimately, prediction of both horizontal and vertical intra-crustal fluid transfer and modelling of associated pore-fluid pressure cycles would provide a new approach to better understand and predict seismic hazard at distance from plate boundaries.

2.3 Interactions between surface processes and lithospheric dynamics

Shortening or stretching the continental lithosphere due to horizontal tectonics involve their thickening or thinning and thus vertical deformation of the Earth's surface and, thus, surface uplift or subsidence. The dismantling of uplifted terrains via erosion and the filling of subsiding basins with sediments contribute facilitates the horizontal motion of plates and the associated strain (Sternai, 2023). Within this framework, convergent mountain belts have been considered as crustal scale accretionary wedges in which lithospheric deformation and erosion are linked in a feedback loop that plays a particularly important role for exhumation of deep crustal and metamorphic rocks normally exposed as metamorphic complexes in the internal zones of orogenic belts (Burkhard & Sommaruga, 1998; Willett, 1999; Malavieille & Konstantinovskaya, 2010) and, as more recently recognized, landscape evolution (Sembroni et al., 2016; Reitano et al., 2022), magmatism (Sternai, 2020; Sternai et al., 2021; Stuewe et al., 2022; Muller et al., 2023), climate and biodiversity (Favre et al., 2015; Sarr et al., 2022; Botsyun et al., 2019; Tian et al., 2022; Xing & Ree, 2017). Probably the best example of the role of surface processes in affecting the deeper dynamics is provided by exhumation of the

high-grade metamorphic Greater Himalayan Sequence, interpreted as the southward 'extrusion' of the Tibetan middle to lower crust ductile flow in the middle to lower crust facilitated by focused erosion along the Himalayan front (Burchfiel & Royden, 1985; Royden, 1996; Grujic et al., 1996; Wu et al., 1998; Beaumont et al., 2001; Zeitler et al., 2001; Thiede & Ehlers, 2013) (Fig. 2.3.1). Finally, parallel to the previous solid Earth studies are paleoclimate modelling studies designed to identify time periods when climate change can induce significant erosional change in tectonically active orogens (Mutz et al., 2018; Mutz & Ehlers, 2019) or to aid in the interpretation of paleoclimate versus surface uplift signals in paleoaltimetry studies (Ehlers & Poulsen, 2009; Botsyun & Ehlers, 2021) (see also section 2.7). More of these types of scientific investigations are needed because often times the regional modern climate configurations are used as long-term proxy to infer past climate forcing on landscape and topography evolution.

The previous theoretical considerations have stimulated a diverse array of observational studies aimed at identifying when and where climate and tectonics operate and may be linked (Whipple, 2009; Whipple, 2014). A fundamental challenge for these communities has been the diverse timescales over which climate and tectonic may be linked, and which methods are best suited for quantifying those interactions. Observational studies have targeted one or more of several approaches. These include: bedrock (hinterland) studies quantifying temporal changes in erosional exhumation over millions of years (e.g., via multiple thermochronometric systems and numerical inverse modelling approaches; (Ehlers & Farley, 2003; Herman et al., 2013)); basin analysis studies investigating the sedimentary record of changes in sedimentation and climate reconstructions from proxy data (Whittaker, 2012; Chen et al., 2018) and (lastly) investigations of recent (millennial timescale) catchment scale sedimentation and erosion rates (e.g., from cosmogenic isotopes, DEM analysis, etc) (Schaller et al., 2016; Starke et al., 2017). Together, these types of approaches have been successfully applied to quantify temporal and spatial variations in erosion and sedimentation, along with inferences on the relative contributions of climate change and tectonic processes in controlling them (Champagnac et al., 2012; Champagnac et al., 2014). One of the best case-study within the TOPO-EUROPE program, would be the European Alps with more than 20 years of scientific research dedicated to the interplay between internal and external forcing mechanisms in Alpine topography evolution (Kuhlemann et al., 2002; Willett, 2006; Champagnac et al., 2007; Fox et al., 2016; Fox et al., 2013; Valla et al., 2021). However, it should be noted that most observational studies focus on identifying spatial or temporal correlations between observed erosion/sedimentation rates with changes in climate

and tectonics. Ultimately, these studies benefit significantly when linked with dynamic, process-based modelling studies where causal relationships can be rigorously tested with physics-based modelling approaches (Sternai et al., 2012; Winterberg & Willett, 2019)

The European Alps have long served as a natural laboratory to highlight relationships between localized thrusting and the topographic/architectural evolution of accretionary mountain belts during convergence. These relationships are well expressed in the Internal Crystalline Complexes (IMC) of the western European Alps (e.g., Monte Rosa, Gran Paradiso and Monviso), where oceanic and continental plate fragments subducted down to ~90 km depth are currently exposed at more than 4500 m above sea level (Schmid et al., 1996; Rosenbaum & Lister, 2005; Handy et al., 2010; Manzotti et al., 2018). The main driver of the exhumation is the shift from subduction to collisional tectonics at ~35 Ma. The localization of brittle deformation along major structures such as the Insubric and Periadriatic lines exerts a major influence on topography and, thus, on erosion (Janots et al., 2009; Malavieille & Konstantinovskaya, 2010). In turn, erosion and sedimentation decrease the topographic slope favouring a change from overcritical to stable to undercritical mechanical state of the wedge (Willett, 1999; Reitano et al., 2022). Alpine models highlight particularly tight relationships between many of the main structures within classical geologic sections across the Swiss Alps and erosion and/or sedimentation during convergence (Malavieille & Konstantinovskaya, 2010) (Fig. 2.3.1a-c). In response to shortening without surface processes, an analogue basement is commonly subject to initial thrusting and imbrication upon inherited structural and sedimentary weaknesses. Then, the homogenous part of the basement underthrusts and a high friction wedge is originated. With erosion and sedimentation, convergence leads to initial thrusting and frontal accretion in the foreland basin, followed by formation of an antiformal stack of duplexes in the internal part (Willett, 2006). Here, protracted strain localization, erosion and exhumation isolates a frontal synformal klippen of formerly imbricated thrust units and the antiformal structure eventually outcrops as a tectonic window, as observed in the natural case studies (Burkhard & Sommaruga, 1998). Climate changes, involving glaciation and precipitation gradients amongst other effects, play a similar role to that of strain regime changes in affecting the exhumation history of tectonics units across the Alps. The External Crystalline Massifs (ECM), for instance, are Paleozoic magmatic and metamorphic complexes of European affinity that were quickly exhumed during the Pliocene along the strike of the western Periadriatic Line and currently form the highest topography of Europe (e.g., the Mont Blanc). Fast exhumation occurs in the last ~1 Ma by erosion of ~1 km of rocks through glacial valley

carving (Valla et al., 2011; Sternai et al., 2012; Fox et al., 2015) across terrains subject to uplift due to mantle dynamics such as slab-break off and/or slab rollback (Fox et al., 2015; Lippitsch et al., 2003; Kästle et al., 2020). The influence of surface processes on orogenic dynamics in the European Alps is also expressed at short timescales. Catchment-wide quantification of millennial-scale erosion rates has suggested a potential "steady-state" between tectonic rock uplift and surface erosion for the Western and Central Alps (Wittmann et al., 2007; Champagnac et al., 2009), in contrast to the Eastern Alps (Norton et al., 2011). Ongoing efforts in further quantification of both modern rock uplift and millennial-scale erosion at the scale of the entire Alps have revealed higher modern uplift rates compared to catchment-wide erosion rates, potentially suggesting ongoing surface uplift for the Central Alps (Delunel et al., 2020). Overall, the influence of surface processes on orogenic dynamics in the European Alps is also expressed at short timescales since at least ~50% of the geodetically measured present-day vertical displacements are currently ascribed to the deglaciation of the Last Glacial Maximum ice-sheet and Plio-Quaternary erosion of the belt (Sternai et al., 2019).

Another important aspect of the interaction between deep and surface processes in orogenic systems has been the documentation of important drainage pattern modifications associated with horizontal movements (Castelltort et al., 2012; Goren et al., 2015), as well as the possibility of large-scale landscape re-organization (Willett et al., 2014). These works have often been benchmarked with numerical and physical models (Guerit et al., 2016; Guerit et al., 2018), but they raise the need for further research on the implications of horizontal advection in mountain ranges, notably for the interpretation of exhumation thermochronometers.

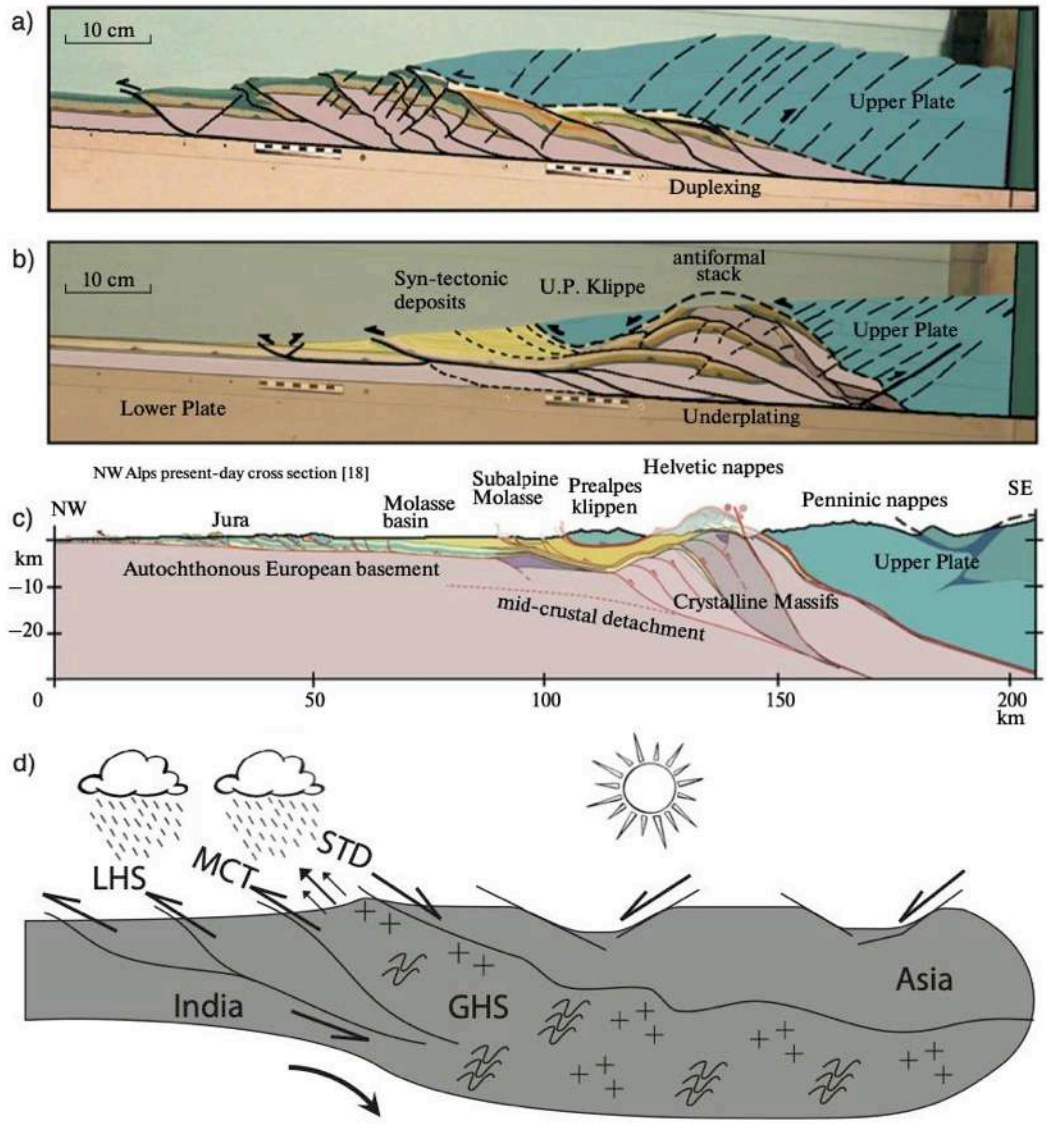

Figure 2.3.1: (a) Analogue models of crustal convergence and orogenic wedge evolution without (a) and with (b) erosion and syn-tectonic sedimentation (Malavieille & Konstantinovskaya, 2010). Modelling results are compared to a classical cross section of the Swiss Alps (c) from Burkhard & Sommaruga, 1998. (d) Crustal tectonic framework of the Himalaya and Southern Tibet where erosion at the mountain front contributes to localized exhumation of weak lower crustal material (e.g., Wu, et al., 1998; Burchfiel, et al., 1992; Beaumont, et al., 2001). LHS, Lesser Himalayan sequence; MCT, Main Central Thrust; STD, South Tibetan Detachment; GHS, Greater Himalayan Sequence

Recently, links between surface processes and volcanism-magmatism are being increasingly recognized and investigated, providing an example of a remarkable breakthrough toward a particularly promising research field. The straightforward concept behind these links is that changes in the crustal stress and strain fields due to variations of the surface load associated to erosion/sedimentation, ice building-melting and/or sea level changes can affect the magma production and upwelling towards the surface. As a result, subaerial volcanic activity can increase during interglacials due to the reduction of surface load by ice melting and erosion (Pagli & Sigmundsson , 2008; Singer et al., 1997; Rivera et

al., 2012; Swindles et al., 2018; Sternai et al., 2016a), whereas submarine volcanic activity can be inhibited by the downstream effect of sea level rise (Crowley et al., 2015; Schindlbeck et al., 2018; Kutterolf et al., 2019). These links pertain not only to individual volcanic edifices but also to entire volcanic arcs, where surface erosion/sedimentation can modulate the production of magmas (Sternai, 2020) and orographic erosion can force an upwind magma ascent toward regions of enhanced surface unloading (Sternai et al., 2021; Stuewe et al., 2022; Muller et al., 2023).

An impressive amount of research performed in just a few decades establishes that deformation, surface uplift or subsidence, erosion or sediment deposition (these latter may act in addition to ice-building/melting or sea level changes), and the magmatic/volcanic activity comprise a dynamic and complex system with feedbacks that links plate tectonics and continental drifting to the evolution of the surface topography.

2.4 Beyond dynamic topography, sea level change, glaciation

The Earth's topography is shaped by external and internal processes that continually shape interact at various time and spatial scales (Sternai, 2023). Mantle flow generates topography through the transport of temperature and density anomalies resulting in deformation of the surface, a mechanism first proposed by (Pekeris, 1935). Over the last few decades, the community of geodynamic models realized the potential implications of mass flow in the upper mantle for vertical motions at the surface of the overlying lithosphere. Major research efforts have been made to advance this field resulting in the concept of 'dynamic topography' as the regional relief generated by the flow-related vertical stresses and/or thermal anomalies acting at the base of the lithosphere resulting from the mantle flow.

Global models of mantle flow and density can be used to predict the Earth's dynamic topography. Current mantle flow models often include density anomalies derived from seismic tomography models (Conrad & Husson, 2009; Hager et al., 1985; Steinberger, 2007), and these density anomalies can be advected backward to several Myr ago (Conrad & Gurnis, 2003). Some mantle flow models use reconstructed surface plate velocities as upper boundary conditions and plate assimilation techniques in forward models (Bower et al., 2015; Liu et al., 2008). Using a wealth of different techniques, previous studies attribute topographic anomalies at wavelengths greater than 10^4 km to convection across the entire mantle (Hager & Richards, 1989; Becker et al., 2014; Arnould et al., 2020). Such large-scale dynamic topography is expected to change at relatively slow rates between 1-80 m/Myr (Flament et

al., 2015). Regional observational constraints, however, suggest the existence of transient (<10 Myr) and local (<3000 km) dynamic topography related to pulses of mantle upwelling or strong local upper mantle convection (Al-Hajri et al., 2009; Hartley et al., 2011). Interpretation of river drainage patterns based on continental margin uplift or subsidence (Pritchard et al., 2009; Roberts et al., 2012) or carbonate platform analysis (Czarnota et al., 2013) indicates rates of dynamic surface elevation change between 75-400 m/Myr. Regional models of dynamic topography and relative sea level change associated with small-scale convection (Petersen et al., 2010) predict surface topography at wavelengths as short as 250 km and on timescales of approximately 2-20 million. (Petersen et al., 2010) showed that small-scale mantle convection can sweep across the surface with an amplitude of about ±300 m and induce a high-frequency stratigraphic sequence with period between 2-20 Myr and lateral wavelength of about 200 km.

A recent global model of present-day topographic anomalies based on global seismic data collected primarily at passive plate margins, confirms that the magnitude of the remnant topography is significant at wavelengths as short as 1000 km (Hoggard et al., 2016). However, most global mantle convection models predict negligible dynamic topography at wavelengths shorter than 5000 km (Hoggard et al., 2016) due to the limited resolution of seismic tomography. Furthermore, the spatial variability of the seismic velocity-density conversion factors to predict mantle flow is uncertain, and chemical effects in the uppermost mantle are often ignored. In addition, lithospheric density anomalies that are commonly not accounted for when dynamic topography is calculated from global or regional upper or whole mantle flow models (Flament et al., 2013; Lithgow-Bertelloni & Silver, 1998; Steinberger, 2007). Recently, (Steinberger et al., 2017), showed that accounting for density heterogeneities in the uppermost mantle from a high-resolution near-surface tomography model in combination with a global S-wave model allows resolving dynamic topography at spatial scales as low as a few hundreds of km.

Studies have also been carried out on European regional scales and a testbed has been the Alpine-Mediterranean area due to the complex plate configuration and associated mantle dynamics. As shown by e.g., (Boschi et al., 2010) for the pan-Mediterranean area, and by (Sternai et al., 2019), for the greater Alpine region, models' predictions are very sensitive to the adopted lithospheric structure and mantle, showing major differences when global low-resolution or regional high-resolution crustal and mantle tomographic data are used. Indeed, considerable debates exist on the magnitude of the mantle contribution to the surface vertical displacements as reviewed by (Molnar et al., 2015; Hoggard et al., 2016). These issues are

important also in the context of linking inherited topography to the record of sea level change (Cloetingh & Haq, 2015), and continuing efforts are made to obtain insights in the connection between long-term sea level changes from Solid Earth processes, including the contribution from dynamic topography (Young et al., 2022) (Fig. 2.4.1). Building upon the research done in the Alpine-Mediterranean domain (Faccenna & Becker, 2020; Sternai et al., 2019; Faccenna et al., 2014; Sternai et al., 2014), the AlpArray and AdriaArray research projects are providing the community with a great deal of new data including seismic anisotropy (Liptai et al., 2022; Rappisi et al., 2022; Lo Bue et al., 2022), Moho and LAB geometry, gravity maps, S- and P-wave structures (Bianchi et al., 2021; Sadeghi-Bagherabadi et al., 2021; Link & Rümpker, 2021; Scarponi et al., 2020) and other geophysical measures.

Improving quantifications of the patterns and magnitudes of mantle contributions to topography changes and vertical displacements is thus a major endeavor in the agenda of future surface-deep Earth research initiatives.

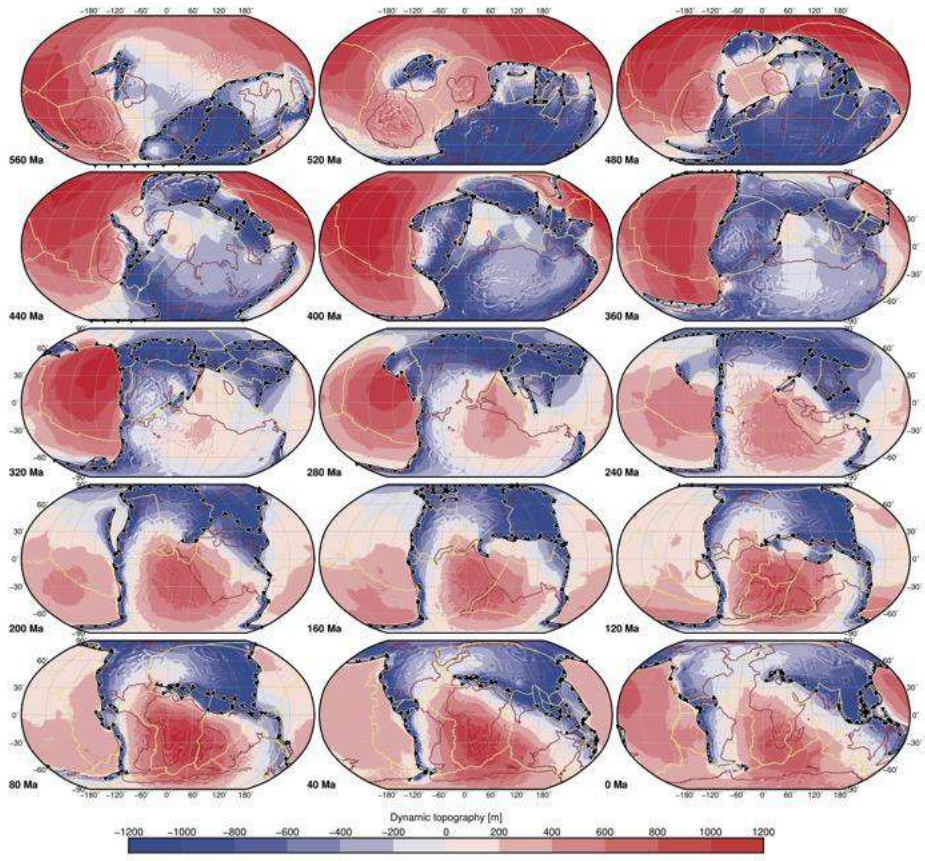

Figure 2.4.1: Dynamic topography estimates since 560 Ma in 40 Myr increments, for sources of buoyancy deeper than 350 km, free-slip boundary conditions and preserving lateral viscosity variations at all depths (Young et al., 2022). Reconstructed subduction locations in black, reconstructed mid-oceanic ridges and transform faults in khaki, and continent-ocean boundary in brown.

2.5. Deciphering the interplay between internal and external forcing in sedimentary basins dynamics

Understanding the structure and evolution of sedimentary basins is important for many societal issues (see chapter 4), in the first place by their nature of a humankind repository for subsurface georesources, both conventional and sustainable, such as geothermal energy or storage as in carbon-capture or hydrogen (Haszeldine, 2009; Cloetingh et al., 2010; Limberger et al., 2018; Jolie et al., 2021). Understanding the feedback mechanisms between internal and external forcing acting in orogens and sedimentary basins systems is important to quantify causal processes, such as linked exhumation and uplift in mountain belts with subsidence in neighbouring basins generating societal-relevant natural hazards (Roure, 2008; Seranne et al., 2015; Matenco et al., 2016; Bernard et al., 2019; Sautter et al., 2019). The interaction between deposition in sedimentary basins with processes in the neighboring orogens driving erosion and transport is in particular challenging because it requires a multi-scale approach where the meters to tens of kilometers scale observations are integrated with numerical modelling across the entire orogen-basin system, including the underlying lithosphere (Fig. 2.5.1a) (Cloetingh & Haq, 2015; Gibson et al., 2015; Noda, 2016; Matenco et al., 2022).

Recent breakthroughs have shown that multi-scale vertical movements associated with erosion control the deposition in sedimentary basins, modulated by sea-level variations and the local climate, or in the case of endorheic basins the balance between precipitation and evapo-transpiration (Nichols, 2011; Andric et al., 2018; Balázs et al., 2017; Ballato et al., 2019; Matenco & Haq, 2020). No matter the specific setting, tectonic drivers of vertical motions controlling the creation or destruction of accommodation space are made up of a wide number of processes that vary in time and space from upper crustal faulting and its individual moments of activation during the seismogenic cycle, the creation of individual basins or their connection in larger sedimentation domains, to the long-term thermo-flexural effects that are usually grouped in the generic term of dynamic topography, driven either by tectonics or mantle convection (Fig. 2.5.1b) (Gurnis, 2002; Ventura et al., 2007; Conrad & Husson, 2009; Braun, 2010; Munteanu et al., 2012; Flament et al., 2013; Bercovici & Ricard, 2014; Sato et al., 2017; Faccenna & Becker, 2020; Tartaglia et al., 2020). The sedimentation patterns observed have a wide range of temporal and spatial scales, creating an often quasi-cyclic deposition than can be observed in the 10 Kyr – 200 Myrs and metres to hundreds of

kilometres scale, depending on the balance between the rate of creating accommodation space and the rate sediment supply, modulated by a wide range of parameters, such as the distribution of faulting, thermal structure of the lithosphere, glacio-isostatic adjustment, the rate of creating the oceanic lithosphere, conditioned by climate and sea-level variations (Sigmundsson & Einarsson, 1992; Cobbold et al., 1993; Garcia-Castellanos et al., 2003; Cederbom et al., 2004; Haq, 2014; Cloetingh & Haq, 2015).

Among the observed large-scale variability of sedimentary basins, tectonic-driven sedimentation can ultimately be defined as being sourced from multiple directions in a quasi-cyclic deposition filling an asymmetric depositional space with an overall triangular geometry that contain steep slopes prone to mass-wasting deposition, creating ultimately generic tectonic successions that are spatial, temporal and sea-level independent (Fig. 2.5.1c) (Matenco & Haq, 2020). While the influence of climate and eurybathic variations, analysed by the classical means of sequence stratigraphy (Van Wagoner et al., 1990; Hardenbol et al., 1998; Catuneau et al., 2009), is undeniable in many tectonically-driven sedimentary wedges, such deposition takes often place in areas located too far in the continental interior, too deep in the oceans or too high in the mountains to be characterized by a global shoreline-fixed terminology (Fig. 2.5.1a). Therefore, the conceptual approach of multi-scale tectonic succession based on the identification of succession boundaries and point of reversals separating sourceward- and basinward- shifting facies tracts (Fig. 2.5.1c) is more appropriately employed for facies predictions in the large variability of syn-kinematic deposition observed. This terminology can be efficiently employed in all types of tectonic settings, from continental rifting and extensional, to transtensional, contractional and foredeeps, with relevant observational or modelling examples that can be applied to the Pannonian Basin, Western Mediterranean, Pyrenees, Alps, Carpathians or various types of south-eastern Asia basins (Matenco et al., 2010; Suades Sala, 2016; Balázs et al., 2016; Andric et al., 2018; Matenco & Haq, 2020; Balázs et al., 2021).

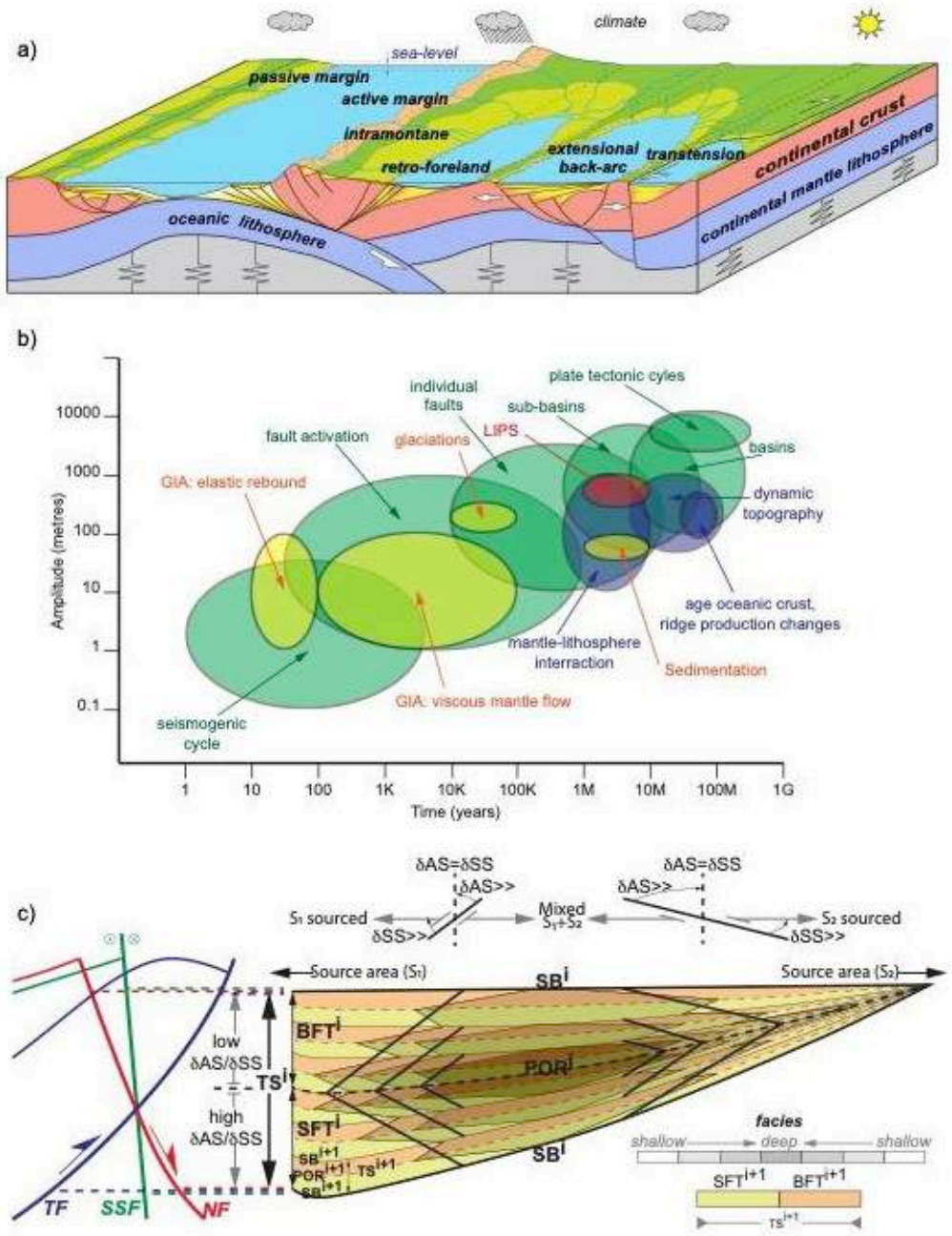

Figure 2.5.1: The multi-scale depositional concept of tectonic successions driven by the coupled evolution of sedimentary basins, orogens and their underlying lithosphere (Matenco and Haq, 2020; Matenco et al., 2022). a) Sketch showing various types of plate tectonic regimes, the formation of depositional space and its infill in sedimentary basins; b) temporal and spatial variability of mechanisms that drive the evolution of depositional space and sea-level variations. LIPS - Large Igneous Provinces; GIA - Glacial Isostatic Adjustment; c) Conceptual definition of low (i) and high order (i+1) tectonic successions (TS) in fault bounded sedimentary basin, which are composed of a sourceward-shifting facies tract (SFT) and a basinward-shifting facies tract (BFT). NF - normal fault(s), TF - thrust fault(s), SSF - strike-slip fault(s) with their sketched offset creating a wedge-shaped depositional space. SB = succession boundaries, POR = point of reversal, δAS = rate of creating accommodation space, δSS = the rate of sediment supply. For further details we refer to Matenco and Haq (2020) and Matenco et al. (2022).

2.6. Quantifying present-day vertical motions

Satellite-based geodesy, and particularly global navigation satellite system (GPS), has rapidly developed in the last two decades, becoming the prime source of information on horizontal motion of the lithosphere. Examples of early regional scale horizontal surface velocity measurements are the studies of (Reilinger et al., 2010), on the westward movement of Anatolia, and (Grenerczy et al., 2005), on the northwestward movement of Adria and its impact on the adjacent lithosphere of the Dinarides Pannonian Carpathian region. This topic has also been an area of active research of TOPO-EUROPE, especially in the Fennoscandia region (van der Wal et al., 2013) and the Mediterranean area (Faccenna et al., 2014). Today, thanks also to the development of pan-European global navigation satellite system (GNSS) initiatives (e.g., EPOS, https://gnss-epos.eu), for large part of the Africa-Eurasia plate boundary zone it is possible to use horizontal geodetic velocities to constrain strain-rates, fault kinematics and lithosphere dynamics with unprecedent spatial details (Piña-Valdés et al., 2022; Pintori et al., 2022; Serpelloni et al., 2022).

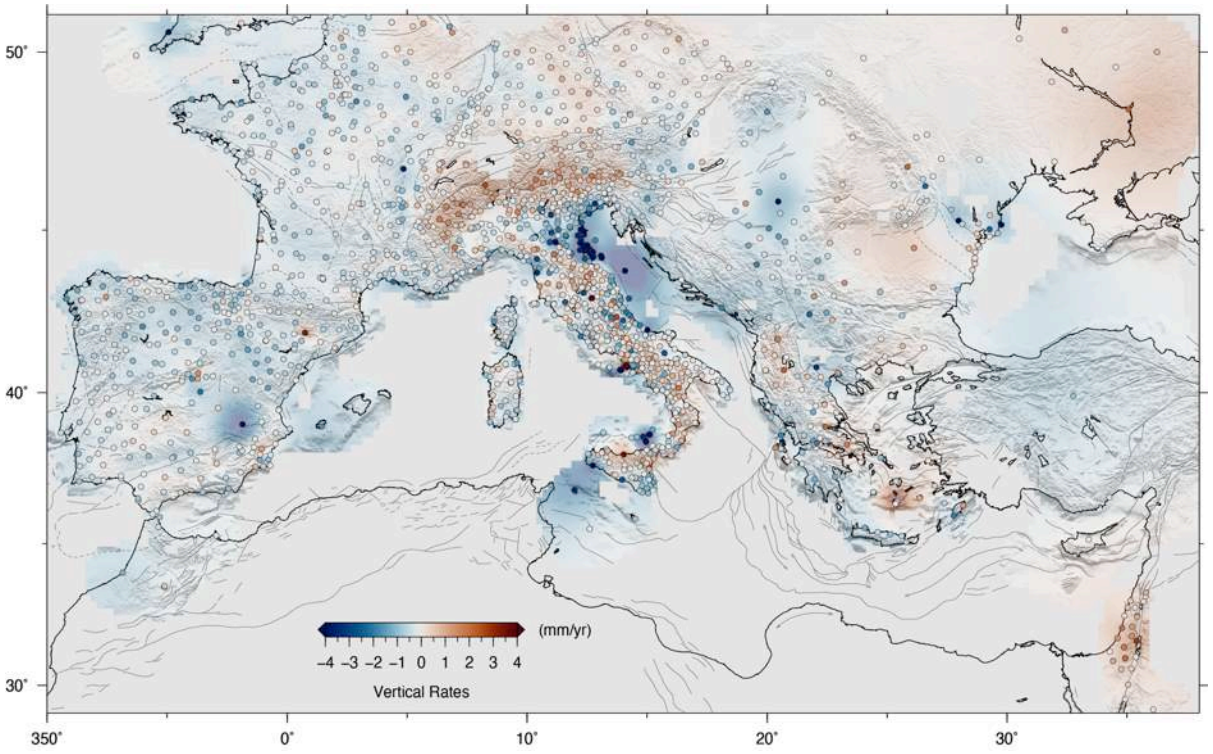

Figure 2.6.1: Map of the absolute observed (colored circles) and continuous vertical GPS velocities of the Mediterranean region (modified after Serpelloni et al., 2022).

A breakthrough has been the development of the capability to extract vertical motions from GPS observations. It is widely known, in fact, that the precision of vertical positions

determined by GPS is typically about 3-5 times lower than for the horizontal. Moreover, GPS measurements of vertical surface motion are susceptible to numerous potential errors and local processes, besides the geometric weaknesses in the height component of GPS in general. However, the increasing GPS series length and stations spatial density now allows to extract spatially consistent, in a statistical sense, features of the vertical geodetic velocity field (Serpelloni et al., 2013; Pintori et al., 2022; Serpelloni et al., 2022; Kreemer et al., 2020). Also in this case, the Alpine-Mediterranean area has been at the forefront. (Serpelloni et al., 2013) detected major differential vertical motions across the Betics, the Apennines and the Alps. In the Iberian micro-plate, for example, (Serpelloni et al., 2013) describe differential vertical motions with a wavelength and spatial pattern consistent with inferences from studies carried out in the context of Topo-Iberia (Fernández-Lozano et al., 2012; Cloetingh et al., 2002) proposing lithospheric folding and a decaying upper mantle thermal anomaly as a prime mechanism for explaining differential vertical motions during late Neogene to present times. (Faccenna et al., 2014), compared vertical GPS velocities and estimates of the crustal isostatic topography along the Apennines to show that a large fraction of the orogens topography is related to the mantle dynamics, particularly the formation and enlargement of a slab window underneath the central Apennines. GPS measurements of surface vertical displacements of the European Alps have also been carefully analyzed (Sternai et al., 2019). Here, a correlation between rock uplift rates and topographic features exists, with uplift at rates of up to ~2–2.5 mm/a in the North-Western and Central Alps and ~1 mm/a across a continuous region from the Eastern to the South-Western Alps. Proposed mechanisms of rock uplift rate include isostatic response to the last deglaciation and/or long-term erosion, detachment of the Western Alpine slab, and surface deflection due to the sub-lithospheric mantle flow. The plausible range of model estimates is large. However, the isostatic adjustment to deglaciation and erosion may explain up to the full observed rate of uplift in the Eastern Alps which, if correct, precludes a contribution from horizontal shortening and crustal thickening and suggests lateral escape of the incoming crustal material toward the Pannonian and Dinaric domains. Alternatively, uplift is a partitioned response to the deglacial/erosional isostatic rebound and crustal shortening and thickening. In the Central and Western Alps, the lithospheric adjustment to deglaciation and erosion likely accounts for roughly half of the rock uplift rate, which points to a noticeable contribution by mantle-related processes such as detachment of the European slab and/or asthenospheric upwelling. Thus, interacting tectonic and surface mass redistribution processes, rather than an individual

forcing, best explain ongoing Alpine elevation changes, which is a further indication of the tight link between the Earth's surface and deep dynamics.

Vertical geodetic velocities provide key information for tectonic and seismogenic potential studies, with important implications, for example, in the Eastern Alps, where tectonic shortening and glacial isostatic adjustment, at least, are certainly simultaneously active (Anderlini et al., 202). Since different multiscale processes are contributing to the total geodetically measured budget of vertical velocities in the Mediterranean, and since each process is characterized by different spatial footprints, the availability of accurate and dense measurements of spatial velocity gradients is important in order to discriminate among their relative contributions. In order to achieve this goal, it is mandatory to increase the precision and accuracy of vertical and horizontal ground velocity measurements, other than increasing the density of measuring stations. It is now possible to exploit the large number of available stations with longer position time-series lengths to estimate spatially correlated common mode errors and common mode signals (mainly associated with hydrological processes occurring at different spatial scales), which can be filtered out resulting in a significant improvement in the precisions and accuracy of GPS velocity estimates (Kreemer & Blewitt, 2021; Pintori et al., 2022) (Fig. 2.5.2). Moreover, the increase in the number of active full-GNSS stations, capable of recording all the GNSS constellations, other than GPS, and the development of new processing techniques, will certainly help improving the accuracy and precisions of vertical and horizontal measurements. Together with the desirable continuous increase in the density of GNSS stations, spatially detailed information on ground deformation at regional or even European scale can be now provided by synthetic aperture radar (SAR) measurements, with a key role played by the Copernicus Sentinel observations (https://sentinels.copernicus.eu). A recent example of the use of multitemporal interferometric SAR observations for the measure of mountain uplift in the western Alps is shown in (Mathey et al., 2022), whereas pan-European InSAR velocity measurements are made available through the Copernicus Service for Ground Motion Mapping and Monitoring (https://land.copernicus.eu/pan-european/european-ground-motion-service; (Costantini et al., 2022)). All together, these recent and ongoing developments in the pan-European space geodetic infrastructures will provide new key information to improve our knowledge on the interactions between surface and deep Earth processes.

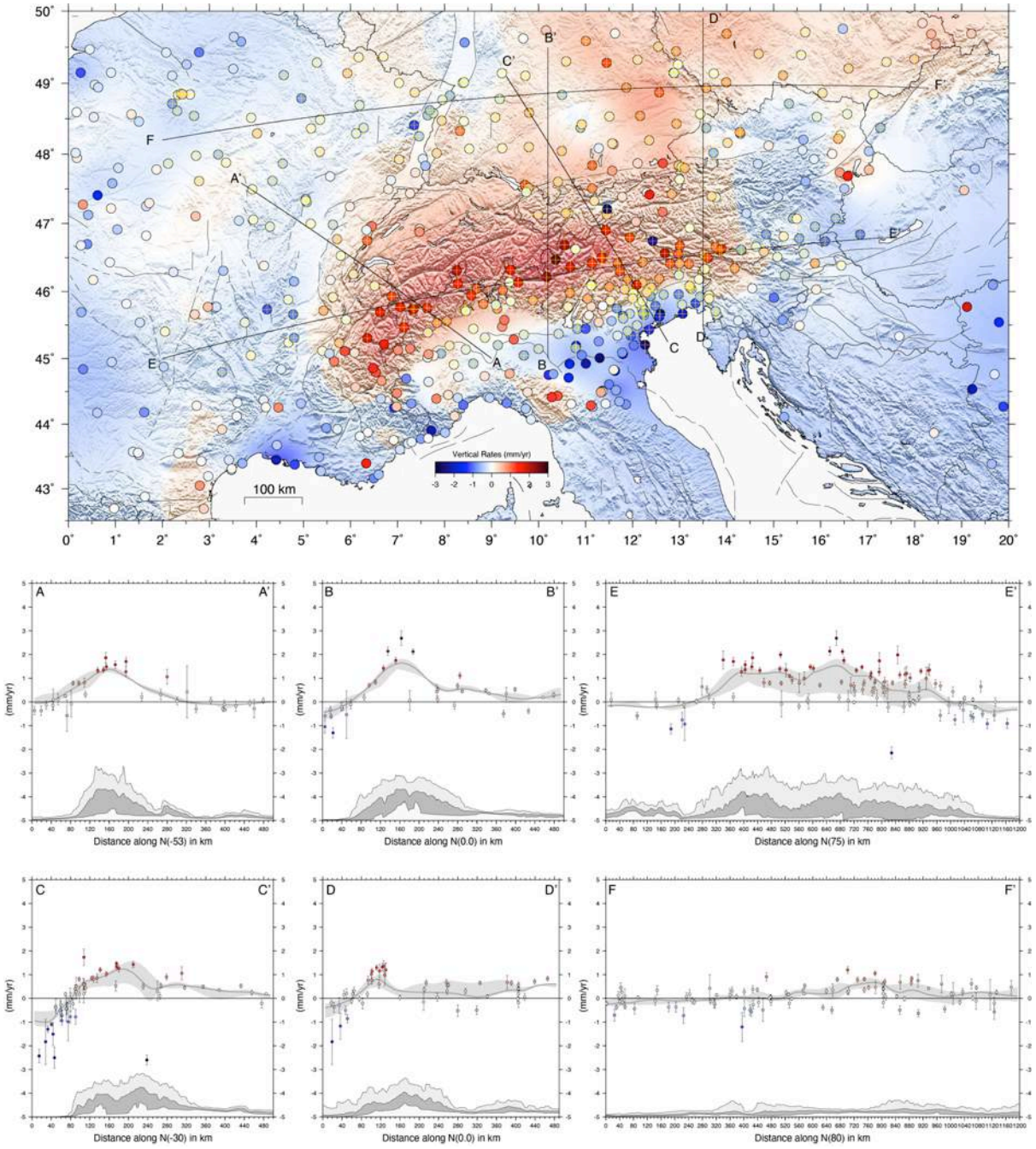

Figure 2.6.2: Map of the common mode signal filtered (colored circles) and continuous vertical GPS velocities of the Alps and velocity cross-section showing the positive correlation between velocities and topography in the western and eastern Alps (from Pintori et al., (2022).

2.7. Quantifying past mountain elevations

Quantifying the uplift history of orogens, including orogenic plateaus and their margins, is essential for understanding the subsurface density structure of orogens, their isostatic compensation, and the interactions between climate, tectonics, and surface processes (Clark, 2007; Molnar et al., 2010; Clift et al., 2010). A wide range of methods have been developed for quantitative estimates of past mountain elevation, e.g., based on

geomorphological evidences, such as river of marine terraces (Hergarten et al., 2010; Legrain et al., 2014), paleontological methods using fossil flora and fauna remains (Forest et al., 1999; Wei et al., 2016; Fauquette et al., 2015), and geochemical methods, such as biomarkers (Hren et al., 2010) and stable water isotopes. Among these methods, paleoaltimetry based on stable isotopes of water is the most widely used. This technique has been extensively applied to Earth's largest mountain ranges, such as the Himalayas and Tibetan Plateau (Ding et al., 2014; Rowley & Currie, 2006), the North America Cordillera (Cassel et al., 2014; Chamberlain et al., 2012), the Andes and Andean Plateau (Garzione et al., 2017; Mulch et al., 2010), but also to smaller mountain ranges such as the Pyrenees (Huyghe et al., 2012), the Tauride Mountains in Anatolia (Meijers et al., 2018), the Southern Alps in New Zealand (Zhuang et al., 2015), the Cascade Mountains (Methner et al., 2016), and the European Alps (Campani et al., 2012; Krsnik et al., 2021). For example, Krskik et al. (2021) apply the stable water isotope paleoaltimetry approach to the Central Alps and suggest that the region surrounding the Simplon Fault Zone attained surface elevations of > 4000 m by the middle Miocene. They propose a change in landscape from a uniform pre- middle Miocene to a more complex one with highly variable topography at the latest in the middle Miocene and attribute this change to the exhumation of the Aar Massif at ~ 20 Ma and the associated reorganization of the Alpine drainage network. Complementary, Fauquette et al. (2015) used pollen data, in combination with other sedimentological and provenance proxy, to reconstruct the topographic evolution of the southwestern Alps since the Eocene. They showed that this region already had topographic elevations over 1900 m as early as the Oligocene, resulting from orogen tectonic building and coincident with a previously documented event of rapid erosional exhumation during the mid-Oligocene. Despite these quantitative studies, little is still known about the topographic evolution of the European Alps over the last 20-30 Myr (e.g., review in Valla et al., 2021 and citation therein).

Despite the success of these data-based paleoaltimetry methods, recent studies have highlighted that a variety of paleoclimate processes can contribute to the isotopic composition of a measured signal used in elevation reconstructions. In some cases, these processes can overprint the elevation signal sought in the proxy data and preclude robust elevation reconstructions (Poulsen et al., 2010; Botsyun et al., 2016). These processes can include: regional, global, and topographic variations in paleotemperature, environmental conditions of an air mass prior to orographic ascent, evapotranspiration, water vapor recycling, and changes in the vapor source. To overcome these uncertainties, it has been proposed to apply

isotope-tracking climate models allowing to estimate changes in paleoclimate during orogen development and associated changes in paleo stable water isotopes due to both climate and topographic changes (Botsyun et al., 2019; Botsyun & Ehlers, 2021). In a recent paper by (Botsyun et al., 2022) on middle Miocene climate in Europe and stable isotopes composition of water, the authors apply a climate model with isotope tracking and designed experiments with variable elevation configurations of the European Alps. This work not only reconciles models and proxy data for European paleotemperature and paleoprecipitation (Fig 2.6.1), but also suggests that only a small fraction of stable water isotope variations in middle Miocene Europe is linked to changes in global climate, thus supporting high elevation of the central Alps in the middle Miocene.

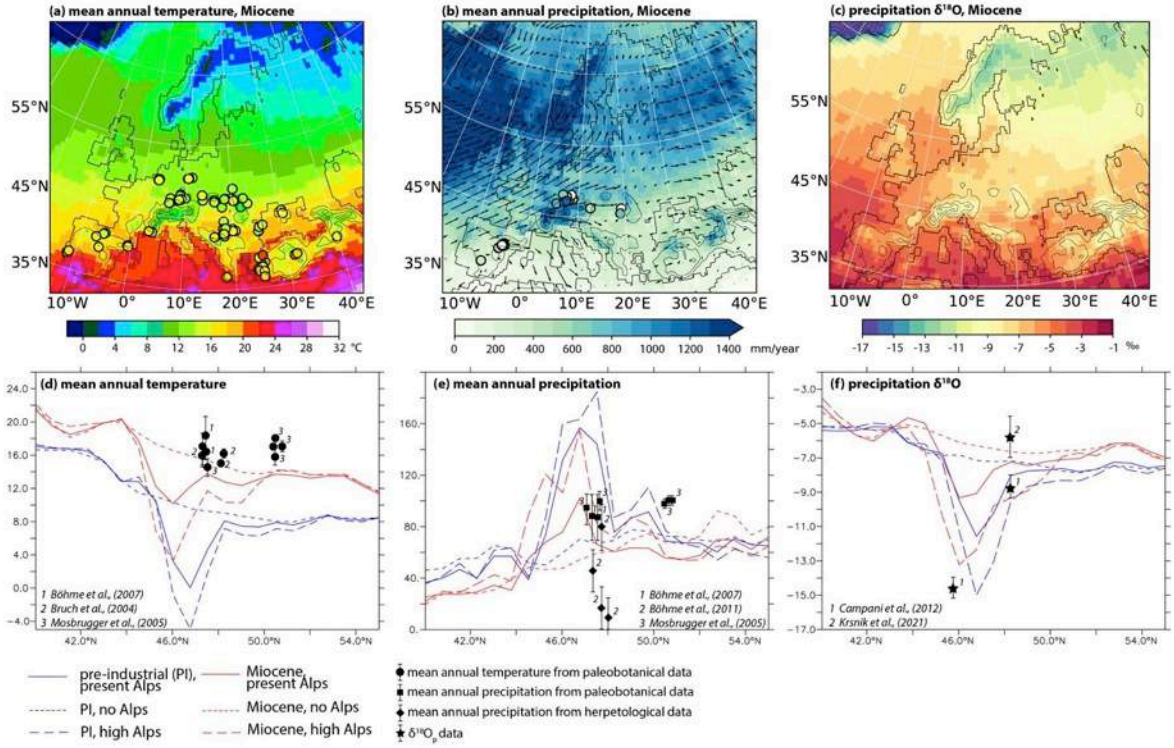

Figure 2.7.1: Results of high-resolution isotope-tracking general circulation model ECHAM5-wiso experiments with Middle Miocene boundary conditions (modified after Botsyun et al., 2022). Maps show Middle Miocene mean annual temperature (a), mean annual precipitation and surface winds (b), and precipitation $\delta^{18}O$ (c). S-N profiles show Middle Miocene and pre-industrial mean annual temperature (d), mean annual precipitation (e), and precipitation $\delta^{18}O$ (f) for experiments with varied topography of the Alps. Color points on subplots (a,b) and black points on on subplots (d,e) show temperatures and precipiation derived from palentological proxy data. Black starts on subplot (f) show $\delta^{18}O$ from carbonate/silicate archives.

Since the NSF Margins Science Plan (MARGINS Office, 2004), source-to-sink studies have proliferated over the last decades, in industry and academia, providing concepts and tools for improved understanding of the uplift history of source terranes preserved in

sedimentary basins, in particular with distinction to climate drivers (Helland-Hansen et al., 2016; Romans et al., 2015). Among others, these S2S studies have delivered important outcomes on the tectonic history of orogens through 1) the development and refinement of methodologies to estimate sediment budgets at the scale of entire orogen-basin systems (Guillocheau et al., 2012; Ortiz et al., 2022), 2) the widespread development of detrital zircons dating for fingerprinting source areas, their exhumation, and their tectono-magmatic origin (Mason et al., 2022) 3) grain size signals and 4) geochemical signals.

3. PERSPECTIVES AND EXAMPLES OF EMERGING FIELDS

3.1. Surface-deep Earth processes coupling in extensional settings

Much of what we know about the climate-tectonics interactions comes from the study of mountain building in convergent tectonic settings. However, prominent topographic ridges and basins generated by dominant extensional tectonics make divergent settings valuable contexts too (Armijo et al., 1996; Petit et al., 2007; Sembroni et al., 2016) and it seems somewhat intuitive that a thinning lithosphere transmits surface stress changes at depth more easily than a thickening one. Recent numerical experiments indicate particularly that syn-extensional sediment deposition within rift basins produced opposite mechanical and thermal effects (Burov & Cloetingh, 1997; Burov & Poliakov, 2001; Buiter et al., 2009; Sternai, 2020; Sternai et al., 2021). The increase in vertical stress involved by the deposition of sediments within rifts basins enhances the lithostatic pressure and, thus, the brittle strength of crustal and mantle rocks. On the other hand, thermal blanketing by sediment deposition prevents crustal rocks to lose heat, thereby enhancing the viscous strain of the lithosphere. By inhibiting localized brittle strain and favouring distributed ductile flow of viscous rocks, sediment deposition above a stretching lithosphere favours lateral migration of the extensional strain in turn allowing for prolonged stretching and delayed continental lithospheric breakup. In a recent contribution (Sternai et al., 2021), investigate how asthenospheric upwelling and orographic precipitation influence the slip along lithospheric shear zones accommodating far-field extension, associated topographic growth, and lithospheric rupturing. The authors derive a relationship between the location of lithospheric rupturing with respect to the asthenospheric plume axis and the lithosphere effective elastic thickness, Te (Burov & Diament, 1995), accounting for asymmetric surface erosion due to orographic precipitation, recognizing striking similarities with the spatial pattern of

lithospheric rupturing, rock exhumation, magmatic activity and topographic evolution of the East African Rift system.

Syn-extensional and post-breakup magmatic units are nearly ubiquitous in extensional settings and in some cases particularly voluminous (White & McKenzie, 1989; Franke, 2013). A particularly promising research direction in the field of the surface-deep Earth processes coupling is provided by the recent recognition that surface processes in extensional settings can significantly affect the magmatic activity (Sternai, 2020). Magmatism likely provides a substantial contribution to lithospheric rupturing (Kendall et al., 2005; Lavecchia et al., 2016) because extensional stresses alone are estimated to be at most just enough to rupture the continental lithosphere (Bott, 1991; Buck, 2004). The magma supply within fracture zones increases the pore fluid pressure, thereby lowering the plastic yield strength of fractured rocks and further localising the strain and topographic uplift or subsidence along weakening fault zones (Turcotte, 1982; Spence et al., 1987; Connolly & Podladchikov, 1998; Gerya & Yuen, 2003; Katz, 2008; Sternai, 2020). In this frame, peaks of igneous activity due to enhanced mantle decompression melting have been ascribed to surface unloading by the deglaciation (Jull & McKenzie, 1996; Singer et al., 1997) and/or erosion (Sternai et al., 2016a) or sea level lowering (Crowley et al., 2015; Sternai et al., 2017). However, the sensitivity of extensional systems to surface processes and the mechanisms that allow these latter to affect the production, transfer and emplacement or eruption of magma are poorly constrained. Numerical modelling suggests that flexural bending of the Moho due to efficient sediment delivery into a rift basin is an efficient mechanism to enhance crustal melting in a stretching and warming lithosphere (Sternai, 2020). On the other hand, surface loading due to efficient filling of the rift basin dampens asthenospheric decompression partial melting by an amount proportional to the rate of basin deepening/filling, the sediment density, and the surface-to-depth stress change transfer of the rift system. For a given erosion/deposition rate, the modulation by surface processes to rock melting in natural rift settings is inversely correlated to the extensional velocity, mantle potential temperature (sensu (McKenzie & Bickle, 1988)) and initial Moho depth. Increasing observational evidence corroborates these modelling results showing that surface load changes in the order of the tens of MPa due to sea level changes during glacial interglacial cycles can modulate the extensional magmatism (Crowley et al., 2015; Schindlbeck et al., 2018; Kutterolf et al., 2019; Satow et al., 2021). Along the Red Sea, convex channel profiles with concave swath profiles west side of the divide, systematic morphologic changes from north to south and the post-12 Ma basaltic volcanism are well interpreted through feedbacks between the onset of ocean spreading,

uplift of the rift shoulders, associated coastal magmatism, and strong orographic rainfall (Stuewe et al., 2022). The recent seismic evidence for failed rifting in the Ligurian basin (Dannowski et al., 2020) can also be explained by the high rate of syn-rift sediment delivery from the western Alpine domain, fostering distributed rather than localized strain and preventing the extensional system to reach the ocean spreading stage.

The main point of this research breakthroughs is that typical changes in the temporal and spatial pattern of surface mass redistribution may result in protracted variations of the strain rate by up to a few orders of magnitude that reach down to sub-lithospheric levels. Such variations imply changes in the location and amount of partial rock melting, with further feedbacks on the strain pattern and topographic evolution. The resulting chain of cause-effect relationships between surface, lithosphere and asthenosphere dynamics are highly non-linear. We thus anticipate that unraveling the substantial modifications to the architectural evolution of extensional systems involved by ever-changing surface processes will be a highly rewarding challenge for future research.

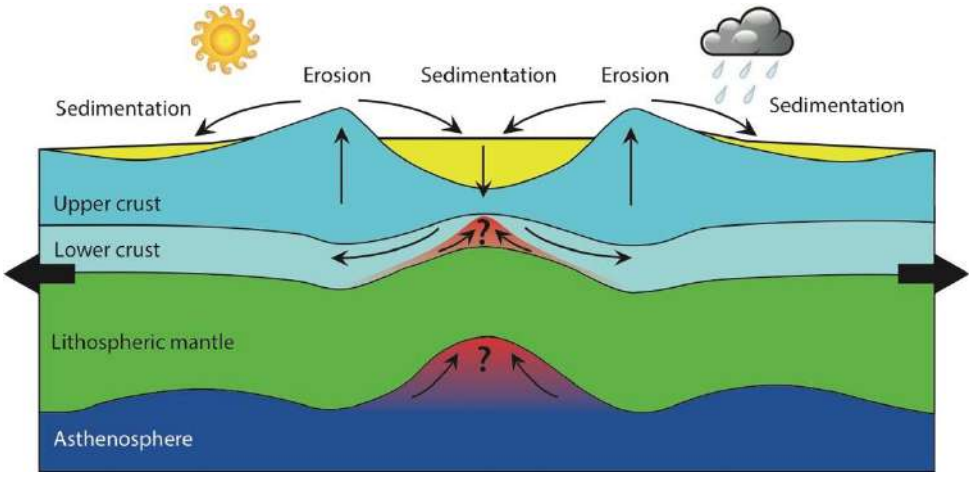

Figure 3.1.1: Schematic representation of the interactions between surface processes and magmatism in an extensional setting (not to scale, modified after Sternai, 2020). Sediments derived from erosion of rift shoulders load the rift basins. The rigid upper crust and lithospheric mantle flex and weaken, while more ductile lower-crustal material flows from the center of the rift outward, facilitating uplift and erosion of the rift shoulders. The associated effects on extensional magmatism (reddish material) are to date poorly constrained and represent a promising emerging research field.

3.2. Surface-deep Earth processes coupling and the geological cycling of carbon and other life-essential elements

At timescales of millions to tens of millions of years the Earth's life-essential elements, among which carbon is of primary relevance, flows between the atmosphere, lithosphere, and mantle in an exchange called the geological volatile cycle (Berner, 2003;

Broecker, 2018; Bodnar et al., 2013; Hayes & Waldbauer, 2006). This cycling, therefore, embodies the coupling between tectonic and climatic changes in that by preventing, for example, all of the Earth's carbon and water from being released into the oceans and atmosphere or to be stored within rocks, it acts as a global long term thermostat, linking the evolution of climate and life to plate tectonics. Geological emissions from volcanic arcs above subduction zones or at divergent margins are a critical input of carbon and oxygen into the atmosphere, whereas the chemical weathering of silicate rocks exhumed at the Earth's surface through erosion of tectonically uplifted terrains (Lee & Lackey, 2015; Kelemen & Manning, 2015; Mason et al., 2017; Bodnar et al., 2013; Vitale Brovarone et al., 2020), and trapping of organic matter in sedimentary basins (Galy et al., 2007; Hage et al., 2022), consume the atmospheric carbon. Recently, analyses of hydrocarbon-rich fluids entrapped in quartz veins in the Swiss Alps have revealed significant fluxes of methane and CO_2 linked with the tectonic burial of organic matter during Miocene nappe emplacement and exhumation (Mangenot et al., 2021). Water-rock interactions at various geodynamic settings spanning mid-ocean ridges and convergent margins can produce fluxes of energy sources and nutrients for microbial life among which natural H_2, methane, ammonia, and hydrogen sulfide are of primary importance (Holm & Charlou, 2001; Kelley et al., 2005; Etiope & Sherwood Lollar, 2013; Vitale Brovarone et al., 2020). Mineral inclusions in super-deep diamonds indicate that the larges of water on Earth is stored in the mantle (Pearson et al., 2014; Nestola & Smyth, 2016). Analyses of the sedimentary archives allow reasonable estimates of the carbon outflux from the atmosphere through erosion, chemical weathering, and preservation of organic matter. Instead, the uncertainty regarding the amounts and driving mechanisms of carbon recycling and emissions from the Earth's interior stands out as one of the most vexing problems facing us in understanding the geological volatile cycle (Berner & Lasaga, 1989; Dasgupta et al., 2007; Burton et al., 2013; Kelemen & Manning, 2015; Orcutt et al., 2019). Available estimates of current carbon fluxes between the Earth's deep and surface reservoirs, for instance, vary by several orders of magnitude (Dasgupta et al., 2007; Kelemen & Manning, 2015; Plank & Manning, 2019), which is indicative of how little we know about this branch of the carbon exchange cycle. Multidisciplinary integrations of geological data and modelling to quantify variations in global emissions due to fundamental geodynamic events throughout the Earth's history and their critical effects on climate change represent a top-priority challenge for future research on the cycling of carbon and other life-essential elements, the quantitative understanding of which is also a fundamental objective of the International Panel on Climate Change - IPCC (www.ipcc.ch).

Mountains are key drivers of global weathering. They represent the main long-term sink of surface CO_2 as they are dominated by rapid mechanical erosion, which increases the amount of minerals available for chemical weathering (Raymo et al., 1988). The proposal that the India-Eurasia collision and uplift of Tibet led to greater global weathering rates and long-term Cenozoic climate cooling (Raymo & Ruddiman, 1992; Molnar & England, 1990) drove research efforts within and outside the TOPO-EUROPE community toward quantifications of past weathering rates (Goddéris et al., 2014) to explain the Cretaceous to Tertiary climate proxy record (Zachos et al., 2001). The currently established weathering-dominated climate paradigm, however, cannot explain the ~10 Ma climate warming preceding post-50 Ma cooling and overlooks changes in volcanic/magmatic /metamorphic CO_2 emissions in driving early Cenozoic climate (Sternai et al., 2020; Chu et al., 2019). This is even more important in the light of recent reinterpretations of Cenozoic climate proxies suggesting overall higher and more variable temperatures than previously determined during the early Eocene (Meckler et al., 2022). Also, recent work further suggests that weaker global Cenozoic silicate weathering fluxes than previously thought (Rugenstein et al., 2019; Tipper et al., 2020) are to some extent compensated by weathering of accessory carbonate and sulfide minerals, a geologically relevant source of CO_2 (Bufe et al., 2021). It is also plausible that elevated rates of 'reverse weathering' - the consumption of alkalinity and generation of acidity during marine authigenic clay formation - enhanced the retention of carbon within the surface reservoirs, leading to elevated past CO_2 concentration baselines (Isson & Planavsky, 2018). The large uncertainty that still exists regarding present-day and past CO_2 and other greenhouse gas emissions from volcanic arcs, the primary natural input of carbon into the ocean and atmosphere, is currently our greatest limitation to the quantitative understanding of the geological carbon cycle. Reconstructing the time history of greenhouse gas emissions thereby marking a turning point in the research about the surface-deep Earth processes coupling will be a priority in the future agenda of TOPO-EUROPE. Ground-breaking techniques that can be used to determine temporal changes in greenhouse gas emissions and assess their geologic drivers and climatic effects are: (1) studies of melt inclusions within magmatic rocks and subsurface fluid records (e.g. calcite/quartz veins), (2) geochemical and organic characterizations of accretionary systems to provide proxies of carbon recycling at subduction-collision zones (3) coupled petro-thermo-mechanical geodynamic, landscape evolution, Earth system and climate carbon cycle numerical modelling to constrain plausible changes in magmatic-volcanic-metamorphic emissions (CO_2 source) as well as weathering and exhumation of silicate minerals but also of organic matter and the trapping of organic

material into sedimentary basin (CO_2 sink). To enhance the understanding of the sedimentary record, it is also important to adopt source-to-sink (S2S) strategies which allow better assessment of the relevant time and space scales, as well as of the potential signal buffering within the sediment routing system (Romans et al., 2015). Engaging into this research allows us to better quantify natural carbon fluxes, assess the drivers of natural climate variability and, by comparison, the climatic consequences of current anthropic emissions.

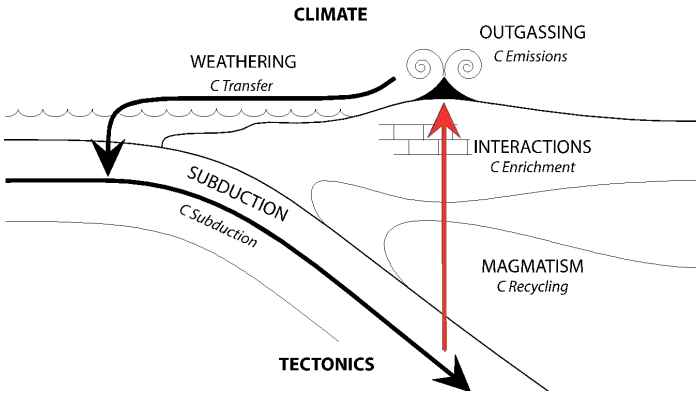

Figure 3.2.1: Schematic representation of the geological carbon cycle (modified after Sternai et al., 2020). The recycling of carbon along subduction zone is a particularly poorly constrained branch of this cycle, but it provides and additional means of linkage between tectonic-magmatic events, climate and surface processes changes.

Another important aspect of the surface-deep Earth processes coupling that involves effects on the geological carbon cycle and has yet to be explored is the role of magmatism in affecting global climate through the intrusion of magmas into organic rich sedimentary basins or, more generally, crustal material. A telling example is the hypothesis formulated by (Svensen et al., 2004) that the intrusion of magmas into organic rich sedimentary rocks of the Norwegian margin during NAIP activity is a potential trigger of a massive and very brief pulse of light Carbon injection into the atmosphere that is a possible responsible for the PETM hyper thermal event. Current research focuses on the tracing of volcanic activity, primarily through mercury concentration (Jones et al., 2019; Tremblin et al., 2022) or mercury isotopes (Jin et al., 2022) among other tracers, into ancient successions to test such hypothesis of deep-surface-climate relationships with impact on the biosphere.

Global estimates on geological carbon emission focus on active volcanoes but disregards diffuse CO_2 emissions away from active volcanoes which may originate in the mantle and travel to the surface through deep shear zones (Caracausi et al., 2015). With this regard, the pargasosphere concept (section 2.1) may provide a new generic model for CO_2 emissions from intraplate settings distant from active volcanic areas. Diffuse gas emissions with upper mantle origin may remain active in formerly active rifted regions long after the

cessation of magmatism and volcanism (Kennedy & Van Soest, 2007). The chemical and isotopic composition of CO_2-rich gas emissions from these areas often show a direct upper mantle origin and a moderate signature of shallow crustal magma chamber processes or carbon reservoirs (Vaselli et al., 2002; Boudoire et al., 2018), which the 'pargasosphere' can help explaining. During gradual cooling of the partially molten asthenosphere beneath young oceans and continents, a small amount (<1 v/v %) of H_2O- and CO_2-bearing basaltic silicate melts or supercritical fluids crystallize or react with the shallower upper mantle respectively (Berkesi et al., 2019). At relatively shallow mantle levels, carbonate minerals are not stable and carbon is not soluble in silicate minerals. Although small proportion of carbon may be incorporated in apatite (Riker et al., 2018), most of the carbon is stored as CO_2 in fluid inclusions of silicate minerals or in free fluids at grain boundaries (Berkesi et al., 2019; Frezzotti & Touret, 2014). The source of CO_2 (and other volatiles) is the in-situ partial melt or incipient fluid present in the cooling asthenosphere a process that can be effective until the 1100 °C isotherm reaches the bottom of the 'pargasosphere' at 100 km depth. The CO_2-rich fluids trapped in fluid inclusions or along grain boundaries eventually migrate to the surface from the upper mantle and contribute to the global carbon cycle (Kovács et al., 2021). In case of CO_2-rich inclusions in upper mantle rocks, the effect of fracturing has been investigated (Yamamoto et al., 2011). These studies suggest that during deformation of the host minerals, fluid inclusions and fluids present at grain boundaries may be mobilized via diffusion or dislocation creep. CO_2-rich fluids can also be liberated along cleavages and migrate quickly toward the surface. The regional stress/strain field and the migration of CO_2-rich fluids thus appear to be tightly related, which is why CO_2 (and associated noble gas) monitoring is tentatively used in earthquakes prediction research (Szakács, 2011).

3.3 Surface-deep Earth processes coupling and direct effects on life

Several elements and nutrients useful to life (besides carbon) are cyclically transferred through surface and deep reservoirs during geological timescales. This implies that, beyond climate and landscape evolution (Antonelli et al., 2018), geodynamic events are intrinsically linked to the biosphere and increasing evidence suggests the establishment of modern-style plate tectonics contributed to the development of complex life on our planet (DePaolo et al., 2008; Sobolev et al., 2011; Stern, 2016; Zaffos et al., 2017; Lee et al., 2018; Hagen et al., 2021; Hagen et al., 2021; Large et al., 2015; Dehant et al., 2019). A global continuously evolving mosaic of lithospheric plates, likely established gradually during the geological past

(Gerya, 2014; Gerya, 2019; Sobolev & Brown, 2019), supplies and withdrawals nutrients resulting in variations of environmental conditions that foster genetic modifications (Zerkle, 2018; Descombes et al., 2018). In this respect, modern-style plate tectonics with its continuously evolving global mosaic of lithospheric plates (Bercovici & Ricard, 2014) is often viewed as a strong promoter of biological evolution (Leprieur et al., 2016; Stern, 2016; Pellissier et al., 2017; Descombes et al., 2018; Zerkle, 2018).

Over geological timescales, volcanic activity of different duration, volume, and origin (e.g., from Large Igneous Provinces to ignimbrites flare-ups) contributed to changes in the composition and availability of trace elements required by life for metabolic functions. Life on Earth uses a small set of proteins to carry out the large majority of redox chemical reactions required for its survival. These proteins, called oxidoreductases enzymes, contain diverse trace elements as catalytic centers used to control redox chemistry. Elements used by life for this purpose include a diverse array of metals and some non-metal (Fe, Cu, Ni, Co, Mo, W, Mn and S among others; (Giovannelli et al., 2022). The environmental availability of these elements is linked to a variety of deep and surface Earth processes, including volcanisms (Edmonds et al., 2018; Liu et al., 2021), redox changes during planetary history (Anbar, 2008) and erosion of diverse rocks (Middelburg et al., 1988; Robbins et al., 2016). The onset of plate tectonics and variations in the coupling of deep and surface Earth processes influencing environmental trace element availability have likely had an effect on the emergence and distribution of life in deep-time, influencing the emergence of modern biogeochemistry and thus influencing climate (Giovannelli, 2022). Besides the effects through the recycling of nutrients and elements, the redistribution of continents, the growth of mountains, the rise and demise of volcanic and magmatic arcs, the opening and closing of marine gateways also produce moderate environmental ‘stress’ that stimulates populations to adapt and evolve (Stern, 2016). Indeed, some of the characteristic timescales of biological evolution are comparable to those at which geodynamic reorganizations occur (Giovannelli et al., 2022), which may be taken as further evidence of the coupling between internal and external dynamics (DePaolo et al., 2008; Hagen et al., 2021). The influences of global tectono-magmatic style are at least twofold and regulate (i) the supply and withdrawal of nutrients (via mantle degassing/ingassing, rock weathering and erosion, sedimentation and burial, subduction-related recycling etc.) and (ii) space-time variations of environmental pressures (including evolution of landmass distribution, landscape, atmosphere, ocean and climate). Zerkle (2018) and Stern (2016) summarized the nutrients-tectonics and environmental pressures-tectonics relations. First, they recognize that life is sustained by a

critical set of elements contained within rock, ocean and atmosphere reservoirs and cycled between Earth's surface and interior via various tectonic, magmatic and surface processes. Over geologic time scales, tectono-magmatic processes play a critical role in providing bioactive elements to the ocean-biosphere system, via outgassing, volcanism, uplift and erosion (Zerkle, 2018). Second, they highlight that tectonic processes such as the redistribution of continents, growth of mountain ranges, formation of land bridges, and opening and closing of oceans provide continuous but moderate environmental pressures that isolate and stimulate populations to adapt and evolve without being capable of extinguishing all life. In addition, mantle plumes and large bolide impacts provide episodic but potentially extreme environmental pressures capable of causing global mass extinctions. A planet with oceans, continents, and modern-style plate tectonics maximizes opportunities for speciation and natural selection, whereas a similar planet without plate tectonics provides fewer such opportunities (Stern, 2016).

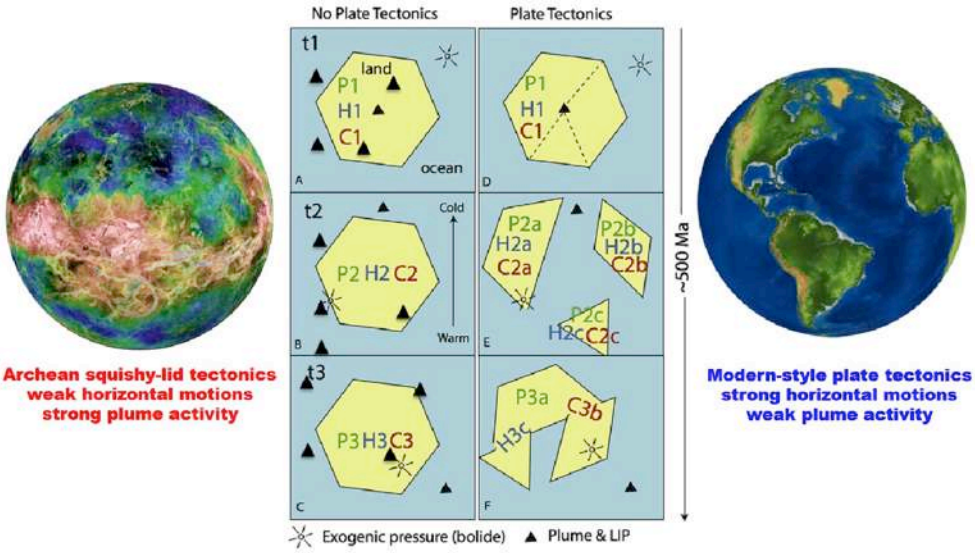

Figure 3.3.1: Cartoon illustrating potential influence of global terrestrial tectonic styles on life evolution (modified after Stern, 2016). Two idealized Earth-like planets without (left, analogous to Hadean-Archean Earth) and with (right, analogous to modern Earth) plate tectonics are compared that possess continents (yellow) and oceans (blue) and three interdependent evolving life forms (plant "P", herbivore "H", and carnivore "C"). Three panels from top to bottom show three different times at ~100 million year intervals (characteristic timescales of the supercontinent cycle). It is assumed that exogenic evolutionary pressures (causing e.g., global mass extinction) depend on meteorite impacts and mantle plume activity including Large Igneous Provinces (LIPS). Plate tectonics causes breakup and movements of continents that provides many opportunities for isolation and diversification under different (geographic, climatic) conditions of natural selection, and evolution. On the other hand, when continents collide, different species comingle and compete and new ecological systems are established that further accelerate life evolution (Stern, 2016).

It is obvious that both nutrients and tectonics aspects are intimately related and must be considered together for better understanding of life evolution and biodiversity distribution. It is important to point out that timescales of biological evolution estimated based on the

analysis of phylogenies and/or fossils are rather long and comparable to geodynamic timescales (Alroy, 2008; Marshall, 2017). In a constant rate birth-death model (Kendall, 1949), new species originate with speciation rate, and species become extinct with extinction rate, typically expressed as rates per lineage per million years (L-1Myr-1). Typically, estimates of speciation and extinction rates fall within the range 0 to 1 L-1Myr-1 (Marshall, 2017) and rarely exceed 1 L-1Myr-1, except within intervals of crisis (Alroy, 2008). The timescales of biological evolution are therefore similar to timescales of tectono-magmatic lithospheric and mantle processes in general and subduction and plate motions timescales in particular. This creates a natural possibility for the coupling of geodynamical simulations with life evolution modelling. Some recent examples of biogeographical modelling coupled to reconstructed plate motions that show strong potential of this modelling direction are shortly described hereafter.

Leprieur et al. (2016) investigated numerically possible roles of plate tectonics in driving tropical reef biodiversity dynamics. The Cretaceous breakup of Gondwana strongly modified the global distribution of shallow tropical seas reshaping the geographic configuration of marine basins. Leprieur et al. (2016) showed that a spatial diversification model constrained by absolute plate motions for the past 140 million years is able to predict the emergence and movement of diversity hotspots on tropical reefs. The simulated spatial dynamics of tropical reefs explains marine fauna diversification in the Tethyan Ocean during the Cretaceous and early Cenozoic and identifies an eastward movement of ancestral marine lineages towards the Indo-Australian Archipelago in the Miocene. A mechanistic model based only on habitat-driven diversification and dispersal yields realistic predictions of current biodiversity patterns for both corals and fishes. Leprieur et al. (2016) therefore concluded that plate tectonics played a major role in driving tropical marine shallow reef biodiversity dynamics.

Pellisier et al. (2017) investigated how changes in the position, connectivity and topography of continents during the last 100 Myr could have shaped the current location of hotspots of endemic richness across the globe. They used palaeogeographies in a numerical model that quantifies, through time and space, the potential dispersal between disconnected habitat areas. As the dynamic coupling to changing plate tectonic environment, Pellisier et al. (2017) used palaeo-reconstructions of the position of continents, coastlines and palaeo-bathymetry from the Early Cretaceous (140 Mya) to the present in 1 Myr steps as boundary conditions for their biogeographical models. They further developed a numerical biogeographical model based on habitat dynamics, which quantifies the amount of potential dispersal into each geographical cell from disconnected patches separated by unsuitable areas

(i.e., of sea for terrestrial species or deep sea and land for marine species). Rare dispersal across such geographic barriers should allow the establishment of new populations, but gene flow is subsequently almost non-existent, leading to in situ speciation. Classical examples of long-distance colonization of remote areas such as islands (Guzmán & Vargas, 2009; Gillespie & Roderick, 2014) followed by local speciation support the possibility of dispersal across straits on geological time scales (Cowie & Holland, 2006), i.e. on the timescales of subduction and plate mosaic evolution. Pellisier et al. (2017) evaluated whether their biogeographical model could pinpoint the locations of hotspots of endemic richness computed from the ranges of 181'603 species across 14 taxonomic groups. As the result, Pellisier et al. (2017) found the significant spatial congruence between the model results and the observed present-day biodiversity thereby providing important quantitative evidence of the contribution of plate tectonics in shaping global biodiversity pattern. Remarkably, the signal of plate tectonics was independent from those of the Quaternary glaciation, topographical heterogeneity and contemporary productivity and was stronger for terrestrial than freshwater and marine taxa (Pellisier et al., 2017). Complex tectonic regions, predominantly located at the confluence of major lithospheric plates such as the Mediterranean, Mesoamerica, Madagascar and South East Asia likely provided favorable environments for allopatric speciation and the emergence of new species across straits (Pellisier et al., 2017). Non-coincidentally, these are also areas strongly affected by various subduction, collision and plate tectonics processes and complex landscape evolution.

Descombes et al. (2018) presented new process-based numerical modelling tool SPLIT that allows to simulate the evolutionary dynamics of species ranges by spatially linking speciation, extinction and dispersal processes to paleo-environmental habitat changes over geological time periods. The SPLIT model provides a mechanistic expectation of speciation and extinction assuming that species are ecologically identical and not interacting. The likelihood of speciation and extinction is equivalent across species and depends on two dispersal parameters interacting with habitat dynamics (d a maximum dispersal distance and ds a distance threshold beyond which gene flow is absent). SPLIT model tracks biodiversity dynamics under paleo-environmental changes and provides multiple expectations that can be compared to empirical patterns. Descombes et al. (2018) illustrated potential real-world applications of SPLIT by whether habitat changes caused by plate tectonics explain the current biodiversity patterns of mangroves. Simulations of the last 100 Myr successfully reproduced the observed longitudinal gradient in species richness, the empirical pattern of beta-diversity and also provided inference on diversification rates (Descombes et al., 2018).

Hagen et al. (2021) presented next generation biogeographical modelling tool GEN3SIS aimed at simulating eco-evolutionary processes coupled to plate tectonics and long-term climate variations. This tool allows to simulate specie's ranges, alpha- and beta-diversity patterns, ecological traits as well as phylogenies that can be compared to observations. This allows to in particular evaluate different paleoclimatic and paleogeographic hypotheses by simulating different Earth history scenarios and comparing numerical results with available observations. As a case study, Hagen et al. (2021) explored the cold-adapted plant biodiversity dynamics throughout the Cenozoic history, based on topo-climatic reconstruction for the India-Asia collision during the last 55 Myr. In this highly elevated region, the first cold niches of the Cenozoic appeared, demanding adaptation from the local living flora. The GEN3SIS model successfully predicted the emergence of current cold-species richness patterns and indicated that cold-adapted flora emerged in the Oligocene, first in the Himalayas, followed by a spread to the Arctic. The later agrees with observed low species richness and high nestedness of Arctic assemblages compared to those of the Himalayan mountain range (Hagen et al., 2021). Development and validation of GEN3SIS is thus an important step toward coupling of biogeographical and climate models.

This very short overview highlights that bio-geodynamical numerical modelling (i.e., coupled modelling of Earth's interior, climate, environment and life evolution) stands out as one of the frontier research tasks in geodynamics, biology, ecology and evolution as well as related disciplines. This is the promising future field, which will explore connections between deep Earth processes, surface processes, and the diversification of life. Accelerated development and application of new global- and regional-scale computational bio-geodynamical numerical modelling tools is needed, that will couple (i) available global and regional geodynamic models of subduction and plate tectonics processes (Crameri et al., 2012; Gerya et al., 2015), (ii) landscape evolution models (Braun & Yamato, 2010; Thieulot et al., 2014; Ueda et al., 2015), (iii) atmospheric, ocean and climate change models (Donnadieu et al., 2006; Donnadieu et al., 2009) and (iv) spatially-explicit models of species speciation, evolution and extinction (Gotelli et al., 2009; Leprieur et al., 2016; Pellissier et al., 2017; Descombes et al., 2018; Hagen et al., 2021). The resulting hybrid bio-geodynamical numerical modelling tools will be used to explore systematically various subduction and plate tectonics scenarios and understand their potential effects for the evolution of the environment, landscape, climate and the diversification of life. To this aim, TOPO-EUROPE will encourage geodynamicists, geologists, (geo)biologists, ecologists, geochemists, palaeontologists, geomorphologists, and climate experts to cooperate and integrate/interpret

biological data with geodynamic, landscape evolution, carbon cycle and climate (*sensu lato*) modelling.

Looking beyond continental drift and the evolution of life (Spencer et al., 2022), biota has been recognized as providing important controls on erosion and weathering processes (Langbein & Schumm, 1958; Istanbulluoglu & Bras, 2005; Heimsath et al., 2012) and river morphodynamics (Métivier & Barrier, 2012; Ielpi et al., 2022). Conversely, the development of topography over geologic timescales creates and destroys ecosystems and influences biodiversity (Antonelli et al., 2018; Hoorn et al., 2013; Boucher et al., 2021). Biota influence erosional processes through interactions with the hydrologic cycle (e.g., interception, infiltration, and runoff), as well as bioturbation and biotic weathering of rocks (Übernickel et al., 2021; Viles et al., 2021). In the absence of climate (or vegetation) change, topography can reach an equilibrium, or steady state, such that the mean of erosion rates over sufficiently long (millennial to million year) time scales reflects that of rock uplift rates (e.g., flux steady state of (Willett & Brandon, 2002)). Superimposed on this tectonic forcing on the landscape are transients in catchment erosion driven by internal dynamics such as river capture (Yanites et al., 2013; Willett et al., 2014), climate change (Tucker & Slingerland, 1997), and vegetation (Starke et al., 2020). The effects of vegetation on erosion are linked to climate change, whereby climate (and topographic) change can lead to variations in the distribution of different plant functional types which then influence catchment average erosions by 5-25% depending on the ecosystem experiencing the change (Langbein & Schumm, 1958; Schmid et al., 2018; Starke et al., 2020). Finally, biota has also long been postulated to exert a strong influence on landscape morphodynamics, such as on river channel patterns and mobility, with potential impact on the transfer of the products of erosion from their source to their ultimate repository in sedimentary basins. Thus, although erosion rates, on the long time scale, are consistent with uplift rates, over shorter timescales climate and vegetation can introduce transients in erosion rates that can potentially obscure the calculation of tectonically driven erosion rates. The previously described interactions highlight that tectonics, and climate and vegetation change have some degree of coupling with each other. More specifically, tectonic processes (from continental drift to mountain building) lead to changes in biomes and ecosystem composition, whereas climate (e.g., orography) and vegetation change influence erosion rates and landscape morphodynamics. Our knowledge of these interactions has grown in the past decade with the rebirth of biogeomorphology as a research area. However, the linkages and feedback between the biosphere, surface processes and solid Earth dynamics remain largely unexplored to date and, as such, present fertile grounds for future research.

In addition to the coupling and direct effects of surface-deep Earth processes on life at the surface of the planet, coupled processes between deep Earth processes, topography, climate and deep subsurface life have been discovered in the last decade of research (D'Hondt et al., 2019; Barry et al., 2019; Vitale Brovarone et al., 2020). Recent advances in environmental microbiology have shown the presence of a vast, diverse and extremely active subsurface biosphere (Magnabosco et al., 2018). The distribution of subsurface life, which is entirely microbial, in the oceanic and continental crust is typically controlled by the 122°C – 150°C isotherms (122°C is the maximum temperature for life growth in laboratory conditions –the so-called "biotic fringe" (Takai et al., 2008)) together with a variety of other parameters (e.g., pore space availability, water activity, presence of electron acceptor and energy sources). Data collected in the last 20 years of subsurface research show that life can penetrate the crust up to 3-5 km (Magnabosco et al., 2018; Kallmeyer et al., 2012), with theoretical studies suggesting that in areas of low heat flow such as those present in cold subduction zones the habitability zone can reach 15-20 km depth (Plümper et al., 2017). Given its global prevalence, diversity and slow but consistent biogeochemical impact over geological time scales (Giovannelli et al., 2022), deep microbial life has been shown to significantly alter the quantity and quality of volatiles recycled through the crust by plate tectonics (Giovannelli et al., 2020; Fullerton et al., 2021) and impact rock weathering through bio-leaching, bio-dissolution and bio-precipitation of minerals in diverse rocks (Lian et al., 2008; Heim, 2011; Samuels et al., 2020). While the extent of the effects of subsurface life on climate-relevant volatile is not constrained, recent papers suggest a tight relationship between deep Earth processes, topography and subsurface microbial communities interactions with element cycling. Recent work on the forearc region of the Costa Rica convergent margin have shown that calcite precipitation in the subsurface can account in a reduction of up to 19% of the carbon originally believed to be delivered to the mantle (Barry et al., 2019). In the same area, subsurface microbes remove through chemolithotrophy an additional 2 to 22 % (Fullerton et al., 2021), which combined with the calcite precipitation described by Barry et al (2019), brings the total amount of carbon removed from deep sequestration up to ~40 %. Calcite and other calcium carbonate minerals are known to be microbially precipitated, either directly or indirectly (Stocks-Fischer et al., 1999) with the microbes acting as nucleating agents (Pacton et al., 2014) or altering the chemical equilibrium (Seifan & Berenjian, 2019). While these papers are focused on the forearc region of the Central American Volcanic Zone, similar processed might be at play in other convergent margins, and their relative intensity might change in relationship to topographic features and deep Earth processes. In the South

American Central Volcanic Zone, the inventory of volatiles recycled through volcanism both in the volcanic arc, forearc and backarc correlates with crustal thickness and heatflow (Barry et al., 2022). The presence of reduced heatflow, for example linked to stable cartons, cold orogenic belts and cold subduction zones, can promote a deeper subsurface ecosystem, allowing for extensive interaction between rock, fluids and microorganisms at depth. Cold thermal regimes do not only favor habitable conditions to depth, but also allow geological processes necessary for microbial life to extend to greater depths and, possibly, to have emerged on Earth. Olivine hydroxylation, also called serpentinization, is a simple, yet fundamental fluid-rock interaction that has attracted broad scientific interest in communities spanning geology, petrology and geochemistry, microbiology, astrobiology, and green energy research. Serpentinization is known to produce reduced fluid species such as H_2 and abiotic CH_4 that act as sources of energy for microbial life (Kelley et al., 2005; Martin et al., 2008), as well as key building blocks of life (Ménez et al., 2018). Cold subduction thermal regimes, which result from the interconnection of multiple surface-deep interactions, favor the extension of serpentinization reaction and H_2 and abiotic CH_4 to greater depths (Vitale Brovarone et al., 2020). This feature sets deep convergent margins fluid-rock reactions as a major feeder of energy for deep –or the deepest– life form on Earth and potentially beyond (Mottl et al., 2003; Ohara et al., 2012; Vitale Brovarone et al., 2020).

While this is a new area of inquiry and data is lacking for diverse tectonic settings globally, the presence of a pervasive subsurface biosphere has the potential to significantly alter volatile cycling over geologic time scales. The feedback mechanisms between deep and surface Earth processes and the biosphere (both surface and subsurface) might have contributed significantly to diverse tipping point in Earth planetary history, and the coevolution between geosphere processes and the biosphere constitute a ripe area of future research.

4. IMPACT ON SOCIETAL CHALLENGES

4.1 Current climate change

Observations of present-day and recent warm climates (e.g., Mid-Piacenzian Warm Period) help understanding climate dynamics and constraining predictions of future climate conditions in response to human activity (Robinson et al., 2008). However, these observations provide limited information about the climatic response to the massive amount

of CO_2 that our societies release into the atmosphere and ocean. To assess climate projections, it is desirable to study past climate changes associated with high atmospheric CO_2 concentrations, similar to those predicted for the near future (i.e., 550 ppm in the next 30–80 years and >1500 ppm in just a few centuries if anthropogenic emissions continue unabated (Caldeira & Wickett, 2003)) and longer than global ocean overturning (i.e., a few millennia). In addition, the tangible narratives of past climate perturbations preserved in rocks, and the story they reveal of their impact on landscapes, biota and even human populations (Zaki et al., 2021) are *per se* efficient communication tools to channel important and complex knowledge to the society (Pancost, 2017), without invoking predictions and the uncertainties they bear that are often misunderstood by the broader public.

Within framework, the Miocene period provides an ideal paleo-example of future climate (Steinthorsdottir et al., 2021), as paleoclimate proxy records document high atmospheric pCO_2 values of up to ~600 ppm, with over 1,000 ppm permissible during the Miocene Climatic Optimum (Rae et al., 2021). Recent modelling efforts to simulate global Miocene climate (MioMIP1 project; (Burls et al., 2021)) show that during the Miocene, the stronger polar greenhouse effect (due to CO2, water vapor, and lapse rate) and decreased surface albedo, are the dominant contributors to the Polar amplified warming – a result consistent with the literature on future climate change (Pithan & Mauritsen, 2014). For Europe, the Miocene is characterized by strong precipitation "bi-directional" precipitation change (Fig. 2.6.1), with a precipitation decrease over the Southern Europe and the Mediterranean and an increase over Scandinavia and Northern Russia (Botsyun et al., 2022). It was been also highlighted that paleoclimatic modelling studies are sensitive to the choice of geological boundary conditions (e.g., paleogeographic reconstruction including surface topography). Therefore, adequate paleoclimate modelling studies require direct integration of latest state-of-the-art of plate tectonic, crustal and paleomagnetic reconstructions, paleotopography, and paleobathymetry.

Another paleo example of what the future climate be similar to is the Early Eocene Climatic Optimum (EECO), between around 53 and 50 million years ago, characterized by much higher CO_2 concentrations and warmer global temperatures (Fig. 4.1.1) (Meckler et al., 2022). At timescales shorter than a few tens of thousands of years, early Eocene hyperthermals show that atmospheric CO_2 concentration and temperature can increase abruptly driven by natural forcing (Barnet et al., 2019). The most prominent hyperthermal, the Palaeocene-Eocene Thermal Maximum (PETM, at ~55 Ma) involving a global

temperature increased by more than 5°C in less than 10 kyr (McInerney & Wing, 2011), is to all effects the most similar known climate aberration to the ongoing global warming (Fig. 4.1.1). Several paleoclimate modelling studies of the PETM (Rush et al., 2021; Shields et al., 2021), have now successfully demonstrated how elevated CO_2 levels could trigger important hydrological response, in particular with atmospheric rivers and shifts in storm tracks, highlighting the potential of future couplings of solid Earth models and high-resolution coupled climate ocean-atmosphere simulations. The early Cenozoic thus includes an ideal ensemble of natural experiments to elucidate the mechanisms and drivers of climate changes and assess by comparison the role of human activity in setting the overall conditions and transience of the global climate (Lunt et al., 2021). The occurrence of past abrupt warming events provides an opportunity to test theories about the physical and biogeochemical interactions in rapidly shifting systems. To achieve this goal, however, it is pivotal to develop a deeper understanding of the complex interactions between the climate system, the biogeochemical cycles and the characteristic processes of the solid Earth, with particular focus on positive and negative feedbacks acting on short geological timescales.

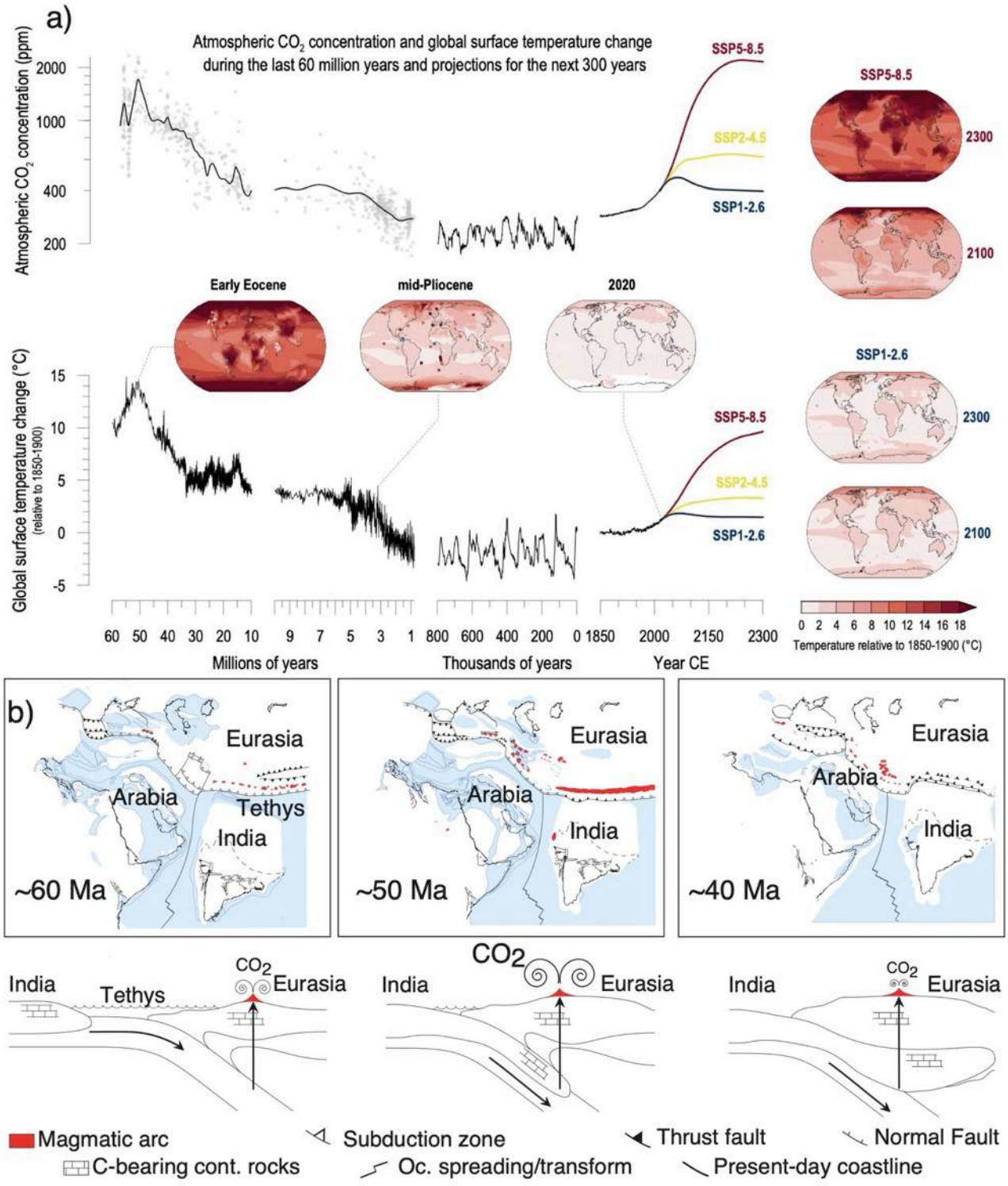

Figure 4.1.1: (a) Changes in atmospheric CO2 and global surface temperature (relative to 1850-1900) throughout the Cenozoic and for the next 300 years (modified after IPCC 2021 report, to which the reader is referred for details on sources and data analyses). (b) Paleotectonic maps and cross-sections of the Neo-Tethyan margin during the lower Cenozoic (modified after the paleotectonic reconstructions by the DARIUS program, 2018, http://istep.dgs.jussieu.fr/darius/maps.html and Sternai et al., 2020).

4.2 Energy

Recent geopolitical events undermined the delicate global economic stability and international security, with seemingly long-term consequences for the European energy policies. As a result, many European countries are moving back to coal or gas production, which shows the weakness of our energy system and the urge for alternative clean and inexpensive sources of energy to prevent further climate and environmental deterioration and safeguard international peace. Many of the 'green' energy and climate mitigation actions are inherently linked to the deep and surface Earth interactions at the very heart of the TOPO-EUROPE initiative. For instance, the long term security of geothermal or nuclear plants can be threatened not only by military actions but also by natural seismicity as well as 'anthropic' earthquakes arising from extraction of hydrocarbons. The development and maintenance of these infrastructures should thus be accompanied by careful monitoring and better understanding of intraplate stresses, 3D fault trajectories, fault reactivation, and both natural and anthropic induced pore fluid pressure cycles nearby.

4.2.1 Geothermal energy and natural H_2

Geothermal resources are most commonly classified based on temperature and thermodynamic properties (Haenel et al., 1988; Hochstein, 1990; Muffler & Cataldi, 1978) which are the most relevant parameters in terms of estimating the amount of energy that can be recovered from a system. An alternative classification scheme referred to as geothermal play types (Moeck, 2014) focuses on the geological and geodynamic controls that have major influence on the thermal, structural, hydrogeological and geochemical characteristics of geothermal reservoirs. Quantitative knowledge of the crust and upper mantle structure and its thermal regime, as well as tectonic regimes and faults structures, enable to link geothermal systems to their plate tectonic settings, therefore, these studies are key for geothermal exploration.

Geothermal energy has high potential for providing sustainable energy in particular in a continent such as Europe, with a relatively hot upper mantle. In the past few decades, there has been a significant increase in both direct heat utilization and geothermal power generation within Europe and worldwide (Huttrer, 2020; Lund & Toth, 2021). The increasing trend in Europe is also predicted for the future, especially in light of the current energy crisis and climate change mitigation actions. By 2050, (Dalla Longa et al., 2020) foresee a level of

880-1050 TWh/yr and_100-210 TWh/year in heating applications and electricity generation, respectively.

Geothermal reservoirs that can provide temperatures of at least 70 °C, suitable for direct heat applications exist in many locations throughout Europe (Limberger et al., 2018), and technologies to utilize such aquifers are already well-established. Geothermal systems that are suitable for economic power generation with temperatures of at least ~120 °C and relatively high flow rates (preferably >100 l s^{-1}) are rather limited within Europe; located for instance close to plate boundaries such as Tuscany and Iceland. Apart from these locations, high temperature basement formations mostly do not have sufficient permeability to host geothermal fluids and require stimulation to create fluid pathways necessary for economic heat recovery, a technology called Enhanced Geothermal System (EGS) (Breede et al., 2013; Lu, 2018; Olasolo et al., 2016). The EGS concept consists essentially of drilling at least two boreholes into deep fractured rock, extracting hot fluid from a production well and injecting the cooled fluid back into the fractured reservoir through an injection well (Fig. 4.2.1). To this end, both boreholes have been stimulated to connect the two wells to the natural surrounding geothermal reservoir by artificially enhancing the permeability of the natural network of fractures in their vicinity.

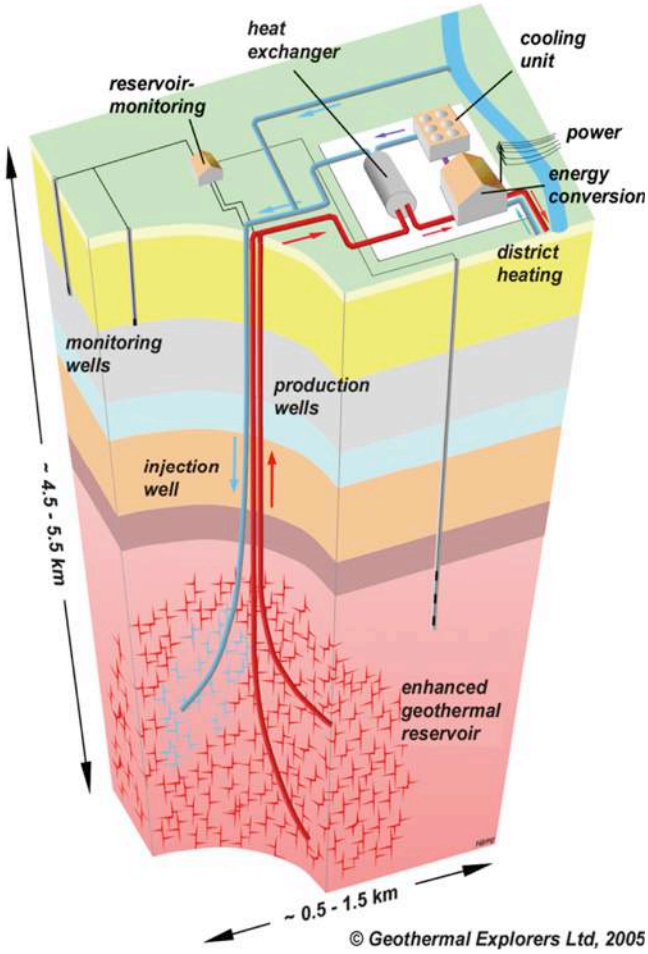

Figure 4.2.1. Main elements of an EGS system consisting of production and injection wells drilled in a deep fractured rocks and surface units for heat and power generation. (Adapted from Geothermal Explorers Ltd, 2005).

Within Europe, the European Cenozoic rift system and the Pannonian basin have excellent conditions for the development of EGS systems. The first successful EGS stimulation in Europe was the Soultz project in eastern France (Gérard et al., 2006). Since then, further projects have been developed in the Upper Rhine Graben near the Soutz site (e.g., Landau, Insheim). The Basel EGS project in Switzerland, which was terminated after an induced earthquake (Deichmann & Giardini, 2009) , is a good example on the potential risks associated with reservoir stimulation. Such risks may be reduced with seismic monitoring and in-depth studies based on local stress conditions and the assessment of the pre-existing fracture network. The number of operating EGS sites in Europe has not increased significantly in the past years, and the share of electricity generation from EGS within Europe is not comparable to other renewables such as wind, solar and hydropower (IEA, 2021). To achieve a significant increase, explorational and technological developments in EGS and further successful demonstration sites are necessary in the future.

The key element of EGS development is the creation of the reservoir, mostly through hydraulic stimulation. For this operation, prediction of the stress field orientation and magnitude is essential. Success in hydraulic stimulation is dependent on the thermo-mechanical properties of the crust. Critically stressed regions, marked by active deformation, require little excess pressure for stimulation and are therefore favourable. In addition, such regions are marked by pre-existing faults and fractures, forming preferential pathways for stimulated flow.

On the exploration side, geological information, world stress map data (Heidbach et al., 2019) and natural seismicity can be used to identify active deforming basins and basement areas which are critically stressed. (Cloetingh et al., 2010) demonstrated the importance of tectonic processes in EGS site selection and development. They point out that distinguishing between local and regional heat flow anomalies is essential for the proper extrapolation of temperature and heat flow data to areas without well control. Tectonic models are able to constrain crustal rheology and stress regime, highlighting actively deforming areas and fault/fracture zones with favorable conditions for hydraulic stimulation.

In recent years, several works on various regions of Europe utilized regional-scale input data such as lithosphere and crustal thickness and composition models, regional heat flow, structural data and models to highlight potential areas for geothermal exploration (Békési et al., 2018; Freymark et al., 2017; Limberger et al., 2018). Such works may shed light on geothermal targets that would have been overlooked without an integrated lithosphere-scale approach.

Apart from EGS systems, deeply buried, fractured and/or karstified carbonate formations can also provide sufficiently high temperatures and flow rates for power generation in Europe. The utilization of such systems for electricity production has already initiated for instance in the German Molasse Basin (Dussel et al., 2016) in the Pannonian Basin (Velika Ciglena power plant in Croatia, Tura power plant in Hungary) (Huttrer, 2020). Such projects can also benefit from basin-scale tectonic and geomechanical models to highlight major fracture zones, and understand the state of stress in locations where no crustal indicators are available (Ziegler & Heidbach, 2020).

As a promising green energy solution, H_2 is receiving increasing attention across several scientific and industrial communities. Although natural H_2 has long been neglected in geological fluids (Smith et al., 2005), discoveries and investigations on natural H_2 shows are increasing fast and set a new horizon in green energy research (Moretti & Webber, 2021; Truche & Bazarkina, 2019; Zgonnik, 2020). Natural H_2 has been identified in multiple forms

such as free gas, in inclusion, and dissolved in water, and in several geological contexts, from mid-ocean ridges, ophiolites, Precambrian shields, coal basins, in terranes ranging in age from Archean to the present day, and from surface to deep mantle conditions (Smith et al., 2005; Zgonnik, 2020; Cannat et al., 2010; Lollar et al., 2014; Vitale Brovarone et al., 2020; Smith et al., 2016). Some shows are associated with large reservoirs (Prinzhofer et al., 2018). Although the identification of natural H_2 shows and the associated H_2 fluxes is still preliminary, the range of identified sources clearly for future collaborative research among geo-bioscientists to identify the mechanisms, fluxes, migration pathways, and reservoirs of this natural resource.

4.2.2 Geological storage of CO_2 and H_2

The rising concentrations of greenhouse gases and the related rising of global temperatures prompted attempts of storing CO_2 in geological reservoirs (Carbon Capture and Storage, or CCS). The basic concept of CCS is to capture CO_2 at a location of anthropogenic emission and inject it underground into a geological formation to prevent emissions into the atmosphere. In many cases, the adopted strategies and reaction pathways mimic natural processes of fluid-rock interaction identified over a broad range of conditions, from shallow to deep. Suitable host geological formations for CCS may be found in sedimentary basins, such as aquifers or depleted oil and gas fields. In these cases, the injected CO_2 is stored in the pore space of the reservoir formation, coexisting with the naturally accumulated fluid phases (brine, hydrocarbons, naturally accumulated CO_2), and relies on seal (low-permeability) formations and trap structures for keeping the injected CO_2 underground. The injected CO_2 is first trapped by the trap structure, and, with time, becomes increasingly consumed by residual trapping, by dissolving into reservoir brines, and by mineralization (Metz et al., 2005). The presence of an extensive subsurface microbial community can directly alter the fate and success of CCS efforts. Microorganisms can in fact use CO2 both as carbon source to produce biomass or as electron acceptor in microbial respiration forming methane and acetate as by products (Tyne et al., In review). While the former, the conversion of CO2 into biomass, can promote sequestration by locking carbon into organic matter at depth, methanogenesis, referred to as CO2 methanation in the field of CCS (Strobel et al., 2020), can alter the chemical and physical properties of the injected carbon, rendering more difficult to predict the long term fate of the CCS efforts. Microbial methanation depend on multiple factors, including reservoir temperature, availability of hydrogen and redox conditions. A

recent paper has demonstrated rapid microbial methanogenesis in CCS reservoir (Tyne et al., 2021), suggesting that deep biosphere interaction with the injected gases might play a key role in the future success of this mitigation technology.

CCS in sedimentary basins has been trialed for decades in frontier projects, such as the Sleipner CCS project, located in offshore Norway, and operating since 1996 (Baklid et al., 1996; Torp & Gale, 2004). Experiences also from other industrial test sites (e.g., In Salah, Snøhvit projects) so far show the general suitability of CCS in porous formations, but also highlight the need for detailed geological models, knowledge of mechanical properties and advanced monitoring-modelling techniques (Chadwick et al., 2010; Eiken et al., 2011; Ringrose, 2020; Williams & Chadwick, 2017). Early successes have been followed by further European initiatives, including research projects focusing on both the aspects of carbon capture (e.g. NANOMEMC2 project, (Ahmadi et al., 2018) and its subsequent geological storage (e.g. ENOS project) (Sohal et al., 2021).

Alternatives to CCS in sedimentary basins are geological formations that undergo relatively rapid chemical reactions in the presence of CO_2. Such rock types are mafic and ultramafic rocks (basalts, peridotites, serpentinites), which may be considered for mineral (reactive) CO_2 storage. The result of mineral storage is the incorporation of the carbon into the mineral structure of carbonates, which results in a much desired “permanent” deposition in the lithosphere and separation from the atmosphere (Oelkers et al., 2008; Snæbjörnsdóttir et al., 2020). Natural examples of such processes include large-scale carbonation, i.e., replacement of silicate by carbonates, of ultramafic rocks in at mid-ocean ridges, in ophiolites and orogenic peridotites such as Oman, Norway, and Newfoundlans among others (Kelemen & Matter, 2008; Matter & Kelemen, 2009; Ludwig et al., 2006; Boschi et al., 2009; Beinlich et al., 2012; Menzel et al., 2018), and possibly large portions of the mantle wedge above subducting slabs (Kelemen & Manning, 2015). Onshore areas in Europe with such oceanic rock types exposed on the surface are not abundant, however, Iceland offers an ideal location for testing and developing this method. This gave rise to the projects CarbFix and CarbFix 2, where reactive mineral storage facilities were established and developed on Iceland, unraveling the optimal conditions and great theoretical potential of this method (Clark et al., 2020; Gislason et al., 2010; Matter et al., 2009). Results have shown that young basalts (not yet affected by weathering) are especially suitable for storing large amounts of carbon (Wiese et al., 2008), making mid-ocean ridges giant potential reservoirs, theoretically capable of storing more carbon than the carbon content of all fossil fuels on Earth (Snæbjörnsdóttir et al., 2020).

CCS projects in sedimentary basins as well as in oceanic rocks have demonstrated the vast geological potential of this method. While improving risk evaluation, technological and monitoring techniques are still essential, the largest barrier for meaningful contribution to climate change mitigation appears to be the lack of attractive business models that would allow for large-scale implementation.

As renewable energy sources become more important, the need for balancing their fluctuating energy output (especially in case of solar and wind energy), which results in periodic energy excesses and deficits, is also growing. One of the possible solutions for this is Underground Hydrogen Storage (UHS), which allows to convert excess electricity to hydrogen through electrolysis ("Power to Gas" method), to store the hydrogen in a geological object, and then to use it later in a period of higher energy demand. UHS is possible in the porous formations of sedimentary basins (aquifers and depleted hydrocarbon fields), in salt caverns or in artificially lined rock caverns.

Storage in low-permeability salt caverns is a proven method, with a Teesside facility in England successfully operating since 1972 (Stone et al., 2009), and new initiatives for example in the Netherlands (Hystock project) and France (Storengy-HyPster project) are further developing the technique. However, suitable salt formations are of limited extent and occurrence in Europe, making the method itself a limited prospect on the scale of European energy transition.

Artificially lined rock caverns also appear to be safe solutions for hydrogen storage: the pilot project HYBRIT in Sweden is building on the experiences of natural gas storage in such facilities (Tengborg et al., 2014) and trying to develop the methodology for hydrogen. While the low risk of hydrogen escape in a lined cavern is an advantage, the cost of cavern mining and artificial lining would certainly require substantial investment when upscaling this technique.

Hydrogen storage in porous formations of sedimentary basins offers far larger theoretical capacity than cavern storage methods. Such potential storage sites require a porous reservoir, a sealing caprock and a trap structure, similarly to hydrocarbon fields. However, the physical-chemical characteristics of hydrogen significantly differ from those of hydrocarbons (Pan et al., 2021), which requires more careful examination of flow patterns, potential chemical (and microbial) reactions and storage integrity (Heinemann et al., 2021). Apart from rising academic interest in this topic, pilot projects for implementation have also started, for example the RAG Underground Sun Storage project in Austria (AG RAG, 2020).

Also, in the case of hydrogen as for CO2, deep microbial communities can impact the results and efficiency of the storage process. Hydrogen is one of the key electron donor in microbial metabolic reactions (Greening et al., 2016), and can be used together with a wide array of electron acceptors some of which might be present in UHS reservoirs (Dopffel et al., 2021). Beside lowering the total amount of hydrogen available for recovery with direct consumption, deep microorganisms are also responsible for the production of unwanted by products, such as sulfide that can sour the recovered gas, affect the infrastructure and alter the pore space structure favoring the precipitation of sulfide minerals. Given the link between the distribution of deep subsurface microbial communities and deep and surface Earth processes, understanding the feedback between microbial and geological processes is a key area of future investigation with potentially multiple contributions to diverse societal challenges.

4.3 Hazards

Much of TOPO-EUROPE research has been dedicated to the analyses of the relationships between lithospheric stress and geohazards, including seismic, hydrogeological and volcanic hazard. Stress fields are also of paramount importance to the understanding of differential vertical motions in the lithosphere and in the discrimination of tectonic and climatic controls on relative sea level variations (Cloetingh & Haq, 2015). In addition, stresses and their interaction with the geomechanics of the lithosphere (Zoback, 1983; Zoback, 2007) are crucial in setting up conduits for fluid transport and melt movements inside the lithosphere, also put forward in a series of recent papers (Sternai et al., 2021; Sternai et al., 2016a; Stuewe et al., 2022; Tibaldi et al., 2010) as tectonic and/or surface stresses changes that guide the processes of magma ascent and emplacement. The resulting magma stress field can produce changes in the basement fault geometry and kinematics. Similarly, the anomalous heat flow in volcanic regions can contribute to modifying the dominant deformation style in the substratum. For example, research carried out in the context of ILP (Tibaldi et al., 2008), through an integrated approach that combines field studies and analogue and numerical modelling, has resulted in a major progress in understanding the tectonic controls on volcanism exerted by a large extent through the interplay of thermal perturbations and stress fields. (Milia et al., 2012) focus on a possible link between faulting, cryptodomes and lateral collapses at the Vesuvius volcano (Italy). The Vesuvius is an active volcano that has been affected by late Quaternary lateral collapses and tectonic faults. Cryptodomes and two debris avalanches, 18 ka-old and 3.5 ka-old, were

previously documented and for the younger avalanche a link between onshore and offshore stratigraphy was reconstructed. Stratigraphic data reveal a remarkable difference between the architecture of the northern and southern volcano sectors that is compatible with the occurrence of the older debris avalanche in the southern volcano sector, broadening the horizons of the Vesuvius volcanic hazard. (Nomikou et al., 2012) addressed submarine cones in the Kolumbo Submarine Volcanic Zone of the Hellenic Arc (Aegean Sea, Greece). The seafloor northeast of the Santorini volcano consists of a small, elongated rifted basin within the Cyclades back-arc region of the present Hellenic subduction zone, where the seafloor of the eastern Mediterranean Sea is descending beneath the Aegean microplate. Nineteen submarine volcanic cones occur within this small rift zone, with Kolumbo, the largest of these, which last erupted explosively in 1650 AD, causing significant damage and fatalities on the nearby island of Santorini. In general, the domes/craters northeast of Kolumbo were found to be sediment-covered and showed little evidence of recent volcanic activity. Another observation by the authors was that volcanic rocks were outcropping in the crater walls and slopes of some of the cones. However, they typically consist of volcanic fragments of pumice and lava that have been cemented together by biological activity, indicative of the lack of recent eruptions. Geochemical analysis of samples collected by Nomikou et al. (2012) on the northeast cones showed evidence of low temperature hydrothermal circulation on the summit and upper flanks in the form of stream-like manganese precipitates emanating from pits and fractures. Since volcanic eruptions are a major threat to our lives and society, they represent a primary connection between surface and deep Earth processes that future TOPO-EUROPE activities will certainly tackle.

Existing meteorological time-series are commonly too short to capture climate oscillations that spans century or millennia and can help modelling and forecasting future climate (Kondrashov et al., 2005; Pèlachs et al., 2011). At such timescales, however, rivers can showcase extremely high sedimentation rates (>1 cm/yr), allowing for the creation of detailed chronology of humid/arid periods and flood events (Knox, 1993; Benito et al., 2015) and the tracking, through mineralogical and geochemical analysis, of the source area of the floods (Mologni et al., 2020). The stratigraphy of deposits formed over century-to-millennial time scale can thus be used as proxies to study the climate variability. The information derived on rainfall dynamics and their localization is not only crucial for paleoclimatology but is also extremely precious for predictions of future climate conditions and extreme meteorological events, long-term planning of agriculture and energetic infrastructures, city zoning and management (Hendrix & Salehyan, 2012; Brunetti et al., 2019). Detailed analysis

of surface processes and sedimentary archives are key source of information to bridge across the time scales of direct measurements of Earth observables and those of the underlying geological processes and Earth dynamics.

5. CONCLUSION AND FORWARD LOOK

All these examples of frontiers research demonstrate the need for a multi-scale approach linking new observational constraints reporting on the Earth's structures and characteristic rates with numerical and experimental modelling of surface and deep Earth processes. They also demonstrate that teamwork and connecting advances in different fields is an intrinsic aspect of research efforts to linking deep Earth and surface processes. The recent advances in this domain have set a stage to build future interfaces with other exciting fields such as research on the biosphere, climate and energy.

The realization of these ambitions requires a dedicated effort for community building from all individuals involved. This Science Agenda has the ambition to provide an up-to-date review of high potential building blocks and opportunities for synergy at their interfaces. Further breakthroughs in coupled surface-deep Earth processes research are a pre-requisite for advancing novel approaches to societal challenges facing the Earth system.

Acknowledgements

The ILP, Academia Europaea, Young Academy of Europe, European Science Foundation, Horizon Europe and numerous national research councils are thanked for continuous support and major grants. Magdala Tesauro, Alexander Koptev, and Pietro Sternai thank the ILP for bestowing them with the Flinn-Hart award to young scientists. This work is part of a project that received funding from the European Research Council (ERC) under the European Union's Horizon 2020 research and innovation program (Grant agreement No. 864045). This work has also been supported by Fondazione Cariplo and Fondazione CDP (Grant n° 2022- 1546_001).

References – Appendix B

Übernickel, K. et al., 2021. Reviews and syntheses: Composition and characteristics of burrowing animals along a climate and ecological gradient, Chile. *Biogeosciences*, 18(20), pp.5573-94.

AG RAG, A., 2020. UNDERGROUND SUN STORAGE, Final Report.

Ahmadi, M. et al., 2018. Performance of mixed matrix membranes containing porous two-dimensional (2D) and three-dimensional (3D) fillers for CO2 separation: A review. *Membranes*, 8(3), p.50.

Al-Hajri, Y., White, N. & Fishwick, S., 2009. Scales of transient convective support beneath Africa. *Geology*, 37(10), pp.883–86.

Alroy, J., 2008. Dynamics of origination and extinction in the marine fossil record. *Proceedings of the National Academy of Sciences*, 105(supplement_1), pp.11536-42.

Anbar, A.D., 2008. Elements and evolution. *Science*, 322(5907), pp.1481-83.

Anderlini, L. et al., 202. New insights into active tectonics and seismogenic potential of the Italian Southern Alps from vertical geodetic velocities. *Solid Earth*, 11(5), pp.1681-98.

Andric, N., Matenco, L., Hilgen, F. & de Bresser, H., 2018. Structural controls on sedimentation during asymmetric extension: The case of Sorbas Basin (SE Spain). *Global and Planetary Change*, 171, pp.185-206.

Antonelli, A. et al., 2018. Geological and climatic influences on mountain biodiversity. *Nature Geoscience*, 11(10).

Armijo, R. et al., 1996. Quaternary evolution of the Corinth Rift and its implications for the Late Cenozoic evolution of the Aegean. *Geophysical Journal International*, 126(1), pp.11-53.

Arnould, M., Coltice, N., Flament, N. & Mallard, C., 2020. Plate tectonics and mantle controls on plume dynamics. *Earth and Planetary Science Letters*, 547.

Artemieva, I.M., 2006. Global 1× 1 thermal model TC1 for the continental lithosphere: implications for lithosphere secular evolution. *Tectonophysics*, 416(1-4), pp.245-77.

Artemieva, I., 2010. Defining the LAB: semantics versus physics. *In Solid Earth-Basic Science for the Human Habitat-ILP's Second Potsdam Conference 2010.*.

Artyushkov, E.V., 1973. Stresses in the lithosphere caused by crustal thickness inhomogeneities. *Journal of Geophysical Research*, 78(32), pp.7675-708.

Audin, L., Avouac, J.P., Flouzat, M. & Plantet, J.L., 2002. Fluid‐driven seismicity in a stable tectonic context: The Remiremont fault zone, Vosges, France. *Geophysical Research Letters*, 29(6), pp.13-1.

Averbuch, O. & Piromallo, C., 2012. Is there a remnant Variscan subducted slab in the mantle beneath the Paris basin? Implications for the late Variscan lithospheric delamination process and the Paris basin formation. *Tectonophysics*, 558, pp.70-83.

Békési, E. et al., 2018. Subsurface temperature model of the Hungarian part of the Pannonian Basin. *Global and Planetary Change*, 171, pp.48-64.

Baklid, A., Korbol, R. & Owren, G., 1996. Sleipner Vest CO2 disposal, CO2 injection into a shallow underground aquifer. *In SPE Annual Technical Conference and Exhibition. OnePetro.*.

Balázs, A. et al., 2017. Tectonic and Climatic Controls on Asymmetric Half‐Graben Sedimentation: Inferences From 3‐D Numerical Modelling. *Tectonics*, 36(10), pp.2123-41.

Balázs, A. et al., 2021. Towards stratigraphic-thermo-mechanical numerical modelling: Integrated analysis of asymmetric extensional basins. *Global and Planetary Change*, 196, p.103386.

Balázs, A. et al., 2016. The link between tectonics and sedimentation in back-arc basins: New genetic constraints from the analysis of the Pannonian Basin. *Tectonics*, 35(6), pp.1526-59.

Ballato, P., Brune, S. & Strecker, M.R., 2019. Sedimentary loading–unloading cycles and faulting in intermontane basins: Insights from numerical modelling and field observations in the NW Argentine Andes. *Earth and Planetary Science Letters*, 506, pp.388-96.

Barnet, J.S. et al., 2019. A high-Fidelity benthic stable isotope record of late Cretaceous–early Eocene climate change and carbon-cycling. *Paleoceanography and Paleoclimatology*, 34(4), pp.672-91.

Barry, P.H. et al., 2022. The helium and carbon isotope characteristics of the Andean Convergent Margin. *Frontiers in Earth Science*, 10, p.897267.

Barry, P.H. et al., 2019. Forearc carbon sink reduces long-term volatile recycling into the mantle. *Nature*, 568(7753), pp.487-92.

Beaumont, C., Jamieson, R.A., Nguyen, M.H. & Lee, B., 2001. Himalayan tectonics explained by extrusion of a low-viscosity crustal channel coupled to focused surface denudation. *Nature*, 414(6865), pp.738-42.

Becker, T.W. et al., 2014. Static and dynamic support of western United States topography. *Earth and Planetary Science Letters*, 402, pp.234-46.

Becker, T.W. et al., 2015. Western US intermountain seismicity caused by changes in upper mantle flow. *Nature*, 524(7566), pp.458-61.

Beinlich, A. et al., 2012. Massive serpentinite carbonation at Linnajavri, N–Norway. *Terra Nova*, 24(6), pp.446-55.

Benito, G. et al., 2015. Recurring flood distribution patterns related to short-term Holocene climatic variability. *Scientific reports*, 5(1), pp.1-8.

Bercovici, D. & Ricard, Y., 2014. Plate tectonics, damage and inheritance. *Nature*, 508, pp.513–16.

Berkesi, M. et al., 2019. Pargasite in fluid inclusions of mantle xenoliths from northeast Australia (Mt. Quincan): evidence of interaction with asthenospheric fluid. *Chemical Geology*, 508, pp.182-96.

Bernard, T. et al., 2019. Lithological control on the post-orogenic topography and erosion history of the Pyrenees. *Earth and Planetary Science Letters*, 518, pp.53-66.

Berner, R.A., 2003. The long-term carbon cycle, fossil fuels and atmospheric composition. *Nature*, 426(6964), p.323.

Berner, R.A. & Lasaga, A.C., 1989. Modelling the geochemical carbon cycle. *Scientific American*, 260(3), pp.74-81.

Bianchi, I., Ruigrok, E., Obermann, A. & Kissling, E., 2021. Moho topography beneath the European Eastern Alps by global-phase seismic interferometry. *Solid Earth*, 12, pp.1185–96.

Bocin, A., Stephenson, R., Matenco, L. & Mocanu, V., 2013. Gravity and magnetic modelling in the Vrancea Zone, south-eastern Carpathians: Redefinition of the edge of the East European Craton beneath the south-eastern Carpathians. *Journal of Geodynamics*, 71, pp.52-64.

Bodine, J.H., Steckler, M.S. & Watts, A.B., 1981. Observations of flexure and the rheology of the oceanic lithosphere. *Journal of Geophysical Research: Solid Earth*, 86(B5), pp.3695-707.

Bodnar, R.J. et al., 2013. Bodnar, R.J., Azbej, T., Becker, S.P., Cannatelli, C., Fall, A. and Severs, M.J., 2013. Whole Earth geohydrologic cycle, from the clouds to the core. *The distribution of water in the dynamic Earth system*..

Boschi, C. et al., 2009. Enhanced CO2-mineral sequestration by cyclic hydraulic fracturing and Si-rich fluid infiltration into serpentinites at Malentrata (Tuscany, Italy). *Chemical Geology*, 265(1-2), pp.209-26.

Boschi, L., Faccenna, C. & Becker, T.W., 2010. Mantle structure and dynamic topography in the Mediterranean Basin. *Geophysical Research Letters*, p.37(20).

Botsyun, S. & Ehlers, T.A., 2021. How can climate models be used in paleoelevation reconstructions? *Frontiers in Earth Science*, 9, p.624542.

Botsyun, S. et al., 2022. Middle Miocene climate and stable oxygen isotopes in Europe based on numerical modelling. *Paleoceanography and Paleoclimatology*, p.p.e2022PA004442.

Botsyun, S. et al., 2019. Revised paleoaltimetry data show low Tibetan Plateau elevation during the Eocene. *Science*, 363(6430), p.eaaq1436.

Botsyun, S., Sepulchre, P., Risi, C. & Donnadieu, Y., 2016. Impacts of Tibetan Plateau uplift on atmospheric dynamics and associated precipitation δ 18 O. *Climate of the Past*, 12(6), pp.1401-20.

Bott, M.H., 1991. Sublithospheric loading and plate-boundary forces. *Phil. Trans. R. Soc. Lond.*, 337, pp.83–93.

Boucher, F.C. et al., 2021. Discovery of cryptic plant diversity on the rooftops of the Alps. *Scientific Reports*, 11(1), pp.1-10.

Boudoire, G. et al., 2018. Extensive CO2 degassing in the upper mantle beneath oceanic basaltic volcanoes: First insights from Piton de la Fournaise volcano (La Réunion Island). *Geochimica et Cosmochimica Acta*, 235, pp.376-401.

Bower, D.J., Gurnis, M. & Flament, N., 2015. Assimilating lithosphere and slab history in 4-D Earth models. *Physics of the Earth and Planetary Interiors*, 238, pp.8–22.

Brace, W.F. & Kohlstedt, D.L., 1980. Limits on lithospheric stress imposed by laboratory experiments. *Journal of Geophysical Research: Solid Earth*, 85(B11), pp.6248-52.

Braun, J., 2010. The many surface expressions of mantle dynamics. *Nature Geoscience*, 3, pp.825-33.

Braun, J. & Yamato, P., 2010. Structural evolution of a three-dimensional, finite-width crustal wedge. *Tectonophysics*, 484(1-4), pp.181-92.

Breede, K., Dzebisashvili, K., Liu, X. & Falcone, G., 2013. A systematic review of enhanced (or engineered) geothermal systems: past, present and future. *Geothermal Energy*, 1(1), pp.1-27.

Broecker, W., 2018. A Collision Changes Everything. *Geochemical Perspectives*, 7(2), pp.142-53.

Brunetti, M., Bertolini, A., Soldati, M. & Maugeri, M., 2019. High-resolution analysis of 1-day extreme precipitation in a wet area centered over eastern Liguria, Italy. *Theoretical and Applied Climatology*, 135(1), pp.341-53.

Buck, W.R., 2004. Consequences of Asthenospheric Variability in Continental Rifting. *in Rheology and Deformation of the Lithosphere at Continental Margins (eds Karner, G. D., Taylor, B., Driscoll, N. W. & Kohlstedt, D. L.) 1–30 (Columbia Univ. Press, New York)*..

Bufe, A. et al., 2021. Co-variation of silicate, carbonate and siulfide weathering drives CO2 release with erosion. *Nature Geoscience*, 14, pp.211-16.

Buiter, S.J., Pfiffner, O.A. & Beaumont, C., 2009. Inversion of extensional sedimentary basins: A numerical evaluation of the localisation of shortening. *Earth and Planetary Science Letters*, 288(3-4), pp.492-504.

Burchfiel, B.C. & Royden, L.H., 1985. North-south extension within the convergent Himalayan region. *Geology*, 13(10).

Burkhard, M. & Sommaruga, A., 1998. Evolution of the western Swiss Molasse basin: structural relations with the Alps and the Jura belt. *Geological Society, London, Special Publications*, 134(1), pp.279-98.

Burls, N.J. et al., 2021. Simulating Miocene warmth: insights from an opportunistic Multi-Model ensemble (MioMIP1). *Paleoceanography and Paleoclimatology*, 36(5), p.2020PA004054.

Burov, E., 2011. Rheology and strength of the lithosphere. *Mar. Petrol. Geol.*, 28, pp.1402–43.

Burov, E.B. & Cloetingh, S., 1997. Erosion and rift dynamics: new thermomechanical aspects of post-rift evolution of extensional basins . *Earth and Planetary Science Letters*, 150, pp.7-26.

Burov, E. & Diament, M., 1995. The effectiveelasticthickness(Te) of continentallithosphere: What doesit really mean? *Journal of Geophysical Research*, 100(B3), pp.3905-27.

Burov, E. & Poliakov, A., 2001. Erosion and rheology controls on synrift and postrift evolution: Verifying old and new ideas using a fully coupled numerical model. *Journal of Geophysical Research: Solid Earth*, 106(B8), pp.16461-81.

Burton, M.R., Sawyer, G.M. & Granieri, D., 2013. Deep Carbon Emissions from Volcanoes. *Reviews in Mineralogy & Geochemistry* , 75, pp.323-354.

Calais, E. et al., 2016. A new paradigm for large earthquakes in stable continental plate interiors. *Geophysical Research Letters*, 43(20), pp.10-621.

Calais, E., Freed, A.M., Van Arsdale, R. & Stein, S., 2010. Triggering of New Madrid seismicity by late-Pleistocene erosion. *Nature*, 466(7306), pp.608-11.

Caldeira, K. & Wickett, M.E., 2003. Anthropogenic carbon and ocean pH. *Nature*, 425(6956), pp.365-65.

Campani, M. et al., 2012. Miocene paleotopography of the Central Alps. *Earth and Planetary Science Letters*, 337, pp.174-85.

Campbell, D.L., 1978. Investigation of the stress-concentration mechanism for intraplate earthquakes. *Geophysical Research Letters*, 5(6), pp.477-79.

Cannat, M., Fontaine, F. & Escartin, J., 2010. Serpentinization and associated hydrogen and methane fluxes at slow spreading ridges. pp.241-64.

Caracausi, A., Paternoster, M. & Nuccio, P.M., 2015. Mantle CO2 degassing at Mt. Vulture volcano (Italy): Relationship between CO2 outgassing of volcanoes and the time of their last eruption. *Earth and Planetary Science Letters*, 411, pp.268-80.

Cassel, E.J. et al., 2014. Profile of a paleo-orogen: High topography across the present-day Basin and Range from 40 to 23 Ma. *Geology*, 42(11), pp.1007-10.

Castelltort, S. et al., 2012. River drainage patterns in the New Zealand Alps primarily controlled by plate tectonic strain. *Nature Geoscience*, 5(10), pp.744-48.

Catuneau, O. et al., 2009. Towards the standardization of sequence stratigraphy. *Earth-Science Reviews*, 92, pp.1-33.

Cederbom, C.E., Sinclair, H.D., Schlunegger, F. & Rahn, M.K., 2004. Climate-induced rebound and exhumation of the European Alps. *Geology*, 32(8), pp.709-12.

Chadwick, A. et al., 2010. Quantitative analysis of time-lapse seismic monitoring data at the Sleipner CO2 storage operation. *The Leading Edge*, 29(2), pp.170-77.

Chamberlain, C.P. et al., 2012. The Cenozoic climatic and topographic evolution of the western North American Cordillera. *American Journal of Science*, 312(2), pp.213-62.

Champagnac, J.D. et al., 2007. Quaternary erosion-induced isostatic rebound in the western Alps. *Geology*, 35, pp.195-98.

Champagnac, J.D., Molnar, P., Sue, C. & Herman, F., 2012. Tectonics, climate, and mountain topography. *Journal of Geophysical Research: Solid Earth*, 117(B2).

Champagnac, J.D. et al., 2009. Erosion-driven uplift of the modern Central Alps. *Tectonophysics*, 474(1-2), pp.236-49.

Champagnac, J.D., Valla, P.G. & Herman, F., 2014. Late-Cenozoic relief evolution under evolving climate: A review. *Tectonophysics*, 614, pp.44-65.

Chen, C. et al., 2018. Estimating regional flood discharge during Palaeocene-Eocene global warming. *Scientific reports*, 8(1), pp.1-8.

Chen, L., Zheng, T. & Xu, W., 2006. A thinned lithospheric image of the Tanlu Fault Zone, eastern China: Constructed from wave equation based receiver function migration. *Journal of Geophysical Research: Solid Earth*, p.111(B9).

Chu, X., Lee, C.T., Dasgupta, R. & Cao, W., 2019. The contribution to exogenic CO2 by contact metamorphism at continental arcs: A coupled model of fluid flux and metamorphic decarbonation. *American Journal of Science*, 319(8), pp.631-57.

Clark, M., 2007. The significance of paleotopography. *Reviews in mineralogy and geochemistry*, 66(1), pp.1-21.

Clark, D.E. et al., 2020. CarbFix2: CO2 and H2S mineralization during 3.5 years of continuous injection into basaltic rocks at more than 250° C. *Geochimica et Cosmochimica Acta*, 279, pp.45-66.

Clift, P.D. et al., 2010. Monsoon control over erosion patterns in the western Himalaya: possible feed-back into the tectonic evolution. *Geological Society, London, Special Publications*, 342(1), pp.185-218.

Cloetingh, S. & Burov, E.B., 1996. Thermomechanical stmcture of European lithosphere: constraints from rheological profiles and EET estimates. *Geophys. J. Int.*, 124, pp.695-723.

Cloetingh, S.A. et al., 2002. Lithospheric folding in Iberia. *Tectonics*, 21(5), pp.5-1.

Cloetingh, S. & Haq, B.U., 2015. Inherited landscapes and sea level change. *Science*, 347(6220), p.1258375.

Cloetingh, S. et al., 2021. Plume-Induced Sinking of Intracontinental Lithospheric Mantle: An Overlooked Mechanism of Subduction Initiation? *Geochemistry, Geophysics, Geosystems*, 22(2), p.2020GC009482.

Cloetingh, S. et al., 2022. Fingerprinting secondary mantle plumes. *Earth and Planetary Science Letters*, 597, p.117819.

Cloetingh, S.A. et al., 2010. Lithosphere tectonics and thermo-mechanical properties: an integrated modelling approach for Enhanced Geothermal Systems exploration in Europe. *Earth-Science Reviews*, 102(3-4), pp.159-206.

Cloetingh, S.A. et al., 2007. TOPO-EUROPE: The geoscience of coupled deep Earth-surface processes. *Global and Planetary Change*, 58(1-4), pp.1-118.

Cobbold, P. et al., 1993. Sedimentary basins and crustal thickening. *Sedimentary Geology*, 86(1-2), pp.77-89.

Connolly, J.A. & Podladchikov, Y.Y., 1998. Compaction-driven fluid flow in viscoelastic rock. *Geodinamica Acta*, 11, pp.55–84.

Conrad, C.P. & Gurnis, M., 2003. Seismic tomography, surface uplift, and the breakup of Gondwanaland: Integrating mantle convection backwards in time. *Geochemistry, Geophysics, Geosystems*, 4(3), pp.1031. https://doi.org/0.1029/2001GC000299.

Conrad, C.P. & Husson, L., 2009. Influence of dynamic topography on sea level and its rate of change. *Lithosphere*, 1(2), pp.110–120. https://doi.org/10.1130/L32.1.

Conrad, C.P. & Lithgow-Bertelloni, C., 2002. How mantle slabs drive plate tectonics. *Science*, 298(5591), pp.207-09.

Costantini, M. et al., 2022. EGMS: Europe-wide ground motion monitoring based on full resolution InSAR processing of all Sentinel-1 acquisitions. *In IGARSS 2022-2022 IEEE International Geoscience and Remote Sensing Symposium*, pp.5093-96.

Courtillot, V., Davaille, A., Besse, J. & Stock, J., 2003. Three distinct types of hotspots in the Earth's mantle. *Earth and Planetary Science Letters*, 205(3-4), pp.295-308.

Cowie, R.H. & Holland, B.S., 2006. Dispersal is fundamental to biogeography and the evolution of biodiversity on oceanic islands. *Journal of Biogeography*, 33(2), pp.193-98.

Craig, T.J., Jackson, J.A., Priestley, K. & McKenzie, D., 2011. Earthquake distribution patterns in Africa: their relationship to variations in lithospheric and geological structure, and their rheological implications. *Geophysical Journal International*, 185(1), pp.403-34.

Crameri, F. et al., 2012. A comparison of numerical surface topography calculations in geodynamic modelling: an evaluation of the 'sticky air'method. *Geophysical Journal International*, 189(1), pp.38-54.

Crowley, J.W. et al., 2015. Glacial cycles drive variations in the production of oceanic crust. *Science*, 347(6227), pp.1237-40.

Czarnota, K., Hoggard, M., White, N. & Winterbourne, J., 2013. Spatial and temporal patterns of cenozoic dynamic topography around Australia. *Geochemistry, Geophysics, Geosystems*, 14, pp.634–58.

Dalla Longa, F. et al., 2020. Scenarios for geothermal energy deployment in Europe. *Energy*, 206, p.118060.

Dannowski, A. et al., 2020. Seismic evidence for failed rifting in the Ligurian Basin, Western Alpine domain. *Solid Earth*, 11(3), pp.873-87.

Dasgupta, R., Hirschmann, M.M. & Smith, N.D., 2007. Water follows carbon: CO2 incites deep silicate melting and dehydration beneath mid-ocean ridges. *Geology*, 35(2), pp.135-38.

Dehant, V. et al., 2019. Geoscience for understanding habitability in the Solar System and beyond. *Space Sci. Rev.*, 215(42), pp.https://doi.org/10.1007/s11214-019-0608-8.

Deichmann, N. & Giardini, D., 2009. Earthquakes induced by the stimulation of an enhanced geothermal system below Basel (Switzerland). *Seismological Research Letters*, 80(5), pp.784-98.

Delunel, R. et al., 2020. Late-Pleistocene catchment-wide denudation patterns across the European Alps. *Earth-Science Reviews*, 211, p.103407.

DePaolo, D.J. et al., 2008. Origin and Evolution of Earth: Research Questions for a Changing Planet. *Committee on Grand Research Questions in the Solid-Earth Sciences, Board on Earth Sciences and Resources, Division on Earth and Life Studies, National Research Council of the National Academies, The National Academies Press, Washington*, p.137.

Descombes, P. et al., 2018. Spatial imprints of plate tectonics on extant richness of terrestrial vertebrates. *Journal of Biogeography*, 44(5), pp.1185-97.

D'Hondt, S., Inagaki, F., Orcutt, B.N. & Hinrichs, K.U., 2019. IODP advances in the understanding of subseafloor life. *Oceanography*, 32(1), pp.198-207.

Ding, L. et al., 2014. The andean-type gangdese mountains: paleoelevation record from the paleocene–eocene linzhou basin. *Earth and Planetary Science Letters*, 392, pp.250-64.

Donnadieu, Y., Goddéris, Y. & Bouttes, N., 2009. Exploring the climatic impact of the continental vegetation on the Mezosoic atmospheric CO 2 and climate history. *Climate of the Past*, 5(1), pp.85-96.

Donnadieu, Y., Pierrehumbert, R., Jacob, R. & Fluteau, F., 2006. Modelling the primary control of paleogeography onCretaceous climate. *Earth and Planetary Science Letters*, 248, pp.426–37.

Dopffel, N., Jansen, S. & Gerritse, J., 2021. Microbial side effects of underground hydrogen storage–Knowledge gaps, risks and opportunities for successful implementation. *International Journal of Hydrogen Energy*, 46(12), pp.8594-606.

Dussel, M. et al., 2016. Forecast for thermal water use from Upper Jurassic carbonates in the Munich region (South German Molasse Basin). *Geothermics*, 60, pp.13-30.

Eaton, D.W. et al., 2009. The elusive lithosphere–asthenosphere boundary (LAB) beneath cratons. *Lithos*, 109(1-2), pp.1-22.

Edmonds, M., Mather, T.A. & Liu, E.J., 2018. A distinct metal fingerprint in arc volcanic emissions. *Nature Geoscience*, 11(10), pp.790-94.

Ehlers, T.A. & Farley, K.A., 2003. Apatite (U–Th)/He thermochronometry: methods and applications to problems in tectonic and surface processes. *Earth and Planetary Science Letters*, 206(1-2), pp.1-14.

Ehlers, T.A. & Poulsen, C.J., 2009. Influence of Andean uplift on climate and paleoaltimetry estimates. *Earth and Planetary Science Letters*, 281(3-4), pp.238-48.

Eiken, O. et al., 2011. Lessons learned from 14 years of CCS operations: Sleipner, In Salah and Snøhvit. *Energy procedia*, 4, pp.5541-48.

Etiope, G. & Sherwood Lollar, B., 2013. Abiotic methane on Earth. *Reviews of Geophysics*, 51(2), pp.276-99.

Faccenna, C. & Becker, T.W., 2020. Topographic expressions of mantle dynamics in the Mediterranean. *Earth-Science Reviews*, 209, p.103327.

Faccenna, C. et al., 2014. Isostasy, dynamic topography, and the elevation of the Apennines of Italy. *Earth and Planetary Science Letters*, 407, pp.163-74.

Fauquette, S. et al., 2015. Quantifying the Eocene to Pleistocene topographic evolution of the southwestern Alps, France and Italy. *Earth and Planetary Science Letters*, 412, pp.220-34.

Favre, A. et al., 2015. Favre, A., Päckert, M., Pauls, S.U., Jähnig, S.C., Uhl, D., Michalak, I. and Muellner-Riehl, A.N., 2015. The role of the uplift of the Qinghai-Tibetan Plateau for the evolution of Tibetan biotas. *Biological Reviews*, 90(1), pp.236-53.

Fernández-Lozano, J. et al., 2012. Integrated gravity and topography analysis in analog models: Intraplate deformation in Iberia. *Tectonics*, 31(6).

Fischer, K.M., Ford, H.A., Abt, D.L. & Rychert, C.A., 2010. The lithosphere-asthenosphere boundary. *Annual Review of Earth and Planetary Sciences*, 38, pp.551-75.

Flament, N., Gurnis, M. & Müller, R.D., 2013. A review of observations and models of dynamic topography. *Lithosphere*, 5(2), pp.189–210. https://doi.org/10.1130/L245.1.

Flament, N. et al., 2015. Influence of subduction history on South American topography. *Earth and Planetary Science Letters*, 430, pp.9–18.

Forest, C.E., Wolfe, J.A., Molnar, P. & Emanuel, K.A., 1999. Paleoaltimetry incorporating atmospheric physics and botanical estimates of paleoclimate. *Geological Society of America Bulletin*, 111(4), pp.497-511.

Forsyth, D. & Uyeda, S., 1975. On the relative importance of the driving forces of plate motions. *Geophys. J. R. Astron. Soc.*, 43, pp.163–200.

Forte, A.M. & Mitrovica, J.X., 1996. New inferences of mantle viscosity from joint inversion of long-wavelength mantle convection and post-glacial rebound data. *Geophysical Research Letters*, 23(10), pp.1147-50.

Forte, A.M. et al., 2007. Descent of the ancient Farallon slab drives localized mantle flow below the New Madrid seismic zone. *Geophysical Research Letters*, 34(4).

Fox, M., Herman, F., Kissling, E. & Willett, S.D., 2015. Rapid exhumation in the Western Alps driven by slab detachment and glacial erosion. *Geology*, 43(5), pp.379-82.

Fox, M., Herman, F., Willett, S.D. & Schmid, S.M., 2016. The exhumation history of the European Alps inferred from linear inversion of thermochronometric data. *American Journal of Science*, 316(6), pp.505-41.

Fox, M.R. et al., 2013. Rock uplift and erosion rate history of the Bergell intrusion from the inversion of low temperature thermochronometric data. *Geochemistry, Geophysics, Geosystems*, 15(4), pp.1235-57.

Franke, D., 2013. Rifting, lithosphere breakup and volcanism: Comparison of magma-poor and volcanic rifted margins. *Marine and Petroleum Geology* , 43, pp.63-87.

French, S.W. & Romanowicz, B., 2015. Broad plumes rooted at the base of the Earth's mantle beneath major hotspots. *Nature*, 525(7567), pp.95-99.

Freymark, J. et al., 2017. Freymark, J., Sippel, J., Scheck-Wenderoth, M., Bär, K., Stiller, M., Fritsche, J.G. and Kracht, M., 2017. The deep thermal field of the Upper Rhine Graben. *Tectonophysics*, 694, pp.114-29.

Frezzotti, M.L. & Touret, J.L., 2014. CO2, carbonate-rich melts, and brines in the mantle. *Geoscience Frontiers*, 5(5), pp.697-710.

Fu, H.Y., Li, Z.H. & Chen, L., 2022. Continental mid-lithosphere discontinuity: A water collector during craton evolution. *Geophysical Research Letters*, p.p.e2022GL101569.

Fullerton, K.M. et al., 2021. Effect of tectonic processes on biosphere–geosphere feedbacks across a convergent margin. *Nature Geoscience*, 14(5), pp.301-06.

Gérard, A. et al., 2006. The deep EGS (enhanced geothermal system) project at Soultz-sous-Forêts (Alsace, France). *Geothermics*, 35(5-6).

Galy, V. et al., 2007. Efficient organic carbon burial in the Bengal fan sustained by the Himalayan erosional system. *Nature*, 450, pp.407–10.

Garate, J. et al., 2015. Topo-Iberia project: CGPS crustal velocity field in the Iberian Peninsula and Morocco. *GPS Solutions*, 19(2), pp.287-95.

Garcia-Castellanos, D., Vergés, J., Gaspar-Escribano, J. & Cloetingh, S., 2003. Interplay between tectonics, climate, and fluvial transport during the Cenozoic evolution of the Ebro Basin (NE Iberia). *Journal of Geophysical Research: Solid Earth*, 108(B7).

Garzione, C.N. et al., 2017. Tectonic evolution of the Central Andean plateau and implications for the growth of plateaus. *Annual Review of Earth and Planetary Sciences*, 45, pp.529-59.

Gerya, T.V., 2014. Precambrian geodynamics: Concepts and models. *Gondwana Research*, 25, pp.442–63.

Gerya, T.V., 2019. Geodynamics of the early Earth: Quest for the missing paradigm. *Geology*, DOI:10.1130/focus-Oct2019..

Gerya, T.V. et al., 2015. Plate tectonics on the Earth triggered by plume-induced subduction initiation. *Nature*, 527(7577), pp.221-25.

Gerya, T.V. & Yuen, D.A., 2003. Characteristics-based marker-in-cell method with conservative finite-differences schemes for modelling geological flows with strongly variable transport properties. *Physics of the Earth and Planetary Interiors*, 140(4), pp.293-318.

Gibson, G.M., Roure, F. & Manatschal, G., 2015. Sedimentary basins and continental margin processes–from modern hyper-extended margins to deformed ancient analogues: an introduction. *Geological Society, London, Special Publications,* 413(8), pp.1-8.

Gillespie, R.G. & Roderick, G.K., 2014. Geology and climate drive diversification. *Nature*, 509(7500), pp.297-98.

Giovannelli, D., 2022. Geosphere and Biosphere coevolution: the role of trace metals availability in the evolution of biogeochemistry. *EarthArxiv*.

Giovannelli, D. et al., 2022. Sampling across large-scale geological gradients to study geosphere-biosphere interactions. *Frontiers in Microbiology*, p.4212.

Giovannelli, D. et al., 2020. Microbial influences on subduction zone carbon cycling. *Eos*, 101.

Girard, J., Chen, J., Raterron, P. & Holyoke, C.W., 2013. Hydrolytic weakening of olivine at mantle pressure: Evidence of [1 0 0](0 1 0) slip system softening from single-crystal deformation experiments. *Physics of the Earth and Planetary Interiors*, 216, pp.12-20.

Gislason, S.R. et al., 2010. Mineral sequestration of carbon dioxide in basalt: A pre-injection overview of the CarbFix project. *International Journal of Greenhouse Gas Control*, 4(3), pp.537-45.

Goddéris, Y. et al., 2014. The role of palaeogeography in the Phanerozoic history of atmospheric CO2 and climate. *Earth-Science Reviews*, 128, pp.122-38.

Goetze, C. & Evans, B., 1979. Stress and temperature in the bending lithosphere as constrained by experimental rock mechanics. *Geophysical Journal International*, 59(3), pp.463-478. ISO 690.

Goren, L., Castelltort, S. & Klinger, Y., 2015. Modes and rates of horizontal deformation from rotated river basins: Application to the Dead Sea fault system in Lebanon. *Geology*, 43(9), pp.843-46.

Gotelli, N.J. et al., 2009. Patterns and causes of species richness: a general simulation model for macroecology. *Ecology letters*, 12(9), pp.873-86.

Greening, C. et al., 2016. Genomic and metagenomic surveys of hydrogenase distribution indicate H2 is a widely utilised energy source for microbial growth and survival. *The ISME journal*, 10(3), pp.761-77.

Grenerczy, G., Sella, G., Stein, S. & Kenyeres, A., 2005. Tectonic implications of the GPS velocity field in the northern Adriatic region. *Geophysical Research Letters*, 32(16).

Grollimund, B. & Zoback, M.D., 2001. Did deglaciation trigger intraplate seismicity in the New Madrid seismic zone? *Geology*, 29(2), pp.175-78.

Grujic, D. et al., 1996. Ductile extrusion of the Higher Himalayan Crystalline in Bhutan: evidence from quartz microfabrics. *Tectonophysics*, 260, pp.21-43.

Guerit, L., Dominguez, S., Malavieille, J. & Castelltort, S., 2016. Deformation of an experimental drainage network in oblique collision. *Tectonophysics*, 693, pp.210-22.

Guerit, L. et al., 2018. Landscape 'stress' and reorganization from χ-maps: Insights from experimental drainage networks in oblique collision setting. *Earth Surface Processes and Landforms*, 43(15), pp.3152-63.

Guillocheau, F. et al., 2012. Quantification and causes of the terrigeneous sediment budget at the scale of a continental margin: a new method applied to the Namibia–South Africa margin. *Basin Research*, 24(1), pp.3-30.

Gung, Y., Panning, M. & Romanowicz, B., 2003. Global anisotropy and the thickness of continents. *Nature*, 422(6933), pp.707-11.

Gurnis, M., 2002. African superplume. *McGraw-Hill Education*.

Guzmán, B. & Vargas, P., 2009. Long-distance colonization of the Western Mediterranean by Cistus ladanifer (Cistaceae) despite the absence of special dispersal mechanisms. *Journal of Biogeography*, 36(5), pp.954-68.

Haenel, R., Rybach, L. & Stegena, L., 1988. Fundamentals of geothermics, Handbook of terrestrial heat-flow density determination. *Springer*, pp.9-57.

Hagen, O. et al., 2021. gen3sis: A gen eral e ngine for e co-e volutionary si mulation s of the processes that shape Earth's biodiversity. *PLoS biology*, 19(7), p.3001340.

Hagen, O. et al., 2021. Earth history events shaped the evolution of uneven biodiversity across tropical moist forests. *Proceedings of the National Academy of Sciences*, 118(40), p.2026347118.

Hager, B.H. et al., 1985. Lower mantle heterogeneity, dynamic topography and the geoid. *Nature*, 313(6003), pp.541–45.

Hage, S. et al., 2022. High rates of organic carbon burial in submarine deltas maintained on geological timescales. *Nature Geoscience*, pp.1-6.

Hager, B. & Richards, M., 1989. Long-wavelength variations in Earth's geoid: Physical models and dynamical implications. *Philo- sophical Transactions of the Royal Society of London A: Mathematical, Physical and Engineering Sciences*, 328(1599), pp.309–327. https://doi.org/10.1098/rsta.1989.0038.

Haldar, C. et al., 2022. Lower crustal intraplate seismicity in Kachchh region (Gujarat, India) triggered by crustal magmatic infusion: Evidence from shear wave velocity contrast across the Moho. *Geosystems and Geoenvironment*, 1(3, p.100073.

Handy, M.R. et al., 2010. Reconciling plate-tectonic reconstructions of Alpine Tethys with the geological–geophysical record of spreading and subduction in the Alps. *Earth-Science Reviews*, 102(3-4), pp.121-58.

Haq, B., 2014. Cretaceous eustasy revisited. *Global and Planetary Change*, 113, pp.44-58.

Hardenbol, J.A. et al., 1998. Mesozoic and Cenozoic sequence chronostratigraphic framework of European basins.

Hartley, R.A., Roberts, G.G., White, N. & Richardson, C., 2011. Transient convective uplift of an ancient buried landscape. *Nature Geoscience*, 4(8), pp.562–565. https://doi.org/10.1038/NGEO1191.

Haszeldine, R.S., 2009. Carbon Capture and Storage: How Green Can Black Be? *Science*, 325, p.1647.

Hayes, J.M. & Waldbauer, J.R., 2006. The carbon cycle and associated redox processes through time. *Philosophical Transactions of the Royal Society B: Biological Sciences*, 361(1470), pp.931-50.

Heidbach, O., Rajabi, M., Reiter, K. & Ziegler, M., 2019. World stress map. *In Encyclopedia of petroleum geoscience. Springer.*, pp.1-8.

Heim, C., 2011. Microbial biomineralization. *An integrated approach to the study of biosignatures in mineralizing biofilms and microbial mats*, p.141.

Heimsath, A.M., DiBiase, R.A. & Whipple, K.X., 2012. Soil production limits and the transition to bedrock-dominated landscapes. *Nature Geoscience*, 5(3), pp.210-14.

Heinemann, N. et al., 2021. Enabling large-scale hydrogen storage in porous media–the scientific challenges. *Energy & Environmental Science*, 14(2), pp.853-64.

Helland-Hansen, W. et al., 2016. Deciphering Earth's natural hourglasses: perspectives on source-to-sink analysis. *Journal of Sedimentary Research*, 86(9), pp.1008-33.

Hendrix, C.S. & Salehyan, I., 2012. Climate change, rainfall, and social conflict in Africa. *Journal of peace research*, 49(1), pp.35-50.

Hergarten, S., Wagner, T. & Stüwe, K., 2010. Age and prematurity of the Alps derived from topography. *Earth and Planetary Science Letters*, 297(3-4), pp.453-60.

Herman , F. et al., 2013. Worldwide acceleration of mountain erosion under a cooling climate. *Nature*, 504.

Hochstein, M.P., 1990. Classification and assessment of geothermal resources. Small geothermal resources: A guide to development and utilization. *UNITAR, New York*, pp.31-57.

Hoggard, M., White, N. & Al-Attar, D., 2016. Global dynamic topography observations reveal limited influence of large-scale mantle flow. *Nature Geoscience*, 9, pp.456–463. https://doi.org/10.1038/NGEO2709.

Holm, N.G. & Charlou, J.L., 2001. Initial indications of abiotic formation of hydrocarbons in the Rainbow ultramafic hydrothermal system, Mid-Atlantic Ridge. *Earth and Planetary Science Letters*, 191(1-2), pp.1-8.

Hoorn, C., Mosbrugger, V., Mulch, A. & Antonelli, A., 2013. Biodiversity from mountain building. *Nature Geoscience*, 6(3), pp.154-54.

Hough, S.E., Armbruster, J.G., Seeber, L. & Hough, J.F., 2000. On the modified Mercalli intensities and magnitudes of the 1811–1812 New Madrid earthquakes. *Journal of Geophysical Research: Solid Earth*, 105(B10), pp.23839-64.

Hren, M.T., Pagani, M., Erwin, D.M. & Brandon, M., 2010. Biomarker reconstruction of the early Eocene paleotopography and paleoclimate of the northern Sierra Nevada. *Geology*, 38(1), pp.7-10.

Huttrer, G.W., 2020. Geothermal power generation in the world 2015-2020 update report. *In Proceedings world geothermal congress*, 1.

Huyghe, D., Mouthereau, F. & Emmanuel, L., 2012. Oxygen isotopes of marine mollusc shells record Eocene elevation change in the Pyrenees. *Earth and Planetary Science Letters*, 345, pp.131-41.

IEA, 2021. IEA. *Renewables*.

Ielpi, A., Lapôtre, M.G., Gibling, M.R. & Boyce, C.K., 2022. The impact of vegetation on meandering rivers. *Nature Reviews Earth & Environment*, 3(3), pp.165-78.

Isacks, B., Oliver, J. & Sykes, L.R., 1968. Seismology and the new global tectonics. *Journal of geophysical research*, 73(18), pp.5855-99.

Isson, T.T. & Planavsky, N.J., 2018. Reverse weathering as a long-term stabilizer of marine pH and planetary climate. *Nature*, 560(7719), pp.471-75.

Istanbulluoglu, E. & Bras, R.L., 2005. Vegetation-modulated landscape evolution: Effects of vegetation on landscape processes, drainage density, and topography. *Journal of Geophysical Research: Earth Surface*, 110(F2).

Janots, E. et al., 2009. Metamorphic rates in collisional orogeny from in situ allanite and monazite dating. *Geology*, 37(1), pp.11-14.

Jin, S. et al., 2022. Mercury isotope evidence for protracted North Atlantic magmatism during the Paleocene-Eocene Thermal Maximum. *Earth and Planetary Science Letters*, 602, p.117926.

Jolie, E. et al., 2021. Geological controls on geothermal resources for power generation. *Nature Reviews Earth & Environment*, 2(5), pp.324-39.

Jones, M.T. et al., 2019. Mercury anomalies across the Palaeocene–Eocene Thermal Maximum. *Climate of the Past*, 15, pp.217–36.

Jull, M. & McKenzie, D., 1996. The effect of deglaciation on mantle melting beneath Iceland. *Journal of Geophysical Research*, 101(B10), pp.21815-28.

Kallmeyer, J. et al., 2012. Global distribution of microbial abundance and biomass in subseafloor sediment. *Proceedings of the National Academy of Sciences*, 109(40), pp.16213-16.

Karousová, H., Plomerová, J. & Vecsey, L., 2012. Seismic tomography of the upper mantle beneath the north-eastern Bohemian Massif (central Europe). *Tectonophysics*, 564, pp.1-11.

Katz, R.F., 2008. Magma dynamics with the enthalpy method: benchmark solutions and magmatic focusing at mid-ocean ridges. *Journal of Petrology*, 49, pp.2099–121.

Kelemen, P.B. & Manning, C.E., 2015. Reevaluating carbon fluxes in subduction zones, what goes down, mostly comes up. *Proceedings of the National Academy of Sciences*, 112(30), pp.E3997-4006.

Kelemen, P.B. & Matter, J., 2008. In situ carbonation of peridotite for CO2 storage. *Proceedings of the National Academy of Sciences*, 105(45), pp.17295-300.

Kelley, D.S. et al., 2005. A serpentinite-hosted ecosystem: the Lost City hydrothermal field. *Science*, 307(5714), pp.1428-34.

Kendall, D.G., 1949. Stochastic processes and population growth. *Journal of the Royal Statistical Society*, Series B (Methodological), 11(2), pp.230-82.

Kendall, J.M. et al., 2005. Magma-assisted rifting in Ethiopia. *Nature*, 433, pp.146-48.

Kennedy, B.M. & Van Soest, M.C., 2007. Flow of mantle fluids through the ductile lower crust: helium isotope trends. *Science*, 318(5855), pp.1433-36.

Kenner, S.J. & Segall, A.P., 2000. A mechanical model for intraplate earthquakes: Application to the New Madrid seismic zone. *Science*, 289(5488), pp.2329-32.

Kästle, E.D. et al., 2020. Slab break-offs in the Alpine subduction zone. *International Journal of Earth Sciences*, 109(2), pp.587-603.

Knox, J.C., 1993. Large increases in flood magnitude in response to modest changes in climate. *Nature*, 361(6411), pp.430-32.

Kondrashov, D., Feliks, Y. & Ghil, M., 2005. Oscillatory modes of extended Nile River records (AD 622–1922). *Geophysical research letters*, 32(10).

Koptev, A., Cloetingh, S. & Ehlers, T.A., 2021. Longevity of small-scale ('baby') plumes and their role in lithospheric break-up. *Geophysical Journal International*, 227(1), pp.439-71.

Koptev, A.I. & Ershov, A.V., 2011. Thermal thickness of the Earth's lithosphere: a numerical model. *Moscow University Geology Bulletin*, 66(5), pp.323-30.

Koulakov, I. et al., 2015. Subduction or delamination beneath the Apennines? Evidence from regional tomography. *Solid Earth*, 6(2), pp.669-79.

Koulakov, I., Kaban, M.K., Tesauro, M. & Cloetingh, S.A., 2009. P-and S-velocity anomalies in the upper mantle beneath Europe from tomographic inversion of ISC data. *Geophysical Journal International*, 179(1), pp.345-66.

Kounoudis, R. et al., 2020. Seismic tomographic imaging of the Eastern Mediterranean mantle: implications for terminal‐stage subduction, the uplift of Anatolia, and the development of the North Anatolian Fault. *Geochemistry, Geophysics, Geosystems*, 21(7), p.p.e2020GC009009.

Kovács, I. et al., 2017. The role of pargasitic amphibole in the formation of major geophysical discontinuities in the shallow upper mantle. *Acta Geodaetica et Geophysica*, 52(2), pp.183-204.

Kovács, I. et al., 2021. The 'pargasosphere'hypothesis: Looking at global plate tectonics from a new perspective. *Global and Planetary Change*, 204, p.p.103547.

Kovacs, I. et al., 2020. The role of water and compression in the genesis of alkaline basalts: Inferences from the Carpathian-Pannonian region. *Lithos*, 354, p.p.105323.

Kreemer, C. & Blewitt, G., 2021. Robust estimation of spatially varying common-mode components in GPS time-series. *Journal of geodesy*, 95(1), pp.1-19.

Kreemer, C., Blewitt, G. & Davis, P.M., 2020. Geodetic evidence for a buoyant mantle plume beneath the Eifel volcanic area, NW Europe. *Geophysical Journal International*, 222(2), pp.1316-32.

Krsnik, E. et al., 2021. Miocene high elevation in the Central Alps. *Solid Earth*, 12(11), pp.2615-31.

Kuhlemann, J. et al., 2002. Post-collisional sediment budget history of the Alps: tectonic versus climatic control. *International Journal of Earth Science*, 91, pp.818-37.

Kuritani, T. et al., 2019. Buoyant hydrous mantle plume from the mantle transition zone. *Scientific reports*, 9(1), pp.1-7.

Kutterolf, S. et al., 2019. Milankovitch frequencies in tephra records at volcanic arcs: The relation of kyr-scale cyclic variations in volcanism to global climate changes. *Quaternary Science Reviews* , pp.1-16.

Langbein, W.B. & Schumm, S.A., 1958. Yield of sediment in relation to mean annual precipitation. *Eos, Transactions American Geophysical Union*, 39(6), pp.1076-84.

Large, R.R. et al., 2015. Cycles of nutrient trace elements in the Phanerozoic ocean. *Gondwana Researc*, 28, pp.1282–93.

Lavecchia, A., Beekman, F., Clark, S.R. & Cloetingh, S.A., 2016. Thermo-rheological aspects of crustal evolution during continental breakup and melt intrusion: The Main Ethiopian Rift, East Africa. *Tectonophysics*, 686, pp.pp.51-62.

Lavecchia, A. et al., 2022. Role of crustal fluids and thermo-mechanical structure for lower crustal seismicity: The Gargano Promontory (southern Italy). *Global and Planetary Change*, 217, p.103929.

Lebedev, S., Schaeffer, S., Fullea, J. & Pease, V., 2018. Seismic tomography of the Arctic region: inferences for the thermal structure and evolution of the lithosphere. , 460(1), pp. *Geological Society, London, Special Publications*, pp.419-40.

Lee, C.T. et al., 2018. Deep mantle roots and continental emergence: implications for whole-Earth elemental cycling, long-term climate, and the Cambrian explosion. *International Geology Review*, 60(4), pp.431-48.

Lee, C.T. & Lackey, J.S., 2015. Global continental arc flare-ups and their relation to long-term greenhouse conditions. *Elements*, 11(2), pp.125-30.

Legrain, N., Stüwe, K. & Wölfler, A., 2014. Incised relict landscapes in the eastern Alps. *Geomorphology*, 221, pp.124-38.

Lei, J. et al., 2009. New seismic constraints on the upper mantle structure of the Hainan plume. *Physics of the Earth and Planetary Interiors*, 173(1-2), pp.33-50.

Leprieur, F. et al., 2016. Plate tectonics drive tropical reef biodiversity dynamics. *Nature Communications*, 7.

Lian, B., Chen, Y., Zhu, L. & Yang, R., 2008. Effect of microbial weathering on carbonate rocks. *Earth Science Frontiers*, 15(6), pp.90-99.

Limberger, J. et al., 2018. Geothermal energy in deep aquifers: A global assessment of the resource base for direct heat utilization. *Renewable and Sustainable Energy Reviews*, 82, pp.961-75.

Limberger, J. et al., 2018. Refining the thermal structure of the European lithosphere by inversion of subsurface temperature data. *Global and Planetary Change*, 171, pp.18-47.

Link, F. & Rümpker, G., 2021. Resolving Seismic Anisotropy of the Lithosphere–Asthenosphere in the Central/Eastern Alps Beneath the SWATH-D Network. *Front. Earth Sci.*, 9, pp.679887. doi: 10.3389/feart.2021.679887.

Lippitsch, R., Kissling, E. & Ansorge, J., 2003. Upper mantle structure beneath the Alpine orogen from high-resolution teleseismic tomography. *J. Geophys. Res.*, 108, pp.108, http://dx.doi.org/10.1029/2002JB002016.

Liptai, N. et al., 2022. Seismic anisotropy in the mantle of a tectonically inverted extensional basin: A shear-wave splitting and mantle xenolith study on the western Carpathian-Pannonian region. *Tectonophysics*, p.229643.

Lithgow-Bertelloni, C. & Silver, P.G., 1998. Dynamic topography, plate driving forces and the African superswell. *Nature*, 395(6699), p.269.

Liu, H., Konhauser, K.O., Robbins, L.J. & Sun, W.D., 2021. Global continental volcanism controlled the evolution of the oceanic nickel reservoir. *Earth and Planetary Science Letters*, 572, p.117116.

Liu, L., Morgan, J.P., Xu, Y. & Menzies, M., 2018. Craton destruction 1: Cratonic keel delamination along a weak midlithospheric discontinuity layer. *Journal of Geophysical Research: Solid Earth*, 123(11), pp.10-040.

Liu, L., Spasojevic, S. & Gurnis, M., 2008. Reconstructing Farallon plate subduction beneath North America back to the Late Cretaceous. *Science*, 322(5903), pp.934–38.

Liu, L. & Zoback, M.D., 1997. Lithospheric strength and intraplate seismicity in the New Madrid seismic zone. *Tectonics*, 16(4), pp.585-95.

Lo Bue, R., Rappisi, F., Vanderbeek, B.P. & Faccenda, M., 2022. Tomographic Image Interpretation and Central-Western Mediterranean-Like Upper Mantle Dynamics From Coupled Seismological and Geodynamic Modelling Approach. *Frontiers in Earth Science*, 10, p.884100.

Lollar, B.S., Onstott, T.C., Lacrampe-Couloume, G. & Ballentine, C.J., 2014. Lollar, B.S., Onstott, T.C., Lacrampe-Couloume, G. and Ballentine, C.J., 2014. The contribution of the Precambrian continental lithosphere to global H2 production. *Nature*, 516(7531), pp.379-82.

Lu, S.M., 2018. A global review of enhanced geothermal system (EGS). *Renewable and Sustainable Energy Reviews*, 81, pp.2902-21.

Ludwig, K.A. et al., 2006. Formation and evolution of carbonate chimneys at the Lost City Hydrothermal Field. *Geochimica et cosmochimica acta*, 70(14), pp.3625-45.

Lund, J.W. & Toth, A.N., 2021. Direct utilization of geothermal energy 2020 worldwide review. *Geothermics*, 90, p.101915.

Lunt, D.J. et al., 2021. DeepMIP: Model intercomparison of early Eocene climatic optimum (EECO) large-scale climate features and comparison with proxy data. *Climate of the Past*, 17(1), pp.203-27.

Ménez, B. et al., 2018. Abiotic synthesis of amino acids in the recesses of the oceanic lithosphere. *Nature*, 564(7734), pp.59-63.

Métivier, F. & Barrier, L., 2012. Alluvial landscape evolution: What do we know about metamorphosis of gravel-bed meandering and braided streams? *Gravel-Bed Rivers: Processes, Tools, Environments*, pp.474-501.

Magnabosco, C. et al., 2018. The biomass and biodiversity of the continental subsurface. *Nature Geoscience*, 11(10), pp.707-17.

Malavieille, J. & Konstantinovskaya, E., 2010. Impact of surface processes on the growth of orogenic wedges: insights from analog models and case studies. *Geotectonics*, 44(6), pp.541-58.

Mangenot, X. et al., 2021. Geochemistry of clumped isotopologues of CH4 within fluid inclusions in Alpine tectonic quartz fissures. *Earth and Planetary Science Letters*, 561, p.116792.

Manzotti, P. et al., 2018. Exhumation rates in the Gran Paradiso Massif (Western Alps) constrained by in situ U–Th–Pb dating of accessory phases (monazite, allanite and xenotime). *Contributions to Mineralogy and Petrology*, 173(3), pp.1-28.

MARGINS Office, 2004. MARGINS Office, 2004. NSF MARGINS Program Science Plans 2004. LDEO, Columbia University.

Marshall, C.R., 2017. Five palaeobiological laws needed to understand the evolution of the living biota. *Nature Ecology & Evolution*, 1(6), pp.1-6.

Martin, W., Baross, J., Kelley, D. & Russell, M.J., 2008. Hydrothermal vents and the origin of life. *Nature Reviews Microbiology*, 6(11), pp.805-14.

Mason, E., Edmonds, M. & Turchyn, A.T., 2017. Remobilization of crustal carbon may dominate volcanic arc emissions. *Science*, 357, pp.290–94.

Mason, C.C. et al., 2022. Cycles of Andean mountain building archived in the Amazon Fan. *Nature Communications*, 13(1), pp.1-10.

Matenco, L. et al., 2022. Advances in the understanding of multi-scale and coupled evolution of orogens, sedimentary basins and the underlying lithosphere. *Global and Planetary Change*, 208, p.103689.

Matenco, L. & Haq, B., 2020. Multi-scale depositional successions in tectonic settings. *Earth-Science Reviews*, 200, p.102991.

Matenco, L. et al., 2010. Characteristics of collisional orogens with low topographic build-up: An example from the Carpathians. *Terra Nova*, 22(3), pp.155-65.

Matenco, L. et al., 2016. The interplay between tectonics, sediment dynamics and gateways evolution in the Danube system from the Pannonian Basin to the western Black Sea. *Science of the Total Environment*, 543, pp.807-27.

Mathey, M. et al., 2022. Spatial Heterogeneity of Uplift Pattern in the Western European Alps Revealed by InSAR Time-Series Analysis. *Geophysical Research Letters*, 49(1), p.e2021GL095744.

Matter, J.M. et al., 2009. Permanent carbon dioxide storage into basalt: the CarbFix pilot project, Iceland. *Energy Procedia*, 1(1), pp.3641-46.

Matter, J.M. & Kelemen, P.B., 2009. Permanent storage of carbon dioxide in geological reservoirs by mineral carbonation. *Nature Geoscience*, 2(12), pp.837-41.

Mazzotti, S. & Stein, S., 2007. Geodynamic models for earthquake studies in intraplate North America. *Special Papers-Geological Society of America*, 425, p.17.

McInerney, F.A. & Wing, S.L., 2011. McInerney, F.A. and Wing, S.L., 2011. The Paleocene-Eocene Thermal Maximum: A perturbation of carbon cycle, climate, and biosphere with implications for the future. *Annual Review of Earth and Planetary Sciences*, 39, pp.489–516.

McKenzie, D. & Bickle, M.J., 1988. The volume and composition of melt generated by extension of the lithosphere. *Journal of petrology*, 29(3), pp.625-79.

Meckler, A.N. et al., 2022. Cenozoic evolution of deep ocean temperature from clumped isotope thermometry. *Science*, 377(6601), pp.86-90.

Medved, I., Polat, G. & Koulakov, I., 2021. Crustal structure of the Eastern Anatolia Region (Turkey) based on seismic tomography. *Geosciences*, 11(2), p.91.

Meijers, M.J. et al., 2018. Rapid late Miocene surface uplift of the Central Anatolian Plateau margin. *Earth and Planetary Science Letters*, 497, pp.29-41.

Menzel, M.D. et al., 2018. Carbonation of mantle peridotite by CO2-rich fluids: the formation of listvenites in the Advocate ophiolite complex (Newfoundland, Canada). *Lithos*, 323, pp.238-61.

Methner, K. et al., 2016. Eocene-Oligocene proto-Cascades topography revealed by clumped (Δ47) and oxygen isotope (δ18O) geochemistry (Chumstick Basin, WA, USA). *Tectonics*, 35(3), pp.546-64.

Metz, B. et al., 2005. IPCC special report on carbon dioxide capture and storage. Cambridge. *Cambridge University Press*.

Middelburg, J.J., van der Weijden, C.H. & Woittiez, J.R., 1988. Chemical processes affecting the mobility of major, minor and trace elements during weathering of granitic rocks. *Chemical geology*, 68(3-4), pp.253-73.

Milia, A., Torrente, M.M. & Belucci, F., 2012. A possible link between faulting, crypto- domes and lateral collapses at Vesuvius volcano (Italy). *Global and Planetary Change*, 90–91, pp.121–34.

Mittag, R.J., 2003. Fractal analysis of earthquake swarms of Vogtland/NW-Bohemia intraplate seismicity. *Journal of Geodynamics*, 35(1-2), pp.173-89.

Moeck, I.S., 2014. Catalog of geothermal play types based on geologic controls. *Renewable and Sustainable Energy Reviews*, 37, pp.867-82.

Molnar, P., Boos, W.R. & Battisti, D.S., 2010. Orographic controls on climate and paleoclimate of Asia: thermal and mechanical roles for the Tibetan Plateau. *Annual Review of Earth and Planetary Sciences*, 38.

Molnar, P. & England, P., 1990. Late Cenozoic uplift of mountain ranges and global climate change: chicken or egg? *Nature*, 346(6279), pp.29-34.

Molnar, P., England, P.C. & Jones, C.H., 2015. Mantle dynamics, isostasy, and the support of high terrain. *Journal of Geophysical Research: Solid Earth*, 120(3), pp.1932-57.

Mologni, C. et al., 2020. Frequency of exceptional Nile flood events as an indicator of Holocene hydro-climatic changes in the Ethiopian Highlands. *Quaternary Science Reviews*, 247, p.106543.

Mooney, W.D., Ritsema, J. & Hwang, Y.K., 2012. Crustal seismicity and the earthquake catalog maximum moment magnitude (Mcmax) in stable continental regions (SCRs): Correlation with the seismic velocity of the lithosphere. *Earth and planetary science letters*, 357, pp.78-83.

Moretti, I. & Webber, M.E., 2021. Natural hydrogen: a geological curiosity or the primary energy source for a low-carbon future. *Renewable Matter, online article.*.

Morgan, W.J., 1971. Convection plumes in the lower mantle. *Nature*, 230(5288), pp.42-43.

Mottl, M.J., Komor, S.C., Fryer, P. & Moyer, C.L., 2003. Deep-slab fluids fuel extremophilic Archaea on a Mariana forearc serpentinite mud volcano: Ocean Drilling Program Leg 195. *Geochemistry, Geophysics, Geosystems*, 4(11).

Muffler, P. & Cataldi, R., 1978. Methods for regional assessment of geothermal resources. *Geothermics*, 7(2-4), pp.53-89.

Mulch, A. et al., 2010. Late Miocene climate variability and surface elevation in the central Andes. *Earth and Planetary Science Letters*, 290(1-2), pp.173-82.

Muller, V.A. et al., 2023. Climatic control on the location of continental volcanic arcs. *Scientific Reports*, Accepted.

Munteanu, I., Matenco, L., Dinu, C. & Cloetingh, S., 2012. Effects of large sea-level variations in connected basins: the Dacian–Black Sea system of the Eastern Paratethys. *Basin Research*, 24(5), pp.583-97.

Mutz, S.G. & Ehlers, T.A., 2019. Detection and explanation of spatiotemporal patterns in Late Cenozoic palaeoclimate change relevant to Earth surface processes. *Earth Surface Dynamics*, 7(3), pp.663-79.

Mutz, S.G. et al., 2018. Estimates of late Cenozoic climate change relevant to Earth surface processes in tectonically active orogens. *Earth Surface Dynamics*, 6(2), pp.271-301.

Nazaruddin, D.A. & Duerrast, H., 2021. Intraplate earthquake occurrence and distribution in Peninsular Malaysia over the past 100 years. *SN Applied Sciences*, 3(7), pp.1-20.

Nestola, F. & Smyth, J.R., 2016. Diamonds and water in the deep Earth: a new scenario. *International Geology Review*, 58(3), pp.263-76.

Nichols, G., 2011. Endorheic Basins. *In: C. Busby and A. Azor (Eds.), Tectonics of Sedimentary BasinsWiley Online Books*, pp.621-32.

Noda, A., 2016. Forearc basins: Types, geometries, and relationships to subduction zone dynamics. *Geological Society of America Bulletin*, 128, pp.879-95.

Nomikou, P. et al., 2012. Exploration of submarine cones in the Kolumbo Submarine Vol- canic Zone of the Hellenic Arc (Aegean Sea, Greece). *Global and Planetary Change*, 90–91, pp.135–51.

Norton, K. et al., 2011. Cosmogenic 10 Be-derived denudation rates of the Eastern and Southern European Alps. *International Journal of Earth Sciences*, 100(5), pp.1163-79.

Nuttli, O.W., 1973. Seismic wave attenuation and magnitude relations for eastern North America. *Journal of Geophysical Research*, 78(5), pp.876-85.

Oelkers, E.H., Gislason, S.R. & Matter, J., 2008. Mineral carbonation of CO2. *Elements*, 4(5), pp.333-37.

Ohara, Y. et al., 2012. A serpentinite-hosted ecosystem in the Southern Mariana Forearc. *Proceedings of the National Academy of Sciences*, 109(8), pp.2831-35.

Olasolo, P., Juárez, M.C., Morales, M.P. & Liarte, I.A., 2016. Enhanced geothermal systems (EGS): A review. *Renewable and Sustainable Energy Reviews*, 56, pp.133-44.

Orcutt, B.N., Daniel, I. & Dasgupta, R., 2019. Deep Carbon: Past to Present. *Cambridge University Press.*.

Ortiz, A. et al., 2022. Siliciclastic sediment volumes and rates of the North Pyrenean retro-foreland basin. *Basin Research.*.

Pèlachs, A. et al., 2011. Potential influence of Bond events on mid-Holocene climate and vegetation in southern Pyrenees as assessed from Burg lake LOI and pollen records. *The Holocene*, 21(1), pp.95-104.

Pacton, M. et al., 2014. Viruses as new agents of organomineralization in the geological record. *Nature communications*, 5(1), pp.1-9.

Page, M.T. & Hough, S.E., 2014. The New Madrid seismic zone: Not dead yet. *Science*, 343(6172), pp.762-64.

Pagli , C. & Sigmundsson , F., 2008. Will present day glacier retreat increase volcanic activity? Stress induced by recent glacier retreat and its effect on magmatism at the Vatnajo ̈kull ice cap, Iceland. *Geophysical Research Letters*, 35.

Pancost, R.D., 2017. Climate change narratives. *Nature Geoscience*, 10(7), pp.466-68.

Pan, B., Yin, X., Ju, Y. & Iglauer, S., 2021. Underground hydrogen storage: Influencing parameters and future outlook. *Advances in Colloid and Interface Science*, 294, p.102473.

Pearson, D.G. et al., 2014. Hydrous mantle transition zone indicated by ringwoodite included within diamond. *Nature*, 507(7491), pp.221-24.

Pekeris, C.L., 1935. Thermal convection in the interior of the Earth. *Geophysical Journal International*, 3, pp.343-67.

Pellissier, L., Heine, C., Rosauer, D.F. & Albouy, C., 2017. Are global hotspots of endemic richness shaped by plate tectonics? *Biological Journal of the Linnean Society*, 123(1), pp.247-61.

Petersen, K.D. et al., 2010. Small-scale mantle convection produces stratigraphic sequences in sedimentary basins. *Science*, 329(5993), pp.827–830. https://doi.org/10.1126/science.1190115.

Petit, C., Fournier, M. & Gunnell, Y., 2007. Tectonic and climatic controls on rift escarpments: Erosion and flexural rebound of the Dhofar passive margin (Gulf of Aden, Oman). *Journal of Geophysical Research: Solid Earth*, 112(B3), p.ISO 690.

Piña-Valdés, J. et al., 2022. 3D GNSS velocity field sheds light on the deformation mechanisms in Europe: effects of the vertical crustal motion on the distribution of seismicity. *Journal of Geophysical Research: Solid Earth*, 127(6), p.e2021JB023451.

Pintori, F., Serpelloni, E. & Gualandi, A., 2022. Common-mode signals and vertical velocities in the greater Alpine area from GNSS data. *Solid Earth*, 13(10), pp.1541-67.

Pithan, F. & Mauritsen, T., 2014. Arctic amplification dominated by temperature feedbacks in contemporary climate models. *Nature geoscience*, 7(3), pp.181-84.

Plümper, O. et al., 2017. Subduction zone forearc serpentinites as incubators for deep microbial life. *Proceedings of the National Academy of Sciences*, 114(17), pp.4324-29.

Plank, T. & Manning, C.E., 2019. Subducting carbon. *Nature*, 574, pp.343–52.

Plomerová, J. et al., 2016. Cenozoic volcanism in the Bohemian Massif in the context of P-and S-velocity high-resolution teleseismic tomography of the upper mantle. *Geochemistry, Geophysics, Geosystems*, pp.3326-49.

Poulsen, C.J., Ehlers, T.A. & Insel, N., 2010. Onset of convective rainfall during gradual late Miocene rise of the central Andes. *Science*, 328(5977), pp.490-93.

Prinzhofer, A., Cissé, C.S. & Diallo, A.B., 2018. Discovery of a large accumulation of natural hydrogen in Bourakebougou (Mali). *International Journal of Hydrogen Energy*, 43(42), pp.19315-26.

Pritchard, D., Roberts, G., White, N. & Richardson, C., 2009. Uplift histories from river profiles. *Geophysical Research Letters*, 36, pp.L24301. https://doi.org/10.1029/2009GL040928.

Rae, J.W. et al., 2021. Atmospheric CO2 over the Past 66 Million Years from Marine Archives. *Annu. Rev. Earth Planet. Sci.*, 49(https://doi.org/10.1146/annurev-earth-082420-063026).

Ranalli, G., 1995. *Rheology of the Earth, Deformation and Flow Processes in Geophysics and Geodynamics*. Chapman & Hall..

Rappisi, F. et al., 2022. Slab Geometry and Upper Mantle Flow Patterns in the Central Mediterranean From 3D Anisotropic P-Wave Tomography. *Journal of Geophysical Research: Solid Earth*, 127(5), p.p.e2021JB023488.

Raymo, M.E. & Ruddiman, W.F., 1992. Tectonic forcing of late Cenozoic climate. *Nature*, 359(6391), pp.117-22.

Raymo, M.E., Ruddiman, W.F. & Froelich, P.N., 1988. Influence of late Cenozoic mountain building on ocean geochemical cycles. *Geology*, 16, pp.649-53.

Reilinger, R. et al., 2010. Geodetic constraints on the tectonic evolution of the Aegean region and strain accumulation along the Hellenic subduction zone. *Tectonophysics*, 488(1-4), pp.22-30.

Reitano, R. et al., 2022. Sediment recycling and the evolution of analogue orogenic wedges. *Tectonics*, e2021TC006951.

Richard, G.C. & Bercovici, D., 2009. Water-induced convection in the Earth's mantle transition zone. *Journal of Geophysical Research: Solid Earth*, 114(B1).

Rickers, F., Fichtner, A. & Trampert, J., 2013. The Iceland–Jan Mayen plume system and its impact on mantle dynamics in the North Atlantic region: evidence from full-waveform inversion. *Earth and Planetary Science Letters*, 367, pp.39-51.

Riker, J. et al., 2018. First measurements of OH-C exchange and temperature-dependent partitioning of OH and halogens in the system apatite–silicate melt. *American Mineralogist: Journal of Earth and Planetary Materials*, 103(2), pp.260-70.

Ringrose, P., 2020. How to store CO2 underground: Insights from early-mover CCS Projects. *Cham, Switz: Springer*, 129.

Ritsema, J., Heijst, H.V. & Woodhouse, J.H., 1999. Complex shear wave velocity structure imaged beneath Africa and Iceland. *Science*, 286(5446), pp.1925-28.

Ritter, J.R., Jordan, M., Christensen, U.R. & Achauer, U., 2001. A mantle plume below the Eifel volcanic fields, Germany. *Earth and Planetary Science Letters*, 186(1), pp.7-14.

Rivera, A., Bown, F., Carrión, D. & Zenteno, P., 2012. Glacier responses to recent volcanic activity in Southern Chile. *Environmental Research Letters*, 7(1), p.014036.

Robbins, L.J. et al., 2016. Trace elements at the intersection of marine biological and geochemical evolution. *Earth-Science Reviews*, 163, pp.323-48.

Roberts, G.G., Paul, J.D., White, N. & Winterbourne, J., 2012. Temporal and spatial evolution of dynamic support from river profiles: A framework for Madagascar. *Geochemistry, Geophysics, Geosystems*, 13, pp.Q04004. https://doi.org/10.1029/2012GC004040.

Robinson, M.M., Dowsett, H.J. & Chandler, M.A., 2008. Pliocene role in assessing future climate impacts. *Eos, Transactions American Geophysical Union*, 89(49), pp.501-02.

Rocha, M.P. et al., 2016. Causes of intraplate seismicity in central Brazil from travel time seismic tomography. *Tectonophysics*, 680, pp.1-7.

Romans, B.W. et al., 2015. Environmental signal propagation in sedimentary systems across timescales. *Earth-Science Reviews*.

Rosenbaum, G. & Lister, G.S., 2005. Rosenbaum, G. and Lister, G.S., 2005. The Western Alps from the Jurassic to Oligocene: spatio-temporal constraints and evolutionary reconstructions. *Earth-Science Reviews*, 69(3-4), pp.281-306.

Roure, F., 2008. Foreland and hinterland basins: what controls their evolution? *Swiss Journal of Geosciences*, 101(1), pp.5-29.

Roure, F. et al., 2010. The use of palaeo-thermo-barometers and coupled thermal, fluid flow and pore-fluid pressure modelling for hydrocarbon and reservoir prediction in fold and thrust belts. *Geological Society, London, Special Publications*, 348(1), pp.87-114.

Roure, F. & Howell, D., 2022. Roure, F. and Howell, D., 2022. Underlying Châteauneuf-du-Pape is a salt diapir and the still active Nîmes Fault of southeastern France. *Mediterranean Geoscience Reviews*, pp.1-28.

Rowley, D.B. & Currie, B.S., 2006. Palaeo-altimetry of the late Eocene to Miocene Lunpola basin, central Tibet. *Nature*, 439(7077), pp.677-81.

Royden, L.H., 1996. Coupling and decoupling of crust and mantle in convergent orogens: implications for strain partitioning in the crust. *J. Geophys. Res.*, 101, pp.17679-705.

Rugenstein, J.K., Ibarra, D.E. & von Blanckenburg, F., 2019. Neogene cooling driven by land surface reactivity rather than increased weathering fluxes. *Nature*, 571(7763), pp.99-102.

Rush, W.D., Kiehl, J.T., Shields, C.A. & Zachos, J.C., 2021. Increased frequency of extreme precipitation events in the North Atlantic during the PETM: Observations and theory. *Palaeogeography, Palaeoclimatology, Palaeoecology*, 568, p.110289.

Rychert, C.A., Fischer, K.M. & Rondenay, S., 2005. A sharp lithosphere–asthenosphere boundary imaged beneath eastern North America. *Nature*, 436(7050), pp.542-45.

Rychert, C.A., Harmon, N., Constable, S. & Wang, S., 2020. The nature of the lithosphere-asthenosphere boundary. *Journal of Geophysical Research: Solid Earth*, 125(10), p.2018JB016463.

Sadeghi-Bagherabadi, A. et al., 2021. High-Resolution Crustal S-wave Velocity Model and Moho Geometry Beneath the Southeastern Alps: New Insights From the SWATH-D Experiment. *Frontiers in Earth Sciences*, 9, pp.641113. doi: 10.3389/feart.2021.641113.

Samuels, T. et al., 2020. Microbial weathering of minerals and rocks in natural environments. *Biogeochemical cycles: Ecological drivers and environmental impact*, pp.59-79.

Sarr, A.C. et al., 2022. Neogene South Asian monsoon rainfall and wind histories diverged due to topographic effects. *Nature Geoscience*, 15(4), pp.314-19.

Sato, H., Ishiyama, T., Matenco, L. & Nader, F.H., 2017. Evolution of fore-arc and back-arc sedimentary basins with focus on the Japan subduction system and its analogues. *Tectonophysics*, 710, pp.1-5.

Satow, C. et al., 2021. Eruptive activity of the Santorini Volcano controlled by sea-level rise and fall. *Nature Geoscience*, 14(8), pp.586-92.

Sautter, B. et al., 2019. Exhumation of west Sundaland: A record of the path of India? *Earth-Science Reviews*, 198, p.102933.

Sbar, M.L. & Sykes, L.R., 1973. Contemporary compressive stress and seismicity in eastern North America: An example of intra-plate tectonics. *Geological Society of America Bulletin*, 84(6), pp.1861-82.

Scarponi, M.G. et al., 2020. New gravity data and 3-D density model constraints on the Ivrea Geophysical Body (Western Alps). *Geophysical Journal International*, 222(3), pp.1977–1991, https://doi.org/10.1093/gji/ggaa263.

Schaller, M. et al., 2016. Timing of European fluvial terrace formation and incision rates constrained by cosmogenic nuclide dating. *Earth and Planetary Science Letters*, 451, pp.221-31.

Schindlbeck , J.C. et al., 2018. 100- kyr cyclicity in volcanic ash emplacement: evidence from a 1.1 Myr tephra record from the NW Pacific. *Sci. Rep.*, pp.https://doi.org/10.1038/s41598-018-22595-0.

Schmid, M. et al., 2018. Effect of changing vegetation and precipitation on denudation–Part 2: predicted landscape response to transient climate and vegetation cover over millennial to million-year timescales. *Earth Surface Dynamics*, 6(4), pp.859-81.

Schmid, S.M. et al., 1996. Geophysical-geological transect and tectonic evolution of the Swiss-Italian Alps. *Tectonics*, 15(5), pp.1036-64.

Schulte, S.M. & Mooney, W.D., 2005. An updated global earthquake catalogue for stable continental regions: reassessing the correlation with ancient rifts. *Geophysical Journal International*, 161(3), pp.707-21.

Seifan, M. & Berenjian, A., 2019. Microbially induced calcium carbonate precipitation: a widespread phenomenon in the biological world. *Appl Microbiol Biotechnol*, 103, pp.4693–4708. doi: 10.1007/s00253-019-09861-5.

Sembroni, A. et al., 2016. Evolution of continental-scale drainage in response to mantle dynamics and surface processes: An example from the Ethiopian Highlands. *Geomorphology*, 261, pp.12-29.

Seranne, M., Lamarche, J. & Agosta, F., 2015. An introduction to Lithosphere dynamics of sedimentary basins–The Circum-Mediterranean basins and analogues. *Bulletin de la Société Géologique de France*, 186(4-5), pp.207-08.

Serpelloni, E. et al., 2022. Surface velocities and strain-rates in the Euro-Mediterranean region from massive GPS data processing. *Frontiers in Earth Science*.

Serpelloni, E. et al., 2013. Vertical GPS ground motion rates in the Euro-Mediterranean region: New evidence of velocity gradients at different spatial scales along the Nubia-Eurasia plate boundary. *J. Geophys. Res.*, 118, pp.6003-24.

Shields, C.A. et al., 2021. Atmospheric rivers in high-resolution simulations of the Paleocene Eocene Thermal Maximum (PETM). *Palaeogeography, Palaeoclimatology, Palaeoecology*, 567, p.110293.

Sigmundsson, F. & Einarsson, P., 1992. Glacio-isostatic crustal movements caused by historical volume change of the Vatnajökull ice cap, Iceland. *Geophysical Research Letters*, 19(21), pp.2123-26.

Singer, B.S. et al., 1997. Volcanism and erosion during the past 930 k.y. at the Tatara–San Pedro complex, Chilean Andes. *GSA Bullettin*, 109(2), pp.127-42.

Sloan, R.A., Jackson, J.A., McKenzie, D. & Priestley, K., 2011. Earthquake depth distributions in central Asia, and their relations with lithosphere thickness, shortening and extension. *Geophysical Journal International*, 185(1), pp.1-29.

Smith, N.J., Shepherd, T.J., Styles, M.T. & Williams, G.M., 2005. Hydrogen exploration: a review of global hydrogen accumulations and implications for prospective areas in NW Europe. *In Geological Society, London, Petroleum Geology Conference series. Geological Society of London.*, 6(1), pp.349-58.

Smith, E.M. et al., 2016. Large gem diamonds from metallic liquid in Earth's deep mantle. *Science*, 354(6318), pp.1403-05.

Snæbjörnsdóttir, S.O. et al., 2020. Carbon dioxide storage through mineral carbonation. *Nature Reviews Earth & Environment*, 1(2), pp.90-102.

Sobolev, S.V. & Brown, M., 2019. Surface erosion events controlled the evolution of plate tectonics on Earth. *Nature*, 570, pp.52–57.

Sobolev, S.V. et al., 2011. Linking mantle plumes, large igneous provinces and environmental catastrophes. *Nature*, 477, pp.312–16.

So, B.D. & Capitanio, F.A., 2017. The effect of plate-scale rheology and plate interactions on intraplate seismicity. *Earth and Planetary Science Letters*, 478, pp.121-131.

Sohal, M.A. et al., 2021. Effect of geological heterogeneities on reservoir storage capacity and migration of CO2 plume in a deep saline fractured carbonate aquifer. *International Journal of Greenhouse Gas Control*, 108, p.103306.

Spencer, C.J. et al., 2022. Composition of continental crust altered by the emergence of land plants. *Nature Geoscience*, 15(9), pp.735-40.

Spence, D.A., Sharp, P.W. & Turcotte, D.L., 1987. Buoyancy-driven crack propagation: a mechanism for magma migration. *Journal of Fluid Mechanics*, 174, pp.135-53.

Starke, J., Ehlers, T.A. & Schaller, M., 2017. Tectonic and climatic controls on the spatial distribution of denudation rates in Northern Chile (18 S to 23 S) determined from cosmogenic nuclides. *Journal of Geophysical Research: Earth Surface*, 122(10), pp.1949-71.

Starke, J., Ehlers, T.A. & Schaller, M., 2020. Latitudinal effect of vegetation on erosion rates identified along western South America. *Science*, 367(6484), pp.1358-61.

Steinberger, B., 2007. Effects of latent heat release at phase boundaries on flow in the Earth's mantle, phase boundary topography and dynamic topography at the Earth's surface. *Physics of the Earth and Planetary Interiors*, 164(1), pp.2–20. https://doi.org/10.1016/j.pepi.2007.04.021.

Steinberger, B., Bredow, E., Lebedev, S. & Schaeffer, A., 2019. Widespread volcanism in the Greenland–North Atlantic region explained by the Iceland plume. *Nature Geoscience*, 12(1), pp.61-68.

Steinberger, B., Conrad, C.P., Tutu, A.O. & Hoggard, M., 2017. On the amplitude of dynamic topography at spherical harmonic degree two. *Tectonophysics*, pp.https://doi.org/10.1016/j.tecto.2017.11.032.

Steinthorsdottir, M. et al., 2021. The Miocene: the future of the past. *Paleoceanography and Paleoclimatology*, 36(4), p.2020PA004037.

Stern, R., 2016. Is plate tectonics needed to evolve technological species on exoplanets? *Geoscience Frontiers*, 7, pp.573-80.

Sternai, P., 2020. Surface processes forcing on extensional rock melting. *Scientific Reports*, doi.org/10.1038/s41598-020-63920-w.

Sternai, P., 2023. *Feedbacks between internal and external dynamics*. In Dynamics of plate tectonics and mantle convection, Editor Joao Duarte, Elsevier.

Sternai, P., Caricchi, L., Castelltort, S. & Champagnac, J.-D., 2016a. Deglaciation and glacial erosion: a joint control on magma productivity by continental unloading. *Geophysical Research Letters*.

Sternai, P. et al., 2017. Magmatic pulse driven by sea-level changes associated with the Messinian salinity crisis. *Nature Geoscience*, DOI: 10.1038/NGEO3032.

Sternai, P. et al., 2020. Magmatic Forcing of Cenozoic Climate? *Journal of Geophysical Research - Solid Earth*, 125, pp.https://doi.org/ 10.1029/2018JB016460.

Sternai, P. et al., 2012. Pre-glacial topography of the European Alps. *Geology*, 40(12), pp.1067-70.

Sternai, P., Jolivet, L., Menant, A. & Gerya, T., 2014. Driving the upper plate surface deformation by slab rollback and mantle flow. *Earth and Planet. Sci. Lett.*, 405, pp.110-18.

Sternai, P. et al., 2021. Effects of asthenospheric flow and orographic precipitation on continental rifting. *Tectonophysics*, 820(229120).

Sternai, P. et al., 2019. Present-day uplift of the European Alps: Evaluating mechanisms and models of their relative contributions. *Earth-Science Reviews*, 190, pp.589-604.

Stocks-Fischer, S., Galinat, J.K. & Bang, S.S., 1999. Microbiological precipitation of CaCO3. *Soil Biology and Biochemistry*, 31(11), pp.1563-71.

Stone, H.B., Veldhuis, I. & Richardson, R.N., 2009. Underground hydrogen storage in the UK. *Geological Society, London, Special Publications*, 313(1), pp.217-26.

Strobel, G., Hagemann, B., Huppertz, T.M. & Ganzer, L., 2020. Underground bio-methanation: Concept and potential. *Renewable and Sustainable Energy Reviews*, 123, p.109747.

Stuewe, K. et al., 2022. A feedback cycle between sea-floor spreading, trade wind and precipitation: the case for the Southern Red Sea. *Nature Communications*, 13(1), pp.1-8.

Suades Sala, E., 2016. Intergrated onshore-offshore study in the northwestern margin of the Alboran Basin, between meridians 5, 30ºW y 3, 30ºW.

Svensen, H. et al., 2004. Release of methane from a volcanic basin as a mechanism for initial Eocene global warming. *Nature*, 429, pp.542–45.

Swindles, G.T. et al., 2018. Climatic control on Icelandic volcanic activity during the mid-Holocene. *Geology*, 46(1), pp.47-50.

Szakács, A., 2011. Earthquake prediction using extinct monogenetic volcanoes: A possible new research strategy. *Journal of volcanology and geothermal research*, 201(1-4), pp.404-11.

Takai, K. et al., 2008. Cell proliferation at 122 C and isotopically heavy CH4 production by a hyperthermophilic methanogen under high-pressure cultivation. *Proceedings of the National Academy of Sciences*, 105(31), pp.10949-54.

Talwani, P., 1988. Talwani, P., 1988. The intersection model for intraplate earthquakes. *Seismological Research Letters*, 59(4), pp.305-10.

Tartaglia, G. et al., 2020. "brittle structural facies" analysis: A diagnostic method to unravel and date multiple slip events of long-lived faults. *Earth and Planetary Science Letters*, 545, p.116420.

Tary, J.B. et al., 2021. Local rift and intraplate seismicity reveal shallow crustal fluid-related activity and sub-crustal faulting. *Earth and Planetary Science Letters*, 562, p.116857.

Tengborg, P., Johansson, J. & Durup, J.G., 2014. Storage of highly compressed gases in underground Lined Rock Caverns–More than 10 years of experience. *In Proceedings of the world tunnel congress.*.

Tesauro, M., Kaban, M.K. & Cloetingh, S.A., 2008. EuCRUST-07: A new reference model for the European crust. *Geophysical Research Letters*, 35(L05313).

Tesauro, M., Kaban, M.K. & Cloetingh, S.A., 2009a. A new thermal and rheological model of the European lithosphere. *Tectonophysics*, 476(3-4), pp.478-95.

Tesauro, M., Kaban, M.K. & Cloetingh, S.A., 2009. How rigid is Europe's lithosphere? *Geophysical Research Letters*, 36(16).

Tesauro, M., Kaban, M.K. & Cloetingh, S.A., 2013. Global model for the lithospheric strength and effective elastic thickness. *Tectonophysics*, 602, pp.78–86.

Tesauro, M., Kaban, M.K. & Mooney, W.D., 2015. Variations of the lithospheric strength and elastic thickness in N orth A merica. *Geochemistry, Geophysics, Geosystems*, 16(7), pp.2197-220.

Tesauro, M., Kaban, M.K., Mooney, W.D. & Cloetingh, S., 2014. NACr14: A 3D model for the crustal structure of the North American Continent. *Tectonophysics*, 631, pp.65-86.

Tesauro, M., Kaban, M.K., Petrunin, A. & Aitken, A.R., 2020. Tesauro, M., Kaban, M.K., Petrunin, A.G. and Aitken, A.R., 2020. Strength variations of the Australian continent: Effects of temperature, strain rate, and rheological changes. *Global and Planetary Change*, 195, p.103322.

Thiede, R. & Ehlers, T.A., 2013. Large spatial and temporal variations in Himalayan denudation. *Earth and Planetary Science Letters*, 371, pp.278-93.

Thieulot, C., Steer, P. & Huismans, R.S., 2014. Three-dimensional numerical simulations of crustal systems undergoing orogeny and subjected to surface processes. *Geochemistry, Geophysics, Geosystems*, 15(12), pp.4936-57.

Thybo, H. & Perchuć, E., 1997. The seismic 8 discontinuity and partial melting in continental mantle. *Science*, 275(5306), pp.1626-29.

Tian, Y. et al., 2022. Introduction to the special issue "Tibetan tectonics and its effect on the long-term evolution of climate, vegetation and environment". *Terra Nova*.

Tibaldi, A. et al., 2008. Influence of substrate tectonic heritage on the evolution of composite volcanoes: predicting sites of flank eruption, lateral col- lapse, and erosion. *Global and Planetary Change*, 61, pp.151–74.

Tibaldi, A., Rust, D., Corazzato, C. & Merri, A., 2010. Setting the scene for self-destruction: from sheet intrusions to the structural evolution of rifted stratovolcanoes. *Geosphere*, 6, pp.1–22.

Tielke, J.A., Zimmerman, M.E. & Kohlstedt, D.L., 2017. Hydrolytic weakening in olivine single crystals. *Journal of Geophysical Research: Solid Earth*, 122(5), pp.3465-79.

Tipper, E.T. et al., 2020. Global silicate weathering flux overestimated because of sediment–water cation exchange. *PNAS*, 118(1), pp.https://doi.org/10.1073/pnas.2016430118.

Torp, T.A. & Gale, J., 2004. Demonstrating storage of CO2 in geological reservoirs: The Sleipner and SACS projects. *Energy*, 29(9-10), pp.1361-69.

Tremblin, M. et al., 2022. Mercury enrichments of the Pyrenean foreland basins sediments support enhanced volcanism during the Paleocene-Eocene thermal maximum (PETM). *Global and Planetary Change*, 212, p.103794.

Truche, L. & Bazarkina, E.F., 2019. Natural hydrogen the fuel of the 21st century. *In E3S Web of Conferences. EDP Sciences.*, 98, p.03006.

Tucker, G.E. & Slingerland, R., 1997. Drainage basin responses to climate change. *Water Resources Research*, 33(8), pp.2031-47.

Turcotte, D.L., 1982. Magma migration. *Annual Review of Earth and Planetary Sciences*, 10(1), pp.397-408.

Turcotte, D.L. & Schubert, G., 2002. *Geodynamics*. Cambridge: Cambridge University Press.

Turrini, C., Lacombe, O. & Roure, F., 2014. Present-day 3D structural model of the Po Valley basin, Northern Italy. *Marine and Petroleum Geology*, 56, pp.266-89.

Tyne, R.L. et al., 2021. Rapid microbial methanogenesis during CO2 storage in hydrocarbon reservoirs. *Nature*, 600(7890), pp.670-74.

Ueda, K., Willett, S.D., Gerya, T. & Ruh, J., 2015. Geomorphological–thermo-mechanical modelling: Application to orogenic wedge dynamics. *Tectonophysics*, 659, pp.12-30.

Valla, P.G., Shuster, D.L. & van der Beek, P.A., 2011. Significant increase in relief of the European Alps during mid-Pleistocene glaciations. *Nature Geoscience*, 4, pp.688-92.

Valla, P.G., Sternai, P. & Fox, M., 2021. How Climate, Uplift and Erosion Shaped the Alpine Topography. *Elements: An International Magazine of Mineralogy, Geochemistry, and Petrology*, 17(1), pp.41-46.

van der Wal, W. et al., 2013. Glacial isostatic adjustment model with composite 3-D Earth rheology for Fennoscandia. *Geophysical Journal International*, 194(1), pp.61-77.

Van Wagoner, J.C., Mitchum, R.M., Campion, K.M. & Rahmanian, V.D., 1990. Siliciclastic sequence stratigraphy in well logs, cores, and outcrops: concepts for high-resolution correlation of time and facies.

Vaselli, O. et al., 2002. A geochemical traverse across the Eastern Carpathians (Romania): constraints on the origin and evolution of the mineral water and gas discharges. *Chemical Geology*, 182(2-4), pp.637-54.

Ventura, G., Cinti, F.R., Di Luccio, F. & Pino, N.A., 2007. Mantle wedge dynamics versus crustal seismicity in the Apennines (Italy). *Geochemistry, Geophysics, Geosystems*, 8(2).

Viles, H.A., Goudie, A.S. & Goudie, A.M., 2021. Ants as geomorphological agents: A global assessment. *Earth-Science Reviews*, 213, p.103469.

Vitale Brovarone, A. et al., 2020. Let there be water: How hydration/dehydration reactions accompany key Earth and life processes. *American Mineralogist: Journal of Earth and Planetary Materials*, 105(8), pp.1152-60.

Vitale Brovarone, A. et al., 2020. Subduction hides high-pressure sources of energy that may feed the deep subsurface biosphere. *Nature communications*, 11(1), pp.1-11.

Wang, Z. & Kusky, T.M., 2019. The importance of a weak mid-lithospheric layer on the evolution of the cratonic lithosphere. *Earth-Science Reviews*, 190, pp.557-69.

Wang, Z., Kusky, T.M. & Capitanio, F.A., 2017. Ancient Continental Lithosphere Dislocated Beneath Ocean Basins Along the Mid-Lithosphere Discontinuity: A Hypothesis. *Geophysical Research Letters*, 44(18), pp.9253-60.

Wang, L., Liu, J., Xu, Q.H. & Xia, Q.K., 2022. Craton destruction induced by drastic drops in lithospheric mantle viscosity. *Earth and Space Science*, p.2022EA002455.

Wei, Y. et al., 2016. Low palaeoelevation of the northern Lhasa terrane during late Eocene: Fossil foraminifera and stable isotope evidence from the Gerze Basin. *Scientific Reports*, 6(1), pp.1-9.

Whipple, K.X., 2009. The influence of climate on the tectonic evolution of mountain belts. *Nature geoscience*, 2(2), p.97.

Whipple, K.X., 2014. Can erosion drive tectonics? *Science*, 346(6212), pp.918-19.

White, R. & McKenzie, D., 1989. Magmatism at rift zones: the generation of volcanic continental margins and flood basalts. *Journal of Geophysical Research*, 94, pp.7685-729.

Whittaker, A.C., 2012. How do landscapes record tectonics and climate? *Lithosphere*, 4(2), pp.160-64.

Wiens, D.A. & Stein, S., 1983. Age dependence of oceanic intraplate seismicity and implications for lithospheric evolution. *Journal of Geophysical Research: Solid Earth*, 88(B8), pp.6455-68.

Wiese, F., Fridriksson, T. & Ármannsson, H., 2008. CO2 fixation by calcite in high-temperature geothermal systems in Iceland. Report from the Iceland Geosurvey (Ísor). *Ísor-2008/003, Reykjavik*.

Willett, S.D., 1999. Orogeny and orography: The effects of erosion on the structure of mountain belts. *Journal of Geophysical Research*, 104(b12), pp.957-81.

Willett, S.D., 2006. *Tectonics, climate, and landscape evolution*. GSA Bookstore.

Willett, S.D. & Brandon, M.T., 2002. On steady states in mountain belts. *Geology*, 30(2), pp.175-78.

Willett, S.D. et al., 2014. Dynamic reorganization of river basins. *Science*, 343(6175), p.1248765.

Willett, S.D. et al., 2014. Dynamic reorganization of river basins. *Science*, 343(6175), p.1248765.

Williams, G.A. & Chadwick, R.A., 2017. An improved history-match for layer spreading within the Sleipner plume including thermal propagation effects. *Energy Procedia*, 114, pp.2856-70.

Winterberg, S. & Willett, S., 2019. Greater Alpine river network evolution, interpretations based on novel drainage analysis. *Swiss journal of geosciences*, 112(1), pp.3-22.

Wittmann, H. et al., 2007. Relation between rock uplift and denudation from cosmogenic nuclides in river sediment in the Central Alps of Switzerland. *Journal of Geophysical Research: Earth Surface*, 112(F4).

Wu, C. et al., 1998. Yadong cross structure and South Tibetan Detachment in the east central Himalaya (89–90 E). *Tectonics*, 17(1), pp.28-45.

Xing, Y. & Ree, R.H., 2017. Uplift-driven diversification in the Hengduan Mountains, a temperate biodiversity hotspot. *Proceedings of the National Academy of Sciences*, 114(17), pp.E3444-51.

Yamamoto, J. et al., 2011. Retentivity of CO2 in fluid inclusions in mantle minerals. *European Journal of Mineralogy*, 23(5), pp.805-15.

Yang, H., Artemieva, I. & Thybo, H., 2022. Yang, H., Artemieva, I. and Thybo, H., 2021. The Mid-Lithospheric Discontinuity caused by channel flow in the cratonic lithosphere. *EarthArxhiv*.

Yanites, B.J. et al., 2013. High magnitude and rapid incision from river capture: Rhine River, Switzerland. *Journal of Geophysical Research: Earth Surface*, 118(2), pp.1060-84.

Young, A. et al., 2022. Long-term Phanerozoic sea level change from solid Earth processes. *Earth and Planetary Science Letters*, 584, p.117451.

Zachos, J. et al., 2001. Trends, rhythms, and aberrations in global climate 65 Ma to present. *Science*, 292(5517), pp.686-93.

Zaffos, A., Finnegan, S. & Peters, S.E., 2017. Plate tectonic regulation of global marine animal diversity. *PNAS*, 114, pp.5653–58.

Zaki, A.S. et al., 2021. Did increased flooding during the African Humid Period force migration of modern humans from the Nile Valley? *Quaternary Science Reviews*, 272, p.107200.

Zeitler, P. et al., 2001. Erosion, Himalayan geodynamics, and the geomorphology of metamorphism. *Gsa Today*, 11(1), pp.4-9.

Zerkle, A.L., 2018. Biogeodynamics: bridging the gap between surface and deep Earth processes. *Phil. Trans. R. Soc.*, A 376, pp.20170401 doi:10.1098/rsta.2017.0401.

Zgonnik, V., 2020. The occurrence and geoscience of natural hydrogen: A comprehensive review. *Earth-Science Reviews*, 203, p.103140.

Zhao, D., 2009. Multiscale seismic tomography and mantle dynamics. *Gondwana Research*, 15(3-4), pp.297-323.

Zhuang, G. et al., 2015. Altitudinal shift in stable hydrogen isotopes and microbial tetraether distribution in soils from the Southern Alps, NZ: Implications for paleoclimatology and paleoaltimetry. *Organic Geochemistry*, 79, pp.56-64.

Zhu, H., Bozdağ, E., Peter, D. & Tromp, J., 2012. Structure of the European upper mantle revealed by adjoint tomography. *Nature Geoscience*, 5(7), pp.493-98.

Ziegler, P.A. & Dèzes, P., 2006. Crustal evolution of western and central Europe. *Geological Society, London, Memoirs*, 32(1), pp.43-56.

Ziegler, M.O. & Heidbach, O., 2020. The 3D stress state from geomechanical–numerical modelling and its uncertainties: a case study in the Bavarian Molasse Basin. *Geothermal Energy*, 8(1), pp.1-21.

Zoback, M.D., 1983. State of stress in the lithosphere. *Reviews of Geophysics*, 21(6), pp.1503-11.

Zoback, M.L., 2007. Reservoir geomechanics: Earth stress and rock mechanics applied to exploration. *Cambridge Press, Production and Wellbore Stability*, p.449.